博士論文（要約）

Role of homogeneous luminescent coupling effect in III-V based multijunction solar cells

(III-V 族多接合太陽電池におけるルミネセンス結合と均質化の効果)

A Dissertation Presented to the
Department of Advanced Interdisciplinary Studies
Graduate School of Engineering
The University of Tokyo

In Partial Fulfillment of the Requirements for the Degree of
Doctor of Engineering

YU JECO Bernice Mae Fetalvero

ユヘコ　ベーニス　メー　フェタルベロ

Supervising Professor:
Prof. OKADA Yoshitaka, Ph. D.

教授　岡田　至崇

March 2020

令和２年　３月

Jeremiah 33:3

‘Call to me and I will answer you and tell you great and unsearchable things you do not know.’

エレミヤ書 33:3

わたしに呼び求めよ、そうすれば、わたしはあなたに答える。そしてあなたの知らない大きな隠されている事を、あなたに示す。

Acknowledgment

I would like to express my sincerest gratitude and warmest appreciation to the following who have been substantial to the completion of this research work instrumental for making me who I am today, kept me going and has changed my life during the pursuit of my doctoral degree.

To my supervisor and one of my foster fathers in Japan, Prof. Yoshitaka Okada, Ph. D. I am very grateful for the freedom, the unwavering support, and the guidance you gave me in executing this research project. I am very blessed to be your student as you have set a great example to me on being a researcher, academician, and a respectable leader in the workplace. I am also grateful for the trusting me with opportunities, for the lessons in science and even in life, and for the responsibilities you have placed in my hands during my Ph. D. journey as they made me who I am right now. I am very thankful as well for supporting my endeavors on science research outreach activities and helping spark the solar technology interest of young scientists from the Philippines by opening your laboratory for science high school internships.

To my direct supervisor, Prof. Nazmul Ahsan, Ph. D. for the guidance, support, sincere concern not only to me but to the laboratory students in general, and inquiries that served as my clues on how to interpret my results and for my next steps. Thank you very much for your questions that had led me to the answers I would not probably realize on the surface of my data without consulting them with you.

To the respectable defense panel members on evaluating this research work, Prof. Takuji Takahashi, Ph. D., Prof. Nazmul Ahsan, Ph. D., Prof. Takaya Kubo, Ph. D., and Prof. Kumiko Oguma, Ph. D. Thank you for your constructive suggestions to improve this research work and help me become a better scientist and a science communicator in the future.

To my research outreach supervisor, Prof. Kumiko Oguma, Ph. D. Thank you very much for accepting me as your honorary student. I am so blessed to have met you through Prof. Okada's recommendation to collaborate with you on water research. I am very grateful for the freedom, the unwavering support, and the guidance you gave me for our research project. Thank you so much for having a big heart to help people in a remote area of my home country. To Mr. Tomoyasu Sado of Oguma Laboratory for sharing his expertise and dedicating his time to contribute to the project. I appreciate the heart you have for the islanders that will benefit from our work.

To the mentors and friends whom I have met at Okada Laboratory, Prof. Tomah Sogabe, Ph. D., Dr. Akio Ogura, Ph. D., Dr. Ryo Tamaki, Ph. D., Dr. Takuya Hoshii, Ph. D., Dr. Dan Farell, Ph. D., Dr. Zacharie Jehl Li-Kao, Ph. D., Dr. Daniel Suchet, Ph. D., Dr. Katsuhisa Yoshida, Ph. D., Dr. Yasushi Shoji, Ph. D., Dr. Naoya Miyashita, Ph. D., Ms. Noriko Fujiki, Ms. Misa Sembommatsu, Ms. Yuiko Nakatomi, Ms. Hisae Nakada, Prof. Kentaroh Watanabe, Ph. D., Dr. Amaury Delamarre, Ph. D., Dr. Hao Xu, Ph. D., Dr. Aobo Ren, Ph. D., Dr. Hsiang-Hung Huang, Ph. D., Dr. Haibin Wang, Ph. D., Dr. Samy Almosni, Ph. D., Dr. Takumi Kinoshita, Ph. D., Dr. Chao-Yu Hung, Ph. D., Dr. Shunya Naito, Ph. D., Jun Osawa, Mizuki Mori, Hokuto Shimomura, Daiki Kimura, Ayaka Matsuoka, Dr. Tetsuya Nakamura, Ph. D., Dr. Maxime Giteau, Ph. D., Meita Asami, Yusuke Oteki, Kei Fukushima, Nanaki Miura, Myeongok Kim, Jonny Qiu, Abhishek, Dr. Logu Thirumalaisamy, Ph. D., Dr. Benoit Behaghel, Ph. D., Lea Tatry,

Omar Belli, Fabien, Edouard De-Moustier, friends from Next-PV, VIT India collaborations, and Saitama University. Thank you for the fun memories that we had and most especially for the lessons not only about device physics but in life that you have imparted onto me and I am grateful for patiently educating me.

To the family and friends whom I have met during my stay in Arizona – from King Lab, Arizona State University: Prof. Richard King, Ph. D., my host/supervising professor and principal investigator of the work presented in Ch. 5, Abhinav Chikhalkar, Sean Babcock, Niranjana Mohan Kumar, Madhan Kumar Arulanandam, Kevin Tyler, Prof. Hala King, Ph. D., and Rocky; from the School of Electrical, Computer and Energy Engineering office Donna Rosenlof and Ginger Rose; QESST administrators Bob Sampson and Katie Taylor; researchers from ASU Research Park (MTW) and Engineering Research Center (ERC): Bill Dauksher, Som Dahal, Srinath Murali, Joseph Karas, Pradeep Balaji, Antony Aguilar, Nicholas Irvin, Tara Nietzold, Yongjie Zou, Dr. Chaomin Zhang, Ph. D., Solar Cell 101 classmates; ASU fire and laboratory safety training staff; all students and professors I met at the fishbowl (ERC); from ASU Nanofab CSSER: Staff and Specialists Carrie Sinclair, Kevin Nordquist, Scott Ageno, Jaime Quintero, Josh Reyes, Arthur Handugan, Kevin Hilgers, Stefan Myhajlenko; from QESST outreach faculty and volunteers: Alex Routhier, Alex Killam, Joe Carpenter, Michael Fitchette (U. Houston), and to Michelle Jordan and Tiffany Rybiski for the outreach collaboration and providing outreach materials for Japan and Philippines; and from Tempe Homestay – Alameda for the excellent host quarters during my stay in Tempe.

To the Director of RCAST, Prof. Ryohei Kanzaki, Ph. D., to my coursework professors, the defense panel members mentioned earlier, Prof. Yu Kosaka, Ph. D., Prof. Hisashi Nakamura, Ph. D., Prof. Maruyama Shigeo, Ph. D., Prof. Yuji Suzuki, Ph. D., Prof. Mamoru Iwabuchi, Ph. D., Prof. Yoshio Mita, Ph. D., Prof. Josiane Zomahoun Ponou, Ph. D., Prof. Yasuyuki Yokono, Ph. D., Prof. Yasumasa Fujii, Ph. D., Prof. Masakazu Sugiyama, Ph. D., Prof. Satoshi Iwamoto, Ph. D., Prof. Kazuro Kikuchi, Ph. D., Prof. Kazuhiko Hirakawa, Ph. D., Prof. Toshiro Hiramoto, Ph. D., Prof. Yasuhiko Arakawa, Ph. D., and Prof. Shinichi Takagi, Ph. D. You are all instrumental in building my fundamental and advanced knowledge about my research work.

To Ms. Yamanaka, Ms. Takeuchi, Ms. Ishii, Mr. Ohtani, the rest of the RCAST/AIS department staff and WINGS-CFS leading graduate school program staff of the Graduate School of Engineering in the University of Tokyo for helping me out with the documents and technicalities during my stay in the department. To the Cooperative Dining Halls at The University of Tokyo, most especially those in Komaba II, thank you very much for providing me balanced meals that helped me function well in my daily activities since my master's degree pursuit.

To my closest collaborators from CEA Leti, France, Dr. Elias Veinberg-Vidal, Ph. D. and Dr. Laura Vauche, Ph. D. Thank you so much for the III-V//Si samples you lent us that lead us to produce articles and a significant portion of my Ch. 3.

To the funding agencies: Ajinomoto Scholarship Foundation for my master's study scholarship, the National Research and Development Agency, New Energy and Industrial Technology Development Organization (NEDO), and Ministry of Economy, Trade, and Industry (METI), Japan for funding our research projects, WINGS-CFS program organizers for my scholarship and providing coursework to expand my perspective on

academia-industry collaborations, the Japan Society for the Promotion of Science (JSPS) Grant-in-Aid 19J13899 for supporting the research project showcased in this dissertation.

To my parents, Benito C. Yu Jeco, Jr. and Maureen F. Yu Jeco. You are the reflection of God's unconditional love for me. Thank you for always understanding me, praying for me, imparting wisdom and speaking words of encouragement to me, most especially during my most trying times in Tokyo. I am truly grateful that with your hard work and sacrifices, I received the privilege of pursuing higher education. I am very blessed to be your daughter.

To the best chemical engineer I know and the love of my life, Engr. Achilles E. Espaldon, M.Sc. I truly appreciate the love we share, the ideas we discuss, the ears you lend, the help you extend most especially in Chemistry, and your very long patience. I thank God that I found you along this journey. You are indeed a blessing to me. I am also grateful to your parents, Miguel and Pacita Espaldon, for bringing you to this world and your siblings, Vis and Lala.

To my siblings, Catherine Sythay, Christine Fausto, and Benedict Yu Jeco, and my aunt, Fe Yu Jeco, I am grateful to have you as my family. Many thanks indeed for your prayers and support during this journey. To my closest aunt and proofreader, Prof. Lucila R. Fetalvero, M.A. I am so blessed to receive your advice on correcting my articles and on statistics. Thank you very much for the wisdom and prayers for me since birth. To my closest cousin, Femalin Mae F. Sison, for keeping company with my mom during my absence and prayers. To my immediate cousins and aunt from Sison Family, Regina, Kenneth, Hubert, John Patrick, and Hermes, to my aunt Milwida Martin, to my cousins Dana, Nadine, and Dominic Alonzo, to my grandmother Adoracion Martin, thank you very much for the prayers, support, and encouragement.

To my blazing furnace friends, Mina Santos, Akemi Kimura, and Jazz MC, most especially during my lowest moments in Japan. To my solid friends, Yvette Buce and family, those since high school, Precious Lean Estacio-Tacdeo, Ma. Christine Sanchez, Loriefe Jane Itable, Veronica Cortez, Ariane San Juan, Maricris Vitalicio, Katherine Perono, Anthony Edward Herrero, Jaimee Mae Javier, the Black Aphoticz: Ma. Clarissa Diño, Lea de Guzman, and Eunice Orallo-Junsay, and those since college, Ma. Fatima Villaflores, Mida Marie Go, Christine Grace Balanaa, Elisha Grace Tarroza, and the rest of the UST-ECE 2011.

To my closest mentors at the University of Santo Tomas, Prof. Darlene Alberto, M.Sc., Prof. Lourdes Baldelomar, M.Sc., Prof. Ma. Theresa Nabor, M.Sc., Prof. Tess Roque, M.Sc., The Dean of Engineering – Prof. Philipina Marcelo, Ph. D., ECE Chair – Prof. Angelo dela Cruz, Ph. D., Engr. Emmanuel Guevara, M.Sc., Prof. Edison Roxas, Ph. D., Prof. Ryan Rhay Vicerra, Ph. D., Prof. Joycelyn Poblete, M.Sc., Prof. Irineo Quinto, Prof. Albert Acosta, M.Sc., and Prof. Ma. Luisa Asilo, M.Eng.

To the friends and mentors from the University of San Agustin and Philippine Science High School – Western Visayas: Prof. Jonel Saludes, Ph. D., Prof. Felicidad Altalaguire, Ph. D., Prof. Nolan Tolosa, Ph. D., Engr. Achilles Espaldon, Engr. Marjorie Carisma, Engr. Reynaldo Ramos, Engr. Mary Abas, Dr. Shena Faith Ganela, Ph. D., Dr. Aris Larroder, Ph. D., Sir Rolando Libutaque, Dr. Angelo Olvido, Ph. D., Sir Jarold Mediodia, Ma'am Athenes Joy Aban, Ma'am Rubi Anne Bito-on, Ma'am Erika Salvador, and Sir Jayson Jolito.

To my foster families in Tokyo, Anna Camille Flores for patiently putting up with me being in the same house, Jay and Rose Landicho, Jarson and Jayvie Silang, and Zacharie

and Lovely Jehl Li-Kao. To my extended family who adopted me during my short trips: Jaleene Gonzales-Ciriales, Janika Gonzales, Jerome Gonzales, Edgardo and Judith Gonzales, Dan and Marian Agas, Vance Ravelo, John Vincent Ravelo, Miguel and Digna Cuerva, Joel and Noemi Martin, Natalie Martin, and Jarryd Martin. I am also grateful to my families, Jo-Ann Martin and Christine Ravelo, for the support and encouragement, most especially during my lost passport stint. Without your help, I won't be able to finish my work in graduate school.

To my extended families, friends and mentors from my previous workplaces in the Philippines – from HP: Fast/Pluto/SBO team 2011-2013, Andrea Carina Padura, Ma. Victoria Migo, Kinney Palma, Noel Camarillo, Ryan Prodigalidad, Jennylee Villarosa-Burgess, James Wang, Paul dela Fuente, Marlon Jay del Monte, Kristian Pimentel, Paul Pena, Aurora Basbas, Vladimir Regoso, Enrico Ceguerra, Jerome Hipolito, Ana Co-Chan, and Erwin Blas, and friends in UST-ECE faculty 2011-2014, Engr. Erika Escandor, M.Sc., Engr. Kanny David, M.Sc., Engr. Rowel Allan Rocaberte, Engr. Seigfred Prado, M.Sc., Prof. Christopher Yalung, Ph. D., Engr. Josyl Rocamora, M.Sc., and Engr. Celdrian Rei Asilo.

To my former students in the University of Santo Tomas, most especially EE Batch 2013 and ECE Beks Batch 2016; those from Philippine Science High School – Western Visayas during 2016 to 2018 Science Immersion Programs in Okada Laboratory, and my current students in the University of San Agustin, most especially the Oguma-USA project water agents and ECE 310 children of God (as I call them).

To all who prayed with me in this journey and to all whom I forgot to mention, but I should be thankful for, thank you.

Last and above all, to the Holy Trinity – to the Almighty Father in Heaven, for always watching over me and providing everything You know that I needed in every moment of my journey as a Ph. D. candidate; to the Son, Jesus Christ, for setting a good example for me. It is never easy to follow You, but thank You for keeping me back on track by reminding me that I am loved and saved by Your grace through the people around me; to the Holy Spirit for being my Daily Guide. Your presence sustained me, most especially during the most challenging times of my journey.

B. Yu Jeco
11/2019

Table of Contents

Review of related literature

Chapter 1

Chapter 1 – Review of Related Literature

Chapter 1 discourses a broad literature review on solar cells. Section 1 contains the recent status of world energy, followed by Sec. 1.2, which focuses on solar energy, a free energy source. This section is succeeded by discussing its basic operating principles and then its fundamental losses. Next, the current world record solar cell efficiencies were discussed. Finally, the end of this chapter showcases the brief introductions to novel design concepts on high-efficiency solar cells, as there may be relevant and essential to conduct this research work on the role of homogeneous luminescent coupling (LC) effect in high-efficiency, III-V based multijunction solar cells (MJSCs).

1.1. World Energy Consumption and Production

1.1.1. Energy consumption

Since the Industrial Revolution, humans have become heavily reliant on energy resources for daily needs; hence, this commenced an increasing demand for exhaustible energy sources such as coal, petroleum, and oil from fossil fuels [1]. Figure 1 shows the historical data of world energy consumption harnessed from different sources. This was gathered from the middle of the Industrial Revolution (1800) up to 2017. Here, it shows that since the 1800s, energy consumption has increased exponentially, brought about by scientific breakthroughs leading to the development of energy-driven technologies. Eventually, this resulted in the commercialization of energy-reliant products, as reflected by the increasing trend of world gross domestic product (GDP) recorded from 1980 to 2017.

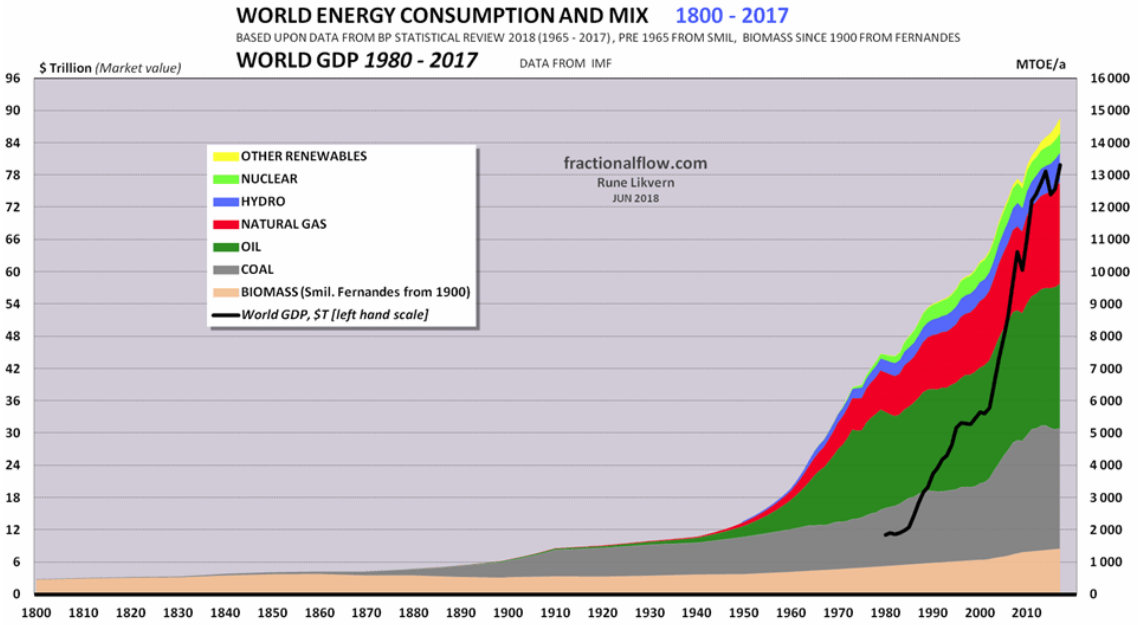

Fig. 1 Historical data on world energy consumption (1800-2017) and on world gross domestic product (1980-2017) [2–4] where 1 MTOE = 4.19×10^{-2} EJ = 1.16×10^{10} kWh.

In parallel with this increase, carbon dioxide (CO_2) emission has also drastically increased up to its critical level of 400 parts per meter (ppm) and even exceeded this level at the time of writing [5]. As shown in Fig. 2, the increase in energy demand from the beginning of the industrial revolution up to the present time has been increasing in proportion with the CO_2 emission in the Earth's atmosphere, where the largest contribution is from coal mining [6].

The world energy consumption history and projections based on country membership to the Organization for Economic Co-operation and Development (OECD) are shown in Fig. 3(a). Additionally, consumption history and projections based on continents where the non-OECD countries belong, having Middle East countries as a separate group from Asia, is shown in Fig. 3(b) [7]. The projections were plotted assuming reference case, i.e.

new policies after conducting their study were not anticipated while the existing energy harvesting technologies were solely considered. For the OECD countries, Japan included, a low increase in energy consumption is projected in the coming years. This low increase was assumed based on the population decline in OECD countries. From 2012 to 2040, the energy consumption of OECD countries is projected to increase from 238 to 282 quadrillion Btu (QBtu), where 1 QBtu = 293 TWh. On the other hand, energy consumption by non-OECD countries is projected to increase by 83% in 2040. This is attributed to the rapid economic growth, specifically of China and India, and the population growth in non-OECD countries in general. From 2012 to 2040, the energy consumption of non-OECD countries is projected to increase from 311 to 533 QBtu.

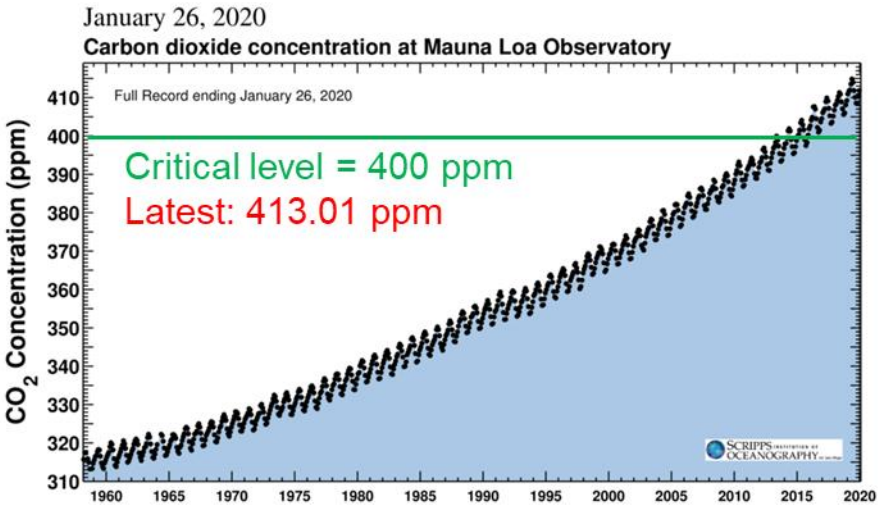

Fig. 2 Concentration of carbon dioxide (CO_2) in the atmosphere from 1700 up to the date of extraction, January 26, 2019, compiled by the Mauna Loa Observatory in Hawaii, USA [5].

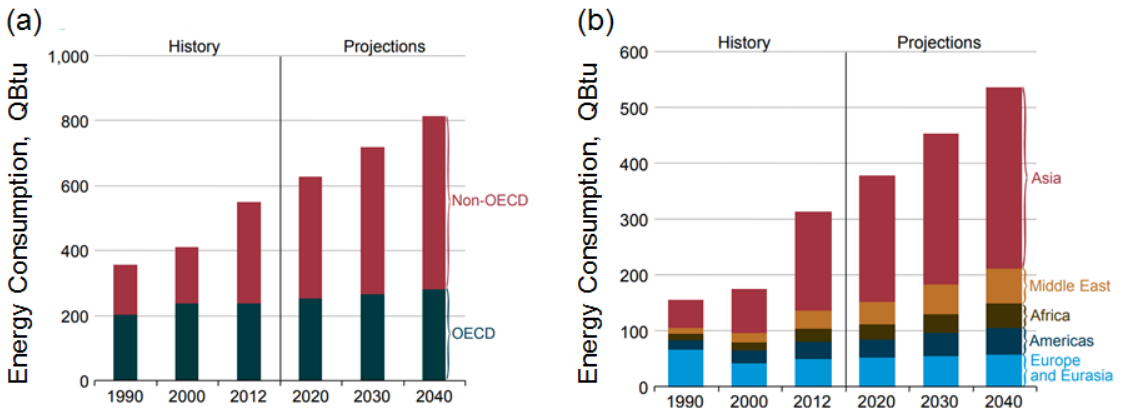

Fig. 3 World energy consumption history and projections assuming reference cases (a) by OECD membership and (b) by continents where the non-OECD countries belong to (1 QBtu = 293 TWh) [7].

Based on the historical data recorded and in anticipation of projected world energy consumption, development and deployment of energy technologies that could meet the world energy demands are becoming accelerated needs.

1.1.2. Energy production vision

The net electricity generation of the world forecast by 2040 based on technology is shown in Fig. 4(a) [7]. Here, the generation share from liquids is projected to decline from 5% to about less than 2% by 2040. This is due to high-priced liquid fuels being replaced by less expensive fuels from other power generation technologies. On the other hand, generation share by nuclear power is expected to slightly increase from about 10.5% to 12.5%. As for coal, which provides the largest power generation share at present, its production share is projected to decrease from 40% in 2012 to 29% by 2040. This is due to the global movement of governments towards renewable energy harvesting by implementing feed-in tariffs and incentives. While natural gas is also an exhaustible energy source, it is considered a more viable energy solution than coal in terms of carbon dioxide emission [8]. Thus, from 22% in 2012, the energy share from natural gas production is expected to increase to 28% by 2040. Then, for the renewables, its energy generation share is projected to increase from 22% to 29%. In summary, the renewables, natural gas and coal are projected to have a similar share of world net electricity generation by 2040, assuming reference case.

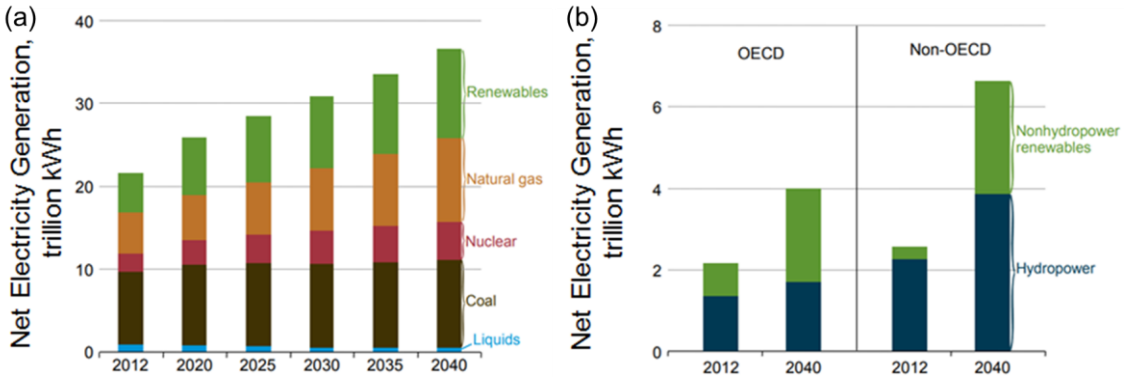

Fig. 4 World net electricity generation (a) share, based on technology from 2012 to 2040 and (b) history (2012) and projections (2040) by OECD and non-OECD countries according to technologies categorized as hydropower and non-hydropower renewables [7].

Considering the renewable energy shares alone, the net electricity generation history and projections by OECD and non-OECD countries according to technologies categorized as hydropower and non-hydropower renewables are shown in Fig. 4(b). For hydropower generation share, smaller production is expected from OECD countries than from non-OECD countries by 2040. This is because most hydropower plants have been fully exploited and developed in OECD countries already. As for the non-hydropower renewable shares, greater production is expected from non-OECD countries due to emerging government policies encouraging renewable energy deployment. Quantitatively, this is an 82% increase from 2012 to 2040.

Beyond 2040, the primary energy supply projections were calculated by the German Advisory Council on Global Change (WBGU). The energy supply forecasts until 2050 and 2100 are shown in Fig. 5. By 2050, it is projected that although coal reliance would decrease, reliance on exhaustible sources will still be around 45% to 50% while the remaining portion is projected to come from renewables, with optimistically higher shares from solar and wind. This agrees with the projection shown for the year 2040 in Fig. 4(b).

By 2100, renewables are anticipated to dominate the energy supply share, with more than 50% coming from solar energy [9–10].

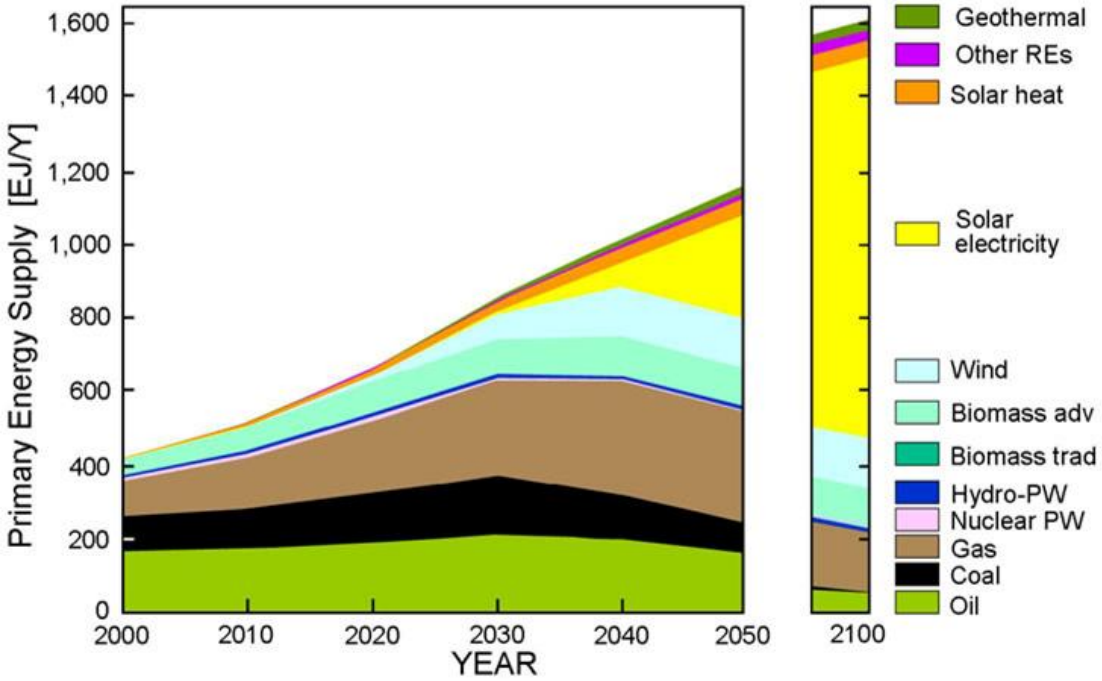

Fig. 5 Energy production forecast for each source until 2050 and 2100 by German Advisory Council on Global Change (WBGU) [9–10], where 1 EJ = 23.88 MTOE = 2.78×10^{11} kWh.

1.1.3. Exhaustible and depletable energy sources

There are 3 widely-known exhaustible energy sources, namely, coal, natural gas, and oil. Harnessing energy from these sources yield CO_2 emissions of 1.0 or higher, where 1.0 is the threshold value and coal emitting the largest portion at 1.8. Additionally, their reserves are predicted to last for another 50 to 100 years [11–12].

Figure 6(a) illustrates the typical sections of a thermal coal-fired power plant. The energy harvesting happens as follows: first, the coal is powdered, then goes into a boiler to undergo high-temperature combustion. The combustion reaction produces heat energy and hot gases which then converts the boiler water into steam. This steam drives the turbine to rotate at high speed, generating a strong magnetic field. This, thereby, produces electricity, which is then transformed into hundreds of kilovolts for grid transmission [13].

Since the 1970s, crude oil price fluctuation has been majorly affected by energy supply constraint and geopolitical situations in the Middle East and by global recession last 2008, hindering smooth investments to harness energy from this source [11]. Figure 6(b) shows the common distribution of harvested oil from the ground. The largest portion per barrel that can be harvested is gasoline. The next largest is the ultra-low sulfur distillate fuel, used for diesel engines. A small portion of jet fuel engines and heating systems can also be harvested while the rest are considered residues.

There are 3 main types of natural gas (NG) sources [12], namely, environmentally benign NG, conventional NG, and unconventional NG. Environmentally benign NG are those with low carbon intensity and high purity. Conventional NG is those found in association with crude oil or those found in reservoirs in an insignificant amount. Last,

unconventional NG are the following: coal bed methane, which are found in bituminous and anthracite coal; tight formation gas, which are trapped in low-permeability sand rock; geo-pressured gas, which are methane gases dissolved in underground water; those gases trapped within fractured shale formations; methane hydrate typically found in permafrost regions or at sea depth levels of 300 to 500 m and beyond; and ultra-deep gases found at reservoirs between 4,600 and 7,600-m below sea level. Some of the different types of NG and where they can naturally be found underground are shown in Fig. 6(c).

As for depletable sources for harnessing electricity from nuclear energy, uranium 238 (U-238) is the most common uranium isotope, having a relative abundance of 99%. However, U-238 cannot sustain a chain reaction in a nuclear reactor; hence, the less abundant U-235 isotope is more preferred for nuclear energy generation. A schematic of the fissile reaction using U-235 atom is illustrated in Fig. 6(d). The fissile reaction occurs as follows. When a neutron collides with a U-235 atom, it produces fission products, such as barium isotope, Ba-139, and krypton isotope, Kr-95, and neutrons that may collide with other U-235 atoms and produce another fissile reaction. Each fissile reaction emits about 200 MeV of energy [14], making nuclear energy potentially lucrative for supplying energy on a national scale. Although harnessing nuclear energy from nuclear reactions essentially does not emit CO_2, the public needs to be assured of their safe confinement in reactors and sustainable disposal of nuclear wastes.

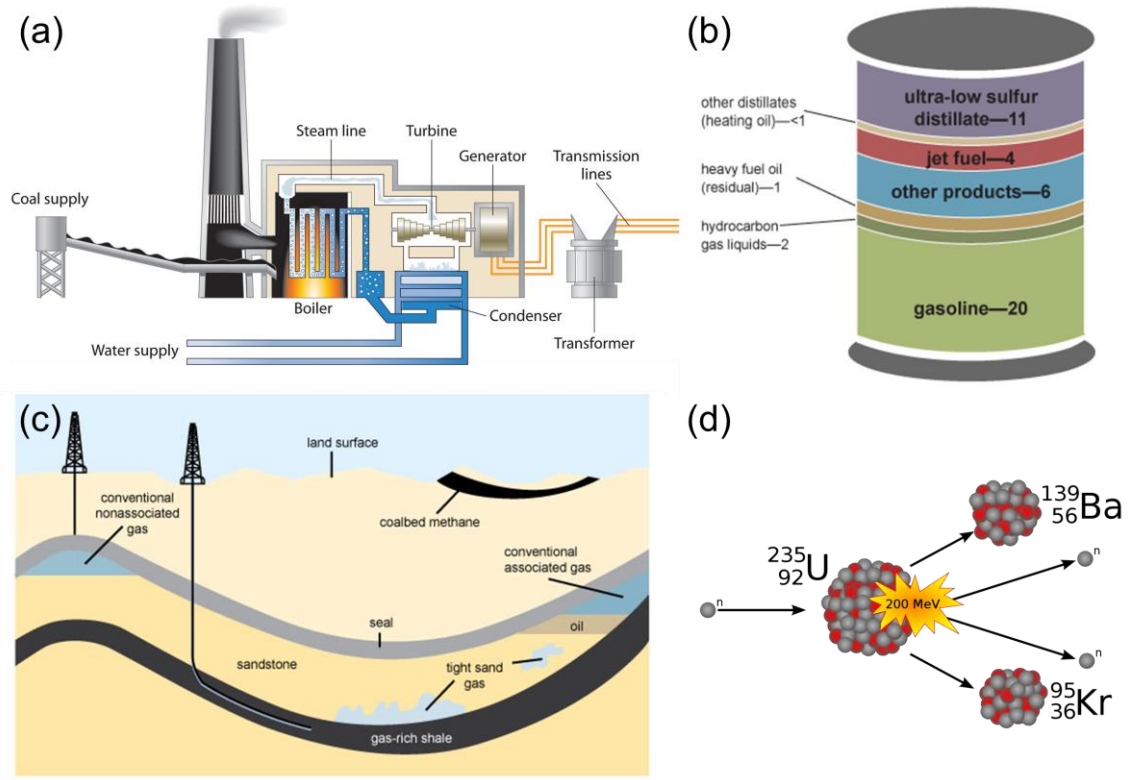

Fig. 6 Illustrations of exhaustible energy sources overview: (a) from thermal coal-fired power plant; (b) harnessed crude oil distribution [15]; (c) natural gas resources [16]. (d) Atomic illustration of an example of uranium 235 isotope (U-235) nuclear fission.

1.1.4. Alternative energy sources

To get away from fossil fuels reliance, which accounts for the majority of the greenhouse gas emissions as shown in Fig. 7, the idea of putting up CO_2 capture-and-storage (CCS) has emerged due to its numerous advantages. For one, the Earth has been surveyed to have a sufficient geological storage capacity over the 21st century. Another advantage is that this solution is cheaper than putting up renewable energy systems [17]. However, the surroundings of CCS plant sites are threatened by gas poisoning in the event of an unacceptable level of CO_2 leakage from these plants [18]. Moreover, not all countries have a potential site to build this kind of storage facility [19]. Thus, more research needs to be conducted on fossil fuel management.

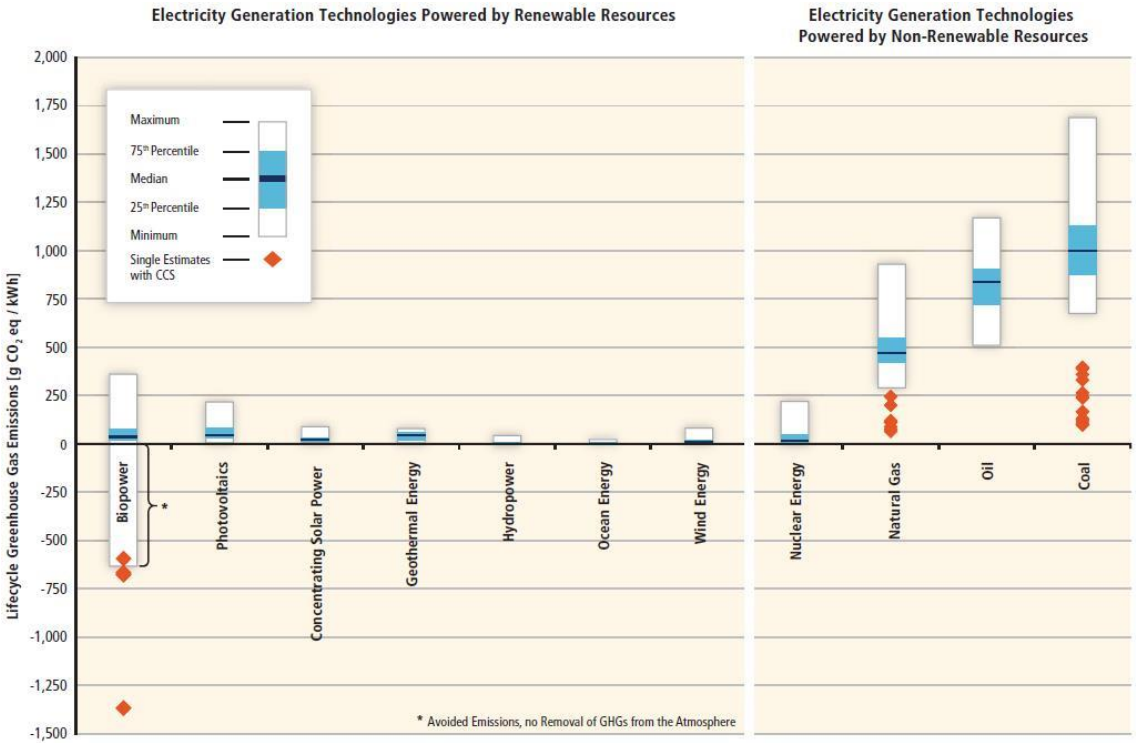

Fig. 7 Greenhouse gas emission levels of different electricity generation technology [20].

High CO_2 emissions due to the aforementioned situation of energy demand and production have led to climate change depicted in the Global Temperature Time Series [21]. This series contains the record of global mean temperature changes from 1840 until 2007. To suppress CO_2 emissions and, in turn, alleviate global warming, shifting to different types of renewable energy sources is recommended, as suggested by low greenhouse gas emission levels from these sources [Fig. 7]. Each energy technology shown in Fig. 8 are broadly classified according to the internal processes involved and the order of energy that these sources can provide [6]. One is involving thermo-mechanical processes that can provide energy within the order of meV. This type harnesses energy from the wind, water or geothermal energy. Another is derived from chemical or photophysical energy which depends on oxidation processes and can provide energy in the order of an eV (biomass). From light energy, one can also harvest direct current (DC) power.

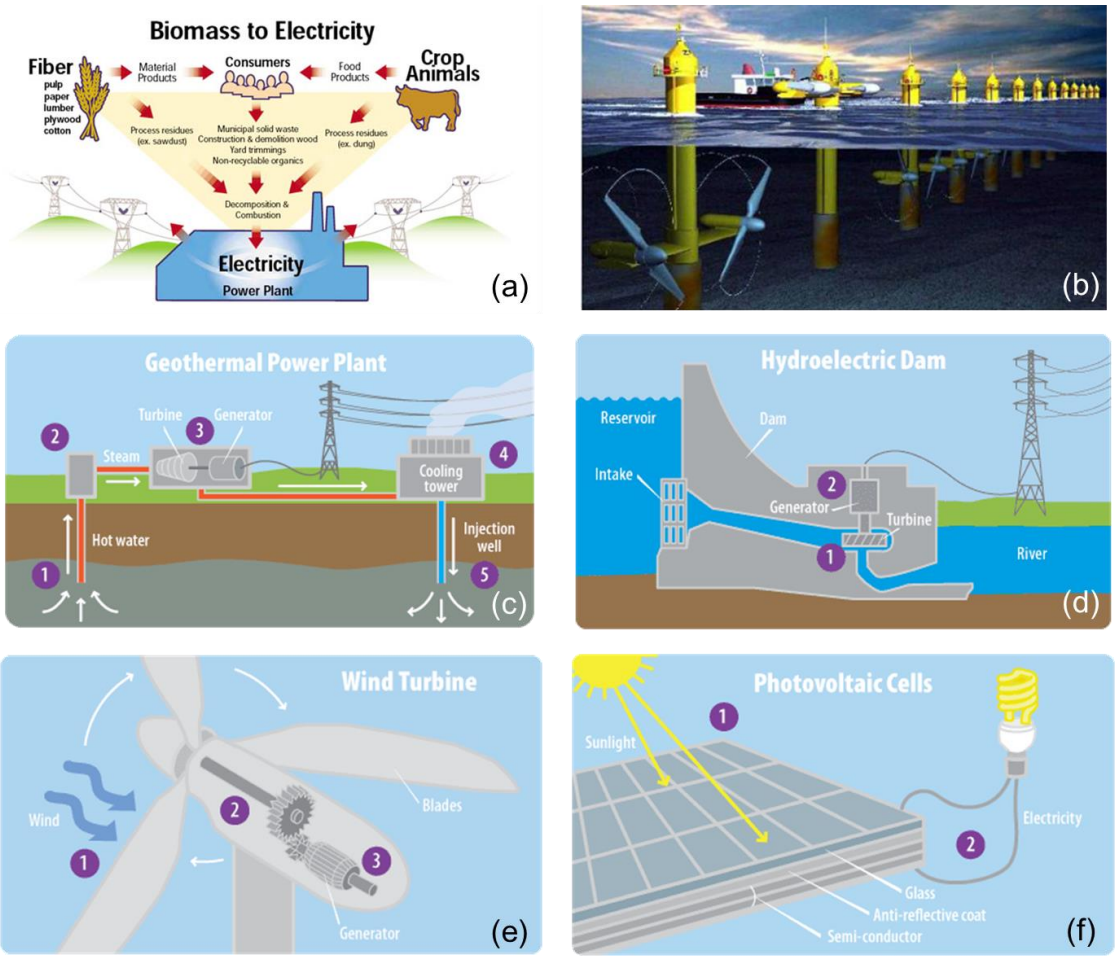

Fig. 8 Illustrations of alternative energy sources overview: (a) from biomass [22]; (b) tidal energy [23]; (c) geothermal energy; (d) hydropower; (e) wind energy; and (f) solar energy [24].

Biomass energy sources are classified into 2, namely plantation type, which can come from agricultural and forestry products such as fuelwood and energy crops, and residual type, which may come from by-products and wastes of food and wood production. It has the potential of supplying 900 Gtoe (1 toe = 11,630 kWh) worldwide [12]. An illustration of biomass energy harvesting is illustrated in Fig. 8(a). Tidal waves and ocean water flow that drives underwater turbines can also produce electricity, as shown in Fig. 8(b). As illustrated in Fig. 8(c), electricity can be also generated by converting the heat of the Earth's core into electrical energy by using steam-driven turbines. From hydroelectric dams [Fig. 8(d)], downward water flow accelerated by gravity can also drive turbines that produce electrical power. Driven by wind strength, windmill turbines can also produce electricity [Fig. 8(e)]. Last, light energy in the form of solar radiation can be converted into electric power through the use of photovoltaic (PV) solar cells [Fig. 8(f)]. Fundamentally, PVs are composed of light-absorbing semiconductor, anti-reflection coating, electrodes, and protective glass.

1.1.5. Solar energy: a free source

There are generally 3 ways to harness energy from the sun. One is by passive solar heating in which the heat from the sun is received by solar collectors, e.g. by windows or panels. Here, the heat is transferred to a certain establishment or water storage tanks while

the lower temperature air or water flows towards the solar collector to cool it down [Fig. 9(a)]. Another method is by collecting the heat of the sun through solar thermal power plants, which then generate steam used for electricity production. As shown in Fig. 9(b), solar thermal energy is received by heliostats and is concentrated towards an energy-collecting tower. The collected energy is passed through a heat exchanger, where the cold fluid is passed to the tower to keep it cool. On the other hand, the heat collected by the tower is sent into the steam turbine, which will cause electricity generation. And the third one is by direct absorption and then conversion of sunlight into electricity using PV cells [25]. As mentioned briefly in Sec. 1.1.4, PV cells are composed of *n*-type and *p*-type light-absorbing semiconductor layers, electrodes or back contacts for electron and hole collection, anti-reflective coating to prevent light escaping from the cells, a glass, and an adhesive layer for encapsulation. The fundamental layers of a complete PV cell are shown in Fig. 9(c).

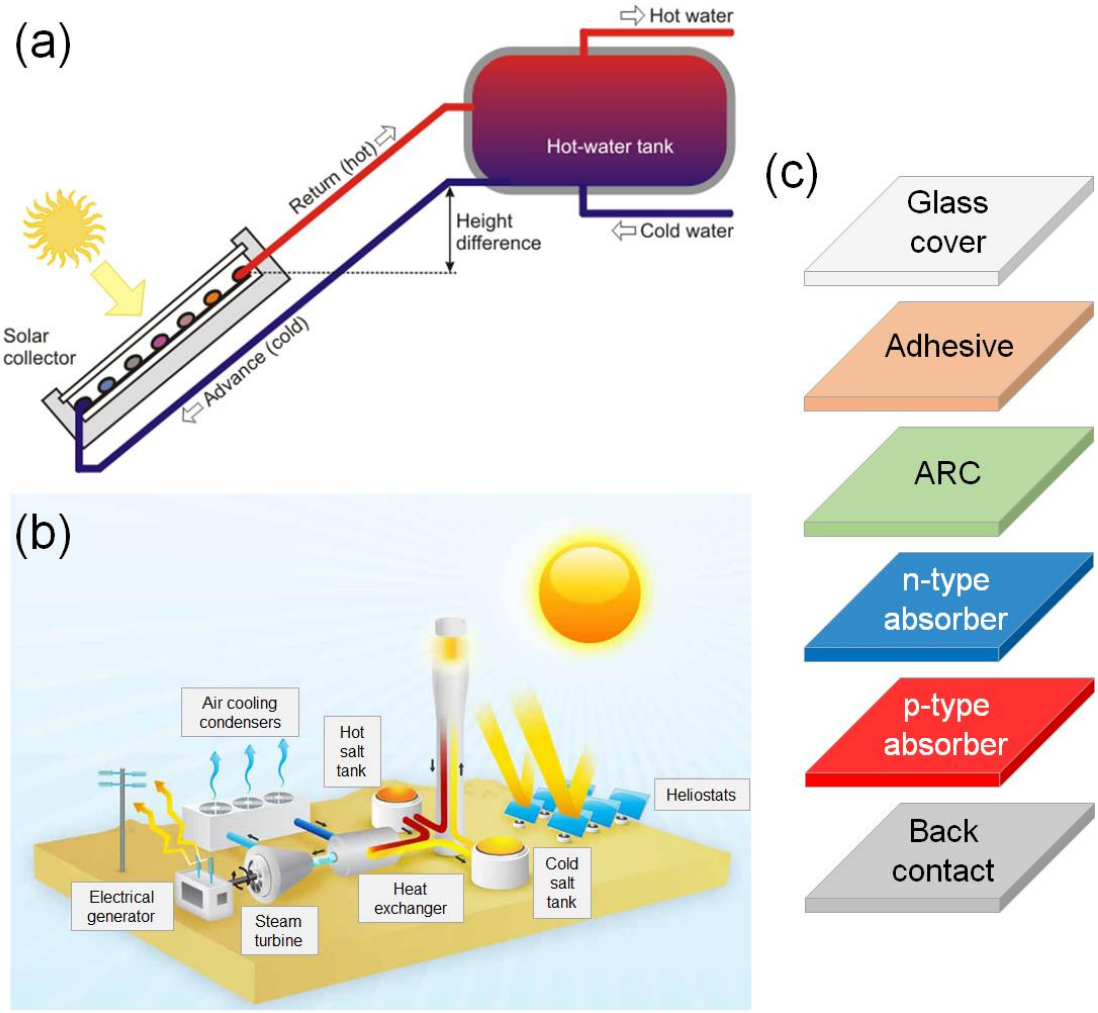

Fig. 9 Schematics of (a) passive solar heating, (b) solar thermal power plant and (c) fundamental layers of a complete photovoltaic cell.

1.2. Fundamental Physics of Solar Cells

1.2.1. Physics in macroscale

Consider an anode plate and a cathode plate parallel to each other which are connected to a battery's positive and negative terminal respectively. When the sun emits light in the form of electromagnetic radiation, also called a photon, and then hits the cathode, the photon is absorbed if its energy exceeds the energy gap or the bandgap of the semiconductor material. When this occurs, an electron is kicked out of the crystal bond of the semiconductor material and gets attracted to the anode; hence, conduction occurs. On the other hand, the photovoltaic phenomenon is described as the generation of current or voltage by a semiconductor material upon the absorption of light [25]. Here, once an atom in a semiconductor crystal absorbs a photon, an electron-hole pair get separated, in which the electron gets elevated to the conduction band, thereby generating current flow. How the photovoltaic phenomenon occurs within a semiconductor material in a macroscale is shown in Fig. 10. The discovery of this effect has paved the way for developing photovoltaic solar cells, beginning from Selenium-based solar cells [24].

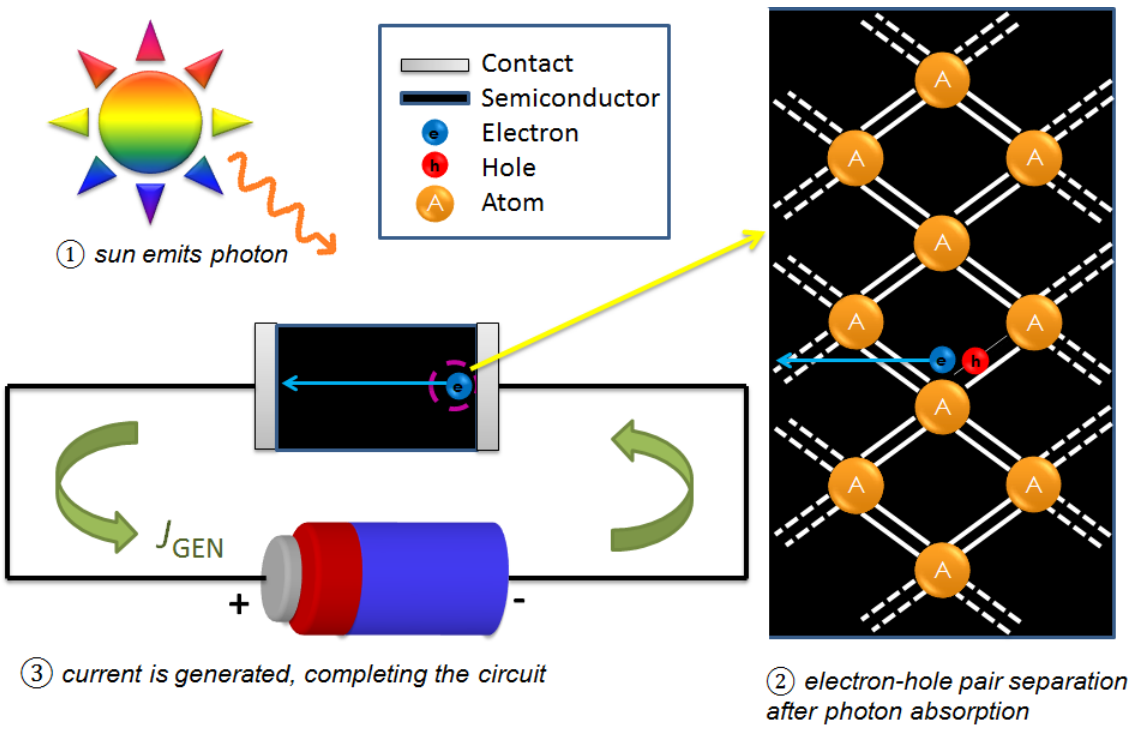

Fig. 10 The photovoltaic phenomenon in a macroscale perspective: from sunlight absorption to energy storage in a battery.

1.2.2. Energy band diagram

While the discussion in Sec. 1.2.1. provides a macroscale picture on how a solar cell works, this subsection discusses the same concept, but in solid-state physics perspective.

The simplest structure of a working solar cell is a *pn* junction, which is made up of a *p*-type and an *n*-type semiconductor. When *p*-type and *n*-type semiconductors are joined together, they form a depletion region [Fig. 11(a)]. In this region, ionized atoms form a barrier that prevents the majority carriers from each type to cross over to the opposite side of the junction. This is necessary to prevent the annihilation of electron-hole pairs (EHP)

generated upon light absorption. Additionally, the electric field in the depletion region originates from the positively-charged ions towards the negatively-charged ions to sweep the moving carriers towards the respective hole and electron contacts and have a higher chance of getting collected to produce electricity.

When the light incident upon a *pn* junction carries energy, E_{PH}, that is equal to or greater than the semiconductor bandgap, E_g, i.e. $E_{PH} \geq E_g$ [Fig. 11(b)], this is absorbed and then elevates an electron from the valence band, E_{VB}, to the conduction band, E_{CB}. This promotion is commonly known as EHP generation [Fig. 11(c)]. Next, the electron and hole are swept into the direction against and towards the electric field, $\vec{E}$, respectively. If the generated carriers do not recombine as they move towards their respective contacts, the hole is then extracted from the left contact [Fig. 11(d)], while the electron gets collected at the right contact [Fig. 11(e)].

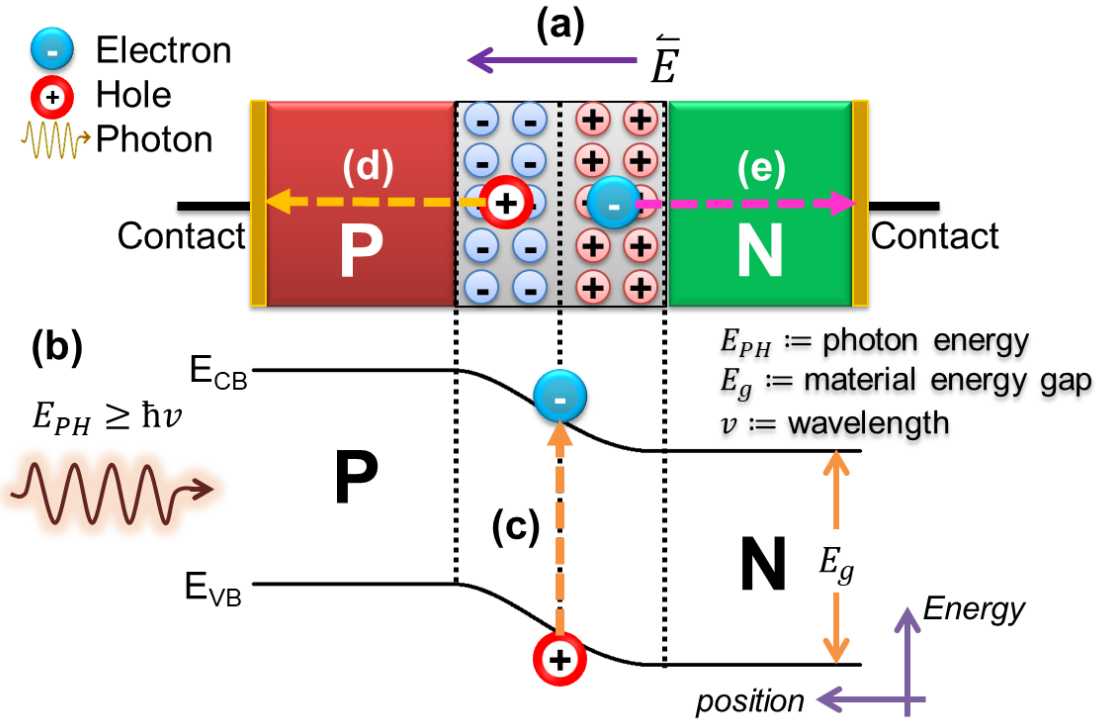

Fig. 11 Simplest solar cell structure: a *pn*-junction, illustrated with its corresponding energy band diagram. Here, (a) the electric field, $\vec{E}$, in the depletion region originates from the hole barriers and terminates at the electron barriers. (b) Incident light whose energy is $E_{PH} \geq E_g$. (c) EHP generation. (d) Hole and (e) electron moving towards the left and right contacts because of $\vec{E}$ in the depletion region.

1.2.3. Analytical form of current-voltage (*J–V*) characteristics

Ideally, the solar cell is mathematically defined as [26]

$$J(V) = J_L - \sum_{i=1}^{n} J_{0i} \left[\exp\left(\frac{qV}{mk_bT}\right) - 1 \right] \quad (1)$$

where the first term, J_L, is the generated photocurrent of the solar cell and the second term describes the total dark current[1] loss due to different mechanisms in the solar cell. Here, $J(V)$ is the net current output of the solar cell at an applied voltage, V, J_{0i} is the diode coefficient of the *i'th* loss mechanism of the solar cell, q is the electron charge, m is the diode ideality factor, k_B is the Boltzmann's constant, and T is the solar cell temperature. However, due to the presence of parasitic resistances in solar cells, eq. (1) expands as

$$J(V) = J_L - \sum_{i=1}^{n} J_{0i}\left[\exp\left(\frac{qV}{mk_bT}\right) - 1\right] - \frac{(V - JR_s)}{R_{sh}} \tag{2}$$

where R_s is the series resistance, mainly affected by contact conductivity and movement of carriers in the lateral and the vertical directions, and R_{sh} is the shunt resistance, which represents cell manufacturing defects. The equivalent electrical circuit model for a solar cell in the presence of parasitic resistances is shown in Fig. 12.

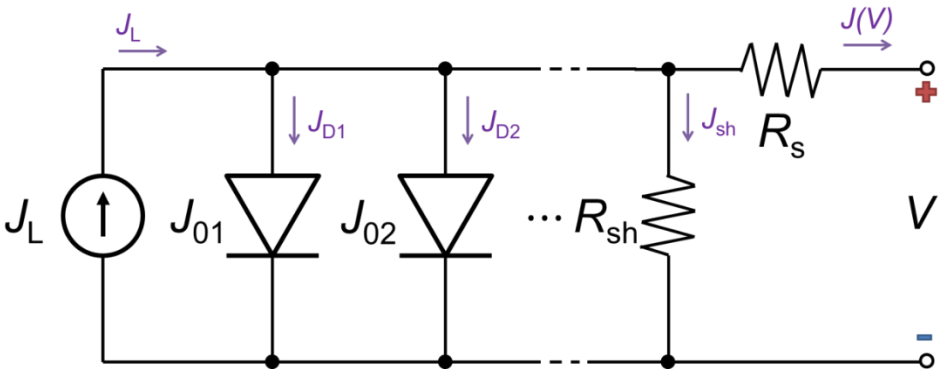

Fig. 12 Equivalent electrical circuit model of a solar cell considering the presence of parasitic resistances.

1.2.4. Fundamental performance evaluation parameters

The solar cell performance is described by the following electrical parameters, namely the short-circuit current, J_{sc}, the open-circuit voltage, V_{oc}, and the fill factor, FF. J_{sc} is the current generated by the solar cell when its terminals are connected, that is $V = 0$ V or in other words, the total dark current is zero. V_{OC} is the voltage generated across the solar cell when its terminals are electrically isolated, i.e. the current flowing through the solar cell is zero. This is the maximum V achievable, that is when the value of the current loss mechanisms is approaching zero based on how eq. (1) simplifies when $J(V)=0$, as in

$$V_{OC} = \frac{mk_BT}{q}\ln\left(\frac{J_{SC}}{J_0} + 1\right) \tag{3}$$

FF is described as the squareness of the solar cell J-V characteristic curve. In elaboration, it is defined by the maximum square area inscribable in the J-V characteristic curve. It is related to J_{sc} and V_{oc} by

[1] In this chapter, the J notations are particularly current densities but was shortened as currents for the ease of reading.

$$FF = \frac{J_m V_m}{J_{sc} V_{oc}} \tag{4}$$

where J_m and V_m are the current and voltage at the maximum power point, P_m, respectively. Then the solar cell conversion efficiency, η, is defined as

$$\eta = \frac{P_m}{P_{in}} = \frac{J_m V_m}{P_{in}}. \tag{5}$$

Here, P_{in} is the power of the light source incident to the solar cell, or simply the input power[2] to the solar cell. The electrical parameters describing the solar cell performance are specified in the sample *J-V* characteristics curve shown in Fig. 13. In the same figure, the three regions of operation of the solar cell device are also specified. At an applied cell voltage of less than zero ($V < 0$ V), the solar cell device operates as a photodiode, thus dissipating power. When the applied voltage is within zero and V_{oc} ($V = 0$ to V_{oc}), the solar cell generates power; hence, the solar cell operating region. And when the applied voltage is greater than V_{oc} ($V > V_{oc}$), the solar cell operates as an LED, which then dissipates power again [26–28].

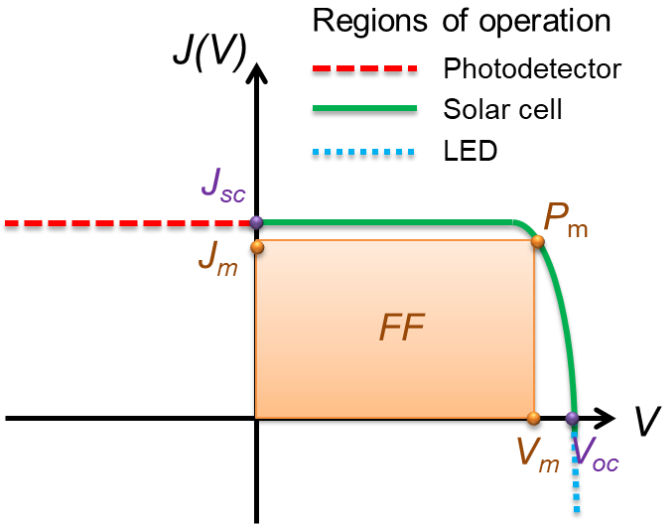

Fig. 13 Typical light *J-V* characteristics of solar cell and its different regions of operation.

1.3. Fundamental Losses in Solar Cells

1.3.1. The maximum sunlight available

As the sunlight reaches the Earth's surface, its intensity decreases due to the reflections by the cloud and ground, and absorption by water and CO_2, particularly in the infrared region. The sunlight distribution is illustrated in Fig. 14. Briefly speaking, about 70% of the total solar irradiation can be absorbed at the surface of the Earth while the remaining 30% of it is either scattered or reflected by the atmosphere. When it is partly cloudy, 19% gets lost through the cloud and atmosphere absorption, thereby leaving only 51%

[2] As *J* notations indicate current densities, so as *P* notations mean power densities.

available sunlight on the ground. Thus, the intermittent shading of clouds results in solar power conversion intermittency [29] – a persisting challenge for solar energy technologies.

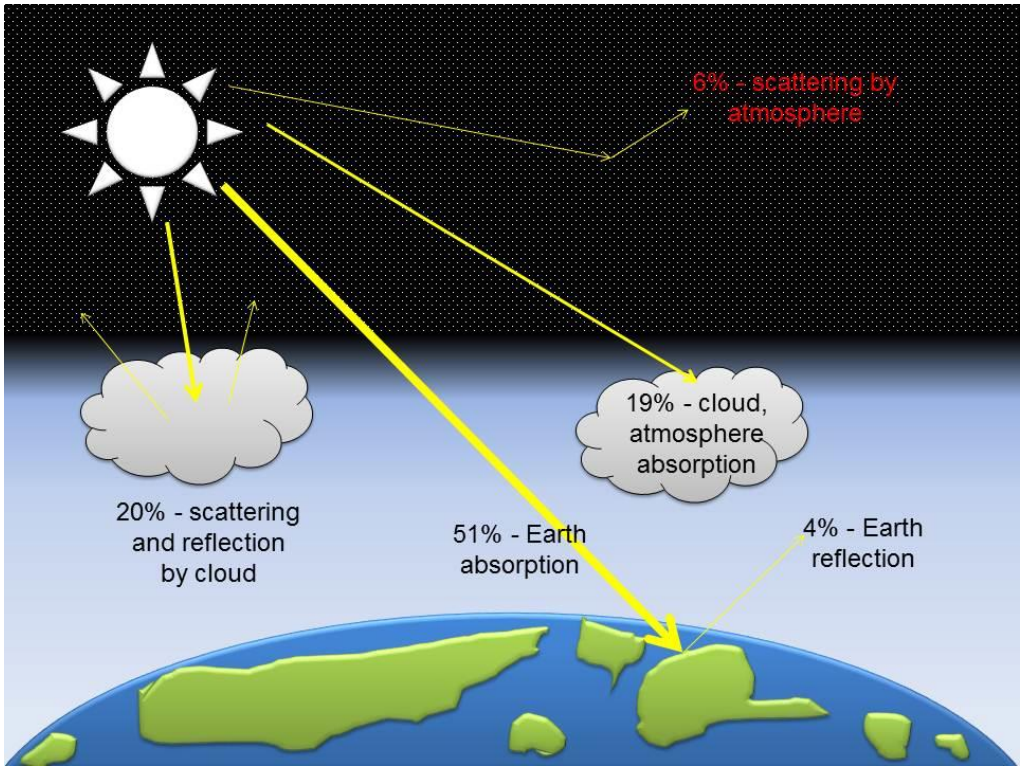

Fig. 14 Intensity distribution of incident sunlight upon reaching the atmosphere of the Earth: without cloud shading, 70% of incident solar energy can be received on the ground.

1.3.2. Shockley-Queisser limit

A solar cell can be considered as a black body due to its ability to absorb or emit light in the form of electromagnetic waves. However, it is not possible to absorb the same amount of light intensity over varying wavelengths consistently. Therefore, it is difficult for a standalone solar cell to achieve very high efficiency. One of the theories explaining this limit is the Shockley-Queisser limit, which assumes that the semiconductor material is a single *pn* junction governed by the blackbody radiation spectrum. Figure 15 shows the theoretical limit calculations for a single-junction solar cell under different sunlight spectra. This limit assumes that the energy is not concentrated and that the energy absorbed over the bandgap of the material becomes thermal energy. Last, it assumes that one photon excites one electron only [30]. Meanwhile, if higher sunlight concentration (measured in suns, where 1 sun is about 1000 W/m^2) is considered, the theoretical limit rises.

From the detailed balance calculations shown in Fig. 15, the optimal solar cell bandgap that may yield the highest conversion efficiency of 32.5% is at 1.31 eV considering blackbody radiation at 1 sun. In Fig. 16, the amount of deliverable power and intrinsic losses in a solar cell having different energy gaps is shown [31]. Here, the largest portion of incident solar energy loss is 29.8% due to thermalization – that is, photons having energies above the semiconductor bandgap lose energy via phonon emission. The next largest are those light carrying energies below a specific bandgap; hence, transparent to

the solar cell. For a 1.31-eV solar cell, it is about 25%. Another is the Boltzmann loss, which accounts for the incident light absorption and emission angle mismatch. Because of the distance of the sun from the Earth's atmosphere, the incident sunlight angle is 0.26° [32], which is very small compared to the luminescence angle by the solar cell device, typically 180°. Meanwhile, Carnot loss refers to the energy loss brought about by converting energy from one form to another and is 2.2% of the incident solar power for a 1.31-eV device. Last is the radiative loss due to photon emission from carrier recombination. For a single-junction solar cell, this loss is about 1.1% of the incident sunlight.

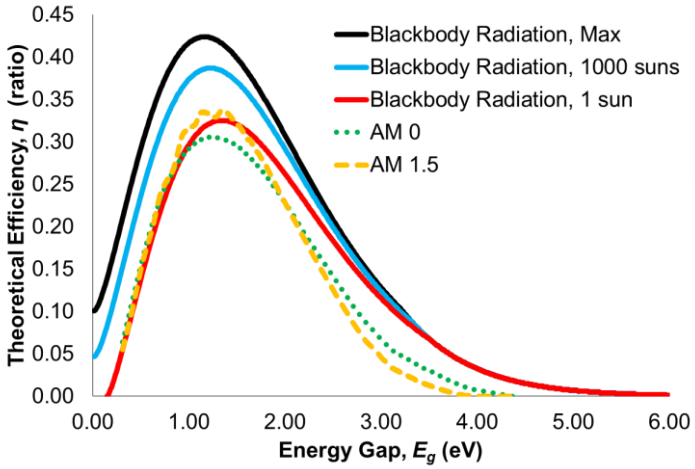

Fig. 15 Theoretical efficiency limit calculations for the single-junction solar cell under different solar spectra.

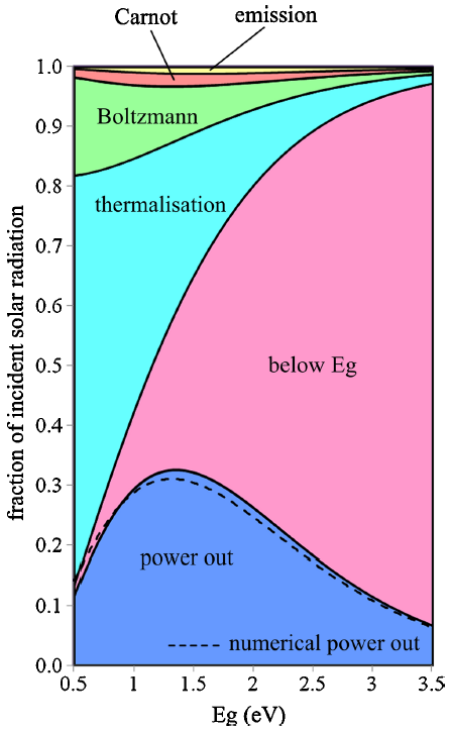

Fig. 16 Intrinsic loss distribution and deliverable power output of a solar cell device having an optimum bandgap of E_g = 1.31 eV under 1 sun illumination [31].

With these occurring in a solar cell, the general challenge for this energy harvesting technology is finding possible ways to minimize these losses. Theoretical conversion efficiency limit prediction has become a catalyst for a wide exploration of various methods to overcome this. This exploration has led to the development of different solar cell structures, categorized according to their technology generations, which are discussed in the later sections.

1.3.3. Parasitic resistances

In a solar cell, parasitic resistances manifest in the contacts and current leakage of the device flowing through the bulk, the side and surface defects. In an electrical model perspective, and as briefly mentioned in Sec. 1.2.3, parasitic resistances have two types, namely the series resistance, R_s, and the shunt resistance, R_{sh}. R_s represents the resistance to current flow within the bulk solar cell material itself, the resistance between the contacts and their interconnections (lateral) and between the metal contacts and the bulk solar cell material (vertical). It is ideally desired to be zero to allow maximum current flow through the device. However, as the photocurrent generation in solar cells increases, this becomes more severe, as indicated by its increase in value. On the other hand, R_{sh} represents the current leakage through the defects in the bulk region and edges and in between contacts with opposite polarity. For better cell efficiency, this material property is desired to be as large as possible, close to infinity [26–28].

1.3.4. Recombination losses

A solar cell device performance is implicitly defined by its dark current-voltage (*J-V*) characteristics. From this curve, the diode coefficients for recombination mechanisms and parasitic resistances can be estimated [33]. Thus, to determine the material properties of the 3JSC sample, its dark *J-V* characteristics must be extracted.

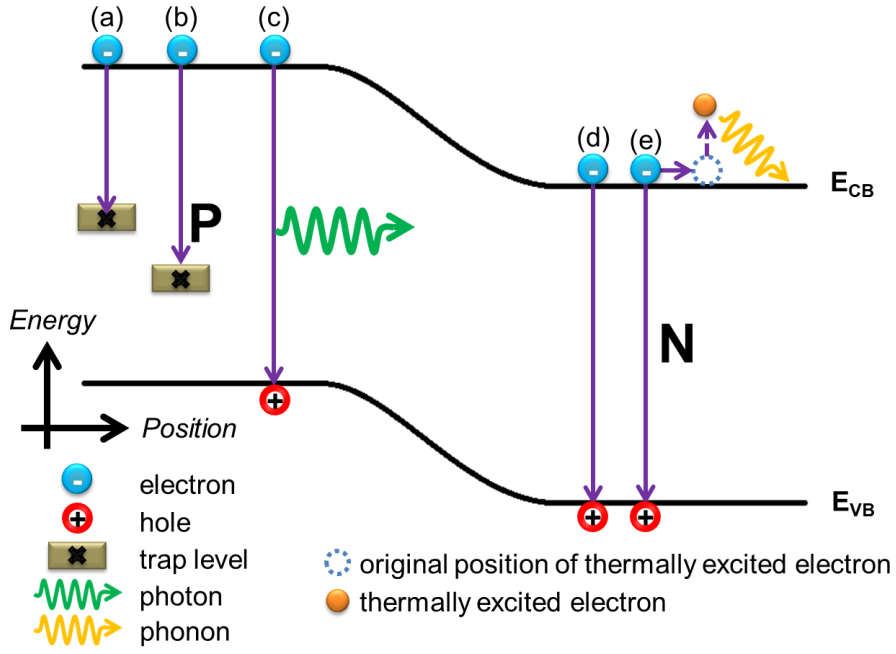

Fig. 17 Recombination mechanisms in a solar cell device: (a) surface and (b) bulk Shockley-Read-Hall recombination, (c) radiative and (d) nonradiative band-to-band recombination, (e) Auger recombination.

The recombination of carriers in a solar cell device translates into a loss of current generation in solar cells. Thus, it is desired to minimize this as much as possible. There are different types of recombination mechanisms that occur within a solar cell device, as illustrated in Fig. 17. Based on where it occurs, recombination can be classified as bulk or surface recombination. Depending on whether it resulted in photon emission or not, it can be categorized as radiative or nonradiative recombination. Aside from these classifications, the fundamental recombination mechanisms are the band-to-band, the Shockley-Read-Hall, and Auger recombination. The band-to-band recombination refers to an electron from the conduction band (CB) recombining to a hole in the valence band (VB). This mechanism has an ideality factor of 1. Shockley-Read-Hall (SRH) recombination refers to the electron-hole pair (EHP) recombining at traps in a solar cell device. This mechanism has an ideality factor of 2. Auger recombination, whose ideality factor is 2/3, refers to EHP recombination in which the electron involved in the recombination has transferred its energy to a nearby electron. This nearby electron thereby becomes thermally excited, then loses energy after some time [27,34].

1.4. World-Record Solar Cell Efficiencies

As of this writing, there are three defined generations of solar cells whose cost and efficiency projections are shown in Fig. 18. The first-generation solar cells are mainly crystalline silicon-based and are currently the most commercialized technology due to its maturity. However, solar cells belonging to this technology have high cost and the recorded conversion efficiencies are yet to reach or overcome the Shockley-Queisser limit. The second-generation solar cells are thin-film based materials such as cadmium telluride (CdTe) and copper-indium-gallium-selenide (CIGS). These thin-film solar cells are typically fabricated by vacuum or by chemical vapor deposition techniques. They are considered more advanced than the first generation solar cells due to their lightness and thinness. Despite the low cost, the technology is extremely challenged on how it will provide higher efficiencies. The efficiency projections for the second generation solar cells are the lowest among all of the generations. The third-generation solar cells are a wide array of novel cell structure concepts that have emerged from the former generations. These solar cells are designed in such a way that the losses within a solar cell material are suppressed and then converted into useful energy. Common approaches include stacking multiple solar cell materials with different bandgaps to absorb a wider range of the solar spectrum, exciting multiple carriers by a single photon, and carrier capture before thermal relaxation. Since third-generation solar cells have promising projections, at present, it is believed that it is practical to spend more research efforts in studying these solar cell technologies to overcome the barriers towards achieving high operating efficiencies [35–38].

The multijunction solar cells (MJSCs) are third-generation solar cell devices that demonstrated efficiencies exceeding 30% for triple-junction and 40% for quadruple junction solar cells under air mass (AM) 1.5 illumination. Based on the current cell efficiency achievement record regularly updated by the National Renewable Energy Laboratory [Fig. 19], the multijunction solar cells can potentially deliver efficiencies as high as 31.1% for dual junction solar cells (2JSCs) under non-concentrated sunlight and 44.4% for triple-junction solar cells (3JSCs) under concentrated sunlight. For six junctions, it can deliver as high as 47.1% under concentrated sunlight [39–41].

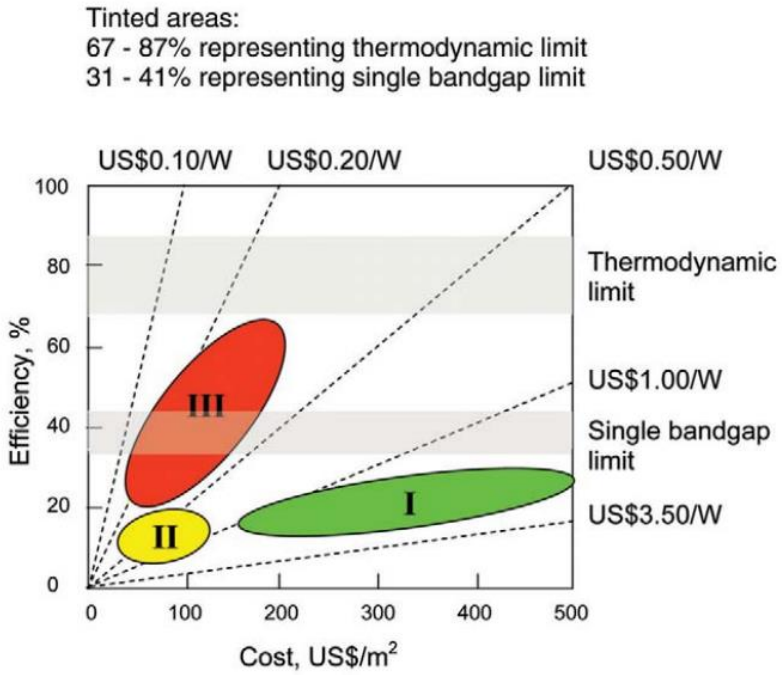

Fig. 18 Cost and efficiency projections for each solar cell generation [38].

1.5. Some Novel Concepts for High-Efficiency Solar Cells

While there is a wide variety of ongoing research on novel high-efficiency solar cells, this section will only discuss those that are highly relevant to this dissertation succinctly.

1.5.1. Multijunction solar cells (MJSCs)

While a solar cell cannot utilize the entire solar spectrum in converting light energy to electricity due to the Shockley-Queisser limit [30], various concepts to overcome this limit have materialized. The most straightforward of these is the use of multiple solar cell materials of different energy bandgaps stacked together, which is called the multijunction solar cell (MJSC). This has the potential to deliver efficiencies higher than 30%, depending on the number of materials stacked together to cover the solar spectrum as wide as possible [31].

MJSCs are made of multiple semiconductor materials with finely tuned bandgaps so that the photon-to-electron conversion is most effective in a specific layer of material [42]. The MJSC power conversion efficiency may be improved by increasing the number of junctions to more than three [31,43–44], by stacking fewer cells that are lattice-matched [45–46], by addition of low-cost optics to reduce the active area requirement [47], as illustrated in Fig. 20(a), or by finding ways to optimize the internal luminescence. The last approach may result to generation of photon [48], which may be reabsorbed in the same subcell by photon recycling [49], in a lower bandgap subcell by luminescent coupling effect [49–56], in a non-active layer of the MJSC or which may be transmitted out of the cell surface.

Each MJ subcell absorbs light to a certain extent depending on the bandgap. An illustration of partitioning the spectrum absorbed by each MJ subcell is shown in Fig. 20(b). The top cell of MJSC is typically the one that has the highest bandgap and absorbs

everything equal to or higher than its bandgap, $E_{g,T}$. Energy below $E_{g,T}$, which is supposed to be lost being transparent in single-junction solar cells, can be then absorbed by the succeeding lower bandgap subcells. Such an approach permits MJSCs to exceed the theoretical limit of single-junction solar cells [30-31].

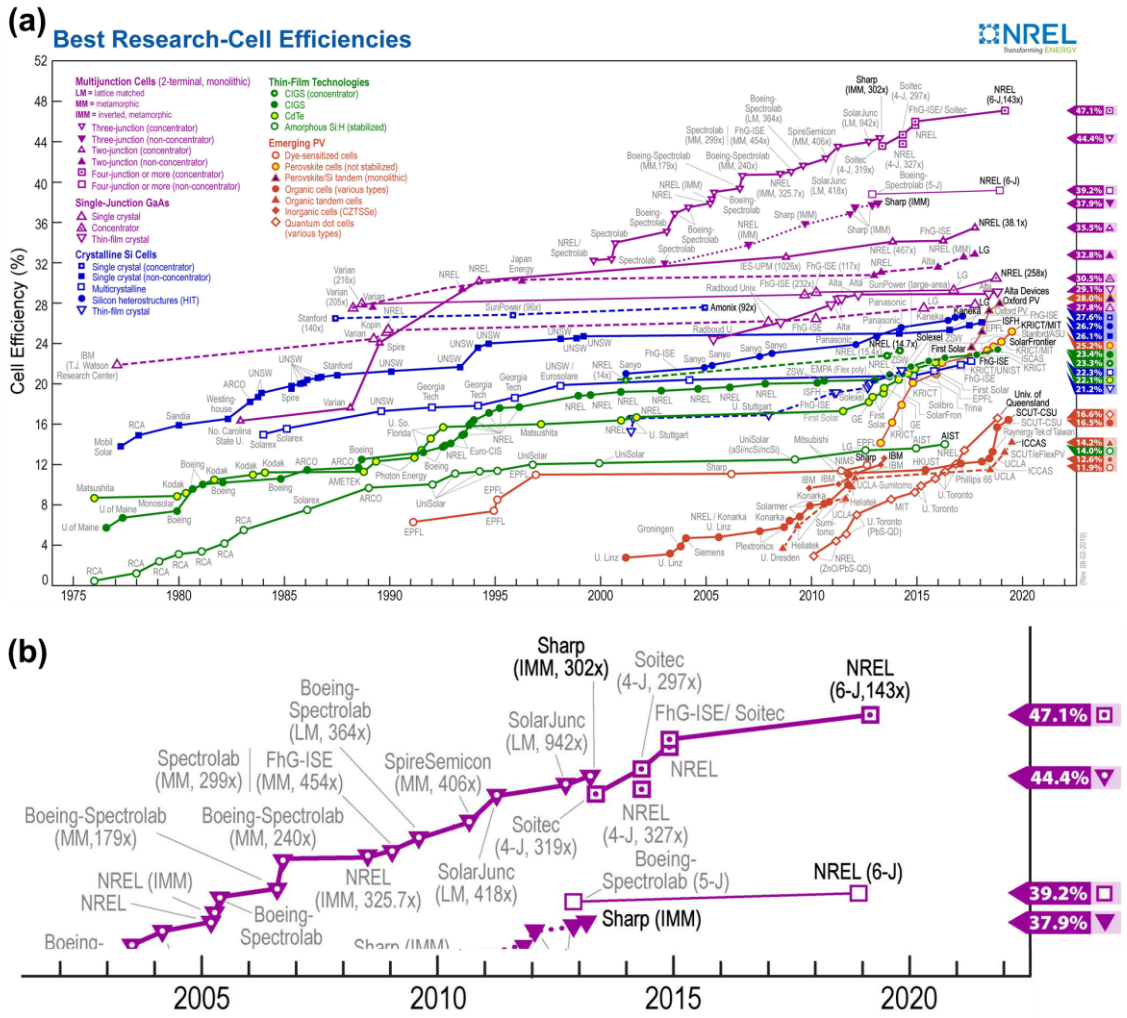

Fig. 19 Recent solar cell efficiency records maintained by the National Renewable Energy Laboratory [40]: (a) all solar cell technology records; and (b) multijunction solar cell records.

MJSCs are designed such that they absorb a wider span of the solar spectrum resulting in increased electric current and, in turn, higher conversion efficiencies [57]. In an MJSC, as the number of subcells increases, the conversion efficiency also increases theoretically. The theoretical limit for an MJSC having an infinite number of layers connected in series is about 86.8% under high sunlight concentration [58] and 68.2% for diffuse sunlight [59]. As of this writing, MJSC holds the highest cell efficiency records. As briefly mentioned earlier, the record is being held by 6-junction solar cells from National Renewable Energy Laboratory, the USA at 39.2% and 47.1% under unconcentrated sunlight and 143 times sunlight concentration, respectively [39–41]. However, there could still be a long way to go until MJSCs reach 50% efficiency. As it appears, increasing the number of junctions alone is not a silver bullet to further boost MJSC efficiency towards 50% and beyond. Hence, other possibilities to do so needs to be explored.

Most MJSCs are based on high-performance III-V compound semiconductors like InGaAs, InGaP, GaAs. However, the availability of these materials poses a challenge in manufacturing them [60]. Besides, the production cost for such high-efficiency semiconductors is considerably expensive, which hinders wide commercial acceptance. As of this writing, MJSCs are generally used in spacecraft applications and are yet to expand in terrestrial applications market optimistically through concentrator PV systems [61].

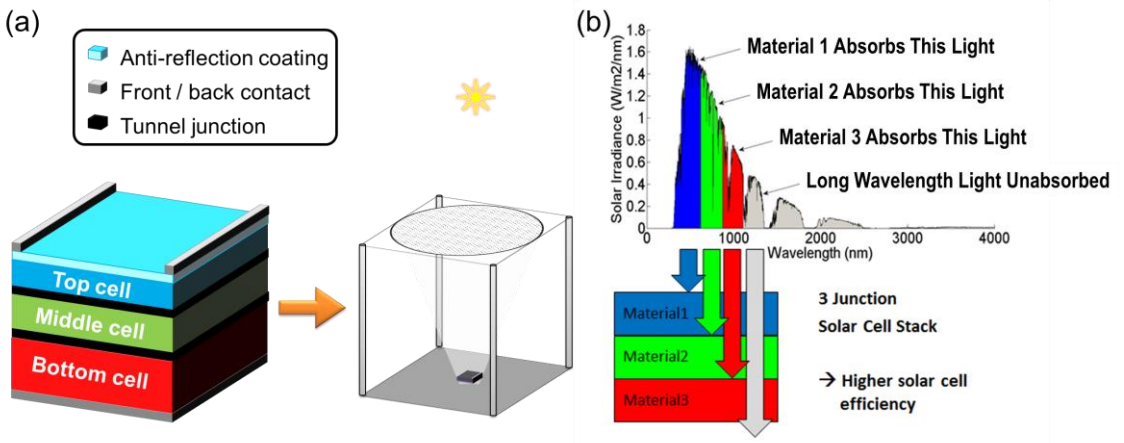

Fig. 20 (a) Simplified schematic of a triple-junction solar cell (3JSC) structure for terrestrial concentrator application. (b) One example of 3JSC absorption spectrum [62].

1.5.2. Quantum dots (QDs) for solar cell applications

A QD is a semiconductor nanocrystal that exhibits discrete electronic states due to quantum confinement. QDs are incredibly small particles, typically having diameters of 2 to 10 nm. Due to their small size, they exhibit quantum mechanical properties [63]. Figures 21(a) and (b) show the size of a QD relative to the exciton Bohr radius and a representation of a bound electron-hole pair [64], called an exciton, respectively.

1.5.2.1. Quantum Confinement

Unlike in bulk semiconductor materials, the charges in QDs are tightly bound to the nuclei of the atoms and thus, the number of free electrons is very small, ranging from less than 10 to a few hundred. In effect, the charges are said to be “confined”. When the carriers (electrons and holes) are confined in a dimension smaller than the exciton Bohr radius, a_B, quantum confinement takes place. Quantum confinement refers to the reduction in the degrees of freedom of charge carriers [63]. In this case, the electron energy levels split into discrete values as shown in the energy band diagram in Fig. 21(c). The energy levels of bulk semiconductor materials are continuous while those of QDs are discrete electronic states; that is, quantized energy levels of the electrons in an atom. For this reason, QDs are sometimes referred to as artificial atoms. Simplified energy band diagrams of a bulk semiconductor and a QD are shown in Fig. 21(d). In a QD, the energy levels are quantized because the carriers are confined in three dimensions [65].

One of the fundamental effects of quantum confinement is its influence on the electronic and optical properties – they become functions of the dot size. An important consequence of this is the ability to tune the QD bandgap across a range of energy levels, such that the QD emits light at a specific wavelength [66]. Thus, the electronic and optical

properties of QDs can be precisely engineered. In this view, QDs may offer some technological breakthroughs for MJSCs. Figure 22(a) shows how the peak emission wavelength of the QDs change with dot size variation. Here, smaller dots have higher bandgaps and emit shorter wavelengths while larger dots have lower bandgaps and emit longer wavelengths when subjected to the illumination of higher energy. This was observed experimentally, that as QD radius increases, i.e. peak emission wavelength increases, the lowest energy transition or, similarly, the energy gap decreases [Fig. 22(b)]. Moreover, the smaller the dots are, the better the quantum confinement experienced by an exciton [Fig. 22(c)]. In addition to its size-dependent emission wavelength, QDs have broad absorption and a narrow emission spectrum, as compared with bulk materials [67]. Besides, the emission quantum yield of a QD is relatively larger than that of an optoelectronic bulk semiconductor material, as shown in Fig. 22(d) for PbSe QDs [68].

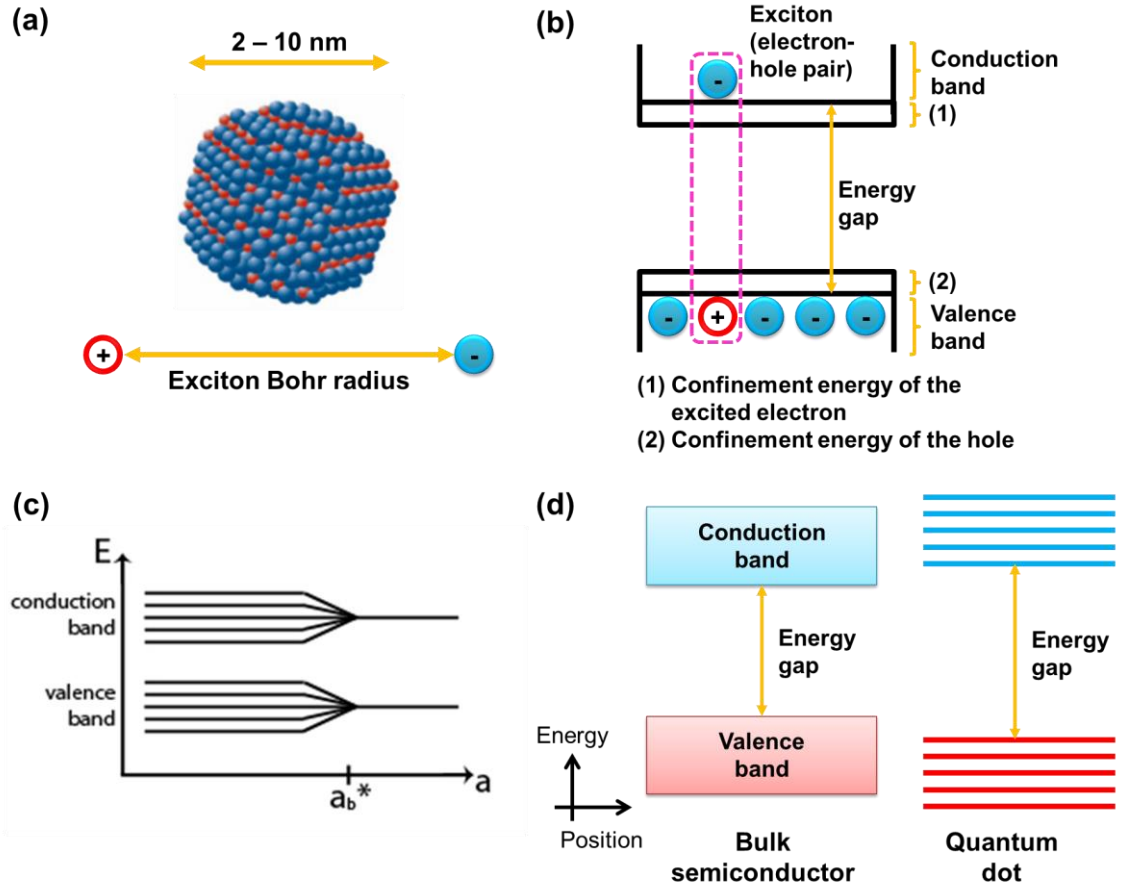

Fig. 21 (a) QD size relative to the exciton Bohr radius. (b) Representation of an exciton. (c) Energy level splitting due to quantum confinement in a QD. (d) Simplified energy band diagram of a bulk semiconductor and a QD showing discrete electronic states.

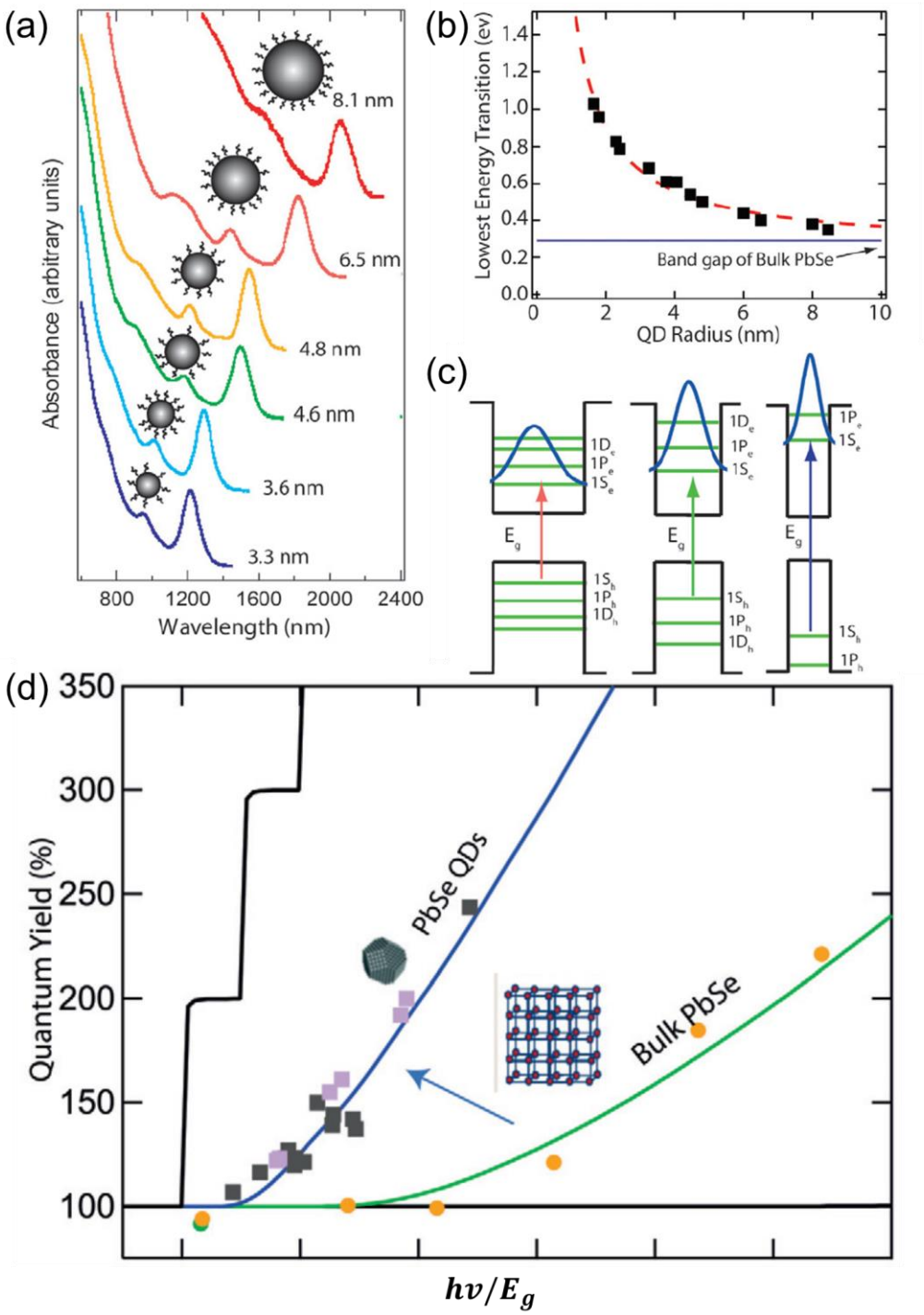

Fig. 22 (a) Absorption spectra of PbSe QDs of sizes between 3.3 nm and 8.1 nm; (b) Quantum confinement increase experienced by 1st exciton with particle size decrease; (c) Approximate variation of PbSe QDs energy gap, E_g, with the inverse of QD radius, $1/r$ [67]. (d) Quantum yield versus hv/E_g, measured by photoluminescence (PL) spectroscopy for bulk PbSe and QD PbSe [68].

1.5.2.2. Fabrication methods

There are two popular methods of producing QDs: first is by epitaxial growth and second is by colloidal synthesis. Examples of epitaxially-grown QDs are III-V semiconductors. Specifically, they are grown by molecular beam epitaxy (MBE) [69–75].

This growth process demands high energy input and complicated pieces of machinery. On the other hand, the colloidal synthesis of QDs offers a more economical and facile method through solution processing that involves only chemical reactions using inexpensive tools and equipment. In this method, QDs are synthesized as colloidal particles suspended in a solvent. Since they are formed from colloidal synthesis, the nanocrystals are usually referred to as colloidal quantum dots (CQDs). In comparison with epitaxially-grown QDs, solution-processed CQDs have the benefit of structural control [76–77]. Another important advantage is that it also allows large-scale production of CQDs at a much lower cost compared to the epitaxially grown QDs [78].

Common CQDs are metal chalcogenide (II-VI) semiconductors like PbS [79–80], PbSe [81], CdS [82], CdSe [83–84], and CdTe [85–87]. Very recently, perovskite CQDs [88–107] are gaining popularity, considering its bulk version being able to increase efficiency by almost 20% in 7 years [41,108]. Integration of CQDs into various substrates can be done using simple solution deposition techniques such as spin coating, inkjet printing, Langmuir-Blodgett deposition, and dip-coating.

CQD nanocrystals are formed by injecting a corresponding metal oleate precursor into a high-temperature solution that contains an organic coordinating solvent [76]. The CQDs are normally terminated by a long chain of organic ligands that make them stable in solution form and maintain colloidal dispersion. In this method, the critical parameter is the reaction or the synthesis temperature which determines the QD size. Generally, the particle size increases with the synthesis temperature. CQDs usually have a core/shell structure wherein an organic core is covered with ligands that serve as stabilizers. The shell capping makes the CQDs more robust during processing and was observed to enhance the room temperature PL quantum yield [109].

1.5.2.3. Quantum Dot Solar Cells (QDSCs)

Although they are challenged by low power conversion efficiencies, colloidal QDSCs are solution-based; hence, they are easy and cheap to prepare as compared with conventional optoelectronic semiconductors such as silicon (Si) and gallium arsenide (GaAs) that requires highly-controlled cleanroom environment.

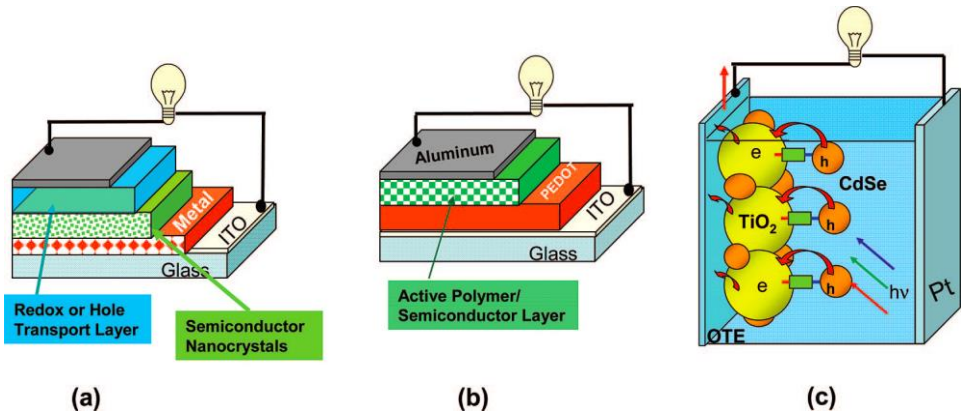

Fig. 23 QDs for solar cell applications (a) metal-semiconductor, (b) polymer-semiconductor (c) semiconductor-semiconductor systems [110].

The recent advances in using quantum dots as light energy harvesters provide more versatile opportunities for the development of third-generation, high-efficiency solar cells [110]. The quantum confinement effect in QDs may be used to compensate for the

fundamental losses in solar cells [31], thereby allowing conversion efficiencies to exceed the theoretical efficiency limits for single-junction solar cells [30]. QDSCs offer the possibility of harvesting light over a wider range of the spectrum, from infrared to visible light. Moreover, the use of QDs in solar cells allows for multiple exciton generation (MEG) [111].

In general, there are three ways to incorporate CQDs in solar cells: (1) metal-semiconductor or Schottky solar cells (2) polymer-semiconductor hybrid solar cells and (3) quantum dot sensitized solar cells (QDSSC) [112]. These strategies are illustrated in Figs. 23 (a) to (c), respectively. In Schottky solar cells, QD arrays are formed where the QDs are electronically coupled to allow for efficient electron/hole conductivity. Meanwhile, in polymer-semiconductor hybrid solar cells, QDs are placed in contact with electron and/or hole conducting polymers. Last, QDSSC involves the use of QDs to sensitize wide-bandgap semiconductors.

1.5.3. Quantum dots for tandem solar cells

To further alleviate the impact of the high cost of high-efficiency III-V solar cell materials, the hybrid concept of employing QDs in MJSCs is proposed recently. Some of them are as follows:

(1) the use of visible light CdSe CQDs on epitaxially-grown InGaP/GaAs dual junction solar cells (2JSCs) for QD-assisted luminescent downshifting [Fig. 24(a)], which demonstrated a power conversion efficiency improvement of 5.78% relative to the reference sample without CQDs [Fig. 24(b), 113];

(2) the use of all-Si tandem solar cells [Fig. 24(c)], which are formed using a combination of a top cell, wide-bandgap QD structure and lower bandgap, thin-film bulk structure [Fig. 24(d), 114]; and

(3) the use of bulk 1.55-eV perovskite on 1.0-eV CQDs, with a maximum theoretical efficiency of 43%, employing radiative coupling that can potentially enhance efficiency by 11-21% [Figs. 24(e) and (f), 115].

From these, QD-assisted luminescence, combined with increasing the number of junctions of III-V-based solar cells, may be a solution worthwhile to investigate in boosting the world record MJSC efficiencies towards 50% and beyond.

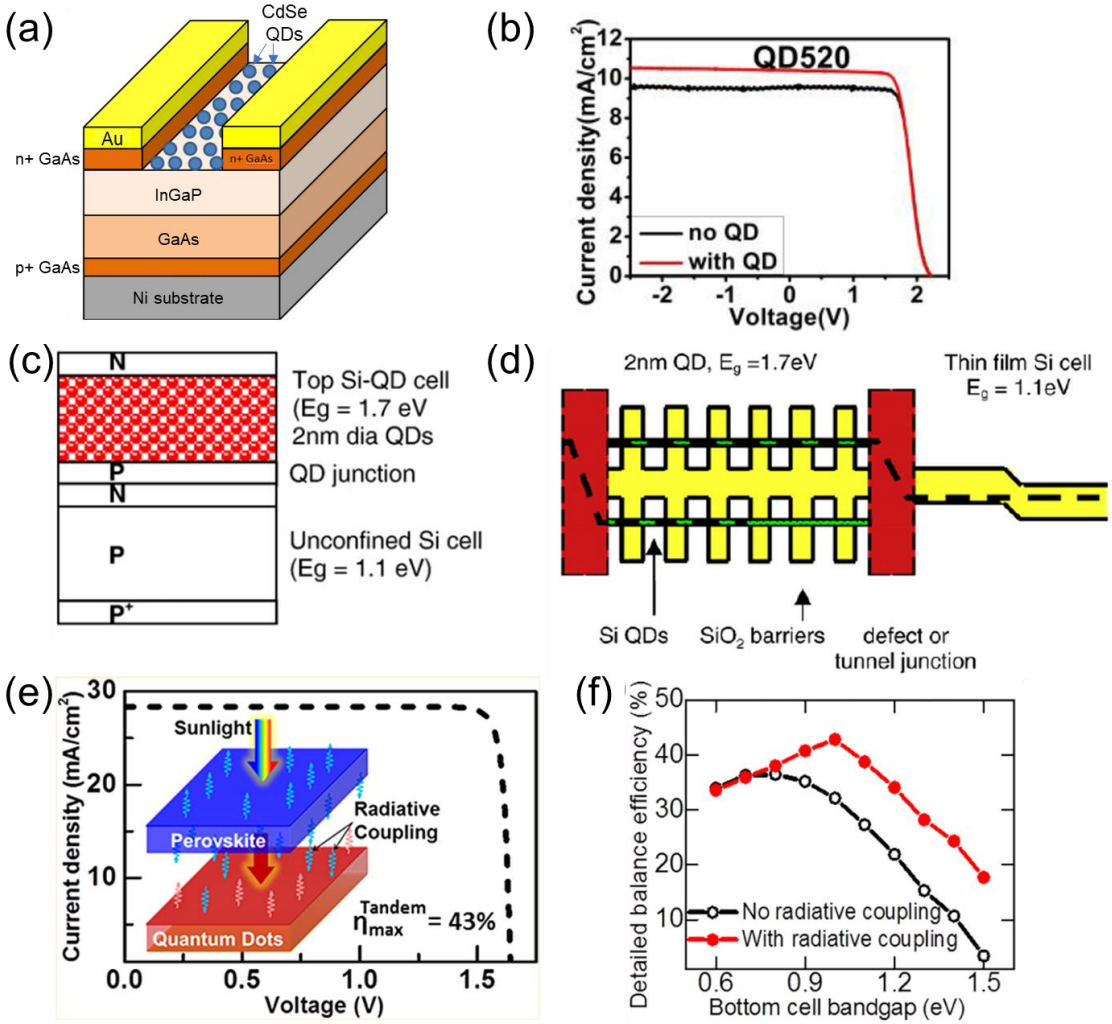

Fig. 24 (a) The schematic diagram and (b) measured *J-V* characteristics of InGaP/GaAs dual junction solar cell with and without CdSe quantum dots [113] (c) Si QD/Si bulk tandem solar cell and (d) its corresponding band diagram [114]. Theoretical (e) *J-V* characteristics, simple schematic and (f) detailed balance efficiency calculation of perovskite on QD tandem solar cell with and without radiative coupling [115].

Luminescent coupling effect in III-V multijunction solar cells

Chapter 2

Chapter 2 – Luminescent coupling effect in III-V multijunction solar cells

Chapter 2 lays down all of the currently available fundamental information that revolves around the luminescent coupling (LC) effect in III-V based multijunction solar cells (MJSCs). This chapter begins with a section of thorough existing and related literature reviews on the LC effect in MJSCs. In Sec. 2.2, the main research problem is introduced through identifying the knowledge gap based on the reviewed literature on the LC effect in III-V based MJSCs. Additionally, the research originality is stated here. This is then followed by the research objectives stated through laying down the general questions which this study will attempt to answer. Finally, this chapter ends with the synopsis of the succeeding dissertation chapters which will attempt to answer research questions that are specific and relevant for each chapter to discourse.

2.1. The Luminescent Coupling (LC) effect

As briefly discussed in Chapter 1, a possible strategy to improve the MJSC efficiency is by finding ways to optimize the internal luminescence resulting in photon generation [48]. In particular, the absorption of photons in the lower bandgap (LBG) subcell is called the LC effect. This is an internal phenomenon caused by photon emission due to radiative recombination from a higher bandgap (HBG) subcell of an MJSC which then results in photocurrent generation in an adjacent LBG subcell. This phenomenon causes carrier redistributions among subcells, thereby reducing current mismatch and wavelength sensitivity that helps boost the conversion efficiency of the MJSC.

In Chapter 1, it was also mentioned that the radiative loss for a 1.31-eV single-junction solar cell is about 1.1% of the incident sunlight. However, as the number of junctions increase, this loss increases as well [31], rendering it as a significant consideration for MJSCs. This has been theoretically studied and is shown in Fig. 1, considering up to 6 junctions having optimal semiconductor bandgaps and are unconstrained. With these, the concept of the LC effect has recently attracted the attention of the scientific community [50–56], making it a timely research topic to explore.

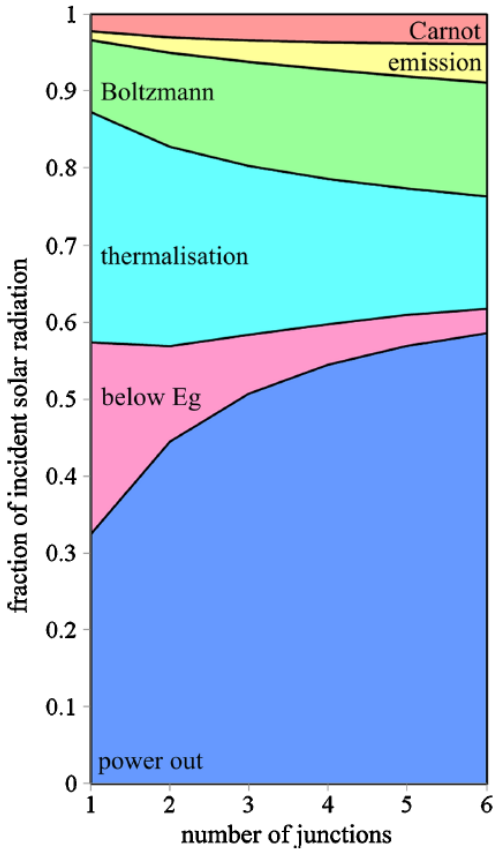

Fig. 1 Calculated junction number dependence of deliverable power (out) and loss mechanisms in an unconstrained, multijunction solar cell under 1 sun illumination [31].

2.1.1. Current matching in series-constrained MJSCs

Fundamentally, MJSCs are series-constrained or monolithic. Having this structure makes current matching imperative, that is, the output current of one subcell is the same as the output of the other. In the case when MJ subcells produce different amounts of current, the one that produces the least current will dictate the overall MJSC performance. Hence, considering subcell current matching can significantly alter the performance of an MJSC device. In Fig. 2(a), an example of a tandem *J-V* curve prediction based on the summation of individual cell voltages is shown. This is the simplest approach one can use to determine the overall *J-V* characteristics of a tandem solar cell. If the limiting cell is shunted, the net tandem *J-V* curve will be shunted as may be dictated by the limiting cell. Another approach, depicted in Fig. 2(b), considers both the forward-reverse voltage compensation in each subcell and whichever current-limits the tandem solar cell. This prediction method is considered more accurate than just summing up the individual cell voltages since it accounts for the possibility of a current-limiting cell changing at each voltage, most especially if the current-limiting cell at lower operating voltages is severely shunted. Meanwhile, Figs. 2(c) to (e) illustrates the change in voltage operating point of individual cells of a tandem solar cell with increasing illumination upon an HBG subcell while keeping the LBG subcell under dark condition. As the illumination upon the HBG subcell increases, the operating voltage increases forwardly. To sustain the total voltage of the tandem solar cell, the LBG subcell gets forced to operate at higher reverse voltages [116].

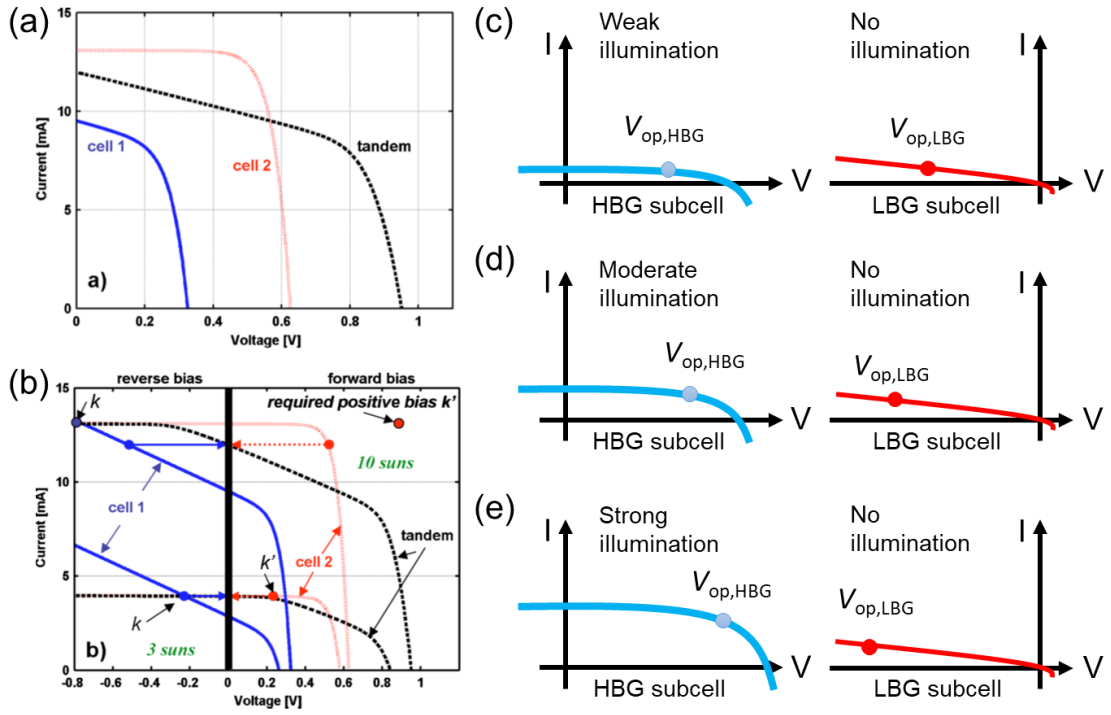

Fig. 2 Individual cells 1 and 2 and series-constrained tandem *I-V* characteristics, where cell 1 is severely shunted, hereby affecting the slope of the total tandem *I-V*. (a) Determining the tandem solar cell I-V curve simply by voltage summation or (b) by considering the forward and reverse voltage compensations and at the same time, which cell current-limits the tandem at each voltage for an AM1.5D solar spectrum at 3 suns and 10 suns [116]. Operating voltages of individual cells at (c) weak, (d) moderate and (e) strong illumination upon HBG subcell (not to scale).

In earlier studies, it was suggested that MJSCs should be evaluated in short-circuit conditions to minimize the LC effect [117]. This is because in a real solar module the top cell is expected to operate at maximum power point at which the LC effect will be remarkably less. Nevertheless, it was found that even in short-circuit conditions, it could not be fully eliminated [118].

2.1.2. LC effect vs photon recycling

There are 2 kinds of recombination – radiative and nonradiative. Focusing on the radiative recombination, the photon emission that this process produces is emitted in all directions. Hence, some parts will exit the cell through the front surface while some portion will still traverse within the cell volume. The latter part will have a chance to be reabsorbed in the semiconductor. This phenomenon is called as photon recycling [49].

The difference between photon recycling and the LC effect is illustrated in Fig. 3. In photon recycling [Fig. 3(a)], the photon produced during radiative recombination is reabsorbed within the cell for 1JSCs or within the same subcell in MJSCs. Photon recycling becomes more effective when the optical absorption coefficient is high for a wide spectrum of wavelengths. It is also more effective when the solar cell material used has high internal light-trapping efficiency [48,119]. On the other hand, the LC effect [Fig. 3(b)] is an internal phenomenon caused by the radiative recombination from an HBG subcell of an MJSC, which then causes photocurrent to be generated in an LBG subcell. This phenomenon causes carrier redistributions between junctions, thereby reducing the current mismatch between adjacent subcells [50–51], as mentioned earlier.

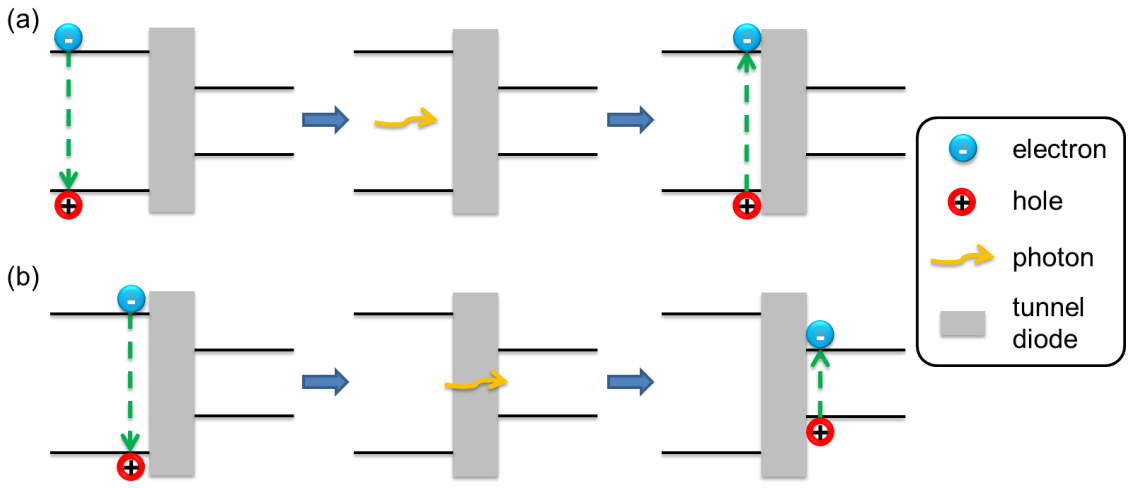

Fig. 3 Simplified energy band diagrams illustrating (a) photon recycling and (b) luminescence coupling.

According to some theoretical studies, photon recycling has a more significant effect on the V_{oc} and little on J_{sc} [120–121]. This is because photon recycling affects the dark current. Moreover, the photon recycling factor needs to be considered in proportion with the radiative recombination coefficient of the solar cell [122]. Furthermore, this depends on the active region thickness and other optical characteristics of the device [123–125]. With these, inaccurate prediction of solar cell performance just by considering nonradiative recombination lifetime alone can be avoided. As shown in Fig. 4, the *J-V* characteristics obtained considering photon recycling for thin-film GaAs solar cells

resemble the observed *J-V* characteristics closer than without photon recycling considered. Numerically, V_{oc} was found to be underestimated by 3.7% without considering photon recycling in the theoretical model. Similarly, it is discussed in the succeeding subsections that excluding the LC effect in theoretical simulations yield underestimated electrical performance parameters for MJSCs.

Aside from III-V based MJSC devices, both photon recycling and LC effect were found to enhance the performance of multijunction photo transducer devices, causing V_{oc} and J_{sc} increase [126] and helpful for the accurate prediction of solar power upon a car-roof PV system [127].

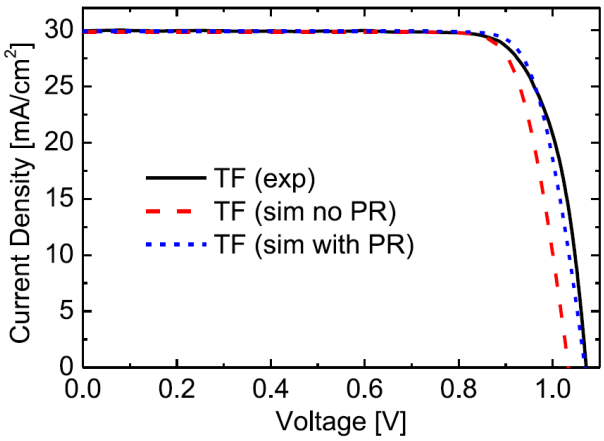

Fig. 4 *J–V* characteristics of the thin-film GaAs solar cell, whose base is 3.5 μm thick at AM1.5G illumination (1000 W/m^2) and T = 300 K, measured (solid line) and simulated with (dotted line) and without photon recycling (dashed line) [125].

2.1.3. Theoretical models

2.1.3.1. Temperature-dependent model for LC effect

The widely-adopted Varshni model for the temperature dependence of semiconductor bandgap is given as [128]

$$E_g(T) = E_g(0) - \frac{\alpha T^2}{\beta + T} \tag{1}$$

where $Eg(0)$ is the semiconductor bandgap at T = 0 K, and α and β are constants. Known literature claims that saturation currents brought about by combined diffusion and radiative recombination, J_{01}, and nonradiative recombination, J_{02}, processes are temperature-dependent. These parameters are given as [129–130]

$$J_{01}(T) = C_1 T^3 \exp\left(\frac{-E_g(T)}{k_B T}\right) \tag{2}$$

and

$$J_{02}(T) = C_2 T^2 \exp\left(\frac{-E_g(T)}{2k_B T}\right) \tag{3}$$

where C_1 and C_2 are constants independent of temperature, T. As radiative recombination process can dominate over the nonradiative recombination at low semiconductor temperatures and vice-versa at high temperatures [131], the temperature dependence of the LC effect needs to be considered during modeling. This is because it was observed to affect the amount of LC current generated in a limiting cell [132]. Furthermore, it needs to be taken into account during outdoor [133–134] and under concentration [135–138] performance evaluation, as PV devices seldom operate at ambient temperatures in these real conditions.

2.1.3.2. One-dimensional (1D) modeling

1.3.2.1. Extension of 2-diode models for MJSC performance prediction

Based on the 2-diode solar cell analytical model, the *J-V* characteristic curve considering the presence of LC effect can be predicted using the equations

$$J(V_i) = J_{L,i} + J_{LC,i-1\rightarrow i} - J_{01,i}\left[\exp\left(\frac{qV_i}{k_BT}\right) - 1\right] - J_{02,i}\left[\exp\left(\frac{qV_i}{2k_BT}\right) - 1\right] \quad (4)$$

$$V_i = \frac{2k_BT}{q}\ln\left[\sqrt{\left(\frac{J_{02,i}}{2J_{01,i}}\right)^2 + 1 + \frac{J_{02,i} + J_{L,i} + J_{LC,i-1\rightarrow i} + J(V_i)}{J_{01,i}}} - \frac{J_{02,i}}{2J_{01,i}}\right] \quad (5)$$

where $J_{LC,i-1\rightarrow i}$ is the LC current of the LBG (i'th) subcell with its adjacent HBG [($i–1$)'th] subcell [53]. Electrically, one can also easily model MJSCs by extending the 2-diode model of a single-junction solar cell. Since the LC effect happens inevitably in MJSCs, this needs to be considered in the electrical model. This can be done by making the LC current in a limiting cell-dependent to the radiative recombination saturation current of its adjacent HBG [($i–1$)'th] subcell, $J_{Rad,i-1}$. Mathematically, this is given as

$$J_{LC,i-1\rightarrow i} = \alpha_{LC}J_{Rad,i-1} \quad (6)$$

where $J_{Rad,i-1}$ is

$$J_{Rad,i-1} = J_{0rad,i-1}\left[\exp\left(\frac{qV_{i-1}}{k_BT}\right) - 1\right]. \quad (7)$$

Here, $J_{0Rad,i-1}$ is the radiative recombination diode coefficient and V_{i-1} is the voltage across the HBG subcell. Also, α_{LC} in eq. (6) is the LC efficiency, alternatively referred to as the LC factor [139] or the LC quantum efficiency between two adjacent subcells, $\eta_{LC}^{T,B}$ [140]. As for the latter definition, the luminescent intensities generated optically and electrically can be plotted against each other to determine the $\eta_{LC}^{T,B}$, which is defined as

$$\eta_{LC}^{T,B} = \frac{\partial I_B}{\partial I} - 1 \quad (8)$$

where $\frac{\partial I_B}{\partial I}$ is the slope of the paired intensities in the external optical bias, I_B, versus external electrical bias, I, as plotted in Fig. 5.

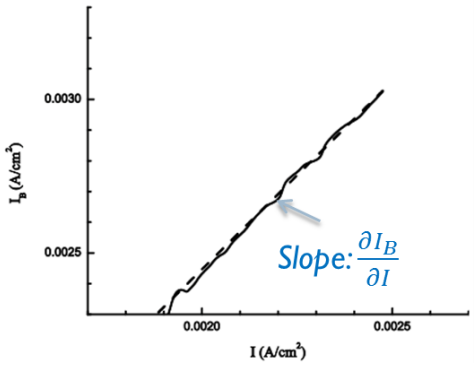

Fig. 5 Plot of the optical bias current, I_B, vs. electrical bias current, I, where $\frac{\partial I_B}{\partial I}$ is the slope of the line needed for determining the LC quantum efficiency, $\eta_{LC}^{T,B}$ [140].

If the LC current is modeled linearly, then it is linearly proportional to the overall radiative dark current. However, it is more realistic to consider the current mismatch between subcells under the influence of the LC effect. Considering a 2JSC wherein the bottom cell is the limiting cell, it is forced to have an overall current equal to that of the bottom cell since the top and the bottom cell are effectively in series. The carriers on the top cell will be forced to recombine, therefore causing LC current generation in the limiting cell. This LC current then adds up to the limiting current, therefore increasing the net current of the 2JSC. For a 3JSC, the LC current from top to bottom cell is neglected since the middle junction is commonly designed to be optically thick at the wavelength of the top junction band edge. The equivalent electrical circuit representations of 2JSC and 3JSC devices with LC effect accounted for are shown in Figs. 6(a) and (b), respectively. Here, $J_{L,i}$ is the photocurrent generation due to external illumination and $J_{LC,i-1\rightarrow i}$ is the LC current generation in the i'th subcell which is dependent on the HBG subcell radiative recombination saturation current, represented by the J_{01} component in Fig. 6 and eqs. (4) and (5), or $J_{Rad,i-1}$ in eqs. (6) and (7).

From the individual subcell *J-V* characteristic curve plot of a 2JSC shown in Fig. 7 and obtained using eq. (4), the following inferences were drawn when there is LC, i.e. the value of the coupling strength, η, is between 0% and 100%. When the device is bottom cell limited, that is, both the net current and voltage increase, thereby improving the overall efficiency of the 2JSC as compared with the no LC plot. On the other hand, when the 2JSC device is top cell limited or subjected to current-matched condition, then only the net voltage improves in the nonlinear portion of the plot as compared with the no LC plot [53].

Meanwhile, the *J-V* characteristic plots for 2JSC and 3JSC subcells from a parallel study [52] are shown in Fig. 8. The large dots in the *J-V* characteristic plots are the operating points during short-circuit conditions. As represented using the electrical models in Fig. 6, no LC component was included for the top cells since there is no LC present in them. Hence, in the top cell limiting case [Figs. 8(a) and (c)], the net *J-V* characteristics only show an increase in voltage, brought about by the increase in top cell V_{oc} and J_{sc}. As for the rest, when a current-limiting cell has a lower bandgap, the LC effect increases the net MJSC current, which is obtained from the middle cell limiting case, as

shown by dotted lines in Fig. 8(d), and in Figs. 8(b) and (e), which are both acquired during the bottom cell limiting case. In these studies though, negligible parasitic resistance effects were assumed [52–53].

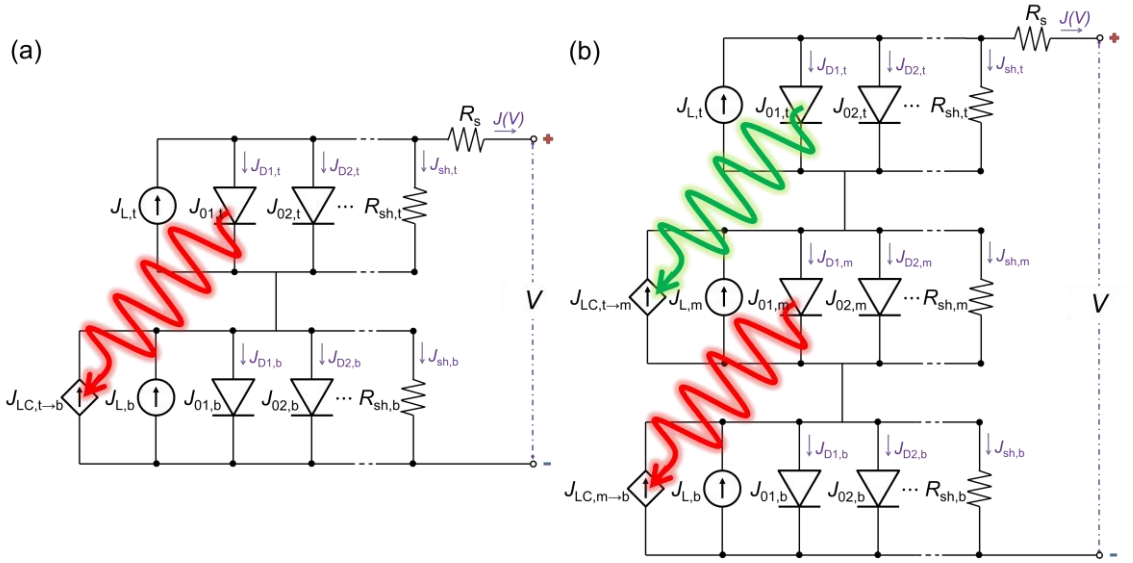

Fig. 6 Equivalent electrical circuit model for (a) 2JSCs and (b) 3JSCs considering LC effect via current-dependent source, $J_{LC,i-1\to i}$.

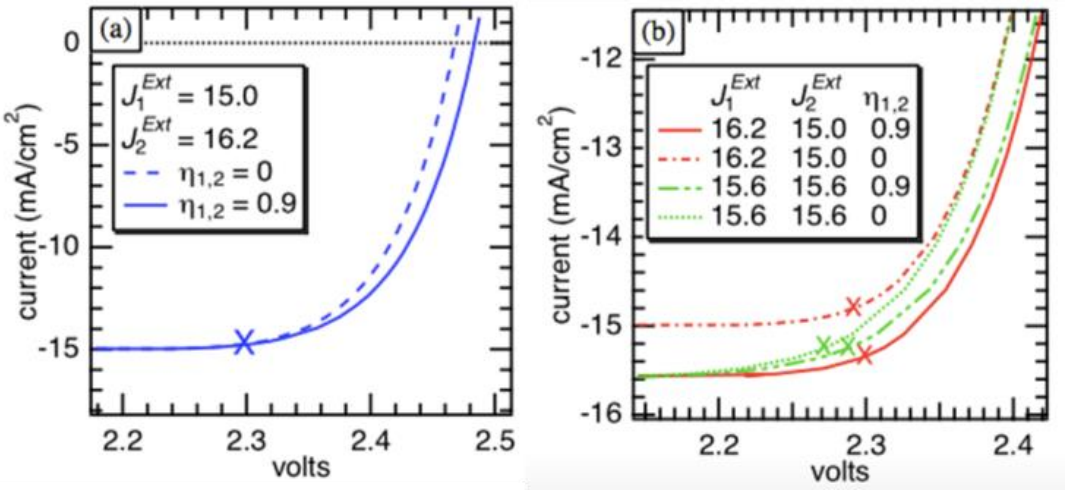

Fig. 7 Current-voltage characteristic plots for top cell limited (external top cell bias photocurrent, J_1^{Ext} < external bottom cell bias photocurrent, J_2^{Ext}), bottom cell limited ($J_1^{Ext} > J_2^{Ext}$), and current-matched ($J_1^{Ext} = J_2^{Ext}$) cases with ($\eta \neq 0$) and without ($\eta = 0$) LC effect [53].

From the *J-V* measurements of MJSCs subjected to severe current mismatch, one can derive the LC yield, γ_{LC}. It is a transfer function that quantifies the amount of adjacent higher bandgap [(*i*-1)'th] subcell radiative current that was successfully transferred into an adjacent lower bandgap (*i*'th) subcell as LC current. γ_{LC} is given as

$$\gamma_{LC} = \frac{J_{LC,i-1\to i}}{J_{rec,i-1}} \tag{9}$$

where $J_{rec,i-1}$ is the total recombination current lost in the higher bandgap subcell [56,116,141]. Here, higher γ_{LC} value indicates better current matching improvement due to the LC effect among 2 adjacent subcells evaluated.

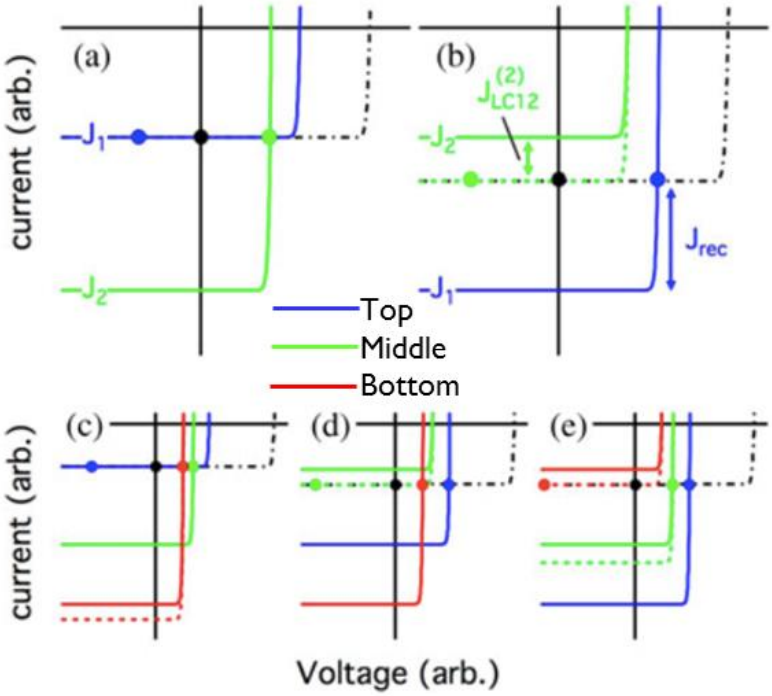

Fig. 8 Individual cells (solid lines) and net *J-V* characteristics (dashed-dotted lines) of 2JSCs at (a) top cell and (b) bottom cell limiting cases, and of 3JSCs at (c) top cell, (d) middle cell, and (e) bottom cell limiting cases [52].

For MJSCs having low or moderate cell quality, parasitic resistance effects cannot be neglected [142]. In the electrical model, non-negligible parasitic resistances are represented by having low shunt resistance and high series resistance, which are expected to affect the generated LC current in a lower bandgap subcell [132]. The impact of parasitic resistances is shown in the γ_{LC} (or γ) plot over increasing photocurrent between adjacent cells in Fig. 9. Having a shunt resistance that is not high enough to be considered infinite results to a high deviation of γ_{LC} from the resistanceless model, where the theoretical results in Fig. 9 were derived. This effect is shown in the low higher bandgap subcell photocurrent (J_{ph}^{HB}) plot. In the high J_{ph}^{HB} regime, the series resistance effects dominate. Here, the higher the series resistance is, the earlier the γ_{LC} breakdown occurs [56]. With these observations, the resistanceless model simulation results fail in representing cells of lower qualities.

To prevent the shunt resistance effects and leakage current to dominate at the low light intensity in real applications, current-limiting cell qualities should be improved. Furthermore, to prevent γ_{LC} breakdown at high J_{ph}^{HB} due to series resistance effects, a moderate solar concentration at around 2000 suns is recommended to be applied to the cell [56].

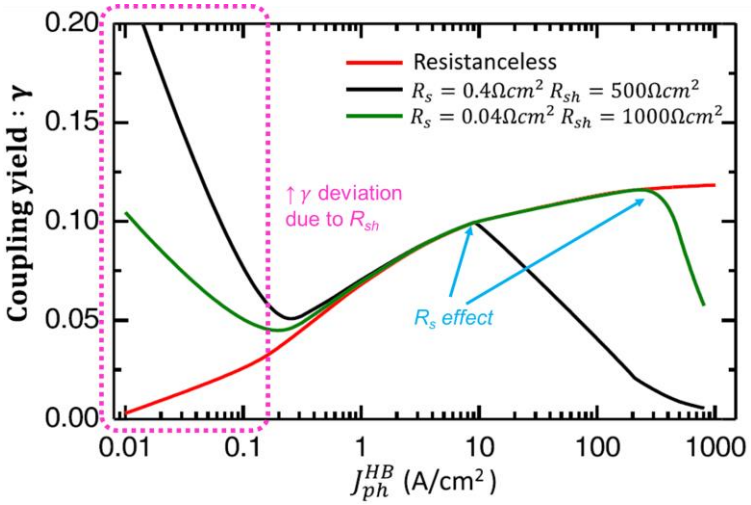

Fig. 9 LC yield (γ) plot against increasing upper bandgap subcell irradiation (J_{ph}^{HB}) subjected to different cases of parasitic resistance effects [56].

1.3.2.2. Nonlinear model for dominant Shockley-Read-Hall (SRH) recombination

In simplified cases, as discussed earlier, the LC factor may be assumed to be linear with the excess current generated in the limiting cell. This is the case if the SRH recombination can be considered negligible. However, in the case of low and moderate quality cells, this effect cannot be neglected as the defects act as additional recombination centers; hence, the equilibrium LC current between adjacent cells must be modeled nonlinearly to account for this process. The nonlinear LC current between the adjacent (i–1)'th and i'th subcells is given as

$$J_{LC,i-1\to i} = \eta_{i-1\to i}\left(\sqrt{\varphi^2 + J_{rec}} - \varphi_i\right)^2 \tag{10}$$

where $\varphi_i = \frac{J_{02}}{2\sqrt{J_{01}}}$ for the nonradiative recombination diode model having an ideality factor of 2 [143].

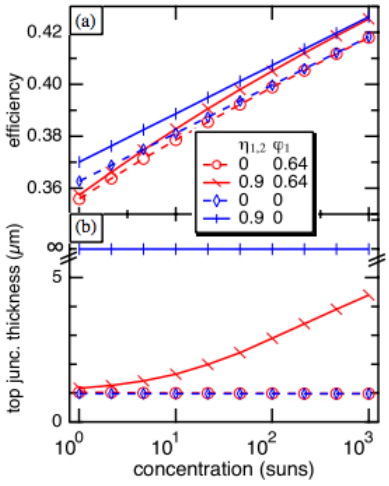

Fig. 10 (a) Cell efficiency and (b) top cell junction thickness as a function of concentration where the blue plots and the red plots correspond to the linear and nonlinear LC models respectively [53,143].

Considering the LC effect in calculating *J-V* characteristics, there is an increase in cell efficiency when LC strength increases with concentration, as depicted in Fig. 10. In addition, it is also illustrated that when the nonlinear model for LC is considered, there is a nonlinear increase in top cell thickness requirement with increasing solar concentration. In using the linear LC model, there was a consistent difference of about 0.75% found in efficiency with increasing solar irradiance. On the other hand, the difference between zero coupling and strong coupling increases with increasing solar irradiance with nonlinear LC model prediction [53,143].

1.3.2.3. Self-consistent numerical modeling

Another approach is by using the self-consistent loop algorithm reported in [56]. Here, the equilibrium J_{sc} of the limiting cell is calculated by the Newton-Raphson iteration method. Assuming that the initial values of photocurrent in each 2JSC subcell are 12 mA and 0 in the top and bottom cell (dark condition), respectively, the LC current at the limiting bottom cell is adjusted per loop iteration. If the recent bottom cell short-circuit current, J_{sc}^{n}, is less than the previous J_{sc}^{n-1}, the LC current is reduced for the next iteration, n+1. Otherwise, the LC current is increased for the next iteration. The loop ends when a converging value has been reached, that is when the difference between the recent and the next iteration LC current is less than or equal to the preset relative approximation error, ε. The algorithm is summarized in Fig. 11(a). Using this simulation algorithm for calculating the *J-V* characteristics of limiting cell that generates LC current, the conversion efficiencies under 1 sun and 1000 suns were estimated to increase to 0.31% and 1.07% respectively, as compared to under no LC effect condition. These results are plotted in Fig. 11(b) [56].

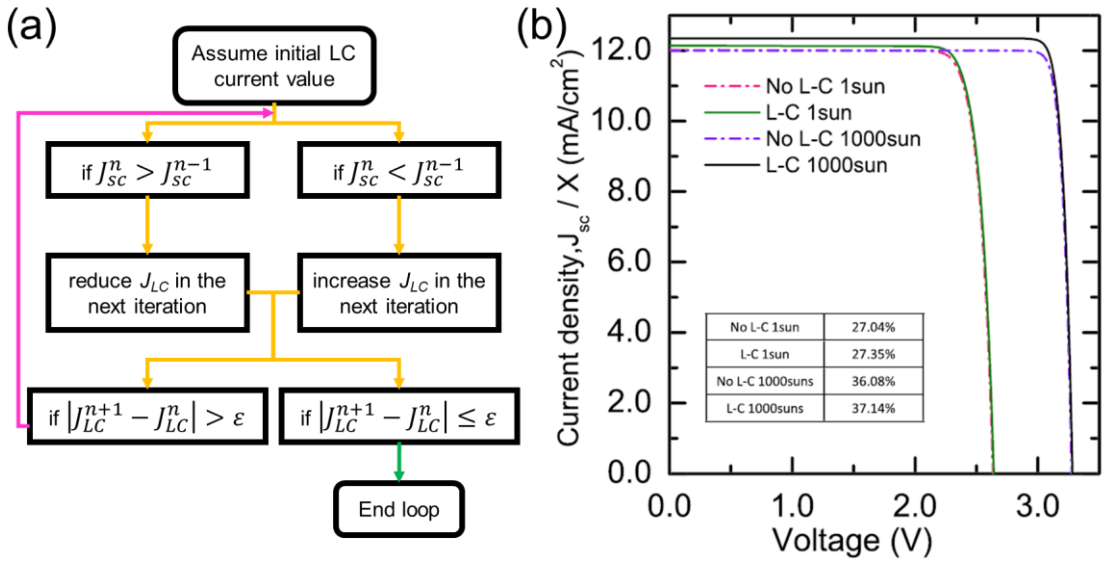

Fig. 11 (a) Summary of self-consistent loop algorithm in finding the equilibrium current between adjacent subcells. (b) Current-voltage (*J-V*) characteristic curves with (solid lines) and without (dashed-dotted lines) LC effect under 1 sun and 1000 sun concentrations [56].

1.3.2.4. Optoelectronic modeling

Since both the electrical bias across an MJSC and the external illumination intensities upon its subcells affect its overall operation performance, a generalized optoelectronic modeling approach (Fig. 12) may be more realistic at any given operating condition than the 2-diode MJSC electrical models illustrated in Fig. 6. Specifically, electrical components such as Zener diodes and tunnel diodes representing the reverse breakdown of a subcell and the carrier tunneling through the tunnel junction were added to the conventional 2-diode MJSC electrical model. Experimental results and generalized optoelectronic model predictions have shown good agreement through empirical fitting [144].

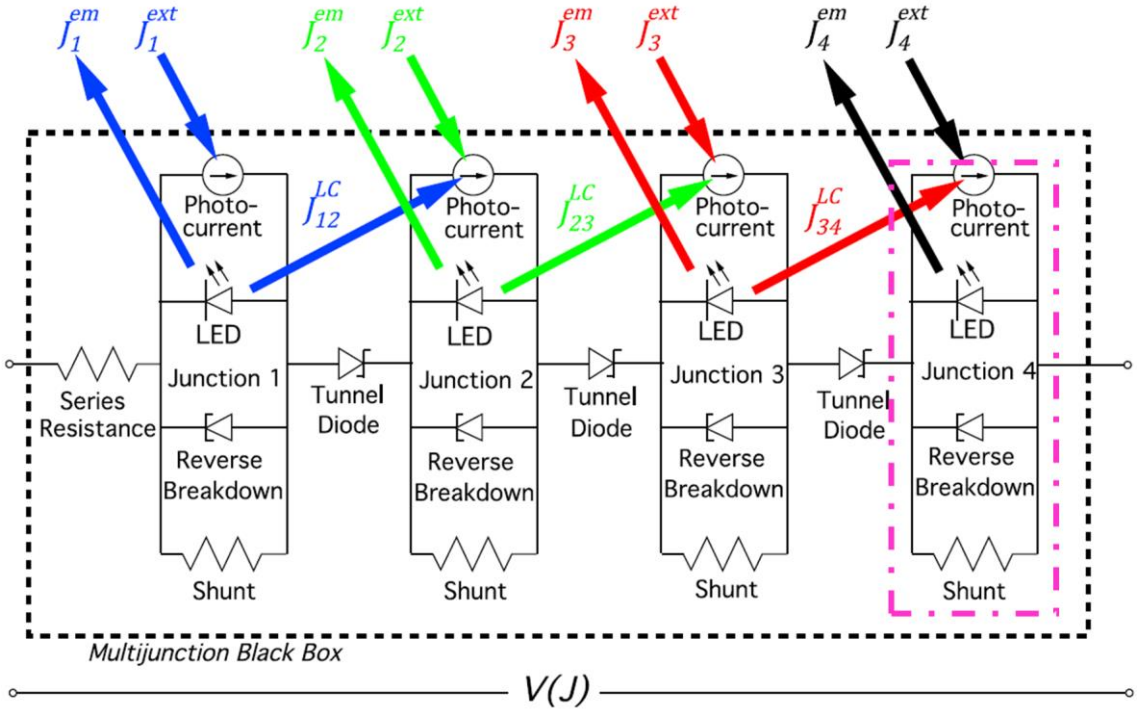

Fig. 12 Equivalent optoelectronic circuit of a series-constrained quadruple junction solar cell, which may be extended to a higher number of junctions by simply adding another tunnel diode and junction subcircuit, enclosed in dashed-dotted box [144].

Quasi-Fermi level (QFL) splitting describes the equilibrium displacement of the electron population in the conduction band and the valence band of a semiconductor separately. QFL splitting is mainly caused by the application of an external voltage or shining light upon the semiconductor that carries energy larger than its bandgap ($E_{light} > E_g$). Hence, treating the dependence of LC efficiency to the applied external voltage across the MJSC and illumination intensity upon an HBG subcell adjacent to a current-limiting cell separately may be essential to understand the interplay between radiative and nonradiative recombination processes. In this context, the LC efficiency, $\eta(V)$, was also treated proportionally to the ratio of radiative recombination current, $J_{rad,HBG}(V)$, and total recombination current, $J_{total,HBG}(V)$, at the HBG subcell, or mathematically given as

$$\eta(V) \propto \frac{J_{rad,HBG}(V)}{J_{total,HBG}(V)} \tag{11}$$

Figure 13 shows the voltage dependence of $\frac{J_{rad,HBG}(V)}{J_{total,HBG}(V)}$ at different light intensities in suns. At low applied voltage, $\frac{J_{rad,HBG}(V)}{J_{total,HBG}(V)}$ remains constant since the QFL splitting is generally affected only by photogeneration. At a certain threshold, carrier injection becomes more apparent, thereby increasing $J_{total,HBG}(V)$. As a result, $\frac{J_{rad,HBG}(V)}{J_{total,HBG}(V)}$ decreases until it reaches a minimum value between the maximum power point voltage, V_m, and open-circuit voltage, V_{oc}. When the applied voltage is further increased, high carrier injection occurs which slows down the $J_{total,HBG}(V)$ increase. Consequently, $\frac{J_{rad,HBG}(V)}{J_{total,HBG}(V)}$ increases again when $V \geq V_{oc}$ [145].

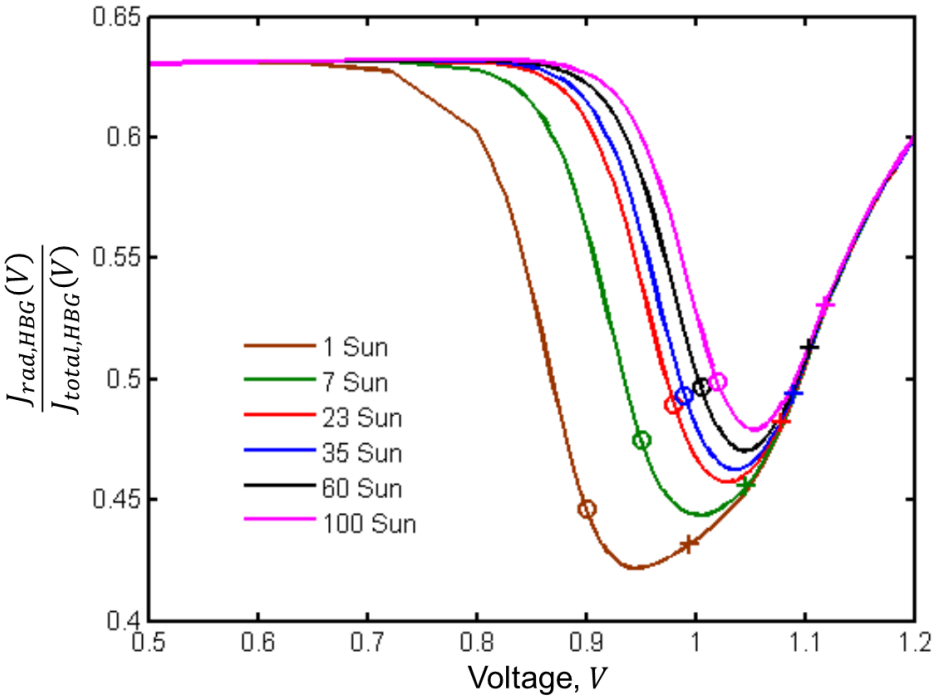

Fig. 13 HBG subcell radiative and total recombination current ratio $\frac{J_{rad,HBG}(V)}{J_{total,HBG}(V)}$ vs applied voltage plot under various illumination intensities, where V_m and V_{oc} points are those points denoted by circles and pluses, respectively [145].

1.3.2.5. Dark current calculation

A more indicative way to determine the LC current is to have the recombination components segregated into radiative and nonradiative components. Upon segregation, the dark current radiative components, I_{rad} collectively, can then be defined as

$$I_{rad} = I_{0,exit} + I_{0,coupling} \tag{12}$$

where $I_{0,exit}$ is the current exiting the surface of the solar cell and $I_{0,coupling}$ is the coupling current traversing to an LBG subcell. This definition assumes that the internally emitted photon either gets reabsorbed in the LBG subcell region or exits through the cell surface,

as illustrated in Fig. 14. In this definition, the internally emitted photon is assumed to be neither reabsorbed in the same junction nor in the non-active layers of the cell. Moreover, it was assumed that there is no significant difference between the indices of refraction of each junction of the 2JSC.

To calculate for $I_{0,exit}$, the cross-section area of the cell, the external incidence angle and the blackbody radiation spectral photon density must be known. The theoretical limit for $I_{0,exit}$ is given by

$$I_{0,exit} = qAn_{air}\int_{E=0}^{\infty} \emptyset_{BB}(E)\cdot 2\pi \times [\int_{\theta_{ext}}^{\frac{\pi}{2}} a(E,\theta)\sin(\theta_{ext})\cos(\theta_{ext})\, d\theta_{ext} dE \quad (13)$$

where n_{air} is the refractive index of air, $a(E,\theta)$ is the absorptance at an incident light angle, θ, θ_{ext} is the escape angle, and the blackbody radiation spectral photon density, $\emptyset_{BB}(E)$, is defined as

$$\emptyset_{BB}(E) = \frac{2}{h^3c^2}\frac{E^2}{\exp\left(\frac{E}{k_BT}\right)-1} \quad (14)$$

In calculating the dark coupling current, the index of refraction, n_{semi}, of absorber layers were determined experimentally. The absorptance is considered to be a hundred percent, that is $a(E,\theta)$=1, when the upper cell absorbs all the incident thermal energy from the lower bandgap subcell; hence, all integral terms for coupling current simplifies to 1/2 [54]. When there is full absorptance, the dark coupling current simplifies to

$$I_{0,coupling} = I_{0,exit}n_{semi}^2 \quad (15)$$

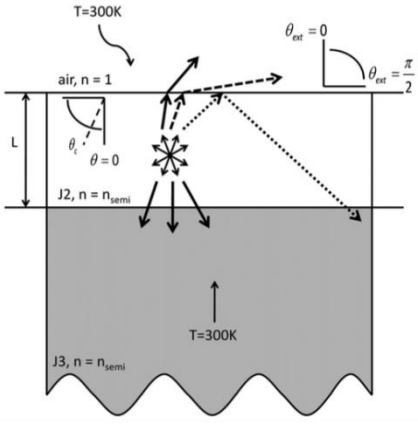

Fig. 14 Schematic diagram of dual junction solar cell under the equilibrium temperature depicting possible paths for radiative emission from the higher bandgap subcell [54].

Thus, the LC current, I_{LC}, can be calculated using

$$I_{LC} = I_{0,coupling}\exp\left(\frac{qV_{final}}{k_BT}\right) \quad (16)$$

where the final voltage, V_{final}, is numerically obtained. Hence, the LC current factor, denoted as X_{LC}, can be determined using the relation

$$X_{LC} \cong \frac{I_{LC}}{I_{SC,Ju} - I_{SC,Jl}} \tag{17}$$

to quantify the amount of LC current present in the cell. Here, $I_{SC,Ju}$ is the short-circuit current of the HBG subcell and $I_{SC,Jl}$ is the short-circuit current of the adjacent LBG subcell. Under the given assumptions, the maximum theoretical LC current factor calculated was approximately 48.17% while the measured one was about 35%. This deviation could be possibly due to other radiative components reabsorbed in the same junction or in the non-active layers of the cell and the nonradiative currents present in the cell which were neglected during the calculation. Moreover, the assumption of both subcells having the same index of refraction may have affected the difference of the calculated and measured results [54].

1.3.2.6. Small-signal electrical model for MJSC external quantum efficiency (EQE)

The EQE evaluation is a conventional method to know how much photons are successfully converted into electrons in a solar cell. Mathematically, EQE is defined as the ratio of the number of photo-generated electrons, *n*, to the number of incident photons, $\emptyset(E)$, that is

$$EQE(E) = \frac{n}{\emptyset(E)} \tag{18}$$

where *E* is the energy possessed by the photon incident to the solar cell [27]. For MJSCs, EQE measurements can be implemented by light bias technique, in which the light sources provide constant illumination upon the solar cell while the monochromated AC light is also in operation. By assimilating the EQE measurements acquired for a solar cell, the short-circuit current, $J_{sc,i}$, can be estimated using

$$J_{sc,i} = \frac{q}{hc} \int_{\lambda_{LL}}^{\lambda_{UL}} \lambda \times EQE(\lambda) \times I_{spec}(\lambda) d\lambda. \tag{19}$$

Here, *h* is Planck's constant, *c* is the speed of light, $I_{spec}(\lambda)$ is the spectral irradiance, $EQE(\lambda)$ is the cell EQE response to incident wavelength, λ, and λ_{UL} and λ_{LL} are the upper and lower limits of the cell absorption range. The subscript *i* is necessary for MJSC J_{sc} calculation, as it is used to refer to a specific subcell.

The EQE of an MJSC is governed by individual subcell properties and interactions between adjacent subcells. To evaluate a specific subcell at a certain voltage, the LEDs must be activated in such a way that this subcell becomes the limiting subcell [146]. Ideally, the subcell photocurrent generated should be equal to the measured output current. If they are not equal, then it could be due to the EQE being nonlinear with respect to varying light intensity [147] or manifestation of a measurement artifact. This artifact has been inferred to either originate from high LC, which corresponds to high shunt

resistance or from very low shunt resistance, which reduces the spectral response of the cell. To measure this artifact, the parameters of small-signal equivalent circuits for subcells are used such as the LC strength, $\alpha_{LC}^{m,b}$, and leakage strength, $\alpha_{LK}^{m,b}$. These parameters can be used to determine the generated photocurrent-output current ratio. If this ratio is equal to 1, then no measurement artifact is present in the evaluated subcell. With these, a tradeoff between high LC and low shunt resistance can be observed. Thus, the optimal light bias is acquired by moderating the shunt resistance or moderating the LC current between adjacent subcells, which can be varied by the applied MJSC voltage [148]. This, in turn, may result in QE response variation since the change in recombination mechanisms may depend on the applied voltage. Besides, optimizing the applied voltage helps compensate for the limiting cell shunt conductance introduced during QE measurements [147].

Typically, EQE measurements employ a dual-channel lock-in technique, in which the incoming EQE signal is multiplied by a signal that is 90° out-of-phase with respect to the reference and then processed through a low-pass filter. Hence, the output signal from the lock-in contains an in-phase (X) and out-of-phase components (Y), where its magnitude, R, and phase shift, φ, are given by

$$R = \sqrt{X^2 + Y^2}; \tan\varphi = \frac{Y}{X} \tag{20}$$

While these values are negligible in low light biasing of nonlimiting subcells, these become significant at high light biasing, which happens under high sunlight concentration. Thus, at high light biasing with significant subcell current mismatch, the current phase shift brought about by lock-in technique should be determined so that the real components of the LC effect and the composite responses may be separated appropriately. Upon doing so, one can determine the optimal voltage that can be applied across the MJSCs during EQE measurements. A simple small-signal electrical circuit representing the tandem solar cell with lock-in phase shift effects during EQE measurements is illustrated in Fig. 15(a) [147].

In a similar study, the EQE signal phase shift from the perspective of measurement artifacts brought about by the combination of LC and shunt resistance effects was studied for 3JSCs [149], but without reactive components for simplicity. The parameters of the small-signal equivalent circuit illustrated in Figs. 15(b) and (c) may be used to determine $\alpha_{LC}^{m,b}$ and $\alpha_{LK}^{m,b}$. These parameters are then used to determine the amount of EQE measurement artifact as given by the relation

$$\frac{i_{out}}{i_{ph}} = \frac{\alpha_{LC}^{m,b} + \alpha_{LK}^{m,b}}{1 + \alpha_{LC}^{m,b}} \tag{21}$$

where i_{out} and i_{ph} are the output current and generated photocurrents respectively. To evaluate the radiative recombination components of a subcell, the external light biases are set such that the light is absorbed by the subcells not being evaluated, and that the evaluated subcell becomes the limiting cell. Here, the adjacent leakage current is the unabsorbed emitted light due to radiative recombination. Additionally, the applied voltage is used for controlling shunt resistance effects, adjustable by changing the load resistance [149].

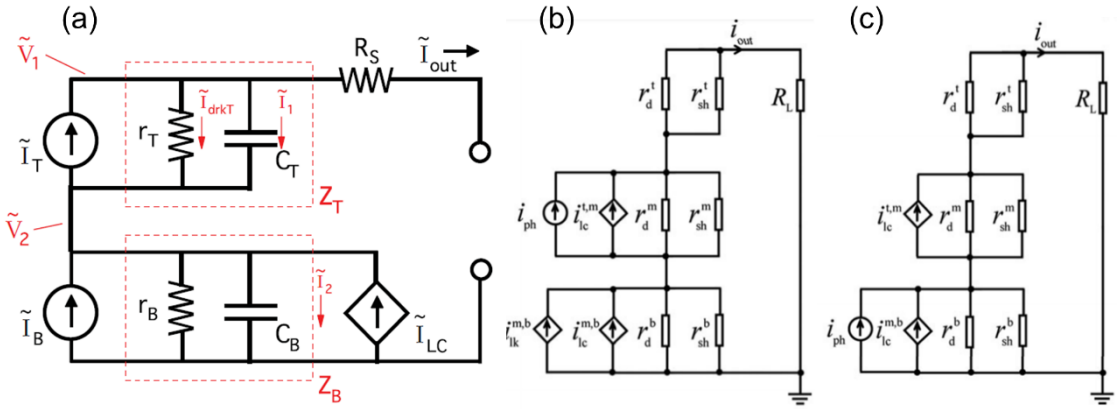

Fig. 15 (a) Small-signal equivalent circuit for tandem solar cells affected by the lock-in phase shift during EQE measurements. Here, diodes were represented by a dynamic resistance and a capacitance, as well as an explicit current source. A dependent current source is also included in the bottom cell to account for the LC effect [147]. The small-signal equivalent circuit for (b) middle cell and (c) bottom cell used for modeling the 3JSC operation during EQE measurements while considering resistive components only [149].

2.1.3.3. Two-dimensional (2D) optical modeling

1.3.3.1. Drift-diffusion modeling of the multijunction photo transducer

Phototransducers have similar structures with MJSCs but are intended for a different application. One application is for laser coupling [150]. While MJSCs are composed of various III-V based semiconductor layers, photo transducer layers can be produced with the same material of different thicknesses. Just like in MJSCs, the LC effect practically occurs in multijunction photo transducer and needs to be accounted for to predict its performance more precisely. Using a 2D drift-diffusion modeling together with realistic recombination parameters, one can properly estimate the internal quantum efficiency (IQE) bandwidth at 90% of the peak for multijunction photo transducer, where IQE is related to EQE as [49]

$$EQE = IQE\big(1 - R(\lambda)\big). \tag{22}$$

Figure 16 (a) shows the 90% IQE bandwidth with an increasing number of junctions. This shows that the IQE bandwidth may be underestimated if the LC effect is neglected. Consequently, EQE [151] and IQE [Fig. 16(b)] predictions for photo transducer may be underestimated when the LC effect is not considered.

1.3.3.2. The physical model for varying shunt defect locations

While most studies assume homogeneous device shunting, defects may exist in random locations in the device bulk in practical situations. Shunt defects affect the LC efficiency [56]; hence, the spatial variation of shunting should be considered for cells of lower qualities. In particular, spatially-resolved physical models may help determine the changes in electric potential, electric field, chemical potential and recombination rate within the vicinity of the defects. An example of a simulated structure and its corresponding physical model with defects included is shown in Fig. 17 [132].

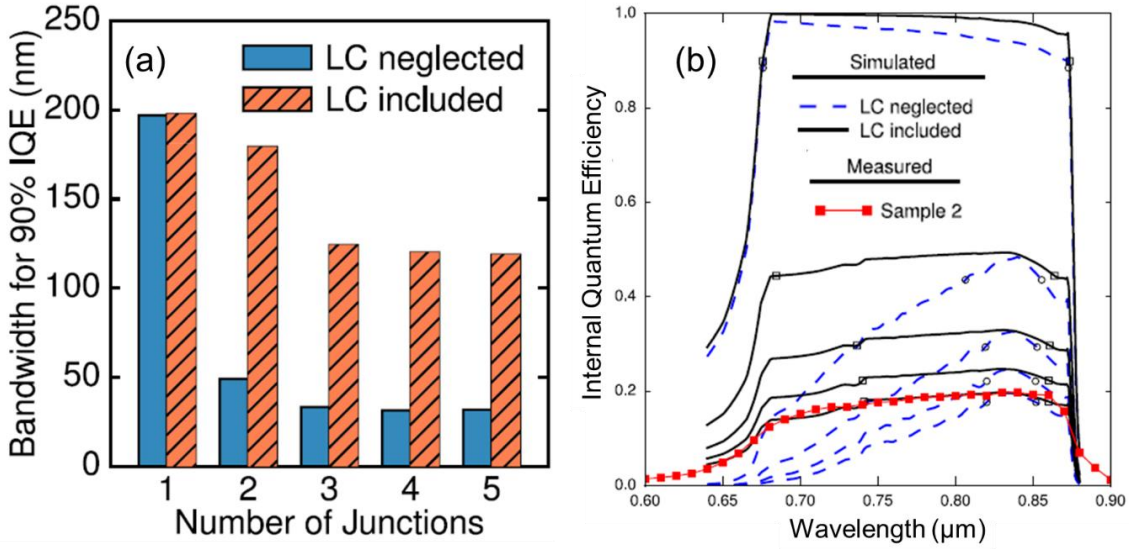

Fig. 16 (a) IQE bandwidth at 90% of peak predicted for 1- to 5- junction photo transducer devices with (hatched bars) and without LC effect (solid bars) considered. (b) Predicted IQE for 1- to 5- junction photo transducer devices with (solid lines) and without LC effect (dashed lines) considered. Here, 90% of the peak is indicated by circles and squares [150].

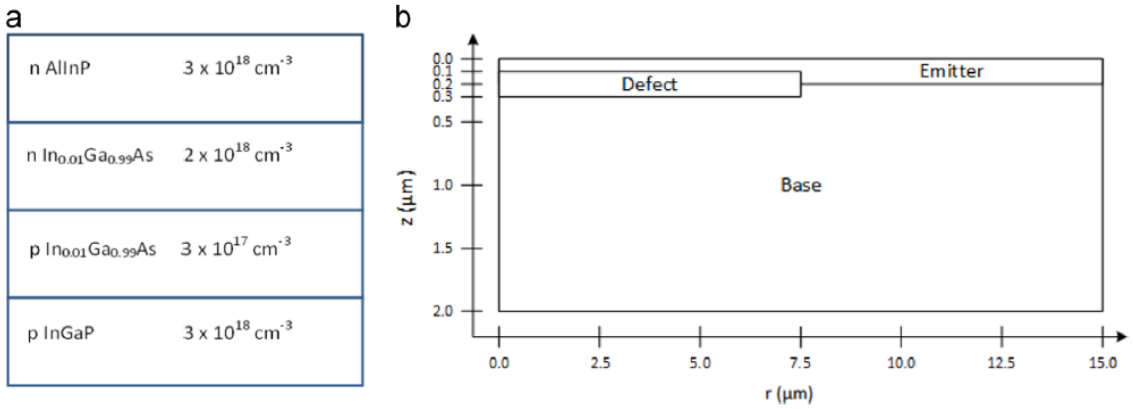

Fig. 17 (a) Schematic illustration of the investigated GaInAs middle-junction and (b) 2D illustration of the modeled junction. Here, the defect has a radius of 7.5 μm and a height of 0.2 μm [132].

1.3.3.3. Derivation of LC efficiency from external luminescence efficiency (ELE) describing photon recycling

The general form of internal luminescence efficiency, $\eta_{int}(\vec{r})$, photon escape probability, $P_{esc}(\vec{r})$, and photon absorption probability, $P_{abs}(\vec{r})$, all varying with position, $\vec{r}$, is related to the external luminescent efficiency, η_{ext}, as

$$\eta_{ext} = \frac{\int \eta_{int}(\vec{r}) P_{esc}(\vec{r}) d\vec{r}}{1 - \int \eta_{int}(\vec{r}) P_{abs}(\vec{r}) d\vec{r}} \tag{23}$$

which can be simplified as

$$\eta_{ext} = \frac{\eta_{int}\overline{P_{esc}}}{1 - \eta_{int}\overline{P_{abs}}} \tag{24}$$

for high-quality solar cells, assuming a uniform distribution of η_{int} over the cell volume. Here, η_{int} is defined as

$$\eta_{int} = \frac{U_{rad}}{U_{rad} + U_{nr}} \tag{25}$$

where U_{rad} is the radiative recombination rate and U_{nr} is the total nonradiative recombination rate. Meanwhile, $\overline{P_{esc}}$ and $\overline{P_{abs}}$ are the averaged photon escape and absorption probabilities over energy, solid angle and cell volume. In principle, high η_{int} in an HBG subcell causes a strong LC effect, which then increases the photogenerated current in an adjacent LBG subcell; hence, a recovery that minimizes parasitic luminescence absorption in the tunnel junctions between the adjacent subcells. For those photons exiting out of an absorber layer but will be reabsorbed through LC effect, LC efficiency definition can be adopted from η_{ext}. This may be then given as

$$\eta_{LC} = \frac{\eta_{int}\overline{P_{LC}}}{1 - \eta_{int}\overline{P_{abs}}} \tag{26}$$

where $\overline{P_{LC}}$ is the averaged luminescent coupling probabilities over energy, solid angle and cell volume [123].

2.1.3.4. Three-dimensional (3D) electrical distributed modeling

Multiple studies have reported the use of 3-dimensional (3D) distributed electrical circuits to study the space-variant LC effects in concentrated MJSCs. A sample 3JSC design is shown in Fig. 18. In 3D modeling, the LC effect is defined in the circuit model either by a voltage-controlled or a current-controlled current source. In verifying the circuit model design, MJSC characterization results by the pulsed bias method [152], EL/PL mapping [153–154] and LBIC mapping [141] at room temperature were assimilated into the 3D model for empirical fitting.

2.1.3.5. Separate treatment of electrical and optical coupling

Another route proposed to increase the accuracy of MJSC modeling with the LC effect is to distinguish its electroluminescence (EL) and PL coupling components and then treat them separately. Particularly, to PL coupling, this is hypothesized to be more significant when the higher bandgap subcell, where the luminescence originates, is operating near or below the maximum power point voltage [145] or when recombination at the junction defects between the coupled subcell dominates. In the case of high-quality MJSC subcells with minimal shunt defects, EL coupling modeling alone is sufficient. However, as discussed earlier on phase shift affecting AC measurements acquired by lock-in technique, the need for optimizing the measurement frequency [155] and also electrical and optical biases upon HBG, nonlimiting cells arises to minimize its reactive components [147]. Figure 19 shows an equivalent steady-state electrical circuit that includes 2 separate current-generation components by EL and by PL coupling [155]. Here, J_i^{Ext} is the external bias photocurrent generation in the *i*'th subcell where *i* is denoted as N-1 (HBG) or N (LBG subcell) in the circuit, J_i^{EL} is the EL coupling current generation, J_i^{PL} is the PL coupling current generation, R_S is the lumped series resistance, $R_{Sh,i}$ is the

subcell shunt resistance, J_i^D is the combined diffusion and radiative recombination saturation current, and J_i^{2D} is the junction recombination saturation current. For the topmost subcell, $J_{EL} = J_{PL} = 0$, since no coupling towards the highest bandgap subcell is possible. This model was validated using EQE measurements.

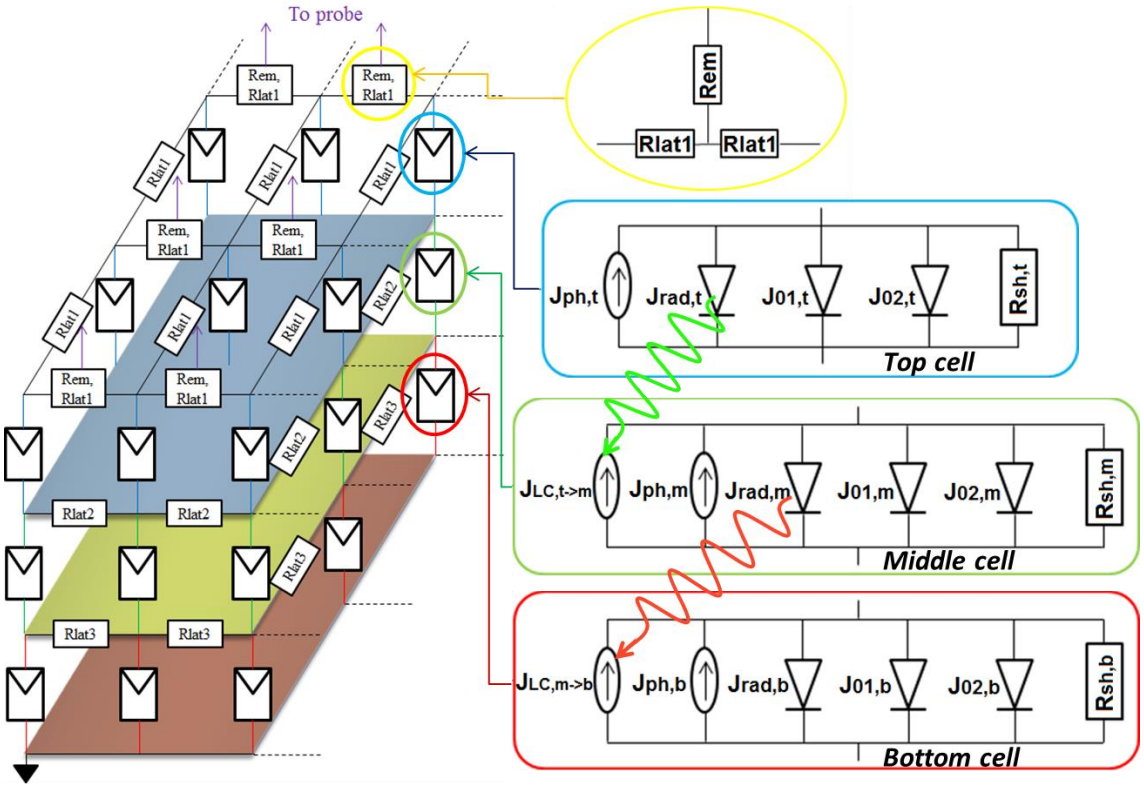

Fig. 18 3-dimensional distributed electrical circuit model of a 3JSC, where $J_{ph,i}$ is the external optical bias photocurrent generation, $J_{LC,i-1\rightarrow i}$ is the LC current, $J_{rad,i}$, $J_{01,i}$ and $J_{02,i}$ are the radiative, diffusion, and SRH recombination diode coefficients, R_{em} is the lumped emitter resistance, $R_{sh,i}$ is the subcell shunt resistance and *RlatN* is the subcell lateral resistance [141].

In the analytical form, the PL coupling efficiency, $\frac{\kappa_{i-1\rightarrow i}}{\beta_{i-1\rightarrow i}}$, from a higher bandgap subcell, *i*-1, to a lower bandgap subcell, *i*, was incorporated into the two-diode equation discussed earlier as [156–157]

$$J(V_i) = (1-\eta_{i,i})J_{01,i}\exp\left(\frac{qV_i}{k_BT}-1\right) + J_{02,i}\exp\left(\frac{qV_i}{mk_BT}-1\right) - \eta_{i-1\rightarrow i}\,J_{01,i}\exp\left(\frac{qV_{i-1}}{k_BT}-1\right) - \frac{\kappa_{i-1\rightarrow i}}{\beta_{i-1\rightarrow i}}J_{L,i-1} - J_{L,i} \quad (27)$$

where $\eta_{i,i}$ is the internal luminescence efficiency and $\eta_{i-1\rightarrow i}$ is the EL coupling efficiency.

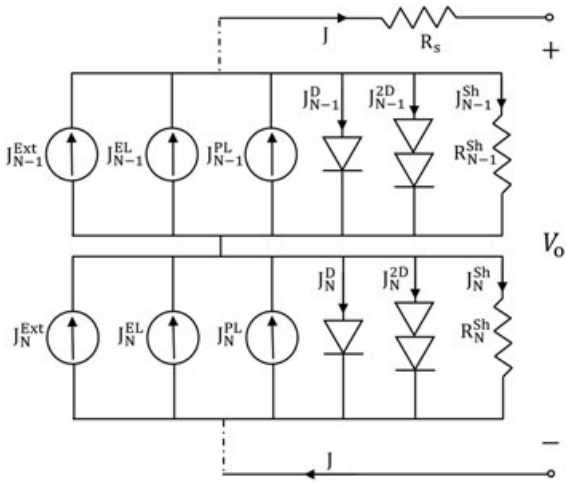

Fig. 19 Schematic diagram of an optoelectronic circuit model for a monolithic tandem solar cell having separate current sources representing EL and PL coupling [155].

2.1.3.6. Bipolar junction transistor (BJT) modeling of MJSCs

In another study, based on a past analytical study on the optical gain of heterojunction phototransistors [158–159], the observed discrepancies between the MJ subcell J_{sc} values and the subcell current derived from QE measurements was explained using *npn* and *pnp* BJT models, focusing more in the EL coupling among subcells [160]. In Fig. 20(a), the electrical circuit model of a 2JSC is represented using a 3-diode model, together with photocurrent sources per subcell, $J_{SC,1}$ and $J_{SC,2}$. Here, the diode between each subcell represents the tunnel junction. Equivalently, the 3-diode model may be also represented using *npn* and *pnp* BJTs, considering the back-to-back connection of the *pn* diodes [Fig. 20(b)]. From this configuration, the net short-circuit current of the 2JSC, $J_{SC,2J}$, considering EL coupling can be calculated using the relation

$$J_{SC,2J} = \frac{\alpha_1\alpha_2 J_{SC,1} + J_{SC,2}}{1 + \alpha_1\alpha_2 - \alpha_2} \tag{28}$$

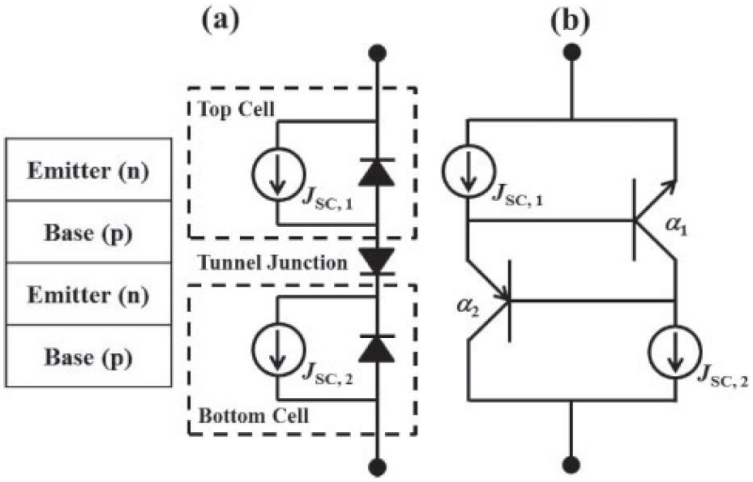

Fig. 20 Equivalent electrical circuit models of *n*-on-*p* 2JSCs using (a) three *p*–*n* diodes and (b) *npn* and *pnp* BJTs [160].

where α_1 is the common base current gain of the *npn* BJT and α_2 is the common base current gain of the *pnp* BJT. If α_1 and α_2 are independent of $J_{SC,i}$, then $J_{SC,1}$ and $J_{SC,2}$ are scalable with solar irradiance. The *npn* BJT base current represents the holes generated in the top cell while its emitter current represents the electrons injected from the top cell emitter. On the other hand, the *pnp* BJT emitter current represents the hole injection into the bottom cell emitter, which is also the base of this transistor. For more quantitative analysis, it was recommended to characterize the potentials at the base of the middle cell and the emitter of the bottom cells [160].

2.1.4. Experimental observations

2.1.4.1. Current-voltage (*J-V*) characteristics

The conventional way to extract the electrical performance of a solar cell in a single picture is by measuring its light *J-V* characteristics. Although outdoor illumination is seldom used due to its intermittency, solar simulators are used in laboratory-scale performance evaluation of solar cells. These simulators are calibrated according to ASTM International G-173-3 reference spectra [161] and are used to characterize MJSCs under spectrally matched conditions.

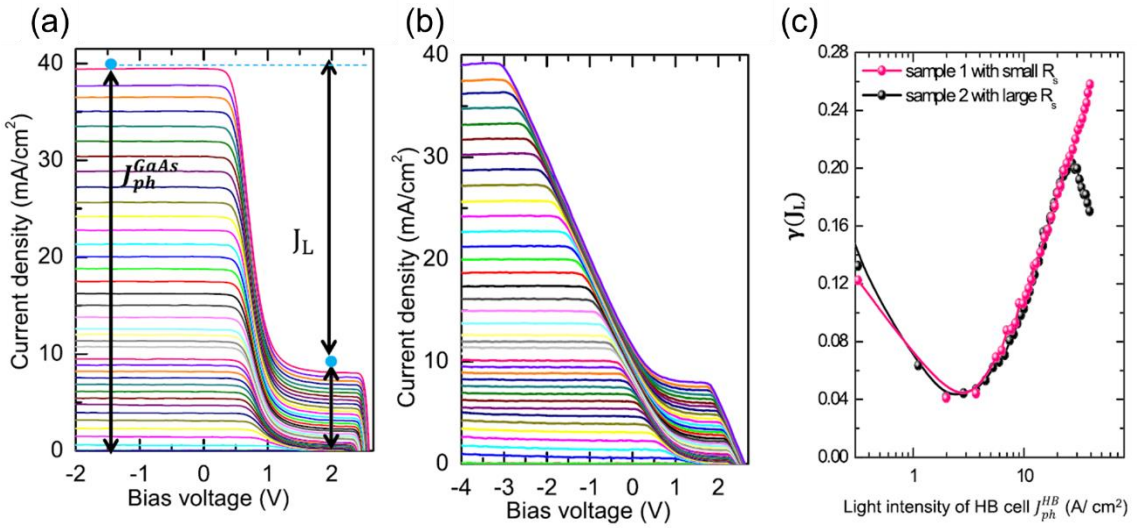

Fig. 21 Measured DC *J-V* characteristics of Ge bottom cell in InGaP/GaAs/Ge 3JSC under various light intensities upon GaAs middle cell (a) with low R_S and (b) with high R_S. (c) LC yield, $\gamma(J_L)$, derived from the experimental results shown in (a) and (b) at an applied 3JSC voltage V = 2.0 V [56].

Meanwhile, it is more convenient to study LC effect under spectrally-mismatched conditions, that is, by modifying optical biases upon nonlimiting cells within their absorption ranges. A way to impose this condition upon series-constrained MJSCs is by using single-wavelength LED biases, as implemented in [56]. In this method, the subcell to be evaluated is made current-limiting by illuminating absorbable single-wavelength LEDs upon the non-evaluated subcells to make them nonlimiting. Figures 21(a) and (b) are measured *J-V* characteristics of Ge bottom cell in InGaP/GaAs/Ge 3JSC samples with low and high series resistance, R_S, respectively. This was implemented by illuminating 430 nm LED at high and fixed intensity upon InGaP and 660 nm LED at various

intensities. From these *J-V* curves, one can derive the LC yield, denoted as $\gamma(J_L)$ in Fig. 21(c) but calculated using the same definition given by eq. (9) [55–56,141].

2.1.4.2. External quantum efficiency (EQE) measurements

Aside from light *J-V* characteristics, EQE measurement artifacts have been discussed in numerous reports as an indicative presence of LC effect in multijunction photo transducer [150] and III-V based MJSCs at low applied external voltage [50,52,142,146,148,162–165]. In some studies, a larger artifact was interpreted as an indication of high subcell quality [166]. Meanwhile, in some EQE measurement observations, the presence of the LC effect between adjacent MJ subcells was claimed to be a source of error since this produces signals outside the wavelength absorption range of the evaluated subcell and then underestimates the signals within its absorption range. Also, inactive layers within the cell are capable of absorbing and reemitting light through radiative recombination processes, which may then contribute to LC current generation in a lower bandgap active subcell [49].

In practice, single-wavelength optical signals are used for separating series-constrained MJ subcells. Figure 22(a) shows the EQE measurement of a lattice-matched, monolithic InGaP/InGaAs/Ge 3JSC. Outside the absorption range of the Ge bottom cell (< 900 nm), one can observe EQE signals at around 15%, indicating the presence of LC effect and treated as an artifact. Meanwhile, in the Ge absorption range (> 900 nm), reduced EQE signals were obtained. The same was acquired from 3-terminal, mechanically-stacked GaInP/GaAs//GaInAsP/GaInAs 4JSC, with GaInP/GaAs and GaInAsP/GaInAs tandems in series connection, as shown in Fig. 22(b). In each tandem, strong LC in GaAs and GaInAs was observed, as indicated by the EQE signal outside their respective absorption ranges. These signals were used for correcting the EQE signals within their absorption ranges.

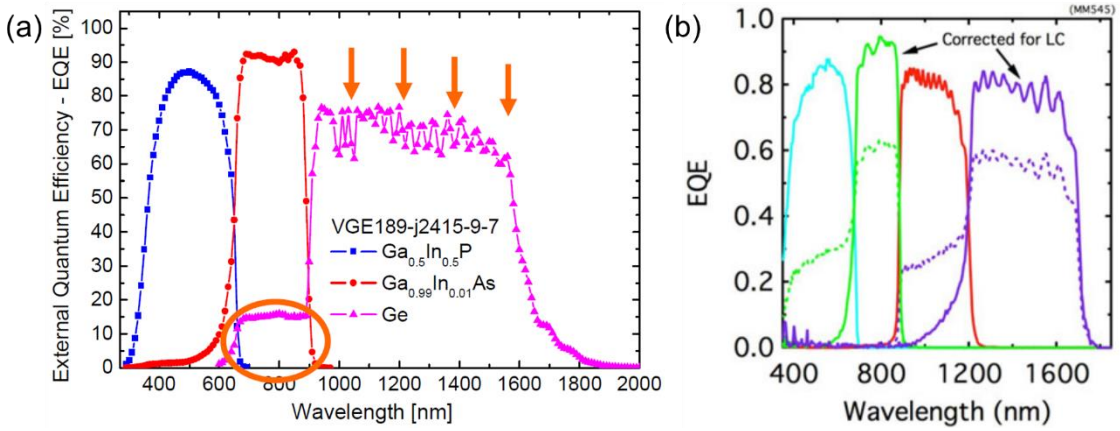

Fig. 22 (a) EQE measurement of lattice-matched, series-constrained GaInP/GaInAs/Ge 3JSC. The artifact outside the Ge bottom cell absorption range (< 900 nm) is enclosed with a circle and the arrows pointing downward indicates an underestimated EQE signal in the Ge absorption range (> 900 nm) [148]. (b) External quantum efficiency of GaInP/GaAs//GaInAsP/GaInAs 4JSC before (dotted line) and after artifact correction (solid line) [163].

Figure 22(b) shows the difference between the EQE measurement before and after the correction. Before the correction, nonzero tails of EQE measurements can be seen before reaching their peak values for GaAs and GaInAs subcells. These tails indicate the presence of LC from GaInP to GaAs and from GaAs to GaInAs subcells respectively.

Applying correction then indicates that the EQE enhancement due to LC effect has been transferred to the lower bandgap subcell, which truly benefits from the said effect, as indicated by EQE increase in GaAs and GaInAs subcells [163,166].

Since the LC effect involves optoelectronic processes and is nonlinear at higher incident light biases upon a higher bandgap subcell, the artifact may differ according to incident wavelength [143]. The EQE measurement artifact defined by eq. (21), as derived from a nonreactive, small-signal circuit model in Fig. 15, may be used to gain further insights about this signal. In InGaP/GaAs/Ge 3JSCs tested, the current generation in Ge bottom cell is found to differ by the optical wavelength applied, as illustrated by the EQE measurement artifact in an LBG subcell (Ge) vs. HBG subcell (InGaAs) incident photocurrent plot in Fig. 23(a). The differences observed were either be attributed to shunt leakage current or LC effect. For 780 nm incident light, which is outside Ge absorption range, the EQE measurement artifact was observed to amplify during the following: (1) with less InGaAs middle cell photocurrent since it becomes less forward biased and its small-signal resistance becomes comparable to that of the shunt resistance of the bottom cell – hence, shunt leakage current-dominated; and (2) with high InGaAs photocurrent since increasing bias light intensity increases its voltage and radiative recombination efficiency, thereby indicating strong LC effect. Consequently, for 980 nm incident light, the artifact decreases with extremely low or high photocurrent [149,162]. These experimental observations confirm that an optimal light bias must be sought after to minimize artifact signal at any incident wavelength during measurements employing a lock-in technique like for EQE.

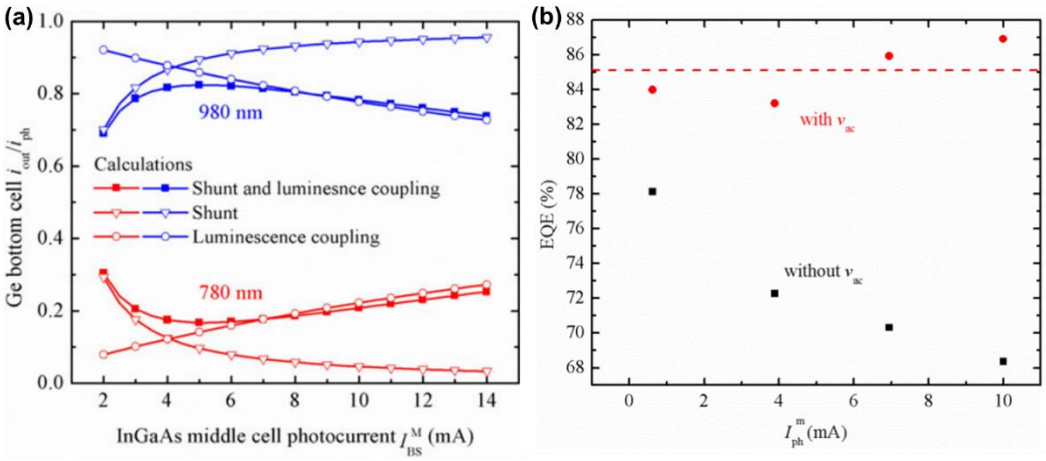

Fig. 23 (a) Bottom cell output-photocurrent ratio with increasing middle cell photocurrent plot [149]. (b) EQE without (squares) and with pulse voltage bias correction (circles) plot [167].

One technique that may be used to correct the measurement artifact is by applying a correcting pulse voltage bias, v_{ac}, upon the cell under evaluation [167]. In Fig. 23(b), the square symbols are the EQE measured using the conventional lock-in method while the circles are those measured with v_{ac} correction. With the latter, the EQE drop observed in the Ge bottom cell was avoided and sustained close to 85% (dashed line), which is the predicted EQE signal. Upon further calibration, one can obtain the true EQE signal of highly shunted lower bandgap subcells or of those subcells that are capable of yielded high LC efficiency. Other methods for EQE artifact correction can be found in [148].

2.1.4.3. Spectral response-voltage (*SR-V*) measurements

To detect the presence of LC, the spectral response-voltage bias (*SR-V*) method can be used. First, the AC light *J-V* characteristics are obtained using pulses of different wavelengths within the absorption range of the evaluated subcell. Figures 24(a) to (c) show the *SR-V* measurements for InGaP, GaAs, and Ge of InGaP/GaAs/Ge 3JSCs, respectively. From these measurements, an equilibrium current between adjacent subcells is numerically determined using the self-consistent model used in [168]. Because current imbalance happens among subcells when a specific light wavelength is an incident upon a specific subcell, after some time the equilibrium current will be reached. Good convergence value of the equilibrium current can be obtained after 15 iterations, as shown in Fig. 24(d) [56]. From this equilibrium current, one can infer the strength of the LC effect, that is, the higher the equilibrium current is, the stronger the LC is. When the first derivative of the *SR-V* curves per subcell is plotted, the linearity with voltage can be observed. The insets of Figs. 24(a) to (c) plots show that *SR-V* is independent of measurement wavelength. Therefore, a single absorbable wavelength will suffice to implement this method [169]. These findings could then imply that using single-wavelength sources may be sufficient for other methods of AC measurements such as laser beam induced current (LBIC) mapping to observe the electrical performance of a specific MJ subcell, as demonstrated recently [141,170–173].

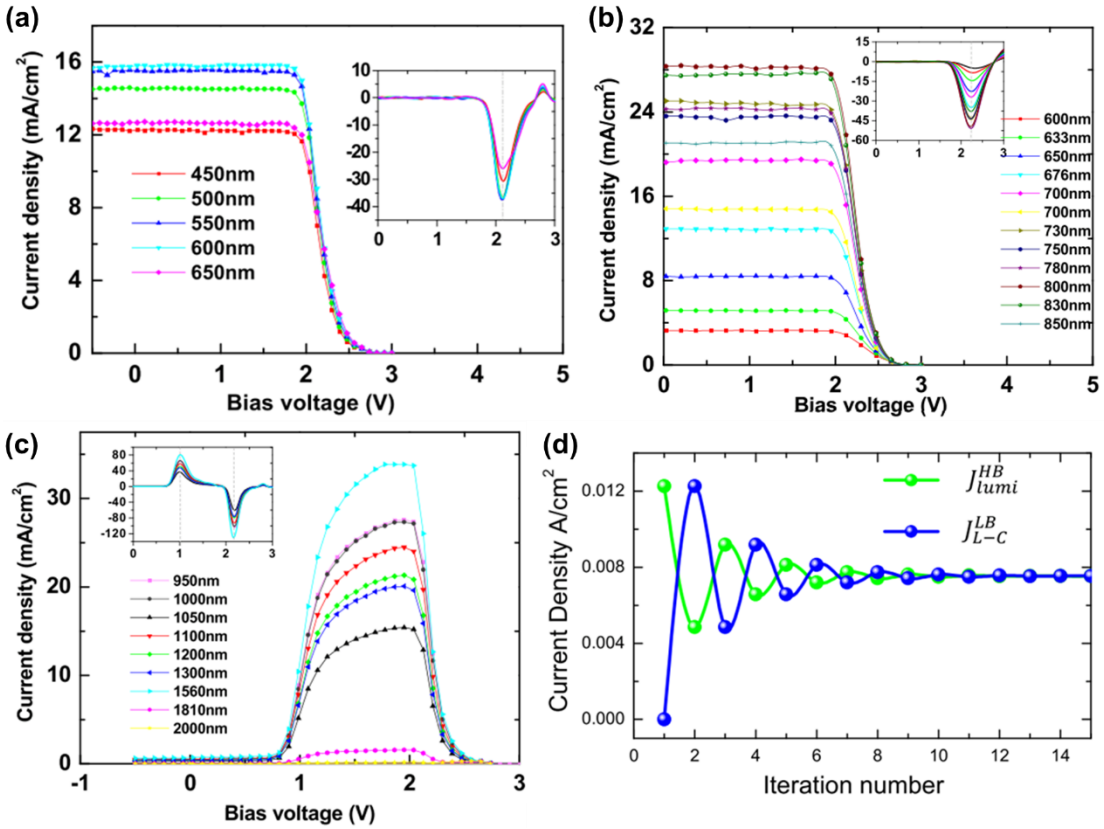

Fig. 24 Measured *SR-V* curves from (a) InGaP top cell, (b) GaAs middle cell and (c) Ge bottom cell of an InGaP/GaAs/Ge 3JSC [169]. (d) Predicted equilibrium LC current after 15 iterations of self-consistent loop calculation [56].

2.1.4.4. High-concentration, pulsed measurements

For MJSC performance evaluation at high concentration, pulsed measurements can be done. This prevents MJSC samples from getting degraded by high radiation and increased operating temperature which may arise when the continuous high-concentration solar simulator is used. In this method, wavelength range-specific light filters upon the variable concentration of solar simulators can be used, as implemented in [55,141]. In Fig. 25(a) illustration, various light filters can be moved along the horizontal plane to make a specific MJ subcell current-limiting during pulsed measurements. By smoothly shifting the opaque shields, one can modify the incident light intensity upon the MJSC sample [55]. The notable difference of this setup with the one used in [141] is that the light filters in the latter were fixed; hence, it needs to be replaced when another subcell at high concentration will be evaluated.

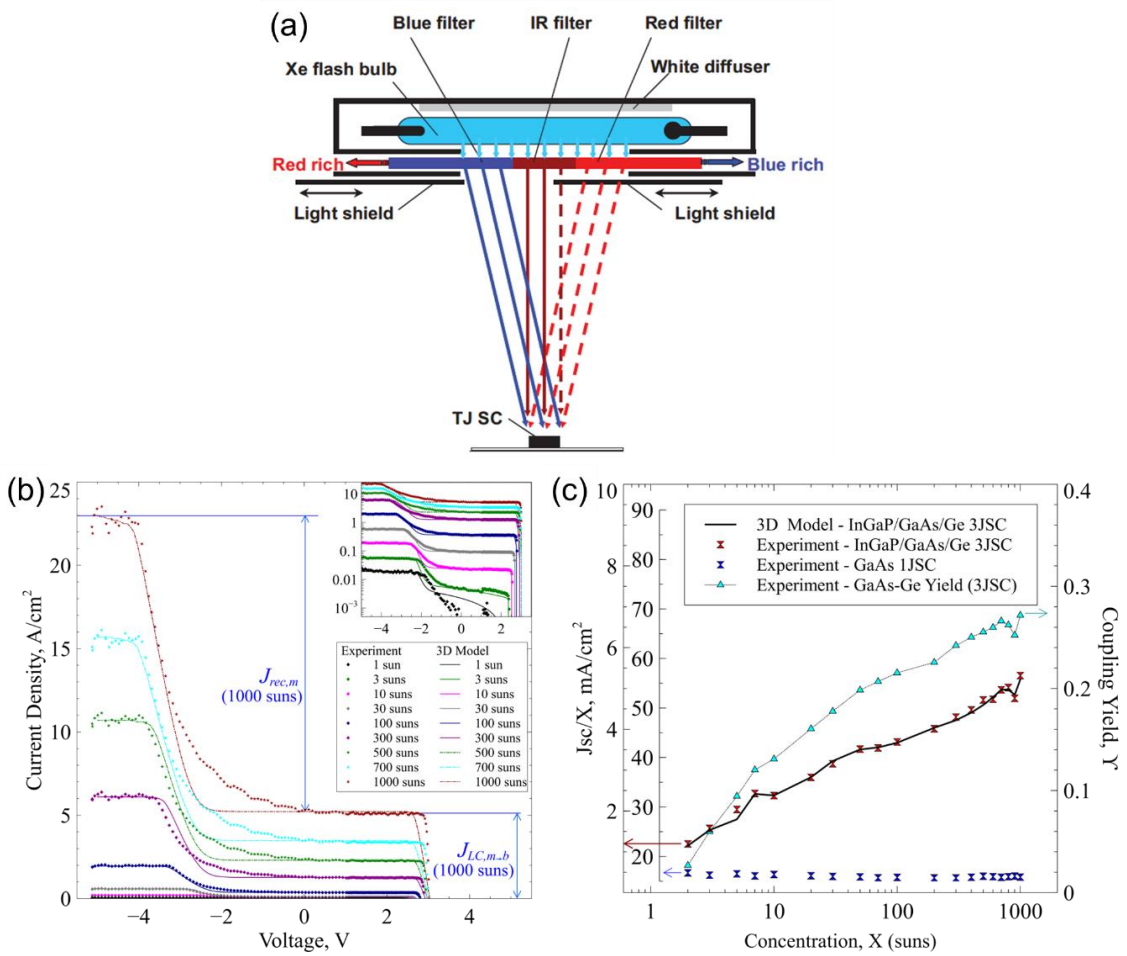

Fig. 25 (a) Schematic illustration of high concentration, pulsed solar simulator measurement setup. (b) DC *J-V* characteristics measured under different concentrations acquired using pulsed light with a short pass filter. This is to current-limit the Ge bottom cell of InGaP/GaAs/Ge 3JSC characterized. The inset shows the set of characteristics curves with current density axis in logarithmic scale. Note that the outer plot and the inset have common legends used. (c) J_{sc} normalized with concentration ratio, X (left axes), and experimental LC yield, γ, (right axis) vs. X plots at an applied 3JSC voltage of 2.0 V. Here, (a) is from [55] and (b) and (c) are from [141].

In Fig. 25(b), the *J-V* curves of Ge bottom cell in InGaP/GaAs/Ge 3JSC samples were acquired by placing a low-pass filter between the solar simulator set at concentrations from 1 to 1000 suns and the cell during measurements [141]. Similarly, the Ge LC yield denoted as γ in Fig. 25(c), and the concentration-normalized J_{sc} of 3JSC compared with that of single-junction GaAs solar cell under various conditions can be derived as well.

Using a 100-times concentrated direct air mass 1.5 (AM 1.5D) spectrum, calculations in Fig. 26(a) show that including LC effect lowers the theoretical efficiency limit by almost 5% [174]. (Meanwhile, the difference between optical coupling and LC was not explicitly stated in [174]. Hence, only with and without LC effect was reviewed in this section.) On the other hand, using an annually obtained AM 1.5D spectrum from a specific location in calculations revealed that with LC effect, the energy efficiency was higher than when there was no LC effect considered [Fig. 26(b)]. In parallel, measured data was obtained using a thermal high-intensity pulsed solar simulator (THIPSS). Notably, the measured data at standard test conditions (STC) was close to the predicted values at STC, that is, the temperature and concentrations beyond 200 to 300 times of AM 1.5D spectrum reduce the energy efficiency of solar cells even when benefiting from LC effect [175].

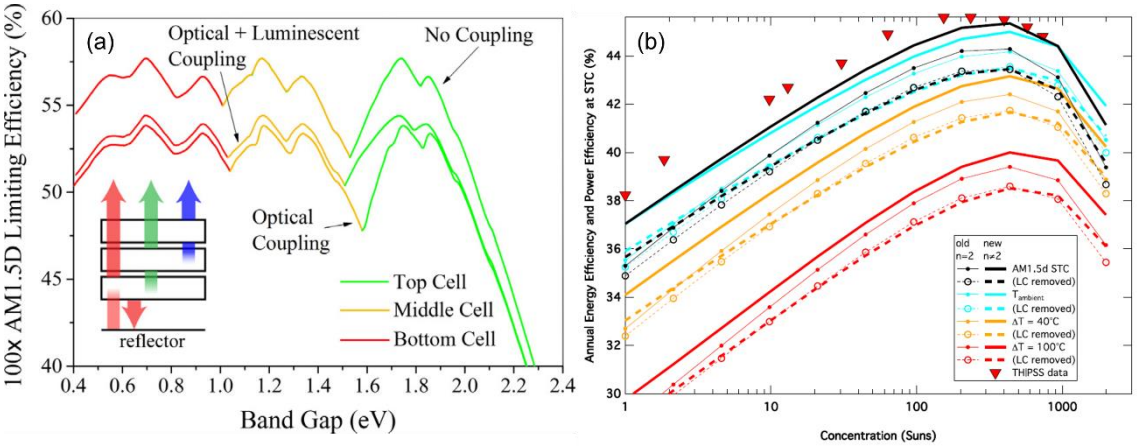

Fig. 26 (a) Theoretical limiting efficiency with respect to varying subcell energy gaps of 3JSC calculated under 100 times concentrated AM1.5D spectrum without any coupling (uppermost line), with both optical coupling and LC effect (middle line) and with optical coupling only (bottom line) [174]. (b) Calculated (solid lines and symbol-lines) and measured (at STC, inverted triangles) annual energy production conversion efficiencies of 4JSC for the annual spectra set obtained at Golden, Colorado, USA considering the cell operating temperatures and concentration with and without LC effect. Here, the old and new data corresponds to the assumed ideality factor equal to 2 and not equal to 2 for the subcell depletion region recombination, respectively [175].

2.1.4.5. Absolute EL measurements

The absolute EL efficiency measurement may be used to characterize the different loss mechanisms in a GaInP/GaAs/Ge 3JSC [176–177]. Furthermore, this technique was proposed to seek a standardized method for measuring individual MJ subcell properties. This measurement method can be implemented using a spectrometer and a photodiode. The different loss mechanisms present in an MJSC such as junction loss, nonradiative loss, radiative loss, thermalization loss, and LC can be quantified using this method. In Fig. 27(a), the absolute EL intensity divided by the number of electrons injected is plotted with respect to increasing photonic energy under different injected current densities. This plot shows that the peaks under different current densities converge at the energy gaps of

the subcells, which are at approximately 1.85 eV and 1.4 eV for GaInP and GaAs respectively. From these plots, the external EL efficiency can be derived by integrating the EL peaks obtained from the absolute EL intensity spectra based on the carrier balance equation introduced in the same paper. From the mentioned equation and the reciprocity relation between EL and EQE, the energy losses per subcell can be obtained. Specifically, the LC energy loss component, $R_{ext,i\rightarrow i+1}$, can be calculated as given by the equation

$$R_{ext,i\rightarrow i+1} = \begin{cases} \left(\frac{a_{bottom}}{a_{top}}\right) n_{i+1}^2 R_{ext,i\rightarrow 0} & (n_{i+1} \leq n_i) \\ \left(\frac{a_{bottom}}{a_{top}}\right) n_i^2 R_{ext,i\rightarrow 0} & (n_{i+1} \geq n_i) \end{cases} \tag{29}$$

where a_{top} and a_{bottom} are the angle-arranged absorptivity or emissivity evaluated experimentally for top and bottom cells respectively. The results are summarized in the schematic in Fig. 27(b). This schematic gives an overview of what makes the cell conversion efficiency degrades. It was reported that 30.5% of the incident light is processed in the top cell, 22.4% is processed in the middle cell and 20.7% is processed in the bottom cell. The missing 26.4% of the incident light accounts for the transmission loss. The overall thermalization loss, nonradiative recombination loss, and junction loss are 18.5%, 6.8%, and 19.6% respectively. With these loss mechanisms present, the overall output was observed to reduce to 28.7%. It is noteworthy that the external emission loss and the LC loss, which were measured to be 1×10^{-5} and 9×10^{-5} respectively are comparatively negligible to other loss mechanisms evaluated. The low loss could be due to the radiative dark current causing current generation in the same (photon recycling) or in the adjacent subcell (LC effect), which are then accounted in the output per subcell [177].

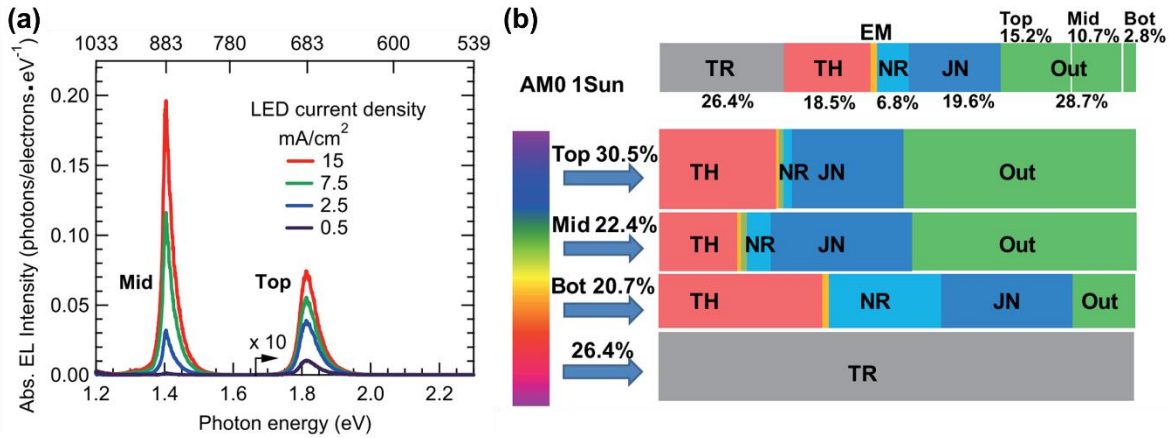

Fig. 27 Absolute EL intensity versus photonic energy plot for the top cell (GaInP) and middle cell (GaAs) of a triple-junction solar cell. (b) Schematic of loss mechanisms in GaInP/GaAs/Ge triple-junction solar cell [177].

2.1.4.6. Suns-open-circuit voltage (Suns-*Voc*) method

In the suns-V_{oc} method, the diode parameters of MJ subcells can be determined using a pulsed, monochromated light upon subcells without having to worry about the junction capacitances [178–179] and the series resistance effects brought about by the

measurement setup probing itself [180]. In this technique, the LC current is treated as a current-generation source, which is dependent on the HBG subcell voltage instead of its radiative recombination current, as defined in eq. (6) [139–140,143]. Figure 28(a) shows the EL/PL setup for implementing the suns-V_{oc} measurement [153]. Here, the *J*-*V* curves are acquired using a sourcemeter and 4-wire probes while a subcell is illuminated uniformly by an LED array whose wavelength is fully absorbed in these subcells and the rest of the subcells are excited by single-wavelength pulsed lasers. Sample V_{oc} measurements at certain amounts of 0.5-ms pulsed external light bias for middle and bottom cells are shown in Figs. 28(b) and (c), respectively.

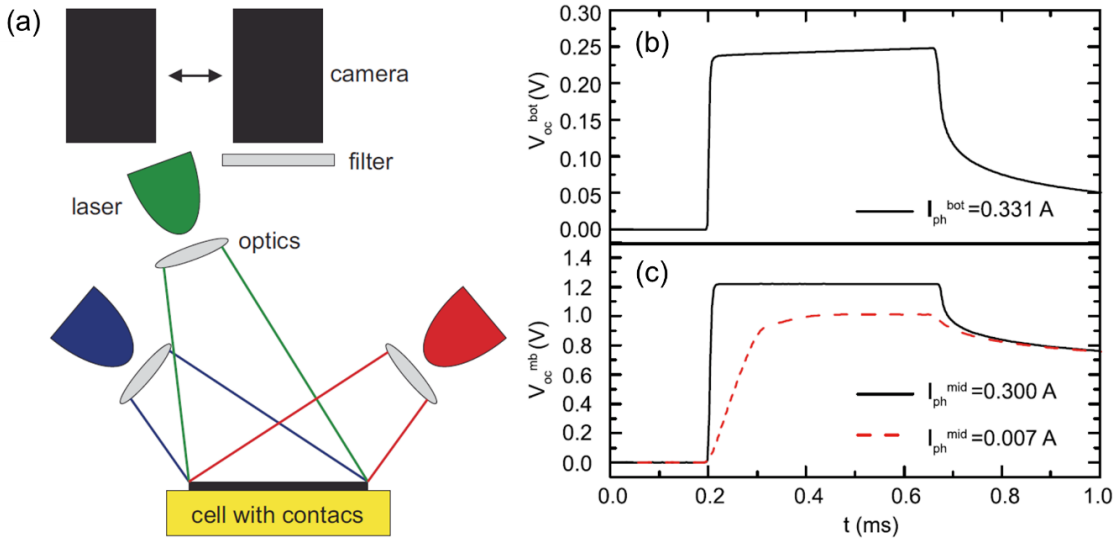

Fig. 28 (a) EL/PL setup employing two movable cameras, light filters, independent light sources illuminating upon the electrically-contacted MJSC [153]. MJSC V_{oc} acquired during a 0.5-ms pulse of illumination upon the (b) bottom cell and (c) middle cell at specified photocurrents [179].

2.1.4.7. Suns-short-circuit current (Suns-J_{SC}) method

Another variation employing variable low sunlight concentration is the suns-J_{sc} measurement [163]. Similar to the measurement of the *J*-*V* characteristic of each MJ subcell, optical biases are used to make evaluated subcell current-limiting. Then, limiting subcell J_{sc} values are to be obtained at each concentration equivalent of the optical biases upon the HBG subcell adjacent to the current-limiting cell while the rest of the nonlimiting subcells are illuminated with high-intensity LEDs. Sample suns-J_{sc} measurements of a mechanically-stacked [163] and an inverted metamorphic (IMM) [181] 4JSC is shown in Fig. 29, together with empirically-fitted LC efficiencies, η_{LC}.

2.1.4.8. Photoreflectance (PR) measurements for LC effect detection

A method to obtain spectral photovoltage measurements that are useful for quantifying the LC effect in MJSCs is by using a PR setup [182–183], as shown in Fig. 30. Here, the front surface is illuminated by two light sources: (1) a single-wavelength pump light that is chopped mechanically and (2) a monochromated probe lamp. During PR scan across the sample, the photovoltage in terms of V_{oc} is fed to an analog-to-digital converter. The reflected probed beam is then detected by a photodiode which is connected to a preamp and a lock-in amplifier. Then, the PR signal is separated into its DC average signal, I_0R, containing the information about the photovoltage and the modulated AC signal, $I_0\Delta R$,

where ΔR is the change in reflectance. In the past, this technique was also found helpful in characterizing multilayer quantum dot solar cell structures [184].

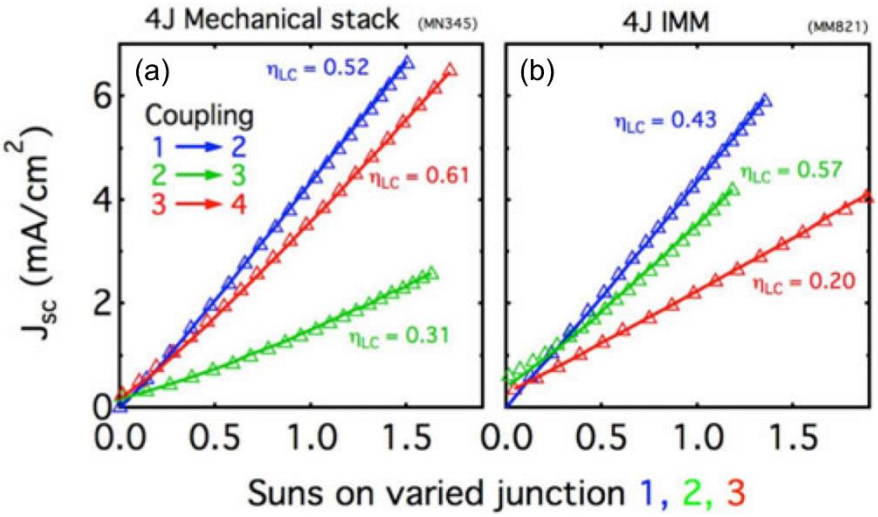

Fig. 29 Suns–J_{sc} measurements from (a) mechanically-stacked GaInP/GaAs//GaInAsP/GaInAs [163] and (b) IMM GaInP/GaAs/GaInAs/GaInAs 4JSCs [181].

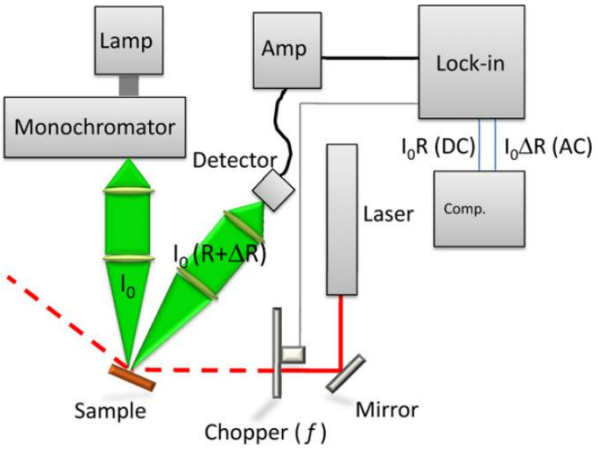

Fig. 30 PR measurement setup for detecting LC effect in MJSCs employing pump and probe illumination sources and lock-in amplifier [184].

2.1.4.9. Laser beam induced current (LBIC) mapping

One can determine the spatially-resolved LC current collection in a limiting lower bandgap MJ subcell using LBIC mapping [141,154,170–173,185–186]. Same as how the DC light *J-V* characteristics per subcell are obtained, the evaluated subcell is first made current-limiting using single-wavelength LEDs that optically bias the other MJ subcells. While the LED biases are switched on, a single-wavelength excitation laser whose wavelength is within the absorption range of the HBG subcell adjacent to the limiting cell is activated. Here, the laser scans upon the MJ sample horizontally and vertically. In acquiring the LBIC map, the laser scanning and switching frequencies depend on the voltage step size and the sampling resolution of the current map, respectively. Also, the pulsed laser is modulated by a lock-in amplifier. Meanwhile, when direct subcell current mapping is desired, the excitation laser wavelength to be used must be within the absorption range of the evaluated limiting subcell. Simple schematics of LBIC map setups

for LC and direct subcell current mapping are shown in Figs. 31(a) and (b). Here, λ_T, λ_M, and λ_B are the single wavelength sources absorbable in the top, middle and bottom cells, respectively.

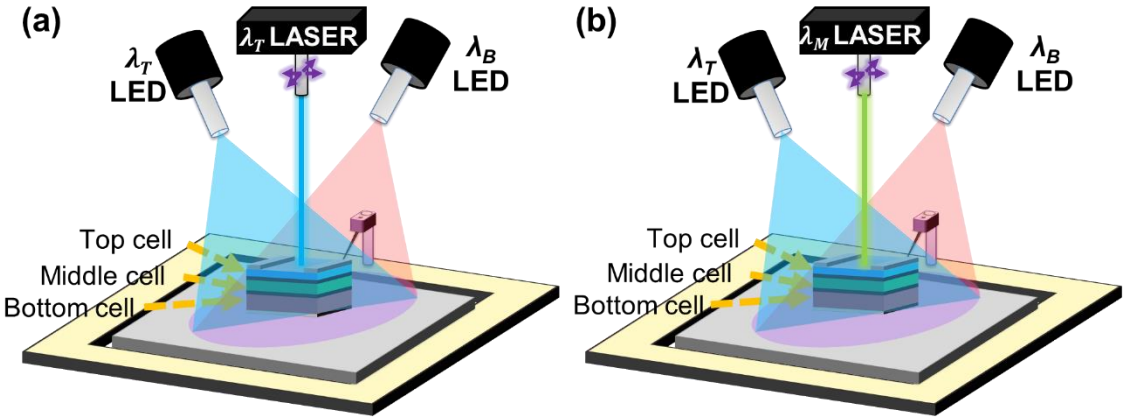

Fig. 31 Schematic illustrations of sample LBIC map setups for (a) top-to-middle cell LC and (b) direct middle cell current collection mapping.

2.2. Research Problem and Novelty Implication

The direction of MJSC research has been so far leaning onto increasing the number of junctions [40–41]. Because the LC efficiency was observed to saturate to about 70% previously [170,187], it becomes more challenging for the LC effect to fully compensate for the current mismatch among MJSC subcells.

Although the luminescent coupling (LC) effect has been extensively studied theoretically through 1D [52–56,132,139–145,147,149,168–169] and quite a few through multi-dimensional modeling of LC effect [132,150,152–154], and experimentally through light *J-V* characteristics [55–56,141] and EQE measurements [50,52,142,146,148,162–166], spatially-resolved LC effect has not been explored thoroughly yet experimentally. Initial studies have revealed that LC-induced current generation is not spatially homogeneous [141,170]. However, very little discussion on the underlying physics of inhomogeneous LC effect can be found in the literature at the time of the study. With this, the need to find out its root cause arises, in the hope of materializing a possible absolute increase of 1.35% in MJSC power conversion efficiency when strong LC effect is made uniform [170]. Furthermore, to the best of the author's knowledge, no study has attempted yet to find solutions to inhomogeneous LC effect techniques. Hence, possible techniques to spatially homogenize the LC effect are yet to be investigated. In addressing these research questions, the role and proof-of-concept in homogenizing LC effect to the power conversion efficiency of III-V based MJSCs may be discovered.

Table 1 summarizes the research groups that have conducted investigations on LC effect using different methods, to the best of the author's knowledge. These works were mainly employing 1-dimensional characterizations. Thus, higher dimension measurements were extensively utilized and studied in this dissertation, making this the first point for research novelty.

Table 1 List of prior studies on LC effect in MJSCs[3] and this work

Research Group	Evaluation method of LC effect reported
M.A. Steiner et al [52–53]	DC light *J-V* characteristics, EQE
T. Sogabe et al [56,169]	DC light *J-V* characteristics (low concentration), *SR-V* characteristics
M.Z. Shvarts et al [187]	DC light *J-V* characteristics (high concentration)
S.H. Lim et al [162]	EQE
J. Jia et al [188]	Small-signal pulsed-bias measurement
This work	Spatially-resolved measurements (LBIC, EL/PL mapping)

2.3. Research Objective

The objective of this dissertation is to find answers to the main research question on the role of homogenizing LC effect on the power conversion efficiency of III-V based MJSCs. Specifically, this work has the following objectives:

1. Investigate the carrier dynamics and light interactions possibly responsible for nonuniform LC current collection using various electrical and optical simulation models;
2. Design and implement electro-optical simulation models for analyzing III-V based MJSC measurements using SPICE, multi-paradigm numerical computation, and 2-dimensional ray tracing;
3. Design and implement LBIC mapping method using continuous bias LEDs to characterize current collection in the limiting subcell of III-V based MJSCs with LC effect;
4. Design and implement EL/PL mapping method using continuous lasers to determine the illumination profiles of a higher bandgap subcell and its adjacent current-limiting lower bandgap subcell of III-V based MJSCs that may cause inhomogeneous LC effect;
5. Compare the LC current collection of different monolithic MJSC structures through electro-optical characterization and data analysis;
6. Design, implement and characterize III-V based MJSC structures that may homogenize the LC current collection in their limiting subcells; and
7. Explore possible applications of III-V based MJSC structures with homogeneous LC effect in practical scenarios:
   a. by structure alteration,
   b. by electrical passivation, and
   c. by photo-passivation.

2.4. Dissertation Framework

This dissertation paper is composed of 7 chapters, with 5 appendices, the first two being the related literature reviews on solar energy in a broad picture and about LC effect in MJSCs, respectively, and the last chapter being the summary of conclusions drawn out of this research work and recommendations for future work. The dissertation framework is summarized as a flowchart in Fig. 32.

[3] Disclaimer: It is possible that other studies on LC effect may have existed at the time of the study but was beyond the author's access or reach.

Chapter III introduces the LBIC mapping method with continuous LEDs as an effective tool to map the LC current collection in III-V based MJSCs. This chapter aims to provide information on the spatial distribution of LC effect and to quantify its degree of inhomogeneity, introduced as the Bern factor, β, in the quasi-2-dimensional electro-optical prediction (Q2DEP) as the light source (LED) intensity upon the higher bandgap subcell is increased, thereby changing the LC strength. Additionally, the temperature dependence of the LC effect homogeneity was investigated.

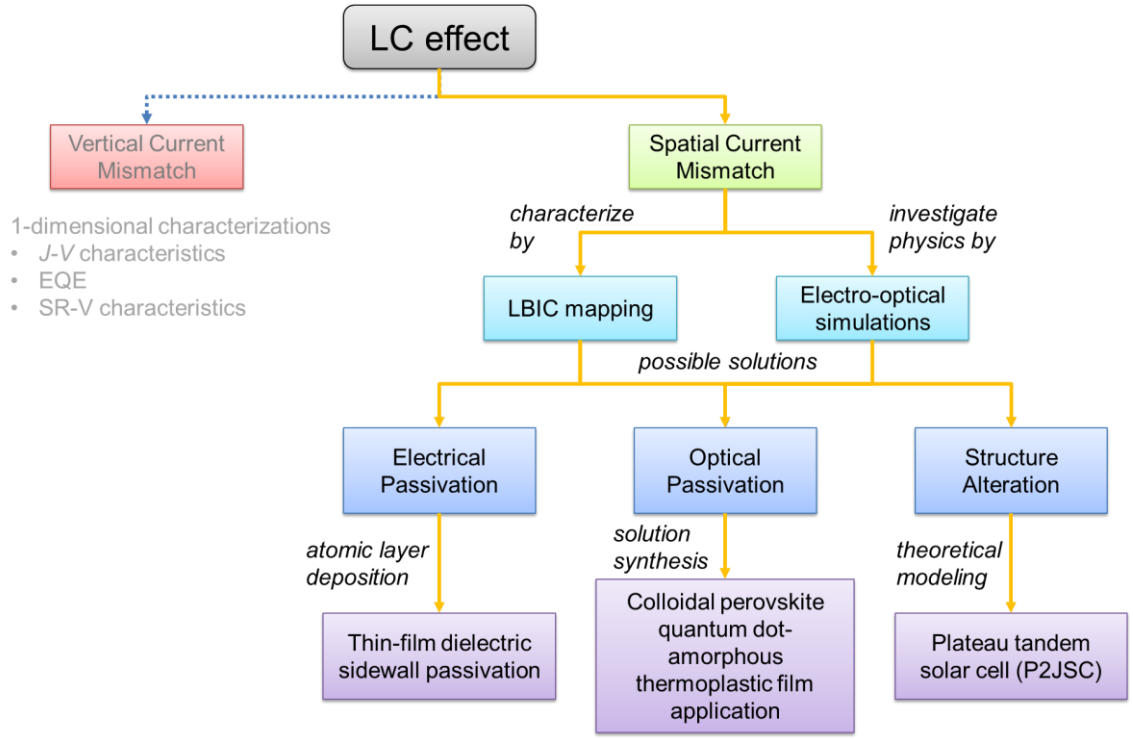

Fig. 32 The dissertation framework. The route that this study pursued is those pointed by solid arrows.

In comparison with the LBIC measurements, Chapter IV explores the LC effect by luminescence mapping of a current-limiting cell of III-V based MJSC and its adjacent higher bandgap subcell. This was done by investigating the effect of increasing the light source (laser) intensity upon the HBG subcell, similar to the illumination conditions imposed during LBIC mapping in Chapter III. Additionally, the effect of high carrier injection to the subcell illumination profile was investigated by varying the applied voltage across the III-V based MJSCs.

Chapters V and VI were dedicated to exploring III-V based MJSC structures that may homogenize the LC current collection in their limiting subcells. In Chapter V, the effect of electrical sidewall passivation by atomic layer deposition (ALD) of thin Al_2O_3 layer on completed III-V based MJSC samples was studied. This was done to answer the question of whether or not the perimeter recombination is one of the root causes of the nonuniform LC effect. On the other hand, Chapter VI discourses an attempt to homogenize LC effect through deposition of all-inorganic perovskite quantum dots (PQDs) on completed III-V based MJSC samples as a photo-passivating technique. Here, all-inorganic PQDs are introduced on the perimeter of the front MJSC surface as photo-emission enhancers. This was done to know if it is possible to compensate for nonuniform

PL from an HBG subcell towards a current-limiting subcell of MJSC. In extension, Appendix A discusses if the area-selective photo-emission by PQDs could induce photon filling effect to the perimeter, which may justify further or disprove perimeter recombination as the main underlying cause of nonuniform LC effect.

In Chapter VII, conclusions gathered in this dissertation are summarized. Additionally, future work is discussed in terms of practical applications of the novel MJSC structures disclosed in Chapters V and VI.

In addition to the solutions in homogenizing LC effect proposed in Chapters V and VI, theoretical modeling and simulation of plateau tandem solar cells (P2JSCs) were probed in Appendix B. Appendix C is focused on the carrier dynamics and light interactions to determine the possible physics behind nonuniform LC effect in III-V based MJSCs. This was investigated by using several theoretical models, namely 2D ray tracing, 3D distributed SPICE modeling of tandem and triple-junction solar cells (3JSCs) and Q2DEP model. Appendix D includes the tools and supplementary materials used in implementing this dissertation. Appendix E contains a list of research publications produced in the course of pursuing this study. This dissertation ends with a list of references.

Laser beam induced current (LBIC) mapping of III-V multijunction solar cells with luminescent coupling effect

Chapter 3

Chapter 3 – Laser beam induced current (LBIC) mapping of III-V multijunction solar cells with luminescent coupling effect

Chapter 3 showcases a thorough observation of spatially-resolved optoelectronic characterization of III-V multijunction solar cells (MJSCs) with luminescent coupling (LC) effect. Here, the laser beam induced current (LBIC) mapping method is introduced as a means of (1) observing LC effect and (2) subcell material quality within the active area of MJSCs, under spectrally-mismatched conditions. The LBIC mapping method using continuous bias LEDs was employed to characterize current collection in the limiting subcell of III-V MJSCs with LC effect.

This chapter is arranged as follows. First, the main research objective for this study is introduced, together with the specific questions. In Sec. 3.2, the methods used for observing and analyzing the LC effect are described. Next, Sec. 3.3 discusses the LBIC measurement results while having the following variables: (1) Group IV bottom cell and substrate material, i.e. germanium (Ge) and silicon (Si), (2) LC strength, (3) temperature, (4) size of the active area, and (5) application, that is, for space or terrestrial. Finally, this chapter ends with the synthesis of the main findings out of III-V MJSC characterizations.

3.1. Research Questions

The main objective of this chapter is to design and implement the LBIC mapping method in characterizing the current collection in the limiting subcell of III-V MJSCs with LC effect. Specifically, this chapter attempts to answer the following questions, in terms of MJ subcell current collection by direct light excitation and by LC effect:

1. What are the observed differences between space-grade and terrestrial concentrator-grade MJSCs?
2. What are the observed differences between Ge-based and Si-based MJSCs?
3. How does the spatial distribution of current production vary with LC strength?
4. How does the spatial distribution of current production vary with the cell operating temperature?
5. How does the spatial distribution of current production vary with the size of the cell's active area?

3.2. Methodology

3.2.1. MJSC samples characterized

In the course of this study, the following two-terminal samples were made available for characterization. One set of samples is from Ge-based III-V MJSC wafers. Specifically, commercial monolithic InGaP/GaAs/Ge triple-junction solar cells (3JSCs) whose active areas are 0.31 cm^2 and 0.99 cm^2 for concentrator samples and 4.00 cm^2 for space-grade samples were characterized. Specification sheets of Ge-based III-V MJSCs characterized can be found in Appendix D and Fig. 1 shows a simple schematic of InGaP/GaAs/Ge 3JSC.

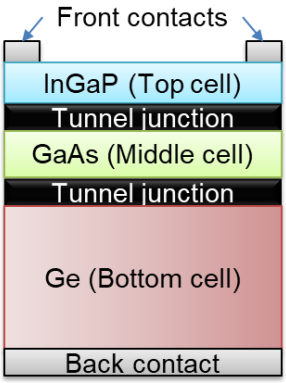

Fig. 1 Simplified schematic of InGaP/GaAs/Ge 3JSC.

Another set of samples characterized is from Si-based III-V MJSC wafers. InGaP/AlGaAs//Si 3JSC samples were fabricated in the same way as reported in [189]. Here, the InGaP/AlGaAs dual-junction (2J) layer was grown inverted on GaAs substrates by Fraunhofer ISE [189–191]. Separately, Si bottom cell was grown by diffusion doping processes to form an n+ emitter at the front surface and p+ back-surface field (BSF) at the back surface [189]. Before bonding the InGaP/AlGaAs 2J and the Si bottom cell, chemical mechanical polishing (CMP) and wet chemical cleaning by sulfur treatment on GaAs and ammonium hydroxide (NH_4OH) scrub on both GaAs and Si surfaces were done

[192–193]. Oxide layers on GaAs and Si surfaces were removed by argon (Ar) beam irradiation. Then, the III-V subcell stacked wafer was bonded on the Si substrate by surface-activated bonding (SAB) under ultra-high vacuum condition [160,189–192]. Next, the GaAs substrate was removed and then, the InGaP/AlGaAs//Si 3JSCs were mesa-etched with $BCl_3/Ar/O_2$ (BCl_3: boron trichloride) etchants for III-Vs and sulfur hexafluoride (SF_6) etchant for Si through dry plasma etching. The front and back metal contacts were evaporated and a 65-nm silicon nitride (SiN_x) anti-reflection coating was deposited through plasma-enhanced chemical vapor deposition (PECVD) [193]. The cross-section of InGaP/AlGaAs//Si 3JSCs is schematically shown in Fig. 2. Four samples were employed, having active areas of 0.25 cm^2, 0.5×1 cm^2, 1 cm^2, and 1×2 cm^2.

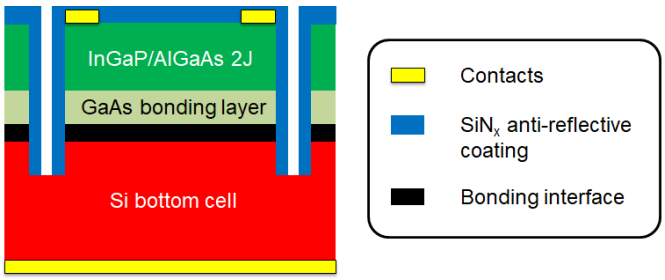

Fig. 2 Cross-section of InGaP/AlGaAs//Si 3JSC structure employed [189].

Each sample was defined by mesa trenches down to 2 µm inside the Si substrate and was mechanically separated by sawing. This process, however, left an exposed Si substrate region. Due to its long minority carrier diffusion length, photo-generated carriers produced outside the active cell area can diffuse to the p-n junction of the Si bottom cell and increase its photocurrent [194–195]. To prevent this, insulated masks were placed on top of the samples during Si bottom cell characterization.

Figure 3(a) shows the 1-cm^2 InGaP/AlGaAs//Si 3JSC sample that has exposed Si substrate. Here, the blue region is the exposed Si substrate, whose length measures about 0.5 mm on each side of the cell. Masked 1 cm^2 sample is shown in Fig. 3(b). Here, the mask was cut in the order of 0.1 mm precision, based on the thickness of the cutting tool used and was insulated with Kapton tape.

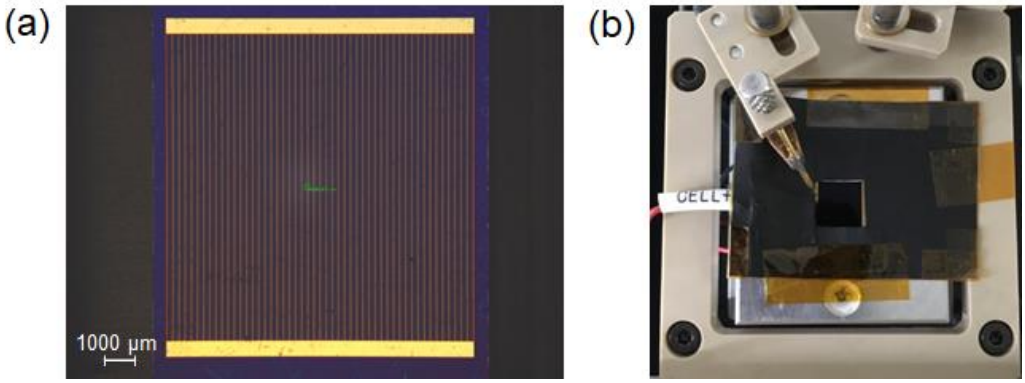

Fig. 3 (a) Unmasked and (b) aluminum-masked 1-cm^2 InGaP/AlGaAs//Si 3JSC sample with exposed Si substrate.

3.2.2. Several assumptions considered

Depending on the characterization conditions implemented, some assumptions were imposed. One is that the LC effect from higher bandgap (HBG) subcells to non-adjacent lower bandgap (LBG) subcells was considered negligible due to the optical thickness of the GaAs middle cell [52,196]. Thus, it was assumed that all photons generated by radiative emission from an HBG subcell towards its adjacent LBG subcell will be reabsorbed by the latter. Another is that negligible tunneling and lateral resistances were assumed for tunnel junctions because typically, the tunnel diode in between subcells are heavily doped [197], producing uniform voltage distribution. And lastly, to model the cell perimeter where the edge recombination occurs, an ideality factor of 2 was assumed [141,170].

3.2.3. Electro-optical characterizations

III-V based MJSCs with LC effect were characterized at various operating conditions by performing a series of DC light *J-V* curve measurements, EQE measurements, and LBIC mapping. Since the subcells of the two-terminal samples characterized are connected in series, the subcell being evaluated was made current-limiting by illuminating other subcells continuously with LEDs. All cases tested were at room temperature (25°C) unless otherwise specified. In the case of varying cell operating temperature, T_c, the Peltier sample stage temperature was varied from 15°C to 95°C through a thermocouple input.

3.2.3.1. DC *J-V* characteristics measurement

To assess the electrical performance of InGaP/GaAs/Ge 3JSC samples with LC effect, DC light *J-V* characteristic curves at room temperature and different T_c were measured from the current-limiting subcell. The current-limiting subcell was preset by irradiating continuous LEDs upon nonlimiting InGaP/GaAs/Ge 3JSC subcells and nothing on the current-limiting subcell being evaluated. In measuring InGaP *J-V* characteristics by LED irradiation, 780-nm, 970-nm, and 1550-nm LED intensities were set at 140.1, 31.4, and 4.2 mW/cm^2, respectively. During the light *J-V* characteristics measurement of the GaAs middle cell with LC effect, 970-nm LED intensity was fixed at 31.4 mW/cm^2 while 440-nm was either fixed at[4] 160.0 mW/cm^2 or was swept from 20.0 mW/cm^2 to 160.0 mW/cm^2 to vary InGaP-to-AlGaAs subcell LC strength [56]. As for Ge bottom cell measurement under fixed and varying LC strength, 660-nm LED intensity was either fixed at 261.1 mW/cm^2 or swept from 22.0 mW/cm^2 to 261.1 mW/cm^2 while 440-nm was fixed at 167.2 mW/cm^2. Applied III-V/Ge 3JSC terminal voltage was typically swept at some values between -10 V and 3.0 V, depending on the bandgap of the subcell being measured.

To determine the electrical performance of InGaP/AlGaAs//Si 3JSC samples with LC effect, DC light *J-V* characteristic curves at room temperature and different T_c were measured from the current-limiting subcell. This was done by irradiating continuous LEDs upon InGaP/AlGaAs//Si 3JSC subcells except for the current-limiting subcell being evaluated. In measuring InGaP *J-V* characteristics by LED irradiation, 780-nm, and 970-nm LED intensities were set at 140.1 and 31.4 mW/cm^2, respectively. During the light *J-V* characteristics measurement of the AlGaAs middle cell with LC effect, 970-nm LED intensity was fixed at 31.4 mW/cm^2 while 440-nm was either fixed at 160.0 mW/cm^2 or

[4] Data acquired before May 2018 made use of a 430-nm LED whose maximum intensity was 47.5 mW/cm^2.

was swept from 20.0 mW/cm^2 to 160.0 mW/cm^2 to vary InGaP-to-AlGaAs subcell LC strength. As for Si bottom cell measurement under fixed and varying LC strength, 660-nm LED intensity was either fixed at 261.1 mW/cm^2 or swept from 22.0 mW/cm^2 to 261.1 mW/cm^2 while 440-nm was fixed at 167.2 mW/cm^2. Applied III-V//Si terminal voltage was typically swept at some values between -10 V and 3.2 V, depending on the bandgap of the subcell being measured.

3.2.3.2. External quantum efficiency (EQE) measurements for subcell concentration difference estimation

To determine the number of incident photons successfully converted into electrons, subcell EQE measurements were performed on the III-V based MJSC samples. First, an external voltage was applied across the 3JSC sample. Then, the evaluated subcell was made current-limiting using continuous LED settings which are the same as described in conducting DC light *J-V* characteristics measurements. In addition to the applied external voltage and continuous LED biases, continuous light from a Xenon lamp source was passed through a monochromator and a chopper to produce an optical AC signal of different wavelengths. The generated AC signal response was then measured using a lock-in amplifier. Finally, the EQE signal generated was recorded in a desktop computer connected to the aforementioned setup components.

In labeling the measurements acquired under different light intensities, varied single-wavelength light source intensities were converted into their equivalent AM 1.5G concentration, C_{LED}, in suns. In the context of this work, C_{LED} means the light concentration difference between the adjacent HBG and LBG subcells. C_{LED} was calculated using [171]

$$C_{LED} = \frac{P(\lambda_{source})}{P(\lambda_{AM1.5G,i-1})}. \quad (1)$$

Here, $P(\lambda_{source})$is the light source intensity upon the HBG or (*i*-1)'th subcell, where the radiative emission originates in the LC effect process, and $P(\lambda_{AM1.5G,i-1})$ is the equivalent AM 1.5G intensity derived from integrated irradiance within the EQE absorption range of the HBG subcell. It is given by

$$P(\lambda_{AM1.5G,i-1}) = \int_{\lambda_{i-1,LL}}^{\lambda_{i-1,UL}} Irr(\lambda)d\lambda, \quad (2)$$

where $Irr(\lambda)$ is the reference AM 1.5G solar spectrum irradiance at each wavelength based on ASTM G173-03 standard [198], and $\lambda_{i-1,UL}$ and $\lambda_{i-1,LL}$ are the upper and lower limits of the (*i*-1)'th subcell absorption range excluding the overlapping regions with other subcell EQE measurements. An example of $P(\lambda_{AM1.5G,i-1})$ at different T_c, including $P(\lambda_{AM1.5G})$ with Si bottom cell being an *i*'th subcell, are listed in Table 1.

A more familiar way to calculate C_{LED} would be through the use of current densities instead of power densities. In this method, the (*i*-1)'th subcell LED current density used in the light *J-V* characteristics measurements of the adjacent LBG or the *i*'th subcell,

$J(\lambda_{LED})$, were converted into its equivalent AM 1.5G concentration, C_{LED}, also in suns, and is given by

Table 1 Global air mass 1.5 (AM 1.5G) intensities per subcell of InGaP/AlGaAs//Si 3JSCs based on the absorption ranges of subcells obtained from EQE measurements at different T_c, where λ_{LL} and λ_{UL} refer to the lower limit and upper limit wavelengths, excluding overlaps, respectively.

Cell Operating Temperature, T_c	AM 1.5 G intensity per subcell, $P(\lambda_{AM1.5G})$ (mW/cm^2)	Absorption range per subcell, λ_{LL} to λ_{UL} (nm)
15°C		
InGaP (top)	39.52	290 to 640
AlGaAs (middle)	22.04	650 to 840
Si (bottom)	17.92	850 to 1150
25°C		
InGaP (top)	39.52	290 to 640
AlGaAs (middle)	22.04	650 to 840
Si (bottom)	18.18	850 to 1160
35°C		
InGaP (top)	39.52	290 to 650
AlGaAs (middle)	22.04	660 to 840
Si (bottom)	18.18	850 to 1160
55°C		
InGaP (top)	40.94	290 to 650
AlGaAs (middle)	21.67	660 to 840
Si (bottom)	18.08	850 to 1180
75°C		
InGaP (top)	40.94	290 to 650
AlGaAs (middle)	21.67	660 to 850
Si (bottom)	18.08	860 to 1180
95°C		
InGaP (top)	40.94	290 to 650
AlGaAs (middle)	21.67	660 to 850
Si (bottom)	18.49	860 to 1190

$$C_{LED} = \frac{J(\lambda_{LED})}{J_{AM1.5G,i-1}}. \quad (3)$$

In this relation, $J(\lambda_{LED})$ is given as

$$J(\lambda_{LED}) = \frac{q}{hc}\lambda_{LED} \times EQE(\lambda_{LED}) \times P(\lambda_{LED}), \quad (4)$$

where λ_{LED} is the varied LED wavelength, q is the electron charge, h is the Planck's constant, c is the speed of light, $EQE(\lambda_{LED})$ is the (i-1)'th subcell external quantum efficiency (EQE) response to λ_{LED}, and $P(\lambda_{LED})$ is the λ_{LED} intensity which was set as a measurement input. Meanwhile, $J_{AM1.5G,i-1}$ is the equivalent AM 1.5G current density

acquired through integrating the solar irradiance within the absorption range of the (*i*-1)'th subcell, where LC effect originated, given by [199–200]

$$J_{AM1.5G,i-1} = \frac{q}{hc} \int_{\lambda_{i-1,LL}}^{\lambda_{i-1,UL}} \lambda \times EQE(\lambda) \times I_{AM1.5G}(\lambda) d\lambda. \quad (17)$$

Here, $I_{AM1.5G}(\lambda)$ is the reference AM 1.5G solar spectrum irradiance at each wavelength based on ASTM G173-03 standard [198], $EQE(\lambda)$ is the (*i*-1)'th subcell EQE response to λ, $\lambda_{i-1,UL}$ and $\lambda_{i-1,LL}$ are the upper and the lower limits of the (*i*-1)'th subcell absorption range. The absorption ranges of the III-V MJ subcells were determined from the EQE measurement.

3.2.3.3. LBIC mapping

The samples were characterized by the LBIC mapping method at room temperature in which a specific subcell was made current limiting [141].

To measure the spatial distribution of the photocurrent generated by direct light source excitation and by LC effect, appropriate continuous LED and modulated laser wavelength were used. Initially, the evaluated subcell was made current-limiting using continuous LEDs. Then, for evaluating the LBG subcell spatial current production, a pulsed laser whose wavelength is within its absorption range was used. As for evaluating the spatial LC current collection originating from radiative emission in the HBG subcell towards its adjacent LBG subcell, the wavelength of the pulsed laser used is within the absorption range of the HBG subcell. In this condition, no external light bias was irradiated upon the *i*'th subcell. Hence, the LBIC maps acquired were assumed to only show LC current production.

The laser used was set to a single value of switching frequency between 2000 and 3500 Hz every series of LBIC measurements for a fair comparison. The lasers have a duty cycle of 50% and scan the stage along the *x*-axis using a Galvano scanner operating at a scanning frequency of 2 Hz and along the y-axis by stage translation. Also, spot diameters of the lasers range between 50 μm and 100 μm, yielding a spatial resolution of about 23.4 × 20.9 pixels/mm^2. Besides, continuous illumination from LEDs was used to make a specific subcell current limiting. As needed, an attenuation filter (transmission, $T \approx 10\%$) for the laser was used to manually vary the laser power. The specifications of the modulated laser sources employed in the setup are summarized in Table 2.

From the power densities of the lasers listed in Table 2, the equivalent concentration of these lasers per spot area in suns was derived using

$$C_{Laser} = \frac{P_{\lambda,Laser}}{P(\lambda_{AM1.5G,i})}, \quad (6)$$

which is similar to eq. (1). Here, the subscript *i* refers to the subcell where the laser can be absorbed.

Table 3 summarizes the LBIC mapping settings used for characterizing InGaP/GaAs/Ge 3JSCs. The InGaP photocurrent collection maps were acquired by switching on continuous 780-nm, 970-nm and 1550-nm LEDs whose intensities are

summarized in Table 3 as condition 1. In addition to the LEDs, a 450-nm pulsed laser was used to excite InGaP top cell.

Table 2 Summary of pulsed laser source specifications used for LBIC measurements.

Laser Wavelength (nm)	Spot Size (μm)	Measured Power, no filter (μW)	Power Density, no filter (mW/cm^2)	Measured Power, with filter[a] (μW)	Power Density, with filter[a] (mW/cm^2)
450	50	51.90	2643.25	6.00	305.58
785	50	51.00	2597.41	5.70	290.30
1064	100	53.40	679.91	5.85	74.48

[a]~10% transmission filter.

The GaAs LC current collection maps were acquired by switching on continuous 440-nm, 970-nm and 1550-nm LEDs whose intensities are summarized in Table 3 as condition 2. A 450-nm pulsed laser was also activated to excite InGaP. Since there was no light bias exciting GaAs, its LC current collection was acquired. The LC current maps were acquired at various 440-nm LED intensities to know how the current collection and the spatial current matching changed with varying LC strengths towards GaAs. Then, the GaAs photocurrent collection maps were acquired by switching on continuous 440-nm, 970-nm and 1550-nm LEDs whose intensities are summarized in Table 3 as condition 3. With these LEDs, a 785-nm pulsed laser was activated to excite GaAs.

Table 3 Settings used for obtaining LBIC maps of each InGaP/GaAs/Ge 3JSC subcell.

Condition	Continuous LED intensity, P_{LED} (mW/cm^2)					Laser wavelength (nm)	Laser spot diameter (μm)
	440-nm	660-nm	780-nm	970-nm	1550-nm		
1. InGaP (top)	*off*	*off*	140.1	31.4	4.2	450	50
2. GaAs LC effect	*	*off*	*off*	31.4	4.2	785	50
3. GaAs (middle)	167.2	*off*	*off*	31.4	4.2	785	50
4. Ge LC effect	167.2	*	*off*	*off*	*off*	785	50
5. Ge (bottom)	167.2	261.1	*off*	*off*	*off*	1064	100

** Either fixed or varied up to maximum intensities of 167.2 and 261.1 mW/cm^2 for 440-nm and 660-nm, respectively.*

For acquiring the spatial LC current generation due to the radiative emission from GaAs middle cell towards the Ge bottom cell, continuous 440-nm and 660-nm LED biases were employed, which is condition 4 in Table 3. These LEDs bias the InGaP top cell and the GaAs middle cell, respectively. Then, a modulated 785-nm scanning laser was activated to excite the GaAs middle cell. Since the Ge bottom cell was not excited by any light bias, this subcell is limiting the current generation of the 3JSC. Last, the current collection by direct Ge excitation was acquired using condition 5 listed in Table 3. This also made use of 440-nm and 660-nm LEDs to current-limit Ge but in this condition, a modulated 1064-nm laser was used.

Table 4 summarizes the LBIC mapping settings used for characterizing InGaP/AlGaAs//Si 3JSCs. Similar to InGaP/GaAs/Ge 3JSCs, the InGaP photocurrent collection maps were acquired by switching on continuous 780-nm and 970-nm LEDs whose intensities are summarized in Table 4 as condition 1. In addition to the LEDs, a 450-nm pulsed laser was used to excite InGaP top cell.

The AlGaAs LC current collection maps were acquired by switching on continuous 440-nm and 970-nm LEDs whose intensities are summarized in Table 4 as condition 2. A 450-nm pulsed laser was also activated to excite InGaP. Since there was no light bias exciting GaAs, its LC current collection was acquired. The LC current maps were acquired at various 440-nm LED intensities to know how the current collection and the spatial current matching changed with varying LC strengths towards GaAs. Then, the GaAs photocurrent collection maps were acquired by switching on continuous 440-nm, 970-nm and 1550-nm LEDs whose intensities are summarized in Table 3 as condition 3. With these LEDs, a 785-nm pulsed laser was activated to excite GaAs.

Table 4 Settings used for obtaining LBIC maps of each InGaP/AlGaAs//Si 3JSC subcell.

Condition	Continuous LED intensity, P_{LED} (mW/cm^2)				Laser wavelength (nm)	Laser spot diameter (μm)
	440-nm	660-nm	780-nm	970-nm		
1. InGaP (top)	*off*	*off*	140.1	31.4	450	50
2. AlGaAs LC effect*	**	*off*	*off*	31.4	–	–
3. AlGaAs (middle)	167.2	*off*	*off*	31.4	1064	100
4. Si LC effect	167.2	**	*off*	*off*	785	50
5. Si (bottom)	167.2	261.1	*off*	*off*	1064	100

** Settings used in DC light J-V measurements only.*
*** Either fixed or varied up to maximum intensities of 167.2 and 261.1 mW/cm^2 for 440-nm and 660-nm, respectively.*

3.2.4. The quasi-2-dimensional electro-optical prediction (Q2DEP) model

3.2.4.1. 2-dimensional SPICE electrical model

To analyze the obtained current maps, a simulation model that satisfies both the photocurrent distribution profiles observed when an MJSC subcell is directly excited and when the LC effect is induced was developed. To implement this model, a 2D electrical circuit model was built initially [201]. Each unit is composed of three subcells representing the top, middle and bottom cells as illustrated in Fig. 4 for InGaP/GaAs/Ge 3JSCs. Here, the illuminated region is represented by units in light fill while the perimeter region is represented by units in gray fill. The units are interconnected by a lumped series resistance R_s, which represents the current movement within the cell and the resistance between the metal contact and the cell. $J_{01,i}$ and $J_{02,i}$ represent the diffusion and the bulk nonradiative recombination diode coefficients with ideality factors of 1 and 2, respectively. $J_{0rad,i}$ is the radiative recombination diode coefficient of the i'th subcell with an ideality factor of 1. $J_{ph,i}$ is the generated photocurrent from external light sources in the i'th subcell. $R_{sh,i}$ is the shunt resistance of the i'th subcell [28,32]. $J_{LC,m\rightarrow b}$ represents the generated LC current in the Ge bottom cell, which is dependent on the radiative

recombination current of GaAs middle cell [139–140]. The values of the parameters fitted with experimental data can be found in Table 5. As for the perimeter region, an ideality factor of 2 was assumed for the diode model per subcell representing the edge recombination [201–207]. In Fig. 4, this is labeled as $J_{02p,i}$. Also, the MJSC operating temperature was set as an input parameter.

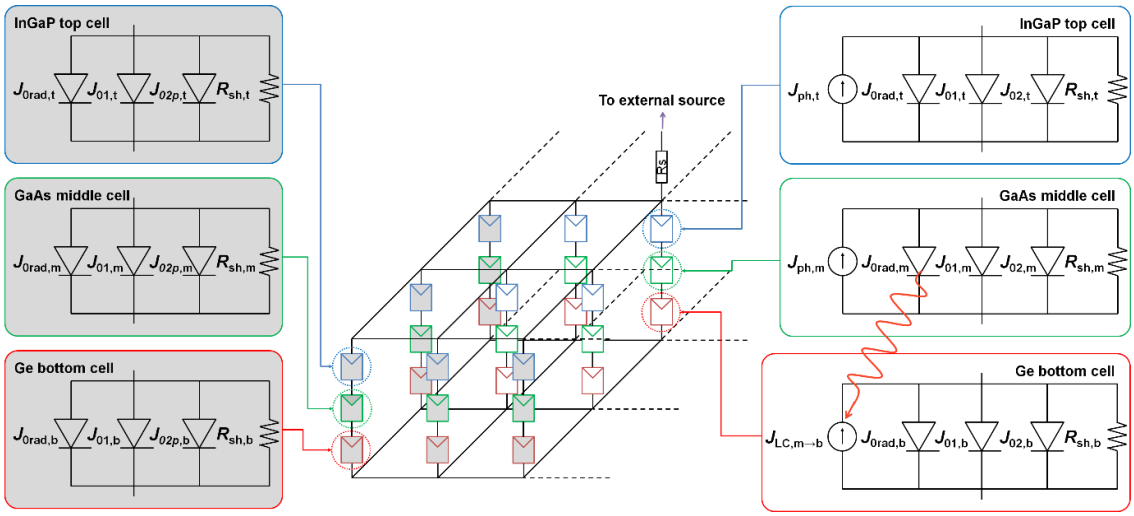

Fig. 4 A portion of the 2D electrical circuit model for InGaP/GaAs/Ge triple-junction solar cell showing 9 cell units. The white-filled units represent those in the illuminated region while the gray-filled units represent those in the perimeter region.

Table 5 Summary of sample parameter values used for each subcell of InGaP/GaAs/Ge triple-junction solar cell fitted into the 2D electrical circuit SPICE model with experiment data. Here, *dA* is the differential cell area.

Parameters Fitted	InGaP Top Cell	GaAs Middle Cell	Ge Bottom Cell
Diffusion diode coefficient, $J_{01,i}$ (mA/*dA*)	1.00×10^{-30}	1.00×10^{-26}	9.00×10^{-12}
Nonradiative recombination diode coefficient, $J_{02,i}$ (mA/*dA*)*	1.20×10^{-18}	1.67×10^{-13}	1.00×10^{-9}
Radiative recombination diode coefficient, $J_{0Rad,i}$ (mA/*dA*)	2.16×10^{-29}	1.64×10^{-21}	6.75×10^{-11}
Shunt resistance, $R_{SH,i}$ (Ω/*dA*)	6.50×10^{14}	1.60×10^{9}	2.50×10^{7}
Lumped series resistance, R_S (Ω)		1.20	

* *The same parameters used for* $J_{02p,i}$.

3.2.4.2. LBIC map empirical fitting procedure

3.2.4.2.1. Dark J-V characteristics fitting (1-dimensional)

To prepare the Q2DEP model for analyzing the characterization results, the optical and electrical properties for each subcell were assimilated into the 2D SPICE electrical model described earlier by fitting the measured *J-V* characteristics. First, dark *J-V* curves were fitted into the 2D SPICE model. Here, the nonradiative saturation current diode coefficient of the *i*'th subcell, $J_{02,i}$, the lumped series resistance, R_s, and the shunt resistance of the *i*'th subcell, $R_{sh,i}$, were obtained by fitting the dark *J-V* curve of the samples into the 2-D SPICE circuit model. Here, the model for $J_{02,i}$ has an ideality factor of 2, R_s represents the combined effects of lateral, electrode, emitter, bonding interface,

tunnel junction, and substrate resistances, and $R_{sh,i}$ represents the i'th subcell defects produced during manufacturing and processing [141,208]. Sample fitted parameters from dark J-V characteristics of InGaP/AlGaAs//Si 3JSC are summarized in Table 6 and the curve fit plots are shown in Fig. 5.

Table 6 Summary of sample values used for each subcell of InGaP/AlGaAs//Si 3JSC fitted into the 2D SPICE electrical model with measured dark J-V curves. Here, dA is the differential cell area.

Parameters Fitted	InGaP Top Cell	AlGaAs Middle Cell	Si Bottom Cell
A_{cell} = 1×2 cm^2			
Nonradiative recombination diode coefficient, $J_{02,i}$ (mA/dA)	1.0×10^{-18}	6.0×10^{-10}	7.0×10^{-7}
Shunt resistance, $R_{sh,i}$ (Ω/dA)	1.2×10^{8}	2.0×10^{6}	4.0×10^{4}
Lumped series resistance, R_s (Ω)		2.0×10^{-3}	
A_{cell} = 1 cm^2			
Nonradiative recombination diode coefficient, $J_{02,i}$ (mA/dA)	3.0×10^{-16}	1.0×10^{-9}	1.0×10^{-9}
Shunt resistance, $R_{sh,i}$ (Ω/dA)	2.0×10^{8}	1.0×10^{7}	4.0×10^{4}
Lumped series resistance, R_s (Ω)		1.0×10^{-4}	
A_{cell} = 0.5×1 cm^2			
Nonradiative recombination diode coefficient, $J_{02,i}$ (mA/dA)	1.0×10^{-19}	1.0×10^{-10}	2.0×10^{-7}
Shunt resistance, $R_{sh,i}$ (Ω/dA)	3.2×10^{8}	4.0×10^{6}	1.0×10^{5}
Lumped series resistance, R_s (Ω)		3.0×10^{-3}	
A_{cell} = 0.25 cm^2			
Nonradiative recombination diode coefficient, $J_{02,i}$ (mA/dA)	4.0×10^{-12}	2.0×10^{-8}	1.0×10^{-14}
Shunt resistance, $R_{sh,i}$ (Ω/dA)	3.0×10^{7}	5.0×10^{5}	3.0×10^{3}
Lumped series resistance, R_s (Ω)		2.5×10^{-3}	

R_s used in the SPICE circuit model was treated as constant for any cell temperature, T_c, range studied, considering its minimal variation observed over various sunlight concentration [209], which is correlated to T_c [138]. Also, $R_{sh,i}$ values were fixed since they represent manufacturing defects. On the other hand, $J_{02,i}$ may vary over T_c. Hence, for varying T_c, a prediction model was used, that is, [130]

$$J_{02,i}(T_c) = C \cdot T_c^2 \exp\left(\frac{-E_{g,i}}{2k_B T_c}\right). \quad (7)$$

Here, C is a temperature-independent proportionality constant, k_B is Boltzmann's constant and $E_{g,i}$ is the i'th subcell bandgap. C was calculated first using the fitted $J_{02,i}$ and the known $E_{g,i}$ at T_c = 25°C [190–191] and was assumed to remain constant over T_c. Then, the rest of $J_{02,i}$ values were calculated using the band absorption edge from the subcell EQE measurements. An example of fitted and predicted J_{02} values for Si bottom cell in InGaP/AlGaAs//Si 3JSC are plotted in Fig. 6(a). Here, fitting was done using the SPICE electrical model, while the predicted values were calculated using eq. (7), where C = 1.33×10^{-4}. The parameters used in the SPICE electrical model and the plot of the fitted

and measured dark *J-V* curves at 25°C are found in Table 7 and Fig. 6(b), respectively. To know how well the SPICE circuit model approximates the observed dark *J-V* characteristics of the samples, the coefficient of determination or R-squared, r^2, of the measured and fitted dark *J-V* curves was calculated. In statistics, r^2 can be used as a measure of evaluating how good a certain model predicts the observed phenomenon [210–211].

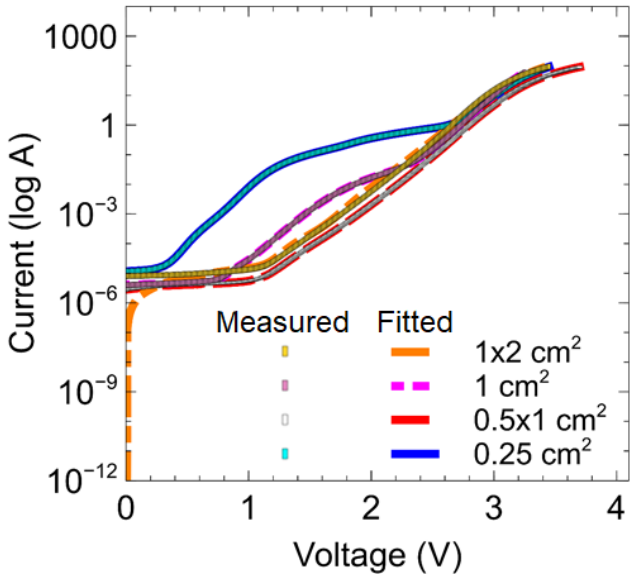

A_c (cm²)	r^2
0.25	0.9982
0.5×1	0.9970
1	0.9960
1×2	0.9948

Fig. 5 Measured (bar symbols) and fitted (solid lines) dark *J-V* curves of InGaP/AlGaAs//Si 3JSC samples, where r^2 is the coefficient of determination [172].

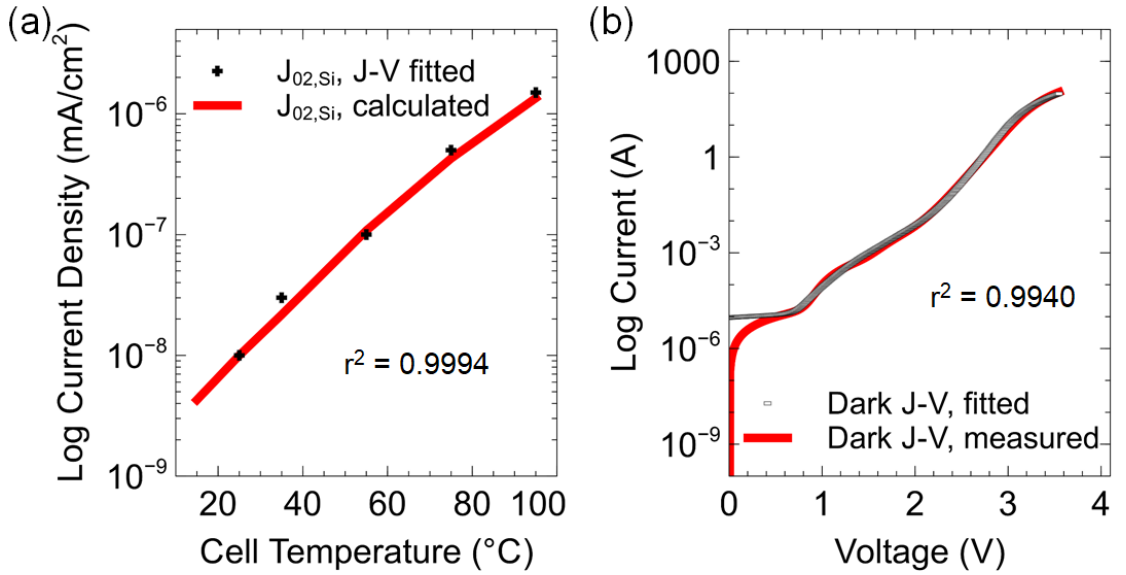

Fig. 6 (a) Fitted (diamond symbol) and calculated (solid line) nonradiative saturation current diode coefficients, $J_{02,Si}$, of Si bottom cell at different T_c, where $C = 1.33\times10^{-4}$. (b) Measured (bar symbol) and fitted (solid line) dark *J-V* characteristic curves of InGaP/AlGaAs//Si 3JSC sample characterized at 25°C. In both figures, r^2 is the coefficient of determination [172–173].

Table 7 SPICE electrical model parameters acquired from measured dark *J-V* characteristic curve fitting of 1 cm^2 InGaP/AlGaAs//Si 3JSC at T_c = 25°C where *dA* is the differential area of the cell.

Parameters Fitted	InGaP Top Cell	AlGaAs Middle Cell	Si Bottom Cell
Nonradiative recombination diode coefficient, $J_{02,i}$ (mA/cm^2)	8.0×10^{-16}	4.0×10^{-11}	1.0×10^{-8}
Shunt resistance, $R_{sh,i}$ (Ω/*dA*)	9.0×10^{7}	1.2×10^{6}	1.0×10^{5}
Lumped series resistance, R_s (Ω)		2.5×10^{-3}	

3.2.4.2.2. Light J-V characteristics fitting

After the dark *J-V* curve fitting, the light *J-V* curves measured at room temperature and different T_c were fitted into the SPICE circuit model. In this step, the combined diffusion and radiative saturation current coefficient of the *i*'th subcell, $J_{01,i}$, was fitted and has an ideality factor of 1. A single value was assumed for $J_{01,i}$ at a certain T_c since the radiative recombination coefficient was observed to vary insignificantly between T_c = 280 K (6.85°C) and 365 K (91.85°C) [212]. Additionally, the photocurrent generated in each subcell by external light sources, $J_{ph,i}$, was fitted. Then, the r^2 of the measured and fitted *J-V* curves was also calculated.

From the light *J-V* characteristics, the following were extracted: the combined diffusion and radiative saturation current coefficient of the *i*'th subcell, $J_{01,i}$, with an ideality factor of 1; the photocurrent generated in the *i*'th subcell by external light sources, $J_{ph,i}$; and LC factor, $\alpha_{LC,i\text{-}1\rightarrow i}$ [56,141]. This describes the efficiency of converting the photons emitted due to radiative recombination from the (*i*-1)'th subcell into the current in its adjacent *i*'th subcell. In the one-dimensional model of the LC effect, the LC current produced in the *i*'th subcell, $J_{LC,i-1\rightarrow i}$ is defined as [139,141]

$$J_{LC,i-1\rightarrow i} = \alpha_{LC,i-1\rightarrow i}\, J_{rad,i-1} = \frac{I_{LC,i-1\rightarrow i}}{A_{cell}}, \tag{8}$$

where $I_{LC,i-1\rightarrow i}$ is the unnormalized LC current and A_{cell} is the cell area. In addition, $J_{LC,i-1\rightarrow i}$ is dependent on the radiative recombination current of the (*i*-1)'th subcell, $J_{rad,i-1}$, which is a portion of the current produced by the diode model whose coefficient is J_{01} and whose ideality factor is 1. Using the fitted parameters, the LC current at each SPICE circuit node, $J_{LC}\big((x-x_0),(y-y_0)\big)$, was extracted. It is given as

$$J_{LC}\big((x-x_0),(y-y_0)\big) = \frac{I_{LC,i-1\rightarrow i}\big((x-x_0),(y-y_0)\big)}{dxdy}, \tag{9}$$

where $dxdy$ is the cell differential area. It is the current produced without considering the illumination profile of the LC effect, hence, laterally uniform as extracted from the 2D SPICE model.

3.2.4.2.3. Extraction of net LC current

Instead of implementing a Gaussian profile, which is typically assumed for modeling the illumination profile for distributed circuits considering spatial dependence of temperature effects in solar cells [213] and chromatic aberration, an optical effect in concentrator MJSC systems [204,214–216], a superellipse profile was assumed. It is since the Gaussian profile contour is circular throughout the plane. On the other hand, the superellipse profile gradually changes from rectangular to rounded rectangular shape towards the center of the cell, which better describes the observed LBIC maps [141]. Hence, after extracting $J_{LC}\big((x-x_0),(y-y_0)\big)$ from the SPICE model, an optical distribution phenomenological model for nonuniform illumination profile of LC effect, $z_{opt}\big((x-x_0),(y-y_0)\big)$ [170,217], was introduced. It is given by the equation of a superellipse

$$z_{opt}\big((x-x_0),(y-y_0)\big)=\left(\frac{s(x-x_0)(y-y_0)}{k^2}\right)^2-\left(\frac{(x-x_0)^{\,2}}{k^2}+\frac{\left(y_{y_0}\right)^2}{k^2}\right)+1 \quad (10)$$

where s defines the sharpness of superellipse corners, $\big((x-x_0),(y-y_0)\big)$ is the map coordinates, (x_0,y_0) is the center of the sample, and k is defined as half of the width of the cell sample. For square or rectangular-shaped solar cells, s = 1. Also, the value of k that closely predicts the optical profile observed during LC current mapping satisfies $k \geq \pm\,(x\text{-}x_0),\,(y\text{-}y_0)$ [218]. Finally, considering z_{opt} which was defined as eq. (10), the net electro-optical LC current, $J_{LC,net}\big((x-x_0),(y-y_0)\big)$, becomes

$$\begin{aligned} J_{LC,net}&\big((x-x_0),(y-y_0)\big) \\ &= \Delta J\big[\beta_{LC} z_{opt}\big((x-x_0),(y-y_0)\big) \\ &\qquad + (1-\beta_{LC})\big]\, J_{LC}\big((x-x_0),(y-y_0)\big), \end{aligned} \quad (11)$$

where ΔJ is an experimental fit parameter accounting for the current production difference between the pure DC light bias and with AC laser excitation and β_{LC} is the Bern factor, which describes the fraction of nonuniformity describing the portion of $J_{LC,net}\big((x-x_0),(y-y_0)\big)$ that was quenched [170,217]. Physically, this spatial nonuniformity is possibly caused by one or a combination of the following phenomena: (1) optical losses due to photon escape through the sides of the MJSC [169], (2) electrical losses due to lateral resistance effects [141,219], (3) high nonradiative recombination rate near the cell perimeter [202–203,205,220], (4) nonuniform material growth [171], and (5) high carrier injection into the higher bandgap subcell resulting in nonuniform radiative emission toward an adjacent lower bandgap subcell [154,186]. In addition, β_{LC} is obtained by fitting the LBIC maps into the Q2D model. The simulated variation of β_{LC} is shown in Fig. 7. In this equation, higher β_{LC} value fitted indicates less uniform LC current distribution.

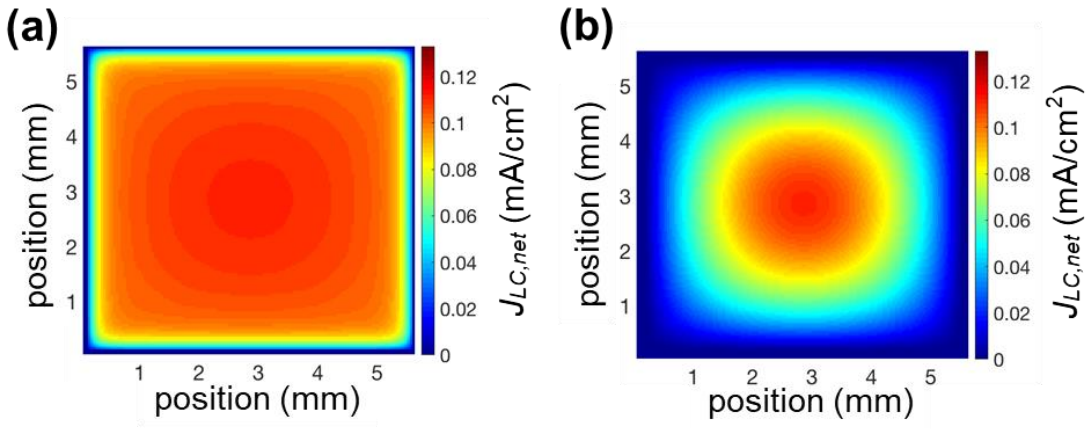

Fig. 7 Color map representation of luminescence coupling (LC) current, $J_{LC,net}$, whose fractions of nonuniformity, β_{LC}, are set to (a) 10% and (b) 100%, respectively. The α_{LC} for both LC current distributions is 0.69, which is the maximum acquired for 0.31 cm^2 sample. The spatial resolution of the maps is 23.4 × 20.9 pixels/mm^2 and the applied InGaP/GaAs/Ge triple-junction solar cell terminal voltage is 1.5 V.

3.2.5. Analytical equations used

The series of equations below were used for analyzing the experimental results obtained from characterizing III-V based MJSCs in this work.

3.2.5.1. Coefficient of determination

In the context of the prediction models used for nonuniform LC current fitting and temperature dependence of subcell bandgaps studied, r^2 is the coefficient of determination or specifically, the squared Pearson correlation coefficient, r, which is an indicator of correlation between the measured and the fitted or calculated data points [211]. It is given by

$$r = \frac{\sum_{i=1}^{n}(x_i - \bar{x})(y_i - \bar{y})}{\sqrt{\sum_{i=1}^{n}(x_i - \bar{x})^2 \sum_{i=1}^{n}(y_i - \bar{y})^2}}, \tag{12}$$

where $\bar{x}$, and $\bar{y}$ are the average of arrays x (predicted) and y (observed), respectively, whose sizes are both n. The closer r and r^2 are to 1.0, the better the correlation and the prediction, respectively.

3.2.5.2. The LC yield

To relate the LC current generation to the total recombination current, the coupling yield [55–56], γ_{LC}, is calculated. It is given by

$$\gamma_{LC} = \frac{J_{LC,i\text{-}1\rightarrow i}}{J_{ph,i\text{-}1} - J_{LC,i\text{-}1\rightarrow i}} \tag{13}$$

$J_{\mathrm{ph},i\text{-}1}$ is the photocurrent collected in an adjacent upper bandgap or (i-1)'th subcell where the luminescence originates. It is derived from the reversed bias region of DC light J-V characteristic curves where the photocurrent saturates. An illustration of where to find this in a J-V characteristic curve is shown in Fig. 8. Subtracting $J_{LC,\mathrm{i}\text{-}1\rightarrow\mathrm{i}}$ from $J_{\mathrm{ph},i\text{-}1}$ gives the total current loss due to nonradiative recombination, due to photons escaping towards

the cell surface and the sides of the cell or due to photons uncollected within the subcells [55–56,141,170].

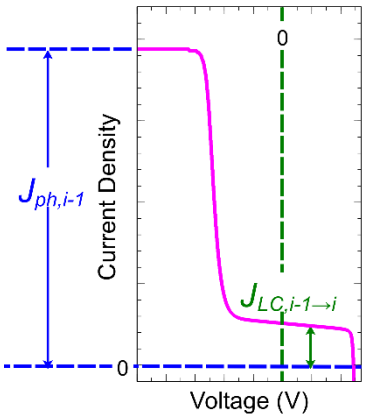

Fig. 8 Values needed for calculating the coupling yield, γ_{LC}, from the *J-V* characteristic curve of current-limiting subcell: photocurrent collected in an HBG (*i*-1) subcell, $J_{ph,i-1}$, and LC current collected in the adjacent LBG (*i*, current-limiting) subcell, $J_{LC,i-1\rightarrow i}$ [170].

3.2.5.3. Adjacent subcell current matching ratio

As an alternative for γ_{LC}, a more straightforward parameter, termed as subcell current matching ratio, $\zeta_{i-1\rightarrow i}$, was used to quantify the current mismatch between the adjacent HBG or (*i*-1)'th and LBG or *i*'th subcells. This is derived from the DC light *J-V* characteristic curve measurements and it is given as

$$\zeta_{i-1\rightarrow i}=\frac{J_{LC,i-1\rightarrow i}(V)}{J_{ph,i-1}} \tag{14}$$

Here, $J_{LC,i-1\rightarrow i}(V)$ is the collected LC current in the *i*'th subcell at an applied terminal voltage, *V*, and $J_{ph,i-1}$ is the photocurrent collected in the (*i*-1)'th subcell. Where to find these values in the *J-V* curve is also illustrated in Fig. 2. The same method was used in [217]. Here, having a $\zeta_{i-1\rightarrow i}$ value closer to 1 implies better current matching between (*i*-1)'th and *i*'th subcells [217].

3.2.5.4. The standard deviation of the current collection

To quantify the severity of nonuniformity or spatial mismatch of LC current collection, the standard deviation of LBIC map values per measurement, σ_{LC}, was calculated using the definition

$$\sigma_{LC}=\sqrt{\frac{1}{N-1}\sum_{l=1}^{N}|J_l-\bar{J}|^2} \tag{15}$$

where *N* is the total number of LC current map points, J_l is the current at *l*-th current map point and $\bar{J}$ is the average of the limiting subcell current acquired at all map points. This value is normalized to the sum of LC current collected in Ge at all map points, which is

indicated as the total J_{LC}. A lower value of normalized σ_{LC} indicates more uniform current distribution.

In some cases, there may be batch spread that can be observed among samples coming from the same wafer. To fairly compare the spatial mismatch of LC current collection at different T_c, the normalized standard deviation of LC current collection, $\sigma_{LC}/J_{LC,Total}$, was calculated using

$$\sigma_{LC}/J_{LC,Total} = \frac{\sqrt{\frac{1}{N-1}\sum_{l=1}^{N}|J_l - \bar{J}|^2}}{J_{LC,Total}} \tag{16}$$

Here, N is the total number of current map points in an LBIC measurement, J_l is the current at l-th current map position, $\bar{J}$ is the average Si bottom cell current obtained at all points in the map and $J_{LC,Total}$ is the sum of LC current collected in Si bottom cell from all points in the map. A lower value of $\sigma_{LC}/J_{LC,Total}$ was interpreted as having better current distribution uniformity [217].

3.2.5.5. Limiting cell conversion efficiency

To calculate for the limiting cell conversion efficiency, the maximum power point voltage, V_{mpp}, from light *J-V* characteristics was determined. From V_{mpp}, the nodal currents and voltages, $J_{mpp}(x,y)$ and $V_{mpp}(x,y)$, were extracted from the 2D electrical circuit model. Then using the Q2DEP simulation model, the nonuniform distribution of the LC effect was incorporated into $J_{mpp}(x,y)$ using eq. (11). The cell conversion efficiency, η_{TOTAL}, was then calculated using

$$\eta_{TOTAL} = \frac{\iint J_{mpp}(x,y)V_{mpp}(x,y)dxdy}{P_{source}} \tag{17}$$

where P_{source} is the incident light power per spot area, or the laser power density as listed in Table 2, Sec. 3.2.3.3, *dxdy* is the differential cell area, and $J_{mpp}(x,y)$ and $V_{mpp}(x,y)$ are the nodal currents and voltages at maximum power point voltage obtained from the *J-V* characteristic curve [170], V_{mpp}. The incident power from the LED biases was not included since the LBIC measurements were conducted in AC mode.

3.2.5.6. Mean LC quantum efficiency, *mLCQE*

For this study, the mean QE of generated LC current, *mLCQE*, has been defined as the averaged ratio of LC current to the incident current, J_{in}. Mathematically, *mLCQE* is given by

$$mLCQE = \frac{\iint J_{LC,net}(x,y)dxdy}{J_{in}A_{cell}} \tag{18}$$

where A_{cell} is the cell area and *dxdy* is the differential area of the InGaP/GaAs/Ge 3JSC sample characterized. Here, larger *mLCQE* indicates a larger number of radiative emission photons induced by J_{in} which were successfully converted to electrons produced by the LC effect. Additionally, J_{in} was derived only from the AC power density of the excitation laser irradiated upon the (i-1)'th subcell during LBIC mapping by LC

excitation, since *mLCQE* calculations were based from LBIC measurements alone. J_{in} is given by

$$J_{in} = \frac{qP_m\lambda_{laser}}{hc}, \tag{19}$$

where P_m is the measured laser power and λ_{laser} is the excitation laser wavelength upon the (*i*-1)'th subcell.

Then, the absolute QE difference of generated LC current, Δ*mLCQE*, is calculated using

$$\Delta mLCQE = mLCQE_{uniform} - mLCQE_{fit} \tag{20}$$

where $mLCQE_{uniform}$ and $mLCQE_{fit}$ are obtained from fitted 3JSC *J-V* characteristics considering uniform (β_{LC} = 0) and nonuniform ($\beta_{LC} \neq 0$, fitted) LC current generation in the limiting Ge bottom cell, respectively. Here, larger Δ*mLCQE* indicates a larger number of uncollected photons emitted by an HBG subcell towards its adjacent LBG subcell, thereby causing spatial LC current mismatch. The mismatch is ascribed to uncollected photons emitted by an (*i*-1)'th subcell towards its adjacent *i*'th subcell that could have either escaped or have been internally reflected, having a higher probability of absorption in the center region [170]. Other possibilities include competition from nonradiative recombination against radiative recombination events [221] occurring at the defects within the bulk region due to material growth inhomogeneity [171] or at the edges of the cell [202–203].

3.2.5.7. Temperature dependence of subcell bandgap, $E_{g,i}(T_c)$ modeling

Different models for III-V based MJSC subcells were used in predicting the semiconductor bandgap at T_c range studied, $E_{g,i}(T_c)$. Equations (21), (22), and (23) defined in Sec. 3.2.5.7.1 to 3.2.5.7.3 hereafter were used to specifically model the $E_{g,i}(T_c)$ of Si, AlGaAs and InGaP subcells, respectively. Predicted $E_{g,i}(T_c)$ were then compared with the *i*'th subcell absorption band edge from EQE measurements including adjacent subcell overlap regions.

3.2.5.7.1. The Varshni model

The Varshni model for temperature dependent-semiconductor bandgap, $E_g(T_c)$, is given as

$$E_g(T_c) = E_g(0) - \frac{\alpha \cdot T_c^2}{T_c + \beta}, \tag{22}$$

where $E_g(0)$ is the semiconductor bandgap at T_c = 0 K and α and β are fit parameters [128]. This was used to calculate the theoretical bandgap of Si bottom cell at various T_c, $E_{g,Si}(T_c)$. The fit parameters used were those published in Ref. [222].

3.2.5.7.2. The Viña model

The Viña model for $E_g(T_c)$ is given by

$$E_g(T_c) = E_B - a_B \left[1 + \frac{2}{\exp\left(\frac{\theta_B}{T_c} - 1\right)} \right], \quad (22)$$

where $E_B - a_B$ is the semiconductor bandgap at T_c = 0 K, a_B is the electron-phonon interaction strength and θ_B is the characteristic temperature describing the effective phonon energy [223–224]. Here, E_B, a_B and θ_B were obtained by experimental data fitting. This approach was used to calculate the theoretical bandgap of $Al_xGa_{1-x}As$ middle cell at various T_c, $E_{g,AlGaAs}(T_c)$. Here, the fit parameters used were from Ref. [225], considering the contribution from thermal expansion. Initially, the reported fit parameters were extrapolated linearly to approximate their values for the known Al content, *x*, of the $Al_xGa_{1-x}As$ middle cell characterized in this study. Then, the $E_{g,AlGaAs}(T_c)$ was then calculated straightforwardly using eq. (22).

3.2.5.7.3. A model considering electron-phonon coupling and volume thermal expansion

To consider the volume thermal expansion of a semiconductor, $E_v(T_c)$, the model introduced in [226] was extended by Ishitani, et al. [227] as

$$E_g(T_c) = E_0 - E_v(T_c) - E_1 \left[\frac{1}{\exp\left(\frac{\theta_1}{T_c}\right) - 1} + \frac{1}{2} \right] - E_2 \left[\frac{1}{\exp\left(\frac{\theta_2}{T_c}\right) - 1} + \frac{1}{2} \right] \quad (28)$$

where E_0, E_1 and E_2 are the fitted energy parameters, and θ_1 and θ_2 are the fitted optical and acoustic phonon temperatures, respectively. This model was used to calculate the theoretical bandgap of $In_{1-x}Ga_xP$ top cell at various T_c, $E_{g,InGaP}(T_c)$. From the literature, the best fit parameters found for $In_{0.5}Ga_{0.5}P$ were E_0 = 2.0536 eV, E_1 = 0.1290 eV, E_2 = 8.6 meV, θ_1 = 515 K and θ_2 = 55 K [227]. These values were extrapolated linearly, together with $E_v(T_c)$ for calculating $E_{g,InGaP}(T_c)$, where x = 0.51 [190–191].

3.3. Results and Discussion

3.3.1. InGaP/GaAs/Ge 3JSCs at Room Temperature [170]

The lateral LBIC map for the GaAs middle cell acquired by direct 785 nm laser excitation is shown in Fig. 9(a). Here we see that the distribution of photocurrent generation is uniform, and an abrupt decrease is seen in the cell edges. Then, the lateral LBIC maps for the Ge bottom cell acquired by LC effect (using 785 nm laser) and by direct 1064 nm laser excitation are shown in Figs. 9(b) and (c) respectively. The photocurrent generation in the Ge bottom cell from direct excitation is uniform while from the LC effect, it shows increasing generation towards the center. To interpret Figs. 9(b) and (c) respectively, consider the illustrations shown in Figs. 9(d), (e), and (f). Figure (d) illustrates the direct excitation from the attenuated 1064 nm scanning laser in which

the Ge bottom cell was excited at its local points. Thus, the spatial distribution of photocurrent, in this case, was expectedly uniform. It is also noted that photocurrent is still high even near the cell edges, suggesting that the size of the perimeter where the edge recombination occurs in Ge bottom cell is negligibly thin in this case. The observation is the same for direct GaAs middle excitation, as shown in Fig. 9(a). On the other hand, Figs. 9(e) and (f) show how the photons are emitted from some of the possible radiative emission spots in GaAs middle cell towards Ge bottom cell. Since the photocurrent generation due to the LC effect was observed to increase towards the cell center, assuming uniform voltage distribution across the Ge bottom cell, this suggests the following. One is that some of the photons emitted from the GaAs middle cell to Ge bottom cell escape towards the edges via escape cone [221], as illustrated in Fig. 9(e). Another is the internal reflection experienced by photons whose incident angle is larger than the escape cone, which may most likely arrive towards the center of the cell and be reabsorbed there, as illustrated in Fig. 9(f). These optical phenomena may thereby induce an in-plane nonuniformity of emission from the higher bandgap subcell [228].

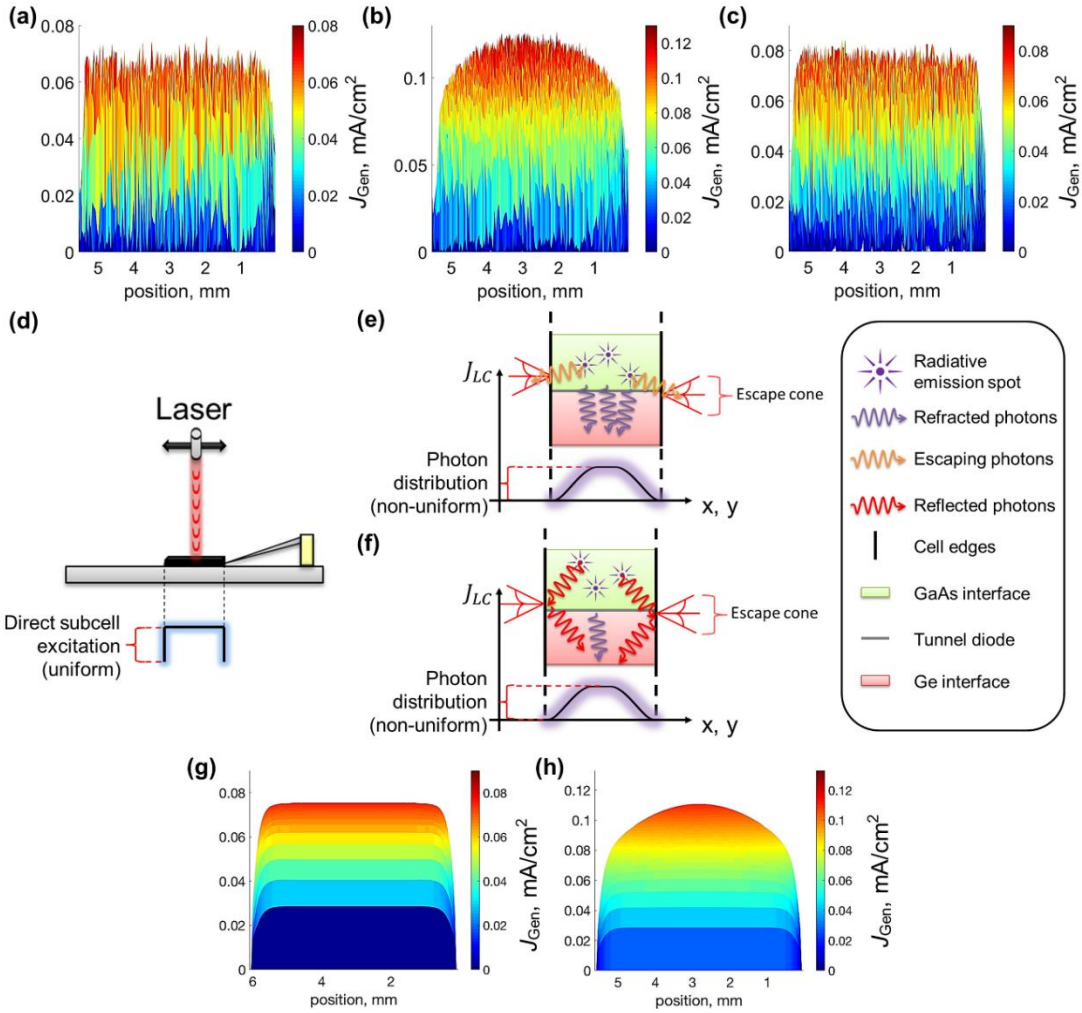

Fig. 9 Lateral LBIC maps of photocurrent generation (a) at GaAs middle cell by direct 785 nm laser excitation with ~90% attenuation filter and at Ge bottom cell (b) by LC effect using 785 nm laser and (c) by direct 1064 nm laser excitation with ~90% attenuation filter. (d) Illustration of 1064 nm laser excitation at a local point in Ge bottom cell. Some of the spontaneous emission spots in GaAs middle cell emitting

photons towards Ge bottom cell, in which some photons are refracted (represented by violet waves), (e) other photons escape towards the cell edges (orange waves), (f) and other photons are internally reflected (red waves) during the LC effect, using 785 nm laser. Lateral view of the Q-2D current map extracts (g) without and (h) with nonuniformity of LC effect considered, respectively. Applied InGaP/GaAs/Ge triple-junction solar cell terminal voltage is 1.5 V and spatial resolution is 23.44×20.98 □/mm^2 for all current maps shown [170].

Figures 9(g) and 9(h) show the lateral current maps without and with nonuniform optical profile considered, respectively. In Fig. 9(g), the lateral current map is uniform because the 2D electrical circuit calculations do not incorporate the nonuniform distribution profile of photons emitted from an adjacent higher bandgap subcell approaching the lower bandgap subcell of an MJSC. On the other hand, Fig. 9(h) shows a nonuniform lateral current map, after considering the nonuniform optical profile assumed. Here, the LC current increases towards the cell center as defined by eq. (11). This assumption shows good agreement with the measured LC current distribution shown in Fig. 9(b). Thus, considering an optical profile, which is assumed as a superellipse distribution, in this case, is necessary for modeling the nonuniform profile of the LC effect. This necessity also suggests that the spatial mismatch of the LC current generation in an MJSC subcell is mainly governed by its internal optics.

To determine how the LC current uniformity changes under different GaAs-to-Ge subcell LC efficiencies, using 785 nm excitation laser we acquired the LBIC maps under varying 660 nm LED intensity, thereby producing different LC efficiencies [56]. Figures 10(a) to (d) show how increasing the GaAs-to-Ge subcell LC efficiency affects the nonuniformity of the LC current distribution map. These figures show that the LC current generated in the Ge bottom cell increases as the LC efficiency increases. However, with increasing LC efficiency, nonuniformity becomes more prominent in the LC current distribution. This is quantitatively confirmed by the standard deviation of LC current map values as summarized in Table 8. Here, a higher σ_{LC} value indicates less uniform current distribution. It is also noteworthy that the minimum and the maximum LC efficiencies derived from LBIC measurements fitting are 8.5% and 69% respectively. 0% LC efficiency cannot be achieved experimentally because of measurement artifacts observed to become more severe at low photocurrent generation. Figures 10(e) to (h) show the simulation results under various LC efficiencies. These results show good agreement with the measured LBIC maps, indicating the same inferences discussed for Figs. 9(b) and (h).

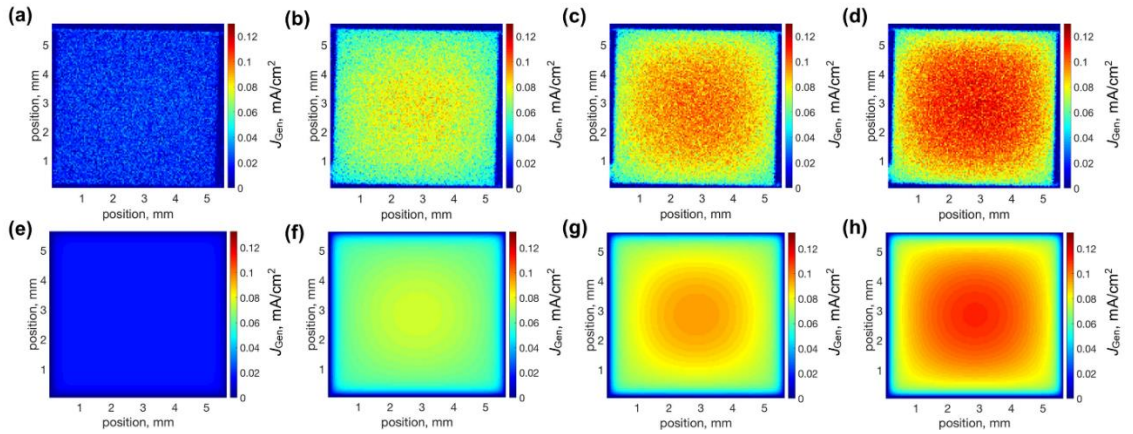

Fig. 10 Color map representations of LC current distribution at Ge bottom cell whose LC efficiencies are (a), (e) 8.5%, (b), (f) 18%, (c), (g) 41%, and (d), (h) 69%. Here, (a) to (d) were experimentally acquired

from LBIC measurements employing 785 nm excitation laser under varying 660 nm LED intensities while (e) to (h) were acquired from Q-2D simulation. Applied InGaP/GaAs/Ge triple-junction solar cell terminal voltage is 1.5 V for all current maps shown [170].

To probe the impact of the nonuniform LC effect on the limiting cell conversion efficiency, the Ge bottom cell conversion efficiency was calculated using eq. (17). The Ge bottom cell conversion efficiency calculations are summarized in Table 8. Considering the nonuniform optical profile of the LC effect, calculations have shown that increasing LC efficiency yields increasing Ge bottom cell efficiency as well. On the other hand, comparing the Ge bottom cell conversion efficiency calculations with ($\beta_{LC} \neq 0$, assimilated from LBIC measurements) and without ($\beta_{LC} = 0$) the optical nonuniformity considered, about 1.35% absolute conversion efficiency reduction is introduced at highest LC efficiency, which is relatively 16.83% of the Ge bottom cell conversion efficiency if the LC effect is uniformly distributed. With this amount of subcell conversion efficiency reduction, spatial current matching becomes an important concept to further improve the MJSC conversion efficiency when benefitting from the LC effect.

Table 8 Summary of the standard deviation of LC current map values obtained from LBIC map and calculated conversion efficiencies from the Q2DEP power distribution maps with increasing GaAs-to-Ge subcell LC efficiencies where Ge bottom cell is limiting. Values shown were rounded up to the nearest hundredths [170].

$P_{LED,660nm}$[a] (mW/cm^2)	$\alpha_{LC,m\to b}$[b] (%)	$\sigma_{J_{LC}}$[c] (μA/cm^2)	η_{TOTAL}[d] (%)		$\Delta\eta_{TOTAL}$[e] (%)	$\eta_{reduction}$[f] (%)
			nonuniform LC (assimilated, $\beta_{LC} \neq 0$)	uniform LC ($\beta_{LC} = 0$)		
35.00	8.50	9.50	0.00	0.00	0.00	0.00
180.00	13.00	21.60	1.34	1.53	0.20	12.77
200.00	18.00	23.40	2.57	2.95	0.38	12.76
225.00	27.00	26.00	3.80	4.40	0.60	13.57
240.00	35.00	27.30	4.58	5.37	0.78	14.62
250.00	41.00	28.40	4.90	5.82	0.92	15.73
270.00	56.00	29.80	6.02	7.15	1.13	15.77
293.46	69.00	33.50	6.67	8.01	1.35	16.83

[a] $P_{LED,660nm}$ is the 660 nm continuous LED light intensity.
[b] $\alpha_{LC,m\to b}$ is the LC efficiency from GaAs to Ge subcell.
[c] $\sigma_{J_{LC}}$ is the standard deviation of LC current map values.
[d] η_{TOTAL} is the Ge bottom cell conversion efficiency.
[e] $\Delta\eta_{TOTAL}$ is the absolute conversion efficiency difference between having uniform ($\beta_{LC} = 0$) and nonuniform ($\beta_{LC} \neq 0$) LC current at Ge bottom cell.
[f] $\eta_{reduction}$ is the relative Ge bottom cell conversion efficiency reduction due to the nonuniform LC effect.

Figure 11 shows the simulated LC current distribution maps with varying spatial LC current distribution profiles and varying perimeter areas. Figures 11(a) and (b) have uniform LC current profile but have thin and thick perimeter areas, respectively. Figure 11(c) is the same as the one shown in Fig. 10(h) and was included in this set of figures for convenience. Comparing Figs. 11(a) and (b), it can be seen that the difference of current distributions between the bulk and the perimeter regions is abrupt. On the other hand, comparing Figs. 11(a) and (c), the current distribution difference between the bulk and the perimeter regions is gradual. Thus, the approach for modeling edge recombination

effects and the optically nonuniform LC effect is not the same as they yield different results. However, through experimental results disclosed in Chapter V and from 3-dimensional distributed SPICE modeling in Appendix C, it will be revealed that the perimeter recombination may be the dominant cause for the nonuniform LC effect. Hence, the model used to acquire Fig. 11 may be insufficient to yield a gradual decrease in the current collection by perimeter recombination.

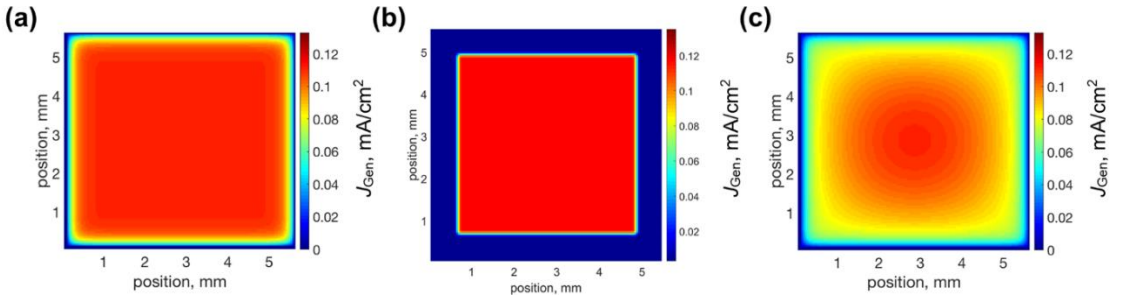

Fig. 11 Simulated Ge bottom cell LC current distribution profiles with (a) uniform profile, thin perimeter area, (b) uniform profile, perimeter area thicker than that in (a), and (c) nonuniform profile, thin perimeter area [170].

3.3.2. InGaP/GaAs/Ge 3JSCs at Different Operating Temperatures [217]

To qualitatively assess the spatial uniformity of LC current distribution in Ge bottom cell, the LBIC maps were acquired at maximum LED intensities as specified in Table 3 and at operating temperatures between 18°C and 72°C. The maps shown in Figs. 12(a) to (e) were compared with the fitted Q2D model results shown in Figs. 12(f) to (j). Here, Figs. 12(a) and (f), (b) and (g), (c) and (h), (d) and (i), and (e) and (j) were acquired at operating temperatures of 18°C, 27°C, 36°C, 54°C, and 72°C, respectively. The terminal voltage of 1.5 V is within the operating region of the 3JSC when Ge is current-limiting. The two sets of results demonstrate qualitative agreement with each other, having the nonuniform profile of the LC current collection considered in the model. This suggests that the Q2D electro-optical model is suitable in determining the in-plane LC effect in MJSCs at various operating temperatures. These maps also show that the LC current collection is highest at 18°C and lowest at 72°C. Therefore, the LC effect is most beneficial to the MJSC when operated at the lowest temperature possible.

Figure 13 (left axis) shows the GaAs-to-Ge subcell LC efficiencies as a function of cell operating temperatures from which the current maps in Fig. 12 were acquired. The LC efficiencies were calculated using eq. (8) by fitting the *J-V* characteristic curves into the Q2D electro-optical model at various operating temperatures. Here, it can be inferred that LC efficiency degrades when the operating temperature increases. This further supports the need for MJSCs to be operated at lower temperatures to allow high photocurrent collection induced by the LC effect.

Also, in Fig. 13, the degree of LC current uniformity, which is indicated by the normalized LC current standard deviation calculations (σ_{JLC}/Total J_{LC}, right axis), is plotted against temperature. This is to determine how the LC current uniformity varies as the operating temperature is increased. In the graph, the LC current uniformity shows negligible variations among different cell operating temperatures. This may imply that the ratio of uncollected photons does not change regardless of the temperature. The calculations from the LBIC measurements (magenta symbols) are slightly larger than those from the Q2DEP model (magenta line) due to the presence of background noise.

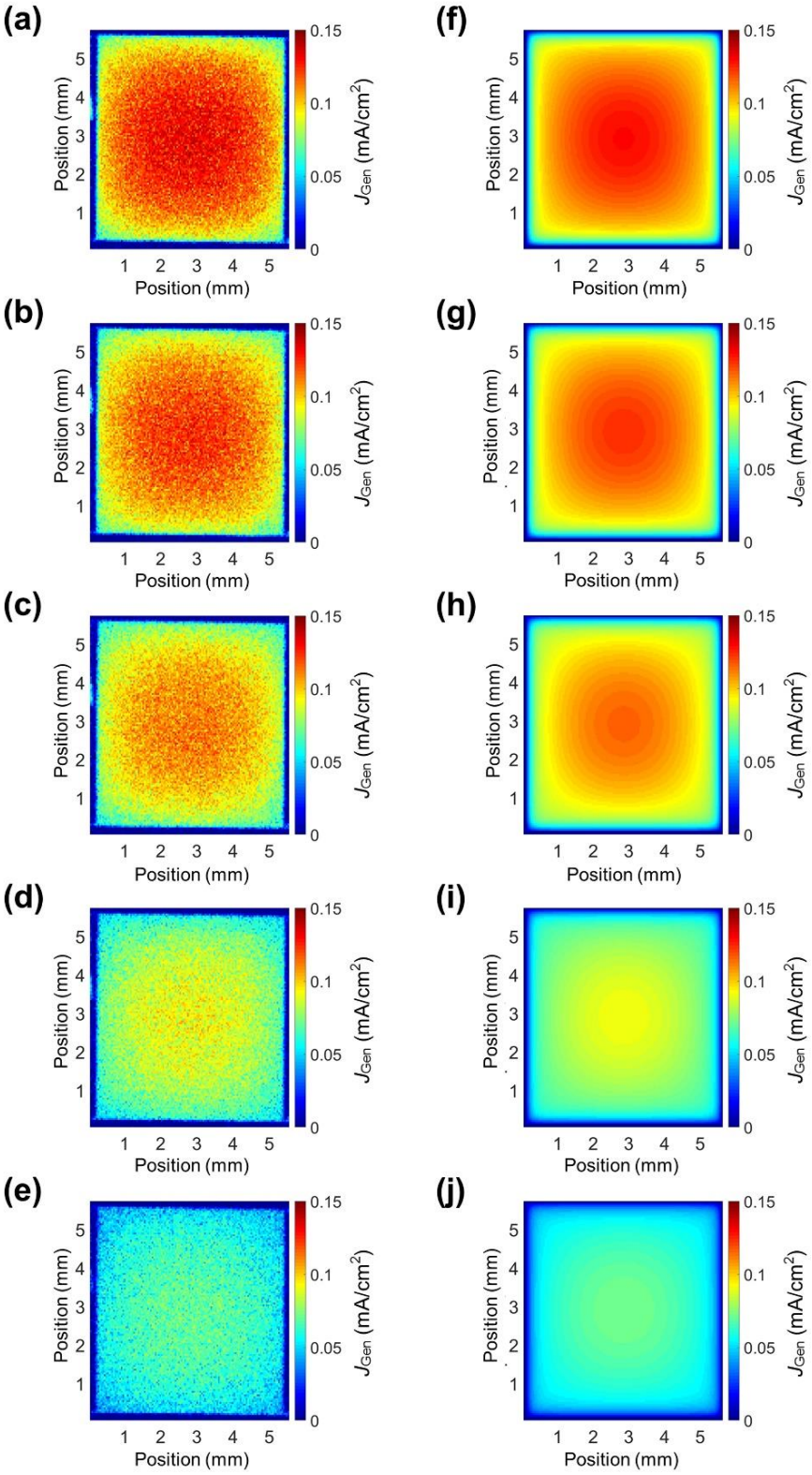

Fig. 12 Color map representations of collected current distribution, J_{Gen}, in the current-limiting Ge bottom cell at operating temperatures of (a), (f) 18°C, (b), (g) 27°C, (c), (h) 36°C, (d), (i) 54°C, and (e), (j) 72°C. Here, (a) to (e) were acquired from LBIC measurements while (f) to (j) were extracted from quasi-2-

dimensional (Q2D) electro-optical model. The spatial resolution of current maps is 23.44×20.93 pixels/mm^2 and the applied InGaP/GaAs/Ge triple-junction solar cell terminal voltage in all cases is 1.5 V [217].

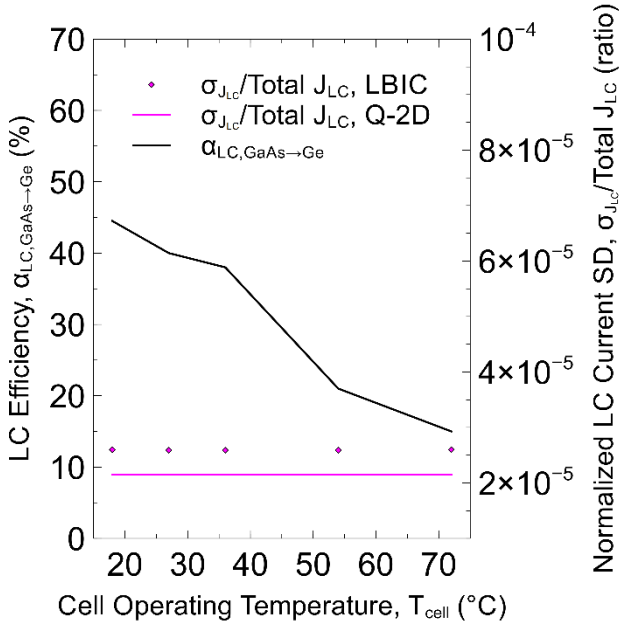

Fig. 13 LC efficiency ($\alpha_{LC,GaAs\rightarrow Ge}$, left axis) and normalized standard deviation of LC current (σ_{JLC}/Total J_{LC}, right axis) as a function of InGaP/GaAs/Ge triple-junction solar cell operating temperature [217].

To derive the coupling yield, γ_{LC}, at different MJSC operating temperatures, the DC light *J-V* characteristic curves were obtained. These were measured at temperatures between 18°C and 72°C and 660-nm LED intensities between 200 mW/cm^2 and 293.5 mW/cm^2. Figure 14(a) shows the series of DC light *J-V* characteristic curves acquired when Ge is current-limiting. Here, the symbols represent the measured *J-V* curves while the solid lines represent the *J-V* curves fitted into the Q2DEP model, having the LC effect considered ($\alpha_{LC,GaAs\rightarrow Ge} \neq 0$). Black arrows indicate measured *J-V* curves when increasing the 660-nm LED intensity. The *J-V* curve series show that as the operating temperature is increased, the LC current collection decreases. This agrees with the trend shown by the LBIC maps in Fig. 12. Besides, when the 660-nm optical bias on the adjacent GaAs middle cell is sufficiently high, that is, $I_{LED}^{660nm} \geq 240$ mW/cm^2, the shunt effect can hardly be noticed from the *J-V* curves at any operating temperature. Quantitatively, the fitted value for shunt resistance, R_{sh}, is in the order of 10^7 Ω. On the other hand, the shunt effect becomes apparent at $I_{LED}^{660nm} \leq 220$ mW/cm^2 and higher temperatures (54°C and 72°C). Here, R_{sh} is in the order of 10^6 Ω. Therefore, to minimize leakage current due to shunt defects and to maximize LC current collection in a current-limiting subcell, the optical bias on its adjacent upper bandgap subcell must be sufficiently high and the MJSC operating temperature must be as low as possible. Although Ge is known to be severely shunted [229], the results in Fig. 14(a) shows that the shunt is not as severe as expected, even for high temperatures. This suggests that shunt defects may have been carrier-filled by weak LC effect and by high-temperature current generation mechanisms. In Fig. 14(b), the same series of *J-V* curves were obtained from the Q2DEP model fit. But in this case, the LC effect was not considered ($\alpha_{LC,GaAs\rightarrow Ge} = 0$). It is shown that the shunt effect is consistently present for any given operating temperature and at any 660-nm LED intensity. However, unlike the trend shown in Fig. 14(a), the current collected in Ge

increases with an increase in MJSC operating temperature when there is no LC effect. Thus, this series of *J-V* curves suggests that aside from shunt leakage current, other mechanisms may have contributed to the current production increase at higher temperatures. These current production mechanisms could be coming from carrier generation by bandgap reduction [128,230] and by thermal excitation [231]. However, results on III-V//Si 3JSCs discussed later in this chapter reveal that bandgap reduction is unlikely to cause significant current generation within the T_c range studied [173].

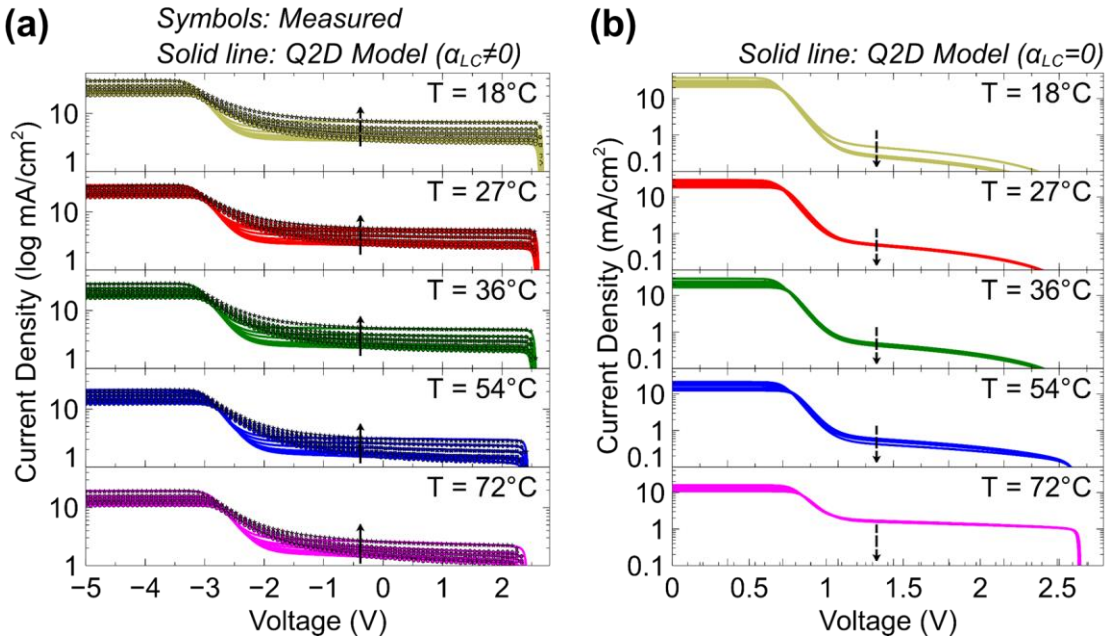

Fig. 14 (a) DC light *J-V* characteristic curve series of Ge bottom cell at varied cell operating temperatures from 18°C to 72°C and at 660-nm LED intensities of 200 mW/cm^2 to 293.5 mW/cm^2. The symbols and the solid lines represent the measured and the Q2D model fitted *J-V* curves *with* LC effect considered ($\alpha_{LC,GaAs\rightarrow Ge} \neq 0$), respectively. (b) Q2D-simulated DC light *J-V* characteristic curves *without* LC effect considered ($\alpha_{LC,GaAs\rightarrow Ge} = 0$). Black dashed arrows indicate increasing 660-nm LED intensity upon GaAs middle cell (I_{LED}^{660nm} = 200, 210, 220, 240, 260 and 293.5 mW/cm^2) [217].

The coupling yield, γ_{LC}, was derived from the light *J-V* characteristic curves shown in Fig. 15. γ_{LC} was calculated using eq. (13) at 660-nm LED intensities varied from 200 mW/cm^2 to 293.5 mW/cm^2, at temperatures from 18°C to 72°C, and at an applied 3JSC terminal voltage of 1.5 V. This was used to determine the ratio of the LC current collected to the uncollected photons emitted by GaAs and current losses due to nonradiative recombination in the current-limiting Ge. Derived γ_{LC} values are plotted in Fig. 15(a). Among the plots shown, the GaAs-to-Ge subcell γ_{LC} is highest at 18°C. This could be due to stronger radiative emission at lower temperatures, which suppresses nonradiative recombination [221]. Also, lower light intensities induced lower γ_{LC}, indicating less LC current collection, a higher number of uncollected photons or a larger number of nonradiative recombination events. This agrees well with the results of previous research findings [56,141]. To determine the difference between having and not having an LC effect at various operating temperatures, γ_{LC} is derived from the *J-V* curve series obtained from the Q2D model fit when $\alpha_{LC,GaAs\rightarrow Ge} = 0$. This is shown in Fig. 15(b). Having all other fitted Q2D parameters retained, γ_{LC} is not zero even when there is no LC effect on the current-limiting Ge bottom cell. On the contrary, it is even increased at higher

temperatures. This further suggests that aside from the LC effect, there must be other mechanisms that allow the current generation at high T_c. Moreover, the decreasing γ_{LC} trend in Fig. 15(b) when the 660-nm LED intensity is increased possibly indicates gradual carrier filling of shunt defects, most especially at higher temperatures (54°C and 72°C) [56,141].

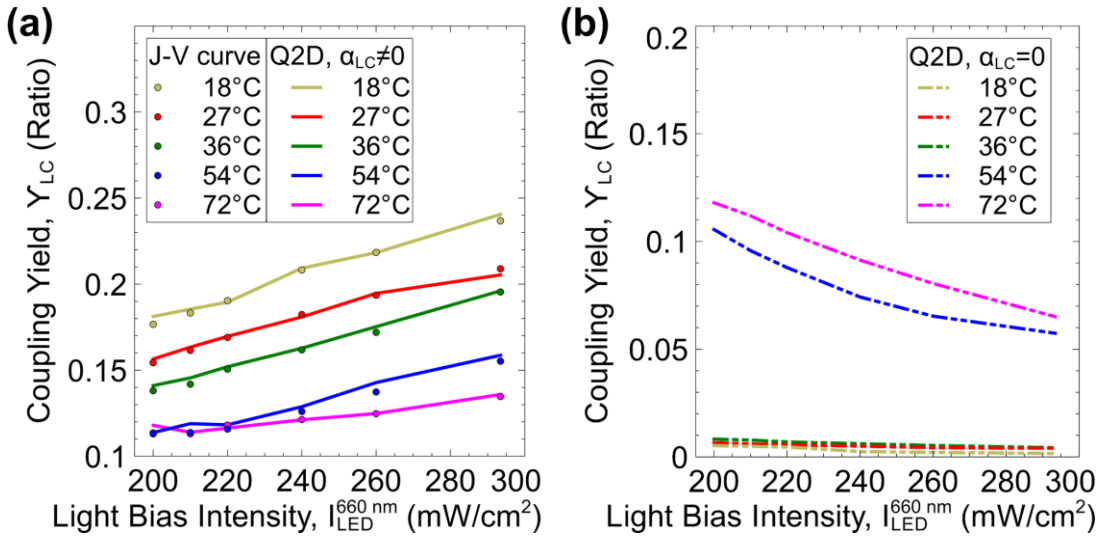

Fig. 15 Coupling yield vs. 660-nm LED intensity plots derived from (a) measured (circles) and quasi-2-dimensional (Q2D) model-fitted (lines) *J-V* characteristic curves *with* GaAs-to-Ge subcell LC effect ($\alpha_{LC,GaAs\rightarrow Ge} \neq 0$) and (b) *without* GaAs-to-Ge subcell LC effect ($\alpha_{LC,GaAs\rightarrow Ge} = 0$, Q2D simulation only) at an applied InGaP/GaAs/Ge triple-junction solar cell terminal voltage of 1.5V. Here, the cell operating temperatures were varied from 18°C to 72°C [217].

To quantify the difference between current-limiting PCEs with and without the LC effect, Ge bottom cell PCEs were calculated from the extracted Q2DEP current and voltage maps using eq. (17). These are summarized in Table 9. By LC effect alone, at an operating temperature of 18°C, the estimated PCE is 6.68%. However, this decreases as the cell operating temperature is increased. On the other hand, at high operating temperatures with no LC effect ($\alpha_{LC,GaAs\rightarrow Ge} = 0$), specifically at 54°C and 72°C, the resulting PCE is 0.01%. Thus, other current generation mechanisms present may have caused the non-negligible PCE, which are most likely due to shunt leakage current and as inferred from Fig. 14(b).

Table 9 Summary of calculated Ge bottom cell conversion efficiencies from the Q2DEP power distribution maps *with* ($\alpha_{LC,GaAs\rightarrow Ge} \neq 0$) and *without* ($\alpha_{LC,GaAs\rightarrow Ge} = 0$) LC effect with increasing InGaP/GaAs/Ge triple-junction solar cell T_c [217].

Cell operating temperature, T_c (°C)	Ge bottom cell conversion efficiency, η_{TOTAL} (%)*	
	with LC	*without* LC
18	6.68	2.37×10^{-5}
27	3.00	5.77×10^{-5}
36	0.22	3.36×10^{-3}
54	0.04	0.01
72	0.01	0.01

* Values shown are rounded up to the nearest hundredths.

To compare the photocurrent collection improvement by LC effect at low and high temperatures, the simulated lateral current distributions of Ge bottom cell with and without LC effect at 18°C and 72°C were obtained. These distributions are shown in Fig. 16. Comparing the current collection difference of Fig. 16(a) with that of Fig. 16(b) at the same operating temperatures, current collection improvement by LC effect is larger at 18°C than at 72°C. Moreover, from Q2DEP simulation without considering the LC effect at 72°C ($\alpha_{LC,\mathrm{GaAs}\rightarrow\mathrm{Ge}} = 0$), the current collection at the limiting cell is not negligible. This agrees with the results shown in Figs. 14(b) and 15(b). Thus, at high temperatures, the results collectively suggest that the current generation is driven by other mechanisms. Since these mechanisms generate more current at higher temperatures, current leakage due to shunt defects would be more severe at lower temperatures without the LC effect taking place in the current-limiting MJSC subcell. Also, the current collection improvement due to the LC effect, which is larger at lower than at higher temperatures, as depicted in Fig. 16, strengthens the inferences made from Figs. 12 to 14 that the photocurrent collection and consequently, the LC efficiency degrades when the operating temperature increases.

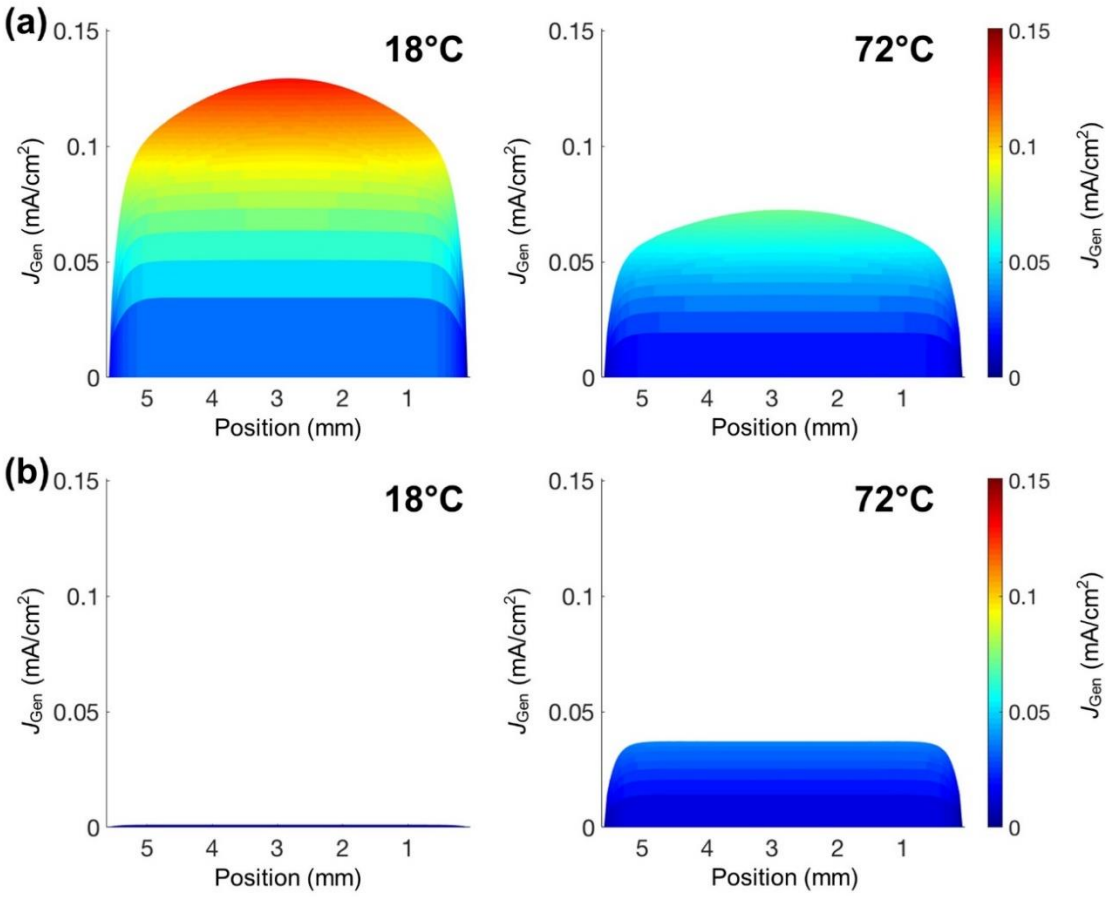

Fig. 16 Simulated lateral maps of collected current distribution, J_{Gen}, in the Ge bottom cell (a) *with* and (b) *without* luminescence coupling (LC) effect at operating temperatures of 18°C and 72°C. The spatial resolution of quasi-2-dimensional (Q2D) simulation maps is 23.44×20.93 pixels/mm^2, with 1.5 V InGaP/GaAs/Ge triple-junction solar cell terminal voltage applied in both cases [217].

To prove the temperature dependence of the LC effect at standard illumination condition, the *J-V* characteristics at operating temperatures between 18°C and 72°C under air mass 1.5 global (AM 1.5G) illumination without and with LED biases activated were acquired. The *J-V* characteristic curves in the case of having no LED biases used are shown in Fig. 17(a). Here, although the open-circuit voltage, V_{OC}, decreases by about 100 mV, the short-circuit current, J_{SC}, increases by approximately 0.1 mA/cm^2 when the operating temperature is increased. Thus, having AM 1.5G illumination only, carrier generation due to shunt leakages at higher temperatures may have allowed larger photocurrent collection, as inferred in Figs. 14(b), 15(b) and 16(b). On the contrary, when LED biases are activated along with the AM 1.5G source, both J_{SC} and V_{OC} decrease with increasing temperature. This is because of the high LED intensities which allow high photocurrent collection in InGaP and GaAs. In this condition, there is a significant current mismatch between GaAs and Ge, which may result in a larger LC current collection in the latter. Thus, if the LC effect becomes pronounced, the increase in the current collection at high operating temperatures becomes unobservable. This would be the case until the operating temperature increases to a certain temperature at which the LC current collection is at its weakest.

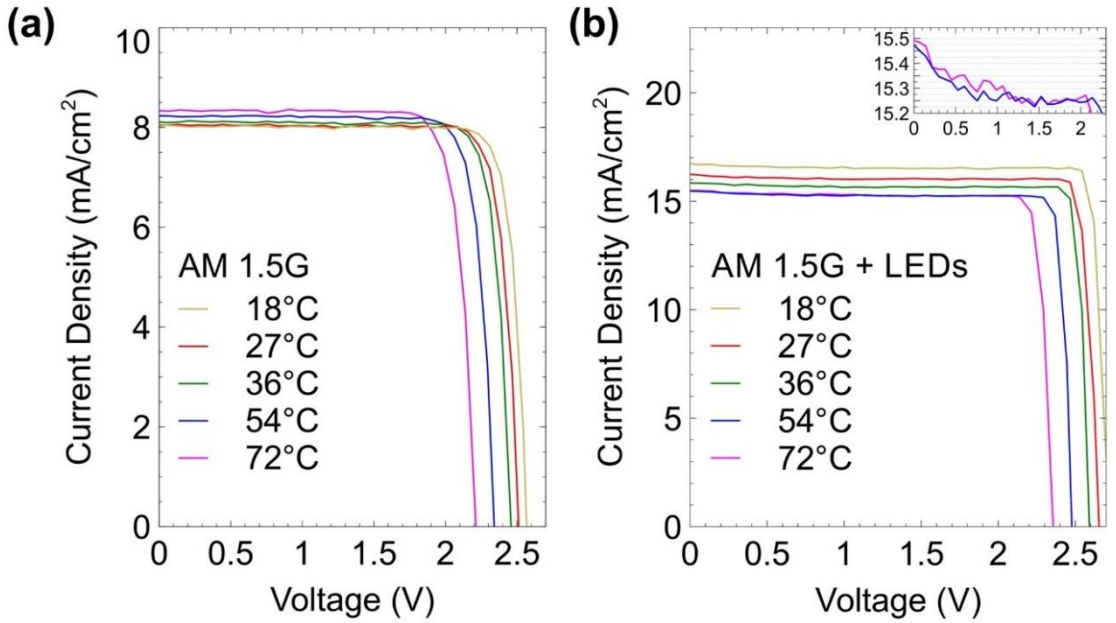

Fig. 17 Collection of DC light *J-V* characteristic curves (a) with global air mass 1.5 illumination at 1 sun (*unobservable* GaAs-to-Ge subcell luminescence coupling, LC) and (b) with global air mass 1.5 illumination at 1 sun, 430-nm LED bias at 47.5 mW/cm^2, and 660-nm LED bias at 293.5 mW/cm^2 (*observable* GaAs-to-Ge subcell LC) [217].

As summarized in Table 10 and as shown in the inset of Fig. 17(b), J_{SC} at 72°C exceeds the J_{SC} at 54°C. This suggests that the LC effect may have been suppressed at operating temperatures above 54°C. Consequently, the bandgap reduction and thermal excitation of carriers may have started to manifest their effect above this temperature where the increase in J_{SC} is about 0.01 mA/cm^2. Thus, when the MJSC operating temperature is high enough, shunt leakage tends to dominate the photocurrent generation by LC effect.

Furthermore, the contribution of the LC effect on the performance of MJSC becomes larger when operated at lower temperatures.

Table 10 Summary of short-circuit currents, J_{SC}, and open-circuit voltages, V_{OC}, obtained from DC light *J-V* characteristic curves with global air mass 1.5 illumination at 1 sun (*unobservable* GaAs-to-Ge subcell LC) and with global air mass 1.5 illumination at 1 sun, 430-nm LED bias at 47.5 mW/cm^2, and 660-nm LED bias at 293.5 mW/cm^2 (*observable* GaAs-to-Ge subcell LC) [217].

Cell operating temperature, T_{cell} (°C)	AM 1.5 G illumination only		AM 1.5 G *with* LED biases	
	J_{SC} (mA/cm^2)	V_{OC} (V)	J_{SC} (mA/cm^2)	V_{OC} (V)
18	8.03	2.58	16.72	> 2.70 *
27	8.04	2.51	16.23	2.66
36	8.10	2.43	15.84	2.58
54	8.24	2.33	15.49	2.48
72	8.34	2.18	15.50	2.33

* Measurements were limited to an applied InGaP/GaAs/Ge triple-junction solar cell terminal voltage of 2.70 V to prevent overcurrent damage to the samples at higher voltages.

3.3.3. InGaP/GaAs/Ge 3JSCs at Various Cell Areas [185]

3.3.3.1. Analysis of LC factor and fraction of nonuniformity

To determine how the LC factor varies upon increasing the incident light bias absorbed by an adjacent HBG subcell, the LC factor, α_{LC}, of 0.31 cm^2 and 0.99 cm^2 samples are plotted against increasing 660-nm LED intensity. This plot is shown in Fig. 18(a). Varying the 660-nm LED intensity varies the LC factor, that is, higher α_{LC} indicates larger LC current generation due to radiative emission from the adjacent GaAs middle cell. For both samples, the α_{LC} increases with the incident light bias on the GaAs middle cell. This agrees well with the previous findings reported [56,141].

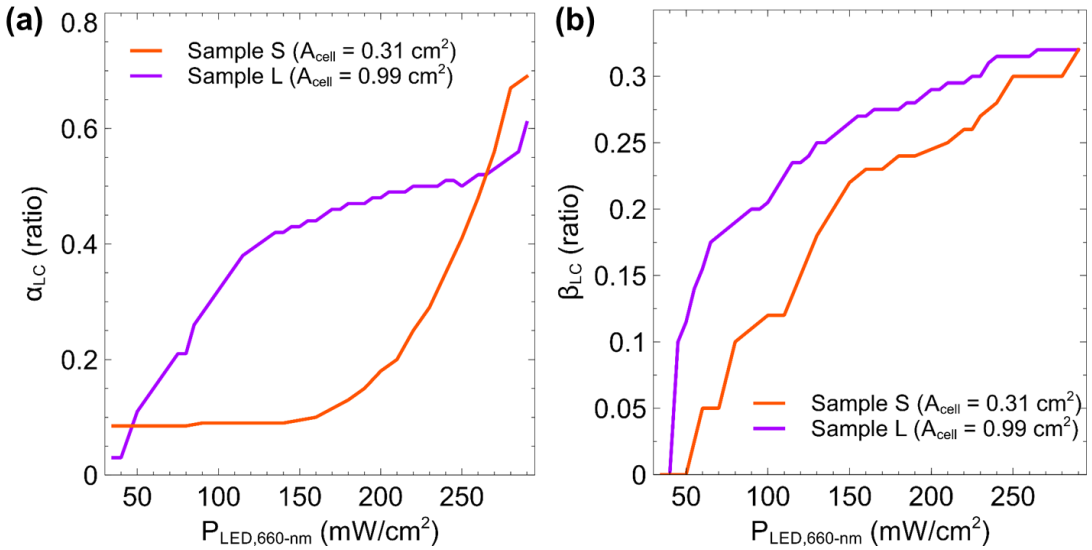

Fig. 18 (a) GaAs-to-Ge subcell luminescence coupling (LC) factor, α_{LC}, and (b) fraction of nonuniformity, β_{LC}, as a function of 660-nm LED intensity, $P_{LED,660\text{-}nm}$ [185].

Also in Fig. 18(a), the difference in the LC factor trend for the samples being studied is apparent. This may be attributed to their differences at which LED intensity will the leakage current from the adjacent GaAs middle cell subjected to low 660-nm LED intensities would dominate over LC current generation [149]. This is indicated by different 660-nm LED intensities at which the minimum LC factors are obtained. For Sample S (0.31 cm^2), the minimum α_{LC} obtained is 0.085 at 660-nm LED intensities from 35 to 85 mW/cm^2. On the other hand, for Sample L (0.99 cm^2), the minimum α_{LC} obtained is 0.03 at 660-nm LED intensities from 35 to 40 mW/cm^2. It should be noted that $\alpha_{LC} = 0$ cannot be obtained due to LBIC measurement artifacts [170]. The leakage current dominance of Sample S that manifested at the larger 660-nm LED intensities may be attributed to the larger edge-active region ratio than that of Sample L.

To know the variation of the spatial mismatch of generated LC current upon increasing the incident light bias absorbed by an adjacent upper bandgap subcell, the fraction of nonuniformity, β_{LC}, of 0.31 cm^2 and 0.99 cm^2 samples are plotted against increasing 660-nm LED intensity. This plot is shown in Fig. 18(b). Here, lower β_{LC} indicates better spatial LC current matching. For both samples, it can be seen that although increasing the 660-nm LED intensity increases α_{LC}, it also increases β_{LC}. This indicates that the stronger the LC effect is, the less uniform the spatial current generation will be. Meanwhile, the value of β_{LC} obtained for both samples have a similar trend upon increasing the 660-nm LED bias intensity. From this trend, it can be inferred that the degree of spatial LC current mismatch is independent of the cell area.

3.3.3.2. Comparison of the spatial LC current distribution for InGaP/GaAs/Ge 3JSC of different areas

To qualitatively compare the number of uncollected photons emitted by the GaAs middle cell towards the limiting Ge bottom cell, the LBIC maps were acquired using the settings listed in Table 3. Figures 19(a) and (b) show the acquired GaAs-to-Ge subcell LC current maps from cell areas of 0.31 cm^2 and 0.99 cm^2, respectively. These were acquired at 660-nm LED intensity of 290 mW/cm^2 and an applied MJSC terminal voltage of 1.5 V, which is within the operating region of the 3JSC for Ge bottom cell limited case. Comparing these LC current maps, it can be seen that the larger the cell area is, the longer the region of current uniformity degradation will be. For cell areas of 0.31 cm^2 and 0.99 cm^2, the steep degradation of LC current uniformity occurs within approximately 1 mm and 2 mm, respectively. As reported previously, this degradation towards the cell edges may originate from photons emitted from the GaAs middle cell escaping through the sides of the cell or subjected to total internal reflection [170]. These results qualitatively show that for larger cell areas, there are more uncollected photons which are emitted from the GaAs middle cell towards the cell edges. As a result, less LC current towards the cell edges is produced at the limiting Ge bottom cell.

To analyze the spatial LC current mismatch observed by LBIC mapping, the LC factor, α_{LC}, and the fraction of nonuniformity, β_{LC}, are fitted into the Q2DEP model. The fitted LC current maps for 0.31 cm^2 and 0.99 cm^2 samples at maximum LED intensities indicated in Table 3 are shown in Figs. 19(c) and (d), respectively. Here, the estimated LC factors for Samples S and L are 0.69 and 0.61, respectively, and the fitted β_{LC} value is 0.32 for both samples at this condition. Comparing the fitted current maps with Figs. 19(a) and (b), the Q2D electro-optical model can replicate the LBIC maps acquired from

Samples S and L. This suggests that this model is suitable for analyzing the nonuniform LC effect.

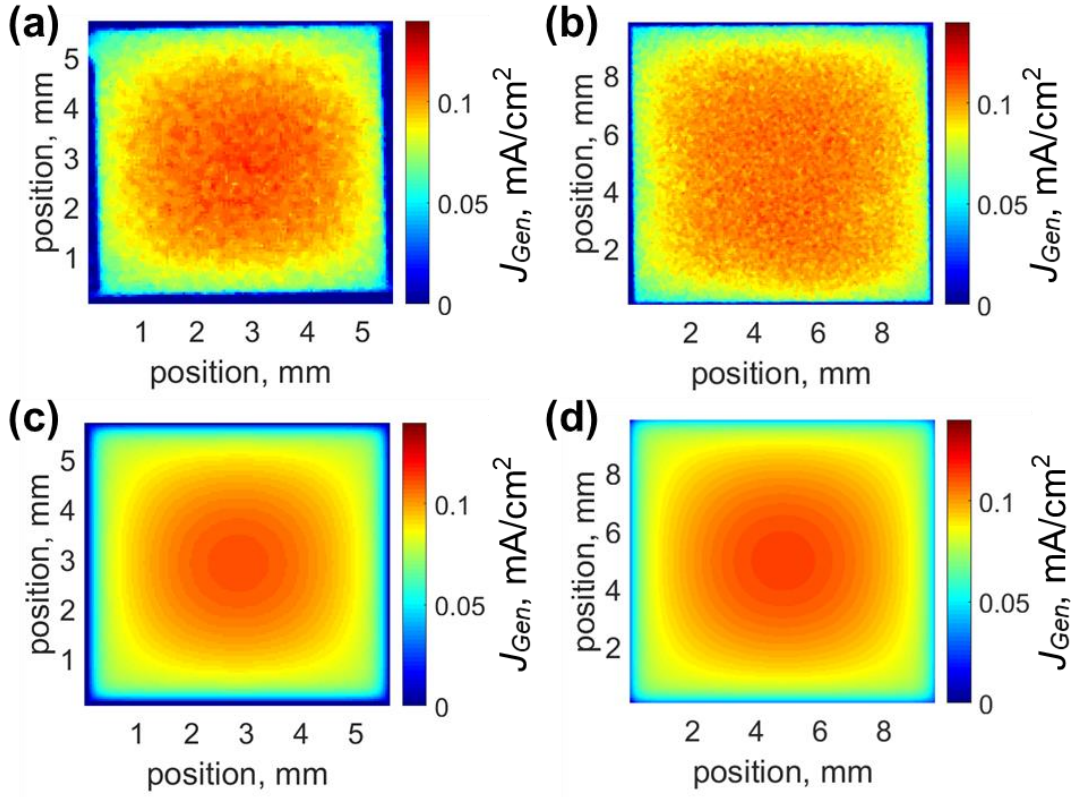

Fig. 19 LBIC maps of photocurrent generated by luminescence coupling (LC) effect, $J_{LC,net}$, at the Ge bottom cell of InGaP/GaAs/Ge triple-junction solar cell whose areas are (a) 0.31 cm^2 and (b) 0.99 cm^2, respectively. LC current maps of (c) 0.31 cm^2 and (d) 0.99 cm^2 samples reproduced by fitting α_{LC} and β_{LC} into the quasi-2-dimensional model. The LC factors for both samples are at maximum (α_{LC} = 0.69 for 0.31 cm^2 and α_{LC} = 0.61 for 0.99 cm^2 sample) and β_{LC} = 0.32 for both samples. The spatial resolution is 23.4 × 20.9 pixels/mm^2 and the applied terminal voltage is 1.5 V for all maps shown [185].

3.3.3.3. Analysis of absolute quantum efficiency reduction due to nonuniform LC effect

To quantify the number of photons emitted by GaAs middle cell successfully converted into LC current in the limiting Ge bottom cell, the mean QE of GaAs-to-Ge subcell LC current was calculated using eq. (18).

Figure 20 shows the mean QE derived from nonuniform (black solid line and black dotted line) and uniform (blue solid line and blue dotted line) LC current distribution plotted against increasing 660-nm LED intensity (for Samples S and L, respectively). The β_{LC} values used upon deriving the mean QEs of nonuniform and uniform LC current distributions are determined by fitting the LBIC measurements and is set to 0, respectively. For maximum LC factors acquired for Sample S (α_{LC} = 0.69) and Sample L (α_{LC} = 0.61), the mean QE estimated for nonuniform LC current distribution was 1.87% and 12.32%, respectively. As for the uniform LC current collection, the mean QE estimated are 2.25% and 14.88%, respectively. From these values, it is inferred that the radiative emission photon to electron conversion in the larger cell by LC effect is more efficient than in the smaller cell. This could be because the samples belong to different wafers, consequently having Sample L to generate an integrated net LC current of 4.02

A/cm^2, which is about 3.2 times larger than that of Sample S (Integrated LC current = 1.26 A/cm^2).

To compare the uncollected photons emitted from GaAs middle cell towards the limiting Ge bottom cell, the absolute QE differences, $\Delta mLCQE$, considering uniform ($\beta_{LC} = 0$) and nonuniform ($\beta_{LC} \neq 0$, fitted) LC current for Samples S and L were obtained using (8). The $\Delta mLCQE$ for Samples S and L are plotted in red solid line and red dotted line in Fig. 20, respectively. Although a higher 660-nm LED intensity yielded higher mean QE, $\Delta mLCQE$ also increased. At incident 660-nm intensity of 290 mW/cm^2, the values of $\Delta mLCQE$ were 0.38% and 2.55% for 0.31 cm^2 and 0.99 cm^2 samples, respectively. These calculations denote that the stronger the LC effect is, which manifests at high bias intensities of the upper bandgap subcell, the larger the number of uncollected photons emitted by GaAs middle cell and carrier generation towards the center of the sample by internal reflection will be. Nevertheless, these calculations suggest that it will help MJSCs to achieve better current generation by addressing the spatial LC current mismatch, most especially for MJSCs having larger active areas. This could be possibly addressed by implementing a light-trapping structure on the sides of the cell to prevent photon escape. This, in turn, may improve the MJSC conversion efficiency.

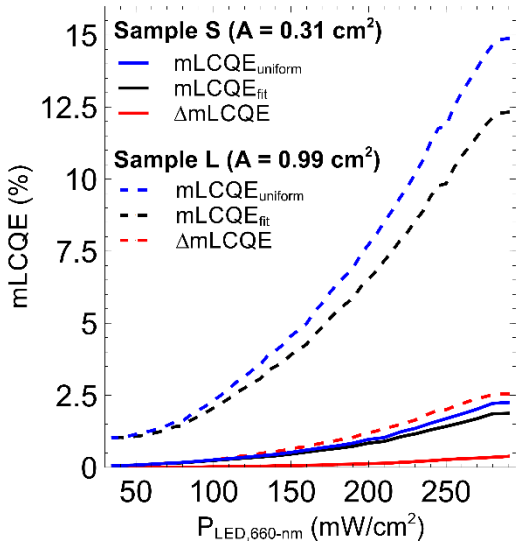

Fig. 20 Mean quantum efficiencies derived from nonuniform ($mLCQE_{fit}$, black solid line and black dotted line, fitted β_{LC}) and uniform ($mLCQE_{uniform}$, blue solid line and blue dotted line, $\beta_{LC} = 0$) LC current distribution and their absolute differences, $\Delta mLCQE$, (red solid line and red dotted line) as a function of 660-nm LED intensity, $P_{LED,660\text{-}nm}$ (for cell areas of 0.31 cm^2 and 0.99 cm^2, respectively) [185].

3.3.4. Space grade InGaP/GaAs/Ge 3JSCs at Room Temperature [171]

3.3.4.1. Concentration differences between adjacent subcells at various single wavelength intensities

Intensities used in measuring the series were converted into their equivalent global air mass 1.5 (AM 1.5G) concentration, C_{LED}, in suns. C_{LED} was calculated using eq. (1). The absorption range was determined from EQE measurement. $P(\lambda_{AM1.5G,i})$ for all InGaP/GaAs/Ge subcells of Samples A and B are summarized in Table 11 and their EQE measurements are shown in Figs. 21(a) and (b), respectively. Here, Sample A is a concentrator grade cell while Sample B is a space-grade cell. The AM 1.5G spectrum

used for C_{LED} calculation was based on the ASTM G173-03 standard table for reference solar spectral irradiances [198].

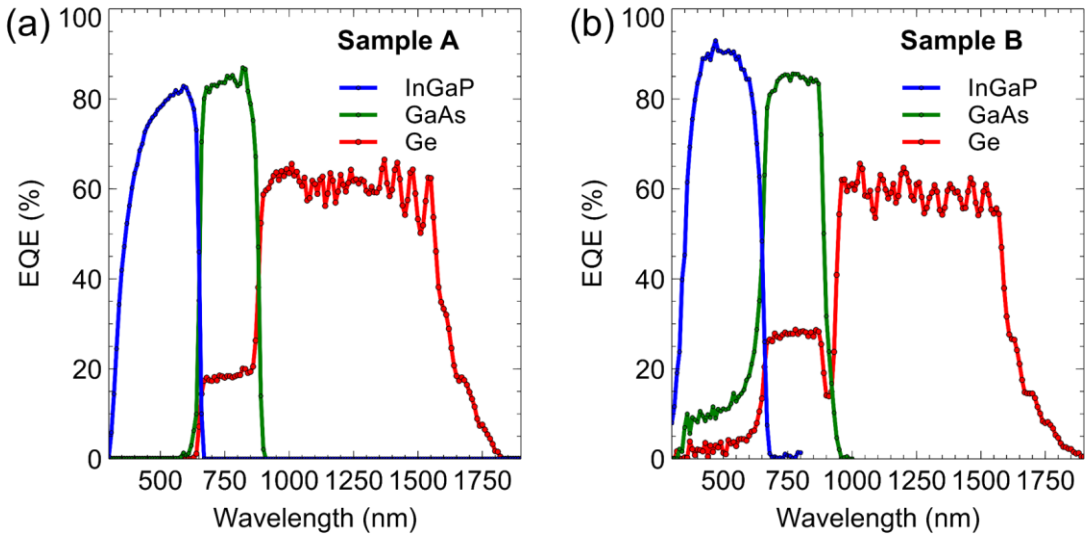

Fig. 21. External quantum efficiency (EQE) measurements of (a) Sample A and (b) Sample B having different InGaP top cell designs [171].

The series of measurements acquired for Samples A and B were then compared by deriving their coupling yields. To quantify how much the LC strength changes when the optical bias intensity upon InGaP is varied, the coupling yield, γ_{LC}, towards GaAs was derived from the DC light *J-V* curve series.

Table 11 Global air mass 1.5 (AM 1.5G) intensities per subcell derived from experimental EQE measurements [171].

3JSC subcell	AM 1.5G Intensity per subcell, $P(\lambda_{AM1.5G,i})$ (mW/cm^2)	
	Sample A	Sample B
InGaP (top)	40.79	40.93
GaAs (middle)	24.54	27.61
Ge (bottom)	28.12	25.63

3.3.4.2. Light *J-V* characteristics

To determine how the strength of the LC effect varies towards GaAs, series of DC light *J-V* characteristic curves were acquired. First, to ensure that GaAs is current-limiting the 3JSC, no direct light excitation on GaAs was applied. Next, Ge was biased by continuous 970-nm and 1550-nm LEDs at fixed intensities of 31.4 mW/cm^2 and 4.2 mW/cm^2, respectively. Lastly, InGaP was biased by a continuous 440-nm LED at various intensities to produce DC light *J-V* characteristic curves at different LC strengths [56,170]. 440-nm LED intensity was varied from 20 mW/cm^2 to 160 mW/cm^2, having a step size of 20 mW/cm^2 per measurement.

To derive the coupling yield, γ_{LC}, which relates the LC current collection to the total amount of current loss by recombination and uncollected photons in a limiting subcell

[56,141], series of DC light *J-V* characteristic curve were acquired. This was done to observe the LC current production trend in GaAs middle cell of Samples A and B as 440-nm LED intensity was increased. Figures 22(a) and (b) show the collection of GaAs DC light *J-V* curve series measured from Samples A and B, respectively. Here, 440-nm LED intensities were converted to their equivalent concentration in suns under AM 1.5G spectrum using eq. (1). Notice that in the plots, Sample B concentrations are slightly lower than those of Sample A, but they were derived from the same values of 440-nm LED intensities. This is because Sample B has a wider InGaP absorption range than Sample A. Excluding the InGaP/GaAs overlap regions, the difference is about 10 nm based on the EQE measurements acquired. Comparing the forward bias regions of these DC light *J-V* curve series, Sample B produced larger LC current generation than Sample A. This suggests that Sample B has a higher LC current production than Sample A. Nevertheless, the negative slope of the DC light *J-V* curves from Sample B is prominent, which may indicate that it has more shunt defects than Sample A. With this, one can expect higher LC yield, γ_{LC}, in Sample B.

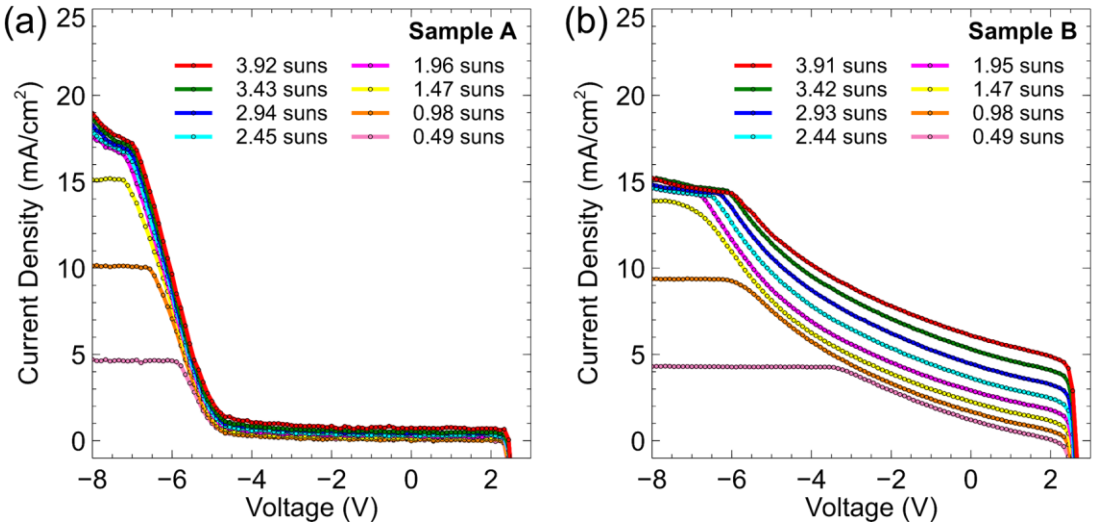

Fig. 22 Light *J-V* characteristic curve measurements under various 440-nm LED intensities, converted to suns, for LC current of GaAs middle cell in (a) Sample A and (b) Sample B having different InGaP top cell designs [171].

From the DC light *J-V* curve series in Fig. 22, the γ_{LC} values for both samples were derived using eq. (13). This was done to quantify how much the LC strength induced in GaAs varies when the optical bias intensity on InGaP is increased. $J_{LC,InGaP\rightarrow GaAs}$ values were first obtained at V = 0.56 V, which is within the operating region of current-limiting subcell, GaAs. For 440-nm LED intensities higher than 1.4 suns, the DC light *J-V* curves in Fig. 22(a) show a breakdown behavior as the reverse voltage was increased beyond V = -7.50 V. Since the saturation for InGaP photocurrent in this region is not visible, $J_{ph,InGaP}$ of Sample A at these intensities were obtained close to the reverse region knee voltage of the curves, at V = - 7.00 V. Meanwhile, for 440-nm LED intensities of about 1.40 suns and lower, the flat region for $J_{ph,InGaP}$ is visible. Hence, $J_{ph,InGaP}$ for these intensities were obtained by averaging the current values between V = -7.5 V and V = -8.0 V. Same was done in obtaining the $J_{ph,InGaP}$ values of Sample B. The γ_{LC} plots derived from GaAs DC light *J-V* curve series of Samples A and B with respect to increasing InGaP optical bias

intensity are shown in Fig. 23. Sample B has significantly larger γ_{LC} than Sample A. This may indicate that Sample B has greater LC current production than Sample A. This may also show that the InGaP top cell of Sample B is more emissive than that of Sample A. However, as mentioned earlier, the DC light *J-V* curves of Sample B at forward voltage region have more prominent negative slopes than those of Sample A. With this, it should be noted that the γ_{LC} values obtained for Sample B may be overestimated as they do not exclude shunt leakage current. Thus, when a current-limiting subcell is severely shunted, J_{LC} should be taken close to the knee voltage at the forward voltage regime. γ_{LC} values were calculated again for $J_{LC,InGaP \rightarrow GaAs}$ at V = 2.00 V. Still, the γ_{LC} trend in Sample B was significantly higher than γ_{LC} of Sample A. This suggests that Sample B was able to produce more LC current than Sample A.

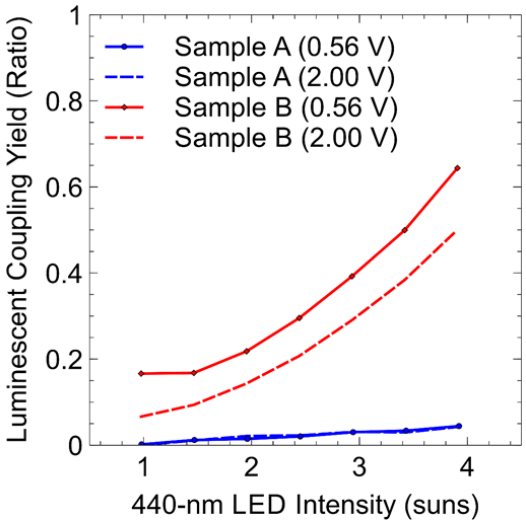

Fig. 23 LC yield, γ_{LC}, derived from measured light *J-V* characteristic curve series of GaAs middle cell for Sample A (blue plots) and Sample B (red plots) under various 440-nm LED intensities, converted to suns [171].

To observe the spatial variation of LC current collection by InGaP/GaAs coupling, LBIC maps were acquired using the settings indicated in Table 4 as condition 2. Figures 24(a) to (c) and 24(d) to (f) show the LC current collection in GaAs middle cell of Samples A and B, respectively. These LBIC maps were measured with increasing 440-nm LED intensity (C_{440nm} in suns listed in Table 12 below) and fixed 450-nm laser spot intensity ($C_{Laser,450nm}$ in suns). The samples were biased at V = 0.5 V for every LBIC measurement obtained. The equivalent concentration of light sources in suns is indicated above each figure as total concentration, $C_T = C_{440nm} + C_{Laser,450nm}$. As C_{440nm} was increased, the LC current collection in GaAs increased for both samples. Comparing these, Sample B produced LC current that is almost one order of magnitude larger than Sample A. This supports the inferences made for γ_{LC} values shown in Fig. 23, that InGaP of Sample B is more emissive than that of Sample A. This then suggests that Sample B has a better InGaP top cell quality than Sample A.

Regarding the spatial variation of LC current collection, LBIC maps of Sample B show more current quench spots than Sample A. This may indicate that Sample B has more defects than Sample A, either in InGaP or in GaAs. From these observations, it may be inferred that aside from photon escape and total internal reflection [170], homogeneity of subcell material growth may also cause spatial variation in LC current production.

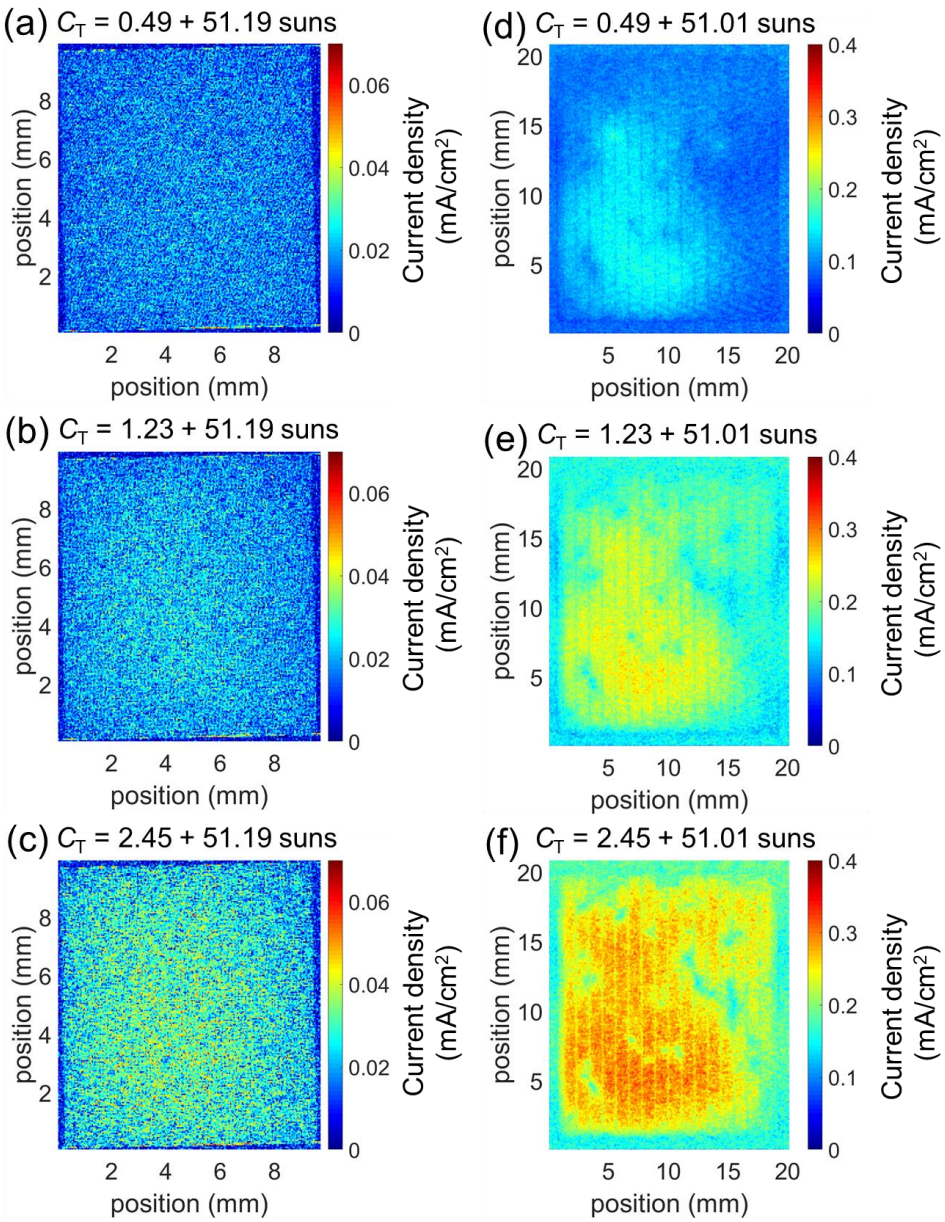

Fig. 24 LC current produced in GaAs middle cell, Sample A (a)-(c) and Sample B (d)-(f), for combined 440-nm LED and 450-nm laser spot equivalent concentration of (a) 0.49 + 51.19 suns, (b) 1.23 + 51.19 suns, (c) 2.45 + 51.19 suns, (d) 0.49 + 51.01 suns, (e) 1.23 + 51.01 suns, and (f) 2.45 + 51.01 suns, respectively. LBIC measurement settings used are summarized in Table I as condition 2. Applied InGaP/GaAs/Ge triple-junction solar cell voltage is 0.5 V for all maps acquired [171].

Table 12 Equivalent concentration derived from 440-nm LED intensities divided with global air mass 1.5 (AM 1.5G) intensities for InGaP top cell [171].

Equivalent AM 1.5G concentration, C_{LED} (suns)	440-nm LED intensity, P_{440nm} (mW/cm^2)	
	Sample A	Sample B
0.49	20.00	20.07
1.23	50.00	50.18
2.45	100.00	100.36

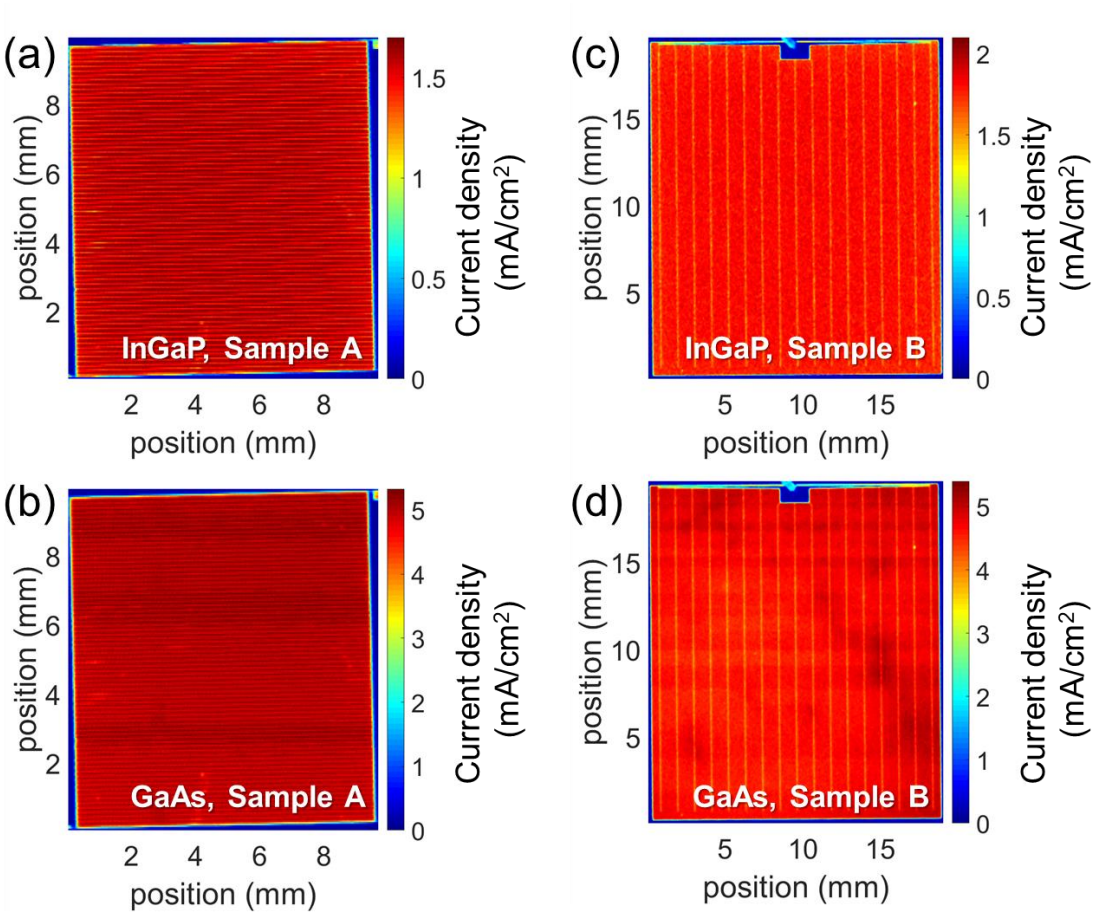

Subcell measured	Sample A		Sample B	
	C_{Laser} (suns per spot)	J_{ave} (mA/cm²)	C_{Laser} (suns per spot)	J_{ave} (mA/cm²)
InGaP top cell	51.19	1.46	51.01	1.68
GaAs middle cell	105.86	4.65	75.63	4.41

Fig. 25 LBIC maps of (a)-(b) Sample A and (c)-(d) Sample B for (a),(c) InGaP top cell and (b),(d) GaAs middle cell, respectively. Measurement settings used are summarized in Table I as conditions 1 and 3, respectively. Applied InGaP/GaAs/Ge triple-junction solar cell voltage is 0.5 V for all maps acquired [171].

To confirm the inferences made about the spatial variation of GaAs LC current generation in Samples A and B, InGaP top cell and GaAs middle cell LBIC maps were obtained by direct laser excitation. LBIC measurement settings used are summarized in Table 3 as conditions 1 and 3, respectively. Figure 25(a)-(b) and (c)-(d) show the photocurrent collection in InGaP and GaAs subcells of Samples A and B, respectively. The average current per spot and equivalent laser concentration per spot under AM 1.5G spectrum are summarized in the table included, also in Fig. 25. These maps were acquired at an applied 3JSC voltage of V = 0.5 V. All maps appear to be uniform, except for Fig. 25(d). Thus, the current quench observed in Figs. 24(d)-(f) may be attributed to nonuniform GaAs middle cell material growth. This agrees with the DC light J-V curve series obtained for Sample B which are severely shunted, as shown in Fig. 22(a). Also,

having uniform photocurrent production of InGaP and GaAs subcells in Sample A could be the reason why no current quench spots were observed in Figs. 24(a)-(c).

As for InGaP photocurrent collection, on average, larger photocurrent was collected in Sample B than in Sample A. This shows that more photons can be absorbed in InGaP of Sample B, which in turn may allow it to emit more photons toward GaAs. As a result, larger LC current was produced in GaAs of Sample B. Since InGaP of Sample B was observed to be a better absorber and, in turn, better emitter, this suggests that the InGaP top cell quality of Sample B is better than that of Sample A. Therefore, in general, upper bandgap subcell quality plays a role in improving the LC current production in a current-limiting lower bandgap subcell in MJSCs.

The results presented suggest that it becomes important to have a high-quality InGaP top cell of an InGaP/GaAs-based III-V MJSC to allow stronger LC effect on current-limiting GaAs middle cell. This may improve current matching between InGaP and GaAs subcells, especially under high concentration.

3.3.5. InGaP/AlGaAs//Si 3JSCs having Various Cell Areas [172]

3.3.5.1. Concentration differences between adjacent subcells at various single wavelength intensities

The absorption ranges of the InGaP/AlGaAs//Si 3JSC subcells were determined from the EQE measurement of 0.25-cm^2 InGaP/AlGaAs//Si 3JSC shown in Fig. 26(a) and the equivalent AM 1.5G current density per subcell are summarized in Table 13, Sec. 3.3.5.1.1. Since all samples were cut from the same wafer, the absorption range of a certain subcell was assumed to have negligible variation. With this assumption, the EQE measurement from one of the samples was considered sufficient. For the latter comparison, the EQE measurement of a 1-cm^2 InGaP/GaAs/Ge 3JSC was also acquired, shown in Fig. 26(b). Meanwhile, its equivalent AM 1.5G current density per subcell is summarized in Table 14, Sec. 3.3.5.1.2.

3.3.5.1.1. InGaP/AlGaAs//Si 3JSC EQE

AM 1.5G equivalent current densities from integrated irradiance, $J_{AM1.5G}$, based on the ASTM G173-03 standard [198] for all InGaP/AlGaAs//Si subcells are summarized in Table 13 and the EQE measurements of a 0.25-cm^2 sample acquired with 10-nm step size is shown in Fig. 26(a).

Table 13 Global air mass 1.5 (AM 1.5G) equivalent current densities per subcell of InGaP/AlGaAs//Si 3JSC derived from EQE measurements [172].

3JSC Subcell	AM 1.5G current density per subcell, $J_{AM1.5G}$ (mA/cm^2)	Absorption range per subcell, λ_{UL} to λ_{LL} (nm)
InGaP (top)	11.59	280 to 640
AlGaAs (middle)	10.03	650 to 840
Si (bottom)	5.79	850 to 1120

3.3.5.1.2. InGaP/GaAs/Ge 3JSC EQE

The absorption ranges of 1-cm^2 InGaP/GaAs/Ge 3JSC subcells were also determined from the EQE measurements shown in Fig. 26(b) [171]. $J_{AM1.5G}$ values of the InGaP/GaAs/Ge 3JSC subcells are summarized in Table 14. They were calculated using the same method for InGaP/AlGaAs//Si 3JSC samples.

Table 14 AM 1.5G equivalent current densities per subcell of InGaP/GaAs/Ge 3JSC derived from EQE measurements [171].

3JSC Subcell	AM 1.5G current density per subcell, $J(\lambda_{AM1.5G})$ (mA/cm^2)	Absorption range per subcell, λ_{UL} to λ_{LL} (nm)
InGaP (top)	12.53	320 to 650
GaAs (middle)	12.19	660 to 880
Ge (bottom)	14.46	890 to 1760

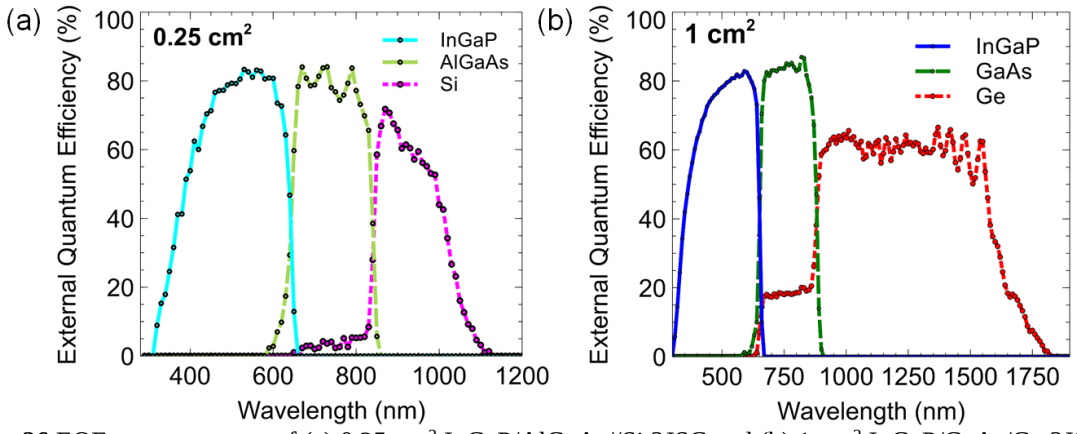

Fig. 26 EQE measurements of (a) 0.25-cm^2 InGaP/AlGaAs//Si 3JSC and (b) 1-cm^2 InGaP/GaAs/Ge 3JSC samples [171].

3.3.5.2. Light *J-V* characteristics curve series of Si bottom cell

Series of light *J-V* curves under different (*i*-1)'th subcell light bias intensities were acquired to determine how the LC current in the *i*'th subcell varies with increasing incident light intensity. Figure 27 shows the light *J-V* curves of 3J Si bottom cell with different active areas. From the *J-V* curves of all samples, it can be seen that increasing AlGaAs optical bias increased J_{sc} noticeably and V_{oc} slightly. On the other hand, all exhibited low shunt resistance, probably dominated by Si bottom cell shunt defects. This could be due to the samples being located near the outermost region of the wafer before cutting and would be typically more susceptible to nonuniform material growth [232].

Light *J-V* curves of the AlGaAs middle cell of InGaP/AlGaAs//Si 3JSC with different active areas are shown in Fig. 28 for all sample sizes. In the measurement setup used, the highest reverse voltage that can be applied across the sample was 10 V. The reverse voltage required to see the photocurrent collection of the adjacent InGaP top cell could have been higher than 10 V. As well, with this voltage, the InGaP/AlGaAs//Si 3JSC may already be operating at its breakdown regime. For these reasons, no further analysis of these *J-V* curves was conducted. Hence, the LC effect analysis was limited to Si bottom cell.

To quantify the amount of current matching improvement due to the LC effect, the AlGaAs-Si current matching ratio, $\zeta_{AlGaAs \rightarrow Si}$, was derived from the DC light *J-V* curves

in Fig. 27. As shown by these curves, shunt resistance representing cell defects dominated at lower forward voltages. Thus, to minimize the influence of shunt leakage current in $\zeta_{AlGaAs \rightarrow Si}$ calculations, the forward voltage chosen was 2.5 V, which is close to the knee point but less than the open-circuit voltage, V_{oc}. The results are plotted in Fig. 29. It was found that the current mismatch between the AlGaAs and Si subcells was reduced when the LC effect was high. This could be explained by the following hypotheses: 1) Since $Al_xGa_{1-x}As$ middle cell has low aluminum content ($x \leq 0.20$), it is considered high quality [233–234]. Because of this, a higher number of radiative recombination events in AlGaAs middle cell may be anticipated, leading to stronger LC effect; 2) A large number of defects in the GaAs and Si bonding interface produced high leakage current. While the leakage current would seem beneficial in this case, this can cause V_{oc} and FF reduction, as shown by the J-V curve measurements in Fig. 27.

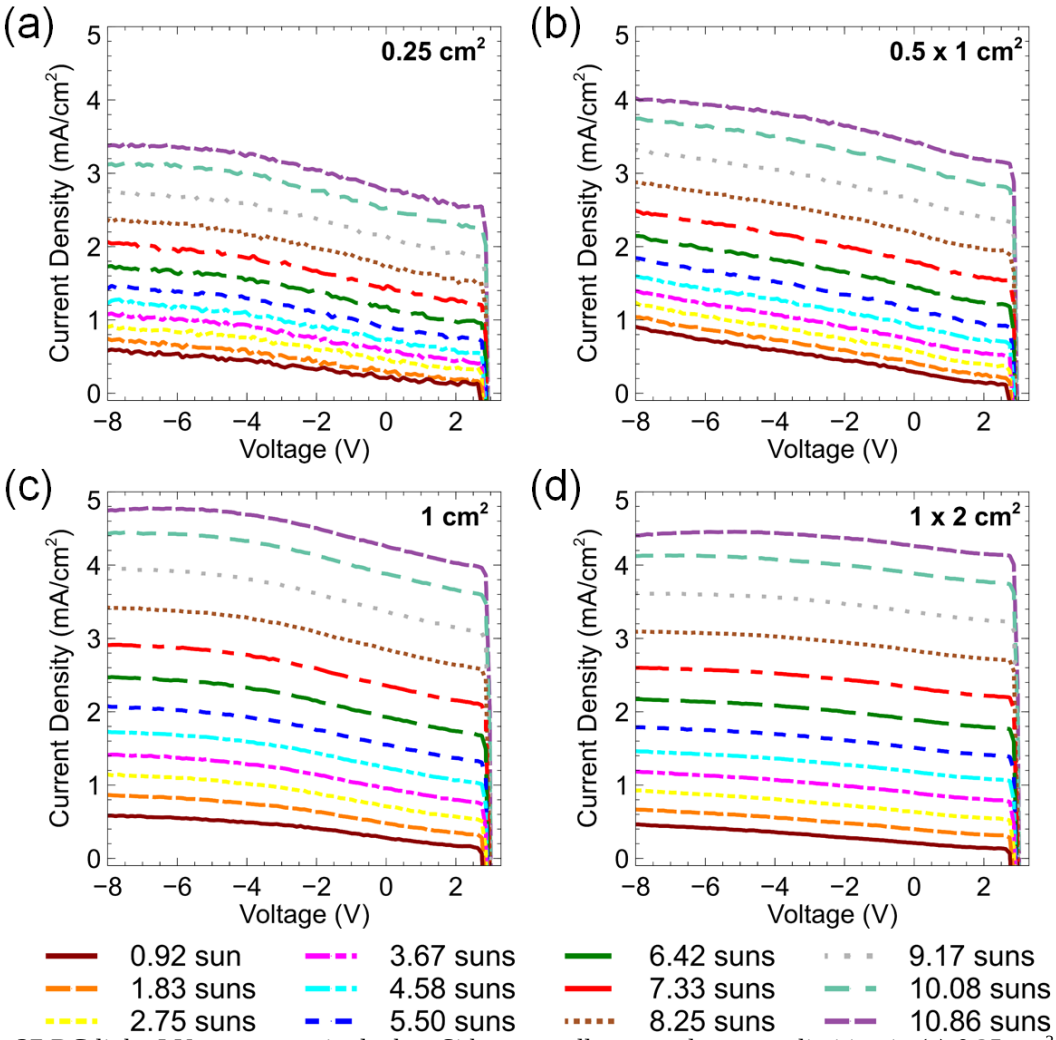

Fig. 27 DC light J-V curves acquired when Si bottom cell was made current limiting in (a) 0.25-cm^2, (b) 0.5×1-cm^2, (c) 1-cm^2 and (d) 1×2-cm^2 InGaP/AlGaAs//Si 3JSCs. These were measured under fixed 440-nm LED intensity and various 660-nm LED intensities between 0.92 sun and 10.86 suns equivalent at 25°C and applied terminal voltages between V = -8 V and V = 3.2 V [172].

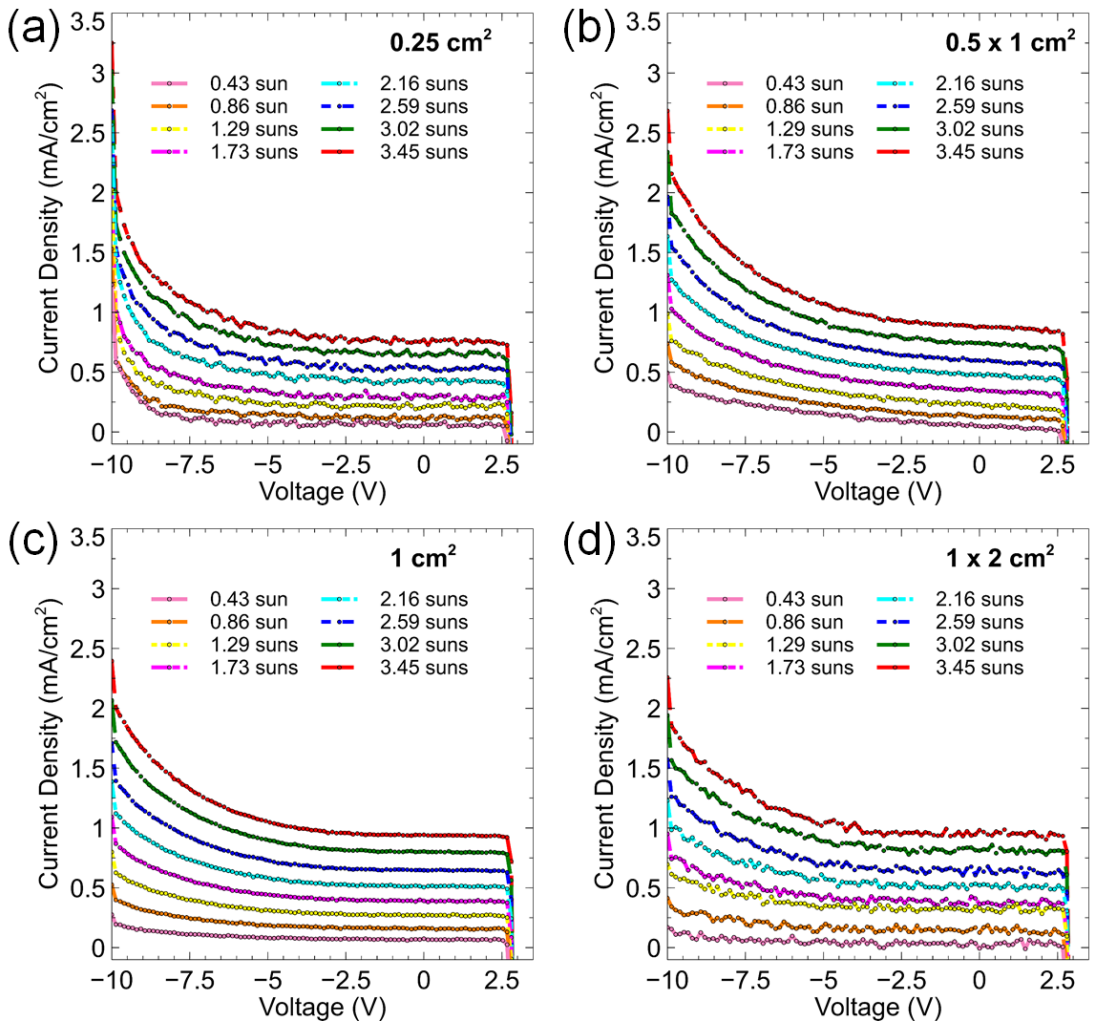

Fig. 28 DC light *J*-*V* curves acquired when AlGaAs middle cell was made current limiting in a (a) 0.25-cm^2, (b) 0.5×1-cm^2, (c) 1-cm^2 and (d) 1×2-cm^2 InGaP/AlGaAs//Si 3JSCs. These were measured under various 440-nm LED intensities between 0.43 sun and 3.45 suns at 25°C and applied terminal voltages between V = -10 V and V = 2.7 V [172].

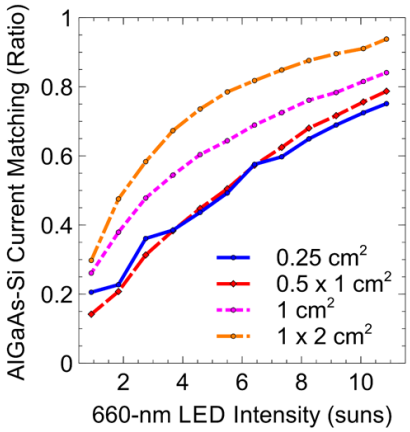

Fig. 29 AlGaAs-Si current matching, $\zeta_{AlGaAs \rightarrow Si}$, derived from the DC light *J*-*V* curves measured from the Si bottom cell of InGaP/AlGaAs//Si 3JSC having different cell areas. $\zeta_{AlGaAs \rightarrow Si}$ was derived from the current produced at an applied terminal voltage of V = 2.5 V with increasing 660-nm LED intensities between 0.92 sun and 10.86 suns [172].

3.3.5.3. Subcell current mapping of the InGaP/AlGaAs//Si 3JSC samples

3.3.5.2.1. Direct subcell excitation

To investigate the subcell material growth uniformity that may affect LC current production [171], maps of photocurrent collection in the InGaP top cell, the AlGaAs middle cell and the Si bottom cell were acquired through LBIC mapping. These are shown in Figs. 30(a), (d), (g), (j), Figs. 30(b), (e), (h), (k), and Figs. 30(c), (f), (i), (l), for cell areas of 0.25 cm^2, 0.5×1 cm^2, 1 cm^2 and 1×2 cm^2, respectively. The maps were obtained at an applied terminal voltage of V = 0 V (short-circuit current, J_{sc}, condition). When directly excited, photocurrent produced in each subcell was generally uniform. In most of the active regions of the cells, the uniform current collection was observed and then abruptly decreased toward the perimeter. However, as shown in Figs. 30(f) and (l), current quenches were seen from the lower right side of the Si bottom cell in 0.5×1-cm^2 and 1×2 -cm^2 samples. As mentioned earlier, since these samples grew at the outermost portions of the wafer, more defects may have been produced in the current-quenched regions [232]. It could also be due to the nonuniformity in GaAs bonding layer thickness or Si bottom cell emitter layer thickness introduced by the CMP step. As for the current quenches observed on the left and the right sides from all subcells of 0.25-cm^2 and 0.5×1-cm^2 samples, this may be attributed to the spatial resolution of LBIC mapping becoming comparable already to the dimensions of the cell. Additionally, perimeter recombination was found to be more prominent with smaller samples [207,219], which may explain the more severe current quenches observed for 0.25-cm^2 and 0.5×1-cm^2 samples.

3.3.5.2.2. LC current production in the Si bottom cell

To determine how the LC current production in a limiting subcell varies with increasing optical bias intensity upon its adjacent higher bandgap subcell, LBIC maps of Si bottom cell induced by LC effect were obtained. Here, the maps shown in Figs. 31(a), (e), (i), (m), Figs. 31(b), (f), (j), (n), Figs. 31(c), (g), (k), (o), and Figs 31(d), (h), (l), (p) were acquired when the 660-nm LED was set to 0.92 sun, 4.58 suns, 6.42 suns, and 9.17 suns equivalent intensities, respectively. Upon acquisition, V = 2.5 V was applied across the sample terminals, in alignment with the $\zeta_{AlGaAs \rightarrow Si}$ calculations discussed for Fig. 29.

The results in Fig. 31 reveal that for all samples, increasing LC strength increased LC current production but became less uniform. These results were also observed for the Ge bottom cell of InGaP/GaAs/Ge 3JSCs previously [141,170–171,186,217]. This poses a potential problem for concentrator III-V on Si MJSC structures, most especially under spectrally mismatched conditions that may cause a stronger LC effect among subcells. Since less current was produced towards the edges of the cell, there may be a higher number of nonradiative recombination events in this region. In this recombination process, excess absorbed energy gets redistributed among electronic excitations or lattice vibrations, making the edges hotter than the rest of the cell [235]. As a result, the cell may become damaged unevenly in the long run, hence reducing its lifespan.

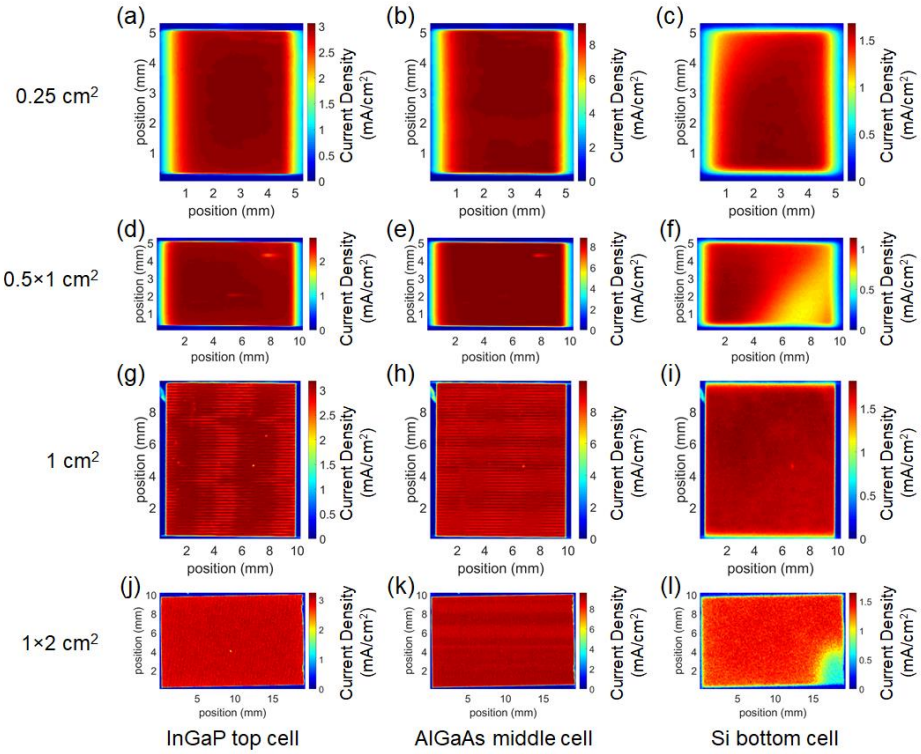

Fig. 30 LBIC maps obtained by direct laser excitation upon InGaP top cell, AlGaAs middle cell, and Si bottom cell of (a)-(c) 0.25-cm^2, (d)-(f) 0.5×1-cm^2, (g)-(i) 1-cm^2, and (j)-(l) 1×2-cm^2 InGaP/AlGaAs//Si 3JSC at V = 0 V (J_{sc}), respectively [172].

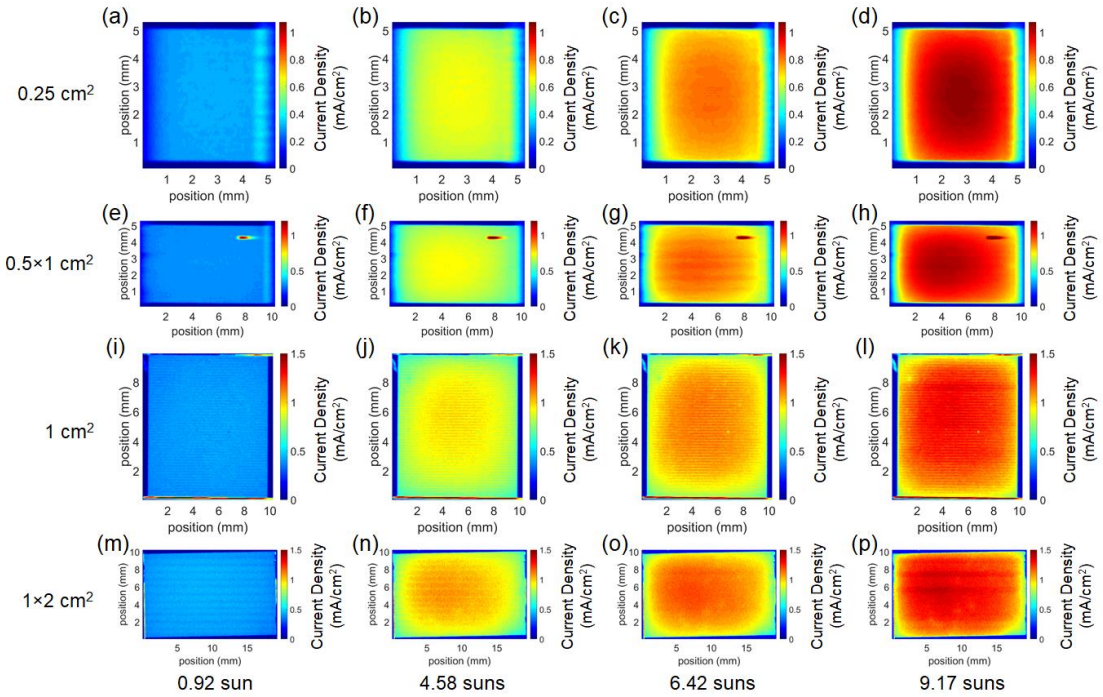

Fig. 31 LBIC maps induced by LC effect towards the Si bottom cell at various 660-nm LED intensity upon the AlGaAs middle cell for (a)-(d) 0.25-cm^2, (e)-(h) 0.5×1-cm^2, (i)-(l) 1-cm^2, and (m)-(p) 1×2-cm^2 InGaP/AlGaAs//Si 3JSC at an applied terminal voltage of V = 2.5 V. 660-nm LED intensity was varied from 22.0 mW/cm^2 (0.92 sun) to 220.4 mW/cm^2 (9.17 suns) [172].

3.3.5.4. Analysis of mean LC quantum efficiencies

As the first step in *mLCQE* analysis, light *J-V* curves were fitted into the 2D SPICE electrical model. The sample light *J-V* curve fits from the Si bottom cell of 0.25-cm^2 InGaP/AlGaAs//Si 3JSC are shown in Fig. 32(a). As indicated by the r^2 values being close to 1.0, good fits at different 660-nm LED intensities were obtained. Hence, the 2D SPICE electrical model is considered appropriate for predicting the *J-V* characteristics of Si bottom cell producing LC current.

Next, the LC current maps were fitted into the Q2DEP model defined by eq. (11). To determine how well the Q2DEP model could predict the LC current collection maps acquired by LBIC measurements, the cross-section plots of the LC current production in the Si bottom cell and the fitted LC current production using (14) are shown in Fig. 32(b). The LBIC measurements were acquired at an applied 3JSC terminal voltage of V = 2.5 V and at 10.86 suns equivalent 660-nm LED intensity upon the AlGaAs middle cell of all InGaP/AlGaAs//Si 3JSC samples. By visual inspection, the Q2DEP model fit looks close to the measured LC current production. Quantitatively, r^2 values were close to 1.0. This suggests that the Q2DEP model may be used to predict spatially-resolved LC current production.

To quantify how severe the nonuniformity of spatial LC current distribution was, the fraction of nonuniformity, $\beta_{LC,AlGaAs\rightarrow Si}$, was determined through LBIC map fitting. In 0.5×1-cm^2, 1-cm^2 and 1×2-cm^2 samples, $\beta_{LC,AlGaAs\rightarrow Si}$ increased with increasing 660-nm LED intensity as shown in Fig. 32(c). This agrees with the observations from Fig. 31, that increasing LC strength increased LC current production but degraded current uniformity. However, at some intensities, the $\beta_{LC,AlGaAs\rightarrow Si}$ of the smaller samples were found higher than those of the larger samples. Hence, $\beta_{LC,AlGaAs\rightarrow Si}$ does not seem to depend on the cell area. The same was observed from InGaP/GaAs/Ge 3JSCs [184]. Meanwhile, high $\beta_{LC,AlGaAs\rightarrow Si}$ was obtained for 0.25 cm^2 at 0.92 sun equivalent 660-nm LED intensity. This may be ascribed to high leakage current due to shunt defects becoming prominent at lower LC strength for this sample [56,141]. As shown in Fig. 32(b), the 1×2-cm^2 cell has the largest current density among the samples. Consequently, the highest $\beta_{LC,AlGaAs\rightarrow Si}$ was obtained for the 1×2-cm^2 sample and was 0.25 at 9.17 suns equivalent 660-nm LED intensity.

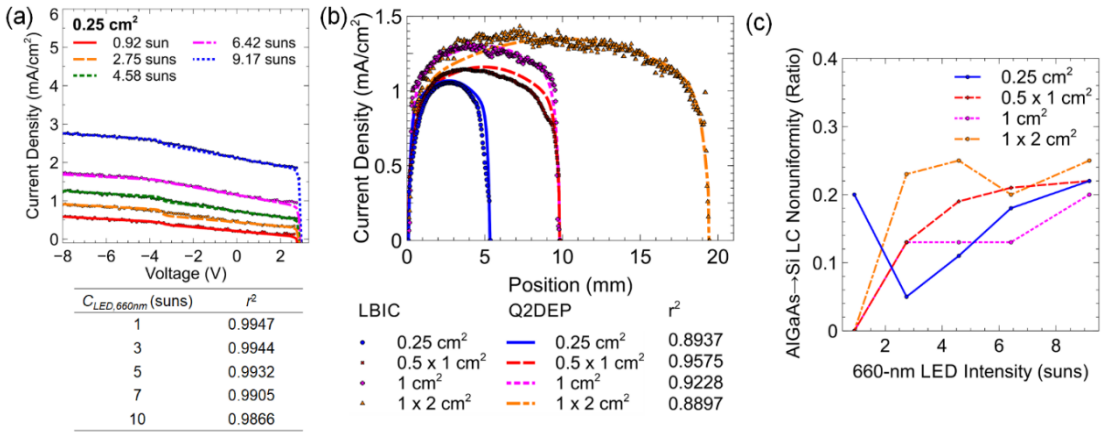

$C_{LED,660nm}$ (suns)	r^2
1	0.9947
3	0.9944
5	0.9932
7	0.9905
10	0.9866

Fig. 32 (a) Measured (solid lines) and fitted (dotted symbols) DC light *J-V* curves acquired when Si bottom cell was made current limiting in a 0.25-cm^2 InGaP/AlGaAs//Si 3JSC. (b) Measured and fitted LC current collection in the Si bottom cell of InGaP/AlGaAs//Si 3JSCs having different areas as a function of position at 9.17 suns equivalent 660-nm LED intensity. In both (a) and (b), r^2 is the coefficient of determination. (c)

AlGaAs-to-Si subcell LC current nonuniformity, $\beta_{LC,AlGaAs\rightarrow Si}$, with increasing 660-nm LED intensity. $\beta_{LC,AlGaAs\rightarrow Si}$ was obtained through LBIC map fitting of LC current production in Si bottom cell for all samples at an applied terminal voltage of V = 2.5 V [172].

To quantify the number of emitted photons that were successfully converted into LC current collected from the Si bottom cell, *mLCQE* was derived using eq. (18) for all samples with an increasing 660-nm LED intensity. Figure 33(a) shows the *mLCQE* calculated from nonuniform ($\beta_{LC,AlGaAs\rightarrow Si} \neq 0$, LBIC map-fitted) and from uniform LC current distributions ($\beta_{LC,AlGaAs\rightarrow Si} = 0$). For all samples, increasing 660-nm LED intensity resulted in increasing *mLCQE*. Moreover, the larger the sample is, the larger was the *mLCQE* value obtained. This agrees with the results attained from InGaP/GaAs/Ge samples in [185], shown in Fig. 33(b). Here, the 660-nm LED intensity equivalents in suns, C_{LED}, of InGaP/GaAs/Ge 3JSC samples were derived using the same method described in Sec. 3.2.3.2. Just as with InGaP/AlGaAs//Si 3JSC samples, C_{LED} indicates the concentration difference between GaAs and Ge. The equivalent 660-nm LED current density under AM 1.5G is summarized in Table 14 and the EQE measurement of a 1.0-cm^2 InGaP/GaAs/Ge sample is shown in Fig. 26(b), Sec. 3.3.5.1.2 [171].

To quantify the number of uncollected photons and electron-hole pair lost to recombination, the absolute LCQE difference, *ΔmLCQE*, was calculated using eq. (19). Figure 34(a) shows the *ΔmLCQE* for all samples. While increasing 660-nm LED intensity increased *mLCQE*, *ΔmLCQE* increased as well. This may indicate an increase in the number of unabsorbed photons that may have escaped through the sides or were subjected to internal reflection [170], thereby causing nonuniform LC current collection as shown in Fig. 31. It could also be due to electron-hole pair recombination in the defects near the cell edges [202–203,205,219], to nonuniform material growth [171] or lateral resistance effects [154,220]. It was also found that although the sample with the largest cell area, which is 1×2 cm^2, delivered the largest *mLCQE*, it also yielded the largest *ΔmLCQE*. The calculated *mLCQE* and *ΔmLCQE* from the 1×2 cm^2 sample were 7.36% and 1.68%, respectively. A similar trend was also observed from InGaP/GaAs/Ge 3JSC samples [185], shown in Fig. 34(b). Thus, among the InGaP/AlGaAs//Si 3JSC samples studied, the 1×2-cm^2 sample has the highest potential for current production improvement. Meanwhile, for 0.25 cm^2 sample, *ΔmLCQE* decreased at low intensities, from 0.92 sun to 2.75 suns difference. This could be due to the high number of shunt defects in the cell that did not get filled by photons, thereby producing leakage current at low intensities [56,141].

From the results presented, the nonuniformity of LC current production becomes significant with a stronger LC effect, brought about by a higher light concentration difference between a higher bandgap subcell and an adjacent lower bandgap subcell. This was found not only for Ge-based III-V MJSCs [185], but also for Si-based III-V MJSCs. Thus, for concentrated sunlight applications, the nonuniform LC effect should be considered in the structure design to improve the current generation which, in turn, may result in conversion efficiency increase, irrespective of the cell size. Moreover, this may also compensate for nonuniform illumination brought about by chromatic aberration of concentrator lenses in CPV systems [204,214]. Another benefit this may have is preventing the cell to develop uneven damage over time [235] through homogenizing current production, thereby allowing III-V on Si MJSCs to function properly until the end of their expected lifespan or even beyond it.

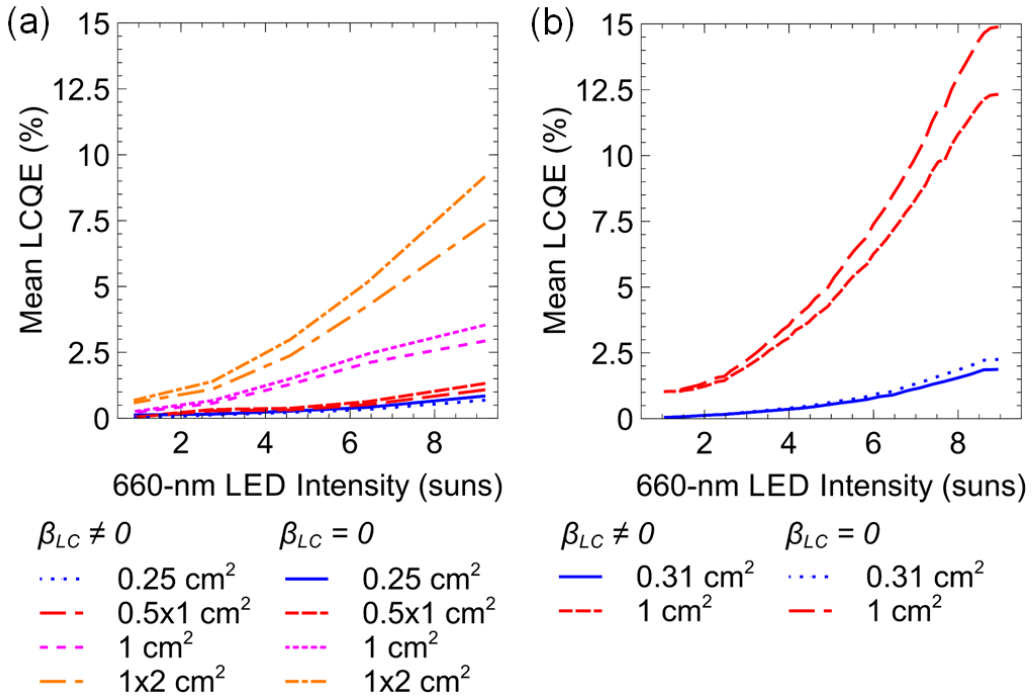

Fig. 33 Mean LCQE plots acquired from LBIC map fitting ($\beta_{LC,AlGaAs \rightarrow Si} \neq 0$) and simulated uniform current collection ($\beta_{LC,AlGaAs \rightarrow Si} = 0$) (a) in Si bottom cell of InGaP/AlGaAs//Si 3JSC samples at V = 2.5 V and (b) in Ge bottom cell of InGaP/GaAs/Ge 3JSC samples at V = 1.5 V [185], respectively [172].

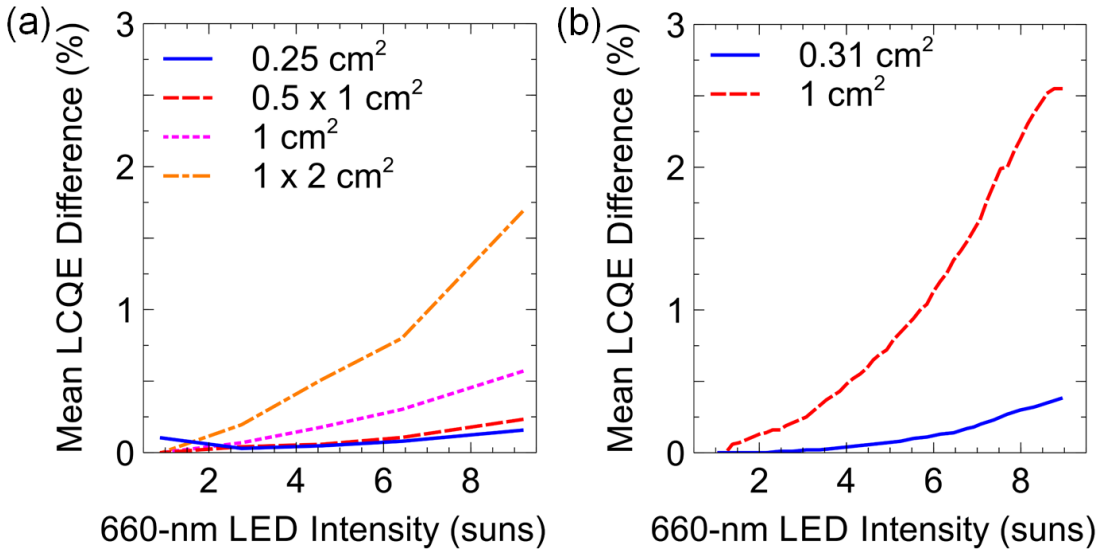

Fig. 34 Consolidated absolute LCQE difference, *ΔmLCQE*, plots derived from the difference between the mean LCQE plots from LBIC map fitting ($\beta_{LC,AlGaAs \rightarrow Si} \neq 0$) and from simulated uniform LC current collection ($\beta_{LC,AlGaAs \rightarrow Si} = 0$) in (a) Si bottom cell for InGaP/AlGaAs//Si 3JSC samples at V = 2.5 V and (b) Ge bottom cell for InGaP/GaAs/Ge 3JSC samples at V = 1.5 V [185], respectively [172].

3.3.6. InGaP/AlGaAs//Si 3JSCs at Different Temperatures [173]

3.3.6.1. Light *J-V* Characteristics of InGaP/AlGaAs//Si 3JSCs

To determine how the electrical performance varies with an increasing cell operating temperature, T_c, series of light *J-V* characteristic curves were measured. Figures 35(a) to

(f) show the light *J-V* curve series measured at T_c = 15°C, 25°C, 35°C, 55°C, 75°C and 95°C, respectively, and at various 660-nm LED intensities. Here, the 660-nm LED intensities in suns indicate the light concentration difference between the AlGaAs middle cell and the Si bottom cell. As T_c was increased and 660-nm LED intensity was decreased at each T_c, both short-circuit current, J_{sc}, and open-circuit voltage, V_{oc}, decreased, which consequently reduced conversion efficiency. Moreover, the influence of shunt defects, indicated by steepening *J-V* curve slopes between V = 0 V and V = 2.0 V became more prominent when T_c was increased. This is because as T_c increases, the overall radiative recombination events decrease due to the elongation of a radiative lifetime with bandgap reduction (BGR) [236]. This was also observed previously for Ge-based MJSCs with LC effect [187,217]. It was hypothesized that BGR and thermally-excited carriers would result in larger current production [128]. However, no increase in current production due to BGR with increasing T_c [230,237] was observed.

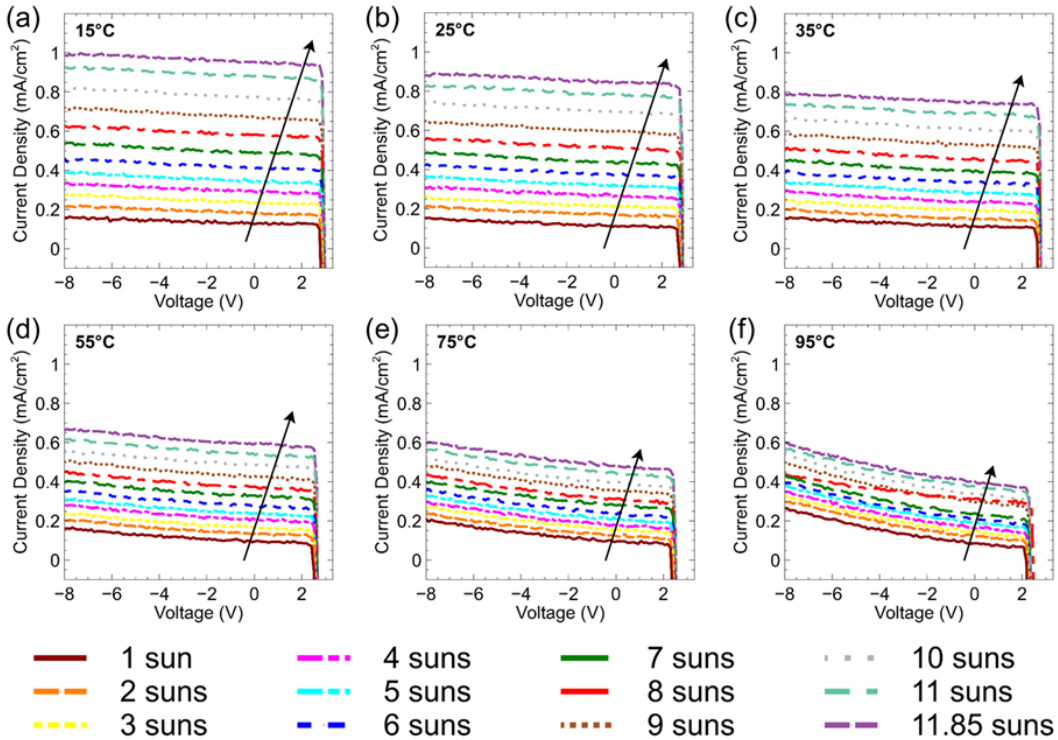

Fig. 35 DC light *J-V* characteristic curve series acquired when the Si bottom cell of InGaP/AlGaAs//Si 3JSC was made current-limiting at cell operating temperatures, T_c, of (a) 15°C, (b) 25°C, (c) 35°C, (d) 55°C, (e) 75°C and (f) 95°C, respectively. These were measured under various 660-nm LED intensities between 1 sun and 11.85 suns and applied terminal voltages from V = -8 V to V = 3.2 V. The arrow direction indicates increasing 660-nm LED intensity [173].

The fitted *J-V* curves acquired at T_c = 15°C to 95°C and when the 660-nm LED intensity was set to 11.85 suns are shown in Fig. 35(a). The goodness of SPICE electrical model prediction of the *J-V* curves was quantified by calculating r^2, as listed in Fig. 36(a) table. As T_c increased, r^2 decreased. This trend can be attributed to the increasing deviation between the measured and the predicted open-circuit voltage, V_{OC}, with increasing T_c and to the nonlinearity of the observed shunt in the *J-V* curves, which is beyond the capacity of the SPICE circuit model used to fit.

To determine current generating mechanisms other than the LC effect at various T_c, *J-V* curves without LC effect were simulated using the parameters determined by light *J-V* curve fitting as 2D SPICE electrical model inputs while having $\alpha_{LC,i-1\rightarrow i}$ set to 0. The *J-V* curves with $\alpha_{LC,i-1\rightarrow i} = 0$ at various T_c is shown in Fig. 36(b). Without the LC effect at T_c = 15°C to 35°C, a negligible shunt leakage current was predicted by the model. On the other hand, the shunt leakage current was forecasted to increase upon increasing T_c. Furthermore, upon comparing the *J-V* curves with and without LC effect over T_c, the current difference decreased. Hence, it may be inferred that at $T_c \geq$ 55°C, the LC effect gets suppressed while the leakage current increases.

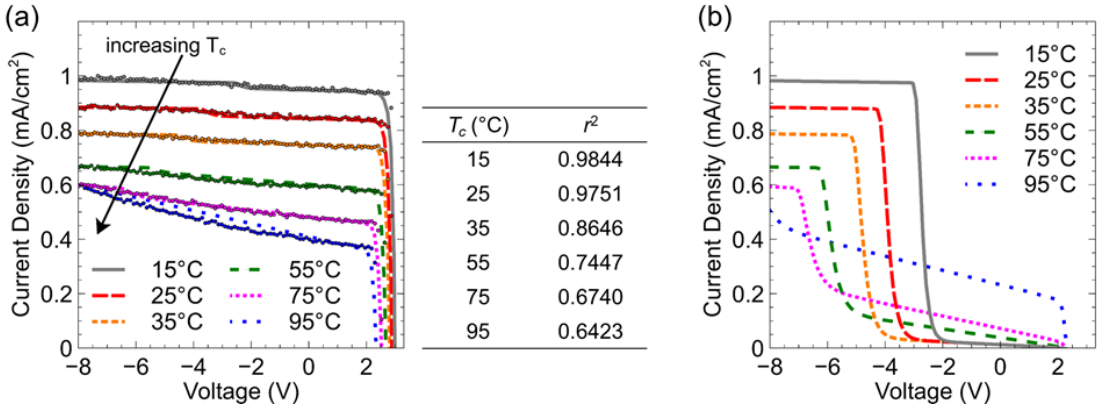

T_c (°C)	r^2
15	0.9844
25	0.9751
35	0.8646
55	0.7447
75	0.6740
95	0.6423

Fig. 36 (a) Collection of measured (dot symbols) and fitted (lines) light *J-V* characteristic curves in the Si bottom cell at 660-nm LED intensity of 11.85 suns between applied terminal voltages of V = -8 and 3.2 V. In the table, r^2 is the coefficient of determination. (b) Light *J-V* characteristic curves in the Si bottom cell simulated without LC effect ($\alpha_{LC,i-1\rightarrow i}$=0) using the 2D SPICE electrical model [173].

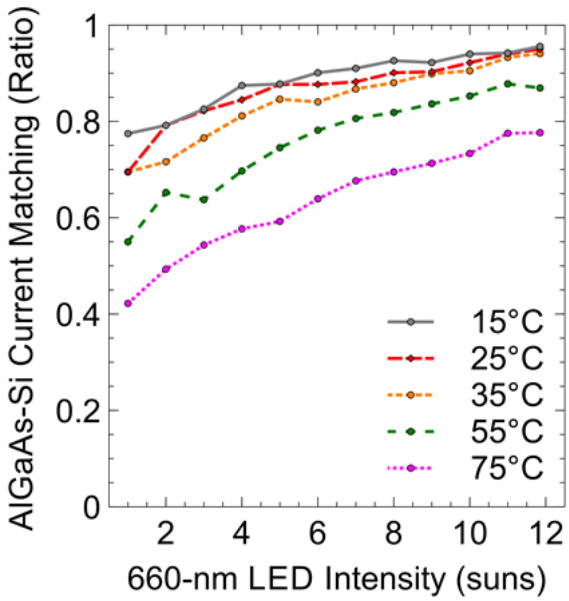

Fig. 37 AlGaAs-Si current matching, $\zeta_{AlGaAs\rightarrow Si}$, derived from the DC light *J-V* characteristic curves of InGaP/AlGaAs//Si 3JSC Si bottom cell measured at different cell operating temperatures, T_c. $\zeta_{AlGaAs\rightarrow Si}$ was derived from the current produced at an applied terminal voltage of V = 2.0 V with increasing 660-nm LED intensities from 1 sun to 11.85 suns [173].

To know how much (*i*-1)'th and adjacent *i*'th subcell current matching changes when T_c is increased, the AlGaAs-Si current matching ratio, $\zeta_{AlGaAs \rightarrow Si}$, was derived from the *J-V* curve series shown in Fig. 35. In Fig. 37, $\zeta_{AlGaAs \rightarrow Si}$ was found to be higher at lower T_c and higher 660-nm LED intensities, indicating better current matching. This is ascribed to a higher number of radiative recombination events at lower temperatures [221] and higher carrier injection levels in III-V subcells caused by higher LED intensities. Both of these conditions are known to yield higher internal radiative efficiencies, thereby resulting in a stronger LC effect upon the Si bottom cell [226]. At higher T_c however, current production was attributed to leakage through the shunt defects, most especially at T_c = 95°C, as inferred from comparing the *J-V* curves with and without LC current in Fig. 35. Thus, as shown in Fig. 35(f), no flat region could be found in the reverse voltage region where $J_{ph,AlGaAs}$ can be found. Consequently, $\zeta_{AlGaAs \rightarrow Si}$ at 95°C was omitted in Fig. 36.

3.3.6.2. EQE of InGaP/AlGaAs//Si 3JSCs

Figure 38(a) shows the subcell EQE measurements at different T_c. At room temperature, short-circuit currents, J_{sc}, derived from these measurements were 12.23, 10.36 and 7.29 mA/cm^2 for InGaP, AlGaAs, and Si subcells, respectively. InGaP top cell EQE shows a negligible increase over temperature. This agrees with the observations reported for InGaP and other III-V MJSC materials such as GaAs and InGaAs [219]. On the other hand, AlGaAs middle cell and Si bottom cell EQE show a small and moderate increase over T_c. This may be attributed to the differences in their pressure coefficients and thermal expansion coefficients, which are related to bandgap change in a subcell [238]. However, the band edges in the EQE plots of AlGaAs and Si subcells did not seem to extend noticeably over wavelength. To confirm this quantitatively, the bandgap temperature dependence of each III-V//Si subcell being studied, $E_{g,i}(T_c)$, were calculated. In Fig. 38(b), the $E_{g,Si}(T_c)$, $E_{g,AlGaAs}(T_c)$, and $E_{g,InGaP}(T_c)$ values predicted using eqs. (21) to (23), respectively, were compared to the subcell absorption band edges observed in the EQE measurements. The goodness of prediction was determined by r^2 calculation. Among the prediction models, the Varshni model given by (21) was able to closely predict $E_{g,Si}(T_c)$. As for other models used for InGaP top cell and AlGaAs middle cell, possible sources of error were identified: (1) the wavelength precision of the EQE measurement, in which the step size used for all measurements was 10 nm, (2) the differences in sample material composition and fabrication conditions used between past literature [225,227] and this report, which would consequently result in fit parameters differences, and (3) the extrapolation of fit parameters reported in past studies by linear prediction may have been insufficient. Nevertheless, the slopes of the experimental and predicted $E_{g,i}$ plots did not vary significantly. As regards to how $E_{g,i}$ changes over T_c, a very small reduction can be noticed. Therefore, mechanisms other than BGR and photo-carrier generation caused the small and the moderate EQE increase over T_c for AlGaAs and Si subcells, respectively. Such mechanisms were possibly related to the increase in leakage current due to shunt defects with increasing T_c, as inferred from the simulated *J-V* curves without LC effect shown in Fig. 36(b). Increasing EQE in Ge, a Group IV material with high shunt defects was also observed in the past [146].

To determine the AC signal response of Si bottom cell at different temperatures to specific wavelengths, the 785 nm and 1064 nm EQE measurements were plotted as a function of T_c. As these wavelengths are the same as those of the pulsed lasers used for

LBIC mapping of Si bottom cell, this may have some implications on the LBIC map results. In Fig. 38(c), it is seen that the measured Si bottom cell EQE response to 785-nm AC signal over the T_c range studied was <3.5%. This suggests that this signal was mostly absorbed in the AlGaAs middle cell for the range of T_c studied. As for 1064-nm, the EQE response of Si bottom cell at T_c > 25°C increased, which may suggest a thermal current increase. However, as inferred from Fig. 38(b), BGR was observed to be negligible between 35°C and 95°C. Thus, this increase may be ascribed to the combination of the following: (1) LC current, which was found to decrease over T_c, and (2) shunt leakage current increase with temperature brought about by nonradiative recombination competing against radiative recombination events [221], in the bulk [171] and edge defects [202–203], and in the imperfectly bonded III-V//Si wafer interface, as also inferred from Fig. 36(b). On the other hand, the 1064-nm EQE response at 15°C (EQE = 17.59%) being slightly larger than that at 25°C (EQE = 17.26%) may be attributed to LC with AlGaAs middle cell.

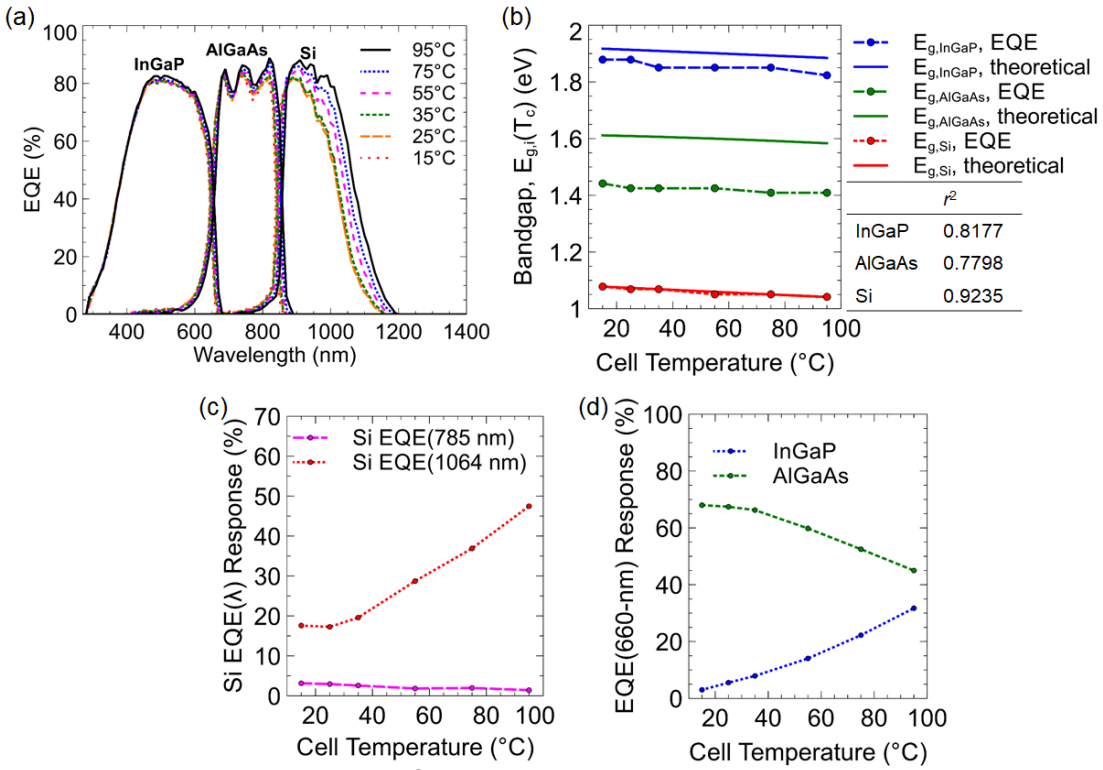

Fig. 38 (a) EQE measurements of 1 cm^2 InGaP/AlGaAs//Si 3JSC samples, (b) calculated and measured subcell bandgap, $E_{g,i}(T_c)$, where r^2 is the coefficient of determination, (c) EQE response of Si bottom cell at 785-nm and 1064-nm chopped monochromated light, and (d) 660-nm signal response of InGaP and AlGaAs subcells observed from EQE measurement acquired at different cell operating temperatures, T_c [173].

In Fig. 38(a), an overlap between InGaP and AlGaAs EQE responses at a 660-nm signal can be seen. Investigating this overlap may be also substantial to interpret the trend of the LC strength with increasing T_c since 660-nm was one of the continuous LED wavelengths used for biasing the AlGaAs middle cell. To investigate this further, the EQE responses of InGaP and AlGaAs subcells to 660-nm signal were plotted as a function of T_c in Fig. 38(d). It is shown that while the InGaP top cell EQE increased, the AlGaAs

middle cell EQE decreased. This decrease correlates with the decreasing LC current trend and $\zeta_{AlGaAs \rightarrow Si}$ observed upon increasing T_c, as shown in Figs. 35 and 37, respectively. This suggests that at higher T_c, the photons supposedly absorbed in the AlGaAs middle cell got absorbed in the InGaP top cell. Because of this, fewer photons would be emitted through radiative recombination, thereby weakening the LC strength towards the Si bottom cell [56,141].

3.3.6.3. LBIC Mapping of InGaP/AlGaAs//Si 3JSCs

To evaluate the material growth uniformity of each subcell [171,208], LBIC mapping by direct subcell excitation was acquired for AlGaAs middle cell and Si bottom cell. Figure 39 shows the maps of the current collection in the AlGaAs middle cell measured at T_c between 15°C and 95°C. In all maps shown here, the current collection was uniform and then decreased abruptly in the perimeter region. Meanwhile, as T_c increased, the current collection also decreased. This trend may be attributed to photon recycling, with AlGaAs being a direct bandgap material [222], and LC from InGaP top cell. This is considering that both degrade over T_c since radiative recombination probability would be higher at lower temperatures [128].

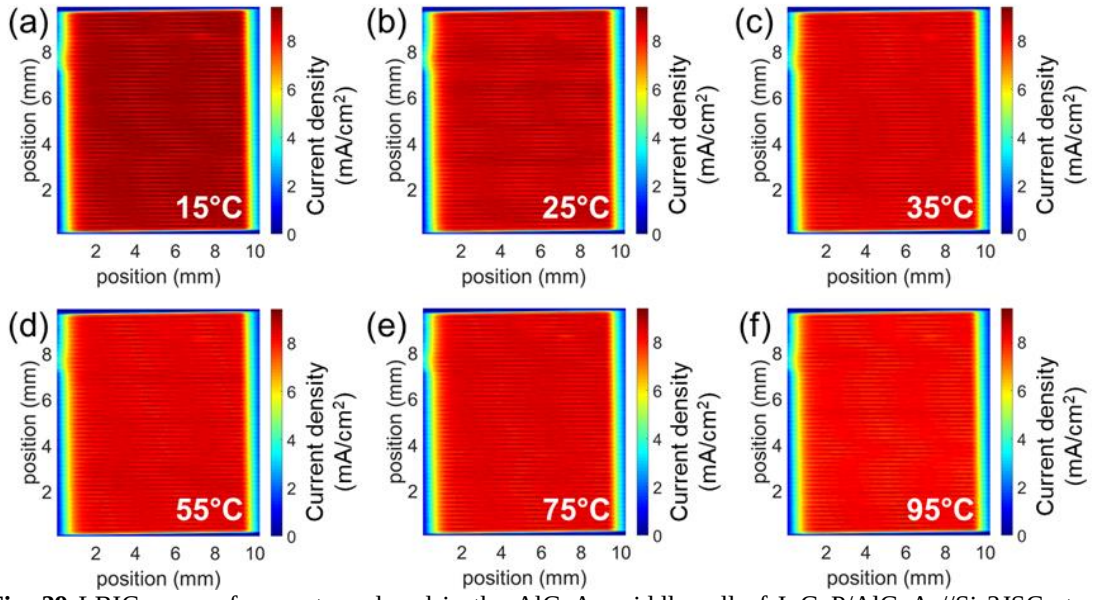

Fig. 39 LBIC maps of current produced in the AlGaAs middle cell of InGaP/AlGaAs//Si 3JSC at cell operating temperatures, T_c, of (a) 15°C, (b) 25°C, (c) 35°C, (d) 55°C, (e) 75°C and (f) 95°C, respectively. These were acquired through exciting InGaP top cell and Si bottom cell with continuous 440-nm and 970-nm LEDs, respectively, and AlGaAs middle cell with a pulsed 785-nm laser at an applied terminal voltage of V = 2.0 V [173].

Figure 40 shows the maps of the current collection in the Si bottom cell acquired by direct 1064-nm laser excitation at T_c between 15°C and 95°C. By comparing Figs. 40(a) and (b), it is inferred that at T_c = 15°C, radiative recombination dominated, resulting in either LC with the AlGaAs middle cell, as interpreted from Fig. 38(c), or photon recycling in the Si bottom cell, which is not likely [239] because Si is an indirect bandgap subcell. Meanwhile, the current collection trend was the opposite of the Si bottom cell at T_c = 35°C and above, as shown in Figs. 40(c)–(f). Since it was inferred from Fig. 38(b) that BGR between T_c = 15°C and 95°C would produce insignificant thermal current, the

current collection at these temperatures was possibly dominated by shunt leakage. Moreover, the data trend at T_c > 35°C shown in Figs. 40(c) to (f) agrees with the trend shown by the *J-V* curves without LC effect and the Si EQE response to 1064-nm pulsed laser plotted in Figs 36(b) and 38(c), respectively.

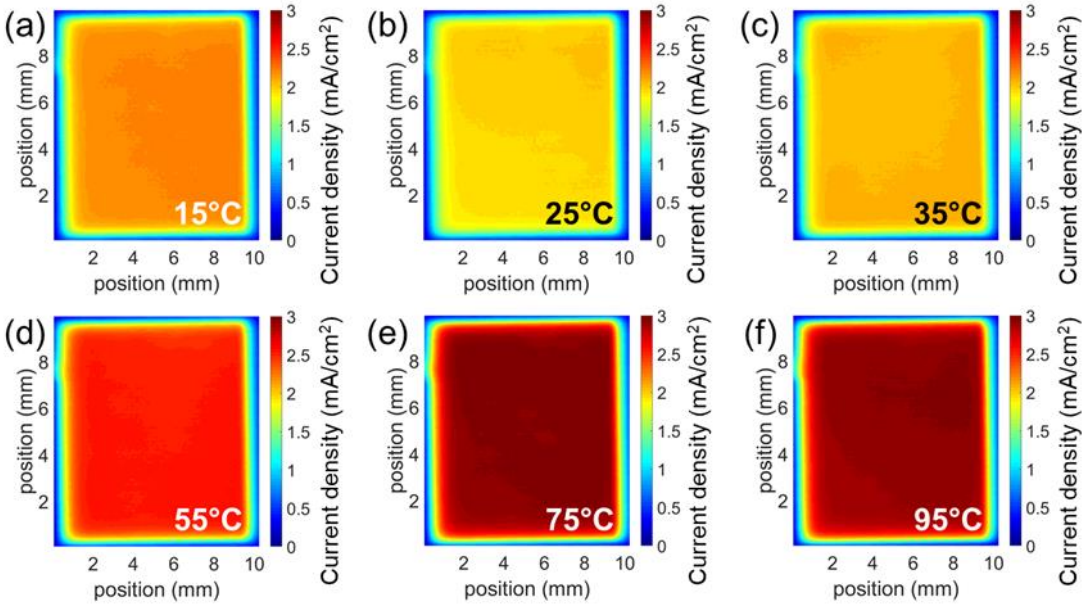

Fig. 40 LBIC maps of current produced in the Si bottom cell of InGaP/AlGaAs//Si 3JSC at cell operating temperatures, T_c, of (a) 15°C, (b) 25°C, (c) 35°C, (d) 55°C, (e) 75°C and (f) 95°C, respectively. These were acquired through exciting InGaP top cell and AlGaAs middle cell with continuous 440-nm and 660-nm LEDs, respectively, and Si bottom cell with a pulsed 1064-nm laser at an applied terminal voltage of V = 2.0 V [173].

To observe how the LC current collection uniformity in the Si bottom cell changes with increasing T_c, LBIC maps of the Si bottom cell were acquired through pulsed 785-nm laser excitation of the AlGaAs middle cell to induce photon emission towards Si bottom cell at T_c between 15°C and 95°C. In all maps acquired, the applied 3JSC terminal voltage was V = 2.0 V and the 660-nm LED intensity upon AlGaAs middle cell of 1 cm^2 InGaP/AlGaAs//Si 3JSC samples was 11.85 suns. As shown in Figs. 41(a)–(f), when T_c was increased, the LC current production decreased. This is attributed to higher radiative recombination events happening at lower temperatures, allowing stronger LC effect from AlGaAs middle cell to Si bottom cell. This agrees with the findings reported in Refs. [187] and [217] for InGaP/GaAs/Ge 3JSCs. Also, this trend can be traced back to the EQE measurements shown in Fig. 38(d), in which the InGaP top cell and the AlGaAs middle cell absorption ranges overlap increases with temperature. Because the InGaP top cell absorbs 660-nm better with temperature increase, the AlGaAs middle cell receives fewer photons at higher temperatures. Under stronger light concentration, a stronger LC effect was observed as shown in Fig. 35 and as inferred from Fig. 37, in agreement to past literatures [56,141,170,187]. However, less current was produced towards the edges of the cell, signifying a higher probability of nonradiative recombination in this region. In this recombination process, excess absorbed energy gets redistributed among electronic excitations or lattice vibrations. As a result, this process could make the edges hotter than the rest of the cell [187]. Furthermore, this could cause uneven damage to the cell, in the

long run, thereby reducing its lifespan. Nevertheless, the heat at the edges might be compensated by operating MJSCs at lower T_c. Thus, to minimize the current mismatch of Si bottom cell with respect to the other subcells and at the same time prevent uneven damage in the active area of the cell, III-V on Si MJSCs should be operated at lower temperatures to maximize the benefits of LC effect.

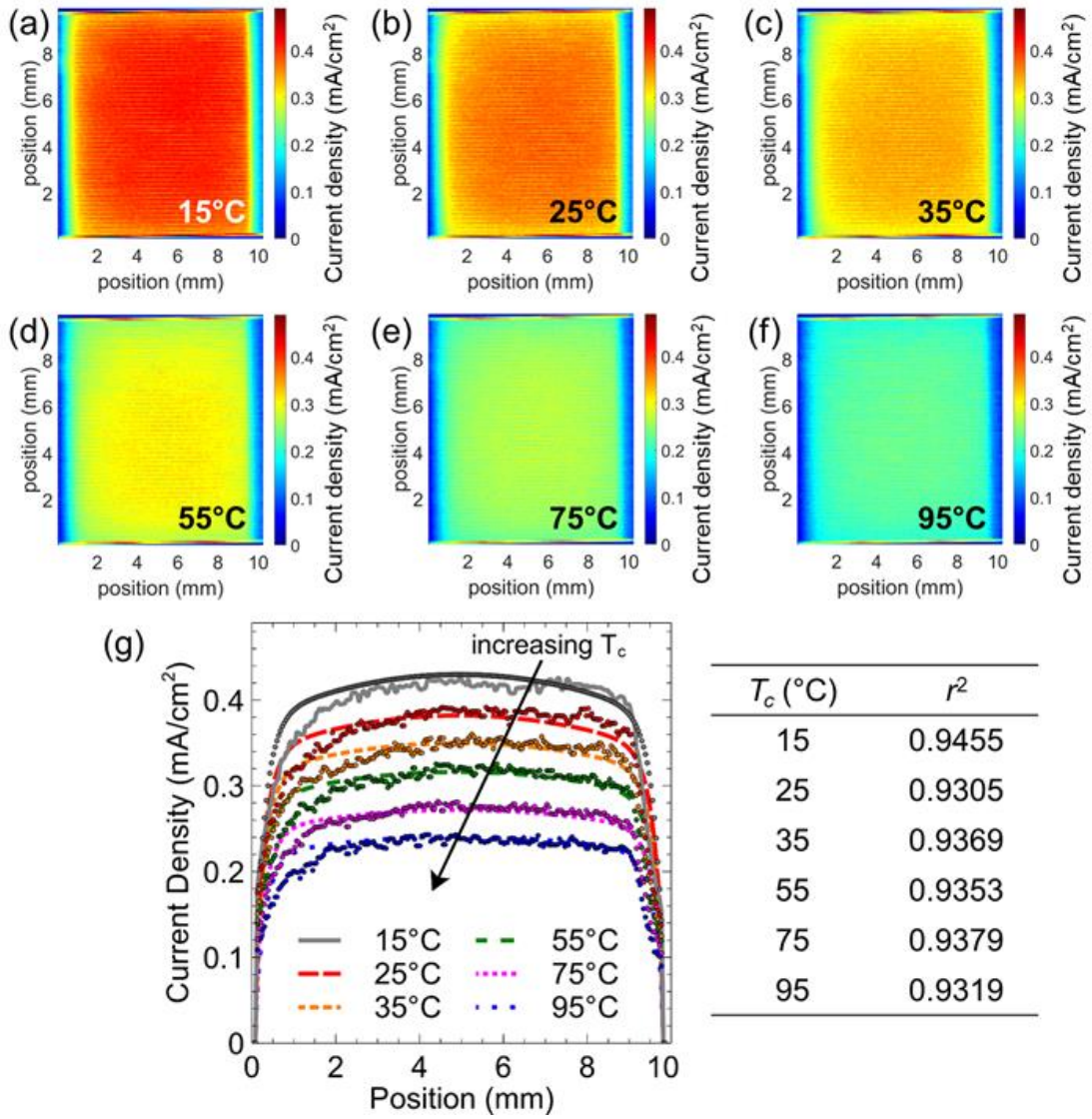

T_c (°C)	r^2
15	0.9455
25	0.9305
35	0.9369
55	0.9353
75	0.9379
95	0.9319

Fig. 41 LBIC maps of current produced in the Si bottom cell of InGaP/AlGaAs//Si 3JSC at cell operating temperatures, T_c, of (a) 15°C, (b) 25°C, (c) 35°C, (d) 55°C, (e) 75°C and (f) 95°C, respectively. These were acquired by inducing photon emission from the AlGaAs middle cell using a 785-nm pulsed laser and a 660-nm LED intensity of 11.85 suns at an applied terminal voltage of V = 2.0 V. (g) Measured and fitted LC current collection in the Si bottom cell of 1 cm^2 InGaP/AlGaAs//Si 3JSC cross-section as a function of position at cell operating temperatures, T_c, of 15°C to 95°C. The measurement data are the same as those in the cross-section of Figs. 40(a)–(f) [173].

Figure 41(g) shows the LC current production in the Si bottom cell cross-section acquired through LBIC mapping and by Q2DEP model fitting at each T_c. By fitting these maps together, $\beta_{LC,AlGaAs\rightarrow Si}$, $mLCQE_U$, $mLCQE_F$, and $\Delta mLCQE$ were obtained. Qualitatively, no change in spatial LC current uniformity at different T_c could be

observed. To confirm this quantitatively, the standard deviation normalized with the total current produced, $\sigma_{LC}/J_{LC,Total}$, was calculated at different T_c using eq. (16). In Fig. 42, $\sigma_{LC}/J_{LC,Total}$ (right axis) values were plotted against T_c. In the same figure, the fitted β_{LC} (left axis) values were also plotted. Although β_{LC} decreased from 0.12 to 0.09, $\sigma_{LC}/J_{LC,Total}$ did not vary significantly with increasing T_c. Thus, regardless of the operating temperature, the spatial nonuniformity of LC current production remains a challenge that needs to be addressed to further improve the current matching between the Si bottom cell and other higher bandgap subcells.

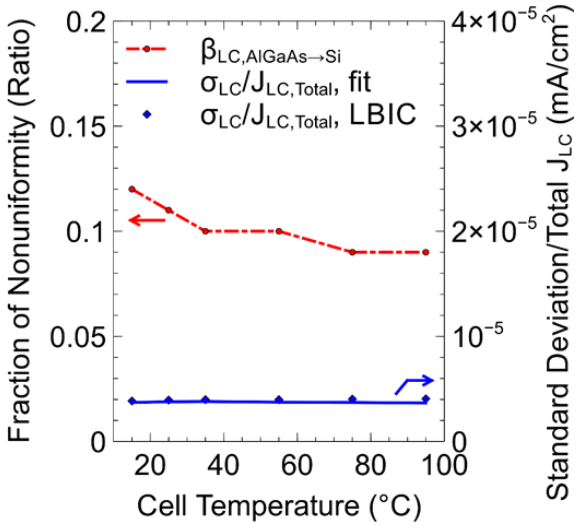

Fig. 42 The fraction of nonuniformity, $\beta_{LC,AlGaAs\rightarrow Si}$, (red plot, left axis) and normalized standard deviation of LC current, $\sigma_{LC}/J_{LC,Total}$, (blue plots, right axis) as a function of InGaP/AlGaAs//Si 3JSC operating temperature, T_c. For $\sigma_{LC}/J_{LC,Total}$, the diamond and solid line plots were derived from measured and fitted LBIC maps using the Q2DEP model, respectively [173].

3.3.6.4. Mean LC Quantum Efficiency Calculations

To quantify how many photons emitted were successfully converted into LC current in the Si bottom cell, the *mLCQE* values at T_c = 15°C to 95°C were derived using eq. (18). These were calculated from nonuniform ($\beta_{LC,AlGaAs\rightarrow Si} \neq 0$, fitted, dotted lines) and uniform ($\beta_{LC,AlGaAs\rightarrow Si} = 0$, dashed-dotted lines) LC current production in the Si bottom cell, termed $mLCQE_F$ and $mLCQE_U$, respectively. The highest $mLCQE_F$ was 1.17%, which was obtained at T_c = 15°C. As shown in Fig. 43, increasing T_c resulted in decreasing *mLCQE*. This agrees with the inferences drawn from Figs. 35, 37, and 41, which suggest that the probability of radiative recombination events decreased, leading to LC effect suppression with increasing T_c. This is also ascribed to the decreasing 660-nm wavelength response of the AlGaAs subcell shown in Fig. 38(d) as discussed earlier.

Lastly, to quantify the number of uncollected photons and electron-hole pair lost to recombination, the absolute LCQE difference, $\Delta mLCQE$, was calculated by subtracting $mLCQE_F$ from $mLCQE_U$. In a previous study [185], $\Delta mLCQE$ was used as an indicator of how much photons were lost through the escape cone or by internal reflection while demonstrating the higher probability of reabsorption in the center region [170]. Additionally, this was used to quantify how much carriers were lost through the edge and bulk nonradiative recombination resulting in nonuniform LC current collection. Conversely, these values indicate potential improvement if LC current production is homogenized. The highest $\Delta mLCQE$ calculated was 0.17%, obtained at 15°C. As shown

in Fig. 43 (solid line), when T_c was increased, $\Delta mLCQE$ decreased. This suggests that the lower the T_c is, the larger the number of unabsorbed photons and carrier loss would be, which may be recovered by homogenizing the LC effect between adjacent MJSC subcells and increase power conversion efficiency.

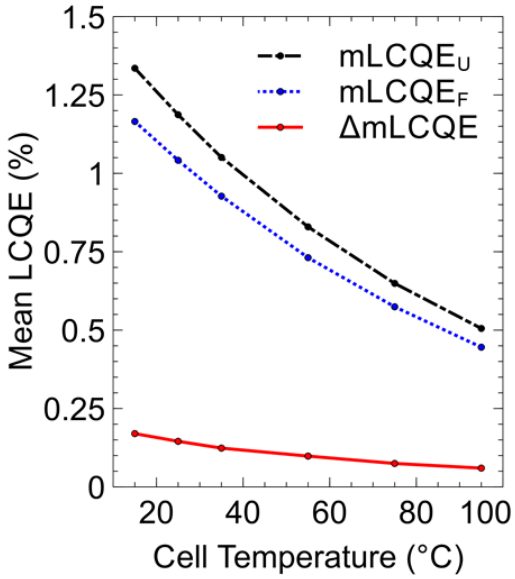

Fig. 43 Mean mLCQE plots acquired through LBIC map fitting, $mLCQE_F$, (dotted line, $\beta_{LC,AlGaAs \rightarrow Si} \neq 0$), simulated uniform current collection, $mLCQE_U$ (dashed-dotted line, $\beta_{LC,AlGaAs \rightarrow Si} = 0$), and absolute LCQE difference, $\Delta mLCQE$, (solid line) derived from the LC current maps of the Si bottom cell of InGaP/AlGaAs//Si 3JSC samples. The cell operating temperatures, T_c, was between 15°C and 95°C and the applied terminal voltage at which the plots were derived was V = 2.0 V [173].

3.4. Summary of Findings

Nonuniform LC current generation was observed in the Ge bottom cell of an InGaP/GaAs/Ge 3JSC when made current limiting. Good agreement of experiment and simulation results suggest that the nonuniform LC effect in MJSCs is optically induced. This is possibly caused by one or a combination of the following phenomena: (1) optical losses due to photon escape through the sides of the MJSC, (2) electrical losses due to lateral resistance effects, (3) perimeter recombination, (4) nonuniform material growth, and (5) high carrier injection into the HBG subcell resulting in nonuniform radiative emission toward an adjacent LBG subcell. At maximum GaAs-to-Ge subcell LC efficiency, although the conversion efficiency of Ge bottom cell that may be achieved was calculated at 8.01% for a cell area of 0.31 cm^2, the absolute conversion efficiency reduction introduced by nonuniform LC effect was calculated at 1.35%. From these results, it can then be inferred that the limiting Ge bottom cell conversion efficiency can be further improved by making the LC current generation spatially uniform. This can be done by finding ways to improve the current generation towards the cell perimeter to compensate for the uncollected photons resulting in nonuniform current generation by strong LC effect, especially for MJSC structures intentionally designed for concentrator photovoltaic systems.

The temperature dependence of the LC effect between GaAs middle cell and Ge bottom cell of the InGaP/GaAs/Ge 3JSC was also investigated. It was found that

operating MJSCs at lower temperatures results in a larger LC current collection. When Ge bottom cell is made current limiting at 18°C and 72°C, conversion efficiencies obtained were 6.68% and 0.01%, respectively. These findings suggest that the LC effect contributes best to MJSC conversion efficiency when it is operated at low temperatures. Current generation mechanisms at low temperatures may be largely attributed to the LC effect. LC current generation decreased until the temperature became high enough to suppress it. Thus, ways to possibly alleviate the reduction of LC current collection should be explored for achieving higher MJSC conversion efficiencies at higher operating temperatures.

The area dependence of GaAs-to-Ge subcell LC current generation was also evaluated by LBIC mapping and analyzed using the Q2DEP model. The following were observed. First, the Q2DEP model reproduced well the spatial distribution of produced LC current, suggesting that this model is appropriate for analyzing nonuniform LC current production. Also, it was found that although stronger incident light bias yields a higher LC factor, the spatial LC current matching degrades. But then, regardless of the LC strength, the degree of spatial LC current mismatch is found to be independent of the cell area. The leakage current dominance and the mean QE of LC current generation were then evaluated in relation to the cell area. The larger cell was found to have less significant leakage current from the adjacent HBG subcell (GaAs middle cell) even at the low incident light bias intensity. Moreover, larger QE was obtained for a larger cell area, indicating better conversion of radiative emission photons to electrons produced by the LC effect. However, it was observed that more photons towards the limiting cell get uncollected, which may have escaped through the sides of the cell. Therefore, if spatial LC current mismatch is solved, it may increase QE up to 2.55% for a cell area of 0.99 cm^2. This, in turn, may increase the MJSC conversion efficiency towards 50% – the current target for the photovoltaics community.

LC effect on current-limiting GaAs middle cells of InGaP/GaAs/Ge 3JSCs having different InGaP top cell designs intended for space-grade and terrestrial concentrator applications were also studied experimentally through the DC light *J-V* characteristic curve and LBIC measurements. Results have shown that higher quality InGaP top cell induced stronger LC effect on the adjacent GaAs middle cell. This may lead to improved current matching between InGaP and current-limiting GaAs, which in turn may improve the MJSC PCE, especially at high concentration conditions.

The active area dependence of LC effect in InGaP/AlGaAs//Si 3JSCs at room temperature was studied. For all sizes, it was found that a stronger LC effect from the AlGaAs middle cell towards the Si bottom cell produced more inhomogeneous LC current distribution. Nonuniformity of LC current collection due to a strong LC effect was found to be most significant for the largest cell area studied, which is 1×2 cm^2. Also, the calculated $\Delta mLCQE$ for this sample was 1.68% at 9.17 suns difference between AlGaAs and Si. This may indicate the maximum possible current collection improvement for 1×2-cm^2 InGaP/AlGaAs//Si 3JSC if the LC effect is made uniform, which may result in power conversion efficiency improvement. Although the larger current collection was achieved for larger cell areas, the degree of LC current nonuniformity did not depend on cell area, as shown by β_{LC} fitting. This agrees with the observations from III-V on Ge 3JSCs discussed. Thus, to avoid uneven damage brought about by nonuniform LC current production for any cell area, ways to homogenize it should be investigated in future studies.

The performance of III-V on Si MJSCs with LC effect under varying T_c was also studied. It was found that the lower the T_c was, the larger the LC current was produced. This was mainly ascribed to higher radiative recombination probability at lower T_c. On the other hand, the spatial LC current uniformity did not have significant variation with temperature. Therefore, nonuniform LC current remains a challenge to be resolved for any T_c, as also observed from III-V on Ge 3JSC samples measured. At 15°C, $mLCQE_F$ and $\Delta mLCQE$ obtained were 1.17% and 0.17%, respectively. Thus, when an InGaP/AlGaAs//Si 3JSC is operated at 15°C, the current production in the limiting Si bottom cell may increase by 0.17% if the LC current is made uniform. This, in turn, directly contributes to solar cell efficiency improvement.

Luminescence imaging of III-V multijunction solar cells with luminescent coupling effect

Chapter 4

Chapter 4 – Luminescence imaging of III-V multijunction solar cells with luminescent coupling effect

To complement the observations made from the spatially-resolved luminescent coupling (LC) effect in III-V multijunction solar cells (MJSCs) by laser beam induced current (LBIC) mapping, another method of spatially-resolved characterization of luminescence from each MJ subcell was implemented. This chapter is dedicated to the spatial mapping of luminescence from MJ subcells involved in the LC effect. Even faster than the LBIC mapping, the electroluminescence/photoluminescence (EL/PL) mapping method was used as a means of observing the (1) LC effect and (2) subcell material quality of the MJSCs. As the main objective for this chapter, the EL/PL mapping method through the aid of continuous lasers was employed to observe the luminescence coming from the lower bandgap (LBG), current-limiting subcell of a III-V MJSC and its adjacent higher bandgap (HBG) subcell where the LC effect originated, in parallel with laser beam induced current (LBIC) mapping. At increasing applied MJSC terminal voltage, it was found that the luminescence profiles of the coupled subcells became less homogeneous. Furthermore, at high MJSC terminal voltage, the luminescence image of the higher bandgap subcell had the same profile as the spatial current collection in the lower bandgap subcell obtained by LBIC mapping. Thus, it may be established that the emission profile of the higher bandgap subcell affects the LC current collection of its adjacent lower bandgap subcell.

Chapter 4 begins with introducing the general objective for using EL/PL mapping to characterize the LC effect in MJSCs, together with the specific questions. In Sec. 4.2, the EL/PL mapping method and the analytical equations used for evaluating luminescence homogeneity are discussed in detail. Next, Sec. 4.3 discourses the EL/PL mapping results while having the laser power illuminating the higher bandgap subcell and the applied MJSC terminal voltage as variables. Finally, this chapter ends with the synthesis of the main findings out of the EL/PL mapping results in comparison with LBIC mapping.

4.1. Research Questions

The main objective of this chapter is to observe the luminescence from each subcell responsible for LC effect in III-V MJSCs by implementing the EL/PL mapping method using single-wavelength continuous lasers having fixed intensities. Specifically, this chapter attempts to answer the following questions:

1. Is the inhomogeneous luminescence from one or both of the adjacent subcells that induce the LC effect a reason for inhomogeneous current collection observed during LBIC mapping of III-V MJSCs with LC effect?
2. At which applied terminal voltage condition will the luminescence from each of the adjacent subcells involved in the LC effect be homogeneous?
3. At which laser power will the luminescence be homogeneous from each of the adjacent subcells involved in the LC effect?

4.2. Methodology

4.2.1. Electroluminescence/Photoluminescence (EL/PL) mapping

Commercial *n*-on-*p* triple-junction solar cells (3JSCs) for terrestrial application and whose area is 0.31 cm^2 were characterized. The top, middle and bottom cells of the 3JSC are indium gallium phosphide (InGaP), gallium arsenide (GaAs) and germanium (Ge), respectively. These subcells are internally connected in series. The samples were characterized by the EL/PL mapping method at room temperature in which the GaAs middle cell was made current limiting.

Figure 1(a) shows an EL setup for capturing MJSC luminescence. Here, long pass and short pass filters whose cutoff wavelengths are less than and greater than the expected emission wavelength of the MJSC subcell are placed between the cell and a charge-coupled device (CCD) camera, respectively. Filters were selected such that the CCD camera will be able to record the emission only from the subcell being studied at the moment of capture. If continuous light sources are added to the EL setup, this becomes a hybrid EL/PL setup.

As inferred from the results discoursed in Chapter 3 and Appendix C on Q2DEP modeling, another possible reason for the nonuniform LC effect in MJSCs could be the nonuniform luminescence from a higher bandgap subcell towards its adjacent lower bandgap subcell. To observe this, EL/PL mapping can be used. This method is known to be much faster and is capable of generating a higher image resolution than LBIC mapping [154,186]. However, this method is limited by the sensitivity level of the detector. Hence, this setup is only capable of capturing luminescence images at high MJSC terminal voltages, i.e. at high carrier injection regime, where the radiative recombination is highly probable to occur. At high terminal voltages, however, the 3JSCs become more susceptible to the series resistance losses. The illustration of the setup used for evaluating luminescence, specifically at GaAs LC effect condition, is shown in Fig. 1(b). Here, the camera detector is Si, which is capable of capturing emissions from InGaP top cell (E_g = 1.87 eV) and GaAs middle cell (E_g = 1.41 eV) of InGaP/GaAs/Ge 3JSC samples. Meanwhile, the long pass and short pass filters used for capturing InGaP emission are 650 nm and 750 nm while 850 nm and 950 nm for capturing GaAs emission, respectively. This condition was specifically used as this is the closest condition that could replicate

those during the LBIC measurements. The continuous lasers used were 532 nm and 1200 nm to illuminate the InGaP and Ge, respectively.

There were two main cases implemented during luminescence measurements – one is the variation of applied 3JSC terminal voltage and the other is the variation of laser power upon the higher bandgap subcell, specifically in InGaP. In both cases, the 1200-nm laser intensity was fixed at 1.6 mW, measured at the sample stage using a visible-light ranged power meter. Meanwhile, the 532-nm laser intensity was varied from 12.8 to 122.9 μW in an attempt to figure out the laser power at which the luminescence from each of the adjacent subcells responsible for the LC effect will be homogeneous. As for varying applied 3JSC terminal voltage, it was varied between 2.2 and 3.0 V.

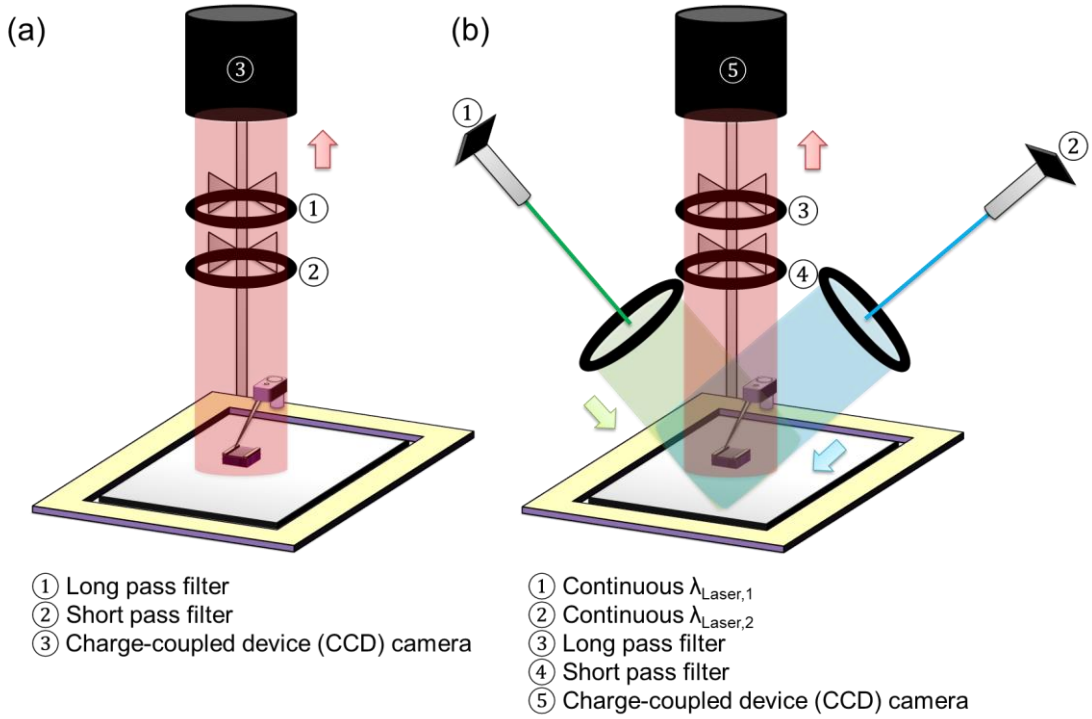

Fig. 1 Setups for (a) EL mapping and (b) EL/PL mapping of InGaP/GaAs/Ge 3JSC.

In monitoring the EL/PL measurement repeatability, it may be cumbersome to measure luminescence maps multiple times due to the huge volume of data each run generates. Hence, the repeatability was observed by measuring dark *J-V* characteristics of the samples before any subcell luminescence measurements, occasionally in between subcell measurements, and after all measurements were taken. These dark *J-V* curves are collectively shown in Fig. 12, Sec. 4.5.

4.2.2. Comparison with LBIC mapping

The EL/PL maps were compared with the LBIC maps, where both sets were acquired at GaAs middle cell current-limiting condition. In the LBIC mapping setup, GaAs was made current limiting by external irradiation upon InGaP using a continuous 440-nm LED at 167.2 mW/cm^2 and upon the Ge bottom cell using continuous 970-nm and 1550-nm LEDs at 31.4 and 4.2 mW/cm^2, respectively. Then, a modulated 450-nm laser was activated at switching and scanning frequencies of 2000 Hz and 2 Hz, respectively. Additionally, this laser locally excites a spot size of 50 μm.

Before EL/PL mapping, in which the power of the 532-nm laser absorbed in InGaP can be adjusted freely using a built-in knob, the power of the 450-nm laser of the LBIC setup was measured without and with 50% and 10% transmission filters at a time. Considering that the power meter used has a detection area, A_{det}, of 73.9 mm^2, which was fully covered by the illumination area of the single wavelength sources used in the EL/PL mapping setup, the 532-nm laser power, $P_{EL/PL}$, was adjusted accordingly using the relation:

$$P_{EL/\,PL} = \frac{A_{det}}{A_{3J}} \times P_{LBIC} \tag{1}$$

Here, A_{3J} is the active area of the InGaP/GaAs/Ge 3JSC sample and P_{LBIC} is the measured 450-nm laser power. While it is difficult to make the power settings exactly equal, they were made close to each other, by at least the same order of magnitude. The power settings and EL/PL mapping laser power equivalent of LBIC mapping laser power calculated using (1) are summarized in Table 1.

Table 1 Measured power of lasers used for InGaP top cell excitation during EL/PL mapping and LBIC mapping and required laser power equivalent for EL/PL setup calculated using eq. (1).

Condition	Measured power (μW)		Calculated 532-nm laser power for EL/PL setup (μW)
	LBIC, 450 nm	EL/PL, 532 nm	
10% light transmission	6.0	12.8	12.2
50% light transmission	28.4	66.0	61.1
100% light transmission (no filter)	51.9	122.9	12.22

4.2.3. Analysis of luminescence homogeneity

In a similar way of analysis done with LBIC measurements, the standard deviation normalized with the average luminescence value, $\sigma_i/\phi_{EL/PL,ave}$, at varying applied terminal voltages and at varying laser power upon the HBG subcell was calculated. $\sigma_i/\phi_{EL/PL,ave}$ is given by the relation:

$$\sigma_i/\phi_{EL/PL,ave} = \frac{\sqrt{\frac{1}{N-1}\sum_{l=1}^{N}\left|\phi_l - \phi_{i,ave}\right|^2}}{\phi_{i,ave}} \tag{2}$$

where the subscript i refers to the subcell from where the emission is being measured, N is the total number of points in an EL/PL map, ϕ_l is the emission captured at a spot, l, and $\phi_{EL/PL,ave}$ is the average EL/PL emission obtained at all points in the map. Here, a lower value of $\sigma_i/\phi_{EL/PL,ave}$ means better luminescence uniformity.

The reason behind normalization with $\phi_{EL/PL,ave}$ is to eliminate the possible differences in carrier collection efficiency among the samples and yield a fair comparison of their luminescence homogeneity.

4.3. Results and Discussions

4.3.1. Varying the applied terminal voltage

To explore the effect of varying the applied MJSC terminal voltages to the luminescence homogeneity of the adjacent subcells at LC effect-induced condition, the luminescence maps from InGaP and GaAs were acquired at different voltages applied across InGaP/GaAs/Ge 3JSC samples, V_{3J}. Here, GaAs was made current limiting, as described in Sec. 4.2.1.

Based on the dark *J-V* curves acquired before, in between, and during EL/PL mapping, all luminescence measurements acquired up to V_{3J} = 2.9 V may be considered reliable enough as the variation of the current in all dark *J-V* lied within less than an order of current magnitude. The dark *J-V* curves are shown in Fig. 12, Sec. 4.5.

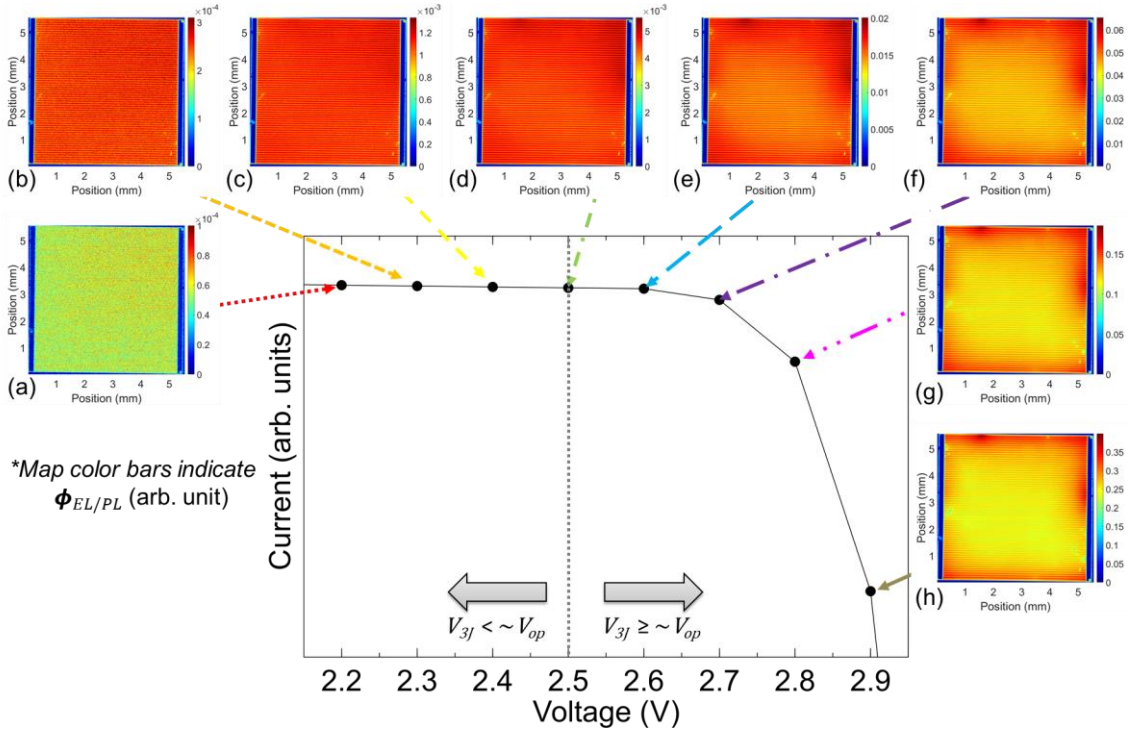

Fig. 2 Spatially-resolved luminescence maps acquired from InGaP top cell of InGaP/GaAs/Ge 3JSC at applied 3JSC terminal voltages of (a) 2.2, (b) 2.3, (c) 2.4, (d) 2.5, (e) 2.6, (f) 2.7, (g) 2.8, and (e) 2.9 V. The arrows directed towards the points on the qualitative *J-V* characteristics curve were added as an aid for indicating the InGaP luminescence of the 3JSC sample at different applied 3JSC terminal voltages, V_{3J}, and at GaAs middle cell current-limiting condition using 532-nm and 1200-nm lasers fixed at 122.9 μW and 1.6 mW, respectively. Here, V_{op} is the approximate operating voltage of the samples characterized.

The InGaP luminescence maps at GaAs current-limiting condition and V_{3J} between 2.2 V and 2.9 V are shown in Figs. 2(a) to (h). Luminescence acquired at voltages lower than 2.5 V was low but uniform. This may be attributed to the low injection of carriers, at which the series resistance effect due to grid contacts. This may also be due to the lateral movement of carriers not yet prevailing at these voltages. On the other hand, as the applied 3JSC terminal voltage was increased from 2.5 V to 2.9 V, the luminescence relatively increased. Since carrier injection increases with increased applied voltage, the probability of radiative recombination may have also increased, thereby intensifying the

emission from InGaP. Furthermore, the luminescence became less uniform, with larger emissions near the perimeter. This suggests that perimeter recombination at higher voltages becomes worse. This inhomogeneity may be also attributed to decreased lateral transport efficiency of carriers towards the lower luminescent regions [154,186]. Additionally, vertical transport of carriers may have been less efficient in the center than on the sides. Referring these maps to the *J-V* characteristics curve shown (not to scale), it may be inferred that when V_{3J} approaches and then exceeds its voltage of operation, V_{op}, the InGaP luminescence profile becomes less uniform. In these voltages, series resistance effects begin to manifest as well, when the current decreases towards V_{OC}; hence, the decreased lateral and vertical transport efficiencies.

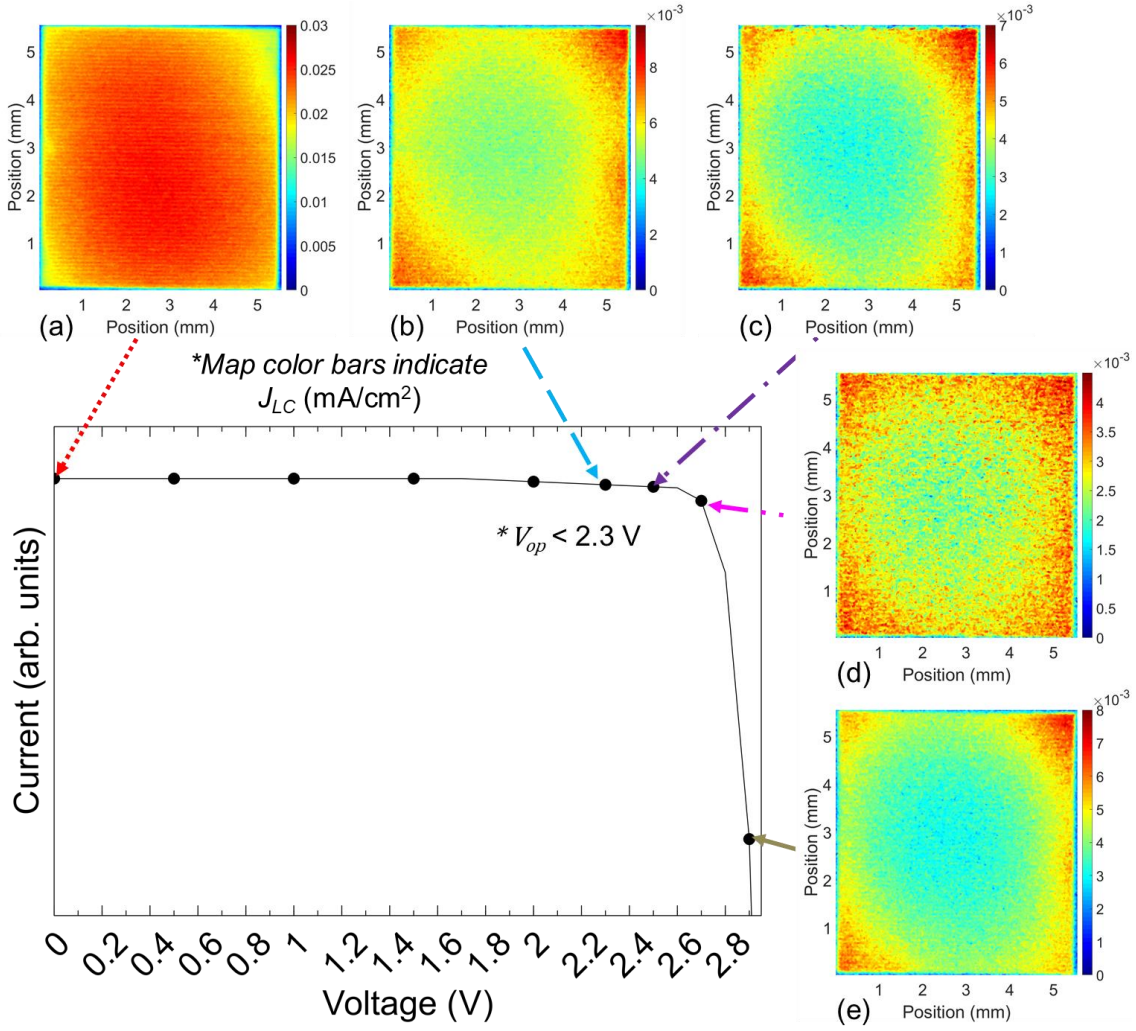

Fig. 3 LBIC maps acquired from GaAs middle cell of InGaP/GaAs/Ge 3JSC at 450-nm laser power (LC effect excitation) of 51.9 μW and applied 3JSC terminal voltages of (a) 0, (b) 2.3, (c) 2.5, (d) 2.7, and (e) 2.9 V, respectively. The arrows directed towards the points on the qualitative *J-V* characteristics curve were added as an aid for indicating the current collection of the 3JSC sample at different applied terminal voltages.

To compare the EL/PL maps with those acquired by LBIC mapping, the LBIC maps measured at 3JSC voltages between 0 V (short-circuit condition) and 2.9 V and GaAs LC condition were acquired using the setup described in Sec. 2.2. These LBIC maps are

shown in Fig. 3. At V_{3J} = 0V, the LC current collection at GaAs was observed to be inhomogeneous, where the larger current was observed at the center and then decreasing towards the perimeter. This agrees with the observations made from GaAs LC current collection at V_{3J} = 0.5 V and at room temperature [171]. On the other hand, at V_{3J} = 2.3 V and higher, the LC current collection was less uniform, with larger collection on the corners. These are similar to the InGaP luminescence maps observed at $V_{3J} \geq$ 2.5 V, shown in Figs. 2(d) to (h).

The slight difference of the LBIC setup with the EL/PL mapping setup in the effective power densities of the light sources upon InGaP and Ge may have caused a change in V_{op}. Thus, the less uniform current collection was already manifesting at 2.3 V, lower than that of the EL/PL map measurements. Another possibility is that starting from V_{3J} = 2.3 V, the LC efficiency may have begun to reduce at the center region, thereby yielding larger LC current near the edges. Nevertheless, these observations suggest that the LC current collection in a limiting LBG MJ subcell is impacted by its adjacent HBG subcell luminescence profile. With this inference, one may then assume that at short-circuit condition (V_{3J} = 0 V) the luminescence profile of the HBG subcell is the same as the LC current collection profile in the limiting LBG subcell.

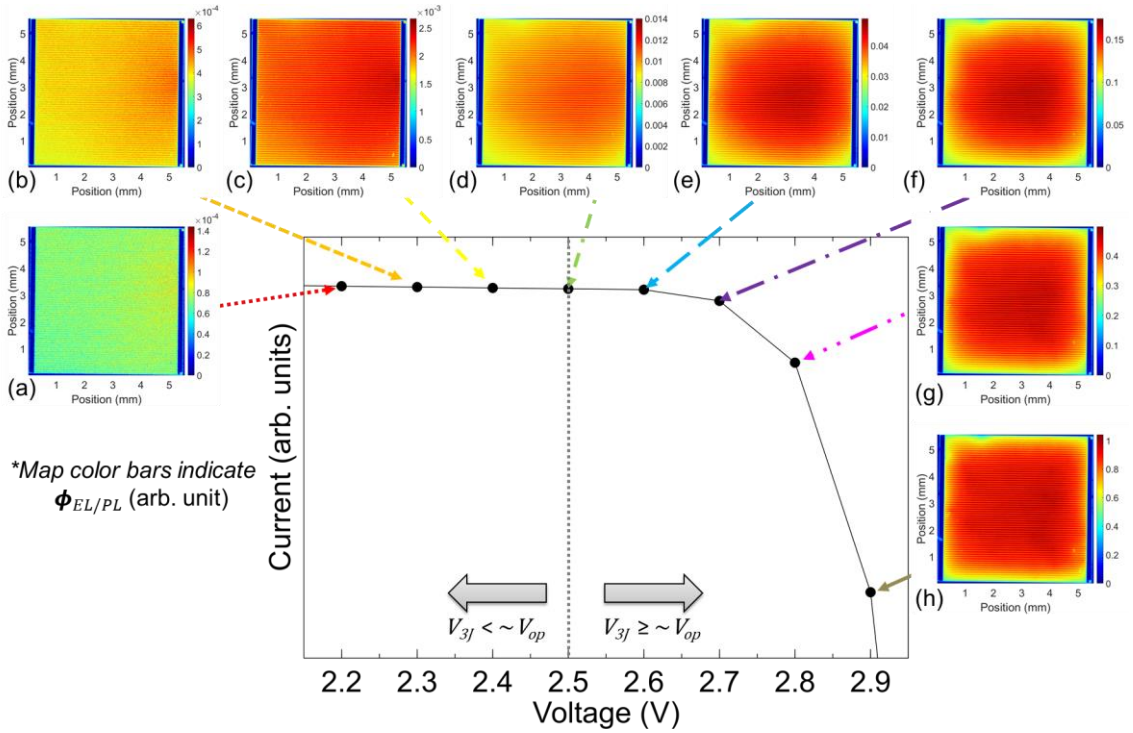

Fig. 4 Spatially-resolved luminescence maps acquired in GaAs middle cell of InGaP/GaAs/Ge 3JSC at applied 3JSC terminal voltages of (a) 2.2, (b) 2.3, (c) 2.4, (d) 2.5, (e) 2.6, (f) 2.7, (g) 2.8, and (e) 2.9 V. The arrows directed towards the points on the qualitative *J-V* characteristics curve were added as an aid for indicating the GaAs luminescence of the 3JSC sample at different applied terminal voltages, V_{3J}, and at GaAs middle cell current-limiting condition using 532-nm and 1200-nm lasers fixed at 122.9 μW and 1.6 mW, respectively. Here, V_{op} is the approximate operating voltage of the samples characterized.

Next, the luminescence maps from GaAs were acquired at varying V_{3J}, from 2.2 V to 2.9 V. At V_{3J} < 2.5 V, also assuming that V_{op} is about 2.5 V, low GaAs luminescence were observed while having larger emission at the right side. The first observation is similarly

attributed to low carrier injection as discussed for InGaP luminescence at low V_{3J} earlier, while the latter observation may be attributed to GaAs material quality, being better at the right portion, or to the InGaP material quality, being better at the left portion of the 3JSC sample characterized. As V_{3J} was increased from 2.5 V though, the peak luminescence in GaAs shifted towards the center. Increasing V_{3J} beyond 2.8 V, the GaAs luminescence was observed to become more uniform. This may suggest that carrier injection becomes very high, that the region closer to the cell perimeter began to experience photo-passivation, which seemingly compensated for the losses due to lateral and vertical carrier transport. This is also considering that the InGaP luminescence was observed to be larger near the perimeter region, as shown in Figs. 2(g) and (h).

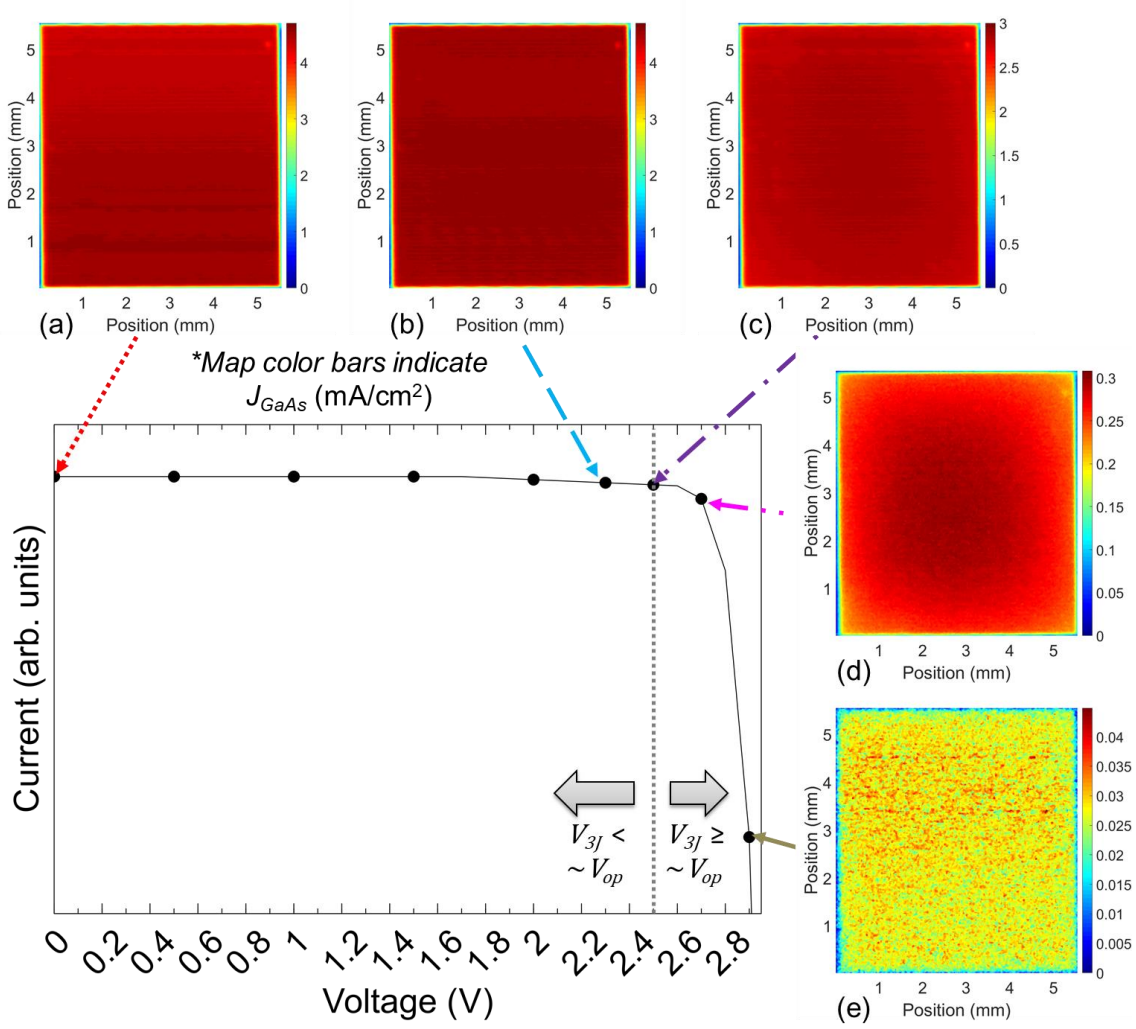

Fig. 5 LBIC maps acquired in GaAs middle cell of InGaP/GaAs/Ge 3JSC at 785-nm laser power (direct GaAs excitation) of 60.2 μW and applied 3JSC terminal voltages of (a) 0, (b) 2.3, (c) 2.5, (d) 2.7, and (e) 2.9 V, respectively. The arrows directed towards the points on the qualitative *J-V* characteristics curve were added as an aid for indicating the current collection of the 3JSC sample at different applied terminal voltages.

The GaAs luminescence maps were then compared with those acquired by LBIC mapping, the LBIC maps measured at 3JSC terminal voltages between 0 V (short-circuit condition) and 2.9 V and at direct GaAs illumination. These maps are shown in Figs. 5(a)

to (e) and were acquired using the setup described in Sec. 2.2, but with a modulated 785-nm laser instead. At $V_{3J} \leq 2.5$ V, GaAs current collection was observed to be uniform, while at $V_{3J} = 2.7$ V, it became less uniform, with larger collection at the center. Similar to the inferences made for GaAs luminescence in Fig. 4, these were attributed to the low carrier injection at $V_{3J} \leq 2.5$ V and increased carrier injection at $V_{3J} = 2.7$ V. Then at $V_{3J} = 2.9$ V, GaAs current collection became more uniform. The GaAs current collection trend observed at $V_{3J} \leq 2.5$ V agree with the InGaP luminescence maps shown in Figs. 2(a) to (d) while that observed between $V_{3J} = 2.7$ V and 2.9 V agree with what was observed from GaAs luminescence shown in Figs. 4(f) to (h). On one hand, it is difficult to comment on the magnitude of the current collection trend in comparison with the trend observed from GaAs luminescence maps due to the use of modulated laser upon GaAs during LBIC mapping.

4.3.2. Varying the optical bias intensity upon an HBG subcell

In Chapter 3, encompassing the literature [141, 170–172,185], it was observed that when the light bias intensity upon the higher bandgap MJ subcell where the LC effect originates was increased, the LC current collection increases but the spatial homogeneity degrades. To know if this observation is influenced by the HBG subcell luminescence, EL/PL mapping was conducted at various light intensities upon this subcell while its adjacent LBG subcell was made current-limiting, that is, the latter was under dark condition.

Figure 6 shows the collection of InGaP luminescence maps measured at low power [Figs. 6(a) to (d)], medium power [Figs. 6(e) to (h)], and at high power [Figs. 6(i) to (l)]. Upon acquiring these maps, the GaAs middle cell was made current-limiting. Here, it can be observed that at low and medium power, no change in the InGaP luminescence profile and magnitude could be explicitly observed, while at high power, the InGaP luminescence was larger at $V_{3J} = 2.3$ V, similar at $V_{3J} = 2.5$ V, while less at $V_{3J} > 2.7$ V. This trend implies the change in V_{op} when the light intensity upon the HBG subcell is varied by at least 1 order of magnitude. This is considering that the low and high 532-nm laser power values differ by 1 order of magnitude. Possibly, these variations could be further observed each time the light intensity upon the HBG subcell is increased to higher orders of magnitude. Hence, in summary, these observations suggest that the LC current collection profile is affected by order of magnitude variations of illumination upon an HBG subcell, which then varies the V_{op} point and then impacts the HBG luminescence profile. These are shown in the mean InGaP luminescence plots in Fig. 12 (a), Sec. 4.5. Here, it can be seen that at $V_{3J} \geq 2.7$ V, the InGaP luminescence is the smallest at high 532-nm laser power. From the mean InGaP luminescence plots comparison, it may be inferred that the V_{op} and V_{OC} points shifted to the right, i.e. larger forward voltage when the 532-nm laser power was increased. Nevertheless, the observations agree with those made by LBIC mapping under varying light bias intensities on the HBG subcell [141, 170–172,185].

The GaAs luminescence maps at different 532-nm laser power were also obtained using the setup described in Sec. 4.2.1. These maps are shown in Fig. 7 for each power setting used at various V_{3J}. No significant profile difference was observed between low (12.8 μW) and medium (66.0 μW) power measurements. On the other hand, there were several differences observed among the sets of GaAs luminescence maps at every V_{3J}. At $V_{3J} = 2.3$ V, the highest luminescence was observed at a low 532-nm laser power. However, for the rest of the maps shown, the highest GaAs luminescence was observed

at medium 532-nm laser power. These observations may be attributed to the variation of V_{op} per laser power setting. Furthermore, the least GaAs luminescence observed at higher 532-nm laser power may be attributed to the higher probability of nonradiative recombination in GaAs, to larger light absorption in InGaP top cell, or both of these. These are comprehensively illustrated in the mean GaAs luminescence plot shown in Fig. 13(b), Sec. 4.5. In this figure, it can be seen that at $V_{3J} \geq 2.7$ V, GaAs luminescence is the smallest at high 532-nm laser power. Comparing all the mean GaAs luminescence plots, it may be inferred that the V_{op} and V_{OC} points shifted to the right, i.e. larger forward voltage when the 532-nm laser power was increased.

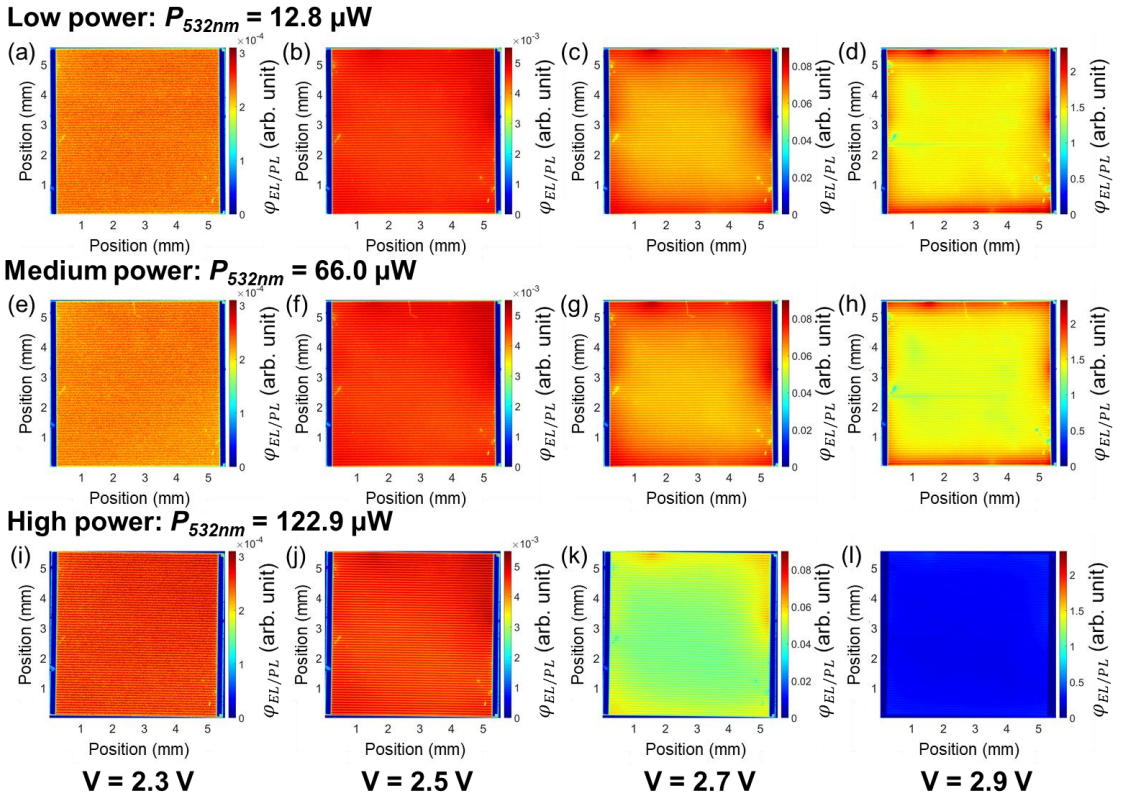

Fig. 6 Spatially-resolved luminescence maps acquired in InGaP top cell of InGaP/GaAs/Ge 3JSC (a)-(d) at low (12.8 µW), (e)-(h) medium (66.0 µW), and (i)-(l) high 532-nm laser power (122.9 µW), at applied 3JSC terminal voltages of 2.3, 2.5, 2.7, and 2.9 V, respectively, and at GaAs middle cell current-limiting condition.

Spatially-resolved maps of LC current collection in GaAs at different 450-nm laser power upon InGaP were measured using the setup described in Sec. 4.2.2. These maps are shown in Fig. 8. From these, it was observed that a higher 450-nm laser power yielded a larger LC current collection at high V_{3J}. Hence, the LC current collection in GaAs may be inferred to be mainly influenced by the InGaP luminescence at a certain V_{3J}. It should be noted that the exact V_{op} is difficult to determine for LBIC mapping due to the presence of continuous 440-nm, 970-nm and 1550-nm LED biases that could affect this. Meanwhile, it can be seen that at V_{3J} = 2.7 V, the LC current collection was the least. This decrease could be due to the V_{3J} approaching the V_{OC} point, where current is 0. Then, the LC current increased again at V_{3J} = 2.9 V. This increase may be attributed to high carrier

injection, possibly yielding a higher probability of radiative emission from InGaP, GaAs, or both subcells, which then increases the chance of carrier collection.

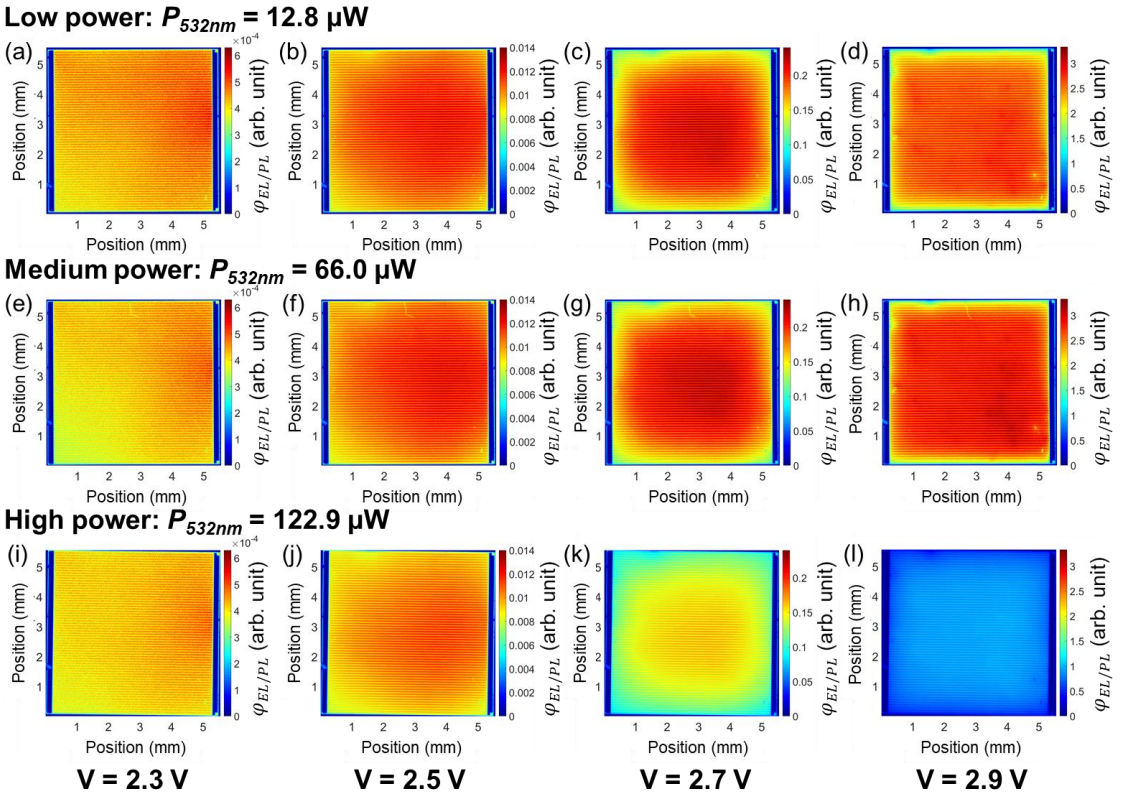

Fig. 7 Spatially-resolved luminescence maps acquired in GaAs middle cell of InGaP/GaAs/Ge 3JSC (a)-(d) at low (12.8 µW), (e)-(h) medium (66.0 µW), and (i)-(l) high 532-nm laser power (122.9 µW), at applied 3JSC terminal voltages of 2.3, 2.5, 2.7, and 2.9 V, respectively, and at GaAs middle cell current-limiting condition.

As for the direct GaAs current mapping, the maps were measured using the setup described in Sec. 4.2.2, while using a modulated 785-nm laser. These maps are shown in Fig. 14, Sec. 4.5 at various applied V_{3J}, close to V_{OC} and V_{op}. When V_{3J} was 2.5 V or less, the current collection in GaAs was uniform with or without transmission filters. It should be noted though, that the irregular fringes observed at these voltages and low [Figs. 14(e) to (h)] and medium [Figs. 14(e) to (h)] 785-nm laser power may be attributed to the opacity of the transmission filter placed between the modulated laser and the sample being scanned during LBIC measurements. On the other hand, when V_{3J} was 2.7 V, the current became less uniform, with less collection near the edges. Because this is similar to the luminescence profile at the same voltages, shown in Figs. 7(c), (g), and (k) for low, medium and high 785-nm laser power, respectively, it may be inferred that the GaAs current collection at V_{3J} = 2.7 V depends on its luminescence profile. Then, at V_{3J} = 2.9 V, the current collection was decreased by an order of magnitude lower than that at V_{3J} = 2.7 V. Moreover, less current was collected at lower 785-nm laser power. These observations imply that the V_{OC} is closer to 2.9 V at lower laser power; hence, the change in V_{op} and V_{OC} points at varying illumination intensities upon the higher bandgap subcell, InGaP. Specifically, as the laser power upon InGaP was increased, the V_{OC} and V_{op} points seemingly shifted to the right, i.e. yielding higher V_{3J}.

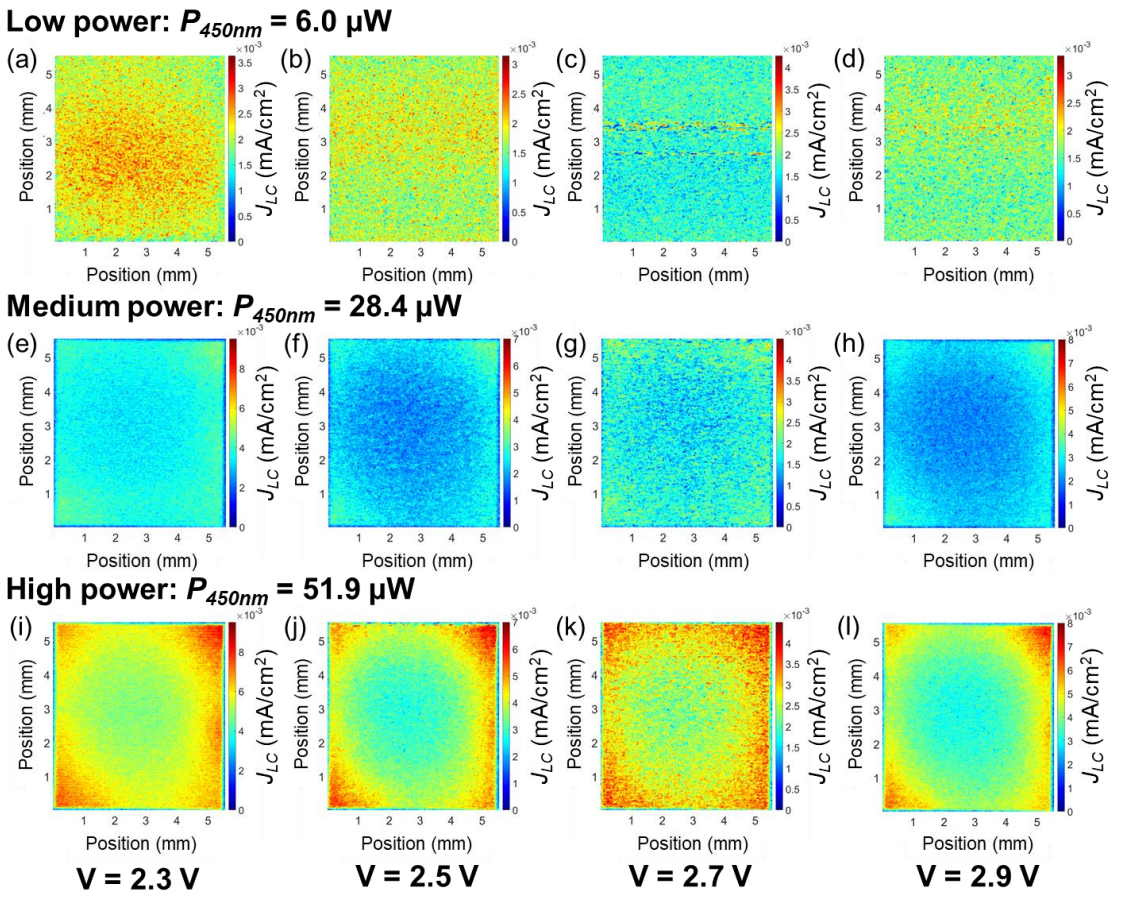

Fig. 8 LBIC maps acquired by LC excitation upon GaAs middle cell of InGaP/GaAs/Ge 3JSC (a)-(d) at low (6.0 μW), (e)-(h) medium (28.4 μW), and (i)-(l) high 450-nm laser power (51.9 μW), at applied 3JSC terminal voltages of 2.3, 2.5, 2.7, and 2.9 V, respectively.

To quantify the variation in luminescence homogeneity of adjacent MJ subcells in LC effect condition, the standard deviation of luminescence map values normalized with their averages, $\sigma_{LC,i}/\phi_{EL/PL,ave}$, was calculated. These were calculated from InGaP and GaAs luminescence maps at V_{3J} from 2.2 V to 3.0 V and at various 532-nm laser power upon InGaP, shown in Figs. 9(a) and (b), respectively. Under varying V_{3J}, the lowest $\sigma_{LC,T}/\phi_{EL/PL,ave}$ and $\sigma_{LC,M}/\phi_{EL/PL,ave}$ values were calculated at $V_{3J} \approx 2.45$ V and 2.4 V, respectively. Hence, the subcell luminescence was most homogeneous at these terminal voltages. As luminescence was observed to be weak at low voltages, the high $\sigma_{LC,T}/\phi_{EL/PL,ave}$ and $\sigma_{LC,M}/\phi_{EL/PL,ave}$ values at $V_{3J} < 2.35$ and 2.3 V, respectively, may be attributed to low signal-to-noise ratio.

In varying the 532-nm laser power, the highest $\sigma_{LC,T}/\phi_{EL/PL,ave}$ was calculated from luminescence maps measured at high power (122.9 μW), as shown in Fig. 9(a). Meanwhile, no significant difference was observed between the $\sigma_{LC,T}/\phi_{EL/PL,ave}$ values acquired at low (12.8 μW) and medium (66.0 μW) power. As this trend was found consistent at $V_{3J} \geq \sim$2.3 V, this suggests that illumination intensity increased by an order of magnitude may yield less homogeneous luminescence in the higher bandgap subcell. This, then, would affect the LC current homogeneity in its adjacent lower bandgap subcell. On the other hand, since no trend of $\sigma_{LC,M}/\phi_{EL/PL,ave}$ could be established from

GaAs luminescence [Fig. 9(b)], in contrast with InGaP [Fig. 9(a)], the influence of GaAs luminescence on its LC current homogeneity could be minimal.

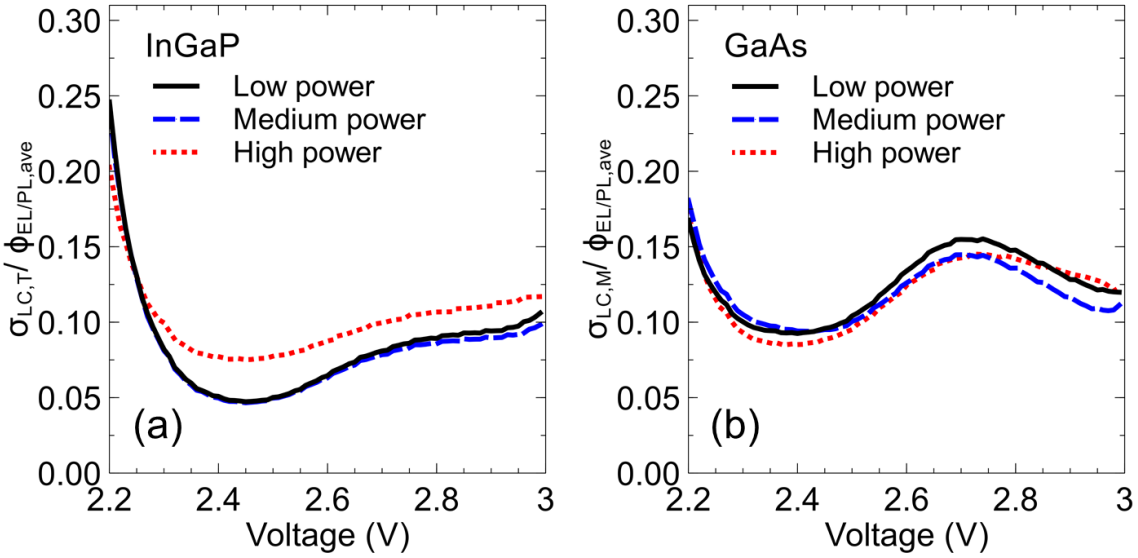

Fig. 9 Normalized standard deviations of luminescence from (a) InGaP top cell, $\sigma_{LC,T}/\phi_{EL/PL,ave}$, and (b) GaAs middle cell, $\sigma_{LC,M}/\phi_{EL/PL,ave}$, of InGaP/GaAs/Ge 3JSC at low (solid lines, 12.8 μW), medium (dashed lines, 66.0 μW), and high (dotted lines, 122.9 μW) 532-nm laser power between applied 3JSC terminal voltages of 2.2 V and 3.0 V.

To expound on the luminescence maps shown earlier, consider the conditions needed to efficiently move carriers within an MJ subcell. Simple schematics of lateral and vertical carrier transport in an *n*-on-*p* tandem cell are shown in Figs. 10(a) and (b), respectively.

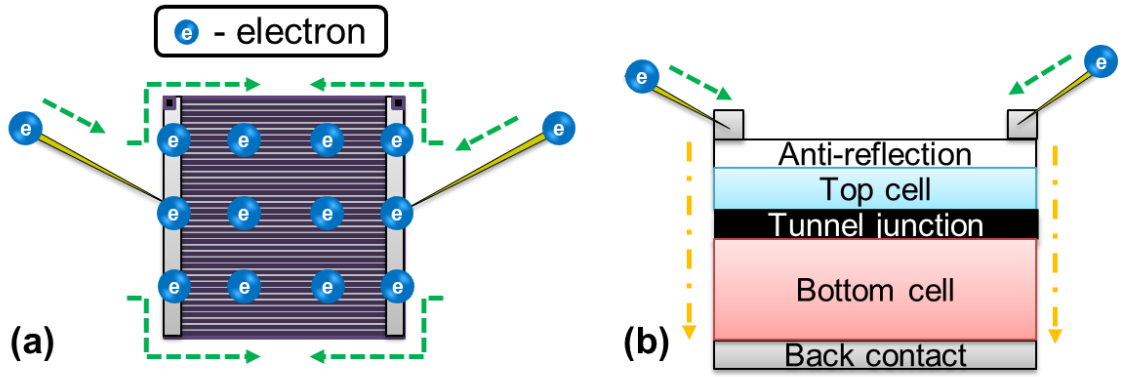

Fig. 10 Simplified schematic illustrations of (a) lateral and (b) vertical transport of carriers in a tandem solar cell, where dashed and dash-dotted arrows represent lateral and vertical electron movements, respectively.

High lateral transport efficiency can be achieved by having high-quality solar cell absorber, allowing carriers to move laterally without experiencing nonradiative recombination in traps or defects. On the other hand, high vertical transport efficiency of carriers can be achieved by having high-quality contacts and tunnel junction between adjacent subcells.

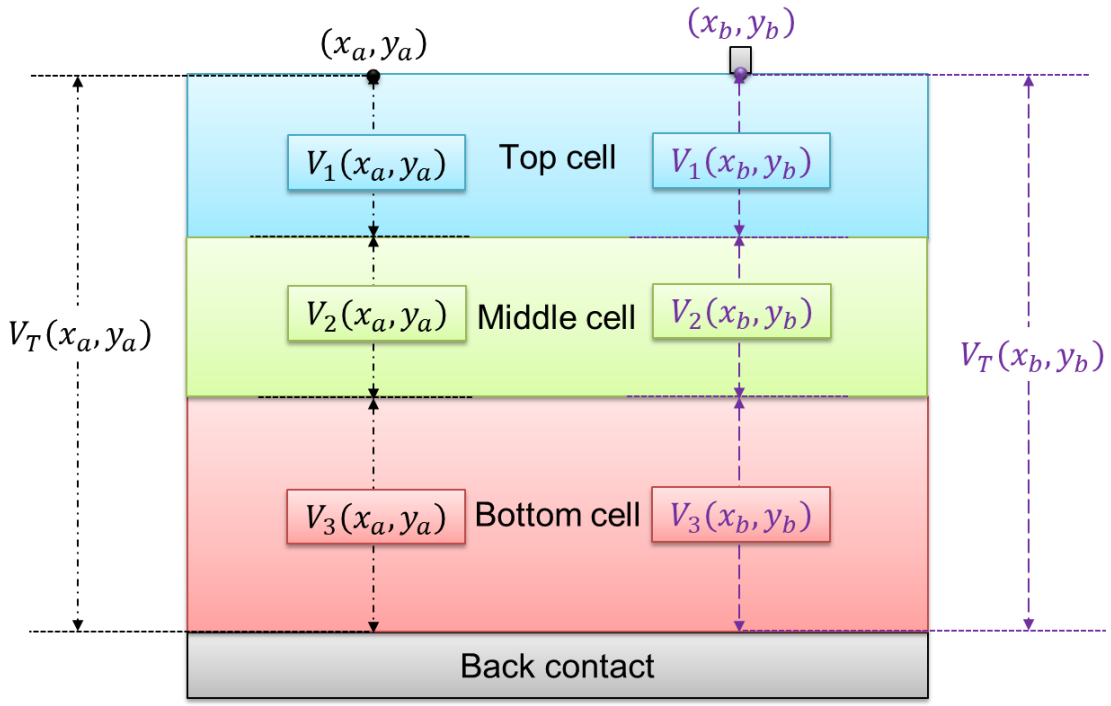

Fig. 11 Schematic illustration of the voltages across the top, middle, and bottom cells, V_1, V_2, and V_3, respectively, and the net voltage across a point on the bulk, $V_T(x_a,y_a)$, and metal grid, $V_T(x_b,y_b)$.

Recalling the luminescence maps discussed earlier at 2.7 V while the LC effect was induced upon GaAs middle cell, the InGaP top cell has higher luminescence on the edges [Figs. 6(c), (g), and (k)], while GaAs has stronger luminescence at the center region [Figs. 7(c), (g), and (k)]. Previous literature has defined luminescence to be proportional to the voltage across a semiconductor device, V, by the relations [153,240]

$$\Phi_{EL} = \int A \cdot E^2 \exp\left(\frac{-E}{k_B T}\right) \exp\left(-\frac{qV}{k_B T}\right) EQE(E) dE \tag{3}$$

for EL [241–244], Φ_{EL}, where E is the photon energy, A is the collective constant for the detector parameters, k_B is the Boltzmann's constant, T is temperature, and q is the electron charge, and

$$\Phi_{PL} \propto \exp\frac{qV}{k_B T} \tag{4}$$

for PL [245], Φ_{PL}. From these, the regions with stronger luminescence may be interpreted to be at higher voltages. It then follows that the observed in-plane voltage was larger in the InGaP perimeter than in the GaAs perimeter. On the other hand, the observed planar voltage was larger in the bulk region of GaAs than in the bulk of InGaP. With these complementary observations from InGaP and GaAs luminescence maps and assuming no change in the in-plane voltage of Ge because 1200-nm laser power was fixed, the net planar voltage at all points in the 3JSC will be equal, though with some reduction at points covered by the metal grid lines due to the series resistance these lines introduce. These are illustrated in the cross-section of a 3JSC shown in Fig. 11, where (x_a, y_a) and (x_a, y_a)

are points on the bulk region and the grid line. Considering this and the downward movement of electrons in an *n*-on-*p* solar cell device, this further suggests that the electron flow direction, the top cell will dictate luminescence for the bottom cell. This was also inferred from comparing the luminescence and LBIC maps shown in Figs. 2 and 3, respectively.

4.4. Synthesis of Findings

In this chapter, the EL/PL measurement was demonstrated to be a useful tool in evaluating the luminescence profile of adjacent MJ subcells involved in manifesting the LC effect. At increasing applied V_{3J}, both MJ subcell homogeneities were found to be less uniform, with larger InGaP and smaller GaAs luminescence on the sides. This was attributed to high carrier injection, which may have led to carrier congestion near the perimeter region. As a result, there could have been a higher probability of photon emission due to radiative recombination in InGaP. This could have then lowered the emission probability in GaAs. Under varying laser power upon a higher bandgap subcell, it was found that the higher its intensity, the less uniform the emission profiles were, both from HBG and LBG subcells, These findings agree with those observed from the LBIC measurements of MJSCs with the LC effect upon increasing the optical bias intensity upon an HBG subcell, wherein the higher the intensity, the less uniform the LC current collection was in the adjacent LBG subcell. Particularly, when the light bias intensity upon the HBG subcell where the LC effect originates is made larger by 1 order of magnitude or higher, noticeable degradation in the HBG subcell luminescence may be observed. The most homogeneous luminescence was observed from InGaP at about 2.45 V in all light intensities. Hence, higher bandgap subcells may be designed to operate at an optimal voltage to possibly induce homogeneous LC effect towards its adjacent lower bandgap subcell.

With these findings, it can be concluded that inhomogeneous luminescence from the HBG MJ subcell affects the LC current production. Hence, under current-mismatched conditions, the nonuniform LC effect may be alleviated when each MJ subcell is illuminated such that each is optimized to operate as close as possible to their respective V_{OC} values.

4.5. Supplementary Information

The dark *J*-*V* characteristic curves measured from the EL/PL setup before any subcell luminescence mapping, in between subcell mapping, and after the last measurement was taken are shown in Fig. 12.

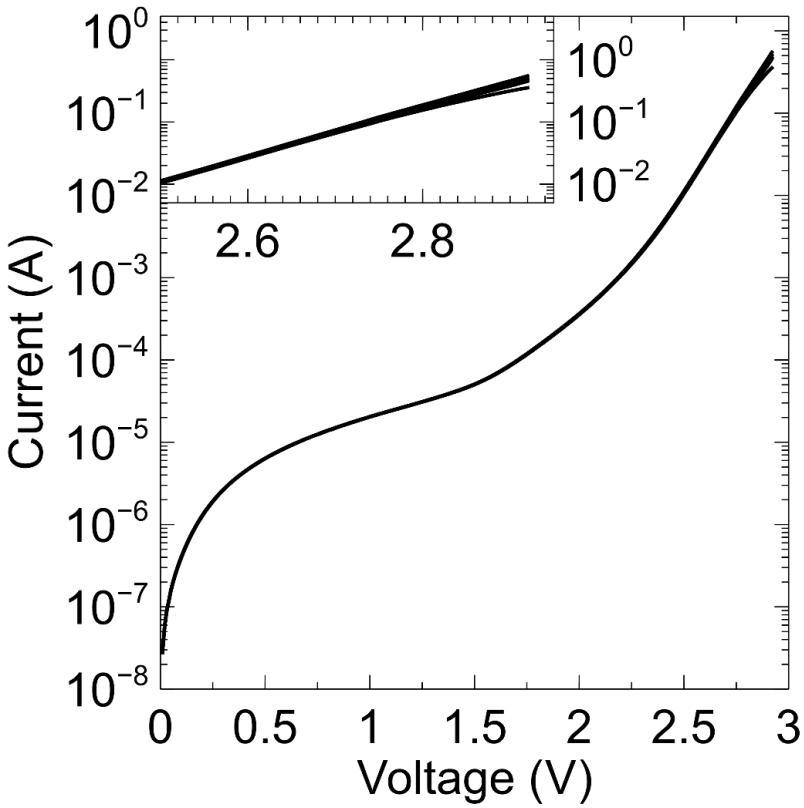

Fig. 12 Dark *J-V* characteristics of InGaP/GaAs/Ge 3JSC measured using the EL/PL mapping setup connected with a sourcemeter. The x- and the y-axes of the inset are voltage in V and current in A.

The averaged InGaP and GaAs luminescence derived from measured EL/PL maps at V_{3J} = 2.2 V to 3.0 V are shown in Figs. 13(a) and (b), respectively. Figure 14 shows the current collection in GaAs middle cell at low [6.3 μW, Figs. 14(a) to (d)], medium [31.2 μW, Figs. 14(e) to (h)], and high [60.2 μW, Figs. 14(i) to (l)] 785-nm laser power.

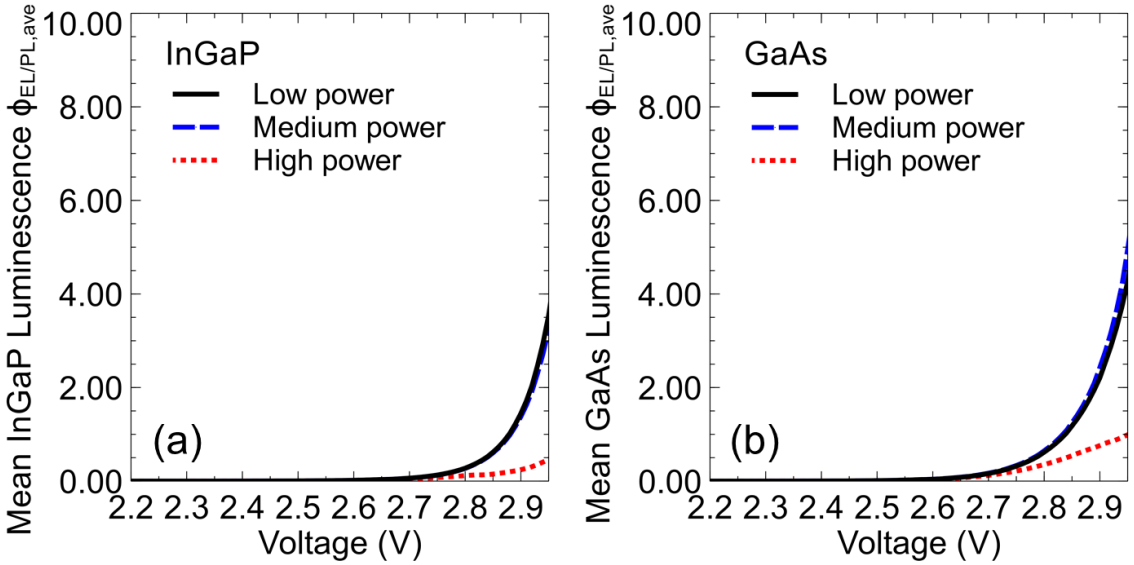

Fig. 13 Mean luminescence, $\phi_{EL/PL,ave}$, from (a) InGaP top cell and (b) GaAs middle cell of InGaP/GaAs/Ge 3JSC at low (solid lines, 12.8 μW), medium (dashed lines, 66.0 μW), and high (dotted lines, 122.9 μW) 532-nm laser power between applied 3JSC voltages of 2.2 V and 2.95 V.

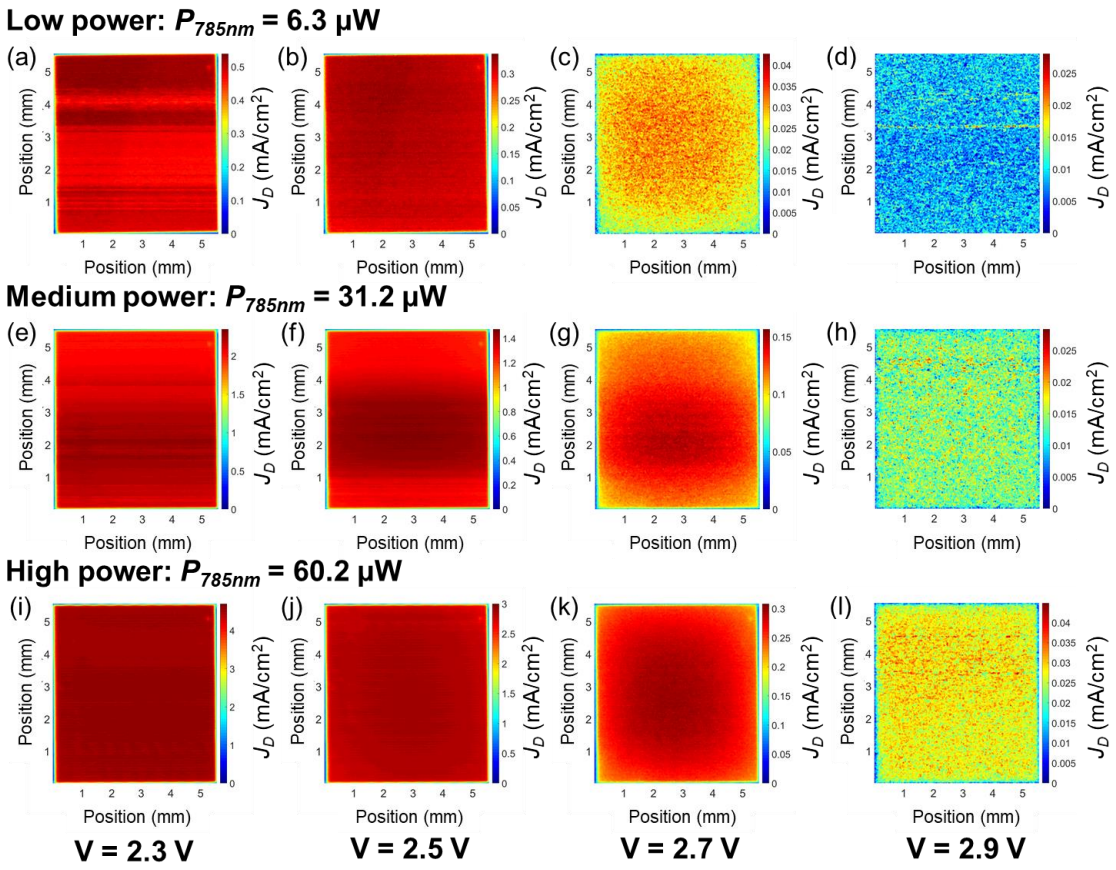

Fig. 14 LBIC maps acquired by direct excitation of GaAs middle cell of InGaP/GaAs/Ge 3JSC (a)-(d) at low (6.3 µW), (e)-(h) medium (31.2 µW), and (i)-(l) high 785-nm laser power (60.2 µW), at applied 3JSC terminal voltages of 2.3, 2.5, 2.7, and 2.9 V, respectively.

Electrical sidewall passivation of III-V multijunction solar cells for homogeneous luminescent coupling effect

Chapter 5

Chapter 5 – Electrical sidewall passivation of III-V multijunction solar cell for homogeneous luminescent coupling effect

Abstract

The nonuniformity of luminescent coupling (LC) effect in III-V based multijunction solar cells (MJSCs) is partly ascribed to recombination at perimeter defects, as identified in Appendix C. In this regard, the electrical passivation of the MJSC sidewalls could be a potential solution to perimeter recombination. An attempt to reduce perimeter recombination was done by sidewall passivation of InGaP/GaAs/Ge triple-junction solar cells (3JSCs) through the atomic layer deposition (ALD) of thin aluminum oxide (Al_2O_3) layer. Results revealed that sidewall passivation of a complete MJSC was observed to increase LC current collection in a limiting GaAs middle cell by 21.9% and enhance its uniformity by 7.2%. Furthermore, the luminescence homogeneities from InGaP and GaAs of the passivated samples were found to be 70.6% and 37.5% better than the reference sample, respectively; hence, demonstrating a non-invasive way to improve current matching among subcells.

Chapter 5, therefore, deals with the use of a thin electrical passivation layer for homogenizing the LC effect in MJSCs. This chapter is introduced by a brief background on semiconductor passivation. Next, the general and specific questions of this chapter are laid down, in connection to the recommendations made at the end of Appendix C. In Sec. 5.3, the simulation and experimental methods used to implement the study are discussed. Then, in Sec. 5.4, the results and inferences are drawn from each method, in an attempt to answer whether the electrical sidewall passivation alleviated the inhomogeneous LC effect or not, are discussed. Last, this chapter ends with the synthesis of the main findings acquired in studying the effect of electrical sidewall passivation to the LC effect homogeneity, together with other performance indicator parameters of the MJSC device itself.

5.1. Background of the Study

Fundamentally, the main reason why we electrically passivate semiconductors is to remove their dangling bonds. Dangling bonds are found on the surfaces of a semiconductor, where atoms have fewer bonding partners than in the bulk. These are illustrated in Fig. 1(a), enclosed in the dashed box. Here, traps are formed, which gives rise to the formation of surface states or unwanted energy levels between the lowest energy level of the conduction band and the highest energy level of the valence band. At these intermediate energy levels, free electrons can be captured easier than without these surface states. As a result, fewer carriers would be available for conduction. The energy band diagram with electrically-active surface states and its corresponding plot (enclosed in dash-dotted box) with respect to the density of surface states, N_{ss}, are shown in Figs. 1(b) and (c), respectively [246].

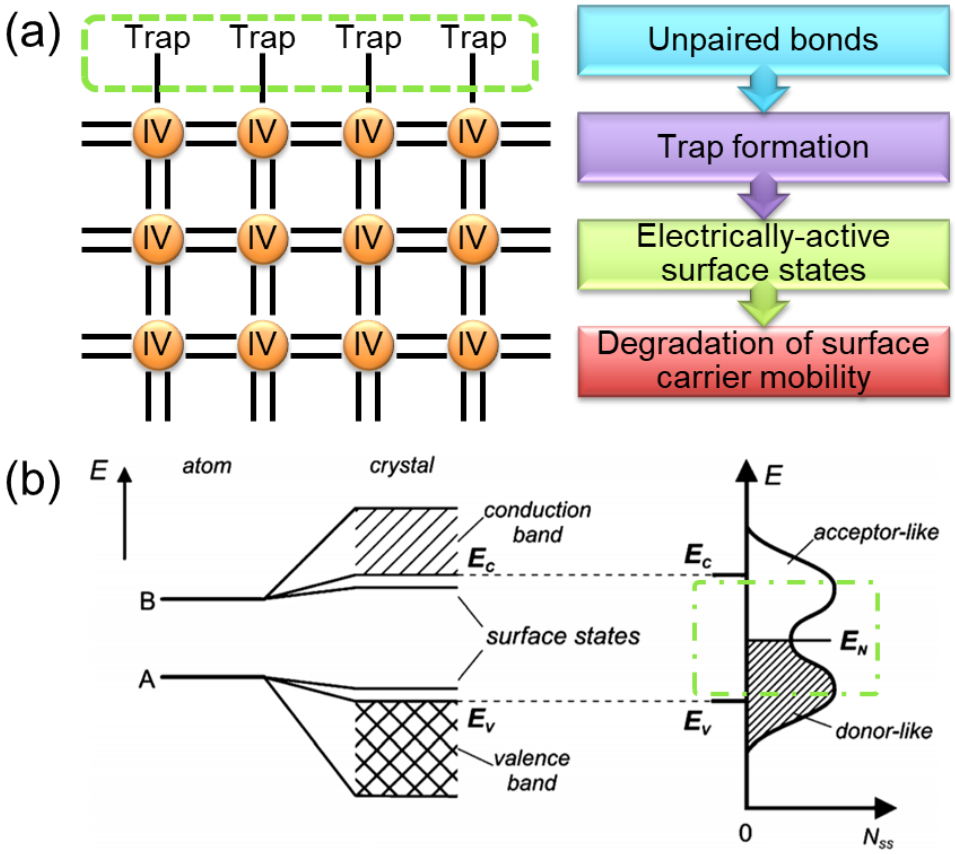

Fig. 1 (a) Simplified schematic of chemical bonds in the surface (dashed box) and bulk regions of a Group IV atom with emphasis on the unpaired surface bonds where traps are formed. (b) Arbitrary energy band diagram of a semiconductor with electrically-active surface states and its approximate plot (dash-dotted box) with respect to the density of surface states, N_{ss} [246].

One way to remove these surface states is by electrical passivation and a method to do so is by ALD of thin-film dielectrics, such as aluminum oxide (Al_2O_3). One cycle of ALD is shown in Fig. 2 [247]. The cycle begins with the pulse release of trimethylaluminum (TMA or $Al(CH_3)_2$ as a chemical formula). In this step, TMA reacts with the hydroxyl

group (OH) on a substrate then releases methane (CH_4). Next, water is pulse-released, then reacts with the remaining methyl groups (CH_3) on the surface to release more CH_4. After 1 cycle, the surface chemistry is restored to its initial OH condition [247]. In the past, Al_2O_3 deposition in III-V semiconductor materials was experimentally proven effective in reducing the native oxides on semiconductor surfaces, which then reduces surface states [248–256]. Doing the same for the solar cell perimeter may help reduce its density of surface states and recombination at the sidewalls. Particularly, a potential solution could, therefore, be passivation of the MJSC sidewalls at the cell perimeter could therefore be passivation of the MJSC sidewalls at the cell perimeter.

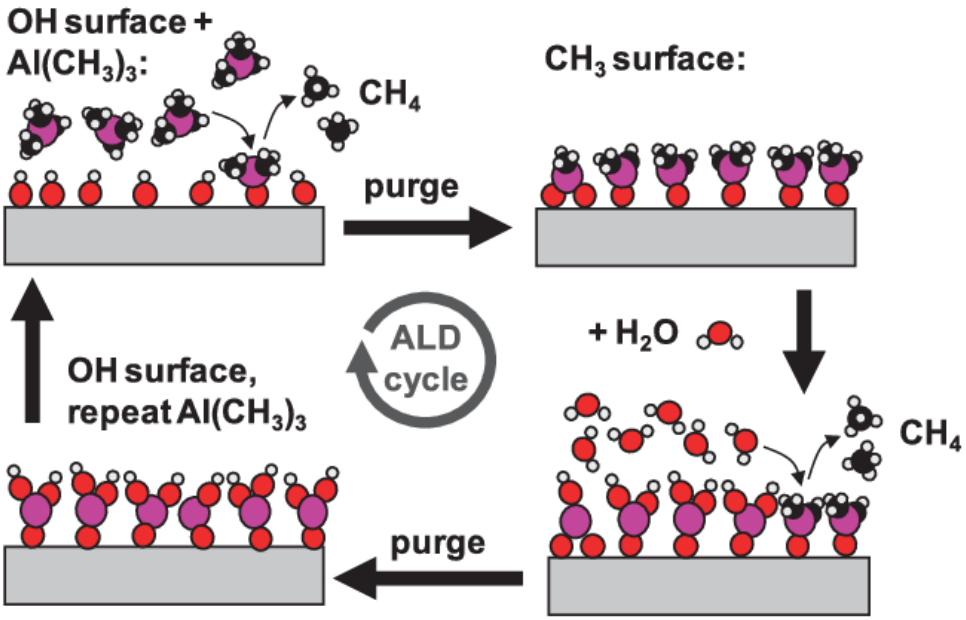

Fig. 2 Schematic illustration of 1 cycle of Al_2O_3 ALD [247].

This study attempts to homogenize the LC effect in a current-limiting cell by Al_2O_3 passivation of a full III-V on Ge MJSC device. This was done experimentally by ALD of Al_2O_3 on the sidewalls of commercial III-V on Ge MJSC samples. These samples were then evaluated by laser beam induced current (LBIC) mapping. Homogenizing LC current production in current-mismatched MJSCs was predicted to increase their power conversion efficiency by 1.35% [170]. Furthermore, this may prevent uneven damage in the cell over time due to nonuniform current production, thereby extending the lifespan of concentrator MJSCs. In a broader picture, the outcome of this study may provide ideas on how to improve MJSC performance non-invasively even after the whole device has been fabricated.

5.2. Research Questions

The main objective of this chapter is to investigate the influence of electrical sidewall passivation on the nonuniform LC effect in MJSCs. Specifically, this chapter attempts to answer the following questions:

1. Will the sidewall deposition of 10-nm aluminum oxide (Al_2O_3) alleviate LC effect inhomogeneity in MJSCs?

a. Will the current collection homogeneity improve or degrade?
b. Will the luminescence homogeneity improve or degrade?

2. Addressing the possible regression of the electrical sidewall passivation to the MJSC performance,
   a. are there other improvements, or
   b. degradation introduced?

5.3. Methodology

5.3.1. Atomic layer deposition (ALD) of Al_2O_3 on MJSC sidewalls

Al_2O_3 was deposited on the MJSC sidewalls by ALD. In this process, 100 cycles of alternating TMA and H_2O precursor pulses were run to deposit 9 to 10-nm thick Al_2O_3 on terrestrial-grade, series-constrained, commercial 1.0-cm^2 InGaP/GaAs/Ge 3JSC samples. The ALD tool used was tested to have an Al_2O_3 deposition homogeneity of 96% within a 4-cm radius. The detailed information on ALD homogeneity can be found in Figs. 20 and 21, Sec. 5.6. Since the back contacts of the samples were resting on the chamber stage, Al_2O_3 was deposited primarily on the sidewalls and front surface exposed to precursor gases. The chamber temperature and pressure were kept at 180°C and within 1 Torr, respectively. After placing the samples into the stage and before closing the ALD chamber, Si pieces were placed as physical masks on the active region of two 3JSC samples, Samples A and B. Two samples were subjected to Al_2O_3 passivation for assessing the repeatability of the results. On the masked region, a significantly thinner Al_2O_3 layer was deposited than on the sidewalls. Last, a reference sample was left unprocessed. Simple top view and cross-section schematics of the reference sample and the passivated sample whose front surface was temporarily masked with Si during ALD are shown in Fig. 3. Additionally, a schematic illustration of the ALD chamber with a temporary Si mask resting on top of a 3JSC sample and the photos of Si masks used on 3JSC samples are shown in Figs. 4(a) and (b), respectively.

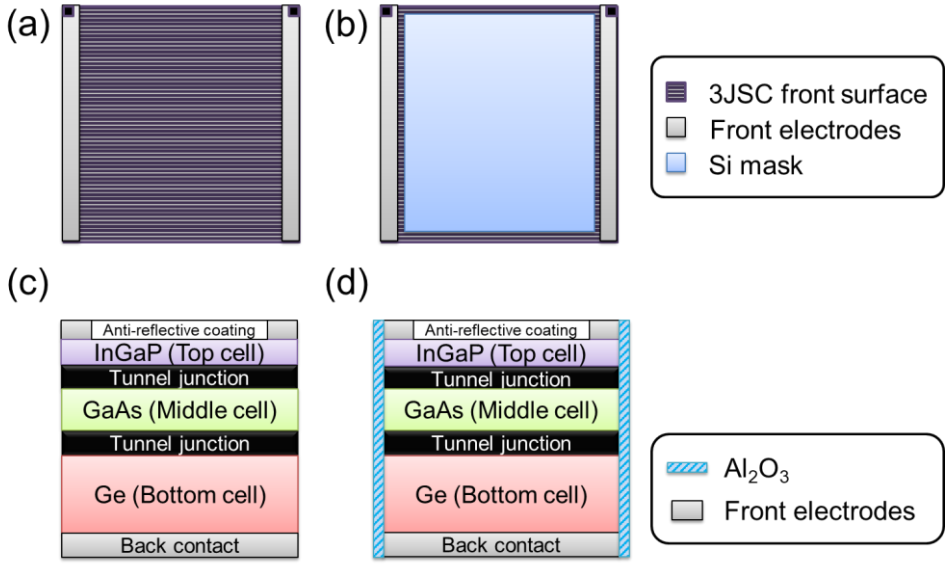

Fig. 3 Top view schematics of (a) reference InGaP/GaAs/Ge 3JSC without Al_2O_3 on the sidewalls and (b) InGaP/GaAs/Ge 3JSC sample subjected to Al_2O_3 sidewall passivation (Samples A and B) that had Si mask

resting on its top during ALD. Cross-section schematics of (c) reference InGaP/GaAs/Ge 3JSC without Al_2O_3 on the sidewalls and (d) InGaP/GaAs/Ge 3JSC sample subjected to Al_2O_3 sidewall passivation (Samples A and B) that had Si mask resting on its top during ALD.

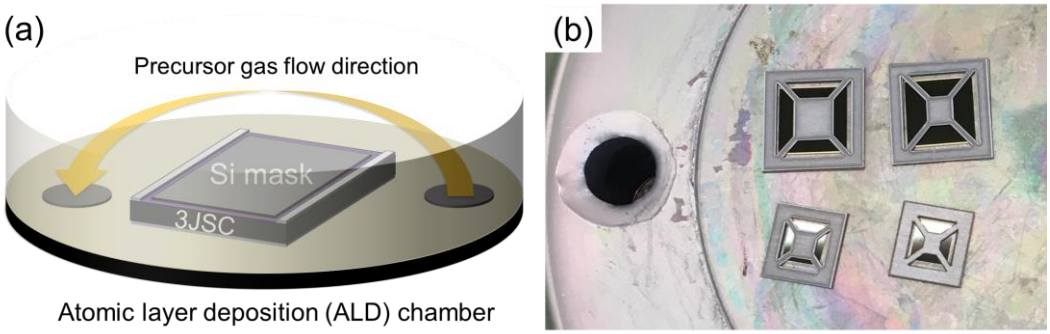

Fig. 4 (a) ALD chamber loaded with temporarily masked InGaP/GaAs/Ge 3JSC sample subjected to Al_2O_3 thin film deposition. (b) Photos of InGaP/GaAs/Ge 3JSC samples with temporary Si masks loaded into the ALD chamber.

5.3.2. Electrical and optical simulations

5.3.2.1. Electrical simulation using 3D distributed SPICE model

To analyze the probable causes of electrical losses causing nonuniform luminescent coupling in InGaP/GaAs/Ge 3JSCs, a 3D distributed SPICE model was used [141,206], as what was done in Appendix C. Focusing on the possible causes for nonuniform LC effect between InGaP top cell and GaAs middle cell, the effect of varying the sheet resistance, R_{lat}, and the InGaP nonradiative recombination diode coefficient, $J_{02,t}$, on current collection homogeneity in GaAs was revisited. As in Appendix C, R_{lat} and $J_{02,t}$ values were varied from 1.0×10^{-3} to 1.0 Ω/cm^2 and 1.0×10^{-15} to 1.0×10^{-3} mA/cm^2, respectively. More details can be found in Appendix C, Sec. C.2.2.

5.3.2.2. Optical simulation using 2D Monte Carlo ray tracer

A 2D Monte Carlo ray-tracing simulation of adding a 10-nm Al_2O_3 layer on MJSC absorbers to photon escape and internal reflection was included in this chapter for the ease of reading. As described in Appendix C, Sec. 2.1.2, the inbound and outbound cases for a III-V or IV solar cell absorber whose both sidewalls are coated with 10-nm Al_2O_3 passivation layer to possibly reduce perimeter recombination [248–256] were investigated.

5.3.2.3. Optical simulation by Transfer Matrix Method (TMM)

As the Si masks placed on top of the 3JSC samples may not be able to perfectly cover their whole front surfaces during ALD, the impact of having a 10-nm Al_2O_3 layer on the approximate final 3JSC structure was investigated theoretically. To complement the 2D ray-tracing calculations intended for MJSC sidewalls, the effect of having an Al_2O_3 layer on the front surface of a III-V solar cell material to its reflection, absorption, and transmission (RAT) spectra was calculated using TMM. Being the top cell material of the samples studied, only InGaP was simulated with and without thin films. Specifically, the RAT spectra were calculated for the following cases: (1) semi-infinite thick InGaP only, (2) 10-nm Al_2O_3 on semi-infinite thick InGaP, (3) 100-nm Si_3N_4 anti-reflection coating (ARC) on semi-infinite thick InGaP, and (4) Al_2O_3/Si_3N_4/InGaP whose thicknesses were

10 nm, 100 nm and semi-infinite, respectively. Cross-section schematic illustrations of all simulation cases are shown in Fig. 5.

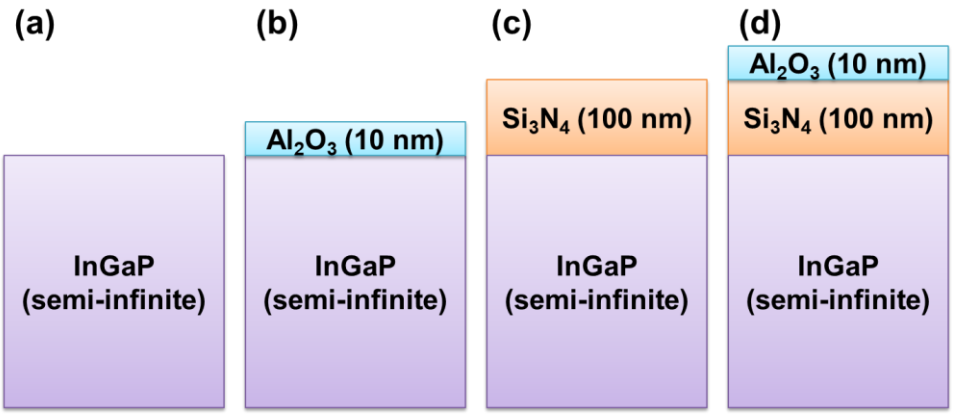

Fig. 5 Cross-section schematic illustrations of (a) semi-infinite InGaP material (b) 10-nm Al_2O_3 on semi-infinite thick InGaP, (c) 100-nm Si_3N_4 ARC on semi-infinite thick InGaP, and (d) Al_2O_3/Si_3N_4/InGaP for reflection, absorption, and transmission (RAT) spectra calculations using TMM.

5.3.3. Electro-optical characterization

5.3.3.1. Current-voltage (*J-V*) characteristics measurements

DC *J-V* characteristics measurements were obtained for InGaP/GaAs/Ge 3JSC samples with and without Al_2O_3 sidewall passivation under three different conditions: (1) at dark, (2) at global air mass 1.5 (AM 1.5G), and (3) when a specific subcell is made current-limiting. In the first condition, no light source was used while injecting electrical current into the samples. For condition 2, a halogen white lamp source was used and was calibrated using a reference cell with known current production at 1 sun. As for the third condition, since all subcells are electrically connected in series, the subcell being evaluated was made current-limiting cell by illuminating other subcells with continuous LEDs. During the light *J-V* characteristics measurement of InGaP top cell with LC effect, 780-nm, 970-nm and 1550-nm LED intensities were fixed at 140.1, 31.4, and 4.2 mW/cm^2, respectively. As for measuring the light *J-V* characteristics of GaAs middle cell with LC effect, 440-nm, 970-nm and 1550-nm LED intensities were fixed at 167.2, 31.4, and 4.2 mW/cm^2, respectively. Last, the light *J-V* characteristics of Ge bottom cell with LC effect were measured using 440-nm and 660-nm LEDs whose intensities were fixed at 167.2 and 261.1 mW/cm^2, respectively. Applied 3JSC terminal voltage was swept from -8.0 V to 2.7 V in all *J-V* curve measurements acquired. The summary of continuous LED intensity settings used for subcell *J-V* curve measurements can be found in Table 1.

Table 1 LED intensity settings used for obtaining the subcell DC light *J-V* characteristics and EQE of InGaP/GaAs/Ge 3JSC samples.

Condition	Continuous LED intensity, P_{LED} (mW/cm^2)				
	440-nm	660-nm	780-nm	970-nm	1550-nm
1. InGaP (top)	*off*	*off*	140.1	31.4	4.2
2. GaAs (middle)	167.2	*off*	*off*	31.4	4.2
3. Ge (bottom)	167.2	261.1	*off*	*off*	*off*

5.3.3.2. External quantum efficiency (EQE) measurements

The electro-optical properties of the 3JSC samples right before and after Al_2O_3 deposition were evaluated by open-circuit voltage (V_{OC}) measurements under AM 1.5G solar simulator and subcell EQE measurements under continuous LEDs and chopped monochromated light[5]. Combinations of 735-nm and 970-nm LEDs, 505-nm and 970-nm LEDs, and 505-nm and 735-nm LEDs were used to current-limit InGaP, GaAs and Ge, respectively, as summarized in Table 2. Also, 0.0 V, 0.0 V, and 1.5 V were applied across the 3JSC terminals during InGaP, GaAs and Ge EQE measurements, respectively. From these measurements, the current density of the limiting subcell, $J_{AM1.5G,i}$, was calculated using

$$J_{AM1.5G,i} = \frac{q}{hc}\int \lambda \cdot EQE(\lambda)\emptyset_{AM1.5G}(\lambda)d\lambda \quad (1)$$

where q is the electron charge, h is the Planck's constant, c is the speed of light, $EQE(\lambda)$ is the measured EQE signal at wavelength, λ, and $\emptyset_{AM1.5G}(\lambda)$ is the global AM 1.5 sunlight irradiance at λ.

For further comparison, EQE before and after[6] Al_2O_3 passivation was acquired using the same continuous LED biases for current limiting each subcell, as listed in Table 1. This was done in parallel with the LBIC measurements.

Table 2 LED current settings used for obtaining the subcell EQE measurements[5] of InGaP/GaAs/Ge 3JSC samples.

Condition	Continuous LED current, I_{LED} (mA)		
	505-nm	735-nm	970-nm
1. InGaP (top)	*off*	50	50
2. GaAs (middle)	50	*off*	50
3. Ge (bottom)	100	100	*off*

5.3.3.3. LBIC mapping settings

The spatial current collection maps of the 3JSC samples with (Samples A and B) and without a 10-nm Al_2O_3 layer on them (reference) were acquired by LBIC mapping. Particularly, current collection from GaAs, which is usually the current-limiting subcell in terrestrial-grade [257] and at the end-of-life of space-grade [258] Ge-based III-V MJSCs, was obtained. First, continuous 440-nm, 970-nm and 1550-nm LEDs whose intensities were set to 167.2, 31.4, and 4.2 mW/cm^2, respectively, were irradiated upon the sample. Here, 440-nm LED was used to generate current in InGaP while 970-nm and 1550-nm LEDs were used to produce current in Ge. In effect, this setting current-limits GaAs, having no light to absorb. To induce an LC effect upon GaAs during LBIC mapping, a 450-nm laser was activated, as illustrated in Fig. 6(a). This wavelength is absorbed in InGaP. On the other hand, the current generation when GaAs was directly

[5] The EQE measurements were done in Arizona State University (ASU) – Solar Power Laboratory within the same week of Al_2O_3 deposition on 3JSC samples, conducted before and after deposition.

[6] This part was done in The University of Tokyo after Al_2O_3 deposition in ASU NanoFab, Arizona, USA.

excited by an external light source was acquired through modulated 785-nm laser irradiation, as shown in Fig. 6(b). As for the current collection in InGaP, continuous 780-nm, 970-nm, and 1550-nm LEDs, together with modulated 450-nm laser were irradiated upon the 3JSC sample. Direct InGaP excitation setup is illustrated in Fig. 6(c). In all measurement conditions, the spot diameter, scanning frequency, switching frequency, time constant, and duty cycle of the lasers used during LBIC measurements were 50 μm, 2 Hz, 2000 Hz, 1 ms and 50%, respectively. Last, the normalized standard deviation of current collection and percent differences of specific parameters between the reference and each of the samples with the Al_2O_3 layer on the sidewalls were calculated from the LBIC measurements. The LBIC mapping settings used can be found in Table 2.

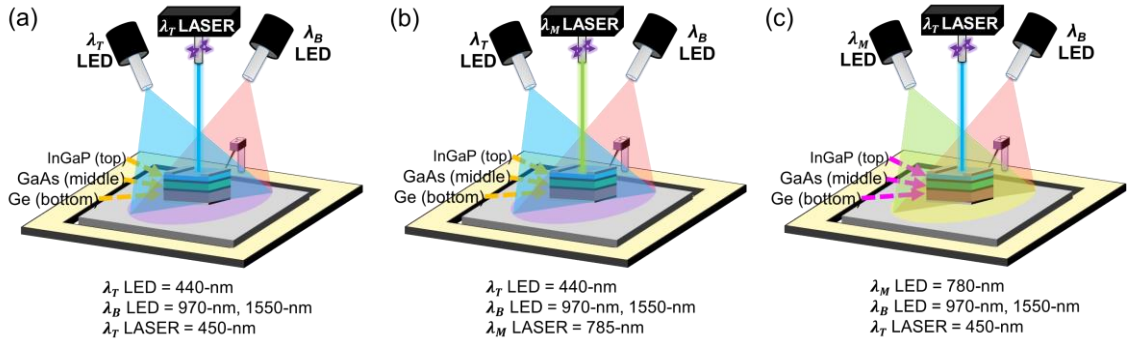

Fig. 6 LBIC measurement setup for (a) GaAs LC effect excitation, (b) direct GaAs middle cell excitation, and (c) direct InGaP top cell excitation.

Table 2 Settings used for obtaining the LBIC maps of InGaP/GaAs/Ge 3JSC samples.

Condition	Continuous LED intensity, P_{LED} (mW/cm^2)				Laser wavelength (nm)	Laser spot diameter (μm)
	440-nm	660-nm	780-nm	970-nm		
1. InGaP (top)	*off*	*off*	140.1	31.4	450	50
2. GaAs (middle)	167.2	*off*	*off*	31.4	785	50
3. Ge (bottom)	167.2	261.1	*off*	*off*	1064	100
4. GaAs LC effect	167.2	*off*	*off*	31.4	450	50
5. Ge LC effect	167.2	261.1	*off*	*off*	785	50

5.3.3.4. Electroluminescence/Photoluminescence (EL/PL) mapping

Another possible reason for the nonuniform LC effect in MJSCs could be the nonuniform luminescence from a higher bandgap subcell towards its adjacent lower bandgap subcell, as concluded in Chapter 4. To probe this on a passivated sample, EL/PL mapping can be used. As this is limited by the sensitivity of the detector, this setup can only capture luminescence images at high voltages, i.e. somewhere close to the open-circuit voltage (V_{OC}) of the device. The illustration of the setup used for evaluating luminescence while inducing LC effect between InGaP and GaAs is shown in Fig. 7(b). Here, the camera detector is Si, which is useful for capturing emissions from InGaP top cell (E_g = 1.87 eV) and GaAs middle cell (E_g = 1.41 eV) of InGaP/GaAs/Ge 3JSC samples. Meanwhile, the long pass and short pass filters used for capturing InGaP emission are 650 nm and 750 nm while 850 nm and 950 nm for capturing GaAs emission,

respectively. The power of 532-nm and 1200-nm lasers used to excite InGaP and Ge were fixed at 10.6 μW and 1.5 mW, respectively.

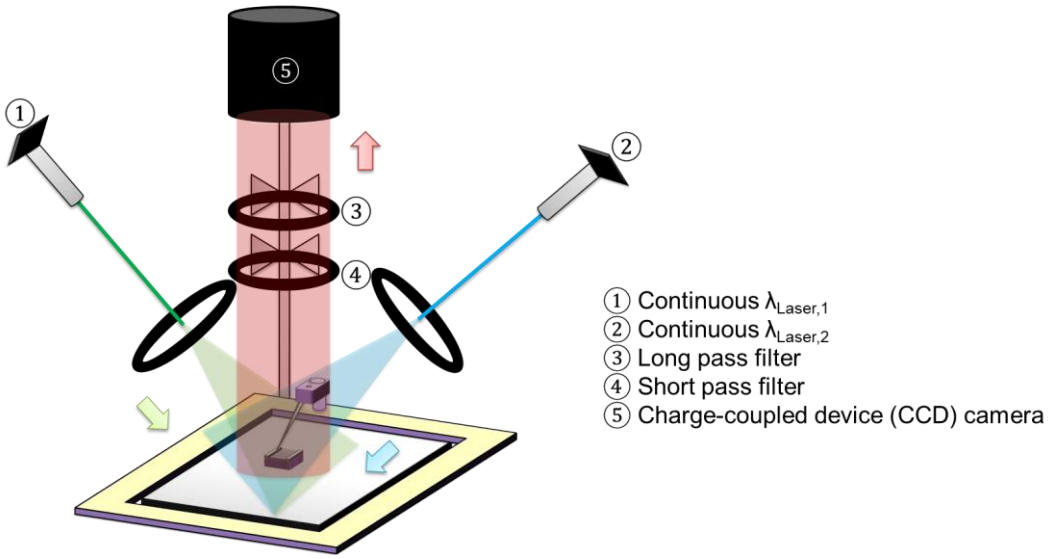

Fig. 7 Schematic illustration of the EL/PL setup used for luminescence mapping of InGaP/GaAs/Ge 3JSC.

5.3.4. Data analysis

5.3.4.1. From EQE measurements

To quantify the change in J_{SC} based on EQE measurements, the percent difference, $\%J_{SC,diff}$, between J_{SC} before ALD, J_{SC1}, and after ALD, J_{SC2}, was calculated using

$$\%J_{SC,diff} = \frac{J_{SC2} - J_{SC1}}{J_{SC1}} \times 100\% \tag{2}$$

Here, positive or negative $\%V_{OC,diff}$ indicates improvement or degradation, respectively. Additionally, and in the same manner, the absolute difference between the V_{OC} before ALD, V_{OC1}, and after ALD, V_{OC2}, was also obtained to quantify its change after ALD. It was calculated using

$$\%V_{OC,diff} = \frac{V_{OC2} - V_{OC1}}{V_{OC1}} \times 100\% \tag{3}$$

5.3.4.2. LBIC measurements analysis

From the LBIC measurements, the normalized standard deviation of the current collection, $\sigma_x/J_{x,max}$, given as

$$\sigma_x/J_{x,max} = \frac{\sqrt{\frac{1}{N-1}\Sigma_{l=1}^{N}|J_l - \bar{J}|^2}}{J_{x,max}} \tag{4}$$

was calculated to quantify the spatial uniformity of current production by inducing LC effect [171,217] or by direct single wavelength excitation upon a current-limiting cell of

the reference sample and Samples A and B. In this equation, the subscript x may either refer to direct subcell (x: DS) or to LC effect (x: LC) excitation, N is the total number of points in an LBIC map, J_l is the current collected at spot, l, $\bar{J}$ is the average GaAs middle cell current obtained at all points in the map, and $J_{x,max}$ is the largest current collection at a spot in GaAs. While a more common method is to calculate σ_x only, this was normalized with $J_{x,max}$. This is to eliminate the possible differences in carrier collection efficiency among the samples and yield a fair comparison of their current production homogeneity. A lower value of $\sigma_x/J_{x,max}$ means better current distribution uniformity.

To compare the reference and the samples subjected to Al_2O_3 sidewall passivation, the percent difference of average current collection based on LBIC measurement results in samples that have Al_2O_3 layer on the sidewalls with respect to the reference sample, $\%\Delta J_{x,ave}$ was calculated using the relation

$$\%\Delta J_{x,ave} = \frac{J_{x,ave(AO)} - J_{x,ave(ref)}}{J_{x,ave(ref)}} \times 100\%. \quad (5)$$

This quantifies the difference in the current generation without Al_2O_3 ($J_{x,ave(ref)}$) and with Al_2O_3 ($J_{x,ave(AO)}$) on the MJSC sidewalls. Here, positive $\%\Delta J_{x,ave}$ indicates current collection increase while negative $\%\Delta J_{x,ave}$ denotes decrease with respect to the reference sample. Furthermore, the percent difference of normalized standard deviation of the current collection in samples that have Al_2O_3 layer on the sidewalls with respect to the reference sample, $\%\Delta\sigma_x/J_{x,max}$ was calculated using the relation

$$\%\Delta\sigma_x/J_{x,max} = \frac{\sigma_x/J_{x,max(AO)} - \sigma_x/J_{x,max(ref)}}{\sigma_x/J_{x,max(ref)}} \times 100\% \quad (6)$$

to quantify the change in current production uniformity without Al_2O_3 ($\sigma_x/J_{x,max(ref)}$) and with Al_2O_3 ($\sigma_x/J_{x,max(AO)}$) on the MJSC sidewalls. Negative $\%\Delta\sigma_x/J_{x,max}$ is interpreted as current production uniformity improvement while positive $\%\Delta\sigma_x/J_{x,max}$ means uniformity degradation.

5.3.4.3. EL/PL measurements analysis

In a similar way of analysis done with LBIC measurements, the standard deviation normalized with the average luminescence value, $\sigma_i/\phi_{i,ave}$, and the percent difference of normalized standard deviation of luminescence in samples with Al_2O_3 sidewall passivation layer, $\sigma_i/\phi_{i,ave(AO)}$, with respect to that of the reference sample, $\sigma_i/\phi_{i,ave(ref)}$, was calculated. The reason behind normalization with $\phi_{i,ave}$ is also to eliminate the possible differences in carrier collection efficiency among the samples and yield a fair comparison of their luminescence homogeneity. $\sigma_i/\phi_{i,ave}$ is given by the following relation:

$$\sigma_i/\phi_{i,ave} = \frac{\sqrt{\frac{1}{N-1}\sum_{l=1}^{N}\left|\phi_l - \phi_{i,ave}\right|^2}}{\phi_{i,ave}} \quad (7)$$

where the subscript i refers to the subcell from where the emission is being measured, N is the total number of points in an EL/PL map, ϕ_l is the emission captured at spot, l, and

$\phi_{i,ave}$ is the average EL/PL emission obtained at all points in the map, and that lower value of $\sigma_i/\phi_{i,ave}$ means better current distribution uniformity. Meanwhile, $\%\Delta\sigma_i/\phi_{i,ave}$ is given as

$$\%\Delta\ \sigma_i/\phi_{i,ave} = \frac{\sigma_i/\phi_{i,ave(AO)} - \sigma_i/\phi_{i,ave(ref)}}{\sigma_i/\phi_{i,ave(ref)}} \times 100\%, \tag{8}$$

in which a negative $\%\Delta\sigma_i/\phi_{i,ave}$ value is interpreted as luminescence uniformity improvement while a positive $\%\Delta\sigma_i/\phi_{i,ave}$ value means uniformity degradation.

5.3.4.4. Two-dimensional (2D) Monte Carlo ray-tracing analysis

From the 2D Monte Carlo ray tracing, one can extract the total photon escape probabilities. As discussed in Appendix C, there are 2 possible scenarios: the inbound case, in which the photon escape happens after external light absorption, and the outbound case, wherein photon escape happens after internal radiative emission. The inbound total photon escape probability, $P_{Tesc,in}$, and the outbound total photon escape probability, $P_{Tesc,out}$, can be calculated using

$$P_{Tesc,in} = \int_{\lambda=300\ nm}^{\lambda_{E_g}} P_{esc}(\lambda)d\lambda \tag{9}$$

and

$$P_{Tesc,out} = \int_{\lambda=300\ nm}^{\lambda_{E_g}} P_{esc}(\lambda) + T(\lambda)d\lambda \tag{10}$$

where $P_{esc}(\lambda)$ is the photon escape probability and $T(\lambda)$ is the transmission at each wavelength, λ. More details can be found at Sec. C.2 of Appendix C.

5.4. Results and Discussions

5.4.1. Main results from the electrical and optical simulation

5.4.1.1. 3D distributed SPICE model simulation and 2D Monte Carlo ray tracing results

SPICE simulation results considering the LC effect between GaAs as the HBG subcell and Ge as the LBG subcell show that the LC current distribution nonuniformity can be significant under the following conditions: (a) when the nonradiative recombination saturation current of the HBG subcell is small, in the order of 10^{-9} mA/cm^2 or lower [Fig. 8(a)]. This is because less nonradiative recombination events allow a higher number of radiative recombination events, which then leads to stronger, less uniform LC effect [141,170]; and (b) when R_{lat} is sufficiently large [Fig. 8(b)], in the order of 1.0 Ω/□, as it represents the lateral transport efficiency of carriers. This becomes more prominent when the operating voltage of the emitting subcell approaches V_{OC}, that is, at high carrier injection voltage regime. Between the parameters varied, the effect of R_{lat} was found to be more significant over length. As shown in Fig. 8(b), the current variation at low R_{lat} was found to be less drastic than that at high R_{lat}, signifying more uniform voltage

distribution at low R_{lat}. This may be attributed to a more uniform distribution of excess carriers.

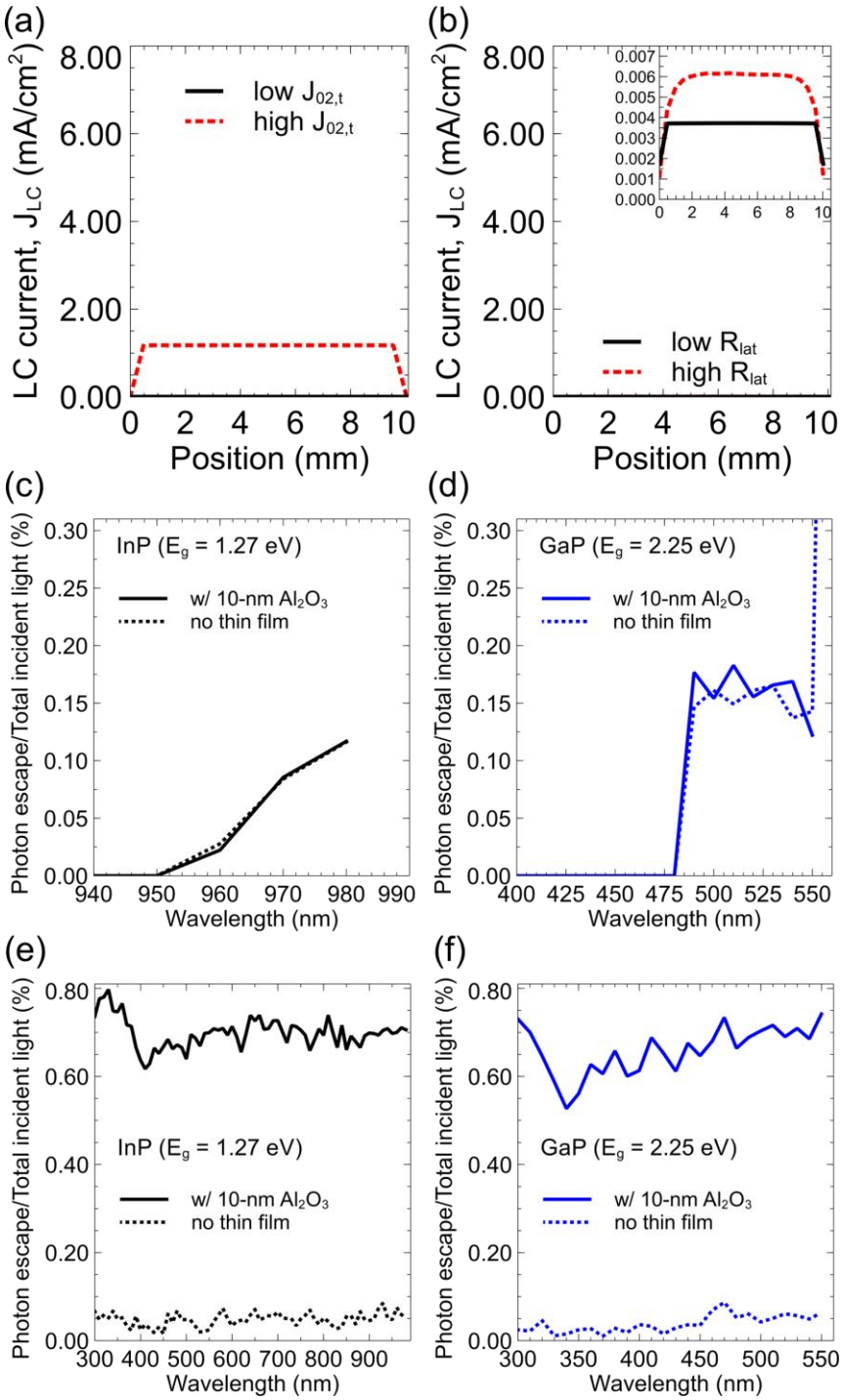

Fig. 8 3D distributed SPICE simulation of GaAs LC current having (a) InGaP top cell nonradiative recombination diode coefficient, $J_{02,t}$, varied from 1×10^{-15} (low) to 1×10^{-3} mA/cm^2 (high) and (b) lateral resistance, R_{lat}, varied from 1×10^{-3} (low) to 1.0 Ω/□ (high). Wavelength-resolved inbound photon escape probabilities of bare (dotted lines) and Al_2O_3-coated (solid lines) (c) InP and (d) GaP solar cell absorbers surrounded by air and having a cell width of 1 mm. Wavelength-resolved outbound photon escape

probabilities of bare (dotted lines) and Al_2O_3-coated (solid lines) (e) InP and (f) GaP solar cell absorbers surrounded by air.

Figures 8(c) and (d) show the inbound photon escape probability, $P_{Tesc,in}$, of InP and GaP solar cell absorbers, respectively, with and without Al_2O_3 thin film coating and having a cell width of 1 mm plotted against incident inbound photon wavelength. No notable difference in $P_{Tesc,in}$ between bare and that with 10-nm Al_2O_3 passivation layer could be observed. Therefore, no issue would be anticipated for adding an Al_2O_3 passivation layer on the front surface of the cell absorber. Then, $P_{Tesc,in}$ values were calculated using eq. (9) and are summarized in Table 4. In adding an Al_2O_3 layer, GaP yielded slightly higher $P_{Tesc,in}$ as compared with the one without it, while InP yielded less $P_{Tesc,in}$ than without it. However, it should be noted that the Al_2O_3 thickness may not yet be the optimum thickness; hence, it may be possible to reduce photon escape further through adding this passivation layer if optimum thickness becomes known. This is also considering that Al_2O_3 has a smaller refractive index (about 1.68 [259]) and is a wide bandgap material (6.4 eV, as reported in [260]).

The wavelength-resolved outbound photon escape probabilities, $P_{Tesc,out}$, for InP and GaP are shown in Figs. 8(e) to (f), respectively. For both materials, it can be seen that for photon emission originating within the solar cell absorber, photon escape is drastically higher for those with a 10-nm Al_2O_3 passivation layer as compared to those having no thin-film layer. To confirm these in numbers, $P_{Tesc,out}$ values were calculated using eq. (10) and are listed in Table 4. There is more than 10 times increase in $P_{Tesc,out}$ for Al_2O_3-coated absorbers than that of the bare, uncoated absorbers. This can be attributed to the refractive indices of the thin film layers being larger than that of air as a surrounding medium to the absorbers. In this sense then, adding thin film layers may aggravate the inhomogeneity of the LC effect, having more photon escape towards the cell edges. Hence, in the optical perspective, adding an Al_2O_3 passivation layer on a III-V material may not be favorable in homogenizing the LC effect.

Table 4 Integrated inbound and outbound photon escape probabilities, $P_{Tesc,in}$ and $P_{Tesc,out}$, of InP and GaP solar cell absorbers with and without Al_2O_3 layer. These structures are surrounded by air.

Semiconductor absorber material	$P_{Tesc,in}$ (%)		$P_{Tesc,out}$ (%)	
	No thin film	10-nm Al_2O_3	No thin film	10-nm Al_2O_3
Indium Phosphide, InP (E_g = 1.27 eV)	0.23	0.22	3.30	48.21
Gallium Phosphide, GaP (E_g = 2.25 eV)	1.06	1.13	1.00	17.15

5.4.1.2. Optical simulations by TMM

5.4.1.2.1. InGaP/GaAs tandem stack with ARC and back contact having finite thicknesses

To determine the optical effect of depositing Al_2O_3 on the front surface of commercial InGaP/GaAs/Ge 3JSCs, optical simulation of InGaP/GaAs tandem structure with (1) silver (Ag) back contact, (2) silicon nitride (SiN_x) anti-reflection coating, and (3) with and without Al_2O_3 was done by transfer matrix method. The simulated structure without and with the Al_2O_3 layer and their corresponding layer thicknesses are shown in Figs. 21(a) and (b), Sec. 5.6, respectively. Since no charges can be generated on Al_2O_3 and

SiN_x layers, no electrical influence on the front 3JSC surface was expected. Hence, only an optical simulation was done between these layers.

The calculated total and each layer absorption without and with 10-nm Al_2O_3 on InGaP/GaAs tandem absorbers are shown in Fig. 21(c), Sec. 5.6. Calculations show that there is an increase in InGaP and GaAs absorption at wavelengths from about 310 to 440 nm and 840 to 900 nm, respectively, with Al_2O_3 sidewall passivation. On the other hand, InGaP and GaAs absorptions at wavelengths from about 440 to 670 nm and 670 to 840 nm, respectively, decreased. Since with the Al_2O_3 layer, the absorption change in each subcell could have compensated between shorter and longer wavelength ranges, deposition on some portions of the front cell surface may have minimal impact on the optical performance of the 3JSC samples.

5.4.1.2.2. Optical spectra of a semi-infinite InGaP with and without thin films

Optical TMM simulation was also done when having a semi-infinite thick InGaP without thin films, with Al_2O_3 only, with SiN_x as an anti-reflection coating only, and with both Al_2O_3 and SiN_x layers. The resultant optical spectra are shown in Figs. 22(a) to (c), Sec. 5.6. In Figs. 22(a) and (b), the reflection reduced, while the absorption increased with the SiN_x layer on InGaP. Additionally, less absorption while larger reflection can be observed at 500- to 650-nm range. This agrees with the $P_{Tesc,out}$ calculated from InP and GaP, as shown in Figs. 8(e) and (f) and as summarized in Table 4. Here, larger $P_{Tesc,out}$ was obtained for the structure with the Al_2O_3 layer than without it. Meanwhile, the spectra are red-shifted when there is an Al_2O_3 layer on SiN_x at wavelengths between 300 and 400 nm. As for Fig. 22(c), a larger transmission was attained from the band edge of InGaP with SiN_x. However, no change was observed with the Al_2O_3 layer addition. Hence, no unabsorbed light in the InGaP top cell coming into the front surfaces of the subsequent LBG subcells could be expected when the Al_2O_3 layer is added on top of an anti-reflection layer such as SiN_x.

5.4.2. EQE measurements

5.4.2.1. Samples with various Al_2O_3 coverages on the front InGaP/GaAs/Ge 3JSC surface[7]

Subcell EQE measurements of Samples X, Y, and Z, having 0.5-mm from the perimeter, 1-mm from the perimeter, and full Al_2O_3 coverage on the front InGaP/GaAs/Ge 3JSC surfaces, respectively, are shown in Fig. 23, Sec. 5.6, together with J_{SC} and V_{OC} summary tables. No significant change after ALD was observed from EQE and J_{SC} of InGaP top cell, regardless of Al_2O_3 size coverage. On the other hand, GaAs and Ge EQE and J_{SC} improved up to 3.00% and 24.90% with increasing Al_2O_3 coverage, respectively. These suggest that both subcells got electrically passivated upon the addition of the Al_2O_3 layer. Since GaAs had consistent improvement for any Al_2O_3 layout and being occasionally the current-limiting cell under terrestrial applications [257], it can be inferred that Al_2O_3 passivation can help improve current matching in InGaP/GaAs/Ge 3JSCs non-invasively. As for V_{OC}, only Samples X and Z got a 20 mV increase. This implies that the Sample Y layout may be the least optimum if higher V_{OC} is desired.

In Fig. 23(a), it can be noticed that there is an EQE drop in Ge between 950 and 1050 nm with Al_2O_3 layer partially deposited on the 3JSC surface of Sample X. While the

[7] Measurements discussed in this subsection were acquired in Solar Power Laboratory, ASU.

origin is unconfirmed, it was speculated to be due to the filter change at a certain wavelength between 950 and 1050 nm. Meanwhile, the Ge EQE of Sample Z was very low as compared with other samples, suggesting that it is severely shunted. This could be due to Ge wafer growth inhomogeneity. Nevertheless, this does not affect the results since the J_{SC} and V_{OC} comparison was done for the same sample before and after Al_2O_3 deposition.

5.4.2.2. Parallel measurements with LBIC mapping[8]

In this section, the EQE measurements were acquired using the same single-wavelength LEDs used in LBIC mapping. These were obtained after Al_2O_3 passivation. Figure 9 shows the EQE measurements of the reference sample (dotted lines), Sample A and Sample B. Compared with the reference sample (no Al_2O_3), both Samples A and B (with Al_2O_3) yielded larger subcell EQE. This is further confirmed by current density calculations obtained using eq. (1) and summarized in Table 5. Hence, these results demonstrated that Al_2O_3 passivation improved current collection in InGaP/GaAs/Ge 3JSCs.

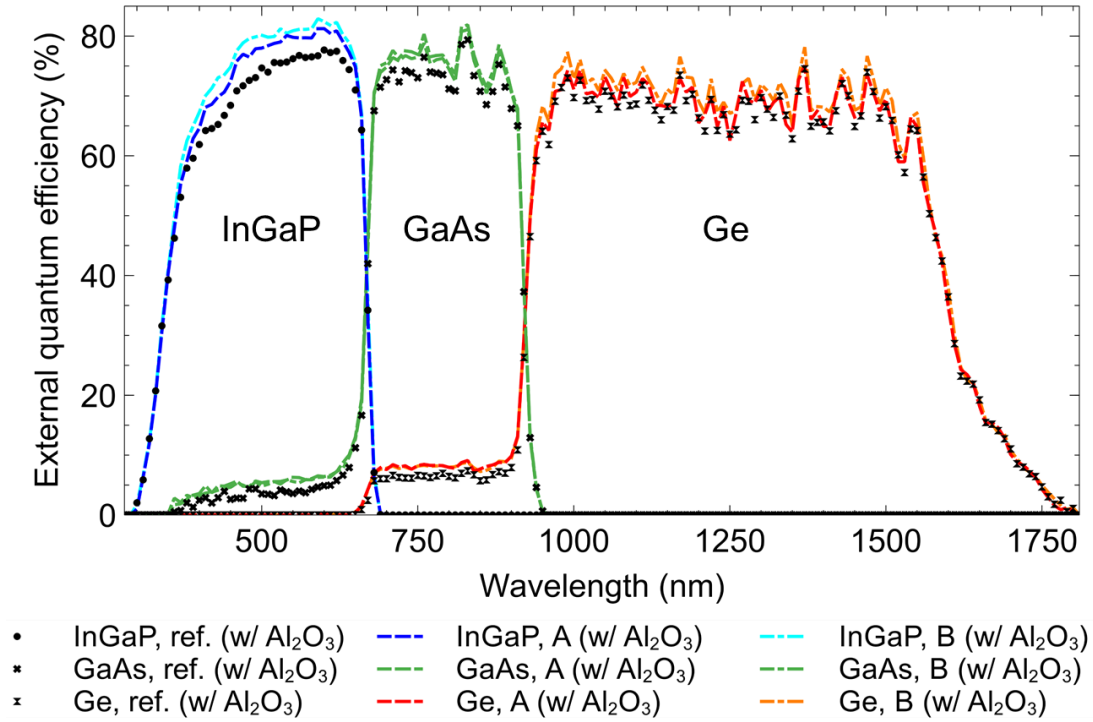

Fig. 9 Subcell EQE measurements acquired from the reference sample (symbols), Sample A with Al_2O_3 (dashed lines), and Sample B with Al_2O_3 passivation (dash-dotted lines).

Table 5 Summary of current density, $J_{AM1.5G,i}$, derived from EQE measurements using eq. (1).

Sample	$J_{AM1.5G,i}(V)$ (mA/cm^2)		
	InGaP	GaAs	Ge
Reference	13.1	12.9	15.9
A	13.7	13.7	16.4
B	14.0	13.8	16.8

[8] These measurements were acquired in The University of Tokyo after Al2O3 deposition in ASU NanoFab, Arizona, USA.

5.4.3. LBIC measurements with and without sidewall passivation[9]

The current generation in GaAs middle cell by LC effect and by direct external light excitation was assessed before and after Al_2O_3 deposition. For the regression check, the current generation in the InGaP top cell was briefly discussed before and after Al_2O_3 deposition.

5.4.3.1. GaAs LC current mapping

To investigate the effect of Al_2O_3 sidewall passivation to the current generation induced by LC effect from the InGaP top cells to the limiting GaAs middle cells of InGaP/GaAs/Ge 3JSC samples, LBIC maps were acquired using the setup illustrated in Fig. 6(a). Figures 10(a) to (c) show the LC current collection in GaAs of the reference (unpassivated) sample, Sample A, and Sample B, respectively. Before passivation, less average current collection, $J_{LC,ave}$, was obtained from Samples A and B, as listed in Table 10, Sec. 5.6. While Sample A had a comparable LC current uniformity with the reference sample, Sample B uniformity before Al_2O_3 deposition was 3.5% better than the reference sample. On the other hand, Figs. 10(d) to (f) show the LC current collection in GaAs of the samples after subjecting A and B to Al_2O_3 deposition. It can be seen that there is a current magnitude difference between the measurement sets before [Figs. 10(a) to (c)] and after ALD [Figs. 10(d) to (f)]. This may be attributed to the change in the 450-nm laser power setting that was done within the period before and after Al_2O_3 deposition. With this, the sets before and after ALD cannot be directly compared. Hence, the percent differences were calculated based on the reference sample. Additionally, this justifies the need to normalize the standard deviations of the current collection with the maximum current collected from a certain spot of the active region of the cell. Comparing Fig. 10(d) with (e) and (f), samples with the Al_2O_3 layer on the sidewalls yielded a larger LC current collection than the reference sample.

Table 6 GaAs LC effect excitation current collection and homogeneity difference between reference InGaP/GaAs/Ge 3JSC sample and samples with Al_2O_3 sidewall passivation layer (A and B).

Sample	**GaAs LC excitation (after ALD)**			
	Average current density, $J_{LC,ave}$ (mA/cm^2)	$J_{LC,ave}$ percent difference (%)	Normalized SD, $\sigma_{LC}/J_{LC,max}$ (ratio)	$\sigma_{LC}/J_{LC,max}$ percent difference (%)
Reference (no Al_2O_3)	0.25	0	1.11×10^{-1}	0
Sample A (w/ Al_2O_3)	0.30	21.9	1.03×10^{-1}	-7.2
Sample B (w/ Al_2O_3)	0.29	14.6	1.04×10^{-1}	-6.7

Using eq. (4), the normalized standard deviation of LC current collection of each sample, $\sigma_{LC}/J_{LC,max}$, was calculated to quantify the change in LC current uniformity. This was derived from the average of 5 LBIC measurement trials. As listed in Table 6, $\sigma_{LC}/J_{LC,max}$ values of Samples A and B were 7.2% and 6.7% less than that of the reference sample, respectively, as computed using eq. (6). Therefore, Al_2O_3 sidewall passivation enhanced the LC current homogeneity, suggesting that perimeter recombination is one of the physical phenomena causing the nonuniform LC effect. Moreover, Samples A and B

[9] In these measurements, as ALD was conducted in ASU, before Al_2O_3 deposition means that the LBIC measurements were acquired prior to traveling to Arizona, USA while after Al_2O_3 deposition means that the measurements were acquired after traveling from Arizona.

with a thin Al_2O_3 layer on the sidewalls resulted in an average LC current increase of 21.9% and 14.6%, respectively, as calculated using eq. (5). This observed increase further suggests that the perimeter recombination in processed MJSCs was reduced after sidewall passivation.

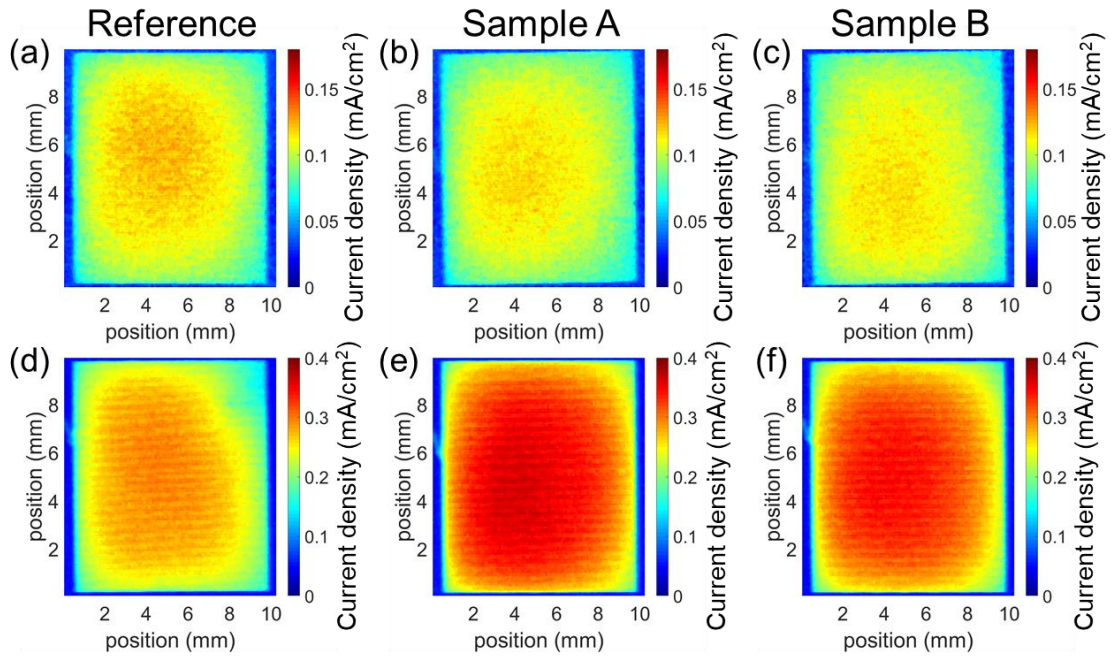

Fig. 10 Spatially-resolved current collection acquired by GaAs LC effect excitation of InGaP/GaAs/Ge 3JSC (a) reference sample, (b) Sample A before Al_2O_3 deposition, and (c) Sample B before Al_2O_3 deposition using a modulated 785-nm laser. Spatially-resolved current collection acquired by GaAs LC effect excitation of InGaP/GaAs/Ge 3JSC (d) reference sample without Al_2O_3, (e) Sample A with Al_2O_3, and (f) Sample B with Al_2O_3 using a modulated 785-nm laser.

5.4.3.2. Direct GaAs middle cell current mapping

To study the effect of Al_2O_3 sidewall passivation to the current production by direct GaAs excitation, LBIC maps were acquired using the setup illustrated in Fig. 6(b). Figures 11(a) to (c) show the current collection when the GaAs middle cells of the reference sample, Sample A and Sample B were directly excited by a modulated 785-nm laser, respectively, before Al_2O_3 deposition. Before ALD, all samples qualitatively had the same amount of current collection. In numbers though, Samples A and B had 3.38% less current collection and were more than 30% less uniform than the reference sample, as summarized in Table 11, Sec. 5.6. However, as mentioned in Sec. 5.4.3.1., this set cannot be fairly compared with the set of measurements obtained after ALD. Hence, the same approach of comparison was done in this part, that is, comparing samples with and without Al_2O_3 from the same wafer.

Figures 11(d) to (f) show the current collection in the GaAs middle cell of the reference sample, Sample A with Al_2O_3 layer, and Sample B with Al_2O_3 layer acquired by 785-nm laser excitation. By visual inspection, Samples A and B had a higher current collection in GaAs than the reference sample while maintaining homogeneity. To confirm this numerically, the normalized standard deviation of current collection by direct GaAs excitation of each sample, $\sigma_{DS}/J_{DS,max}$, was calculated using eq. (4). This was obtained from the average of 5 trials of LBIC measurements to account for the experimental

variation. Comparing with the reference sample using eq. (6), the current collection homogeneity in GaAs middle cell of Samples A and B increased by 13.2% and 23.1%, respectively. However, as these values are relative and $\sigma_{DS}/J_{DS,max}$ values obtained were in the hundredth order of magnitude, a portion of these percentages may be attributed to the measurement noise. Nevertheless, as calculated using eq. (5), Samples A and B with a thin Al_2O_3 layer on the sidewalls resulted in average GaAs current increase of 16.3% and 15.1%, respectively. These results agree with the inferences made from GaAs LC current production earlier, that the perimeter recombination was reduced after Al_2O_3 sidewall passivation. Calculated values after ALD are summarized in Table 7.

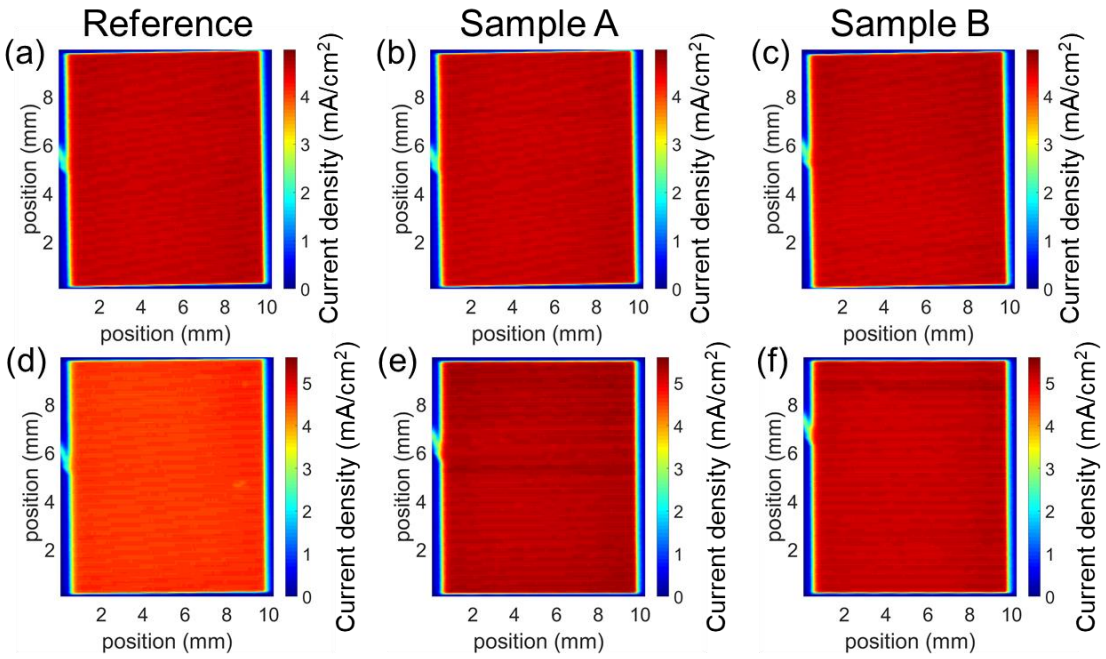

Fig. 11 Spatially-resolved current collection acquired in GaAs middle cell of InGaP/GaAs/Ge 3JSC (a) reference sample, (b) Sample A before Al_2O_3 deposition, and (c) Sample B before Al_2O_3 deposition using a modulated 785-nm laser. Spatially-resolved current collection acquired in GaAs middle cell of InGaP/GaAs/Ge 3JSC (d) reference sample without Al_2O_3, (e) Sample A with Al_2O_3, and (f) Sample B with Al_2O_3 using a modulated 785-nm laser.

Table 7 Direct GaAs excitation current collection and homogeneity difference between reference InGaP/GaAs/Ge 3JSC sample and samples with Al_2O_3 sidewall passivation layer (A and B).

Sample	**Direct GaAs excitation (after ALD)**			
	Average current density, $J_{DS,ave}$ (mA/cm^2)	$J_{DS,ave}$ percent difference (%)	Normalized SD, $\sigma_{DS}/J_{DS,max}$ (ratio)	$\sigma_{DS}/J_{DS,max}$ percent difference (%)
Reference (no Al_2O_3)	4.48	0	1.86×10^{-2}	0
Sample A (w/ Al_2O_3)	5.21	16.3	1.61×10^{-2}	-13.2
Sample B (w/ Al_2O_3)	5.15	15.1	1.43×10^{-2}	-23.1

5.4.3.3. Direct InGaP top cell current mapping

To determine if Al_2O_3 sidewall passivation affected the current production in the InGaP top cell, LBIC maps were acquired by direct InGaP excitation using a modulated 450-nm laser, as illustrated in Fig. 6(c). Figures 24(a) to (c), Sec. 5.6 show the current

collection when the InGaP top cells of the reference sample before Al_2O_3 deposition, Sample A and Sample B were directly excited by a modulated 450-nm laser, respectively. Here, Samples A and B had a less current collection in InGaP than the reference sample although the current homogeneity seemed to be unchanged. The same trend among the samples was observed after Al_2O_3 deposition, as shown in Figs. 24(d) to (f). Meanwhile, there is a magnitude difference between the two sets of LBIC measurements. Same as discussed earlier on GaAs LC current collection before and after Al_2O_3 deposition, the magnitude difference between the measurement sets before and after ALD may be attributed to the change in the 450-nm laser power setting that was done within the period before and after Al_2O_3 deposition. With this, InGaP current collection sets before and after ALD cannot be directly compared. Therefore, the comparison was also made between the reference and the passivated samples. From these observations, it may be inferred that the Al_2O_3 sidewall deposition did not cause any significant improvement or degradation to the InGaP current collection.

5.4.4. EL/PL measurements with and without sidewall passivation

The EL/PL measurements were acquired to observe the luminescence homogeneity in the emitting HBG subcell and in the LBG subcell where the LC current was collected. These were obtained at forward voltages close to the V_{OC} of the samples, after Al_2O_3 deposition. Figures 12(a) to (d), (e) to (h), and (i) to (l) show the luminescence maps of InGaP of the reference sample, Sample A, and Sample B, normalized with the average InGaP luminescence, $\phi_{T,ave}$, at applied 3JSC terminal voltages of 2.3, 2.5, and 2.7 V, respectively. In these images, it can be seen that the passivated samples, A and B, luminescence are more uniform than that of the reference sample in all voltages. Numerically, this is the case in all voltages at which the luminescence maps were acquired, as plotted in Fig. 13(a). Specifically, the normalized standard deviation, $\sigma_T/\phi_{T,ave}$, at 2.5 V was found to be 14.3% less for Samples A and B than that of the reference sample, as calculated using eq. (8) and are summarized in Table 8. This suggests that the luminescence from InGaP top cell where the LC effect originates towards the current-limiting GaAs middle cell would be more uniform if the Al_2O_3 sidewall passivation layer is added to full 3JSCs.

Table 8 GaAs LC effect excitation luminescence and homogeneity difference between reference InGaP/GaAs/Ge 3JSC sample and samples with Al_2O_3 sidewall passivation layer (A and B) at an applied 3JSC terminal voltage of 2.5 V.

Sample	**InGaP top cell (at 2.5 V)**		**GaAs middle cell (at 2.5 V)**	
	Normalized SD, $\sigma_T/\phi_{T,ave}$ (arbitrary units)	$\sigma_T/\phi_{T,ave}$ percent difference (%)	Normalized SD, $\sigma_M/\phi_{M,ave}$ (arbitrary units)	$\sigma_M/\phi_{M,ave}$ percent difference (%)
Reference (no Al_2O_3)	0.17	0	0.16	0
Sample A (w/ Al_2O_3)	**0.05**	**-70.6**	**0.10**	**-37.5**
Sample B (w/ Al_2O_3)	**0.07**	**-58.8**	**0.12**	**-25.0**

As for the GaAs middle cell emission, shown in Fig. 15, the reference sample luminescence maps [Figs. 14(a) to (d)] had less uniform emission than those of Samples A [Figs. 14(e) to (h)] and B [Figs. 14(i) to (l)]. Having less $\sigma_M/\phi_{M,ave}$ for Samples A and B

than the reference sample at voltages between 2.2 V and 3.2 V were also shown in Fig. 13(b) plot. At 2.5 V, the luminescence uniformities of Samples A and B were found to be 37.5% and 25.0% better than that of the reference sample. These values were calculated using eq. (8) and are also summarized in Table 8. Although Al_2O_3 sidewall passivation may have contributed to this, the improved homogeneity may also be attributed to the difference in the homogeneity of GaAs middle cell quality over space. This was inferred from the spots observed with higher luminescence in the reference sample, most especially at higher applied 3JSC terminal voltages.

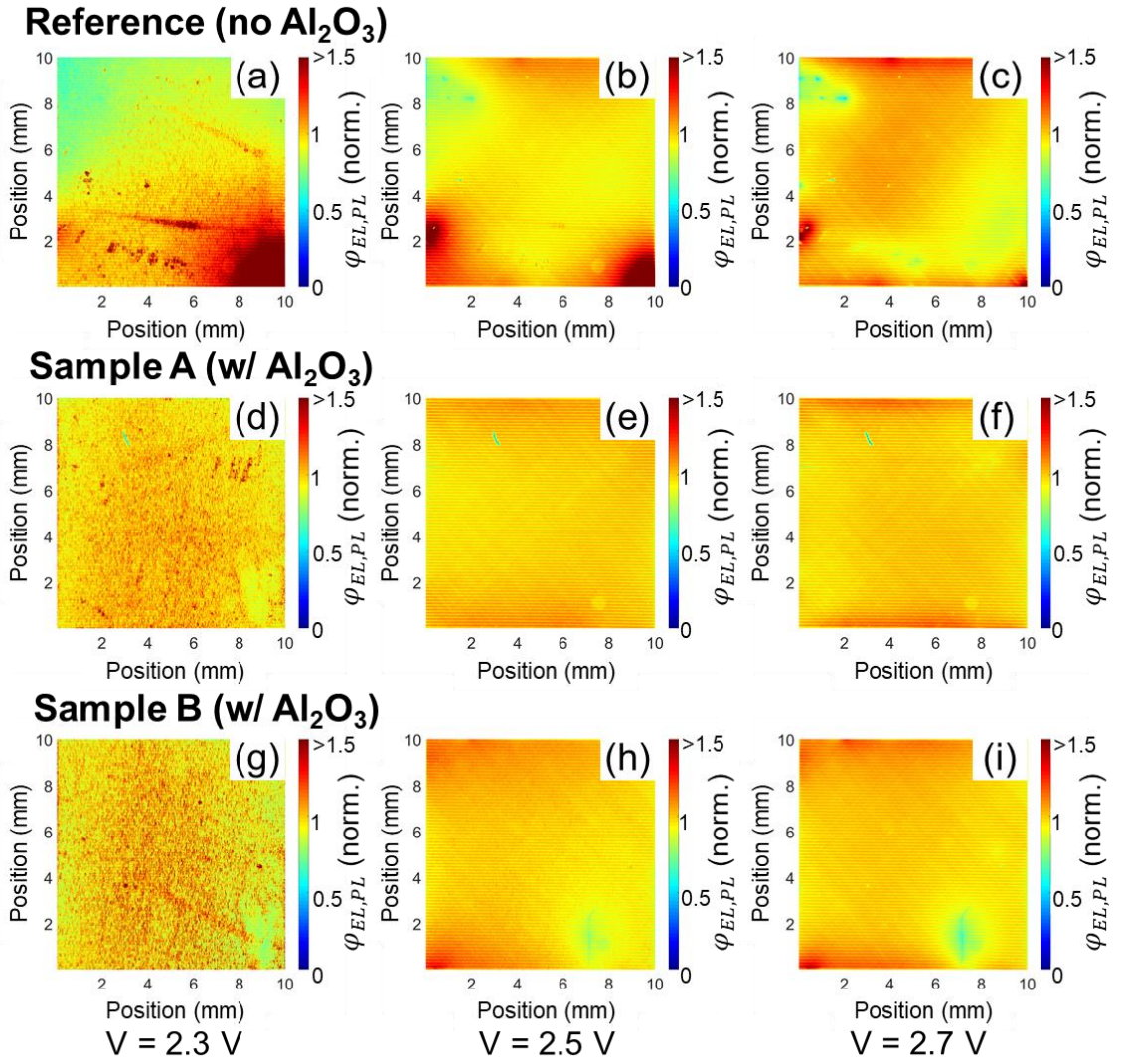

Fig. 12 Spatially-resolved luminescence maps acquired in InGaP top cell of InGaP/GaAs/Ge 3JSC (a)-(c) reference sample, (d)-(f) Sample A with Al_2O_3, and (g)-(i) Sample B with Al_2O_3 under GaAs middle cell current-limiting condition at applied 3JSC terminal voltages of 2.3, 2.5, and 2.7 V, respectively.

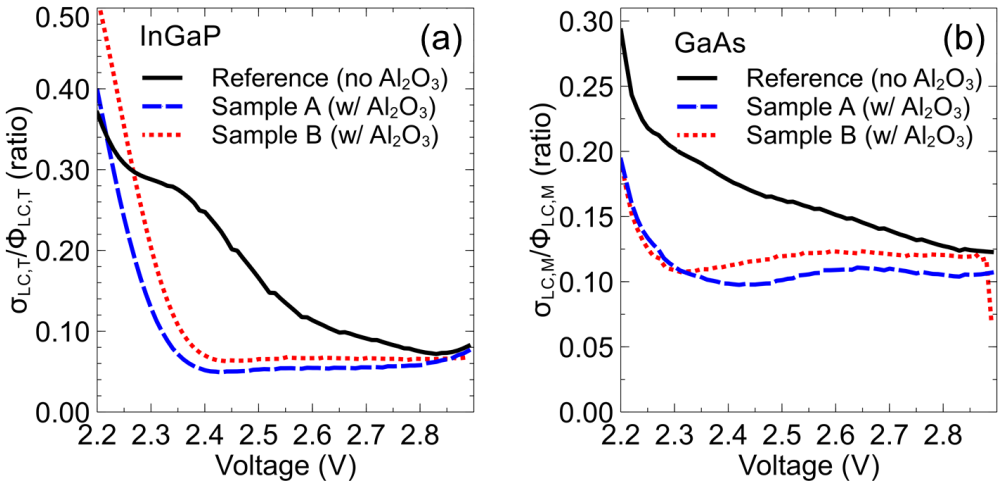

Fig. 13 Normalized standard deviations of luminescence from (a) InGaP top cell and (b) GaAs middle cell of InGaP/GaAs/Ge 3JSC reference sample (solid lines), Sample A with Al_2O_3 (dashed lines), and Sample B with Al_2O_3 (dotted lines) under GaAs middle cell current-limiting case between applied 3JSC voltages of 2.2 V and 2.9 V.

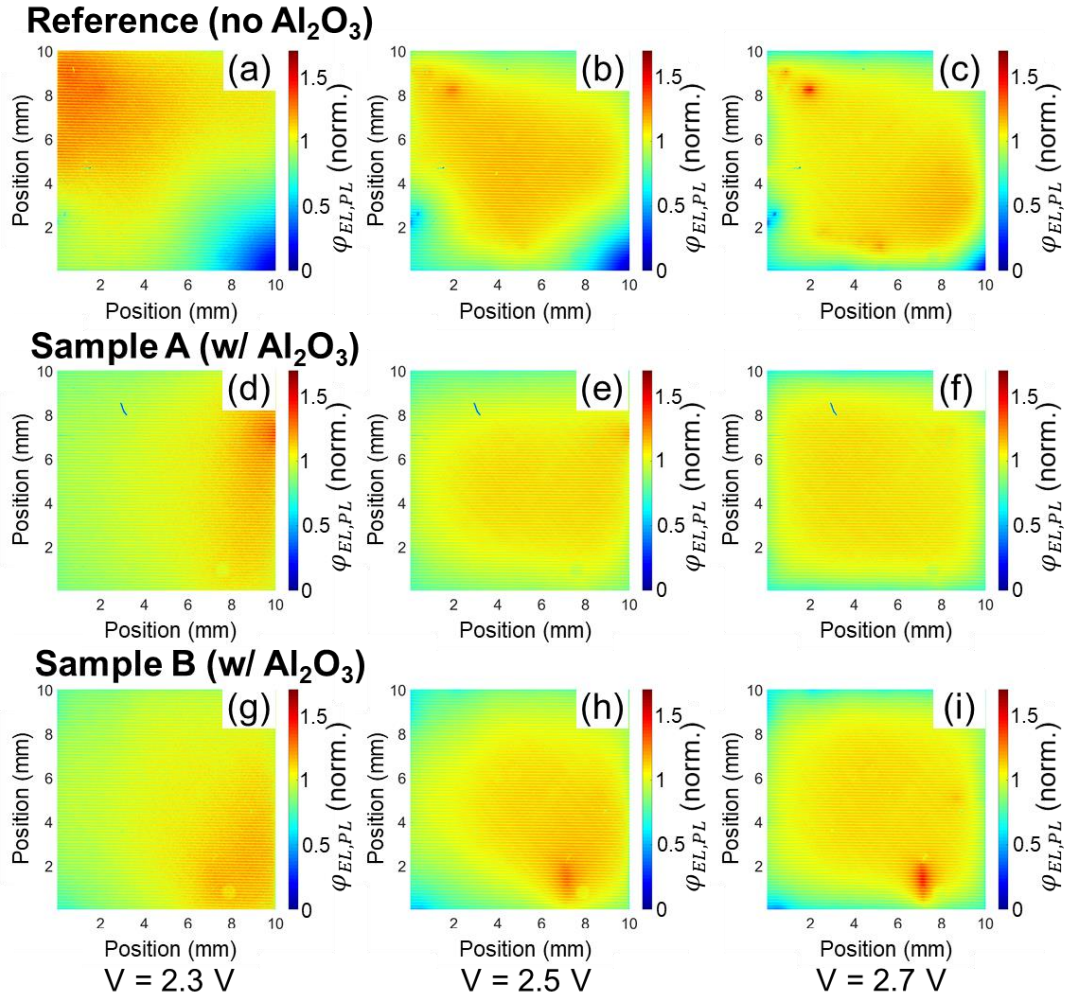

Fig. 14 Spatially-resolved luminescence maps acquired in GaAs middle cell of InGaP/GaAs/Ge 3JSC (a)-(c) reference sample, (d)-(f) Sample A with Al_2O_3, and (g)-(i) Sample B with Al_2O_3 under GaAs middle cell current-limiting condition at applied 3JSC terminal voltages of 2.3, 2.5, and 2.7 V, respectively.

5.4.5. Regression tests by *J-V* characteristics measurement[10]

As the main objective of MJSC sidewall passivation is to homogenize the LC current collection in a current-limiting MJSC subcell, this may have consequences to the electrical performance of the processed samples. To investigate the effect of Al_2O_3 sidewall passivation, *J-V* characteristics measurements under AM 1.5 G spectrum at 1 sun, under extreme current mismatch, and under dark were obtained.

5.4.5.1. Global air mass (AM 1.5G) measurement

Single one-sun AM 1.5G *J-V* curve measurements of all samples being studied were acquired before and after Al_2O_3 sidewall passivation by ALD. Before ALD [Fig. 15(a)], it can be seen that among the samples, the reference sample had the best *J-V* characteristics, as shown by the cross symbols in Fig. 16 box plots for J_{SC} [Fig. 16(a)], *FF* [Fig. 16(c)], and η [Fig. 16(d)], respectively. These agree with the GaAs LC current collection before Al_2O_3 deposition, upon comparing Figs. 10(a) to (c).

It is noticeable as well that Sample A had high series resistance before ALD, as shown by gradual negative slope between applied 3JSC voltages of about 1.8 V to 2.6 V. This could be due to its position in the wafer where it was cut from. The wafer map of the samples is shown in Fig. 25, Sec. 5.6. Here, the reference sample, Sample A, and Sample B were taken from column-row wafer positions 32-10, 28-9, and 29-9, respectively. As position 28-9 is close to the wafer edge, it was more susceptible to produce inactive regions that oppose carrier movement within the solar cell material, thereby leading to higher series resistance [261].

Table 9 Electrical performance summary of reference InGaP/GaAs/Ge 3JSC sample and samples with Al_2O_3 sidewall passivation layer (A and B) at 1-sun AM 1.5G.

Sample	AM 1.5G, 1-sun electrical performance (average, after ALD)			
	J_{SC} (mA/cm^2)	V_{OC} (V)	*FF* (ratio)	η (%)
Reference (no Al_2O_3)	12.08	2.546	0.87	26.76
Sample A (w/ Al_2O_3)	**12.37**	**2.549**	**0.88**	**27.81**
Sample B (w/ Al_2O_3)	**12.52**	**2.547**	**0.88**	**27.94**

The *J-V* measurements acquired under 1-sun, AM 1.5G spectrum after Al_2O_3 sidewall passivation are shown in Fig. 15(b). These measurements were acquired for 5 trials to eliminate equipment precision as an additional factor to consider in interpreting the results. From the measurements, it can be seen that Samples A and B produced larger J_{SC} than the reference one while no apparent difference in V_{OC} among all samples. These observations were put into numbers by the electrical performance box plots calculated from the *J-V* curves after Al_2O_3 sidewall passivation. These are shown in the box plots in Fig. 16. In general, J_{SC} [Fig. 16(a)], V_{OC} [Fig. 16(b)], *FF* [Fig. 16(c)], and η [Fig. 16(d)] values were found to be larger in Samples A and B than in the reference sample. However, it can be noticed that the V_{OC} values of the samples before ALD were higher. This could

[10] In these measurements, as ALD was conducted in ASU, before Al_2O_3 deposition means that the LBIC measurements were acquired prior to traveling to Arizona, USA while after Al_2O_3 deposition means that the measurements were acquired after traveling from Arizona.

be attributed to oxidation when the samples were in transit under ambient air conditions. On one hand, as summarized in Table 9, the calculated η for samples with Al_2O_3 sidewall passivation was more than 1% larger than that of the reference sample. Hence, this further suggests that Al_2O_3 sidewall passivation was effective in reducing perimeter recombination, as complemented by LBIC mapping and EL/PL mapping results discussed earlier.

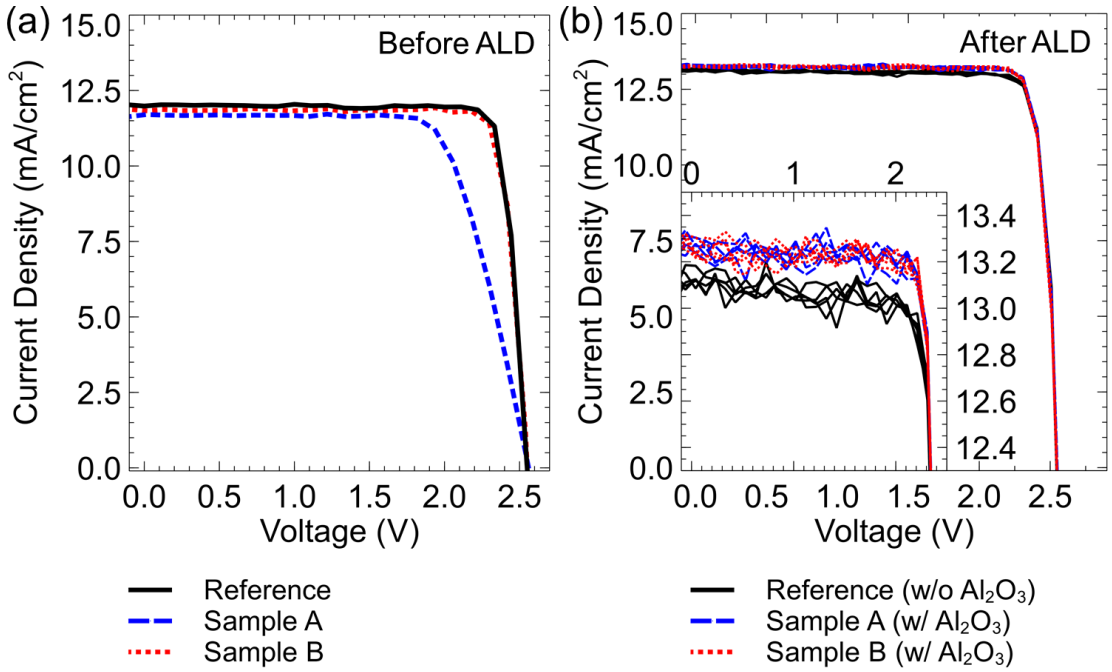

Fig. 15 *J-V* characteristics of the reference sample (solid lines), Sample A with Al_2O_3 (dashed lines), and Sample B with Al_2O_3 (dotted lines) (a) before and (b) after Al_2O_3 sidewall passivation measured at 1 sun, AM 1.5G spectrum. The x- and y- axes of the inset are voltage in V and current densities in mA/cm^2.

5.4.5.2. Investigation of current-limiting subcell cases

As another angle for investigating the possible regression of InGaP/GaAs/Ge 3JSC performance after Al_2O_3 sidewall passivation, the individual subcell DC light *J-V* characteristics were measured using the continuous LED settings listed in Table 1. The *J-V* curves of InGaP, GaAs, and Ge before ALD and after ALD are shown in Figs. 17(a) to (c) and (d) to (f), respectively. Single measurement for the set of *J-V* curves before ALD was taken while 5 measurement trials were acquired after ALD to determine the repeatability of the results and eliminate the experimental error as a factor to consider in interpreting the results.

Comparing the InGaP *J-V* curves before [Fig. 17(a)] and after ALD [Fig. 17(b)], Samples A and B, both with Al_2O_3 sidewall layers, did not have a significant difference with their *J-V* characteristics before ALD. As for the reference sample (solid lines), the low to moderate voltage regime of its *J-V* curve yielded a more negative slope. The negative slope suggests that the reference sample developed more shunt defects during the study. This could also be due to oxidation as the samples were often brought in transit within ambient air conditions.

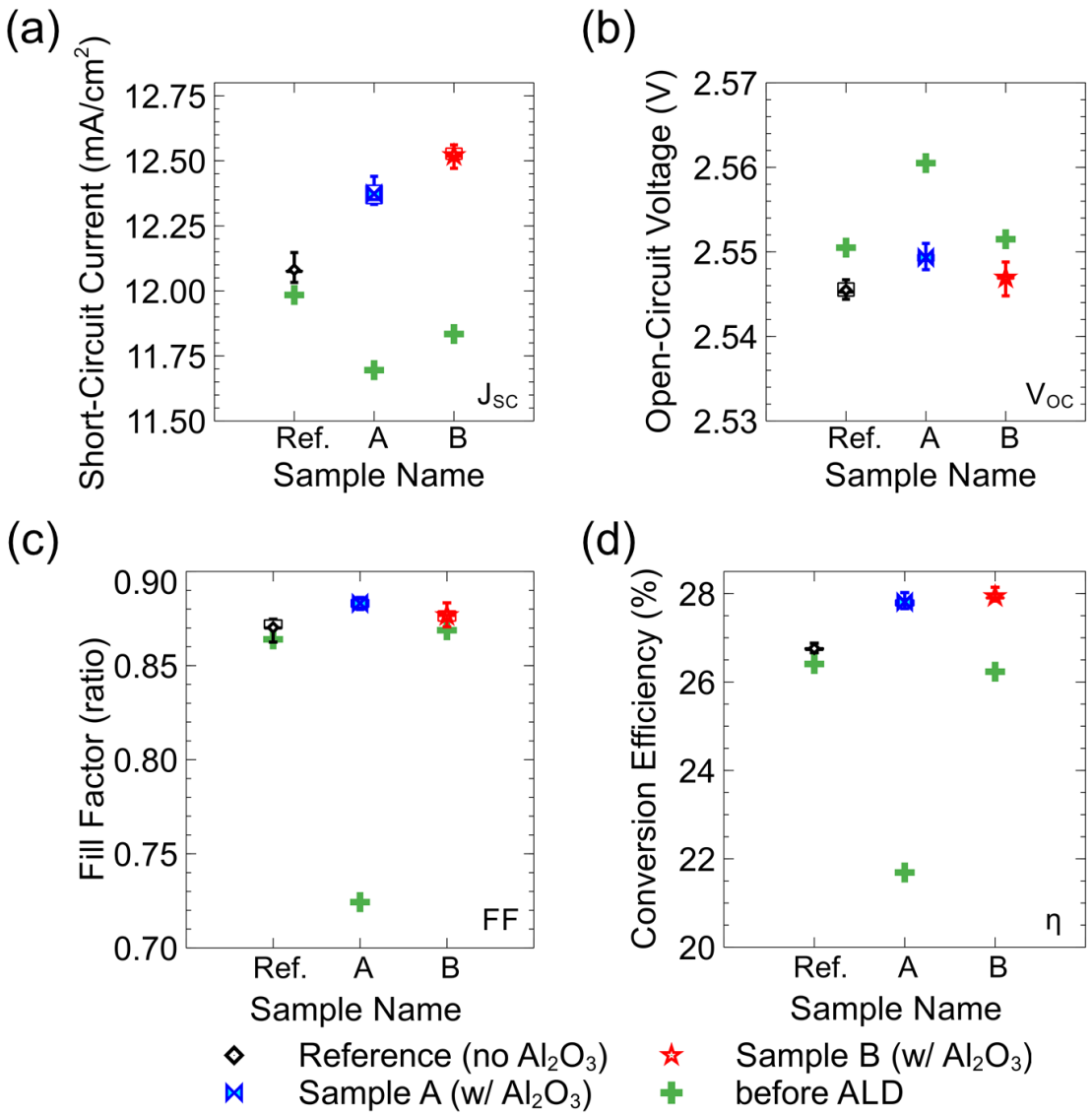

Fig. 16 (a) J_{SC}, (b) V_{OC}, (c) *FF*, and (d) η of the reference InGaP/GaAs/Ge 3JSC sample, Sample A with Al_2O_3, and Sample B with Al_2O_3 before (single measurement, cross symbols) and after Al_2O_3 sidewall passivation (5 trials, box plots) derived from 1 sun, AM 1.5G spectrum measurements.

As for GaAs *J-V* characteristics before ALD [Fig. 17(b)], which includes the LC current production induced by the adjacent InGaP top cell, no significant difference among the *J-V* curves of all samples can be observed. After ALD [Fig. 17(e)] however, it can be seen that there is an increase in current production in Samples A and B, while no change was observed from the reference sample. Hence, this further confirms that the GaAs middle cell performance was improved by Al_2O_3 passivation, as observed from the direct GaAs LBIC mapping of Samples A and B, shown in Figs. 11(e) and (f), respectively.

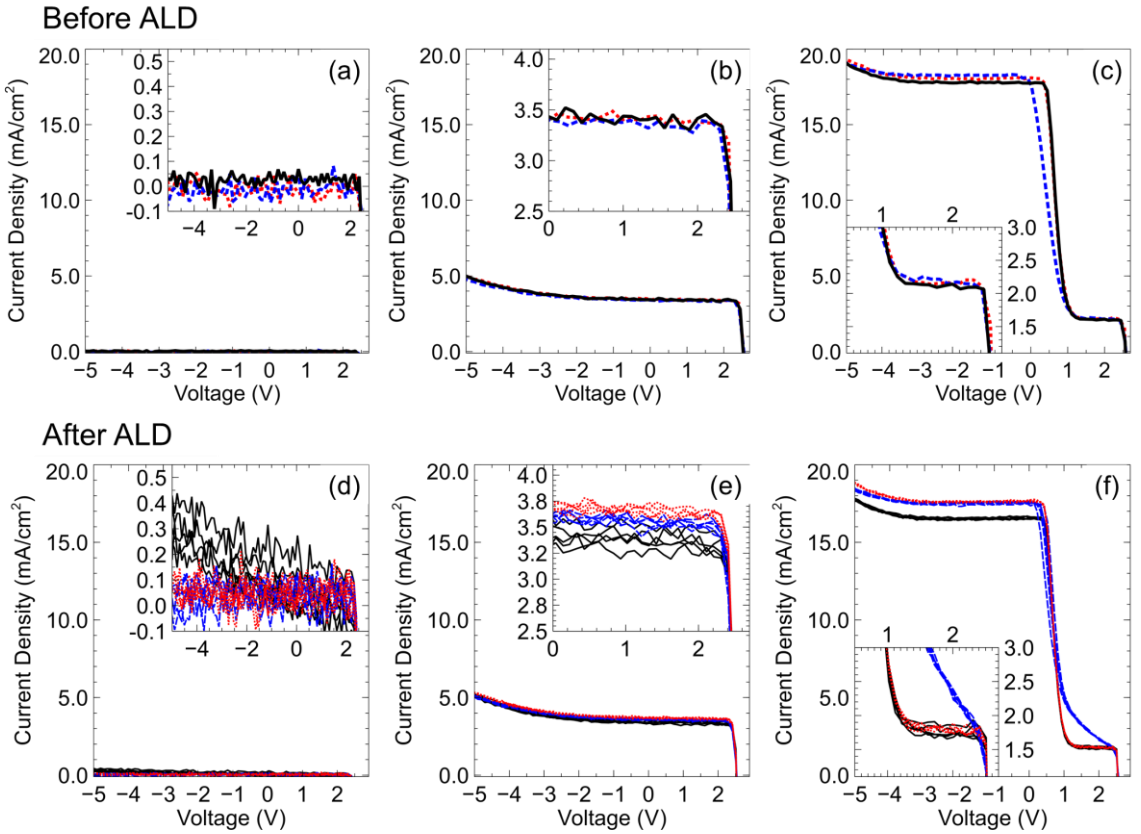

Fig. 17 *J-V* characteristics of (a), (d) InGaP top cell, (b), (e) GaAs middle cell, and (c), (f) Ge bottom cell before (single measurement) and after Al_2O_3 sidewall passivation (5 measurement trials) of the reference InGaP/GaAs/Ge 3JSC sample (solid lines), Sample A with Al_2O_3 (dashed lines), and Sample B with Al_2O_3 (dotted lines) measured at 1 sun, AM 1.5G spectrum, respectively. The *x*- and *y*- axes of the insets for all plots are voltages in V and current densities in mA/cm^2.

Finally, no significant difference was found between the *J-V* curves of Ge bottom cell (at $V > 0.5$ V) of the reference sample and Sample B before and after ALD [Figs. 17(c) and (f)]. As for Sample A, the Ge bottom cell *J-V* curve became more shunted. This could be due to its imperfections in the tunnel junction between GaAs and Ge subcells.

Commenting about Sample A before ALD, the slope in the series resistance region of the inferred GaAs middle cell characteristics in Fig. 17(c), that is, between -1.0 V to 0.5 V, agrees with the measured AM 1.5G *J-V* characteristics curve before ALD, shown in Fig. 15(a). This confirms that with the continuous LED illumination conditions imposed on current-limiting Ge bottom cell, the adjacent characteristics curve reflected is from the adjacent GaAs middle cell.

From the previous statement then, for applied voltages of $V < 0.5$ V of Figs. 17(c) and (f), inferences can be made about GaAs. Comparing the GaAs *J-V* characteristics at $V <$ 0.5 V of Figs. 17(c) and (f), it can be seen that after ALD, the larger current was collected from Samples A and B, while no significant change in the current collection was observed from the reference sample.

Therefore, a general conclusion that can be derived from the subcell *J-V* curves is that aside from current collection and luminescence homogeneity improvement, the electrical performance of GaAs was enhanced by Al_2O_3 sidewall passivation as well.

5.4.5.3. Dark *J-V* measurements

Dark *J-V* characteristics curves contain rough information about solar cell material properties. These were measured for samples with and without the Al_2O_3 sidewall passivation layer. Figure 18(a) shows the collection of dark *J-V* curves before (dotted lines) and after ALD (solid lines) measured using the MJSC evaluator, which contains the LBIC mapper and continuous LEDs used for measuring subcell DC light *J-V* curves and EQE. Since the MJSC evaluator has low sensitivity at lower voltages, only voltages between 2 V and 2.8 V can be acquired with minimal equipment noise. Before ALD, it can be seen that the reference sample and Sample B had better series resistance, as indicated by larger current at $V > 2.6$ V. On the other hand, a more positive slope at $V <$ 2.6V can be noticed for Sample A, possibly indicating that it has lower ideality factor, closer to 1.0 than the reference sample and Sample B. In electrical circuit modeling, radiative recombination saturation current is associated with the diode model whose ideality factor is 1.0 and J_{01} coefficient. This could mean that before ALD, sample A may have had radiative recombination more dominant than its nonradiative recombination as compared with the other samples. After ALD, all samples had a similar slope in the series resistance regime, at approximately $V > 2.6$ V. This agrees with the AM 1.5 G *J-V* curves shown in Fig. 16(b). Meanwhile, the exact origin of the differences in the dark current before and after ALD cannot be pinpointed. But one possibility could be the adjustment on the MJSC evaluator machine between these two different times of measurements that could have affected the measurement's sensitivity.

Since there was limited information that can be seen from MJSC evaluator dark *J-V* measurements, these were measured again after ALD using sourcemeters from two different setups – a single junction solar cell evaluator and the EL/PL mapping setup shown in Fig. 7 and was used for acquiring luminescence maps discussed in Sec. 5.4.4. Sourcemeters have acceptable sensitivities to current values up to the nA order; hence, clear low voltage information can be obtained. Figures 18(b) and (c) show the dark *J-V* curves measured using the 1JSC evaluator sourcemeter and the EL/PL mapper sourcemeter for 5 measurement trials per sample. In the literature [262], smaller current at voltages close to 0 V is associated with the solar cell having desirable or high shunt resistance, which then indicates less presence of material defects where the leakage current may pass through within the device. Also, a lower curve slope at moderate voltages, approximately between 0.5 and 1.5 V for the InGaP/GaAs/Ge 3JSC samples evaluated in this study, suggested that the ideality factor is closer to 2.0, which is associated with nonradiative recombination current. The measurements shown in Figs. 18(b) and (c) confirm that Samples A (dashed lines) and B (dotted lines), both with Al_2O_3 sidewall passivation layers had higher shunt resistance (near $V = 0$ V) and less dominance of low slope regions within moderate voltages (approximately between 0.5 and 1.5 V), as compared with those of the reference sample. These results suggest that with Al_2O_3 sidewall passivation, shunt defects are reduced, as also inferred from the DC light *J-V* curves under AM 1.5G and subcell limited cases in Figs. 15 and 17, respectively. Furthermore, the radiative recombination dominance may have been enhanced, as suggested by the numerical treatment of LBIC and luminescence maps earlier.

Considering the relationship for V_{OC}, that is,

$$V_{OC} = \frac{k_B T}{q} \ln\left[\frac{J_{SC}}{J_0} + 1\right] \tag{11}$$

it was hypothesized that there should be an increase in V_{OC} of Samples A and B after ALD if their J_{SC}/J_0 ratio is higher than that of the reference sample (where J_0 is the dark current diode coefficient). This hypothesis agrees with the larger J_{SC} while less dark current related to J_0 observed from Samples A and B than those of the reference sample, shown in Figs. 18(b) and (c). However, just a very small increase in V_{OC} was observed from the passivated samples, as shown in Figs. 15(b) and 16(b) and as listed in the V_{OC} column of Table 9. This could be due to the photoconduction through the Al_2O_3 passivation layer. This was observed previously in thin nanocrystalline zinc oxide (nc-ZnO) films in higher amounts when mixed with a *p*-type π-conjugated polymer (i.e. MDMO-PPV) on hybrid polymer solar cells synthesized, in which the J_{SC} increased but the V_{OC} decreased [263]. Since only one value of Al_2O_3 thickness was used during the sidewall passivation of various samples, this may not yet be the optimum. Hence, its optimum thickness on a full III-V based MJSC may be investigated in future work.

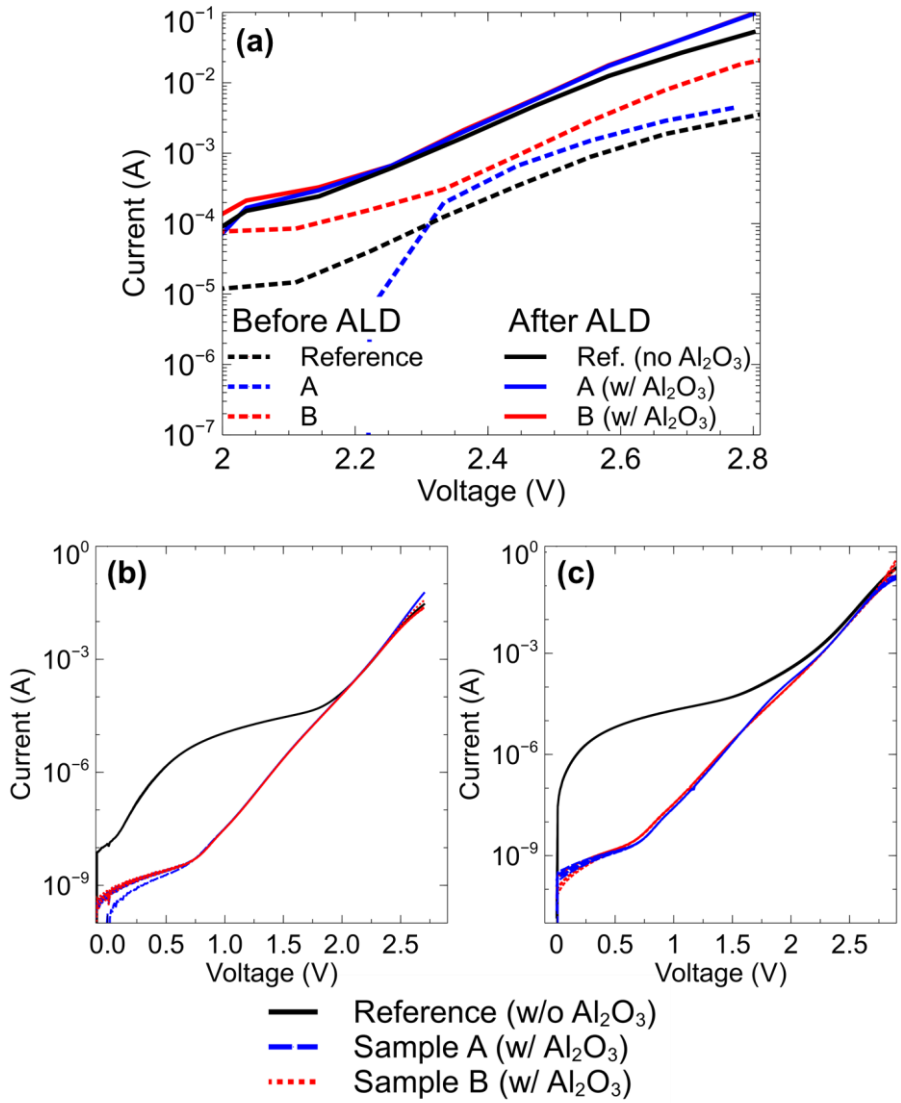

Fig. 18 Dark *J-V* characteristics of the reference, Sample A with Al_2O_3 sidewall passivation, and Sample B with Al_2O_3 sidewall passivation measured using three different setups: (a) MJSC evaluator with low voltage

sensitivity, (b) 4-wire probed sourcemeter of a single-junction solar cell evaluator, and (c) 4-wire probed sourcemeter of the EL/PL mapping setup. Single dark *J-V* curve measurements in (a) were acquired in Tokyo, Japan before and after Al_2O_3 deposition while those in (b) and (c) were obtained after Al_2O_3 deposition.

5.5. Synthesis of Findings

Thin Al_2O_3 passivation layer was successfully deposited on commercial III-V on Ge 3JSCs by the ALD technique non-invasively. Results revealed that the Al_2O_3 sidewall passivation can enhance the LC current production homogeneity in a limiting cell of InGaP/GaAs/Ge 3JSC by about 7.2%. Furthermore, the current production by LC effect and by direct excitation of the limiting GaAs middle cell increased by about 21.9% and 16.3% relative to the sample without the Al_2O_3 layer on the sidewalls, respectively. Generally, a cell conversion efficiency difference of more than 1.0% was found between the reference and the samples with Al_2O_3 sidewall passivation. These results were further confirmed through the following: (1) improvement in the luminescence homogeneity of the HBG subcell where LC effect originates by 70.6% and in the current-limiting cell by 37.5%; (2) subcell *J-V* characteristics showing increased current collection at GaAs; and (3) the increased dominance of radiative recombination over nonradiative recombination inferred from the dark *J-V* characteristics. These findings show that perimeter recombination was reduced with sidewall passivation, making it an important consideration for homogenizing current production in III-V on Ge MJSCs.

Since this technique is non-invasive in increasing the current collection in a limiting subcell, this may serve as an additional guideline on fabricating high-efficiency III-V MJSCs. Alternatively, this may be useful for post-fabrication maintenance of complete solar cells, thereby extending their lifespan. Therefore, it is possible to increase MJSC conversion efficiency by homogenizing the LC effect through electrical sidewall passivation.

For continuity, the optimal thickness of the Al_2O_3 sidewall passivation layer should be sought after that may yield better V_{OC} increase, which then may boost the MJSC conversion efficiency further.

5.6. Supplementary Information

Figure 19 shows the Al_2O_3 deposition uniformity profile on a 4" Si wafer. The growth rate was found to be 1.0 Å per deposition cycle, based on the calculated slope of the thickness versus the number of cycle deposition plotted in Fig. 20. Also, the deposition nonuniformity was found to be 3.94% and the average thickness deposited was 512.41 Å on a 4" Si wafer. These data were provided by ASU NanoFab [264].

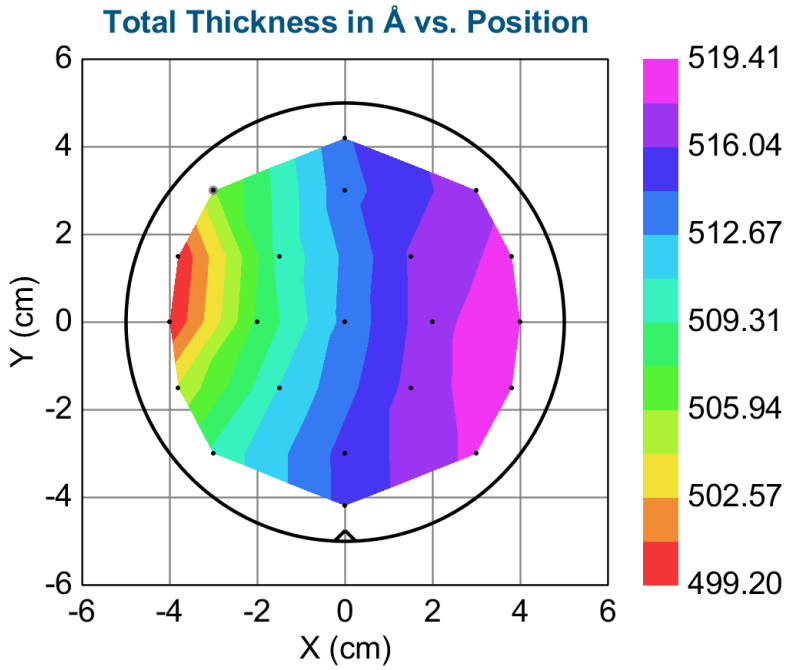

Fig. 19 Al_2O_3 layer thickness (Å) profile on a 4" flat Si wafer produced from 500-cycle run [264].

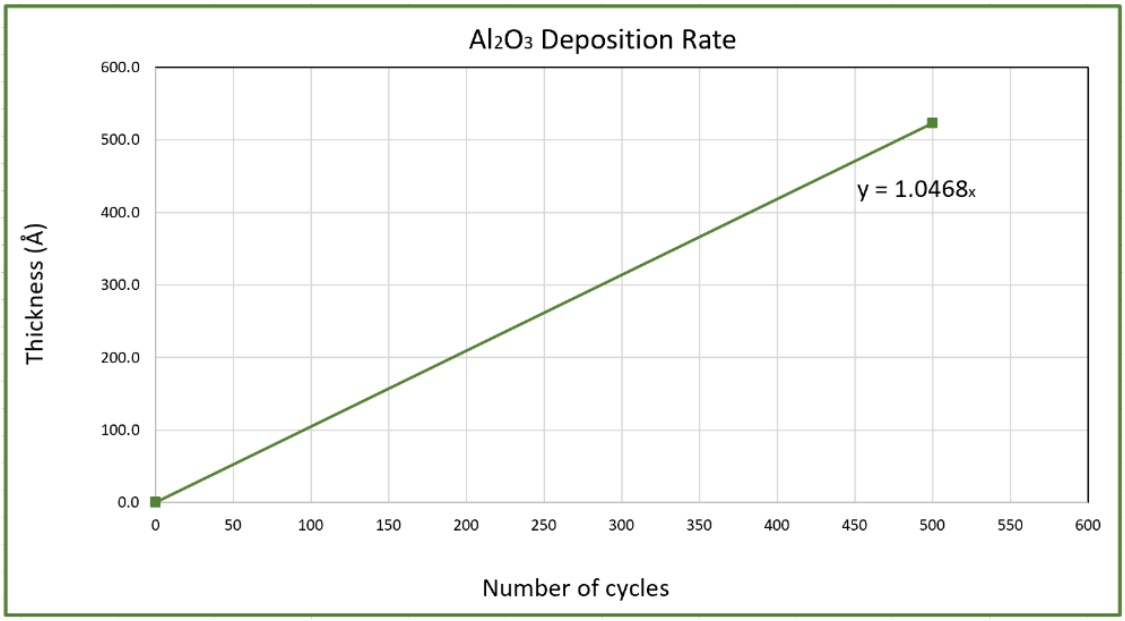

Fig. 20 Al_2O_3 layer thickness (Å) vs the number of deposition cycles on a 4" flat Si wafer.

Figure 21 shows the tandem solar cell structures with and without Al_2O_3 simulated by TMM. Figure 22 shows the optical spectra of a semi-infinitely thick InGaP absorber with and without thin dielectric layers used as anti-reflection coating or passivation.

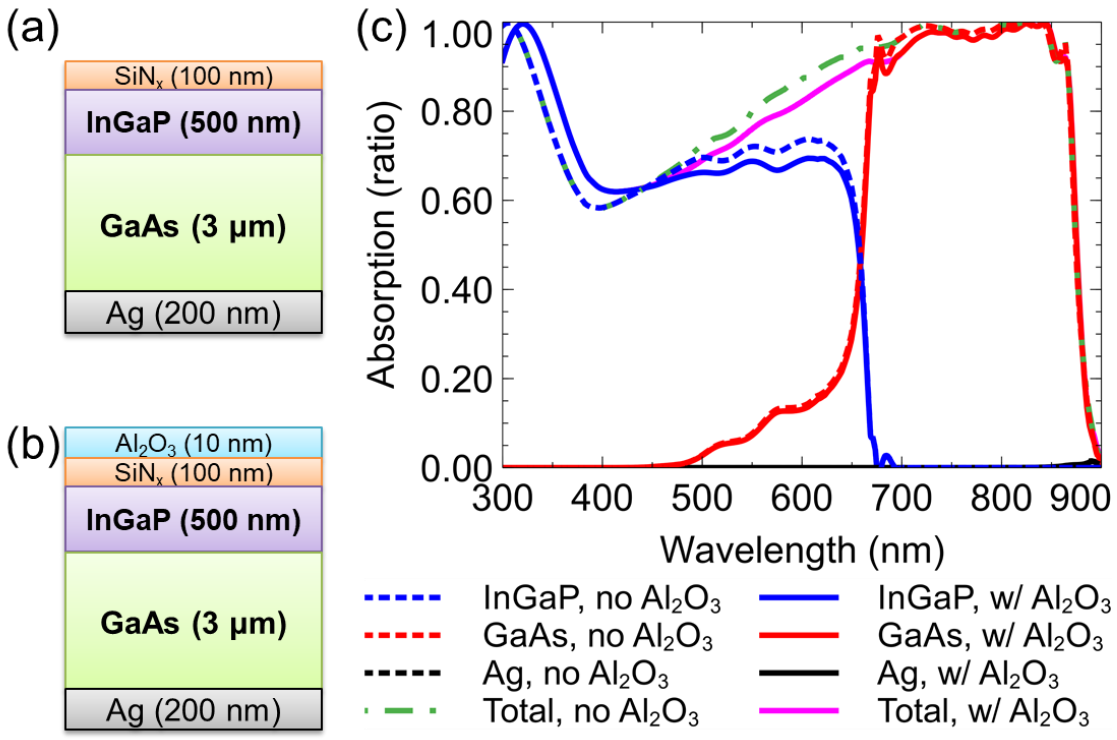

Fig. 21 Schematic of InGaP/GaAs tandem absorber structure (a) without and (b) with Al_2O_3 layer and both with SiNx anti-reflection coating and Ag back contact simulated using TMM. (c) Calculated absorption in the InGaP layer, GaAs layer, and Ag back contact without Al_2O_3 and with Al_2O_3 calculated between 300 nm and 900 nm of the incident light.

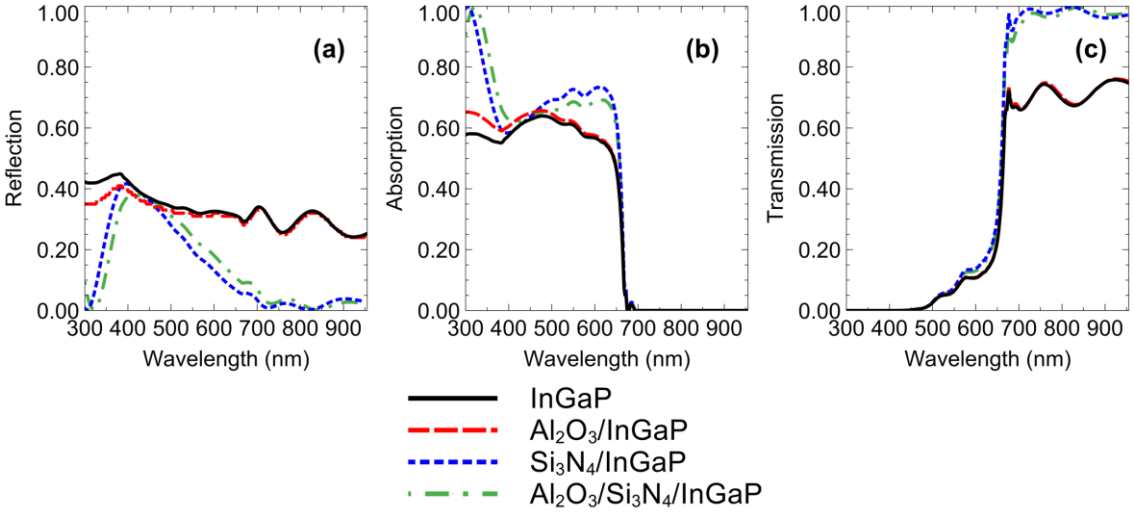

Fig. 22 (a) Reflection, (b) absorption, and (c) transmission spectra of semi-infinitely thick InGaP with and without thin films calculated using TMM.

Figure 23 shows the EQE measurement results from and J_{SC} and V_{OC} summary tables of 3JSC samples having different Al_2O_3 coverages on their front surfaces. These were measured within the same week of deposition, before (solid lines) and after (dashed lines) ALD.

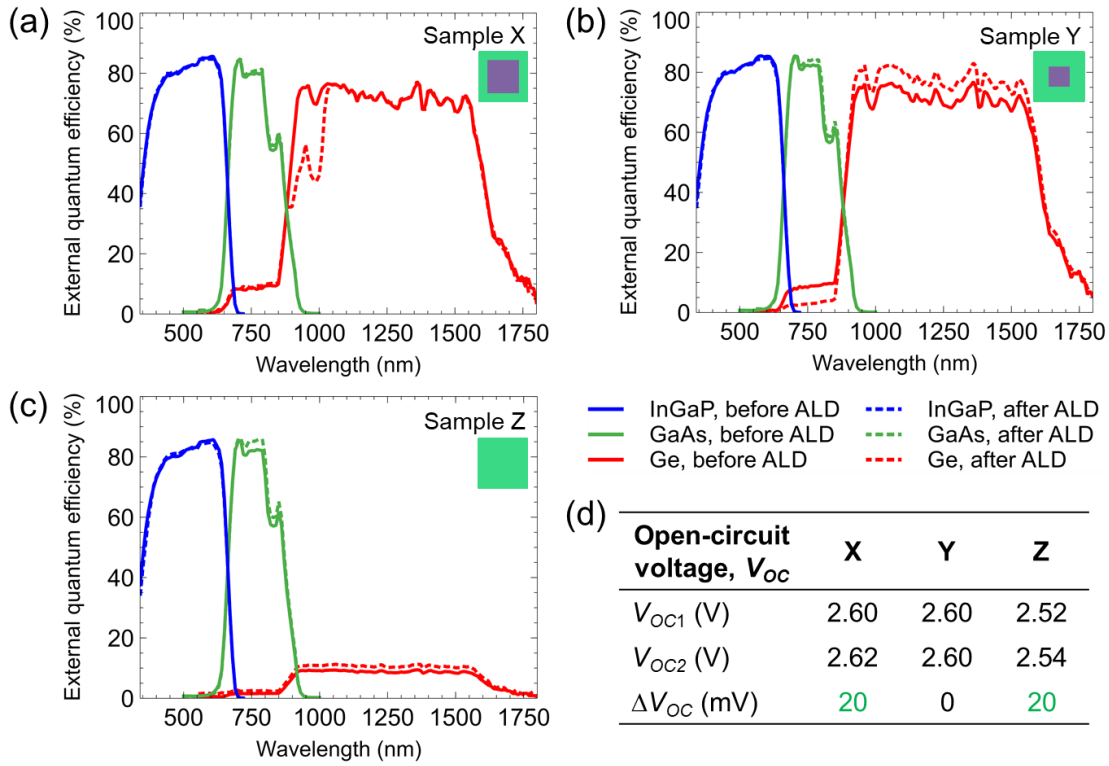

(d)

Open-circuit voltage, V_{OC}	X	Y	Z
V_{OC1} (V)	2.60	2.60	2.52
V_{OC2} (V)	2.62	2.60	2.54
ΔV_{OC} (mV)	20	0	20

(e)

Short-circuit current, J_{SC}	InGaP			GaAs			Ge		
	X	Y	Z	X	Y	Z	X	Y	Z
J_{sc1} (mA/cm^2)	14.01	14.00	14.04	11.04	11.36	11.33	19.19	19.05	2.45
J_{sc2} (mA/cm^2)	14.00	13.94	13.97	11.16	11.57	11.67	17.88	19.67	3.06
$\%_{Jsc,diff}$	-0.07	-0.43	-0.50	1.09	1.85	3.00	-6.83	3.25	24.90

Fig. 23 Subcell EQE measurements of (a) Sample X with 0.5-mm Al_2O_3 coverage from each side of the front surface perimeter, (b) Sample Y with 1-mm coverage, and (c) Sample Z with full coverage, followed by summary tables of (d) J_{SC} and $\%_{Jsc,diff}$ and (e) V_{OC} and ΔV_{OC} calculations before and after ALD. These measurements were acquired at Arizona State University – Solar Power Laboratory. Calculations in green texts indicate improvement while those in red indicate degradation.

Table 10 GaAs LC effect excitation current collection and homogeneity difference between reference InGaP/GaAs/Ge 3JSC sample and samples before subjected to Al_2O_3 sidewall passivation (A and B).

Sample	GaAs LC excitation (before ALD)			
	Average current density, $J_{LC,ave}$ (mA/cm^2)	$J_{LC,ave}$ percent difference (%)	Normalized SD, $\sigma_{LC}/J_{LC,max}$ (ratio)	$\sigma_{LC}/J_{LC,max}$ percent difference (%)
Reference	0.11	0	9.81×10^{-2}	0
Sample A (before Al_2O_3 deposition)	0.10	-9.09	9.72×10^{-2}	-0.9
Sample B (before Al_2O_3 deposition)	0.10	-9.09	9.47×10^{-2}	-3.5

Tables 10 and 11 summarizes the current collection by LC effect and direct excitation of GaAs, respectively, and homogeneity difference between the unpassivated reference sample and the passivated samples A and B.

Table 11 Direct GaAs excitation current collection and homogeneity difference between reference InGaP/GaAs/Ge 3JSC sample and samples before subjected to Al_2O_3 sidewall passivation (A and B).

Sample	**Direct GaAs excitation (before ALD)**			
	Average current density, $J_{DS,ave}$ (mA/cm^2)	$J_{DS,ave}$ percent difference (%)	Normalized SD, $\sigma_{DS}/J_{DS,max}$ (ratio)	$\sigma_{DS}/J_{DS,max}$ percent difference (%)
Reference (no Al_2O_3)	4.74	0	1.40×10^{-2}	0
Sample A (before Al_2O_3 deposition)	4.58	-3.38	1.94×10^{-2}	38.5
Sample B (before Al_2O_3 deposition)	4.58	-3.38	1.83×10^{-2}	30.7

Figure 24 shows the InGaP top cell current collection in the reference InGaP/GaAs/Ge 3JSC sample, Sample A, and Sample B when directly excited by a modulated 450-nm laser.

Figure 25 shows the InGaP/GaAs/Ge 3JSC wafer map, which serves as a reference to which part each sample used in this study was grown and taken from the wafer.

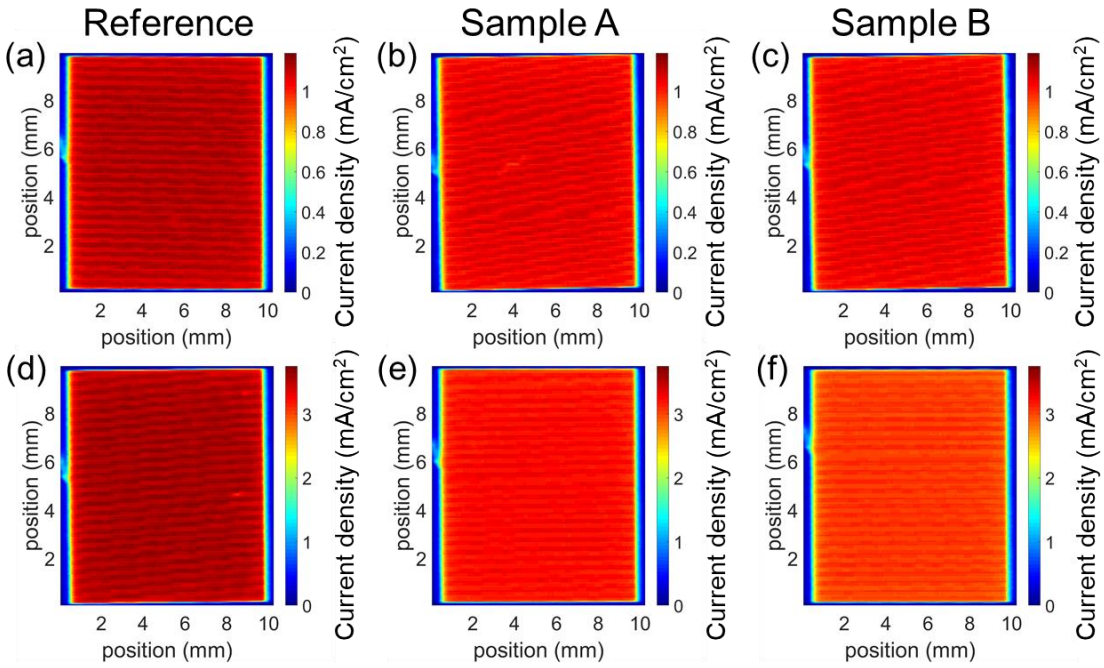

Fig. 24 Spatially-resolved current collection acquired in InGaP top cell of InGaP/GaAs/Ge 3JSC (a) reference sample, (b) Sample A before Al_2O_3 deposition, and (c) Sample B before Al_2O_3 deposition using a modulated 450-nm laser. Spatially-resolved current collection acquired in InGaP top cell of InGaP/GaAs/Ge 3JSC (d) reference sample without Al_2O_3, (e) Sample A with Al_2O_3, and (f) Sample B with Al_2O_3 using a modulated 450-nm laser.

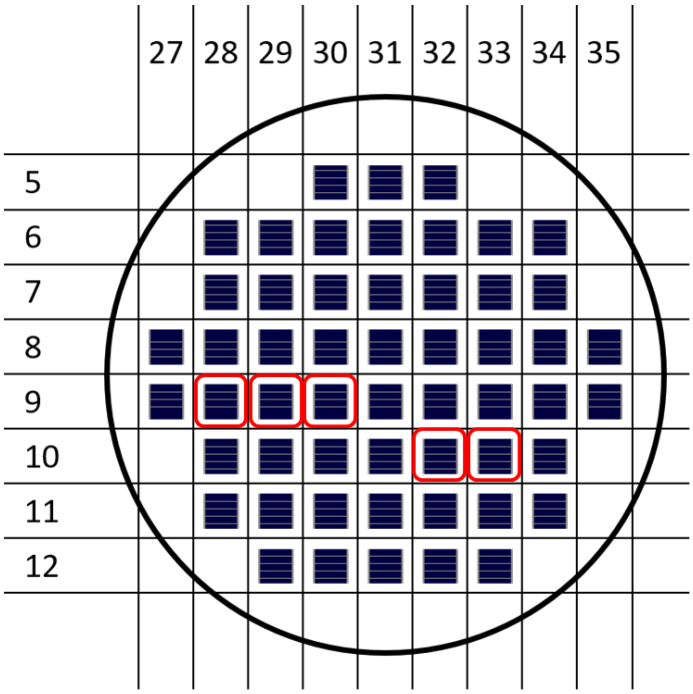

Fig. 25 InGaP/GaAs/Ge 3JSC wafer map locations of the reference sample (32-10), Sample A (28-9), Sample B (29-9), and others used for this study (33-10 and 30-9).

Application of perovskite quantum dots on assisting luminescent coupling effect in III-V multijunction solar cells

Chapter 6

Chapter 6 – Application of perovskite quantum dots on assisting luminescent coupling effect in III-V multijunction solar cells

*** Omitted in the Abridged Vesion ***

Conclusions and recommendations

Chapter 7

Chapter 7 – Conclusions and Recommendations

7.1. Conclusion

The role of homogeneous luminescent coupling (LC) effect in III-V multijunction solar cells (MJSCs) was probed. It was found that homogenizing the LC effect may increase the conversion efficiency of III-V MJSCs. This was experimentally demonstrated by electrical passivation, which garnered an efficiency increase of 1.05% to 1.18% with respect to a reference cell. This is close to the 1.35% efficiency increase predicted from modeling an MJSC with homogeneous LC current collection. The possibility was also demonstrated by photo-passivation. In this part, current redistribution onto lower bandgap subcells and more homogenized current collection on the benefitting subcells were observed. Theoretically, a homogeneous LC effect may be achieved by designing a plateau-stack of III-V MJSCs, in which the topmost subcell has the smallest lateral area. The larger the proportion between adjacent subcells, the lenient the choices for the material's energy gap will be, based on the detailed balance calculations made.

7.1.1. Ways to observe spatial LC effect

It was found that the laser beam induced current (LBIC) mapping is a useful technique in observing spatial LC current collection in III-V MJSCs. The key components in measuring it are the single wavelength LEDs used in irradiating the non-evaluated subcells, while no external irradiation was shone upon the subcell being evaluated. To get a perspective on the emission profile of adjacent subcells where the LC effect occurs, one may implement the electroluminescence/photoluminescence (EL/PL) mapping. Aside from high carrier injection by application of external voltage, single-wavelength light sources were also used for nonlimiting subcell irradiation, similar to the LBIC mapping approach. It was found that the emission profile of the higher bandgap subcell where the LC effect originated was the same as that of the LC current collection in its adjacent lower bandgap subcell. Therefore, exploring these techniques while inducing the LC effect has led us to confirm that the LC current collection in a lower bandgap subcell will depend on the emission profile of its adjacent higher bandgap subcell.

7.1.2. Structures with inhomogeneous LC effect

The nonuniform LC effect in III-V MJSCs was observed among the adjacent subcells of Ge-based and Si-based samples characterized. The nonuniformity was found to get severe as the intensity of external irradiation upon a higher bandgap subcell was increased. Upon comparing the LC current collection in terrestrial- and space-grade samples, it was inferred that the higher bandgap subcell quality and design will affect the LC effect towards its adjacent lower bandgap subcell. By quality, it pertains to the number of defects acting as carrier traps or recombination centers present. On the other hand, design refers to which part of the solar spectrum the MJSCs can absorb more easily. Meanwhile, no change in LC effect homogeneity was observed for any cell temperature. Hence, it prevails as a problem in any cell temperature. In a broader perspective, this is an issue for concentrator systems, as terrestrial MJSCs typically operate at 85°C and beyond under high sunlight concentration [137–138]. As for various cell sizes, while the degree of LC nonuniformity did not vary at every higher bandgap subcell irradiation

tested, the larger the cell area, the larger the losses observed due to the inhomogeneity of the LC effect.

7.1.3. Underlying physics behind inhomogeneous LC effect

To investigate the physics behind nonuniform LC effect, 3-dimensional distributed simulation program with integrated circuit emphasis (SPICE) electrical model, 2-dimensional Monte Carlo ray tracer, and a quasi-2-dimensional electro-optical prediction (Q2DEP) model developed in the course of this study were used. Before the implementation of these models, it was hypothesized that the nonuniform LC effect is possibly caused by the following physics: (1) lateral resistance effect resulting to nonuniform radiative emission within the MJ subcells at high carrier injection, (2) nonuniform material growth, (3) perimeter recombination, and (4) photon escape through the MJSC sidewalls. Although the nonuniformity also depends on the III-V or IV material defect distribution itself, the lateral resistance effects and perimeter recombination were identified to be the dominant causes of the inhomogeneous LC effect. On the other hand, low photon escape probabilities obtained from optical simulations of III-V and IV solar cell materials suggested that photon escape is not a prevalent cause of inhomogeneous LC effect.

7.1.4. Homogenizing the LC effect

7.1.4.1. By electrical sidewall passivation

Experimentally, it was found that perimeter recombination is mainly responsible for the inhomogeneity of the LC effect since this was observed to be alleviated by electrical passivation of the sidewalls of InGaP/GaAs/Ge triple-junction solar cells. The sidewall passivation was made possible by atomic layer deposition of thin Al_2O_3 film on full MJSCs with contacts and anti-reflection coating. Results revealed that this method increased the LC current collection in a limiting MJ subcell by 21.9% and enhance its uniformity by 7.2%. Furthermore, the luminescence homogeneity from the limiting MJ subcell was observed to improve by 37.5% after Al_2O_3 passivation at 2.5 V, when the MJSC was operated near its open-circuit voltage. Last, under standard global air mass 1.5 (AM 1.5G) condition at 1 sun concentration, the power conversion efficiency of the electrically-passivated III-V 3JSC increased by 1.05% to 1.18%; hence, close to the predicted value [170] of 1.35% and demonstrating a non-invasive way to improve current matching among MJ subcells.

7.1.4.2. By plateau MJSC structure (theoretical)

Aside from electrical sidewall passivation, MJSC dimension modification was also probed as a possible solution to the nonuniform LC effect. This was investigated theoretically by the detailed balance calculation of a tandem solar cell, in which the top cell was designed to have a larger bandgap and a smaller active area than those of the bottom cell. Also, this was simulated using a 2-dimensional SPICE electrical model with a lumped series resistance model and Q2DEP model mentioned earlier. Simulation results revealed that if the active area of a current-limiting, lower bandgap MJ subcell is made at least 1.23 times larger than that of the light-emitting higher bandgap subcell, the nonuniformity of the LC effect may be eliminated. Furthermore, this may allow a larger current collection near the MJSC edges, which may then alleviate the perimeter recombination due to sidewall defects and oxidation over time.

7.1.4.3. By photo-passivation

Another potential solution explored was the deposition of all-inorganic metal halide perovskite quantum dots (PQDs) – an amorphous thermoplastic mixture on the selected area near the edges of a III-V semiconductor material by dip-coating technique. This was hypothesized to allow a larger amount of light emission towards the edges of a current-limiting lower bandgap subcell, which then may yield larger LC current generation specifically near the edges by photo-passivation or "photon healing" effect. At the same time, the amorphous thermoplastic provided a moisture barrier for the PQDs. Experimentally, this proposed solution was tested preliminarily on single substrates such as glass and undoped, semi-insulated III-V substrate to study its fundamental optoelectronic properties. It was found that the perovskite quantum dot-coated III-V substrates had larger photoluminescence peaks near the III-V substrate bandgap than the bare samples, suggesting that it can potentially induce LC effect when deposited on a III-V MJSC. Interestingly found as well, higher PL intensities were acquired from the PQD-coated samples than the pure GaAs samples in their GaAs emission regime. These results demonstrated the proof-of-concept of optical coupling between a low-dimensional PQD structure and a III-V material; hence, paving a possibility to finely tune current matching among III-V-based MJSC subcells. Also, its stability on single substrates was observed for some time, as perovskites were known to be weak against humidity and moisture when unencapsulated. With amorphous thermoplastic mixed with quantum dot solution, PL emission was observed to be sustainable for at least 10 weeks. On the other hand, without thermoplastic, the PL emission quenched within 3 hours after deposition. Hence, the weakness of perovskite against moisture, one of its greatest challenges, has been addressed in this work by the use of thermoplastics as a moisture barrier in the solution phase. Last, perovskite quantum dots were deposited on full III-V based MJSC devices, covering their entire front surface. From a fully dip-coated MJSC device with a moderate number of dipping cycles, desirable current redistribution among subcells was achieved; hence, a demonstration of current matching control among MJ subcells.

7.1.4.3. New guidelines suggested in III-V based MJSC fabrication with uniform LC effect

In summary, there are three pathways to possibly homogenize and increase current collection in a limiting cell of a III-V MJSC device – one is by growing smaller active area of the top cell, another is by electrical sidewall passivation using thin-film dielectrics, and the other is by photo-passivation of shunt defects in MJSCs using a PQD-amorphous thermoplastic film.

The electrical sidewall passivation was experimentally observed to homogenize and increase current collection in a subcell benefitting from the LC effect. Hence, the electrical sidewall passivation of full MJSC devices is an additional step recommended in fabricating high-efficiency MJSCs with homogeneous current production, just after the fabrication of the semiconductor stack or after electrode fabrication, provided that the electrodes are masked during passivation layer growth.

The PQD-amorphous thermoplastic films on a full III-V MJSC device successfully demonstrated current redistribution from the top cell into its lower subcells. Thus, for enhanced MJSC current matching, it is recommended to use a photo-assistive layer like PQD-amorphous thermoplastic films. This film can be deposited after growing the III-V stack, but before the deposition of anti-reflective coating (ARC). Alternatively, if the

MJSC is already fabricated, the limiting subcell current should be determined first, then, an optimum PQD-thermoplastic film should be fabricated.

Applying these solutions may reach the conversion efficiency increase by 1.35% in MJSCs, based on the estimation made in Chapter 3.

7.2. Recommended Future Work

Although the proofs-of-concept in homogenizing LC effect in III-V MJSCs have been put in place, more work needs to be done in perfecting the novel technologies presented. For one, the optimal thickness of the Al_2O_3 passivation layer on the MJSC sidewalls was not explored yet. The question of how thick the Al_2O_3 passivation layer should be to yield high J_{SC} and V_{OC} at the same time remains at this time. While it was raised that the non-increase of the V_{OC} after passivation could be due to photoconduction through the Al_2O_3 layer, this is yet to be confirmed in a future investigation.

Another issue that has not been explored yet is the PQD-COC film deposition technique that could produce the most uniform film. As concluded earlier, the film uniformity affects the luminescence homogeneity of the higher bandgap subcell where the LC effect originates, which, then, impacts the LC current collection uniformity in its adjacent lower bandgap subcell. It is suggested that aside from the dip-coating technique, other film deposition methods should be probed to find out the one that could produce the most uniform film. On top of this issue, the optimal thickness of the PQD-COC film on a full III-V MJSC device seemed to depend on the degree of a current mismatch at least between 2 adjacent subcells having the least current production. Hence, further exploration of the optimal thickness of PQD-COC film fully covering the III-V MJSC front surface is recommended as future work.

Last, the technical issues on how to transfer the film from a dummy substrate into the full MJSC device remain as challenges, as briefly investigated and discussed in Appendix A and should be addressed in continuing work. At this point, the hypothesis on selective area application of PQD film with optimal thickness as a photo-passivating layer could not be discarded yet just because the preliminary results were undesirable. A cleaner and automated way of selective area deposition, while maintaining the integrity of the film produced and of the host material such as III-V based MJSCs, should be sought after.

Record of publications

Record of Publications

Journal publications

[1] **Yu Jeco, B.M.**, Sogabe, T., Tamaki, R., Ahsan, N. and Okada, Y. (2017), Impact of Optically non-uniform Luminescence Coupling Effect to the Limiting Cell Conversion Efficiency in InGaP/GaAs/Ge Triple-junction Solar Cell, Journal of Photonics for Energy, Vol. 7, No. 3, p. 035501, https://doi.org/10.1117/1.JPE.7.035501. **(Chapter 3)**

[2] **Yu Jeco, B.M.**, Sogabe, T., Ahsan, N. and Okada, Y. (2018), Temperature Dependence of Luminescence Coupling Effect in InGaP/GaAs/Ge Triple-junction Solar Cells, Journal of Photonics for Energy, Vol. 8, No. 2, p. 022602, https://doi.org/10.1117/1.JPE.8.022602. **(Chapter 3)**

[3] Barrios, J.P.L.G., Cortez, J.R., Herman, G.M., Larroder, A., **Yu Jeco, B.M.**, Watanabe, K. and Okada, Y. (2018), The Use of Convex Lens as Primary Concentrator for Multi-junction Solar Cells, Emergent Scientist, Vol. 2, p. 5, https://doi.org/10.1051/emsci/2018004.

[4] **Yu Jeco, B.M.**, Veinberg-Vidal, E., Vauche, L., Ahsan, N. and Okada, Y. (2019), Temperature dependence of wafer-bonded III-V on silicon multijunction solar cells with luminescent coupling effect, Journal of Photonics for Energy, Vol. 9, No. 1, p. 015503, https://doi.org/10.1117/1.JPE.9.015503. **(Chapter 3)**

[5] **Yu Jeco, B.M.**, Veinberg-Vidal, E., Vauche, L., Yoshida, K., Tamaki, R., Ahsan, N. and Okada, Y. (2019), Luminescent coupling effect in wafer-bonded III-V on silicon multijunction solar cells, Journal of Photonics for Energy, Vol. 9, No. 1, p. 015504, https://doi.org/10.1117/1.JPE.9.015504. **(Chapter 3)**

[6] Xu, H., Delamarre, A., **Yu Jeco, B.M.**, Johnson, H., Watanabe, K., Okada, Y., Guillemoles, J.F., Nakano, Y., and Sugiyama, M. (2019), Current transport efficiency analysis of multi-junction solar cells by luminescence imaging, Progress in Photovoltaics: Research and Applications, *in press*, https://doi.org/10.1002/pip.3140. **(Chapter 4)**

[7] **Yu Jeco, B.M.**, Larroder, A. and Oguma, K. (2019), Technosocial feasibility analysis of solar-powered UV-LED water treatment system in a remote island of Guimaras, Philippines, Journal of Photonics for Energy – Special Section on Solar Energy Solutions for Electricity and Water Supply in Rural Areas, Vol. 9, No. 4, https://doi.org/10.1117/1.JPE.9.043105.

Conference proceedings

Oral presentations:

[1] **O Yu Jeco, B.M.**, Yoshida, K., Tamaki, R., Ahsan, N. and Okada, Y. (2017), Analysis of Current Generation in InGaP/GaAs/Ge Triple-junction Solar Cells with Optically Non-Uniform Luminescence Coupling Effect, 33rd European Photovoltaic Solar Energy Conference (EUPVSEC-33) and Exhibition, pp. 1236-1240, https://doi.org/10.4229/EUPVSEC20172017-4DO.4.5. **(Chapter 3)**

[2] **O Yu Jeco, B.M.**, Hosoi, Y. and Oguma, K. (2019), Solar-powered ultraviolet light-emitting diodes (UV-LED) for inactivation of *Escherichia coli* in water, 53rd Annual Conference of Japan Society on Water Environment (JSWE).

[3] **O Yu Jeco, B.M.**, Wang, H., Espaldon, A.E., Jehl Li-Kao, Z., Kubo, T., Segawa, H., and Okada, Y. (2020), Cyclic Olefin Copolymer (COC) as Moisture Barrier for All-Inorganic Perovskite Quantum Dots on III-V Optoelectronic Materials, 6th World Congress on Smart Materials 2020 (WCSM-2020). **(Chapter 6)**

Poster presentations:

[1] **O Yu Jeco, B.M.**, Tamaki, R., Nakamura, T., Imaizumi, M., Ahsan, N. and Okada, Y. (2018), Spatial Evaluation of Luminescent Coupling Effect in a Current-limiting Subcell of InGaP/GaAs/Ge Triple-junction Solar Cells, 7th World Conference on Photovoltaic Energy Conversion (WCPEC-7), pp. 969-974, **Award Nominee** https://doi.org/10.1109/PVSC.2018.8547432. **(Chapter 3)**

[2] O Amboy, J., **O Yu Jeco, B.M.**, Wang, H, Kinoshita, T., Jehl Li-Kao, Z., Shoji, Y., Ahsan, N., Kubo, T. and Okada, Y. (2018), Cesium Lead Halide Perovskite Quantum Dot Deposition on GaAs Substrates by Dip-coating, 7th World Conference on Photovoltaic Energy Conversion (WCPEC-7), pp. 467-471, https://doi.org/10.1109/PVSC.2018.8548078. **(Chapter 6)**

[3] Jehl Li-Kao, Z., Suchet, D., Miyashita, N., Behagel, B., Giteau, M., Delamarre, A., **O Yu Jeco, B.M.**, O Guillemoles, J.F., and Okada, Y. (2018), Hot Carrier Extraction Using Energy Selective Contacts And Feedback On The Remaining Distribution, 7th World Conference on Photovoltaic Energy Conversion (WCPEC-7), pp. 1814-1816, https://doi.org/10.1109/PVSC.2018.8548164.

[4] O Xu, H., Delamarre, A., Jia, J., **Yu Jeco, B.M.**, Watanabe, K., Okada, Y., Guillemoles, J.F., Nakano, Y. and Sugiyama, M. (2018), Transport Efficiency Imaging in Multi-junction Solar Cells by Luminescence Analysis, 7th World Conference on Photovoltaic Energy Conversion (WCPEC-7), pp. 2261-2265, **Award Nominee** https://doi.org/10.1109/PVSC.2018.8548208. **(Chapter 4)**

[5] **O Yu Jeco, B.M.**, Chikhalkar, A., Giteau, M., Tamaki, R., Ahsan, N., King, R. and Okada, Y. (2019), The influence of Al_2O_3 passivation of III-V on Ge multijunction solar cells to the spatial distribution of luminescent coupling effect, IEEE 46th Photovoltaic Specialists Conference (PVSC), *in print*. **(Chapter 6)**

References

References

[1] A. Grubler, T.B. Johansson, L. Muncada, N. Nakicenovic, S. Pachauri, K. Riahi, H.H. Rogner, and L. Strupeit, "Energy Primer," in Global Energy Assessment - Toward a Sustainable Future, p. 34, Vienna, Cambridge University Press (2012).

[2] British Petroleum (BP), "Full report – BP Statistical Review of World Energy 2018," available June 13, 2018, accessed May 14, 2019 https://www.bp.com/content/dam/bp/business-sites/en/global/corporate/pdfs/energy-economics/statistical-review/bp-stats-review-2018-full-report.pdf.

[3] International Monetary Fund, "World GDP," (1980-2017).

[4] R. Likvern, "The Powers of Fossil Fuels, an Update with Data per 2017," available June 14, 2018, accessed May 14, 2019 https://runelikvern.online/2018/06/14/the-powers-of-fossil-fuels-an-update-with-data-per-2017/#more-1287.

[5] Scripps Institution of Oceanology, "Latest CO_2 reading – Keeling Curve," available May 12, 2019, accessed May 14, 2019 https://scripps.ucsd.edu/programs/keelingcurve/.

[6] M. S. Dresselhaus and I. L. Thomas, "Alternative energy technologies," Nature 414(6861), pp. 332-337 (2001) https://doi.org/10.1038/35104599.

[7] U.S. Energy Information Administration (EIA), "International Energy Outlook 2016," DOE/EIA-0484, available May 2016, accessed August 2017 https://www.eia.gov/outlooks/ieo/pdf/0484(2016).pdf.

[8] J.A. De Gouw, D.D. Parrish, G.J. Frost, and M. Trainer, "Reduced emissions of CO_2, NO_x, and SO_2 from US power plants owing to switch from coal to natural gas with combined cycle technology," Earth's Future 2(2), pp.75-82 (2014) https://doi.org/10.1002/2013EF000196.

[9] German Advisory Council on Global Change (WBGU), "World in Transition 3 – Towards Sustainable Energy Systems 1st edition," Routledge, London (2003) https://doi.org/10.4324/9781315071961.

[10] ISPRE, "Research and Development on Renewable Energies: A Global Report on Photovoltaic and Wind Energy," International Science Panel on Renewable Energies, Paris (2009) https://council.science/cms/2017/05/ISPRE_Photovoltaic_and_Wind.pdf.

[11] British Petroleum (BP), "BP Statistical Review of World Energy 2015" (2016).

[12] The Institute of Energy Economics, Japan (IEEJ) via Y. Fujii, "Overview of Energy Systems – Lecture 3," Department of Nuclear Engineering and Management, The University of Tokyo (2016).

[13] World Coal Association (WCA), "Coal and Electricity," accessed May 22, 2019 https://www.worldcoal.org/coal/uses-coal/coal-electricity.

[14] R. Murray and K.E. Holbert, "Chapter 6 – Fission," in *Nuclear energy: an introduction to the concepts, systems, and applications of nuclear processes*, Elsevier, p. 93 (2014).

[15] United States Energy Information Administration (EIA), Petroleum Supply Monthly (2018).

[16] United States Energy Information Administration (EIA), "Natural Gas Production in the United States," U.S. Geological Survey Fact Sheet 0113-01 (2002) https://pubs.usgs.gov/fs/fs-0113-01/.

[17] H. Herzog and D. Golomb, "Carbon capture and storage from fossil fuel use," Encyclopedia of Energy 1(6562), pp. 1-11 (2004) retrieved here.

[18] B. van der Zwaan and K. Smekens, "CO_2 capture and storage with leakage in an energy-climate model," Environmental Modeling & Assessment 14(2), pp. 135-148 (2009) https://doi.org/10.1007/s10666-007-9125-3.

[19] Y. Fujii, "Overview of Energy Systems – Lecture 8," Department of Nuclear Engineering and Management, The University of Tokyo (2016).

[20] O. Edenhofer, R. Pichs-Madruga, Y. Sokona, K. Seyboth, P. Matschoss, S. Kadner, T. Zwickel, P. Eickemeier, G. Hansen, S. Schlömer and C. von Stechow, "IPCC Special Report on Renewable Energy Sources and Climate Change Mitigation," Cambridge University Press, Cambridge, UK and New York, NY, USA (2011).

[21] S. Solomon, ed., "Climate change 2007–the physical science basis: Working group I contribution to the fourth assessment report of the IPCC, vol. 4," Cambridge University Press (2007).

[22] California Energy Commission, "Waste to Energy & Biomass in California," accessed December 1, 2016 http://www.energy.ca.gov/biomass/.

[23] Power Technology, "Strangford Lough Tidal Turbine, Northern Ireland, United Kingdom," accessed December 1, 2016 https://www.power-technology.com/projects/strangford-lough/.

[24] United States Environmental Protection Agency, "A student's guide to global climate change," accessed December 1, 2016 http://www.epa.gov/climatestudents/solutions/technologies/index.html (dead link as of May 30,2019).

[25] W. Smith, "Effect of Light on Selenium during the passage of an Electric Current," SPIE Milestone Series MS 56, p. 3-3, 1992.

[26] J. Nelson, "Chapter 1 – Introduction," in *The Physics of Solar Cells*, Imperial College, London (2003).

[27] J.L. Gray and A. Luque and S. Hegedus (eds.), "Chapter 3 – The Physics of the Solar Cell," in *Handbook of Photovoltaic Science and Engineering*, John Wiley & Sons, Ltd., West Sussex (2011).

[28] M. A. Green, "Chapter 5 – Efficiency Limits, Losses and Measurement," in *Solar Cells: Operating Principles, Technology, and System Applications*, The University of New South Wales, New South Wales (1998).

[29] M. Boxwell, "Surveying your Site," in *Solar Electricity Handbook: A Simple, Practical Guide to Solar Energy: How to Design and Install Photovoltaic Solar Electric Systems*, Greenstream Publishing (2010).
[30] W. Shockley and H.J. Queisser, "Detailed balance limit of efficiency of p-n junction solar cells," Journal of Applied Physics 32(3), pp. 510-519 (1961) https://doi.org/10.1063/1.1736034.
[31] L.C. Hirst and N.J. Ekins-Daukes, "Fundamental losses in solar cells," Progress in Photovoltaics: Research and Applications 19(3), pp. 286-293 (2011) https://doi.org/10.1002/pip.1024.
[32] J. Nelson, "Chapter 2 – Photons In, Electrons Out: Basic Principles of PV," in *The Physics of Solar Cells*, Imperial College, London (2003).
[33] A. Kaminski, J.J. Marchand, A. Fave, and A. Laugier, "New method of parameters extraction from dark IV curve," Proc. 26th IEEE Photovoltaics Specialist Conference (PVSC-26), pp. 203-206 (1997) https://doi.org/10.1109/PVSC.1997.654064.
[34] J. Nelson, "Chapter 4 – Generation and Recombination," in *The Physics of Solar Cells*, Imperial College, London (2003).
[35] The University of Washington, "Solar Technologies," accessed September 30, 2016 http://depts.washington.edu/cmditr/modules/opv/solar_technologies.html.
[36] M. A. Green, "Third generation photovoltaics: Ultra-high conversion efficiency at low cost," Progress in Photovoltaics: Research and Applications 9(2), pp. 123-135 (2001) https://doi.org/10.1002/pip.360.
[37] M. A. Green, "Third generation photovoltaics: advanced solar energy conversion," Physics Today 57(12), pp. 71-72 (2004).
[38] G. Conibeer, "Third-generation photovoltaics," Materials Today 10(11), pp. 42-50 (2007) https://doi.org/10.1016/S1369-7021(07)70278-X.
[39] M. A. Green, K. Emery, Y. Hishikawa, W. Warta and E. D. Dunlop, "Solar cell efficiency tables (Version 45)," Progress in Photovoltaics: Research and Applications 23(1), pp. 1-9 (2015) https://doi.org/10.1002/pip.2573.
[40] National Renewable Energy Laboratory, "Best research-cell efficiencies," accessed November 18, 2019 https://www.nrel.gov/pv/cell-efficiency.html.
[41] M.A. Green, E.D. Dunlop, D.H. Levi, J. Hohl-Ebinger, M. Yoshita, and A.W. Ho-Baillie, "Solar cell efficiency tables (Version 54)," Progress in Photovoltaics: Research and Applications 27(7), pp. 565-575 (2019) https://doi.org/10.1002/pip.3171.
[42] F. Dimroth and S. Kurtz, "High-efficiency multijunction solar cells," MRS bulletin 32(3), pp. 230-235 (2007) https://doi.org/10.1557/mrs2007.27.
[43] D.J. Friedman, "Progress and challenges for next-generation high-efficiency multijunction solar cells," Current Opinion in Solid State and Materials Science 14(6), pp. 131-138 (2010) https://doi.org/10.1016/j.cossms.2010.07.001.
[44] G. Letay, C. Baur, and A. Bett, "Theoretical investigations of III-V multi-junction concentrator cells under realistic spectral conditions," Proc. 19th European Photovoltaic Solar Energy Conference (EUPVSEC-19) vol. 7, p. 11 (2004) retrieved here.
[45] M. Wiemer, V. Sabnis, and H. Yuen, "43.5% efficient lattice matched solar cells," Proc. SPIE High and Low Concentrator Systems for Solar Electric Applications VI 8108 p. 810804 (2011) https://doi.org/10.1117/12.897769.
[46] R. R. King, D. C. Law, K. M. Edmondson, C. M. Fetzer, G. S. Kinsey, H. Yoon, R. A. Sherif, and N. H. Karam, "0% efficient metamorphic GaInP/GaInAs/Ge multijunction solar cells," Applied Physics Letters 90(18), p. 183516 (2007) https://doi.org/10.1063/1.2734507.
[47] C. Algora and I. Rey-Stolle, "The interest and potential of ultra-high concentration," in *Next Generation of Photovoltaics*, Springer, Berlin, Heidelberg, pp. 23-60 (2012).
[48] W.P. Dumke, "Spontaneous radiative recombination in semiconductors," Physical Review 105(1), p. 139 (1957) https://doi.org/10.1103/PhysRev.105.139.
[49] C. Domínguez and P. García-Linares, "Characterization of multijunction concentrator solar cells," in *High Concentrator Photovoltaics*, Springer, Cham, pp. 39-84 (2015).
[50] C. Baur, M. Hermle, F. Dimroth, and A.W. Bett, "Effects of optical coupling in III-V multilayer systems," Applied Physics Letters 90(19), p. 192109 (2007) https://doi.org/10.1063/1.2737927.
[51] K.H. Lee, K.W. Barnham, J.P. Connolly, B.C. Browne, R.J. Airey, J.S. Roberts, M. Fuhrer, T.N. Tibbits, and N.J. Ekins-Daukes, "Demonstration of photon coupling in dual multiple-quantum-well solar cells," IEEE Journal of Photovoltaics 2(1), pp. 68-74 (2011) https://doi.org/10.1109/JPHOTOV.2011.2177444.
[52] M.A. Steiner, J.F. Geisz, T.E. Moriarty, R.M. France, W.E. McMahon, J.M. Olson, S.R. Kurtz, and D.J. Friedman, "Measuring IV curves and subcell photocurrents in the presence of luminescent coupling," IEEE Journal of Photovoltaics 3(2), pp. 879-887 (2012) https://doi.org/10.1109/JPHOTOV.2012.2228298.
[53] D.J. Friedman, J.F. Geisz, and M.A. Steiner, "Analysis of multijunction solar cell current–voltage characteristics in the presence of luminescent coupling," IEEE Journal of Photovoltaics 3(4), pp. 1429-1436 (2013) https://doi.org/10.1109/JPHOTOV.2013.2275189.

[54] D. Derkacs, D.T. Bilir, and V.A. Sabnis, "Luminescent coupling in GaAs/GaInNAsSb multijunction solar cells," IEEE Journal of Photovoltaics 3(1), pp. 520-527 (2012) https://doi.org/10.1109/JPHOTOV.2012.2213579.
[55] M.Z. Shvarts, M.A. Mintairov, V.M. Emelyanov, V.V. Evstropov, V.M. Lantratov, and N.K. Timoshina, "Method for direct measurements of luminescent coupling efficiency in concentrator MJ SCs," AIP Conference Proceedings 1556(1), pp. 147-151 (2013) https://doi.org/10.1063/1.4822219.
[56] T. Sogabe, A. Ogura, C. Y. Hung, V. Evstropov, M. Mintairov, M. Shvarts and Y. Okada, "Experimental characterization and self-consistent modeling of luminescence coupling effect in III-V multijunction solar cells," Applied Physics Letters 103(26), p. 263907 (2013) https://doi.org/10.1063/1.4858970.
[57] A.S. Brown and M.A. Green, "Limiting efficiency for current-constrained two-terminal tandem cell stacks," Progress in Photovoltaics: Research and Applications 10(5), pp. 299-307 (2002) https://doi.org/10.1002/pip.425.
[58] A. Marti and G.L. Araújo, "Limiting efficiencies for photovoltaic energy conversion in multigap systems," Solar Energy Materials and Solar Cells 43(2), pp. 203-222 (1996) https://doi.org/10.1016/0927-0248(96)00015-3.
[59] A. De Vos, "Detailed balance limit of the efficiency of tandem solar cells," Journal of Physics D: Applied Physics 13(5), p. 839 (1980) https://doi.org/10.1088/0022-3727/13/5/018.
[60] A. Feltrin and A. Freundlich, "Material considerations for terawatt level deployment of photovoltaics," Renewable Energy 33(2), pp. 180-185 (2008) https://doi.org/10.1016/j.renene.2007.05.024.
[61] G.K. Singh, "Solar power generation by PV (photovoltaic) technology: A review," Energy 53, pp. 1-13 (2013) https://doi.org/10.1016/j.energy.2013.02.057.
[62] Solar Junction, "Multi-junction solar cell," accessed May 22, 2019 http://www.sj-solar.com/technology/.
[63] L. Banyai and S.W. Koch, "Chapter 2 – Theoretical Concepts," in *Semiconductor Quantum Dots*, World Scientific Series on Atomic, Molecular and Optical Physics (1993).
[64] Y.Z. Hu, H. Gie, N. Peyghambarian, and S.W. Koch, "Microscopic theory of optical gain in small semiconductor quantum dots," Physical Review B 53(8), p. 4814 (1996) https://doi.org/10.1103/PhysRevB.53.4814.
[65] S.E. Laux and F. Stern, "Electron states in narrow gate-induced channels in Si," Applied Physics Letters 49(2), pp. 91-93 (1986) https://doi.org/10.1063/1.97361.
[66] L.E. Brus, "Electron–electron and electron-hole interactions in small semiconductor crystallites: The size dependence of the lowest excited electronic state," The Journal of Chemical Physics 80(9), pp. 4403-4409 (1984) https://doi.org/10.1063/1.447218.
[67] O.E. Semonin, J.M. Luther, and M.C. Beard, "Quantum dots for next-generation photovoltaics," Materials Today 15(11), pp. 508-515 (2012) https://doi.org/10.1016/S1369-7021(12)70220-1.
[68] M.C. Beard, A.G. Midgett, M.C. Hanna, J.M. Luther, B.K. Hughes, and A.J. Nozik, "Comparing multiple exciton generation in quantum dots to impact ionization in bulk semiconductors: implications for enhancement of solar energy conversion," Nano Letters 10(8), pp. 3019-3027 (2010) https://doi.org/10.1021/nl101490z.
[69] P.M. Petroff and S.P. DenBaars, "MBE and MOCVD growth and properties of self-assembling quantum dot arrays in III-V semiconductor structures," Superlattices and Microstructures 15(1), p. 15 (1994) https://doi.org/10.1006/spmi.1994.1004.
[70] D. Bimberg, M. Grundmann, N.N. Ledentsov, S.S. Ruvimov, P. Werner, U. Richter, J. Heydenreich, V.M. Ustinov, P.S. Kop'ev, and Z.I. Alferov, "Self-organization processes in MBE-grown quantum dot structures," Thin Solid Films 267(1-2), pp. 32-36 (1995) https://doi.org/10.1016/0040-6090(95)06597-0.
[71] R. Oshima, A. Takata, and Y. Okada, "Strain-compensated InAs/GaNAs quantum dots for use in high-efficiency solar cells," Applied Physics Letters 93(8), p. 083111 (2008) https://doi.org/10.1063/1.2973398.
[72] S.F. Tang, S.Y. Lin, and S.C. Lee, "Near-room-temperature operation of an InAs/GaAs quantum-dot infrared photodetector," Applied Physics Letters 78(17), pp. 2428-2430 (2001) https://doi.org/10.1063/1.1362201.
[73] K. Akahane, N. Yamamoto, and T. Kawanishi, "Fabrication of ultra-high-density InAs quantum dots using the strain-compensation technique," Physica Status Solidi (a) 208(2), pp. 425-428 (2011) https://doi.org/10.1002/pssa.201000432.
[74] Y.J. Chun, S. Nakajima, Y. Okada, and M. Kawabe, "The role of atomic hydrogen for formation of quantum dots by self-organizing process in MBE," Physica B: Condensed Matter 227(1-4), pp. 299-302 (1996) https://doi.org/10.1016/0921-4526(96)00425-5.
[75] Y. Okada, R. Oshima, and A. Takata, "Characteristics of InAs/GaNAs strain-compensated quantum dot solar cell," Journal of Applied Physics 106(2), p. 024306 (2009) https://doi.org/10.1063/1.3176903.
[76] C.B. Murray, M. Nirmal, D.J. Norris, and M.G. Bawendi, "Synthesis and structural characterization of II–VI semiconductor nanocrystallites (quantum dots)," Zeitschrift für Physik D Atoms, Molecules and Clusters 26(1), pp. 231-233 (1993) https://doi.org/10.1007/BF01425674.

[77] M. Danek, K.F. Jensen, C.B. Murray, and M.G. Bawendi, "Synthesis of luminescent thin-film CdSe/ZnSe quantum dot composites using CdSe quantum dots passivated with an overlayer of ZnSe," Chemistry of Materials 8(1), pp. 173-180 (1996) https://doi.org/10.1021/cm9503137.
[78] J. Tang, K.W. Kemp, S. Hoogland, K.S. Jeong, H. Liu, L. Levina, M. Furukawa, X. Wang, R. Debnath, D. Cha, and K.W. Chou, "Colloidal-quantum-dot photovoltaics using atomic-ligand passivation," Nature Materials 10(10), p. 765 (2011) https://doi.org/10.1038/nmat3118.
[79] S.A. McDonald, G. Konstantatos, S. Zhang, P.W. Cyr, E.J. Klem, L. Levina, and E.H. Sargent, "Solution-processed PbS quantum dot infrared photodetectors and photovoltaics," Nature Materials 4(2), p. 138 (2005) https://doi.org/10.1038/nmat1299.
[80] H. Wang, T. Kubo, J. Nakazaki, T. Kinoshita, and H. Segawa, "PbS-quantum-dot-based heterojunction solar cells utilizing ZnO nanowires for high external quantum efficiency in the near-infrared region," The Journal of Physical Chemistry Letters 4(15), pp. 2455-2460 (2013) https://doi.org/10.1021/jz4012299.
[81] B.L. Wehrenberg and P. Guyot-Sionnest, "Electron and hole injection in PbSe quantum dot films," Journal of the American Chemical Society 125(26), pp. 7806-7807 (2003) https://doi.org/10.1021/ja035369d.
[82] Y. Chen and Z. Rosenzweig, "Luminescent CdS quantum dots as selective ion probes," Analytical Chemistry 74(19), pp. 5132-5138 (2002) https://doi.org/10.1021/ac0258251.
[83] K.J. Nordell, E.M. Boatman, and G.C. Lisensky, "A safer, easier, faster synthesis for CdSe quantum dot nanocrystals," Journal of Chemical Education 82(11), p. 1697 (2005) https://doi.org/10.1021/ed082p1697.
[84] X. Peng, L. Manna, W. Yang, J. Wickham, E. Scher, A. Kadavanich, and A.P. Alivisatos, "Shape control of CdSe nanocrystals," Nature 404(6773), p. 59 (2000) https://doi.org/10.1038/35003535.
[85] T. Rajh, O.I. Micic, and A.J. Nozik, "Synthesis and characterization of surface-modified colloidal cadmium telluride quantum dots," The Journal of Physical Chemistry 97(46), pp. 11999-12003 (1993) https://doi.org/10.1021/j100148a026.
[86] S.F. Wuister, I. Swart, F. van Driel, S.G. Hickey, and C. de Mello Donegá, "Highly luminescent water-soluble CdTe quantum dots," Nano Letters 3(4), pp. 503-507 (2003) https://doi.org/10.1021/nl034054t.
[87] Y. Zheng, S. Gao, and J.Y. Ying, "Synthesis and cell-imaging applications of glutathione-capped CdTe quantum dots," Advanced Materials 19(3), pp. 376-380 (2007) https://doi.org/10.1002/adma.200600342.
[88] J. Song, J. Li, X. Li, L. Xu, Y. Dong, and H. Zeng, "Quantum dot light-emitting diodes based on inorganic perovskite cesium lead halides ($CsPbX_3$)," Advanced Materials 27(44), pp. 7162-7167 (2015) https://doi.org/10.1002/adma.201502567.
[89] J. Pan, L.N. Quan, Y. Zhao, W. Peng, B. Murali, S.P. Sarmah, M. Yuan, L. Sinatra, N.M. Alyami, J. Liu, and E. Yassitepe, "Highly Efficient Perovskite-Quantum-Dot Light-Emitting Diodes by Surface Engineering," Advanced Materials 28(39), pp. 8718-8725 (2016) https://doi.org/10.1002/adma.201600784.
[90] X. Li, Y. Wu, S. Zhang, B. Cai, Y. Gu, J. Song, and H. Zeng, "$CsPbX_3$ quantum dots for lighting and displays: room-temperature synthesis, photoluminescence superiorities, underlying origins and white light-emitting diodes," Advanced Functional Materials, 26(15), pp. 2435-2445 (2016) https://doi.org/10.1002/adfm.201600109.
[91] Z. Shi, Y. Li, Y. Zhang, Y. Chen, X. Li, D. Wu, T. Xu, C. Shan, and G. Du, "High-efficiency and air-stable perovskite quantum dots light-emitting diodes with an all-inorganic heterostructure," Nano Letters 17(1), pp.313-321 (2016) https://doi.org/10.1021/acs.nanolett.6b04116.
[92] C. Sun, Y. Zhang, C. Ruan, C. Yin, X. Wang, Y. Wang, and W.W. Yu, "Efficient and stable white LEDs with silica-coated inorganic perovskite quantum dots," Advanced Materials 28(45), pp. 10088-10094 (2016) https://doi.org/10.1002/adma.201603081.
[93] Y. Wang, X. Li, V. Nalla, H. Zeng, and H. Sun, "Solution-processed low threshold vertical cavity surface emitting lasers from all-inorganic perovskite nanocrystals," Advanced Functional Materials 27(13), p.1605088 (2017) https://doi.org/10.1002/adfm.201605088.
[94] R.J. Sutton, G.E. Eperon, L. Miranda, E.S. Parrott, B.A. Kamino, J.B. Patel, M.T. Hörantner, M.B. Johnston, A.A. Haghighirad, D.T. Moore, and H.J. Snaith, "Bandgap-tunable cesium lead halide perovskites with high thermal stability for efficient solar cells," Advanced Energy Materials 6(8), p. 1502458 (2016) https://doi.org/10.1002/aenm.201502458.
[95] G. Nedelcu, L. Protesescu, S. Yakunin, M.I. Bodnarchuk, M.J. Grotevent, and M.V. Kovalenko, "Fast anion-exchange in highly luminescent nanocrystals of cesium lead halide perovskites ($CsPbX_3$, X= Cl, Br, I)," Nano Letters 15(8), pp. 5635-5640 (2015) https://doi.org/10.1021/acs.nanolett.5b02404.
[96] R.E. Beal, D.J. Slotcavage, T. Leijtens, A.R. Bowring, R.A. Belisle, W.H. Nguyen, G.F. Burkhard, E.T. Hoke, and M.D. McGehee, "Cesium lead halide perovskites with improved stability for tandem solar cells," The Journal of Physical Chemistry Letters 7(5), pp. 746-751 (2016) https://doi.org/10.1021/acs.jpclett.6b00002.
[97] Y. Wang, X. Li, J. Song, L. Xiao, H. Zeng, and H. Sun, "All-inorganic colloidal perovskite quantum dots: a new class of lasing materials with favorable characteristics," Advanced Materials 27(44), pp. 7101-7108 (2015) https://doi.org/10.1002/adma.201503573.

[98] Y. Su, X. Chen, W. Ji, Q. Zeng, Z. Ren, Z. Su, and L. Liu, "Highly controllable and efficient synthesis of mixed-halide $CsPbX_3$ (X= Cl, Br, I) perovskite QDs toward the tunability of entire visible light," ACS Applied Materials & Interfaces 9(38), pp. 33020-33028 (2017) https://doi.org/10.1021/acsami.7b10612.
[99] A. Swarnkar, A.R. Marshall, E.M. Sanehira, B.D. Chernomordik, D.T. Moore, J.A. Christians, T. Chakrabarti, and J.M. Luther, "Quantum dot–induced phase stabilization of α-CsPbI3 perovskite for high-efficiency photovoltaics," Science 354(6308), pp. 92-95 (2016) https://doi.org/10.1126/science.aag2700.
[100] L. Protesescu, S. Yakunin, M.I. Bodnarchuk, F. Krieg, R. Caputo, C.H. Hendon, R.X. Yang, A. Walsh, and M.V. Kovalenko, "Nanocrystals of cesium lead halide perovskites ($CsPbX_3$, X= Cl, Br, and I): novel optoelectronic materials showing bright emission with wide color gamut," Nano Letters 15(6), pp. 3692-3696 (2015) https://doi.org/10.1021/nl5048779.
[101] E. Yassitepe, Z. Yang, O. Voznyy, Y. Kim, G. Walters, J.A. Castañeda, P. Kanjanaboos, M. Yuan, X. Gong, F. Fan, and J. Pan, "Amine-free synthesis of cesium lead halide perovskite quantum dots for efficient light-emitting diodes," Advanced Functional Materials 26(47), pp. 8757-8763 (2016) https://doi.org/10.1002/adfm.201604580.
[102] Z.K. Tan, R.S. Moghaddam, M.L. Lai, P. Docampo, R. Higler, F. Deschler, M. Price, A. Sadhanala, L.M. Pazos, D. Credgington, and F. Hanusch, "Bright light-emitting diodes based on organometal halide perovskite," Nature Nanotechnology 9(9), p. 687 (2014) https://doi.org/10.1038/nnano.2014.149.
[103] H. Cho, S.H. Jeong, M.H. Park, Y.H. Kim, C. Wolf, C.L. Lee, H.J. Heo, A. Sadhanala, N. Myoung, S. Yoo, and S.H. Im, "Overcoming the electroluminescence efficiency limitations of perovskite light-emitting diodes," Science 350(6265), pp. 1222-1225 (2015) https://doi.org/10.1126/science.aad1818.
[104] H. Huang, F. Zhao, L. Liu, F. Zhang, X.G. Wu, L. Shi, B. Zou, Q. Pei, and H. Zhong, "Emulsion synthesis of size-tunable $CH_3NH_3PbBr_3$ quantum dots: an alternative route toward efficient light-emitting diodes," ACS Applied Materials & Interfaces 7(51), pp. 28128-28133 (2015) https://doi.org/10.1021/acsami.5b10373.
[105] Y.H. Kim, H. Cho, J.H. Heo, T.S. Kim, N. Myoung, C.L. Lee, S.H. Im, and T.W. Lee, "Multicolored organic/inorganic hybrid perovskite light-emitting diodes," Advanced Materials 27(7), pp. 1248-1254 (2015) https://doi.org/10.1002/adma.201403751.
[106] H. Huang, A.S. Susha, S.V. Kershaw, T.F. Hung, and A.L. Rogach, "Control of emission color of high quantum yield $CH_3NH_3PbBr_3$ perovskite quantum dots by precipitation temperature," Advanced Science 2(9), p. 1500194 (2015) https://doi.org/10.1002/advs.201500194.
[107] Z. Shi, X. Li, and C. Shan, "Perovskite Quantum Dot Light-Emitting Diodes," in *Quantum-dot Based Light-emitting Diodes*, IntechOpen, p.47 (2017).
[108] W.S. Yang, B.W. Park, E.H. Jung, N.J. Jeon, Y.C. Kim, D.U. Lee, S.S. Shin, J. Seo, E.K. Kim, J.H. Noh, and S.I. Seok, "Iodide management in formamidinium-lead-halide–based perovskite layers for efficient solar cells," Science 356(6345), pp. 1376-1379 (2017) https://doi.org/10.1126/science.aan2301.
[109] M.A. Hines and P. Guyot-Sionnest, "Synthesis and characterization of strongly luminescing ZnS-capped CdSe nanocrystals," The Journal of Physical Chemistry 100(2), pp. 468-471 (1996) https://doi.org/10.1021/jp9530562.
[110] P.V. Kamat, "Quantum dot solar cells. Semiconductor nanocrystals as light harvesters," The Journal of Physical Chemistry C 112(48), pp. 18737-18753 (2008) https://doi.org/10.1021/jp806791s.
[111] O.E. Semonin, J.M. Luther, S. Choi, H.Y. Chen, J. Gao, A.J. Nozik, and M.C. Beard, "Peak external photocurrent quantum efficiency exceeding 100% via MEG in a quantum dot solar cell," Science 334(6062), pp. 1530-1533 (2011) https://doi.org/10.1126/science.1209845.
[112] A.J. Nozik, "Quantum dot solar cells," Physica E: Low-dimensional Systems and Nanostructures 14(1-2), pp. 115-120 (2002) https://doi.org/10.1016/S1386-9477(02)00374-0.
[113] S.-C. Hsu, Y.-C. Kao, H.-V. Han, H.-C. Kuo, R.-H. Horng, C.-C. Lin, "Colloidal quantum dot enhanced dual-junction tandem solar cells," Proc. 43rd IEEE Photovoltaic Specialists Conference (PVSC-43), pp. 144-146 (2016) https://doi.org/10.1109/PVSC.2016.7749565.
[114] G. Conibeer, M. Green, E.C. Cho, D. König, Y.H. Cho, T. Fangsuwannarak, G. Scardera, E. Pink, Y. Huang, T. Puzzer, and S. Huang, "Silicon quantum dot nanostructures for tandem photovoltaic cells," Thin Solid Films 516(20), pp. 6748-6756 (2008) https://doi.org/10.1016/j.tsf.2007.12.096.
[115] A. Karani, L. Yang, S. Bai, M.H. Futscher, H.J. Snaith, B. Ehrler, N.C. Greenham, and D. Di, "Perovskite/colloidal quantum dot tandem solar cells: theoretical modeling and monolithic structure," ACS Energy Letters 3(4), pp. 869-874 (2018) https://doi.org/10.1021/acsenergylett.8b00207.
[116] A. Braun, N. Szabó, K. Schwarzburg, T. Hannappel, E.A. Katz, and J.M. Gordon, "Current-limiting behavior in multijunction solar cells," Applied Physics Letters 98(22), p. 223506 (2011) https://doi.org/10.1063/1.3596444.
[117] S. Essig, J.F. Geisz, M.A. Steiner, A. Merkle, R. Peibst, J. Schmidt, R. Brendel, S. Ward, D.J. Friedman, P. Stradins, and D.L. Young, "Development of highly-efficient GaInP/Si tandem solar cells," Proc. 42nd IEEE Photovoltaic Specialists Conference (PVSC-42), pp. 1-4 (2015) https://doi.org/10.1109/PVSC.2015.7355602.

[118] M. A. Steiner, M. W. Wanlass, J. J. Carapella, A. Duda, J. S. Ward, T. E. Moriarty, K. A. Emery, "A Monolithic Three-terminal GaInAsP/GaInAs Tandem Solar Cell," Progress in Photovoltaics: Research and Applications 17(8), pp. 587-593 (2009) https://doi.org/10.1002/pip.913.
[119] S.M. Durbin and J.L. Gray, "Numerical modeling of photon recycling in solar cells," IEEE Transactions on Electron Devices 41(2), pp. 239-245 (1994) https://doi.org/10.1109/16.277372.
[120] J.L. Balenzategui, A. Martí, and G.L. Araújo, "Numerical modeling of photon recycling effects in solar cells using PC-1d," Proc. 13th European Photovoltaic Solar Energy Conference (EUPVSEC-13) p. 1223-1226 (1995).
[121] J.L. Balenzategui and A. Marti, "Detailed modeling of photon recycling: application to GaAs solar cells," Solar Energy Materials and Solar Cells 90(7-8), pp. 1068-1088 (2006) https://doi.org/10.1016/j.solmat.2005.06.004.
[122] P. Asbeck, "Self-absorption effects on the radiative lifetime in GaAs-GaAlAs double heterostructures," Journal of Applied Physics 48(2), pp. 820-822 (1977) https://doi.org/10.1063/1.323633.
[123] M.A. Steiner, J.F. Geisz, I. Garcia, D.J. Friedman, A. Duda, and S.R. Kurtz, "Optical enhancement of the open-circuit voltage in high quality GaAs solar cells," Journal of Applied Physics 113(12), p. 123109 (2013) https://doi.org/10.1063/1.4798267.
[124] T. Kraus, O. Höhn, H. Hauser, and B. Bläsi, "Optoelectronic simulation of GaAs solar cells with angularly selective filters," Journal of Applied Physics 115(5), p. 053103 (2014) https://doi.org/10.1063/1.4863775.
[125] A.W. Walker, O. Höhn, D.N. Micha, B. Bläsi, A.W. Bett, and F. Dimroth, "Impact of photon recycling on GaAs solar cell designs," IEEE Journal of Photovoltaics 5(6), pp. 1636-1645 (2015) https://doi.org/10.1109/JPHOTOV.2015.2479463.
[126] M. Wilkins, C.E. Valdivia, S. Chahal, M. Ishigaki, D.P. Masson, S. Fafard, and K. Hinzer, "Performance impact of luminescent coupling on monolithic 12-junction phototransducers for 12 V photonic power systems," Proc. SPIE Physics, Simulation, and Photonic Engineering of Photovoltaic Devices V 9743, p. 97430W (2016) https://doi.org/10.1117/12.2213727.
[127] K. Araki, Y. Ota, K.H. Lee, T. Sakai, K. Nishioka, and M. Yamaguchi, "Analysis of fluctuation of atmospheric parameters and its impact on performance of CPV," AIP Conference Proceedings 2012(1), p. 080002 (2018) https://doi.org/10.1063/1.5053530.
[128] Y. P. Varshni, "Temperature dependence of the energy gap in semiconductors," Physica 34(1), pp. 149-154 (1967) https://doi.org/10.1016/0031-8914(67)90062-6.
[129] P. Würfel, *Physics of solar cells: From principles to new concepts*, Verlag GmbH & Co KGaA (2005).
[130] M. Ochoa, M.A. Steiner, I. García, J.F. Geisz, D.J. Friedman, and C. Algora, "Influence of temperature on luminescent coupling and material quality evaluation in inverted lattice-matched and metamorphic multi-junction solar cells," Progress in Photovoltaics: Research and Applications 24(3), pp. 357-367 (2016) https://doi.org/10.1002/pip.2714.
[131] E. F. Schubert, "Chapter 5 – Theory of radiative recombination," in *Light-Emitting Diodes*, 3rd ed., Cambridge University Press, New York, pp. 91-93 (2018).
[132] V. Paraskeva, C. Lazarou, M. Hadjipanayi, M. Norton, M. Pravettoni, G.E. Georghiou, M. Heilmann, and S. Christiansen, "Photoluminescence analysis of coupling effects: The impact of shunt resistance and temperature," Solar Energy Materials and Solar Cells 130, pp. 170-181 (2014) https://doi.org/10.1016/j.solmat.2014.07.008.
[133] R.G. Ross, Jr. and M.I. Smokler, "Electricity from photovoltaic solar cells: flat-plate solar array project final report," Volume VI: Engineering Sciences and Reliability, JPL Publication 86–31, NASA, Springfield, Virginia (1986).
[134] R.G. Ross, Jr., "Flat-plate photovoltaic array design optimization," Proc. 14th IEEE Photovoltaic Specialist Conference (PVSC-14), pp. 1126-1132 (1980).
[135] M.A.M. Shaltout, A. Ghettas, and M. Sabry, "V-trough concentrator on photovoltaic full tracking system at hot desert climate," Renewable Energy 6(5-6), pp. 527-532 (1995) https://doi.org/10.1016/0960-1481(95)00055-O.
[136] A. Akbarzadeh and T. Wadowski, "Heat pipe-based cooling systems for photovoltaic cells under concentrated solar radiation," Applied Thermal Engineering 16(1), pp. 81-87 (1996) https://doi.org/10.1016/1359-4311(95)00012-3.
[137] P. Rodrigo, E.F. Fernández, F. Almonacid, and P.J. Pérez-Higueras, "Review of methods for the calculation of cell temperature in high concentration photovoltaic modules for electrical characterization," Renewable and Sustainable Energy Reviews 38, pp. 478-488 (2014) https://doi.org/10.1016/j.rser.2014.06.008.
[138] G.S. Kinsey, P. Hebert, K.E. Barbour, D.D. Krut, H.L. Cotal, and R.A. Sherif, "Concentrator multijunction solar cell characteristics under variable intensity and temperature," Progress in Photovoltaics: Research and Applications 16(6), pp. 503-508 (2008) https://doi.org/10.1002/pip.834.
[139] D.J. Friedman, J.F. Geisz, and M.A. Steiner, "Effect of luminescent coupling on the optimal design of multijunction solar cells," IEEE Journal of Photovoltaics 4(3), pp. 986-990 (2014) https://doi.org/10.1109/JPHOTOV.2014.2308722.

[140] C.R. Allen, S.H. Lim, J.J. Li, and Y.H. Zhang, "Simple method for determining luminescence coupling in multi-junction solar cells," Proc. 37th IEEE Photovoltaic Specialist Conference (PVSC-37), pp. 452-453 (2011) https://doi.org/10.1109/PVSC.2011.6185991.
[141] B.M.F. Yu Jeco, T. Sogabe, A. Ogura, N. Miyashita, R. Tamaki, and Y. Okada, "Laser beam induced current (LBIC) mapping of InGaP/GaAs/Ge triple-junction solar cells with luminescence coupling," Proc. 43rd IEEE Photovoltaic Specialist Conference (PVSC-43), pp. 1229-1234 (2016) https://doi.org/10.1109/PVSC.2016.7749810.
[142] J.P. Babaro, K.G. West, and B.H. Hamadani, "Spectral response measurements of multijunction solar cells with low shunt resistance and breakdown voltages," Energy Science & Engineering 4(6), pp. 372-382 (2016) https://doi.org/10.1002/ese3.141.
[143] M.A. Steiner and J.F. Geisz, "Non-linear luminescent coupling in series-connected multijunction solar cells," Applied Physics Letters 100(25), p. 251106 (2012) https://doi.org/10.1063/1.4729827.
[144] J.F. Geisz, M.A. Steiner, I. García, R.M. France, W.E. McMahon, C.R. Osterwald, and D.J. Friedman, "Generalized optoelectronic model of series-connected multijunction solar cells," IEEE Journal of Photovoltaics 5(6), pp. 1827-1839 (2015) https://doi.org/10.1109/JPHOTOV.2015.2478072.
[145] Y. Miao, J. Jia, Y. Kang, Y. Huo, M. Mazouchi, Y. Chen, H. Deng, P. Supaniratisai, S.H. AlQahtani, L. Zhao, and J.S. Harris, "Dependency of Luminescent Coupling Efficiency on Bias Voltage and Illumination Intensity," Proc. OSA Optical Nanostructures and Advanced Materials for Photovoltaics, pp. PTu3C-3 (2014) https://doi.org/10.1364/PV.2014.PTu3C.3.
[146] M. Meusel, C. Baur, G. Létay, A. W. Bett, W. Warta, and E. Fernandez, "Spectral response measurements of monolithic GaInP/Ga (In) As/Ge triple-junction solar cells: Measurement artifacts and their explanation," Progress in Photovoltaics: Research and Applications 11(8), pp. 499-514 (2003) https://doi.org/10.1002/pip.514.
[147] M.A. Steiner, S.R. Kurtz, J.F. Geisz, W.E. McMahon, and J.M. Olson, "Using phase effects to understand measurements of the quantum efficiency and related luminescent coupling in a multijunction solar cell," IEEE Journal of Photovoltaics 2(4), pp. 424-433 (2012) https://doi.org/10.1109/JPHOTOV.2012.2206566.
[148] G. Siefer, C. Baur, and A. W. Bett, "External quantum efficiency measurements of germanium bottom subcells: Measurement artifacts and correction procedures," Proc. 35th IEEE Photovoltaic Specialist Conference (PVSC-35), pp. 704-707 (2010) https://doi.org/10.1109/PVSC.2010.5616919.
[149] J.J. Li, S.H. Lim, C.R. Allen, D. Ding, and Y.H. Zhang, "Combined effects of shunt and luminescence coupling on external quantum efficiency measurements of multijunction solar cells," IEEE Journal of Photovoltaics 1(2), pp. 225-230 (2011) https://doi.org/10.1109/JPHOTOV.2011.2172188.
[150] M. Wilkins, C.E. Valdivia, A.M. Gabr, D. Masson, S. Fafard, and K. Hinzer, "Luminescent coupling in planar opto-electronic devices," Journal of Applied Physics 118(14), p. 143102 (2015) https://doi.org/10.1063/1.4932660.
[151] C.E. Valdivia, M.M. Wilkins, B. Bouzazi, A. Jaouad, V. Aimez, R. Arès, D.P. Masson, S. Fafard, and K. Hinzer, "Five-volt vertically-stacked, single-cell GaAs photonic power converter," Proc. SPIE Physics, Simulation, and Photonic Engineering of Photovoltaic Devices IV 9358, p. 93580E (2015) https://doi.org/10.1117/12.2079824.
[152] J. Jia, F. Suarez, T. Bilir, V. Sabnis, and J. Harris, "3-D modeling of luminescent coupling effects in multijunction concentrator solar cells," AIP Conference Proceedings 1616(1), pp. 3-7 (2014) https://doi.org/10.1063/1.4897016.
[153] H. Nesswetter, P. Lugli, A.W. Bett, and C.G. Zimmermann, "Electroluminescence and photoluminescence characterization of multijunction solar cells," Proc. 38th IEEE Photovoltaic Specialist Conference (PVSC-38) 2, pp. 1-6 (2012) https://doi.org/10.1109/PVSC-Vol2.2012.6656769.
[154] H. Xu, A. Delamarre, J. Jia, B.M.F. Yu Jeco, K. Watanabe, Y. Okada, J.-F. Guillemoles, Y. Nakano, and M. Sugiyama, "Transport efficiency imaging in multi-junction solar cells by luminescence analysis," Proc. 7th IEEE World Conference on Photovoltaic Energy Conversion (WCPEC-7) pp. 2261-2265 (2018) https://doi.org/10.1109/PVSC.2018.8548208.
[155] D. Lan and M.A. Green, "Photoluminescent and electroluminescent couplings in monolithic tandem solar cells," Progress in Photovoltaics: Research and Applications 24(12), pp. 1566-1576 (2016) https://doi.org/10.1002/pip.2750.
[156] Z. Ren, H. Liu, Z. Liu, C.S. Tan, A.G. Aberle, T. Buonassisi, and I.M. Peters, "The GaAs/GaAs/Si solar cell–Towards current matching in an integrated two terminal tandem," Solar Energy Materials and Solar Cells 160, pp. 94-100 (2017) https://doi.org/10.1016/j.solmat.2016.10.031.
[157] D. Lan, J.F. Geisz, M.A. Steiner, I. Garcia, D.J. Friedman, and M.A. Green, "Improved modeling of photoluminescent and electroluminescent coupling in multijunction solar cells," Solar Energy Materials and Solar Cells 143, pp. 48-51 (2015) https://doi.org/10.1016/j.solmat.2015.06.036.
[158] R.A. Milano, T.H. Windhorn, E.R. Anderson, G.E. Stillman, R.D. Dupuis, and P.D. Dapkus, "$Al_{0.5}Ga_{0.5}As$-GaAs heterojunction phototransistors grown by metalorganic chemical vapor deposition," Applied Physics Letters 34(9), pp. 562-564 (1979) https://doi.org/10.1063/1.90867.

[159] N. Chand, P.A. Houston, and P.N. Robson, "Gain of a heterojunction bipolar phototransistor," IEEE Transactions on Electron Devices 32(3), pp. 622-627 (1985) https://doi.org/10.1109/T-ED.1985.21988.
[160] N. Shigekawa, J. Liang, R. Onitsuka, T. Agui, H. Juso, and T. Takamoto, "Current–voltage and spectral-response characteristics of surface-activated-bonding-based InGaP/GaAs/Si hybrid triple-junction cells," Japanese Journal of Applied Physics 54(8S1), p.08KE03 (2015) https://doi.org/10.7567/JJAP.54.08KE03.
[161] American Society for Testing and Materials (ASTM), "ASTM-G173-03 Standard Tables for Reference Solar Spectral Irradiances: Direct Normal and Hemispherical on 37° Tilted Surface," accessed via National Renewable Energy Laboratory (NREL) website (2012) https://www.nrel.gov/grid/solar-resource/assets/data/astmg173.xls.
[162] S.H. Lim, J.J. Li, E.H. Steenbergen, and Y.H. Zhang, "Luminescence coupling effects on multijunction solar cell external quantum efficiency measurement," Progress in Photovoltaics: Research and Applications 21(3), pp. 344-350 (2013) https://doi.org/10.1002/pip.1215.
[163] M.A. Steiner, J.F. Geisz, J.S. Ward, I. Garcia, D.J. Friedman, R.R. King, P.T. Chiu, R.M. France, A. Duda, W.J. Olavarria, and M. Young, "Optically enhanced photon recycling in mechanically stacked multijunction solar cells," IEEE Journal of Photovoltaics 6(1), pp. 358-365 (2016) https://doi.org/10.1109/JPHOTOV.2015.2494690.
[164] M.Z. Shvarts, V.M. Emelyanov, V.V. Evstropov, M.A. Mintairov, E.D. Filimonov, and S.A. Kozhukhovskaia, "Overcoming the luminescent coupling effect in experimental search for the actual quantum efficiency values in multi-junction solar cells," AIP Conference Proceedings 1766(1), p. 060005 (2016) https://doi.org/10.1063/1.4962095.
[165] T. Tayagaki, K. Makita, H. Mizuno, R. Oshima, and T. Sugaya, "Investigation of the open-circuit voltage in mechanically stacked InGaP/GaAs//InGaAsP/InGaAs solar cells," Japanese Journal of Applied Physics 56(8S2), p.08MC01 (2017) https://doi.org/10.7567/JJAP.56.08MC01.
[166] M.A. Steiner, J.F. Geisz, J.S. Ward, I. García, D.J. Friedman, R.R. King, P.T. Chiu, R.M. France, A. Duda, W.J. Olavarria, and M. Young, "Mechanically stacked four-junction concentrator solar cells," Proc. 42nd IEEE Photovoltaic Specialist Conference (PVSC-42) pp. 1-3 (2015) https://doi.org/10.1109/PVSC.2015.7356151.
[167] J.J. Li and Y.H. Zhang, "Accurate measurement of the external quantum efficiency of multi-junction solar cells," Proc. OSA CLEO: Science and Innovations, pp. CF1J-4 (2012) https://doi.org/10.1364/CLEO_SI.2012.CF1J.4.
[168] T. Sogabe, A. Ogura, M. Ohba, and Y. Okada, "Self-consistent electrical parameter extraction from bias dependent spectral response measurements of III-V multi-junction solar cells," Progress in Photovoltaics: Research and Applications 23(1), pp. 37-48 (2015) https://doi.org/10.1002/pip.2392.
[169] T. Sogabe, A. Ogura, and Y. Okada, "Analysis of bias voltage dependent spectral response in $Ga_{0.51}In_{0.49}P/Ga_{0.99}In_{0.01}As$/Ge triple-junction solar cell," Journal of Applied Physics 115(7), p. 074503 (2014) https://doi.org/10.1063/1.4866321.
[170] B.M.F. Yu Jeco, T. Sogabe, R. Tamaki, N. Ahsan, and Y. Okada, "Impact of optically nonuniform luminescence coupling effect to the limiting cell conversion efficiency in InGaP/GaAs/Ge triple-junction solar cell," Journal of Photonics for Energy 7(3), p.035501 (2017) https://doi.org/10.1117/1.JPE.7.035501.
[171] B.M.F. Yu Jeco, R. Tamaki, T. Nakamura, M. Imaizumi, N. Ahsan, and Y. Okada, "Spatial evaluation of luminescent coupling effect in a current-limiting subcell of InGaP/GaAs/Ge triple-junction solar cells," Proc. 7th IEEE World Conference on Photovoltaic Energy Conversion (WCPEC-7) pp. 969-974 (2018) https://doi.org/10.1109/PVSC.2018.8547432.
[172] B.M.F. Yu Jeco, E. Veinberg-Vidal, L. Vauche, K. Yoshida, R. Tamaki, N. Ahsan, and Y. Okada, "Luminescent coupling effect in wafer-bonded III-V on silicon multijunction solar cells," Journal of Photonics for Energy 9(1), p.015504 (2019) https://doi.org/10.1117/1.JPE.9.015504.
[173] B.M.F. Yu Jeco, E. Veinberg-Vidal, L. Vauche, N. Ahsan, and Y. Okada, "Temperature dependence of wafer-bonded III-V on silicon multijunction solar cells with luminescent coupling effect," Journal of Photonics for Energy 9(1), p.015503 (2019) https://doi.org/10.1117/1.JPE.9.015503.
[174] S.P. Bremner, C. Yi, I. Almansouri, A. Ho-Baillie, and M.A. Green, "Optimum band gap combinations to make best use of new photovoltaic materials," Solar Energy 135, pp. 750-757 (2016) https://doi.org/10.1016/j.solener.2016.06.042.
[175] J.F. Geisz, I. García, W.E. McMahon, M.A. Steiner, M. Ochoa, R.M. France, A. Habte, and D.J. Friedman, "Energy yield determination of concentrator solar cells using laboratory measurements," AIP Conference Proceedings 1679(1), p. 040005 (2015) https://doi.org/10.1063/1.4931516.
[176] M. Yoshita, L. Zhu, C. Kim, T. Mochizuki, T. Nakamura, M. Imaizumi, S. Chen, H. Kubota, Y. Kanemitsu, and H. Akiyama, "Calibration standards and measurement accuracy of absolute electroluminescence and internal properties in multi-junction and arrayed solar cells," Proc. SPIE Physics, Simulation, and Photonic Engineering of Photovoltaic Devices V 9743, p. 97430D (2016) https://doi.org/10.1117/12.2211726.

[177] S. Chen, L. Zhu, Y. Masahiro, T. Mochizuki, C. Kim, H. Akiyama, M. Imaizumi and Y. Kanemitsu, "Thorough subcells diagnosis in a multi-junction solar cell via absolute electroluminescence-efficiency measurements," Scientific reports 5, p. 7836 (2015) https://doi.org/10.1038/srep07836.
[178] H. Nesswetter, N.R. Jost, P. Lugli, A.W. Bett, and C.G. Zimmermann, "Determination of subcell I–V characteristics of multijunction solar cells using optical coupling," Progress in Photovoltaics: Research and Applications 24(6), pp. 760-773 (2016) https://doi.org/10.1002/pip.2722.
[179] H. Nesswetter, N.R. Jost, P. Lugli, A.W. Bett, and C.G. Zimmermann, "Determination of subcell IV parameters by a pulsed suns-Voc method including optical coupling," Applied Physics Letters 106(2), p. 023903 (2015) https://doi.org/10.1063/1.4906237.
[180] M. Wolf and H. Rauschenbach, "Series resistance effects on solar cell measurements," Advanced Energy Conversion 3(2), pp. 455-479 (1963) https://doi.org/10.1016/0365-1789(63)90063-8.
[181] R.M. France, J.F. Geisz, I. Garcia, M.A. Steiner, W.E. McMahon, D.J. Friedman, T.E. Moriarty, C. Osterwald, J.S. Ward, A. Duda, and M. Young, "Quadruple-junction inverted metamorphic concentrator devices," IEEE Journal of Photovoltaics 5(1), pp. 432-437 (2014) https://doi.org/10.1109/JPHOTOV.2014.2364132.
[182] D.F. Marrón, E. Barrigón, M. Ochoa, and I. Artacho, "Quantitative determination of luminescent coupling in multijunction solar cells from spectral photovoltage measurements," Physical Review Applied 6(1), p. 014001 (2016) https://doi.org/10.1103/PhysRevApplied.6.014001.
[183] T.K. Sharma and T.J. Hosea, "A Method of Obtaining Simultaneous Complementary Spectroscopic Information on Self-Assembled Quantum Dots," Japanese Journal of Applied Physics 48(8R), p. 082301 (2009) https://doi.org/10.1143/JJAP.48.082301.
[184] D.F. Marrón, E. Cánovas, I. Artacho, C.R. Stanley, M. Steer, T. Kaizu, Y. Shoji, N. Ahsan, Y. Okada, E. Barrigón, and I. Rey-Stolle, "Application of photoreflectance to advanced multilayer structures for photovoltaics," Materials Science and Engineering: B 178(9), pp. 599-608 (2013) https://doi.org/10.1016/j.mseb.2012.11.012.
[185] B.M.F. Yu Jeco, K. Yoshida, R. Tamaki, N. Ahsan, and Y. Okada, "Analysis of current generation in InGaP/GaAs/Ge triple-junction solar cells with optically non-uniform luminescence coupling effect," Proc. 33th European Photovoltaic Solar Energy Conference (EUPVSEC-33), pp. 1236-1240 (2017) https://doi.org/10.4229/EUPVSEC20172017-4DO.4.5.
[186] H. Xu, A. Delamarre, B.M.F. Yu Jeco, H. Johnson, K. Watanabe, Y. Okada, J.-F. Guillemoles, Y. Nakano, and M. Sugiyama, "Current transport efficiency analysis of multi-junction solar cells by luminescence imaging," Progress in Photovoltaics: Research and Applications, *forthcoming* https://doi.org/10.1002/pip.3140.
[187] M. Shvarts, V. Emelyanov, M. Mintairov, V. Evstropov, and N. Timoshina, "Temperature influence on luminescent coupling efficiency in concentrator MJ SCs," AIP Conference Proceedings 1679, p. 120003 (2015) https://doi.org/10.1063/1.4931560.
[188] J. Jia, Z. Lyu, M. Yuan, Y. Chen, Y. Huo, T. Bilir, Y. Miao, M. Xue, and J.S. Harris, "Accurate characterization of luminescent coupling effects with voltage and light bias adjustment," Proc. 43rd IEEE Photovoltaic Specialist Conference (PVSC-43), pp. 1229-1234 (2016) https://doi.org/10.1109/PVSC.2016.7749809.
[189] L. Vauche, E. Veinberg-Vidal, C. Jany, C. Morales, J. Decobert, C. Dupré, and P. Mur, "Development of III-V on Si multijunction photovoltaics by wafer bonding," Proc. 33th European Photovoltaic Solar Energy Conference (EUPVSEC-33), pp. 1228-1231 (2017) https://doi.org/10.4229/EUPVSEC20172017-4DO.4.3.
[190] R. Cariou, J. Benick, P. Beutel, N. Razek, C. Flötgen, M. Hermle, D. Lackner, S.W. Glunz, A.W. Bett, M. Wimplinger, and F. Dimroth, "Monolithic two-terminal III–V//Si triple-junction solar cells with 30.2% efficiency under 1-Sun AM1. 5G," IEEE Journal of Photovoltaics 7(1), pp. 367-373 (2016) https://doi.org/10.1109/JPHOTOV.2016.2629840.
[191] R. Cariou, J. Benick, F. Feldmann, O. Höhn, H. Hauser, P. Beutel, N. Razek, M. Wimplinger, B. Bläsi, D. Lackner, M. Hermle, G. Siefer, S.W. Glunz, A.W. Bett, and F. Dimroth, "III–V-on-silicon solar cells reaching 33% photoconversion efficiency in two-terminal configuration," Nature Energy 3(4), pp. 326 (2018) https://doi.org/10.1038/s41560-018-0125-0.
[192] L. Vauche, E. Veinberg-Vidal, C. Weick, C. Morales, V. Larrey, C. Lecouvey, M. Martin, J.D. Fonseca, C. Jany, T. Desrues, and C. Brughera, "Wafer bonding approaches for III-V on Si multi-junction solar cells," Proc. 44th IEEE Photovoltaic Specialists Conference (PVSC-44) (2017) https://doi.org/10.1109/PVSC.2016.7749565.
[193] E. Veinberg-Vidal, C. Dupré, P. Garcia-Linares, C. Jany, R. Thibon, T. Card, T. Salvetat, P. Scheiblin, C. Brughera, F. Fournel, and Y. Desieres, "Manufacturing and characterization of III-V on silicon multijunction solar cells," Energy Procedia 92, pp. 242-247 (2016) https://doi.org/10.1016/j.egypro.2016.07.066.
[194] J. Nelson, "Chapter 7 – Monocrystalline Solar Cells," in *The Physics of Solar Cells*, Imperial College, London (2003).
[195] E.D. Stokes and T.L. Chu, "Diffusion lengths in solar cells from short-circuit current measurements," Applied Physics Letters 30(8), pp. 425-426 (1977) https://doi.org/10.1063/1.89433.

[196] H.C. Casey, Jr., D.D. Sell, K.W. Wecht, "Concentration dependence of the absorption coefficient for n− and p− type GaAs between 1.3 and 1.6 eV," Journal of Applied Physics 46(1), pp. 250-257 (1975) https://doi.org/10.1063/1.321330.
[197] M. Yamaguchi, T. Takamoto, K. Araki, and N. Ekins-Daukes, "Multi-junction III–V solar cells: current status and future potential," Solar Energy 79(1), pp.78-85 (2005) https://doi.org/10.1016/j.solener.2004.09.018.
[198] ASTM Standard Reference Spectra G173-03, "Standard tables for reference solar spectral irradiances: direct normal and hemispherical on 37° tilted surface," ASTM International, West Conshohocken, Pennsylvania (2012).
[199] D.J. Aiken, "Antireflection coating design for series interconnected multi-junction solar cells," Progress in Photovoltaics: Research and Applications 8(6), pp. 563-570 (2000) https://doi.org/10.1002/1099-159X(200011/12)8:6<563::AID-PIP327>3.0.CO;2-8.
[200] A.W. Walker, J.F. Wheeldon, O. Thériault, M.D. Yandt, and K. Hinzer, "Temperature dependent external quantum efficiency simulations and experimental measurement of lattice matched quantum dot enhanced multi-junction solar cells," Proc. 37th IEEE Photovoltaic Specialists Conference (PVSC-37), pp. 564-569 (2011) https://doi.org/10.1109/PVSC.2011.6186018.
[201] K. Nishioka, T. Takamoto, W. Nakajima, T. Agui, M. Kaneiwa, Y. Uraoka, and T. Fuyuki, "Analysis of triple-junction solar cell under concentration by SPICE," Proc. 3rd IEEE World Conference on Photovoltaic Energy Conversion (WCPEC-3) 1, pp. 869-872 (2003) http://ieeexplore.ieee.org/document/1305421/.
[202] K. R. McIntosh and C. B. Honsberg, "The influence of edge recombination on a solar cell's IV curve," roc. 16th Photovoltaic Solar Energy Conference and Exhibition (PVSEC-16), 1651-1654 (2000).
[203] M. Hermle, J. Dicker, W. Warta, S.W. Gulnz, and G. Willeke, "Analysis of edge recombination for high-efficiency solar cells at low illumination densities," Proc. 3rd IEEE World Conference on Photovoltaic Energy Conversion (WCPEC-3) 2, pp. 1009-1012 (2003) http://ieeexplore.ieee.org/document/1306082/.
[204] I. García, P. Espinet-González, I. Rey-Stolle, and C. Algora, "Analysis of chromatic aberration effects in triple-junction solar cells using advanced distributed models," IEEE Journal of Photovoltaics 1(2), pp. 219-224 (2011) https://doi.org/10.1109/JPHOTOV.2011.2171671.
[205] P. Espinet-González, I. Rey-Stolle, C. Algora, and I. García, "Analysis of the behavior of multijunction solar cells under high irradiance Gaussian light profiles showing chromatic aberration with emphasis on tunnel junction performance," Progress in Photovoltaics: Research and Applications 23(6), pp. 743-753 (2015) https://doi.org/10.1002/pip.2491.
[206] B. Galiana, C. Algora, I. Rey-Stolle, and I.G. Vara, "A 3-D model for concentrator solar cells based on distributed circuit units," IEEE Transactions on Electron Devices 52(12), pp. 2552-2558 (2005) https://doi.org/10.1109/TED.2005.859620.
[207] P. Espinet-González, I. Rey-Stolle, M. Ochoa, C. Algora, I. García and E. Barrigón, "Analysis of perimeter recombination in the subcells of GaInP/GaAs/Ge triple-junction solar cells," Progress in Photovoltaics: Research and Applications 23(7), pp. 874-882 (2015) https://doi.org/10.1002/pip.2501.
[208] J. Bajaj, L.O. Bubulac, P.R. Newman, W.E. Tennant, and P.M. Raccah, "Spatial mapping of electrically active defects in HgCdTe using laser beam-induced current," Journal of Vacuum Science & Technology A: Vacuum, Surfaces, and Films 5(5), pp. 3186-3189 (1987) https://doi.org/10.1116/1.574834.
[209] A. Cheknane, H.S. Hilal, J.P. Charles, B. Benyoucef, and G. Campet, "Modeling and simulation of InGaP solar cells under solar concentration: Series resistance measurement and prediction," Solid State Sciences 8(5), pp. 556-559 (2006) https://doi.org/10.1016/j.solidstatesciences.2006.01.001.
[210] N. J. Salkind, Encyclopedia of Research Design, Vol. 1, Sage, Thousand Oaks, California, p. 409 (2010).
[211] R. Lyman Ott and M. Longnecker, An Introduction to Statistical Methods & Data Analysis 7th ed., Chapter 3: Data Description, Cengage Learning, Boston MA USA (2015).
[212] H.T. Nguyen, S.C. Baker-Finch, and D. Macdonald, "Temperature dependence of the radiative recombination coefficient in crystalline silicon from spectral photoluminescence," Applied Physics Letters 104(11), p. 112105 (2014) https://doi.org/10.1063/1.4869295.
[213] E. Franklin and J. Coventry, "Effects of highly nonuniform illumination distribution on electrical performance of solar cells," ANZSES Solar Conference (2002) http://hdl.handle.net/1885/40832.
[214] M. Victoria, R. Herrero, C. Domínguez, I. Antón, S. Askins, and G. Sala, "Characterization of the spatial distribution of irradiance and spectrum in concentrating photovoltaic systems and their effect on multi-junction solar cells," Progress in Photovoltaics: Research and Applications 21(3), pp. 308-318 (2013) https://doi.org/10.1002/pip.1183.
[215] R. Herrero, M. Victoria, C. Domínguez, S. Askins, I. Antón, and G. Sala, "Concentration photovoltaic optical system irradiance distribution measurements and its effect on multi-junction solar cells," Progress in Photovoltaics: Research and Applications 20(4), pp. 423-430 (2012) https://doi.org/10.1002/pip.1145.

[216] P. Sharma, M.M. Wilkins, H.P. Schriemer, and K. Hinzer, "Concentrating optical system optimization for 3-and 4-junction solar cells: impact of illumination profiles," Journal of Photonics for Energy 7(1), p.014501 (2017) https://doi.org/10.1117/1.JPE.7.014501.
[217] B.M.F. Yu Jeco, T. Sogabe, N. Ahsan, and Y. Okada, "Temperature dependence of luminescence coupling effect in InGaP/GaAs/Ge triple-junction solar cells," Journal of Photonics for Energy 8(2), p.022602 (2018) https://doi.org/10.1117/1.JPE.8.022602.
[218] M. F. Guasti and M. D. L. C. Heredia, "Diffraction pattern of a circle/square aperture," Journal of modern Optics, 40(6), 1073-1080 (1993) https://doi.org/10.1080/09500349314551141.
[219] H. Nesswetter, W. Dyck, P. Lugli, A.W. Bett, and C.G. Zimmermann, "Luminescence based series resistance mapping of III-V multijunction solar cells," Journal of Applied Physics 114(19), p. 194510 (2013) https://doi.org/10.1063/1.4831749.
[220] M. Ochoa, C. Algora, P. Espinet-González, and I. Garcia, "3-D modeling of perimeter recombination in GaAs diodes and its influence on concentrator solar cells," Solar Energy Materials and Solar Cells 120, pp. 48-58 (2014) https://doi.org/10.1016/j.solmat.2013.08.009.
[221] E. F. Schubert, "Chapter 4 – Radiative and non-radiative recombination," in *Light-Emitting Diodes*, 3rd ed., Cambridge University Press, New York (2003).
[222] S.M. Sze and K.K. Ng, "Chapter 13 – Photodetectors and Solar Cells," in *Physics of Semiconductor Devices*, 3rd ed., John Wiley & Sons, Hoboken, New Jersey, p. 677 (2006).
[223] L. Viña, S. Logothetidis, and M. Cardona, "Temperature dependence of band gaps in Si and Ge," Physical Review B 30(4), p. 1979 (1984) https://doi.org/10.1103/PhysRevB.30.1979.
[224] S. Logothetidis, M. Cardona, and M. Garriga, "Temperature dependence of the dielectric function and the interband critical-point parameters of $Al_xGa_{1-x}As$," Physical Review B 43(14), p. 11950 (1991) https://doi.org/10.1103/PhysRevB.43.11950.
[225] S.A. Lourenco, I.F.L. Dias, J.L. Duarte, E. Laureto, L.C. Poças, D.O. Toginho Filho, and J.R. Leite, "Thermal expansion contribution to the temperature dependence of excitonic transitions in GaAs and AlGaAs," Brazilian Journal of Physics 34(2A), pp. 517-525 (2004) http://dx.doi.org/10.1590/S0103-97332004000300031.
[226] P. Lautenschlager, P.B. Allen, and M. Cardona, "Temperature dependence of band gaps in Si and Ge," Physical Review B 31(4), p. 2163 (1985) https://doi.org/10.1103/PhysRevB.31.2163.
[227] Y. Ishitani, S. Minagawa, and T. Tanaka, "Temperature dependence of the band-gap energy of disordered GaInP," Journal of Applied Physics 75(10), pp. 5326-5331 (1994) https://doi.org/10.1063/1.355735.
[228] B. E. Saleh and M. C. Teich, Fundamentals of Photonics, John Wiley & Sons, Inc., New Jersey (2007).
[229] P. Pérez-Higueras and E. F. Fernández, eds. High concentrator photovoltaics: fundamentals, engineering and power plants, Springer, London (2015).
[230] D. M. Tobnaghi, R. Madatov, and D. Naderi, "The effect of temperature on electrical parameters of solar cells," International Journal of Advanced Research in Electrical, Electronics and Instrumentation Engineering 2(12), 6404–6407 (2013).
[231] P.P. Altermatt, A. Schenk, F. Geelhaar, and G. Heiser, "Reassessment of the intrinsic carrier density in crystalline silicon in view of band-gap narrowing," Journal of Applied Physics 93(3), pp. 1598-1604 (2003) https://doi.org/10.1063/1.1529297.
[232] I. Dimitrios, A.M. Kremer, D.R. McKenna, and K.F. Jensen, "Complex flow phenomena in vertical MOCVD reactors: Effects on deposition uniformity and interface abruptness," Journal of Crystal Growth 85(1-2), pp. 154-164 (1987) https://doi.org/10.1016/0022-0248(87)90217-X.
[233] S. Heckelmann, D. Lackner, F. Dimroth, and A.W. Bett, "Material quality frontiers of MOVPE grown AlGaAs for minority carrier devices," Journal of Crystal Growth 464, pp. 49-53 (2017) https://doi.org/10.1016/j.jcrysgro.2016.09.069.
[234] S. Heckelmann, D. Lackner, C. Karcher, F. Dimroth, and A.W. Bett, "Investigations on $Al_xGa_{(1-x)}As$ Solar Cells Grown by MOVPE," IEEE Journal of Photovoltaics 5(1), pp. 446-453 (2015) https://doi.org/10.1109/JPHOTOV.2014.2367869.
[235] A.M. Stoneham, "Non-radiative transitions in semiconductors," Reports on Progress in Physics 44(12), p. 1251 (1981) https://doi.org/10.1088/0034-4885/44/12/001.
[236] R. Paschotta, "Radiative lifetime," in Encyclopedia of Laser Physics and Technology (2008) https://www.rp-photonics.com/radiative_lifetime.html (20 November 2018).
[237] H. Schlangenotto, H. Maeder, and W. Gerlach, "Temperature dependence of the radiative recombination coefficient in silicon," Physica Status Solidi (a) 21(1), pp. 357-367 (1974) https://doi.org/10.1002/pssa.2210210140.
[238] V. Alex, S. Finkbeiner, and J. Weber, "Temperature dependence of the indirect energy gap in crystalline silicon," Journal of Applied Physics 79(9), pp. 6943-6946 (1996) https://doi.org/10.1063/1.362447.
[239] M.A. Green and S.R. Wenham, "Novel parallel multijunction solar cell," Applied Physics Letters 65(23), pp. 2907-2909 (1994) https://doi.org/10.1063/1.112526.

[240] U. Rau, "Superposition and reciprocity in the electroluminescence and photoluminescence of solar cells," IEEE Journal of Photovoltaics 2(2), pp.169-172 (2012) https://doi.org/10.1109/JPHOTOV.2011.2179018.
[241] U. Rau, "Reciprocity relation between photovoltaic quantum efficiency and electroluminescent emission of solar cells," Physical Review B 76(8), p.085303 (2007) https://doi.org/10.1103/PhysRevB.76.085303.
[242] A. Delamarre, L. Lombez, and J.F. Guillemoles, "Characterization of solar cells using electroluminescence and photoluminescence hyperspectral images," Journal of Photonics for Energy 2(1), p.027004 (2012) https://doi.org/10.1117/1.JPE.2.027004.
[243] T. Kirchartz, J. Nelson, and U. Rau, "Reciprocity between charge injection and extraction and its influence on the interpretation of electroluminescence spectra in organic solar cells," Physical Review Applied 5(5), p.054003 (2016) https://doi.org/10.1103/PhysRevApplied.5.054003.
[244] A. Delamarre, L. Lombez, K. Watanabe, M. Sugiyama, Y. Nakano, and J.F. Guillemoles, "Experimental demonstration of optically determined solar cell current transport efficiency map," IEEE Journal of Photovoltaics 6(2), pp.528-531 (2016) https://doi.org/10.1109/JPHOTOV.2016.2516249.
[245] K. Schick, E. Daub, S. Finkbeiner, and P. Würfel, "Verification of a generalized Planck law for luminescence radiation from silicon solar cells," Applied Physics A 54(2), pp.109-114 (1992) https://doi.org/10.1007/BF00323895.
[246] H. Lüth, "Chapter 6 – Electronic Surface States," in *Solid Surfaces, Interfaces and Thin Films – Graduate Texts in Physics*, Springer-Verlag Berlin Heidelberg (2015) https://doi.org/10.1007/978-3-319-10756-1_6.
[247] G.N. Parsons, S.M. George, and M. Knez, "Progress and future directions for atomic layer deposition and ALD-based chemistry," MRS Bulletin 36(11), pp.865-871 (2011) https://doi.org/10.1557/mrs.2011.238.
[248] M. L. Huang, Y. C. Chang, C. H. Chang, Y. J. Lee, P. Chang, J. Kwo, T. B. Wu, and M. Hong, "Surface passivation of III-V compound semiconductors using atomic-layer-deposition-grown Al_2O_3," Applied Physics Letters 87(25), p. 252104 (2005) https://doi.org/10.1063/1.2146060.
[249] S.M. George, "Atomic layer deposition: an overview," Chemical reviews 110(1), pp. 111-131 (2009) https://doi.org/10.1021/cr900056b.
[250] J. Schmidt, A. Merkle, R. Brendel, B. Hoex, M.V. de Sanden, and W.M.M. Kessels, "Surface passivation of high-efficiency silicon solar cells by atomic-layer-deposited Al_2O_3," Progress in Photovoltaics: Research and Applications 16(6), pp. 461-466 (2008) https://doi.org/10.1002/pip.823.
[251] C.L. Hinkle, A.M. Sonnet, E.M. Vogel, S. McDonnell, G.J. Hughes, M. Milojevic, B. Lee, F.S. Aguirre-Tostado, K.J. Choi, H.C. Kim, and J. Kim, "GaAs interfacial self-cleaning by atomic layer deposition," Applied Physics Letters 92(7), p. 071901 (2008) https://doi.org/10.1063/1.2883956.
[252] P. Poodt, A. Lankhorst, F. Roozeboom, K. Spee, D. Maas, and A. Vermeer, "High-speed spatial atomic-layer deposition of aluminum oxide layers for solar cell passivation," Advanced materials 22(32), pp. 3564-3567 (2010) https://doi.org/10.1002/adma.201000766.
[253] J. Benick, A. Richter, M. Hermle, and S.W. Glunz, "Thermal stability of the Al_2O_3 passivation on p-type silicon surfaces for solar cell applications," Physica Status Solidi (RRL)–Rapid Research Letters 3(7-8), pp. 233-235 (2009) https://doi.org/10.1002/pssr.200903209.
[254] P. Saint-Cast, J. Benick, D. Kania, L. Weiss, M. Hofmann, J. Rentsch, R. Preu, and S.W. Glunz, "High-efficiency c-Si solar cells passivated with ALD and PECVD aluminum oxide," IEEE Electron Device Letters 31(7), pp. 695-697 (2010) https://doi.org/10.1109/LED.2010.2049190.
[255] J.A. Van Delft, D. Garcia-Alonso, and W.M.M. Kessels, "Atomic layer deposition for photovoltaics: applications and prospects for solar cell manufacturing," Semiconductor Science and Technology 27(7), p. 074002 (2012) https://doi.org/10.1088/0268-1242/27/7/074002.
[256] G. Dingemans and W.M.M. Kessels, "Status and prospects of Al_2O_3-based surface passivation schemes for silicon solar cells," Journal of Vacuum Science & Technology A: Vacuum, Surfaces, and Films 30(4), p. 040802 (2012) https://doi.org/10.1116/1.4728205.
[257] J.H. Ermer, R.K. Jones, P. Hebert, P. Pien, R.R. King, D. Bhusari, R. Brandt, O. Al-Taher, C. Fetzer, G.S. Kinsey, and N. Karam, "Status of C3MJ+ and C4MJ production concentrator solar cells at spectrolab," IEEE Journal of Photovoltaics 2(2), pp. 209-213 (2012) https://doi.org/10.1109/JPHOTOV.2011.2180893.
[258] T. Takamoto, M. Kaneiwa, M. Imaizumi, and M. Yamaguchi, "InGaP/GaAs-based multijunction solar cells," Progress in Photovoltaics: Research and Applications 13(6), pp. 495-511 (2005) https://doi.org/10.1002/pip.642.
[259] R. Boidin, T. Halenkovič, V. Nazabal, L. Beneš, and P. Němec, "Pulsed laser deposited alumina thin films," Ceramics International 42(1), pp. 1177-1182 (2016) https://doi.org/10.1016/j.ceremint.2015.09.048.
[260] N.V. Nguyen, O.A. Kirillov, W. Jiang, W. Wang, J.S. Suehle, P.D. Ye, Y. Xuan, N. Goel, K.W. Choi, W. Tsai, and S. Sayan, "Band offsets of atomic-layer-deposited Al_2O_3 on GaAs and the effects of surface treatment," Applied Physics Letters 93(8), p. 082105 (2008) https://doi.org/10.1063/1.2976676.

[261] D. A. Neamen, "Chapter 5 – Carrier Transport Phenomena," in *Semiconductor Physics and Devices: Basic Principles*, 4th ed., McGraw-Hill Companies Inc., New York, pp. 164-166 (2012).
[262] C. Honsberg and S. Bowden, "Chapter 8.2 – Other IV Measurements, Dark I-V Measurements," PV Education, accessed 8/19/2019 https://www.pveducation.org/pvcdrom/characterisation/dark-iv-measurements.
[263] W.J. Beek, M.M. Wienk, and R.A. Janssen, "Efficient hybrid solar cells from zinc oxide nanoparticles and a conjugated polymer," Advanced Material 16(12), pp. 1009-1013 (2004) https://doi.org/10.1002/adma.200306659.
[264] A. Handugan and J. Quintero, Cambridge Nanotech ALD Standard operation procedure Arizona State University NanoFab (Rev C) received Jan 25, 2019.
[265] D.B. Mitzi, C.A. Feild, W.T.A. Harrison, and A.M. Guloy, "Conducting tin halides with a layered organic-based perovskite structure," Nature 369(6480), p. 467 (1994) https://doi.org/10.1038/369467a0.
[266] Y. Li, X. Zhang, H. Huang, S.V. Kershaw, and A.L. Rogach, "Advances in metal halide perovskite nanocrystals: Synthetic strategies, growth mechanisms, and optoelectronic applications," Materials Today (2019) https://doi.org/10.1016/j.mattod.2019.06.007.
[267] J.M. Ball, M.M. Lee, A. Hey, and H.J. Snaith, "Low-temperature processed meso-superstructured to thin-film perovskite solar cells," Energy & Environmental Science 6(6), pp. 1739-1743 (2013) https://doi.org/10.1039/C3EE40810H.
[268] H. Wang, L. Whittaker-Brooks, and G.R. Fleming, "Exciton and free charge dynamics of methylammonium lead iodide perovskites are different in the tetragonal and orthorhombic phases," The Journal of Physical Chemistry C 119(34), pp. 19590-19595 (2015) https://doi.org/10.1021/acs.jpcc.5b04403.
[269] H.J. Snaith, "Perovskites: the emergence of a new era for low-cost, high-efficiency solar cells," The Journal of Physical Chemistry Letters 4(21), pp. 3623-3630 (2013) https://doi.org/10.1021/jz4020162.
[270] A. Kojima, K. Teshima, Y. Shirai, and T. Miyasaka, "Organometal halide perovskites as visible-light sensitizers for photovoltaic cells," Journal of the American Chemical Society 131(17), pp. 6050-6051 (2009) https://doi.org/10.1021/ja809598r.
[271] A.L. Rogach, A. Eychmüller, S.G. Hickey, and S.V. Kershaw, "Infrared-emitting colloidal nanocrystals: synthesis, assembly, spectroscopy, and applications," Small 3(4), pp. 536-557 (2007) https://doi.org/10.1002/smll.200600625.
[272] S.V. Gaponenko, "Chapter 5 – Absorption and emission of light by semiconductor nanocrystals," in *Optical properties of semiconductor nanocrystals* vol. 23, Cambridge University Press, London (1998).
[273] V.L. Klimov, A.A. Mikhailovsky, S. Xu, A. Malko, J.A. Hollingsworth, A.C. Leatherdale, H.J. Eisler, and M.G. Bawendi, "Optical gain and stimulated emission in nanocrystal quantum dots," Science 290(5490), pp. 314-317 (2000) https://doi.org/10.1126/science.290.5490.314.
[274] G. Hodes, "Comparison of dye-and semiconductor-sensitized porous nanocrystalline liquid junction solar cells," The Journal of Physical Chemistry C 112(46), pp. 17778-17787 (2008) https://doi.org/10.1021/jp803310s.
[275] B.E. Hardin, H.J. Snaith, and M.D. McGehee, "The renaissance of dye-sensitized solar cells," Nature Photonics 6(3), p. 162 (2012) https://doi.org/10.1038/nphoton.2012.22.
[276] F. Liu, Y. Zhang, C. Ding, S. Kobayashi, T. Izuishi, N. Nakazawa, T. Toyoda, T. Ohta, S. Hayase, T. Minemoto, and K. Yoshino, "Highly luminescent phase-stable $CsPbI_3$ perovskite quantum dots achieving near 100% absolute photoluminescence quantum yield," ACS Nano 11(10), pp.10373-10383 (2017) https://doi.org/10.1021/acsnano.7b05442.
[277] J.H. Im, C.R. Lee, J.W. Lee, S.W. Park, and N.G. Park, "6.5% efficient perovskite quantum-dot-sensitized solar cell," Nanoscale 3(10), pp. 4088-4093 (2011) https://doi.org/10.1039/C1NR10867K.
[278] M.M. Lee, J. Teuscher, T. Miyasaka, T.N. Murakami, and H.J. Snaith, "Efficient hybrid solar cells based on meso-superstructured organometal halide perovskites," Science 338(6107), pp. 643-647 (2012) https://doi.org/10.1126/science.1228604.
[279] A. Goodrich and M. Woodhouse, "A Manufacturing Cost Analysis Relevant to Single-and Dual-Junction Photovoltaic Cells Fabricated with III-Vs and III-Vs Grown on Czochralski Silicon," PR-6A20-60126, National Renewable Energy Lab. (NREL), Golden, CO, United States (2013).
[280] J.S. Ward, T. Remo, K. Horowitz, M. Woodhouse, B. Sopori, K. VanSant, and P. Basore, "Techno-economic analysis of three different substrate removal and reuse strategies for III-V solar cells," Progress in Photovoltaics: Research and Applications 24(9), pp. 1284-1292 (2016) https://doi.org/10.1002/pip.2776.
[281] J. Jean, P.R. Brown, R.L. Jaffe, T. Buonassisi, and V. Bulović, "Pathways for solar photovoltaics," Energy & Environmental Science 8(4), pp. 1200-1219 (2015) https://doi.org/10.1039/C4EE04073B.
[282] C. Hu, T. Aubert, Y. Justo, S. Flamee, M. Cirillo, A. Gassenq, O. Drobchak, F. Beunis, G. Roelkens, and Z. Hens, "The micropatterning of layers of colloidal quantum dots with inorganic ligands using selective wet etching," Nanotechnology 25(17), p. 175302 (2014) https://doi.org/10.1088/0957-4484/25/17/175302.

[283] D. Bryant, N. Aristidou, S. Pont, I. Sanchez-Molina, T. Chotchunangatchaval, S. Wheeler, J.R. Durrant, and S.A. Haque, "Light and oxygen induced degradation limits the operational stability of methylammonium lead triiodide perovskite solar cells," Energy & Environmental Science 9(5), pp. 1655-1660 (2016) https://doi.org/10.1039/C6EE00409A.
[284] X. Guo, C. McCleese, W. Gao, M. Wang, L. Sang, and C. Burda, "Investigation of moisture stability and PL characteristics of terpineol-passivated organic–inorganic hybrid perovskite," Materials for Renewable and Sustainable Energy 5(4), p. 17 (2016) https://doi.org/10.1007/s40243-016-0081-1.
[285] A. Babayigit, A. Ethirajan, M. Muller, and B. Conings, "Toxicity of organometal halide perovskite solar cells," Nature Materials 15(3), p. 247 (2016) https://doi.org/10.1038/nmat4572.
[286] C. Caddeo, M.I. Saba, S. Meloni, A. Filippetti, and A. Mattoni, "Collective Molecular Mechanisms in the $CH_3NH_3PbI_3$ Dissolution by Liquid Water," ACS Nano 11(9), pp. 9183-9190 (2017) https://doi.org/10.1021/acsnano.7b04116.
[287] C. Caddeo, D. Marongiu, S. Meloni, A. Filippetti, F. Quochi, M. Saba, and A. Mattoni, "Hydrophilicity and Water Contact Angle on Methylammonium Lead Iodide," Advanced Materials Interfaces 6(3), p. 1801173 (2019) https://doi.org/10.1002/admi.201801173.
[288] C. Müller, T. Glaser, M. Plogmeyer, M. Sendner, S. Döring, A.A. Bakulin, C. Brzuska, R. Scheer, M.S. Pshenichnikov, W. Kowalsky, and A. Pucci, "Water infiltration in methylammonium lead iodide perovskite: Fast and inconspicuous," Chemistry of Materials 27(22), pp. 7835-7841 (2015) https://doi.org/10.1021/acs.chemmater.5b03883.
[289] J. Yang, B.D. Siempelkamp, D. Liu, and T.L. Kelly, "Investigation of $CH_3NH_3PbI_3$ degradation rates and mechanisms in controlled humidity environments using in situ techniques," ACS Nano 9(2), pp. 1955-1963 (2015) https://doi.org/10.1021/nn506864k.
[290] R.K. Misra, S. Aharon, B. Li, D. Mogilyansky, I. Visoly-Fisher, L. Etgar, and E.A. Katz, "Temperature-and component-dependent degradation of perovskite photovoltaic materials under concentrated sunlight," The Journal of Physical Chemistry Letters 6(3), pp. 326-330 (2015) https://doi.org/10.1021/jz502642b.
[291] Y. Han, S. Meyer, Y. Dkhissi, K. Weber, J.M. Pringle, U. Bach, L. Spiccia, and Y.B. Cheng, "Degradation observations of encapsulated planar $CH_3NH_3PbI_3$ perovskite solar cells at high temperatures and humidity," Journal of Materials Chemistry A 3(15), pp. 8139-8147 (2015) https://doi.org/10.1039/C5TA00358J.
[292] S. Yang, W. Fu, Z. Zhang, H. Chen, and C.Z. Li, "Recent advances in perovskite solar cells: efficiency, stability and lead-free perovskite," Journal of Materials Chemistry A 5(23), pp. 11462-11482 (2017) https://doi.org/10.1039/C7TA00366H.
[293] G.E. Eperon, G.M. Paterno, R.J. Sutton, A. Zampetti, A.A. Haghighirad, F. Cacialli, and H.J. Snaith, "Inorganic caesium lead iodide perovskite solar cells," Journal of Materials Chemistry A 3(39), pp. 19688-19695 (2015) https://doi.org/10.1039/C5TA06398A.
[294] E.M. Sanehira, A.R. Marshall, J.A. Christians, S.P. Harvey, P.N. Ciesielski, L.M. Wheeler, P. Schulz, L.Y. Lin, M.C. Beard, and J.M. Luther, "Enhanced mobility $CsPbI_3$ quantum dot arrays for record-efficiency, high-voltage photovoltaic cells," Science advances 3(10), p. eaao4204 (2017) https://doi.org/10.1126/sciadv.aao4204.
[295] J. Jiang, H. Jun Tao, S. Chen, B. Tan, N. Zhou, L. Zhu, Y. Zhao, Y. Wang, and J. Tao, "Efficiency enhancement of perovskite solar cells by fabricating as-prepared film before sequential spin-coating procedure," Applied Surface Science 371, pp. 289-295 (2016) https://doi.org/10.1016/j.apsusc.2016.02.206.
[296] B.D. Chernomordik, A.R. Marshall, G.F. Pach, J.M. Luther, and M.C. Beard, "Quantum dot solar cell fabrication protocols," Chemistry of Materials 29(1), pp. 189-198 (2016) https://doi.org/10.1021/acs.chemmater.6b02939.
[297] D. Grosso, "How to exploit the full potential of the dip-coating process to better control film formation," Journal of Materials Chemistry 21(43), pp. 17033-17038 (2011) https://doi.org/10.1039/C1JM12837J.
[298] C.J. Brinker, A.J. Hurd, G.C. Frye, K.J. Ward, and C.S. Ashley, "Sol-gel thin film formation," Journal of Non-Crystalline Solids 121(1-3), pp. 294-302 (1990) https://doi.org/10.1016/0022-3093(90)90147-E.
[299] L. Landau and B. Levich, "Dragging of a liquid by a moving plate," in Dynamics of Curved Fronts, pp. 141-153 (1988) https://doi.org/10.1016/B978-0-08-092523-3.50016-2.
[300] W. Deng, X. Xu, X. Zhang, Y. Zhang, X. Jin, L. Wang, S.T. Lee, and J. Jie, "Organometal Halide Perovskite Quantum Dot Light-Emitting Diodes," Advanced Functional Materials 26(26), pp. 4797-4802 (2016) https://doi.org/10.1002/adfm.201601054.
[301] L. Li, P. Gao, W. Wang, K. Müllen, H. Fuchs, and L. Chi, "Growth of ultrathin organic semiconductor microstripes with thickness control in the monolayer precision," Angewandte Chemie International Edition 52(48), pp. 12530-12535 (2013) https://doi.org/10.1002/anie.201306953.
[302] P.N. Tananaev, I.A. Boginskaya, I.V. Bykov, I.V. Trofimov, I.A. Rodionov, I.A. Ryzhikov, G.M. Yankovskiĭ, and A.V. Baryshev, "Fabricating thin films with colloidal quantum dots on planar substrates using polymethyl methacrylate," Journal of Optical Technology 85(3), pp. 136-143 (2018) https://doi.org/10.1364/JOT.85.000136.

[303] N. Reitinger, A. Hohenau, S. Köstler, J.R. Krenn, and A. Leitner, "Radiationless energy transfer in CdSe/ZnS quantum dot aggregates embedded in PMMA," Physica Status Solidi (a) 208(3), pp. 710-714 (2011) https://doi.org/10.1002/pssa.201026590.
[304] A. Abdelghani, "Atomic force microscopy on bare and thiol monolayer covered gallium arsenide," Materials Letters 50(2-3), pp. 73-77 (2001) https://doi.org/10.1016/S0167-577X(00)00416-X.
[305] A. Gocalinska, K. Gradkowski, V. Dimastrodonato, L.O. Mereni, G. Juska, G. Huyet, and E. Pelucchi, "Wettability and "petal effect" of GaAs native oxides," Journal of Applied Physics 110(3), p. 034319 (2011) https://doi.org/10.1063/1.3619797.
[306] J.M. Amboy, B.M.F. Yu Jeco, H. Wang, T. Kubo, T. Kinoshita, Z. Jehl Li-Kao, Y. Shoji, N. Ahsan, H. Segawa, Y. Okada, and J.J.R. Balbin, "Cesium lead halide perovskite quantum dot deposition on GaAs substrates by dip-coating," Proc. 7th IEEE World Conference on Photovoltaic Energy Conversion (WCPEC-7) pp. 467-471 (2018) https://doi.org/10.1109/PVSC.2018.8548078.
[307] Y. Dong, Y. Wang, S.T. Wu, J. He, H. Chen, and J. Chen, "Methods of making highly stable perovskite-polymer composites and structures using same," University of Central Florida Research Foundation Inc. (UCFRF), U.S. Patent Application 15/204,171, filed July 7, 2016 (2018).
[308] Y. Dong, Y. Wang, S.T. Wu, J. He, H. Chen, and J. Chen, "Methods of making highly stable perovskite-polymer composites and structures using same," University of Central Florida Research Foundation Inc. (UCFRF), Worldwide Patent Application WO/2018/009530, filed July 7, 2016 (2018).
[309] Z. Yu, H. Li, X. Shan, "Perovskite-polymer composite materials, devices, and methods," The Florida State University Research Foundation, Inc., Worldwide Patent Application WO/2019/195517, filed April 9, 2019 (2019).
[310] M. Meyns, M. Perálvarez, A. Heuer-Jungemann, W. Hertog, M. Ibáñez, R. Nafria, A. Genç, J. Arbiol, M.V. Kovalenko, J. Carreras, and A. Cabot, "Polymer-enhanced stability of inorganic perovskite nanocrystals and their application in color conversion LEDs," ACS Applied Materials & Interfaces 8(30), pp. 19579-19586 (2016) https://doi.org/10.1021/acsami.6b02529.
[311] J. He, A. Towers, Y. Wang, P. Yuan, Z. Jiang, J. Chen, A.J. Gesquiere, S.T. Wu, and Y. Dong, "In situ synthesis and macroscale alignment of $CsPbBr_3$ perovskite nanorods in a polymer matrix," ACS Nanoscale 10(33), pp. 15436-15441 (2018) https://doi.org/10.1039/C8NR04895A.
[312] Y. Wang, J. He, H. Chen, J. Chen, R. Zhu, P. Ma, A. Towers, Y. Lin, A.J. Gesquiere, S.T. Wu, and Y. Dong, "Ultrastable, highly luminescent organic–inorganic perovskite–polymer composite films," Advanced Materials 28(48), pp. 10710-10717 (2016) https://doi.org/10.1002/adma.201603964.
[313] R.R. Lamonte and D. McNally, "Cyclic olefin copolymers," Advanced Materials and Processes 159(3), pp. 33-36 (2001) http://www.elite-plastic.com.tw/COC-1.pdf.
[314] T. Nielsen, D. Nilsson, F. Bundgaard, P. Shi, P. Szabo, O. Geschke, and A. Kristensen, "Nanoimprint lithography in the cyclic olefin copolymer, Topas®, a highly ultraviolet-transparent and chemically resistant thermoplast," Journal of Vacuum Science & Technology B: Microelectronics and Nanometer Structures Processing, Measurement, and Phenomena 22(4), pp. 1770-1775 (2004) https://doi.org/10.1116/1.1771665.
[315] S. Baek, S. Kim, J.Y. Noh, J.H. Heo, S.H. Im, K.H. Hong, and S.W. Kim, "Development of Mixed-Cation $Cs_xRb_{1-x}PbX_3$ Perovskite Quantum Dots and Their Full-Color Film with High Stability and Wide Color Gamut," Advanced Optical Materials 6(15), p. 1800295 (2018) https://doi.org/10.1002/adom.201800295.
[316] Topas ® Advanced Polymers "Specification sheet – Topas ® COC Polymers," https://topas.com/sites/default/files/PRODUCTS-E-13.06.19.pdf.
[317] Y. Zhou and K. Zhu, "Perovskite solar cells shine in the "Valley of the Sun"," ACS Energy Letters 1(1), pp. 64-67 (2016) https://doi.org/10.1021/acsenergylett.6b00069.
[318] W. Mi, J. Tian, W. Tian, J. Dai, X. Wang, and X. Liu, "Temperature dependent synthesis and optical properties of CdSe quantum dots," Ceramics International 38(7), pp. 5575-5583 (2012) https://doi.org/10.1016/j.ceramint.2012.03.077.
[319] S. Maruyama, E. Einarsson, Y. Murakami, and T. Edamura, "Growth process of vertically aligned single-walled carbon nanotubes," Chemical Physics Letters 403(4-6), pp. 320-323 (2005) https://doi.org/10.1016/j.cplett.2005.01.031.
[320] M. Schubert, V. Gottschalch, C.M. Herzinger, H. Yao, P.G. Snyder, and J.A. Woollam, "Optical constants of $Ga_xIn_{1-x}P$ lattice matched to GaAs," Journal of Applied Physics 77(7), pp. 3416-3419 (1995) https://doi.org/10.1063/1.358632.
[321] G.E. Jellison, Jr., "Optical functions of GaAs, GaP, and Ge determined by two-channel polarization modulation ellipsometry," Optical Materials 1(3), pp. 151-160 (1992) https://doi.org/10.1016/0925-3467(92)90022-F.
[322] M.R. Vogt "Development of physical models for the simulation of optical properties of solar cell modules," Doctoral dissertation, Technische Informationsbibliothek (TIB) (2016).
[323] J. Mistrik S. Kasap H.E. Ruda, C. Koughia and J. Singh, S. Kasap and P. Capper (eds.), "Chapter 3 – Optical Properties of Electronic Materials: Fundamentals and Characterization," in *Springer Handbook of Electronic and Photonic Materials*, Springer Handbooks. Springer, Cham (2017) https://doi.org/10.1007/978-3-319-48933-9_3.

[324] Q. Lin, H. Huang, Y. Jing, H. Fu, P. Chang, D. Li, Y. Yao, and Z. Fan, "Flexible photovoltaic technologies," Journal of Materials Chemistry C 2(7), pp. 1233-1247 (2014) https://doi.org/10.1039/C3TC32197E.
[325] J. De Roo, M. Ibáñez, P. Geiregat, G. Nedelcu, W. Walravens, J. Maes, J.C. Martins, I. Van Driessche, M.V. Kovalenko, and Z. Hens, "Highly dynamic ligand binding and light absorption coefficient of cesium lead bromide perovskite nanocrystals," ACS Nano 10(2), pp. 2071-2081 (2016) https://doi.org/10.1021/acsnano.5b06295.
[326] N.G. Anderson, W.D. Laidig, R.M. Kolbas, and Y.C. Lo, "Optical characterization of pseudomorphic In x Ga1− x As–GaAs single-quantum-well heterostructures," Journal of Applied Physics 60(7), pp. 2361-2367 (1986) https://doi.org/10.1063/1.337146.
[327] F. Capasso and G.F. Williams, "A proposed hydrogenation/nitridization passivation mechanism for GaAs and other III–V semiconductor devices, including InGaAs long wavelength photodetectors," Journal of the Electrochemical Society 129(4), pp. 821-824 (1982) https://doi.org/10.1149/1.2123979.
[328] W. Nie, H. Tsai, R. Asadpour, J.C. Blancon, A.J. Neukirch, G. Gupta, J.J. Crochet, M. Chhowalla, S. Tretiak, M.A. Alam, and H.L. Wang, "High-efficiency solution-processed perovskite solar cells with millimeter-scale grains," Science 347(6221), pp. 522-525 (2015) https://doi.org/10.1126/science.aaa0472.
[329] M.V. Kovalenko and M.I. Bodnarchuk, "Lead halide perovskite nanocrystals: From discovery to self-assembly and applications," CHIMIA International Journal for Chemistry 71(7-8), pp. 461-470 (2017) https://doi.org/10.2533/chimia.2017.461.
[330] M.V. Kovalenko, L. Protesescu, and M.I. Bodnarchuk, "Properties and potential optoelectronic applications of lead halide perovskite nanocrystals," Science 358(6364), pp. 745-750 (2017) https://doi.org/10.1126/science.aam7093.
[331] Y. Zhang, J. He, P.N. Wang, J.Y. Chen, Z.J. Lu, D.R. Lu, J. Guo, C.C. Wang, and W.L. Yang, "Time-dependent photoluminescence blue shift of the quantum dots in living cells: effect of oxidation by singlet oxygen," Journal of the American Chemical Society 128(41), pp. 13396-13401 (2006) https://doi.org/10.1021/ja061225y.
[332] P. Häring and R. Kötz, "Nanoscale thickness changes of nickel hydroxide films during electrochemical oxidation/reduction monitored by in situ atomic force microscopy," Journal of the Electroanalytical Chemistry 385(2), pp. 273-277 (1995) https://doi.org/10.1016/0022-0728(94)03869-5.
[333] W.W. Yu and X. Peng, "Formation of high-quality CdS and other II–VI semiconductor nanocrystals in noncoordinating solvents: tunable reactivity of monomers," Angewandte Chemie International Edition 41(13), pp. 2368-2371 (2002) https://doi.org/10.1002/1521-3773(20020703)41:13<2368::AID-ANIE2368>3.0.CO;2-G.
[334] Q. Dai, S. Kan, D. Li, S. Jiang, H. Chen, M. Zhang, S. Gao, Y. Nie, H. Lu, Q. Qu, and G. Zou, "Effect of ligands and growth temperature on the growth kinetics and crystal size of colloidal CdSe nanocrystals," Materials Letters 60(24), pp. 2925-2928 (2006) https://doi.org/10.1016/j.matlet.2006.02.015.
[335] J. Zhang, R.W. Crisp, J. Gao, D.M. Kroupa, M.C. Beard, and J.M. Luther, "Synthetic conditions for high-accuracy size control of PbS quantum dots," The Journal of Physical Chemistry Letters 6(10), pp. 1830-1833 (2015) https://doi.org/10.1021/acs.jpclett.5b00689.
[336] X. Peng, J. Wickham, and A.P. Alivisatos, "Kinetics of II-VI and III-V colloidal semiconductor nanocrystal growth:"focusing" of size distributions," Journal of the American Chemistry Society 120(21), pp. 5343-5344 (1998) https://doi.org/10.1021/ja9805425.
[337] D. Battaglia and X. Peng, "Formation of high quality InP and InAs nanocrystals in a noncoordinating solvent," Nano Letters 2(9), pp. 1027-1030 (2002) https://doi.org/10.1021/nl025687v.
[338] S. Abdul Hadi, E.A. Fitzgerald, and A. Nayfeh, "Theoretical efficiency limit for a two-terminal multi-junction "step-cell" using detailed balance method," Journal of Applied Physics 119(7), p.073104 (2016) https://doi.org/10.1063/1.4942223.
[339] K.R. McIntosh and M.D. Abbott, "Wafer ray tracer," PV Lighthouse (2016) available https://www.pvlighthouse.com.au/calculators/wafer%20ray%20tracer/wafer%20ray%20tracer.html.
[340] D.E. Aspnes and A.A. Studna, "Dielectric functions and optical parameters of Si, Ge, GaP, GaAs, GaSb, InP, InAs, and InSb from 1.5 to 6.0 eV," Physical Review B 27(2), pp. 985-1009 (1983) https://doi.org/10.1103/PhysRevB.27.985.
[341] D.E. Aspnes, S.M. Kelso, R.A. Logan, and R. Bhat, "Optical properties of $Al_xGa_{1-x}As$," Journal of Applied Physics 60(2), pp. 754-767 (1986) https://doi.org/10.1063/1.337426.
[342] E. Palik, "Handbook of Optical Constants of Solids Vol I," Academic Press p. 508 (1985).
[343] E. Palik, "Handbook of Optical Constants of Solids Vol I," Academic Press pp. 577-580 (1985).
[344] H.K. Raut, V.A. Ganesh, A.S. Nair, and S. Ramakrishna, "Anti-reflective coatings: A critical, in-depth review," Energy & Environmental Science 4(10), pp. 3779-3804 (2011) https://doi.org/10.1039/C1EE01297Es.
[345] J. Page and T. Markvart, A. McEvoy, and L. Castaner (eds.), "Chapter I – The Role of Solar Radiation Climatology in the Design of Photovoltaic Systems," in *Practical handbook of photovoltaics: fundamentals and applications*, Elsevier, p. 12 (2003).

[346] C. Kittel, *Introduction to Solid State Physics, 6th Ed.*, John Wiley: New York, p. 185 (1986).
[347] P. Campbell and M.A. Green, "Light trapping properties of pyramidally textured surfaces," Journal of Applied Physics 62(1), pp. 243-249 (1987) https://doi.org/10.1063/1.339189.
[348] A.W. Smith and A. Rohatgi, "Ray tracing analysis of the inverted pyramid texturing geometry for high efficiency silicon solar cells," Solar energy materials and solar cells 29(1), pp. 37-49 (1993) https://doi.org/10.1016/0927-0248(93)90090-P.

Preliminary trials on the selective area application of perovskite quantum dot-amorphous thermoplastic film on III-V multijunction solar cells intended for luminescent coupling effect enhancement

Appendix A

Appendix A – Preliminary trials on the selective area application of perovskite quantum dot-amorphous thermoplastic film on III-V multijunction solar cells intended for luminescent coupling effect enhancement

As the next step to full dip-coating of III-V multijunction solar cells (MJSCs), selective all-inorganic perovskite quantum dot-cyclic olefin copolymer (PQD-COC) film application on InGaP/GaAs/Ge 3JSCs having different layouts were done. An extension to Chapter 6, this supplementary dissertation chapter was added to specifically discuss the preliminary findings on photo-passivating a selected III-V MJSC area. This was done in an attempt to achieve a homogeneous LC effect upon a current-limiting cell, where the photo-emission originates from all-inorganic (PQD-COC) films. The main goal of this supplementary study is to find the lateral film layout that could yield homogeneous LC current collection in III-V based MJSCs. The films were first deposited on a substrate mold, then mechanically removed and transferred on the front surface of the MJSC samples. Results revealed that although homogeneity cannot be achieved, some increase in LC current production was observed in the lower bandgap subcells of the host MJSC devices after the application of a film in the center of the active region. On the other hand, the current homogeneity remains as a challenge and could be solved in future work by addressing technical concerns such as the film deposition uniformity itself.

A.1. Application on the perimeter front surface

The first selective area layout tried was the PQD-COC film deposited on a Si/SiO_2 glass mold. Here, the Si has an area of about 0.5 × 0.5 mm^2 and was fixed on glass using a cyanoacrylate thermosetting adhesive. After dip-coating, the film was punctured on the center region covering the Si layer using a precision knife. Then, the film was transferred by hand onto the III-V MJSC mounted on a Cu plate with In as the back-contact paste. This layout is shown in Fig. 4(a), Sec. A.3.

To determine the effect of PQD-COC film application to the perimeter front surface of InGaP/GaAs/Ge 3JSC to LC current homogeneity, LBIC measurements before and after film application were obtained. From these measurements, σ_x and $\%\Delta\sigma_x$, including J_{ave}, were obtained using eqs. (9) and (10) in Chapter 6, respectively[11]. The LBIC maps acquired, together with the summary tables containing the J_{ave}, σ_x and $\%\Delta\sigma_x$ values are shown in Fig. 1. After the film transfer, current production decreased [Figs. 1(a) to (c), (h) and (k)] and current homogeneity degraded in all subcells as compared with those before film transfer [Figs. 1(d) to (f), (i) and (l)]. These were regardless of the excitation condition and are supported by the following data presented in Fig. 5, Sec. A.3.1: the decrease in measured subcell EQE [Fig. 5(a)] translated to subcell current reduction as calculated using eq. (3) [Fig. 5(b)]; some increase in dark current [Fig. 5(c)]; reduction in AM 1.5G current density as shown in Fig. 5(d); and increases in subcell *J-V* curves which most likely indicate the presence of shunt leakage current [Fig. 5(e) to (g)] in InGaP, GaAs, and Ge, respectively, under extreme current mismatch conditions. Additionally, these observations were numerically confirmed by J_{ave}, σ_x and $\%\Delta\sigma_x$ calculations listed in Figs. 1(g), (j) and (m) for direct subcell, GaAs LC, and Ge LC excitation, respectively. Therefore, PQD-COC film applied manually without machine intervention on the perimeter front surface of III-V MJSCs is a difficult approach to alleviating inhomogeneous subcell current production.

Another layout tried was the application of PQD-COC/Polyamine film punctured with a precision knife by hand on the center region of InGaP/GaAs/Ge 3JSC, shown in Fig. 4(b), Sec. A.3. To determine the effect of having this film layout to the LC current homogeneity, LBIC measurements before and after film application were obtained. From these measurements, σ_x and $\%\Delta\sigma_x$, including J_{ave}, were also obtained using eqs. (9) and (10), respectively. The LBIC maps acquired, together with the summary tables containing the J_{ave}, σ_x and $\%\Delta\sigma_x$ values are shown in Fig. 2. After the film transfer, current production decreased [Figs. 2(a) to (c), (h) and (k)] as compared with those before film transfer [Figs. 2(d) to (f), (i) and (l)], regardless of the excitation condition. These are supported by the following data presented in Fig. 6, Sec. A.3.2: decrease in measured subcell EQE [Fig. 6(a)] translated to subcell current reduction as calculated[12] using eq. (3) [Fig. 6(b)]; some increase in dark current [Fig. 6(c)]; reduction in AM 1.5G current density as shown in Fig. 6(d); and increases in subcell *J-V* curves which most likely indicate the presence of shunt leakage current [Fig. 6(e) to (g)] in InGaP, GaAs, and Ge, respectively, under extreme current mismatch conditions. Although current homogeneity degraded severely upon direct subcell excitations, it was observed to be better by 25.0% and 22.7% at GaAs LC and Ge LC effect excitation conditions, respectively. These observations were numerically confirmed by J_{ave}, σ_x and $\%\Delta\sigma_x$ calculations listed in

[11] Refer to Sec. 6.3.7.4, Chapter 6.
[12] Refer to Sec. 6.3.6.1, Chapter 6.

Figs. 2(g), (j) and (m) for direct subcell, GaAs LC, and Ge LC effect excitation, respectively. Therefore, PQD-COC/Polyamine film application to the perimeter front surface of III-V MJSCs might help alleviate inhomogeneous LC current production but may also regress when producing current under different excitation conditions. Moreover, the improved current homogeneity at LC effect excitation condition may be also attributed to the decrease in LC efficiencies between adjacent subcell after dip-coating which lead to LC current collection decreases. Hence, the current decrease brought about by film application should be addressed in a future study.

A.2. Application on the center region

As the perimeter film application did not yield larger subcell currents, another layout tested was the application of a small piece of PQD-COC/Polyamine film on the center region of InGaP/GaAs/Ge 3JSC, shown in Fig. 4(c), Sec. A.3. To determine the effect of having this film layout to the LC current homogeneity, LBIC measurements before and after film application were obtained. From these measurements, σ_x and $\%\Delta\sigma_x$, including J_{ave}, were also obtained using eqs. (9) and (10), respectively. The LBIC maps acquired, together with the summary tables containing the J_{ave}, σ_x and $\%\Delta\sigma_x$ values are shown in Fig. 3. After the film transfer, current production decreased [Figs. 3(a) to (c), and (h)] as compared with those before film transfer [Figs. 3(d) to (f), and (i)], except for Ge LC effect excitation condition [before transfer: Fig. 3(k) and after transfer: Fig. 3(l)]. The latter observation is supported by the increase in current density observed from Ge *J-V* characteristics shown in Fig. 7(g), Sec. A.3.3. Additionally, current homogeneity degraded in all conditions except for the Ge LC effect excitation condition, with an improvement of 2.7%. These observations were numerically confirmed by J_{ave}, σ_x and $\%\Delta\sigma_x$ calculations listed in Figs. 3(g), (j) and (m) for direct subcell, GaAs LC, and Ge LC effect excitation, respectively. On the other hand, no significant differences were observed from the following measurements presented in Fig. 7, Sec. A.3.3: subcell EQE [Fig. 7(a)] translated to subcell current densities calculated using eq. (3) [Fig. 7(b)] and dark *J-V* characteristics [Fig. 7(c)]; InGaP and GaAs *J-V* curves [Fig. 7(e) and (f)] under extreme current mismatch conditions. It can be noticed that after the film application, particularly from LBIC mapping by Ge LC effect excitation [Fig. 3(l)], the current collection on the perimeter region did not change at all. Therefore, PQD-COC/Polyamine film application to the center region of III-V MJSCs would not help alleviate inhomogeneous subcell current production.

As the area covered with films for any layout yielded less current collection, thinner films are recommended for future investigations and must emit towards any MJ subcell except for the topmost cell. Additionally, just like in full coverage of III-V MJSC with PQD-COC showcased in Chapter 6, Sec. 6.4.3.1, the current collection follows the homogeneity of the PQD-COC film as well. Hence, the deposition uniformity of PQD-COC film on a substrate mold should be treated as an additional consideration to address subcell current homogeneity using this approach.

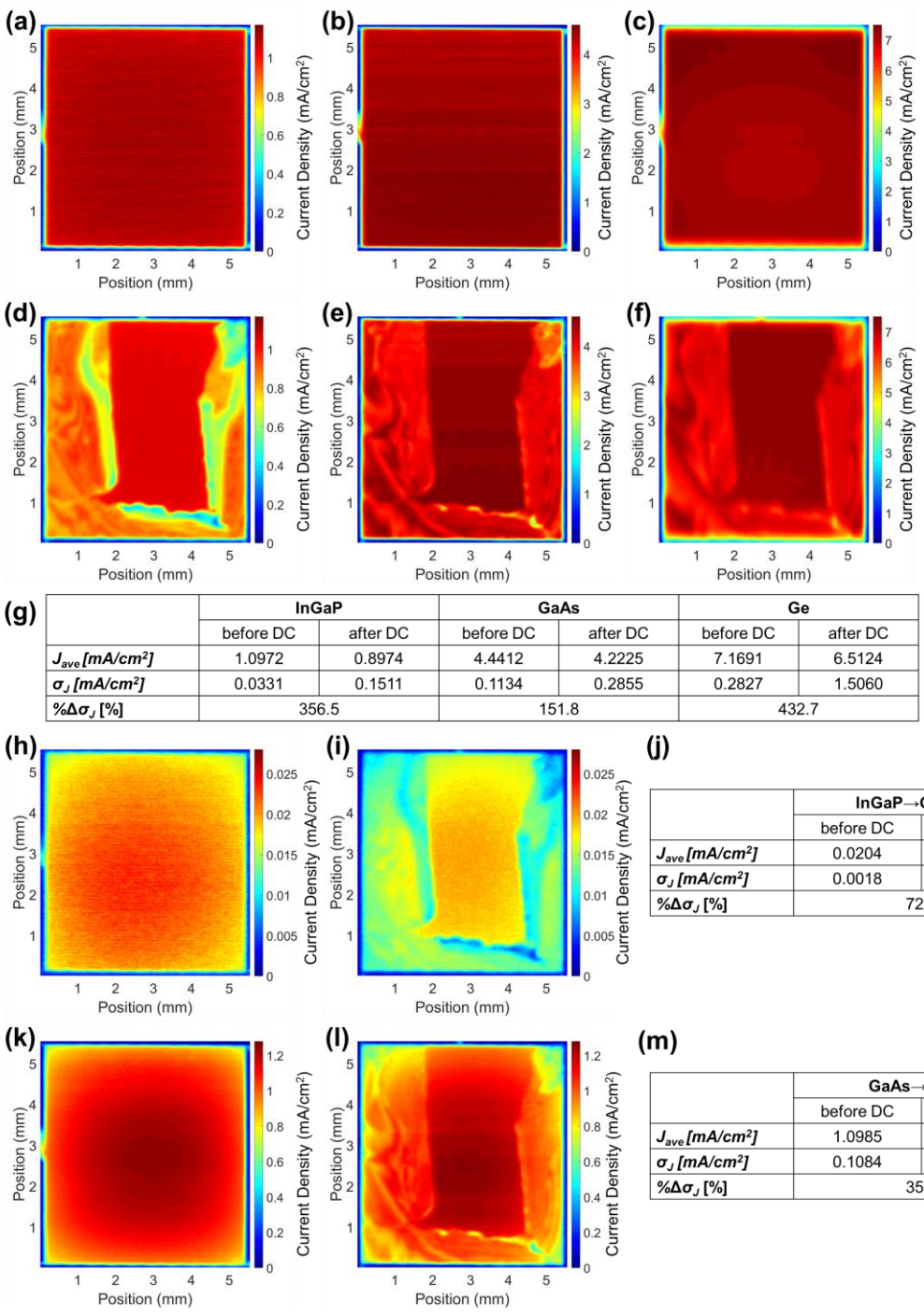

(g)

	InGaP		GaAs		Ge	
	before DC	after DC	before DC	after DC	before DC	after DC
J_{ave} [mA/cm²]	1.0972	0.8974	4.4412	4.2225	7.1691	6.5124
σ_J [mA/cm²]	0.0331	0.1511	0.1134	0.2855	0.2827	1.5060
$\%\Delta\sigma_J$ [%]	356.5		151.8		432.7	

(j)

	InGaP→GaAs LC	
	before DC	after DC
J_{ave} [mA/cm²]	0.0204	0.0153
σ_J [mA/cm²]	0.0018	0.0031
$\%\Delta\sigma_J$ [%]	72.2	

(m)

	GaAs→Ge LC	
	before DC	after DC
J_{ave} [mA/cm²]	1.0985	1.0318
σ_J [mA/cm²]	0.1084	0.1470
$\%\Delta\sigma_J$ [%]	35.6	

Fig. 1 Direct subcell LBIC mapping of InGaP/GaAs/Ge 3JSC topped with $CsPbX_3$ PQD-COC film as shown in Fig. 4(a): before film transfer – (a) InGaP, acquired using 450-nm laser, (b) GaAs, acquired using 785-nm laser, and (c) Ge, acquired using 450-nm laser; after film transfer – (d) InGaP, (e) GaAs, and (f) Ge; (g) summary table of average current density, $J_{DS,ave}$, standard deviation, σ_{DS}, and percent difference of standard deviation before and after DC, $\%\Delta\sigma_{DS}$. LBIC mapping by LC effect excitation of InGaP/GaAs/Ge 3JSC topped with $CsPbX_3$ PQD-COC film: before film transfer – (h) GaAs LC, acquired using 450-nm laser, and (k) Ge LC, acquired using 785-nm laser; (j) summary table of J_{ave}, σ_J, and $\%\Delta\sigma_J$ from GaAs LC current mapping before and after DC; current maps after film transfer – (i) GaAs LC and (l) Ge LC; (m) summary table of $J_{LC,ave}$, σ_{LC}, and $\%\Delta\sigma_{LC}$ from Ge LC current mapping before and after DC.

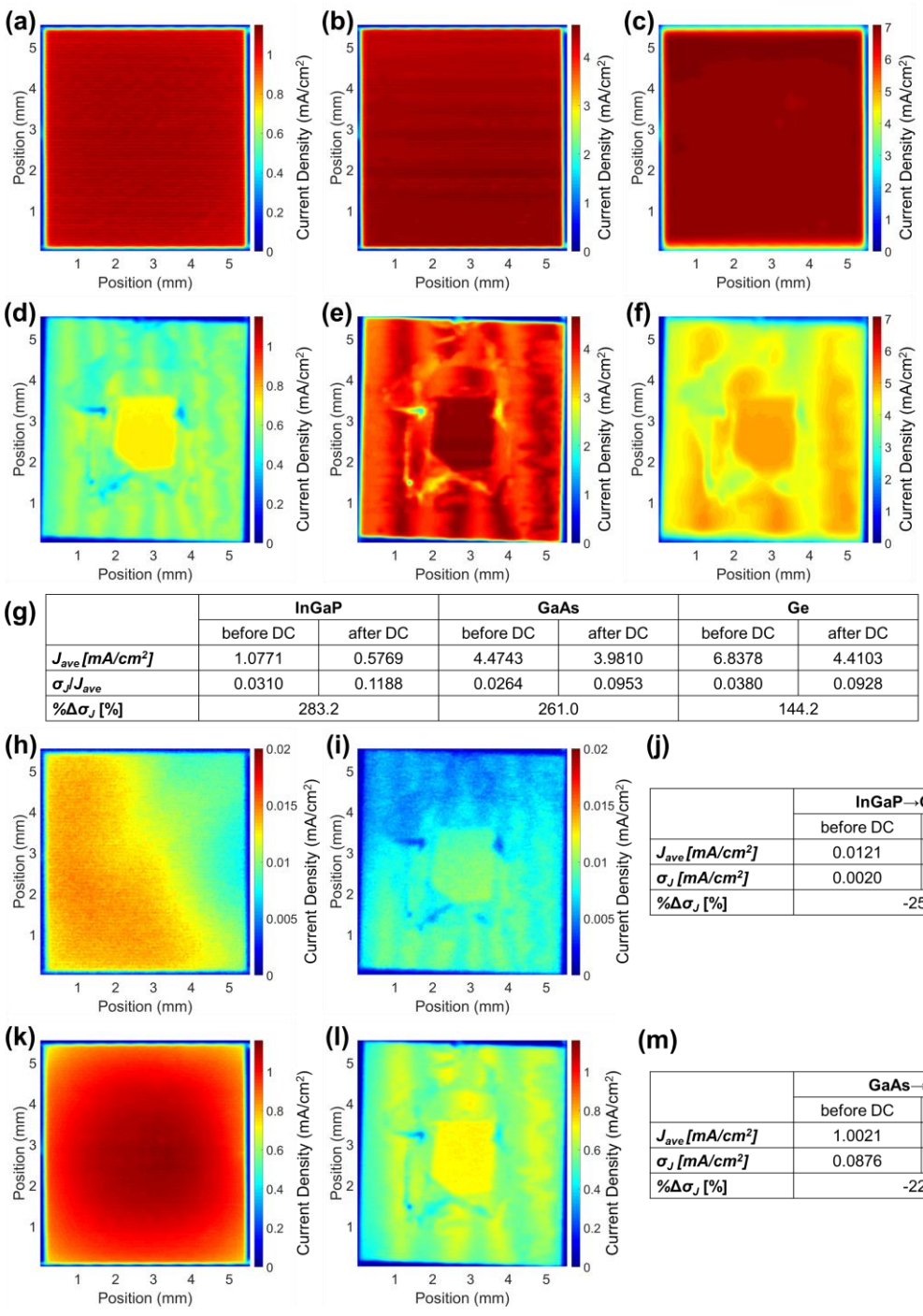

(g)

	InGaP		GaAs		Ge	
	before DC	after DC	before DC	after DC	before DC	after DC
J_{ave} [mA/cm²]	1.0771	0.5769	4.4743	3.9810	6.8378	4.4103
σ_J/J_{ave}	0.0310	0.1188	0.0264	0.0953	0.0380	0.0928
$\%\Delta\sigma_J$ [%]	283.2		261.0		144.2	

(j)

	InGaP→GaAs LC	
	before DC	after DC
J_{ave} [mA/cm²]	0.0121	0.0075
σ_J [mA/cm²]	0.0020	0.0015
$\%\Delta\sigma_J$ [%]	-25.0	

(m)

	GaAs→Ge LC	
	before DC	after DC
J_{ave} [mA/cm²]	1.0021	0.6015
σ_J [mA/cm²]	0.0876	0.0677
$\%\Delta\sigma_J$ [%]	-22.7	

Fig. 2 Direct subcell LBIC mapping of InGaP/GaAs/Ge 3JSC topped with $CsPbX_3$ PQD-COC/Polyamine film as shown in Fig. 4(b): before film transfer – (a) InGaP, acquired using 450-nm laser, (b) GaAs, acquired using 785-nm laser, and (c) Ge, acquired using 450-nm laser; after film transfer – (d) InGaP, (e) GaAs, and (f) Ge; (g) summary table of average current density, $J_{DS,ave}$, standard deviation, σ_{DS}, and percent difference of standard deviation before and after DC, $\%\Delta\sigma_{DS}$. LBIC mapping by LC effect excitation of InGaP/GaAs/Ge 3JSC 3JSC topped with $CsPbX_3$ PQD-COC/Polyamine film: before film transfer – (h) GaAs LC, acquired using 450-nm laser, and (k) Ge LC, acquired using 785-nm laser; (j) summary table of J_{ave}, σ_J, and $\%\Delta\sigma_J$ from GaAs LC current mapping before and after DC; current maps after film transfer – (i) GaAs LC and (l) Ge LC; (m) summary table of $J_{LC,ave}$, σ_{LC}, and $\%\Delta\sigma_{LC}$ from Ge LC current mapping before and after DC.

A.3. Supplementary information

Figure 4 shows the PQD-COC film applied on InGaP/GaAs/Ge 3JSCs in different layouts. In addition, Figs. 5 to 7 showcase a series of optoelectronic characterization of InGaP/GaAs/Ge 3JSCs before and after PQD-COC film application on their front surface at different configurations: partially cut PQD-COC film after deposition on a Si/SiO_2 glass mold [Fig. 5], and partially cut PQD-COC films on polyamine after deposition on glass with the latter [Figs. 6 and 7].

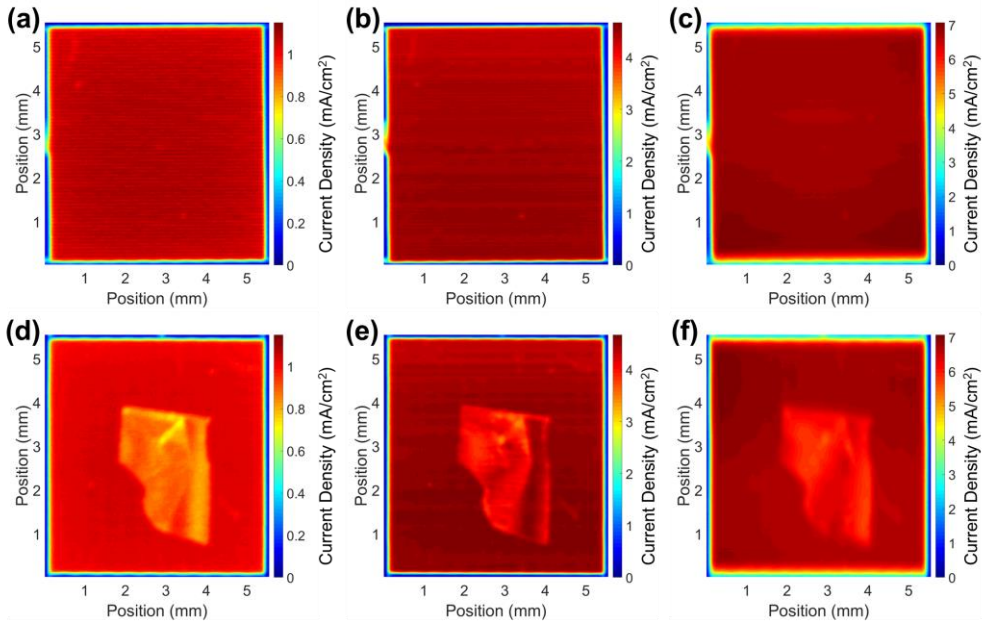

(g)

	InGaP		GaAs		Ge	
	before DC	after DC	before DC	after DC	before DC	after DC
J_{ave} [mA/cm²]	1.0678	0.9931	4.4513	4.4426	6.7659	6.5681
σ_J [mA/cm²]	0.0347	0.0682	0.1211	0.1983	0.2633	0.3587
$\%\Delta\sigma_J$ [%]	96.5		63.7		36.2	

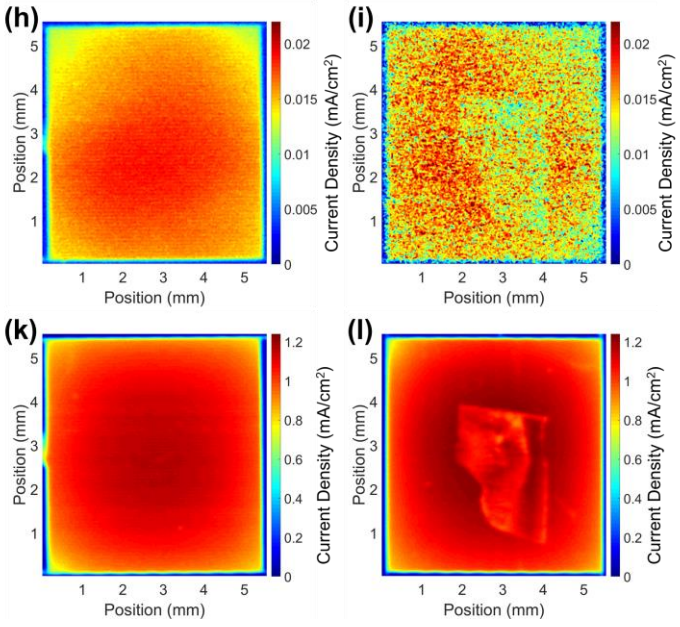

(j)

	InGaP→GaAs LC	
	before DC	after DC
J_{ave} [mA/cm²]	0.0163	0.0144
σ_J [mA/cm²]	0.0016	0.0030
$\%\Delta\sigma_J$ [%]	87.5	

(m)

	GaAs→Ge LC	
	before DC	after DC
J_{ave} [mA/cm²]	1.0486	1.0817
σ_J [mA/cm²]	0.0886	0.0862
$\%\Delta\sigma_J$ [%]	-2.7	

Fig. 3 Direct subcell LBIC mapping of InGaP/GaAs/Ge 3JSC topped with $CsPbX_3$ PQD-COC/Polyamine film as shown in Fig. 4(c): before film transfer – (a) InGaP, acquired using 450-nm laser, (b) GaAs, acquired using 785-nm laser, and (c) Ge, acquired using 450-nm laser; after film transfer – (d) InGaP, (e) GaAs, and (f) Ge; (g) summary table of average current density, $J_{DS,ave}$, standard deviation, σ_{DS}, and percent difference of standard deviation before and after DC, $\%\Delta\sigma_{DS}$. LBIC mapping by LC effect excitation of InGaP/GaAs/Ge 3JSC 3JSC topped with $CsPbX_3$ PQD-COC/Polyamine film: before film transfer – (h) GaAs LC, acquired using 450-nm laser, and (k) Ge LC, acquired using 785-nm laser; (j) summary table of J_{ave}, σ_J, and $\%\Delta\sigma_J$ from GaAs LC current mapping before and after DC; current maps after film transfer – (i) GaAs LC and (l) Ge LC; (m) summary table of $J_{LC,ave}$, σ_{LC}, and $\%\Delta\sigma_{LC}$ from Ge LC current mapping before and after DC.

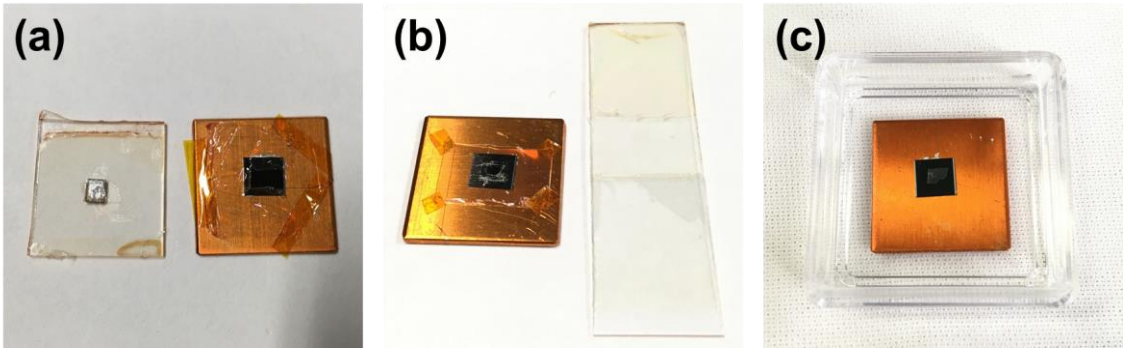

Fig. 4 Images of InGaP/GaAs/Ge 3JSC after mechanical film transfer. (a) The PQD-COC film was formed on a Si/SiO_2 glass mold dip-coated for 5 times and was punctured by about 4.0 mm × 2.0 mm in the middle. (b) The PQD-COC/Polyamine film was formed on a glass-covered with polyamine that was dip-coated for 5 times and was punctured by about 1.8 mm × 1.8 mm in the middle. (c) The PQD-COC/Polyamine film was formed on a glass-covered with polyamine that was dip-coated 5 times, cut into about 3.0 mm × 2.0 mm and then placed on the center of the 3JSC front surface.

A.3.1. PQD-COC film cut on the center region then transferred on InGaP/GaAs/Ge 3JSC:

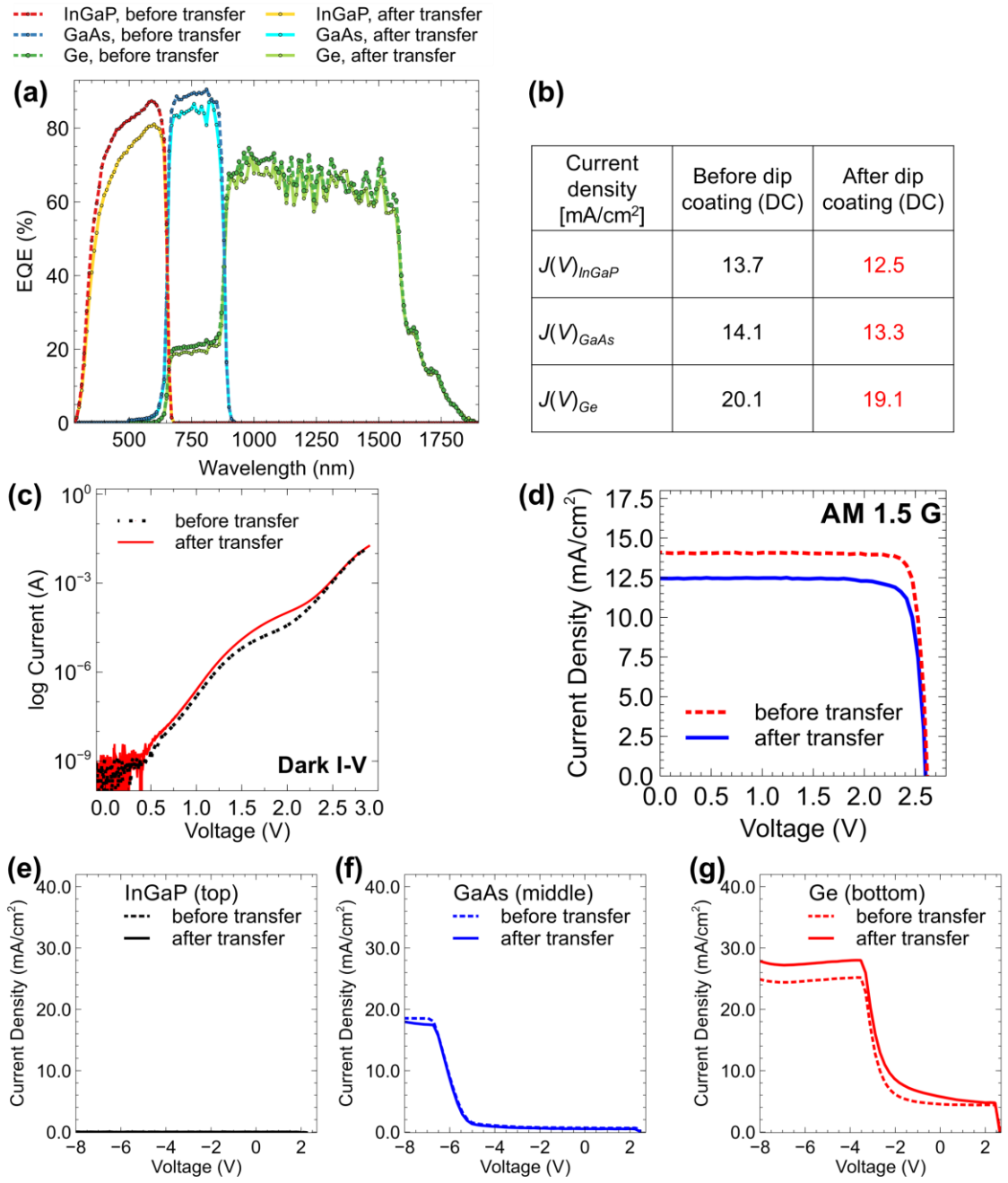

Current density [mA/cm^2]	Before dip coating (DC)	After dip coating (DC)
$J(V)_{InGaP}$	13.7	12.5
$J(V)_{GaAs}$	14.1	13.3
$J(V)_{Ge}$	20.1	19.1

Fig. 5 Optoelectronic characterizations before and after the manual transfer of $CsPbX_3$ PQD-COC film on the InGaP/GaAs/Ge 3JSC perimeter front surface: (a) EQE measurements; (b) summary of current densities derived from subcell EQE measurements using eq. (3); LED *J-V* curves of (c) InGaP, (d) GaAs, and (e) Ge; (f) dark and (g) AM 1.5G at 1 sun *J-V* curve measurements.

A.3.2. PQD-COC film cut on the center region then transferred on InGaP/GaAs/Ge 3JSC:

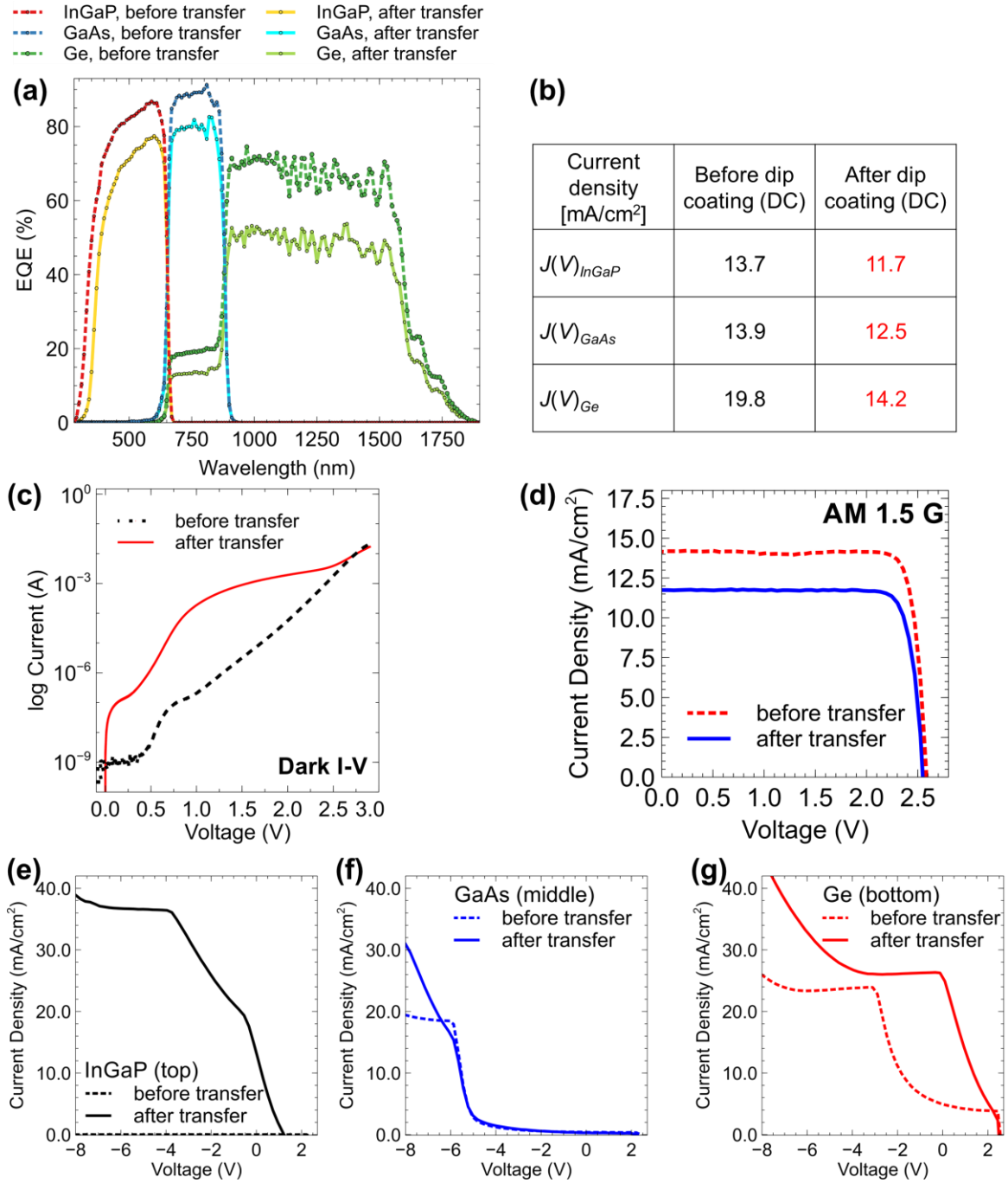

Current density [mA/cm^2]	Before dip coating (DC)	After dip coating (DC)
$J(V)_{InGaP}$	13.7	11.7
$J(V)_{GaAs}$	13.9	12.5
$J(V)_{Ge}$	19.8	14.2

Fig. 6 Optoelectronic characterizations before and after the manual transfer of $CsPbX_3$ PQD-COC/Polyamine film on the InGaP/GaAs/Ge 3JSC perimeter front surface: (a) EQE measurements; (b) summary of current densities derived from subcell EQE measurements using eq. (3); LED *J-V* curves of (c) InGaP, (d) GaAs, and (e) Ge; (f) dark and (g) AM 1.5G at 1 sun *J-V* curve measurements.

A.3.3. Small piece of PQD-COC/Polyamine film transferred on InGaP/GaAs/Ge 3JSC:

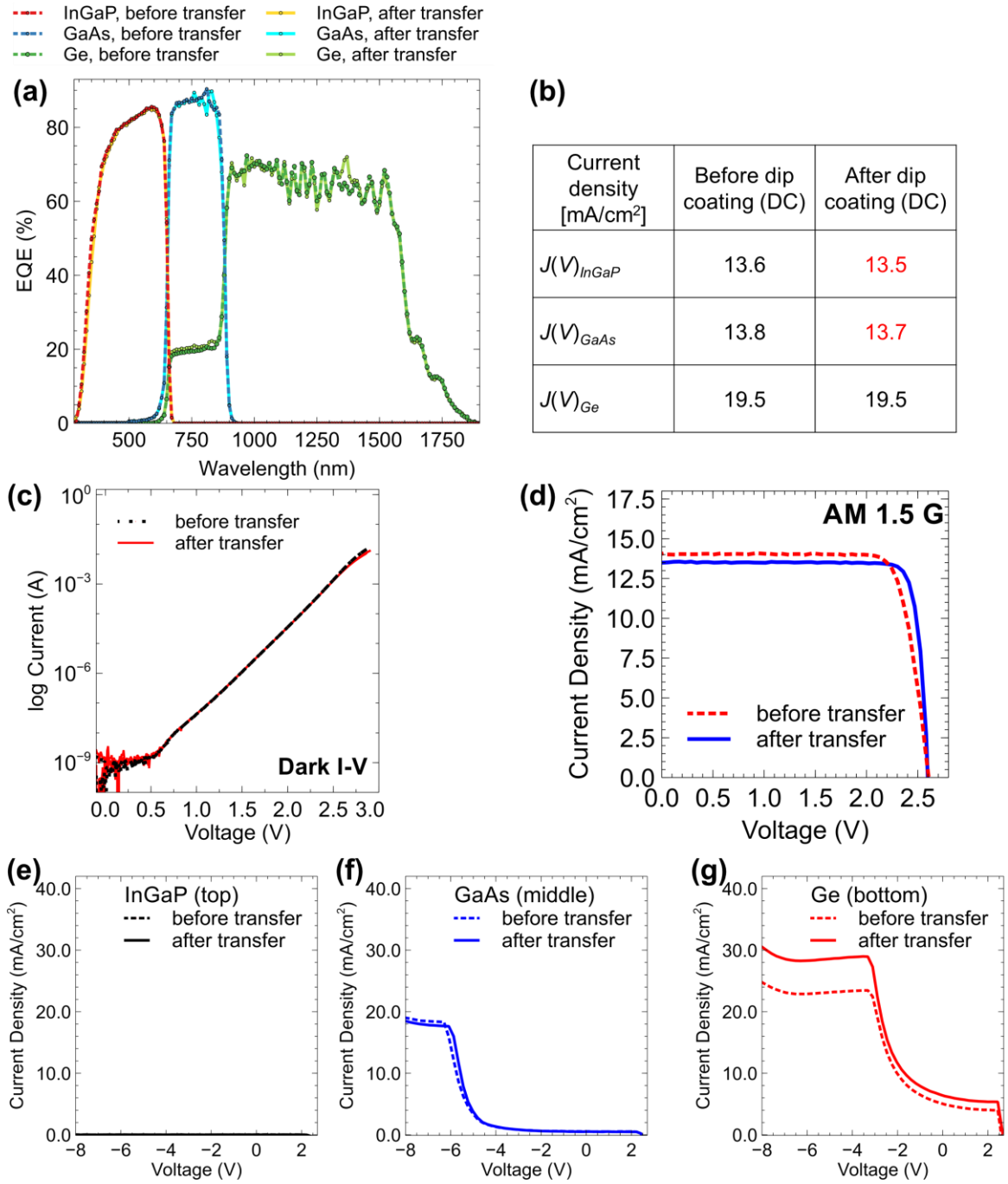

Current density [mA/cm^2]	Before dip coating (DC)	After dip coating (DC)
$J(V)_{InGaP}$	13.6	13.5
$J(V)_{GaAs}$	13.8	13.7
$J(V)_{Ge}$	19.5	19.5

Fig. 7 Optoelectronic characterizations before and after the manual transfer of $CsPbX_3$ PQD-COC/Polyamine film on the InGaP/GaAs/Ge 3JSC perimeter front surface: (a) EQE measurements; (b) summary of current densities derived from subcell EQE measurements using eq. (3); LED *J-V* curves of (c) InGaP, (d) GaAs, and (e) Ge; (f) dark and (g) AM 1.5G at 1 sun *J-V* curve measurements.

Theoretical design and simulation of plateau tandem solar cells for homogeneous luminescent coupling

Appendix B

Appendix B – Theoretical design and simulation of plateau tandem solar cells for homogeneous luminescent coupling

Abstract

Another possible solution to the nonuniform luminescent coupling (LC) effect in III-V multijunction solar cells explored was the alteration of a multijunction solar cell (MJSC) structure. In this supplementary dissertation chapter, the theoretical design and simulation of plateau tandem solar cell structure were discoursed briefly. Different proportions of bottom-to-top cell areas, the latter being reduced in increments, were tested to see which design could yield a homogeneous LC effect. Simulation results revealed that the bottom-to-top cell of 1.28 or larger may yield homogeneous LC current in the bulk region.

.

B.1. Research Question

The main objective of this supplementary chapter is to design and implement a theoretical model for plateau tandem solar cells (P2JSC). This is to test whether it is feasible or not to increase the photocurrent generation towards the cell sides, which in turn may homogenize LC current by modifying the architecture of conventional multijunction solar cell (MJSC) designs. Typically, MJSCs have subcells of the same active areas.

B.2. Methodology

B.2.1. Detailed balance calculation

In the past, a step-cell tandem structure was theoretically studied by detailed balance calculation [338]. By step-cell tandem structure, it means that the top cell has a smaller active region than the lower cell, while the top cell usually has a larger bandgap than the bottom cell. To calculate the detailed balance calculation, the current generation in the top cell, I_T, are given as

$$I_T = A_{Top} \times q \int_{E_{gT}}^{\infty} \emptyset(E)\, QE(E)\, dE \tag{1}$$

and the bottom cell, I_B, as

$$I_B = A_{Top} \times q \int_{E_{gB}}^{E_{gT}} \emptyset(E) QE(E) dE + A_{exp} \times q \int_{E_{gB}}^{\infty} \emptyset(E) QE(E) dE \tag{2}$$

where A_{Top} is the active area of the top cell, A_{exp} is the bottom cell active area that is directly exposed to a light source, q is the electron charge, E_{gT} and E_{gB} are the top and bottom cell bandgaps, respectively, $\emptyset(E)$ is the photon flux at energy, E, and $QE(E)$ is the quantum efficiency. To get the top cell and the bottom cell current densities, J_T and J_B, I_T and I_B should be normalized with A_{Top} and the total bottom cell area (which is the sum of A_{Top} and A_{exp}), respectively.

If all sides of a bottom cell are extended outward for a certain proportion, as illustrated in Fig. 1, it then becomes the P2JSC. Hence, as a first step, the detailed balance calculation for P2JSCs was conducted to determine the theoretical efficiencies of such design at various bottom-to-top cell ratios. Since in terms of subcell active areas, the step-cell and the P2JSC are similar, eqs. (1) and (2) were used for top cell and bottom cell current calculations. Also, the theoretical conversion efficiency limits, η, were calculated using

$$\eta = \frac{P_{out}}{P_{in}} = \frac{\min(J_T, J_B) \times V_{mpp,Total}}{P_{in}} \tag{3}$$

for different top cell and bottom cell bandgap combinations. Here, $\min(J_T, J_B)$ is the subcell producing the lower current density sought after, $V_{mpp,Total}$ is the total maximum

power point voltage across the P2JSC, and P_{in} is the incident light intensity tested. For a realistic picture, the power density at unconcentrated (1-sun) AM 1.5G spectrum was used, that is, P_{in} = 100 mW/cm^2.

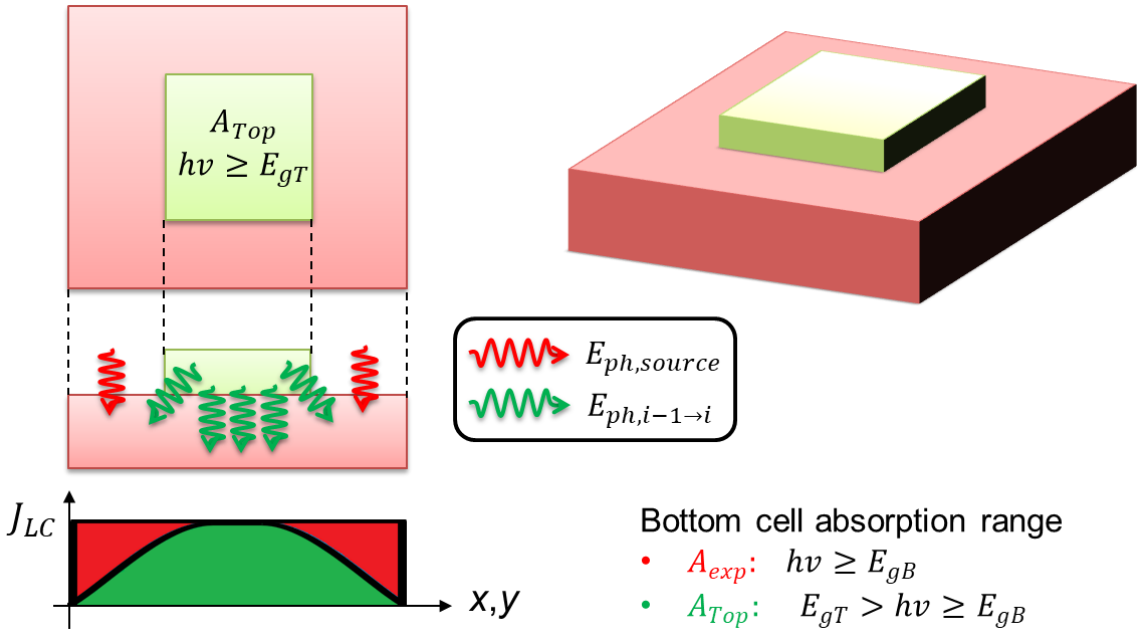

Fig. 1 Schematic illustration of the proposed P2JSC structure for homogenizing the LC effect in MJSCs. Here, $E_{ph,source}$ is the incoming photon directly from the light source and $E_{ph,i-1\rightarrow i}$ is the photon emission from the top cell to the bottom cell.

B.2.2. 3-dimensional modeling of plateau tandem solar cell (P2JSC)

A 3D model was developed to simulate different top and bottom cell area proportions and seek the optimal proportion that may yield a homogeneous LC effect. This was done by implementing a combination of SPICE and Q2DEP modeling (see Appendix C, Sec 3 for a detailed description of the Q2DEP model). Figure 2 shows a simplified electrical circuit illustration of the P2JSC in 3D [Fig. 2(a)] and its cross-section [Fig. 2(b)]. In these illustrations, $J_{B,exp}$, $J_{B,in}$, and J_{Total} are the currents from the exposed bottom cell region, from the bottom cell region covered by top cell, and the total P2JSC current.

The first step in developing this model was to set the bottom-to-top cell ratio. As the size of the SPICE model was limited by the calculation capacity of the computer used, a fixed value of 30×30 unit cells were built for the top cell, while the unit cells in the bottom cell ranged between 30×30 to 40×40. Based on these sizes, the bottom-to-top cell ratios were calculated, which may serve as a possible guide on the optimal areas for top and bottom cell that may result in uniform LC current. Similarly, this could be a useful guideline for selective area application of all-inorganic perovskite quantum dot-cyclic olefin copolymer (PQD-COC) film on MJSCs achieve homogeneous LC effect. The summary of test cases is listed in Table 1, Sec. B.5. Next, using the SPICE parameters listed in Table 2, Sec. B.5, the current collection map of the P2JSC was acquired, in which the bottom cell was made current-limiting. The resultant current map was incorporated into the Q2DEP model to consider nonuniform ($\beta \neq 0$) and uniform LC current ($\beta = 0$) cases by setting the Bern factor, β, which is the fraction of nonuniform LC current [170,172–

173,185,217]. Based on previous LC current measurement fits [170,185], β was then set to 32% for all bottom-to-top cell ratios implemented.

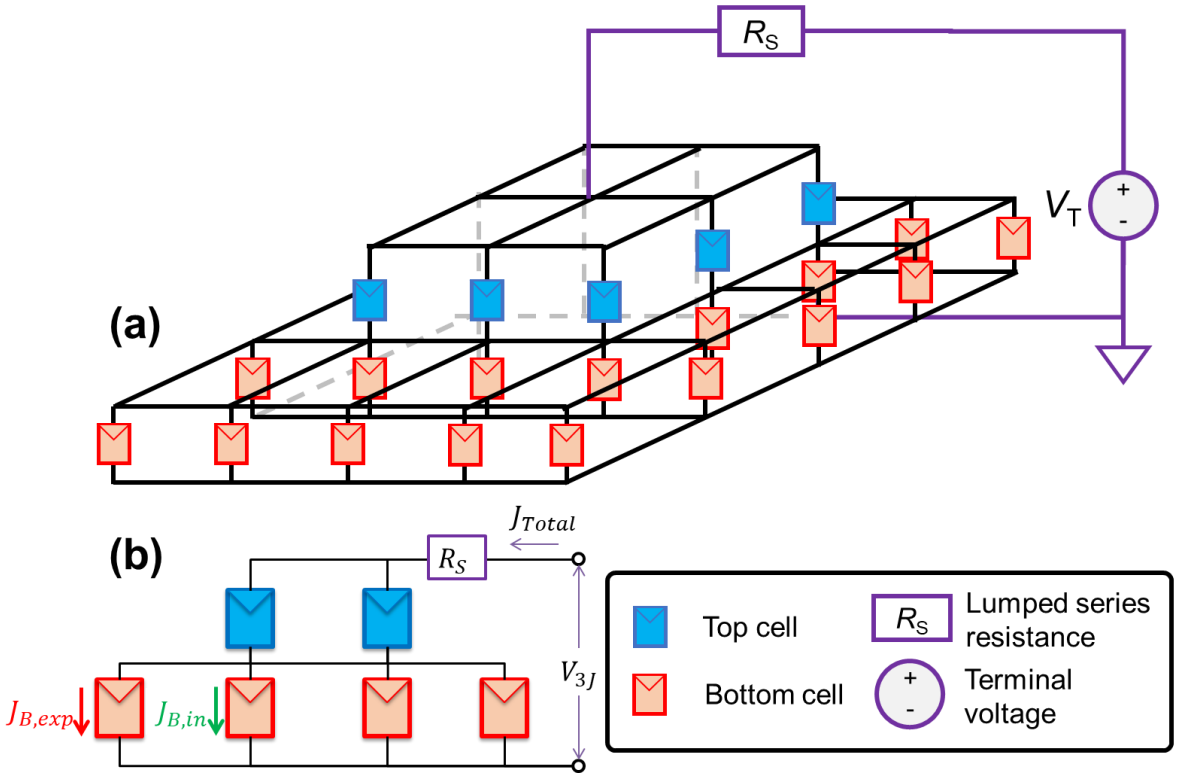

Fig. 2 Schematic illustration of P2JSC electrical model (a) in 3D perspective and (b) its cross-section. Here, $J_{B,exp}$, $J_{B,in}$, and J_{Total} are the currents from the exposed bottom cell region, from the bottom cell region covered by the top cell, and the total P2JSC current.

B.3. Results and Discussions

The optimal E_{gB} and E_{gT} combinations with the highest theoretical efficiency limits were calculated for P2JSC using eq. (3). Shown in Fig. 5, the theoretical limits for P2JSC (triangle) at different bottom-to-top cell proportions, A_{Bottom}/A_{Top} were plotted with the optimal E_{gB} and E_{gT} combinations that resulted in the highest theoretical limits for a step cell (dot symbols [338]). Among the A_{Bottom}/A_{Top} ratios implemented, A_{Bottom}/A_{Top} = 1.1, with bandgap combinations of E_{gB} = 0.948 eV and E_{gT} = 1.543 eV, yielded the highest theoretical efficiency of 45.9%.

However, in real applications, it is difficult to produce solar cell absorber materials having the exact values of E_{gB} = 0.948 eV and E_{gT} = 1.543 eV. Hence, for a broader picture of the optimal E_{gB} and E_{gT} combinations, the theoretical efficiency maps were plotted at different A_{Bottom}/A_{Top} ratios and various E_{gB} and E_{gT} combinations. These are shown in Fig. 3. With larger total to top cell area ratio, the number of optimal E_{gB} and E_{gT} combinations increases as indicated by the dashed boxes on the plots. This suggests that less top cell material will be needed; hence, promoting better efficiency in upper cell material usage. In MJSCs, InGaP is typically used as a top cell, in which In is known to be limited on Earth [60]. Hence, P2JSC design may be a more sustainable option than the conventional MJSC architecture, in which all subcells have the same active area.

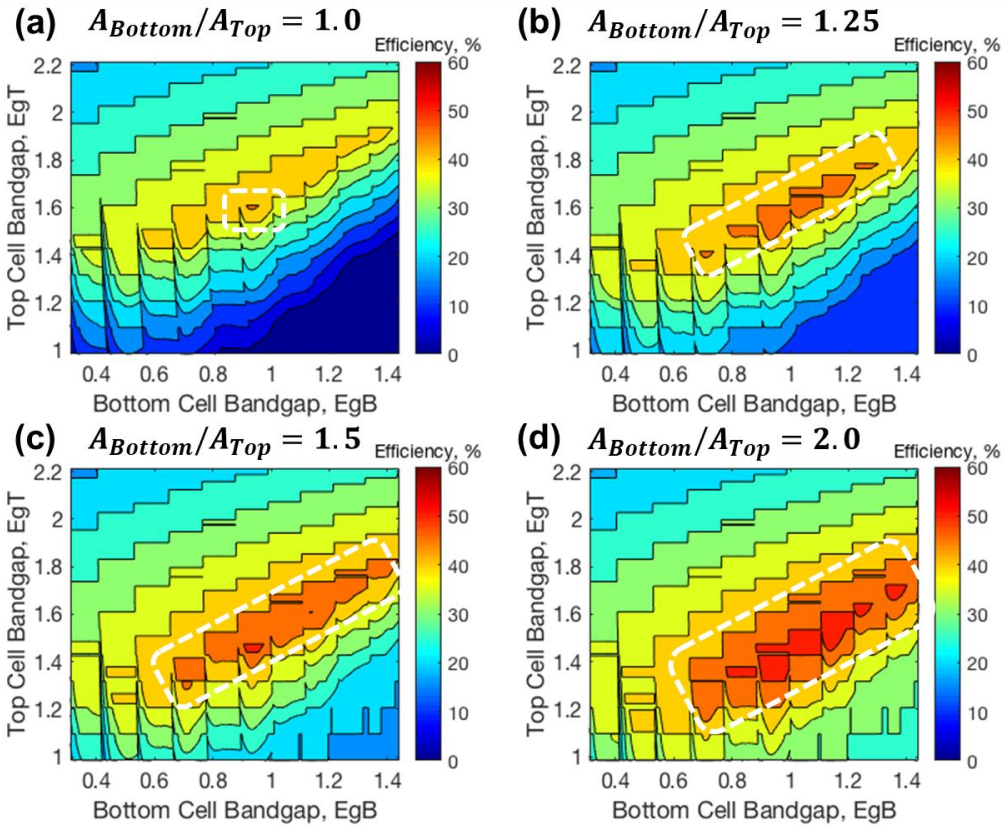

Fig. 3 Theoretical efficiency limit maps obtained from different E_{gB} and E_{gT} combinations and at different bottom-to-top cell proportions.

Different A_{Bottom}/A_{Top} proportions were also tested for LC current collection using SPICE electrical and Q2DEP models described in Section B-2. The series of current maps produced by uniform (β=0) and nonuniform LC effect ($\beta\neq0$) are shown in Figs. 4(a) and (b), respectively. From the current maps produced by the uniform LC effect [Fig. 4(a)], the current collection was high in all regions. However, with A_{Bottom}/A_{Top} ratios of 1.28 and beyond, less current collection was obtained in the region covered by the top cell as compared with those collected in the bottom cell region modeled to be directly exposed to the light source. As for nonuniform LC current maps [Fig. 4(b)], at ratios of 1 to 1.14, the inhomogeneous LC effect is still prevalent. On the other hand, when the ratio was increased to 1.28 or higher, the current collection in the region covered by the top cell became homogeneous. Hence, LC nonuniformity may be eliminated when the bottom cell is at least 1.28 times larger than the top cell.

However, less LC current collection was obtained from the central region while the exposed region produced more LC current. This is the same as observed from simulations for uniform LC current shown in Fig. 4(a). The distinct current collection between these two different regions observed could be due to the electrical model not being able to consider carrier diffusion.

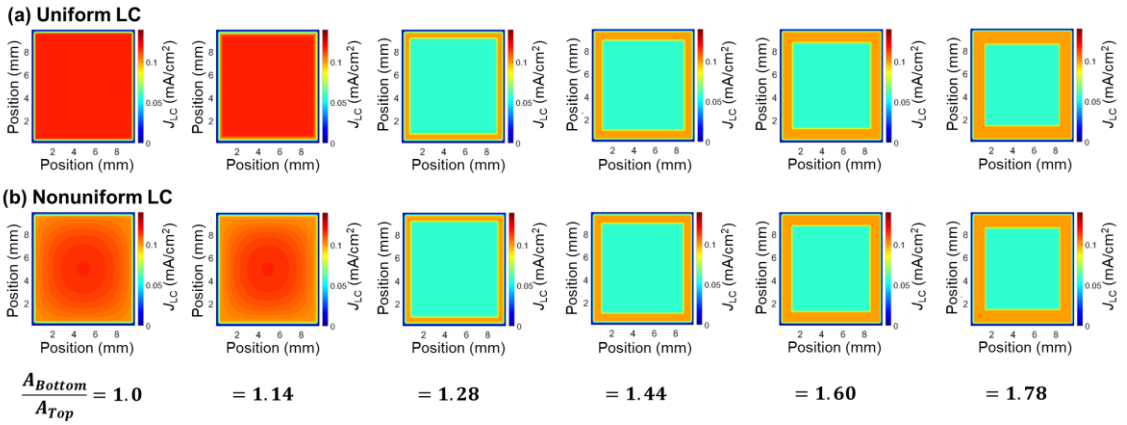

Fig. 4 Current collection maps obtained using SPICE and Q2DEP models at different A_{Bottom}/A_{Top} proportions at (a) uniform LC effect, i.e. $\beta = 0$, and (b) nonuniform LC effect, i.e. $\beta \neq 0$.

Although the highest theoretical efficiency limit was obtained at A_{Bottom}/A_{Top} of 1.1 for a certain E_{gB} and E_{gT} combinations, the LC current was homogenized at A_{Bottom}/A_{Top} of 1.28 or larger. Therefore, as there may be a tradeoff between the cell efficiency and the current collection homogeneity, an optimal A_{Bottom}/A_{Top} should be sought after while considering available materials with E_{gB} and E_{gT} combination being favorable to the overall performance of plateau MJSC designs.

B.4. Conclusion

A theoretical model for plateau tandem solar cells (P2JSC) was designed and simulated to determine if such architecture is capable of homogenizing LC current in MJSCs. An A_{Bottom}/A_{Top} ratio of 1.28 or higher resulted in a more uniform LC current collection in the bottom cell region covered by the top cell. Hence, LC nonuniformity may be eliminated when the bottom cell is at least 1.28 times larger than the top cell. However, these configurations suffered less current collection than what was generated in their exposed regions. This could be possibly addressed by optimizing the A_{Bottom}/A_{Top} while considering available E_{gB} and E_{gT} combinations and will be favorable to the overall performance of plateau MJSC designs. Also, dedicated supercomputers for a more precise calculation of current collection while considering carrier diffusion from the exposed regions to the region covered by the top cell. Needless to say, another next step recommended is to fabricate this structure and test it experimentally.

B.5. Supplementary Information

Table 1 shows the summary of the 3D SPICE model considering 6 different proportions between the top cell and the bottom cell.

Figure 5 shows the optimal 2J bandgap combinations for step cells [338] and P2JSC that yield the highest theoretical efficiencies obtained from detailed balance calculation using eq. (3).

Table 2 contains the parameters used in 3D SPICE simulation, in which the bottom cell within the same area covered by the top cell was made current-limiting.

Table 1 Summary of bottom cell nodes implemented in electrical SPICE modeling of P2JSC with their corresponding bottom-to-top cell ratios.

Bottom cell nodes, $n \times n$ (unit cells)	Bottom-to-top cell ratio, A_{Total}/A_{Top}
30×30	1.00
32×32	1.14
34×34	1.28
36×36	1.44
38×38	1.60
40×40	1.78

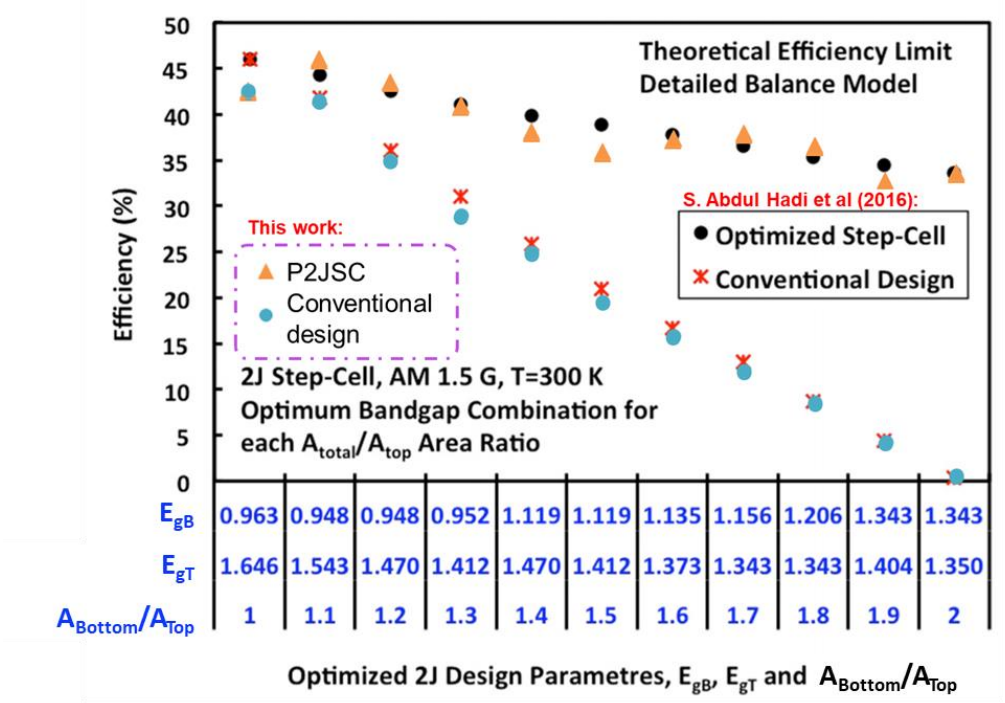

Fig. 5 Best E_{gB} and E_{gT} combinations with highest theoretical efficiency limits for step cell (dark dot symbols [338]) and their corresponding efficiencies for P2JSC (triangle symbols) at different bottom-to-top cell proportions, A_{Bottom}/A_{Top}. Here, conventional design (step cell: cross symbol [338] and P2JSC: light dot symbols) means $A_{Bottom}/A_{Top} = 1$ for all E_{gB} and E_{gT} combinations.

Table 2 Summary of parameter values used for the top and bottom cells of P2JSC in electrical SPICE modeling. Here, dA is the differential cell area.

Parameter	Top cell	Bottom cell within A_{Top}	Bottom cell outside A_{Top} (exposed)
Photocurrent generation, $J_{ph,i}$ (mA/dA)	20.0	0	1.0
Diffusion diode coefficient, $J_{01,i}$ (mA/dA)	1.00×10^{-20}	9.00×10^{-6}	9.00×10^{-9}
Nonradiative recombination diode coefficient, $J_{02,i}$ (mA/dA)	1.00×10^{-8}	2.50×10^{-1}	1.00×10^{-6}
Radiative recombination diode coefficient, $J_{0Rad,i}$ (mA/dA)	1.00×10^{-17}	1.00×10^{-6}	6.75×10^{-8}
Shunt resistance, $R_{SH,i}$ (Ω/dA)	1.95×10^{5}	1.00×10^{4}	1.00×10^{4}
Lumped series resistance, R_S (Ω)		3.00×10^{-3}	
LC efficiency, $\alpha_{LCi\text{-}1\rightarrow i}$		0.61	

Simulation of carrier dynamics and light interactions affecting the spatial distribution of luminescent coupling effect

Appendix C

Appendix C – Simulation of carrier dynamics and light interactions affecting the spatial distribution of luminescent coupling effect

Abstract

This supplementary chapter is dedicated to the investigation of the underlying physics behind nonuniform luminescent coupling (LC) effect in multijunction solar cells (MJSCs) observed in past studies, which were thoroughly discussed in Chapter 2. This chapter begins stipulating the main research objective, that is, to find out the possible causes behind nonuniform LC effect by electrical and optical simulations, followed by listing down the specific questions that may lead to the answers for the general question of this supplementary chapter. In Sec. C.2, the simulation methods used are discussed. Next, Sec. C.3 discusses the simulation results and inferences drawn from each method in relation to the inhomogeneous LC effect. Last, this chapter ends with the synthesis of the main findings acquired during the theoretical investigation of the carrier dynamics and light interactions possibly causing an inhomogeneous LC effect in MJSCs.

C.1. Research Questions

The main objective of this supplementary chapter is to find out the underlying carrier dynamics and light interactions possibly responsible for nonuniform LC current collection using various electrical and optical simulation models. Specifically, this chapter attempts to answer the following questions:

1. What causes the nonuniform LC effect among the following?
   a. Is it photon escape?
   b. Is it the lateral series resistance leading to degraded carrier transport efficiency?
   c. Is it the nonradiative recombination in the emitting higher bandgap subcell?
   d. Is it the nonradiative recombination in the current-limiting lower bandgap subcell where the photons are reabsorbed?
   e. Is it the shunt defects in the higher bandgap subcell?
   f. Is it the shunt defects in the lower bandgap subcell?
2. What are the possible ways to homogenize the LC effect?
   a. By surface texturing?
   b. By electrical passivation?
   c. By applying anti-reflective coating (ARC) on the sidewalls?
3. What electro-optical simulation model design could be implemented for analyzing the observed nonuniform LC effect in III-V based MJSCs?

C.2. Methodology

C.2.1. Two-dimensional ray tracing

In the previous chapter, along with some recent reports [141,170–173,185,217], photon escape was speculated to be one of the underlying causes behind the nonuniform LC effect. To theoretically investigate photon escape in common semiconductors used as solar cell absorber materials, a 2-dimensional (2D) Monte Carlo ray-tracer by PV lighthouse was used [339]. The 2D ray tracer used is available online and is a free optical simulation tool. However, because it is an open access simulator, it has the following limitations: (1) the longest wavelength that can be simulated without fee is 1300 nm; (2) the simulator does not account for photon recycling; and (3) reflection, R, absorption, A, and transmission, T, are calculated as probabilities. Considering these limitations, only the following semiconductors were simulated, namely, gallium phosphide (GaP) [340], aluminum gallium arsenide ($Al_xGa_{1-x}As$, $x = 0.099$) [341], gallium arsenide (GaAs) [340], indium phosphide (InP) [342], and silicon (Si) [343].

In conducting 2D ray tracing, two general cases were considered. One is the inbound case, in which the light is coming from outside the solar cell absorber, then hits it. In this case, the photons of different wavelengths that penetrated through it are calculated as transparent, absorbed, or reflected. Another is the outbound case, where the light emission is coming from the solar cell absorber, then calculate if the photons would escape the absorber, i.e. by transmission or photon escape or if the photons would be internally reflected. To find possible answers to question 2 of this chapter, different interfaces were considered. One is when a bare absorber material is planar and is simply surrounded by air as an ambient material. Next is when the absorber material has a thin film coating,

which is either intended as an anti-reflection coating (ARC) [344] or an electrical passivation material [248–256]. Last is when a bare absorber material is textured and is surrounded by air as an ambient material.

C.2.1.1. Planar solar cell absorbers

As a base case, planar solar cell absorbers of different materials and cell widths were initially investigated using 2D Monte Carlo ray tracer. Varying the cell width may help identify what cell size would be ideal to suppress photon escape, and in turn, could assist homogenizing strong LC effect in III-V based MJSCs.

The inbound case for a bare solar cell absorber surrounded by air is illustrated in Fig. 1(a). Here, the sunlight spectrum used was isotropic global air mass 1.5 (AM 1.5G), releasing a maximum of 50,000 photon rays, with a 0.001% limit of the total intensity (exact value not specified in the simulator). Practically, this light source may be considered as the diffuse light, which is about 10% of the total sunlight under cloudless conditions [345]. Based on the refractive index of the absorber material, there are three possible outcomes that the incident external photons may experience: (1) external reflection, that is, photons subjected to this process never entered the absorber material; (2) escape, in which photons were able to enter the absorber material but then eventually exited through the escape cones; and, (3) transmission, where the photons possessing energies below the absorber bandgap just pass through the material and has no chance of being absorbed. These processes are governed by Snell's law [131], given as:

$$\frac{\sin\theta_{absorber}}{\sin\theta_{ambient}} = \frac{n_{ambient}}{n_{absorber}} \tag{1}$$

where $n_{absorber}$ and $n_{ambient}$ are the refractive indices of the solar cell absorber material and the material surrounding it (in this case, air; hence $n_{ambient} = 1$), respectively. Here, $\theta_{absorber}$ and $\theta_{ambient}$ are the photon angles measured from the normal with respect to the interface. Whether a photon will escape or be internally reflected is determined by calculating the critical angle, θ_c, using the relation:

$$\sin\theta_c = \frac{n_{ambient}}{n_{absorber}}. \tag{2}$$

If the angle of the photon within the absorber, θ_{photon}, with respect to the normal of the air-absorber interface is less than or equal to θ_c, i.e. $\theta_{photon} \leq \theta_c$, the photon will escape. On the other hand, if $\theta_{photon} > \theta_c$, the photon will undergo total internal reflection.

The outbound case for a bare solar cell absorber surrounded by air is shown in Fig. 1(b). Being the only generic option available from the free version of 2D ray tracer, the sunlight spectrum used for the outbound emission was also AM 1.5G. A maximum of 50,000 photon rays was released as well, having a limit of 0.001% of the total intensity. In this scenario, there are two possible processes that the internally emitted photons may undergo: (1) internal reflection, that is, photons subjected to this process never escaped the absorber material; and (2) escape, in which photons were able to enter the absorber material but then eventually exited through the escape cones. These processes are also governed by the Snell's law, as described by eqs. (1) and (2).

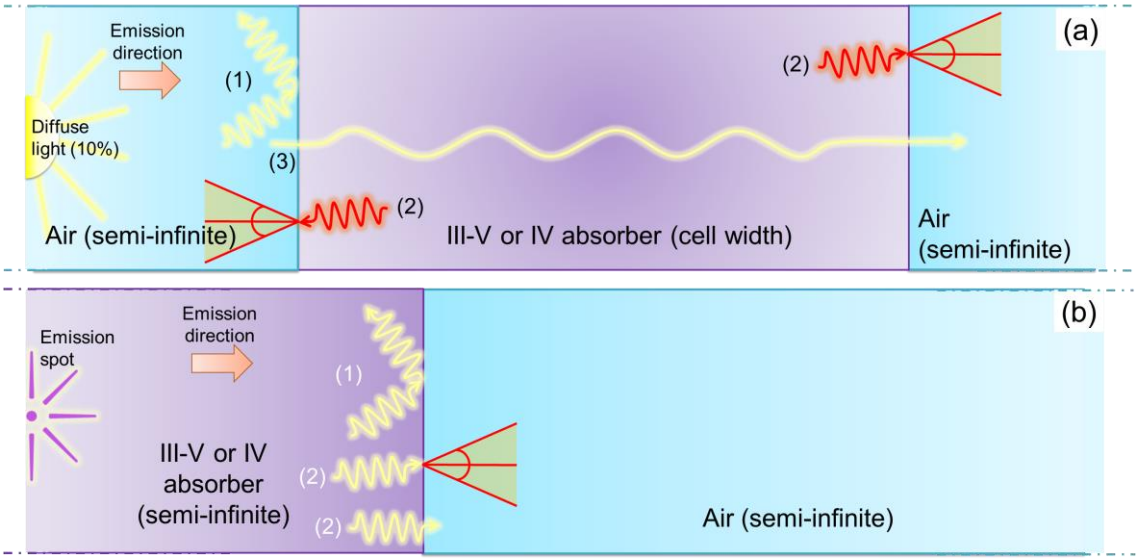

Fig. 1 (a) Schematic illustration of the (diffuse) sunlight coming through a sidewall of a III-V or IV semiconductor absorber material. Here processes (1), (2), and (3) correspond to external reflection, photon escape, and transmission, respectively. (b) Schematic illustration of light emission within the absorber. Here, processes (1) and (2) correspond to internal reflection and photon escape, respectively. Specific to photon escape, this process is a combination of reflected photons escaping and transmitted, as both indicate that the photon exited from the absorber.

Aside from the light source parameters, such as the radiation direction (isotropic or direct), spectrum (AM 1.5G or D), intensity limit, and the total number of rays released during simulation, the following parameters need to be encoded into the 2D ray tracer to simulate the inbound and outbound cases for a bare solar cell absorber material surrounded by air. One is the material stack, in which for the inbound and the outbound cases, the surrounding materials are air and the III-V or IV material, respectively. Another is the material thickness, in which the maximum possible thickness that can be set in the free version is 10,000 μm (10 mm). Another is the wavelength-resolved refractive index to be used based on the available literature compiled by the 2D ray tracer developers. Then, one can also specify the maximum number of ray bounces, the wavelength range to simulate, where the lower and upper limits for the free version are 300 and 1300 nm, respectively, the wavelength step size, and the number of rays to release per calculation cycle. Sample inputs for the inbound and the outbound cases are shown in Figs. 17(a) and (b), Sec. C.5, respectively.

The processes accounted for the inbound and the outbound cases are indicated in the sample output window shown in Figs. 18(a) and (b), Sec. C.5, respectively. From this window, one can determine the probable amount of incident light subjected to each possible process in terms of current densities and their percentages of the total incident light. While processes for the inbound case are straightforwardly described in the output section [Fig. 18(a)], further elaboration on the output section for the outbound case is needed. As listed in Fig. 18(b), processes (1) and (2) correspond to internal reflection and photon escape, respectively, as discussed earlier about Fig. 1(b). Specific to the output section, process (1) is indicated as "Reflected – external" while process (2) is the sum of both "Reflected – escape" and "Transmitted" as photons subjected to these processes exited out of the absorber.

As for the photon escape probabilities in each material and both cases, one can extract a spreadsheet file after the ray tracing run is finished. Note that during simulations, data shown in this section of the 2D ray tracer must be stored manually as the raw spreadsheet data that can be extracted will not contain this information. For the inbound case, the total photon escape probability, $P_{Tesc,in}$, is extracted from the "Reflected – escape" column by integrating the values in this column from 300 nm up to the equivalent energy gap of the simulated absorber material in terms of wavelength, λ_{E_g}, at 300 K [346]. Mathematically, this is

$$P_{Tesc,in} = \int_{\lambda=300\,nm}^{\lambda_{E_g}} P_{esc}(\lambda)d\lambda \tag{3}$$

where $P_{esc}(\lambda)$ is the photon escape probability at each wavelength, λ. On the other hand, for calculating the outbound photon escape probability, $P_{Tesc,out}$, it is extracted from the sum of "Reflected – escape" and "Transmitted" columns, as both cases indicate that the photon exited the absorber material. The sum of these columns is then integrated from 300 nm up to λ_{E_g} at 300 K, that is,

$$P_{Tesc,out} = \int_{\lambda=300\,nm}^{\lambda_{E_g}} P_{esc}(\lambda) + T(\lambda)d\lambda \tag{4}$$

where $T(\lambda)$ is the transmission probability per λ.

C.2.1.2. Solar cell absorbers coated with thin films

Depending on their bandgap and optical properties, thin films can be used as ARC layers for solar cells to improve light absorption and light trapping. Furthermore, thin films can be used to electrically passivate solar cells to decrease dangling bonds that may act as surface recombination centers. Hence, these layers could homogenize the LC effect when deposited to III-V based MJSC sidewalls. The same 2D ray tracer used for simulating the cases discussed in Section 2.1.1 was also used to simulate the effect of adding a thin film coating on III-V and IV solar cell absorbers to photon escape. The inbound and outbound light emission schematics of a thin film on solar cell absorbers are shown in Figs. 2(a) and (b), respectively. Here, thin films simulated were 10-nm aluminum oxide (Al_2O_3), which is widely used for electrical passivation of a solar cell to reduce surface recombination [248–256] and 100-nm silicon nitride (SiN_x), which is commonly used as an ARC film for solar cell front surfaces [344].

The inbound case for a solar cell absorber coated by thin film and then surrounded by air is illustrated in Fig. 2(a). Here, the sunlight spectrum used was isotropic AM 1.5G, releasing a maximum of 50,000 photon rays, with a 0.001% limit of the total incident light intensity. Based on the refractive indices of the thin film and the absorber material, there are three possible outcomes that the incident external photons may experience: (1) external reflection, that is, photons subjected to this process never entered the absorber material; (2) escape, in which photons were able to enter the absorber material but then eventually exited through the escape cones; (3) transmission, where the photons possessing energies below the absorber bandgap just pass through the material and has no chance of being absorbed; (4) and (5) are thin-film absorption on the light entry and

exit sides of the cell, respectively. These processes are also governed by Snell's law, in which the photon angles are measured from the normal with respect to the interface. In this case, there are 2 interfaces considered, which are the absorber-thin film and the thin film-air interfaces. For the absorber-thin film interface, the relationship based on Snell's law is given as:

$$\frac{\sin\theta_{absorber}}{\sin\theta_{TF}} = \frac{n_{TF}}{n_{absorber}} \tag{5}$$

where n_{TF} and θ_{TF} are the refractive index and the thin-film light angle measured from the normal with respect to the absorber-thin film interface, respectively. On the other hand, the Snell's law for the thin-film interface is given as:

$$\frac{\sin\theta_{TF}}{\sin\theta_{ambient}} = \frac{n_{ambient}}{n_{TF}} \tag{6}$$

Whether a photon will escape or be internally reflected is determined by the critical angles for each interface, θ_{c1} and θ_{c2}, defined as:

$$\sin\theta_{c1} = \frac{n_{ambient}}{n_{TF}} \tag{7}$$

and

$$\sin\theta_{c2} = \frac{n_{TF}}{n_{absorber}} \tag{8}$$

for thin film-air and absorber-thin film interfaces, respectively. If the photon angle within the absorber or the thin film, θ_{photon}, with respect to the normal of the thin film-air or absorber-thin film interface is less than or equal to θ_{c1} or θ_{c2}, i.e. $\theta_{photon} \leq \theta_{c1}$ or θ_{c2}, respectively, the photon will escape. On the other hand, if $\theta_{photon} > \theta_{c1}$ or θ_{c2}, the photon will undergo total internal reflection.

The outbound case for a bare solar cell absorber coated by thin film and then surrounded by air is shown in Fig. 2(b). In this case, the sunlight spectrum used for outbound emission was also AM 1.5G. A maximum of 50,000 photon rays was released as well, having a limit of 0.001% of the total intensity. In this scenario, three possible processes may happen to the internally emitted photons: (1) internal reflection, that is, photons subjected to this process never escaped the absorber material; (2) escape, in which photons were able to enter the absorber material but then eventually exited through the escape cones; and (3) thin-film absorption. These processes are also governed by Snell's law, as described by eqs. (5) to (8).

Aside from the light source parameters, such as the radiation direction, spectrum, intensity limit, and the total number of rays released during simulation, the following parameters need to be encoded in the 2D ray tracer to simulate the inbound and outbound cases for a thin film-coated absorber material surrounded by air. Just like in the bare solar cell absorber material cases, one is the material stack, where the surrounding medium is air. For the inbound case, a front and back thin film were included, which represent the

entry and exit surfaces of light escaping from the absorber layer. As for the outbound cases, the surrounding medium is the III-V or IV material, with a single layer of thin-film separating it from the air. In the outbound case, only the front film was added since the emission direction that could be anticipated is only through a single film layer. Another parameter set is the material thickness (maximum = 10 mm). The wavelength-resolved refractive index to be used based on the available literature compiled by the 2D ray tracer developers is also a set parameter. Then, one can also specify the maximum number of ray bounces, the wavelength range to simulate, where the lower and upper limits for the free version are 300 and 1300 nm, respectively, the wavelength step size, and the number of rays to release per calculation cycle. Sample inputs for inbound and outbound cases for coated solar cell absorbers are shown in Figs. 19(a) and (b), Sec. C.5, respectively.

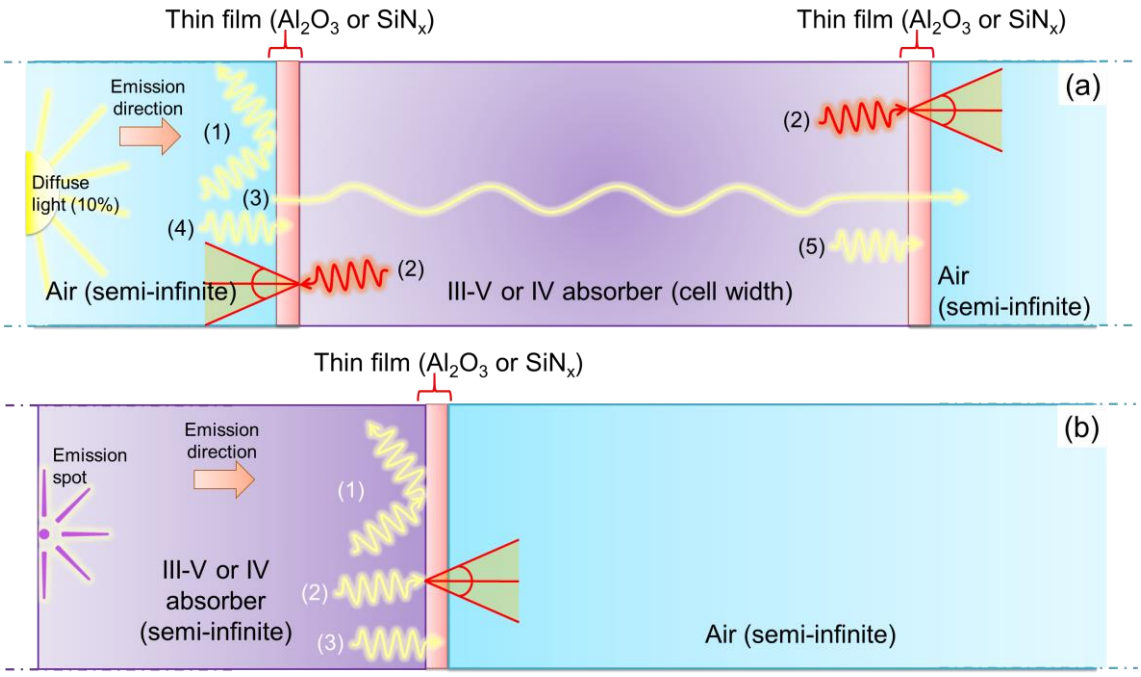

Fig. 2 (a) Schematic illustration of light coming through a sidewall of a III-V or IV semiconductor absorber material coated with a thin film anti-reflective coating or electrical passivation layer. Here processes (1), (2), (3), (4) and (5) correspond to external reflection, photon escape, transmission, and thin-film absorption at the left and at the right sides, respectively. (b) Schematic illustration of light emission within the absorber. Here, processes (1), (2), and (3) correspond to internal reflection, photon escape, and thin-film absorption, respectively. Specific to photon escape, this process is a combination of reflected photons escaping and transmitted, as both indicate that the photon exited from the absorber.

The processes accounted for the inbound and the outbound cases are indicated in the sample output section shown in Figs. 20(a) and (b), respectively. While processes listed in Fig. 20(a) are straightforward, processes (1), (2), and (3) in Fig. 20(b) correspond to internal reflection, photon escape, and thin-film absorption, respectively, as discussed earlier Fig. 2(b). Specific to the output section, process (1) is indicated as "Reflected – external", process (2) is the sum of both "Reflected – escape" and "Transmitted" as photons subjected to these processes exited out of the absorber, and process (3) is indicated as "Absorbed – front films".

For the inbound case, the total photon escape probability, $P_{Tesc,in}$, is extracted from the "Reflected – escape" column by integrating the values in this column from 300 nm up

to the equivalent energy gap of the simulated absorber material in terms of wavelength, λ_{E_g}, at 300 K [346], as defined in eq. (3) earlier. On the other hand, for the outbound case, $P_{Tesc,out}$ is extracted from the sum of "Reflected – escape" and "Transmitted" columns, as both cases, indicate that the photon exited the absorber material. The sum of these columns is then integrated from 300 nm up to λ_{E_g} at 300 K, as defined by eq. (4).

C.2.1.3. Textured solar cell absorbers

Textured surfaces are known to enhance the light absorption and light trapping in solar cells [259,347–348]; hence, texturing the solar cell sidewalls may assist in homogenizing the LC effect in III-V based MJSCs. Using the 2D ray tracer, the effect of textured sidewall surfaces on photon escape was probed. The inbound and outbound light emission schematics of textured solar cell absorber surfaces are shown in Figs. 3(a) and (b), respectively. Textures simulated were upright pyramid [Fig. 3(c)], inverted pyramid [Fig. 3(d)] and periodically grooved surfaces [Fig. 3(e)].

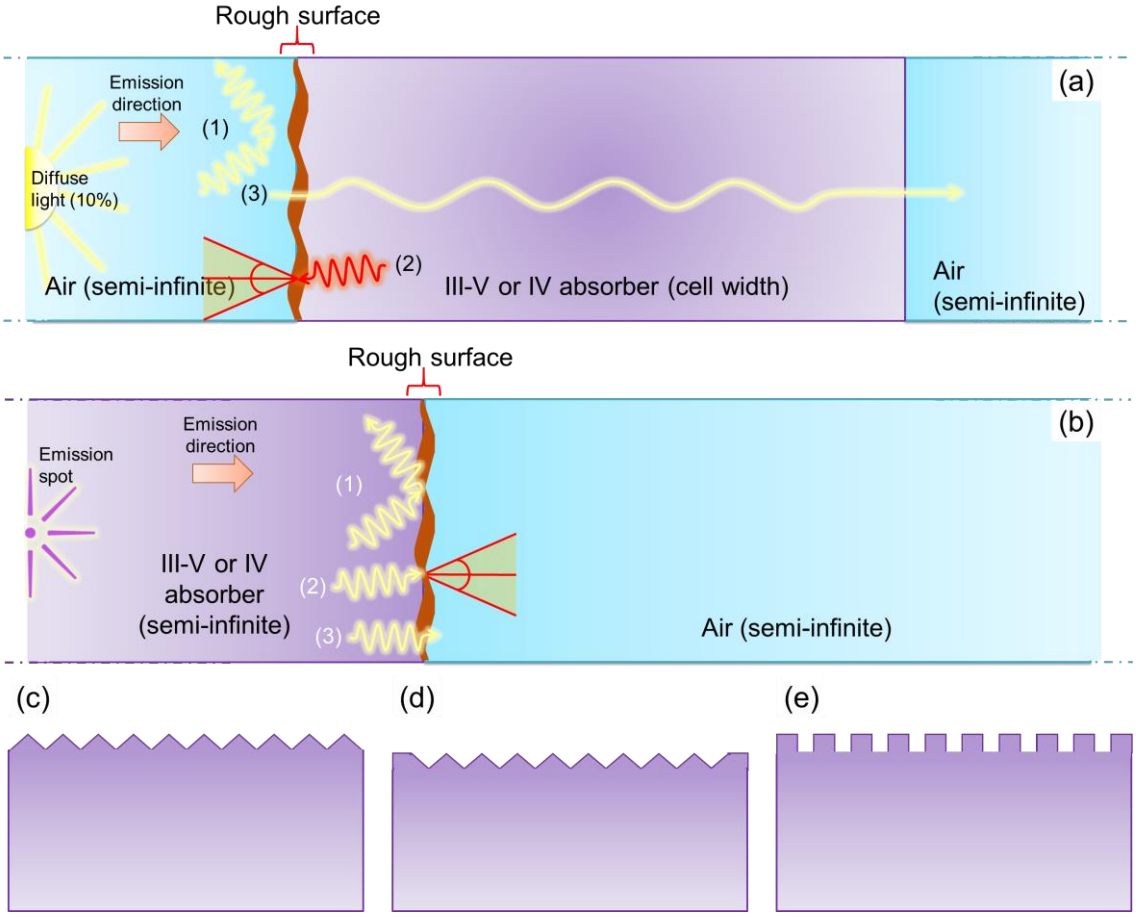

Fig. 3 (a) Schematic illustration of light coming through a textured sidewall of a III-V or IV semiconductor absorber material. Here processes (1), (2), and (3) correspond to external reflection, photon escape, and transmission, respectively. (b) Schematic illustration of light emission within the textured absorber. Here, processes (1) and (2) correspond to internal reflection and photon escape, respectively. Specific to photon escape, this process is a combination of reflected photons escaping and transmitted, as both indicate that the photon exited from the absorber. Schematic illustrations of different solar cell absorber material textures: (c) upright pyramid, (d) inverted pyramid, and (e) X-groove textures.

The inbound case for a textured solar cell absorber surrounded by air is illustrated in Fig. 3(a). Here, the sunlight spectrum used was isotropic AM 1.5G, releasing a maximum of 50,000 photon rays, with a 0.001% limit of the total intensity. Based on the refractive index of the absorber material, there are three possible processes that the incident external photons may undergo: (1) external reflection, that is, photons subjected to this process never entered the absorber material; (2) escape, in which photons were able to enter the absorber material but then eventually exited through the escape cones; and, (3) transmission, where the photons possessing energies below the absorber bandgap just pass through the material and has no chance of being absorbed. These processes are governed by Snell's law [131] defined as eq. (1) earlier, but with additional influence from the textured surface angles. Moreover, θ_c is also given by eq. (2).

The outbound case for a textured solar cell absorber surrounded by air is shown in Fig. 3(b). Being the only generic option available from the free version of 2D ray tracer, the light source used for outbound emission was also AM 1.5G. A maximum of 50,000 photon rays was released like in other cases, with a total intensity limit of 0.001%. In this case, there are two possible processes that the incident external photons may undergo: (1) internal reflection, that is, photons subjected to this process never escaped the absorber material; and (2) escape, in which photons were able to enter the absorber material but then eventually exited through the escape cones. These processes are also governed by Snell's law, as described by eqs. (1) and (2).

Aside from the light source parameters, such as the radiation direction, spectrum, intensity limit, and the total number of rays released during simulation, the following parameters have to be entered in the 2D ray tracer to simulate the inbound and outbound cases for a textured solar cell absorber material surrounded by air. One is the material stack, in which for the inbound and the outbound cases, the surrounding media are air and the III-V or IV material, respectively. Another is the material thickness (maximum = 10 mm). There is also the wavelength-resolved refractive index based on the available literature compiled by the 2D ray tracer developers. Then, one can also specify the maximum number of ray bounces, the wavelength range to simulate, where the lower and upper limits for the free version are 300 and 1300 nm, respectively, the wavelength step size, and the number of rays to release per calculation cycle. Sample inputs for inbound and outbound cases are shown in Figs. 21(a) and (b), Sec. C.5, respectively.

The processes accounted for the inbound and the outbound cases are indicated in the sample output section shown in Figs. 22(a) and (b), respectively. Although the inbound case processes are straightforwardly described in the output section [Fig. 22(a)], further elaboration on the output section for the outbound case is needed. As listed in Fig. 22(b), processes (1) and (2) correspond to internal reflection and photon escape, respectively, as discussed earlier about Fig. 3(b). Specific to the output section, process (1) is indicated as "Reflected – external" while process (2) is the sum of both "Reflected – escape" and "Transmitted" as photons subjected to these processes exited out of the absorber. Similar to the planar case, $P_{Tesc,in}$ and $P_{Tesc,out}$ are calculated using eqs. (3) and (4), respectively.

C.2.2. Three-dimensional SPICE electrical modeling of MJSCs with LC effect

To study the electrical losses possibly causing nonuniform luminescent coupling in III-V based 3JSCs, a 3D distributed SPICE electrical model was used [141,206]. In this

model, the lateral sheet resistance, R_{lat}, and the nonradiative recombination diode coefficient of the adjacent or coupled subcells, $J_{02,i-1}$ and $J_{02,i}$, whose ideality factor, m, is 2, and the shunt resistances of the adjacent subcells, $R_{sh,i-1}$ and $R_{sh,i}$, were varied at a time. These three parameters were chosen to be varied due to the following reasons:

1. R_{lat} represents the carrier transport efficiency, which becomes more pronounced at higher applied terminal voltages in the forward regime [154,186]. Hence, this may affect the spatial carrier collection of the MJSC.
2. $J_{02,i}$ represents the nonradiative recombination in a specific subcell. Thus, the higher this value is, the larger the number of recombination centers present in the subcell is, which may be greatly influenced by unwanted defects in it [171].
3. $R_{sh,i}$ represent the manufacturing defects in an MJSC subcell, which is similar to how J_{02} is described in item 2. Shunt defects are pathways to leakage current, thereby affecting the carrier collection homogeneity as well [141].

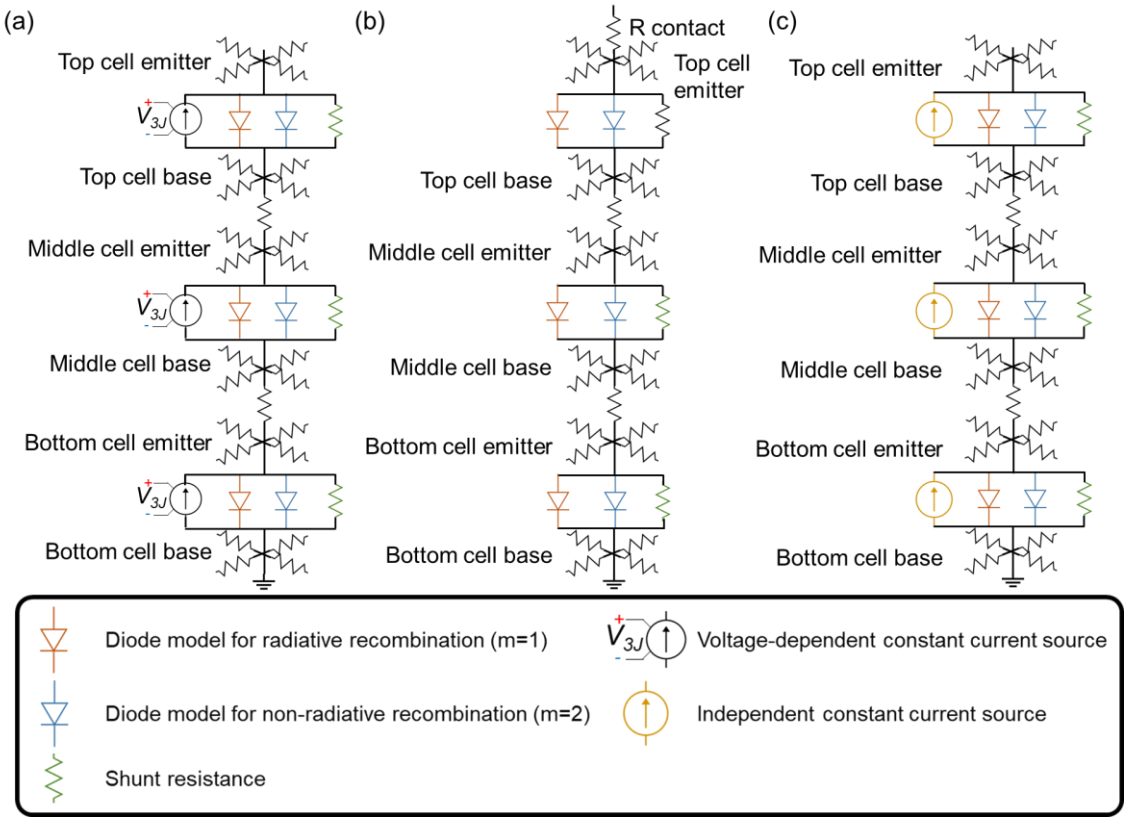

Fig. 4 Unit schematic diagram used in 3D distributed SPICE electrical modeling of III-V based 3JSCs in each differential region of the cell: (a) perimeter region, (b) metal (busbar) region, and (c) active region.

Figure 4 shows the schematic diagram per differential area of a 3JSC. The unit circuit models for the perimeter region, the metal region representing the grid and the busbars of the 3JSC, and the active region are shown in Figs. 4(a) to (c), respectively. Aside from those mentioned earlier, each subcell in the perimeter region contains the following: a voltage-dependent constant-current source, which represents the current generation at the cell perimeter based on the applied 3JSC terminal voltage, and radiative recombination diode whose coefficient is $J_{01,i}$, and has an ideality factor of 1. On the other hand, the active region has an independent constant-current source, which represents the current

production due to external light bias. Additionally, the metal region does not have any constant current source. The default SPICE simulation parameters used for each region per unit subcell are summarized in Table 1. These values are based on those published in [172] for terrestrial-grade InGaP/GaAs/Ge 3JSCs.

Table 1 Summary of the default parameters used for each subcell at the active region, metal (busbar) region and perimeter region of a triple-junction solar cell modeled using a 3-dimensional distributed SPICE electrical circuit. Here, *dA* is the differential cell area.

Parameter	Top Cell	Middle Cell	Bottom Cell
Lumped lateral series resistance, R_{lat} (Ω/*dA*)		1.00×10^{-3}	
Temperature (°C)		25	
Active region			
Photocurrent generation, $J_{ph,i}$ (mA/*dA*)			
• Middle cell current-limiting	1.00×10^{-2}	0	1.00×10^{-2}
• Bottom cell current-limiting	1.00×10^{-2}	1.00×10^{-2}	0
Diffusion diode coefficient, $J_{01,i}$ (mA/*dA*)	1.00×10^{-27}	1.00×10^{-23}	9.00×10^{-8}
Luminescent coupling factor/efficiency (%)			
• Middle cell current-limiting, $\alpha_{LC,T\rightarrow M}$		70.0	
• Bottom cell current-limiting, $\alpha_{LC,M\rightarrow B}$		70.0	
Nonradiative recombination diode coefficient, $J_{02,i}$ (mA/*dA*)	1.00×10^{-15}	1.00×10^{-9}	1.00×10^{-4}
Shunt resistance, $R_{sh,i}$ (Ω/*dA*)	1.00×10^{7}	1.00×10^{7}	1.00×10^{4}
Metal (busbar) region			
Diffusion diode coefficient, $J_{01,i}$ (mA/*dA*)	1.00×10^{-27}	1.00×10^{-23}	1.00×10^{-8}
Diffusion diode breakdown voltage, $V_{BR,J01,i}$ (V)	3.73	3.06	0.30
Nonradiative recombination diode coefficient, $J_{02,i}$ (mA/*dA*)	1.00×10^{-15}	1.00×10^{-9}	1.00×10^{-4}
Shunt resistance, $R_{sh,i}$ (Ω/*dA*)	1.00×10^{7}	1.00×10^{7}	1.00×10^{4}
Perimeter region			
Photocurrent generation, $J_{ph,i}$ (mA/*dA*)	Applied 3J voltage-dependent, $J_{ph,i}(V_{3J})$*		
Diffusion diode coefficient, $J_{01,i}$ (mA/*dA*)	1.00×10^{-27}	1.00×10^{-23}	1.00×10^{-8}
Diffusion diode breakdown voltage, $V_{BR,J01,i}$ (V)	3.73	3.06	0.30
Nonradiative recombination diode coefficient, $J_{02,i}$ (mA/*dA*)	1.00×10^{-15}	1.00×10^{-9}	1.00×10^{-4}
Shunt resistance, $R_{sh,i}$ (Ω/*dA*)	1.00×10^{7}	1.00×10^{7}	1.00×10^{4}

** Modeled using voltage-dependent constant-current source.*

As the 3D distributed model was limited by the calculation capacity of the computer used and the SPICE software itself, the active region of the cell was defined by 20×20 units of illuminated 3JSC region, as shown in Fig. 5. Moreover, the metal region was lumped into two 1×20 units. Last, the perimeter region is represented by surrounding the metal and the active regions with 1 external unit. Hence, the whole 3D distributed model for the 3JSC is comprised of a total of 24×22 units.

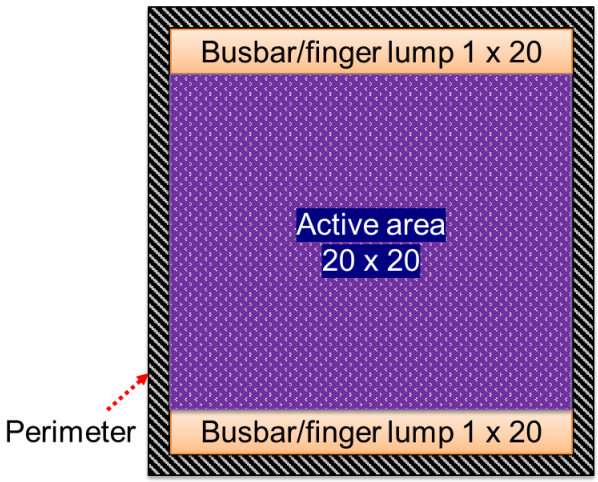

Fig. 5 Simplified top view schematic illustration of the 3D distributed model for III-V based 3JSC using SPICE electrical circuit.

C.2.3. Quasi-two-dimensional electro-optical prediction (Q2DEP) model

As discussed in Chapter 3, a spatially-resolved Q2DEP model was developed for analyzing the nonuniform LC effect in III-V based MJSCs. Here, the material properties of the 3JSC samples and the illumination profile of the LC effect were modeled using a 2D SPICE electrical model and 3D superellipse model, respectively [170,185,217]. In Fig. 6(a), the 2D SPICE electrical model for a 3JSC is shown, while Fig. 6(b) shows the 3D phenomenological superellipse model for the inhomogenous LC effect. It was mentioned in Chapter 3, as described by eq. (2) there, that β_{LC} is the fraction of nonuniformity describing the portion of the LC current that was quenched, particularly those near the cell edges. This nonuniformity is ascribed to photon escape [170,217], to perimeter recombination [202–203,207,219], to nonuniform material growth [171], or high carrier injection into a higher bandgap (HBG) or (*i*-1)th subcell resulting to nonuniform illumination towards an adjacent limiting lower bandgap (LBG) or *i*th subcell [154,220]. As defined by eq. (2) in Chapter 3, higher β_{LC} value indicates less uniform LC current distribution. A detailed description of the model can be found in Chapter 3, Sec. 3.2.4.

The coefficient of determination or R-squared, r^2, can be used as a statistical measure of evaluating how good a certain model predicts the observed phenomenon [210]. In the context of the prediction models used for nonuniform LC current fitting and temperature dependence of subcell bandgaps studied, r^2 is the squared Pearson correlation coefficient, r, which is an indicator of correlation between the measured and the fitted or calculated data points [211]. It is given by

$$r = \frac{\sum_{i=1}^{n}(x_i - \bar{x})(y_i - \bar{y})}{\sqrt{\sum_{i=1}^{n}(x_i - \bar{x})^2 \sum_{i=1}^{n}(y_i - \bar{y})^2}} \tag{9}$$

where $\bar{x}$, and $\bar{y}$ are the average of arrays x (predicted) and y (observed), respectively, whose sizes are both n. The closer r and r^2 are to 1.0, the better the correlation and the prediction, respectively.

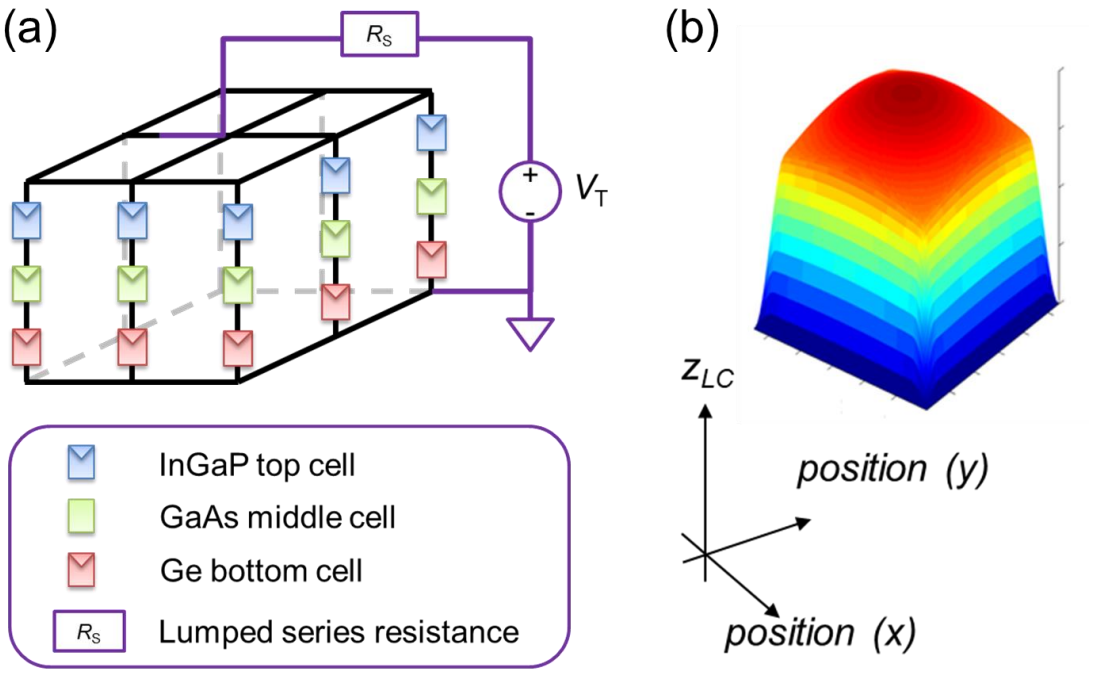

Fig. 6 Main components of the Q2DEP model: (a) 2D SPICE electrical circuit and (b) superellipse phenomenological model for spatially nonuniform LC effect.

C.3. Results and Discussions

C.3.1. Optical simulation using 2D Monte Carlo ray tracer

C.3.1.1. Case 1 – Photon escape in planar solar cell absorbers

Figures 7(a) to (e) show the inbound photon escape probability of each bare solar cell absorber having various cell widths, W_c, plotted against incident inbound photon wavelength. Among the different absorbers simulated, GaAs yielded zero probability when the light emission is inward for all values of W_c. While InP and Si showed a clear decreasing trend in the inbound probability with larger cell width or area, no obvious trend could be established for both GaP and $Al_xGa_{1-x}As$ (x = 0.099) just by looking at Figs. 7(a) and 7(b), respectively. As for the wavelength-resolved outbound photon escape probability, all materials exhibited similar probabilities. However, in terms of integrated probabilities, these materials would differ based on their respective bandgaps.

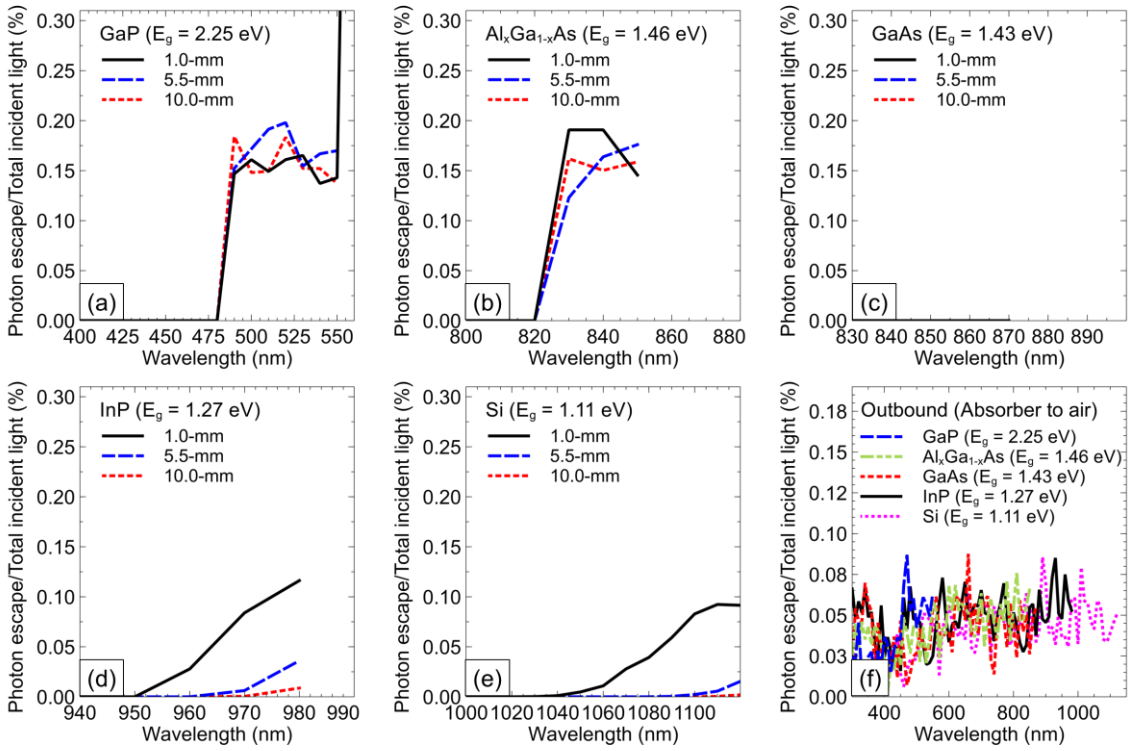

Fig. 7 Wavelength-resolved inbound photon escape probabilities of bare (a) GaP, (b) $Al_xGa_{1-x}As$; x = 0.099, (c) GaAs, (d) InP, and (e) Si solar cell absorbers surrounded by air and having different cell widths. (f) Wavelength-resolved outbound photon escape probabilities of various solar cell absorbers having a cell width of 1 mm.

Table 2 Integrated inbound photon escape probabilities of various bare III-V, IV solar cell absorber materials surrounded by air and having different cell widths, W_c.

Semiconductor absorber material	Photon escape probability (%)		
	W_c = 1.0 mm	W_c = 5.5 mm	W_c = 10.0 mm
Gallium Phosphide, GaP (E_g = 2.25 eV)	1.06	1.20	1.11
Aluminum Gallium Arsenide, $Al_xGa_{1-x}As$; x=0.099 (E_g = 1.46 eV)	0.53	0.46	0.47
Gallium Arsenide, GaAs (E_g = 1.43 eV)	0	0	0
Indium Phosphide, InP (E_g = 1.27 eV)	0.23	0.04	0.01
Silicon, Si (E_g = 1.11 eV)	0.41	0.02	0

Using eq. (3), the integrated inbound photon escape probability, $P_{Tesc,in}$, of each solar cell absorber having various W_c was calculated based on the absorber's bandgap at 300 K [346]. Calculations are summarized in Table 2. Among the different absorbers simulated, GaAs yielded zero $P_{Tesc,in}$ for all W_c values tested when the light emission is inward. Meanwhile, InP and Si showed a decreasing trend in $P_{Tesc,in}$ with larger cell width or area. Hence, for inbound light emission, using single-junction InP or Si solar cells with a larger cell area may eliminate photon escape almost completely. On the other hand, no definite trend of $P_{Tesc,in}$ can be established for both GaP and $Al_xGa_{1-x}As$ (x=0.099). Nevertheless, these values do not seem to deviate from 1.1% and 0.5%, respectively. The $P_{Tesc,in}$ values listed in Table 2 are the maximum amount of photon losses that could be prevented to

escape the solar cell by homogenizing the LC effect. Meanwhile, it should be noted that some of these photons may escape through the front and back surfaces.

Last, the integrated outbound photon escape probability, $P_{Tesc,out}$, of each solar cell absorber was calculated using eq. (4), considering bandgaps at 300 K [346]. These values are summarized in Table 3. Simulation results revealed that $P_{Tesc,out}$ is about 1.0 to 3.3 % for bare solar cell absorbers with air as the surrounding medium. Among the different materials, InP suffers the highest amount of loss due to photon escape, which was estimated to be $P_{Tesc,out}$ = 3.3%. Meanwhile, GaP yielded the least $P_{Tesc,out}$ of 1.0%. Hence, when these two are combined to form a ternary compound, $In_xGa_{1-x}P$, one III-V compound may compensate for the other in terms of photon escape losses. While some of these photons may escape through the front and the back surfaces, calculated $P_{Tesc,out}$ may indicate the maximum amount of photon losses that could be prevented to escape the solar cell by homogenizing the LC effect.

Table 3 Integrated outbound photon escape probabilities of various bare III-V, IV solar cell absorber materials surrounded by air.

Semiconductor absorber material	Photon escape probability (%)
Gallium Phosphide, GaP (E_g = 2.25 eV)	1.00
Aluminum Gallium Arsenide, $Al_xGa_{1-x}As$; x=0.099 (E_g = 1.46 eV)	2.39
Gallium Arsenide, GaAs (E_g = 1.43 eV)	2.35
Indium Phosphide, InP (E_g = 1.27 eV)	3.30
Silicon, Si (E_g = 1.11 eV)	3.14

C.3.1.2. Case 2 – Photon escape in solar cell absorbers coated with thin films

Figures 8(a) to (e) show the inbound photon escape probability of each solar cell absorber with and without thin film coating and having a cell width of 1 mm plotted against incident inbound photon wavelength. Here, two different coatings were tested – a 10-nm Al_2O_3 layer and a 100-nm SiN_x layer. From these plots, the following can be observed and inferred. For GaP, InP, and Si [Figs. 8(a), (d) and (e), respectively], photon escape reduction is noticeable for the one with a 100-nm SiN_x ARC layer, while there is no notable difference between bare and the one with 10-nm Al_2O_3 passivation layer. Therefore, no issue would be anticipated for adding a passivation layer and may even be better when an ARC layer is deposited. As for $Al_xGa_{1-x}As$, where x = 0.099 [Fig. 8(b)], both coated materials yielded less photon escape that the bare material, with the SiN_x-coated one yielding the least photon escape; hence, photon escape reduction may be expected when a passivation layer or an ARC layer is deposited on the sidewalls. Same as for the bare GaAs absorber, GaAs with any of the two thin films did not yield any amount of photon escape loss [Fig. 8(c)]. Hence, no potential issue regarding photon escape after inbound light absorption would be expected for GaAs with ARC or passivation layer on the sidewalls.

To confirm the inferences made from Fig. 8 quantitatively, the $P_{Tesc,in}$, was calculated using eq. (3) and are summarized in Table 4. Among the simulated sidewall structures, only GaAs yielded zero $P_{Tesc,in}$ with or without thin film coating. Meanwhile, all other structures yielded less $P_{Tesc,in}$ with a 100-nm SiN_x ARC layer than without it. As for adding an Al_2O_3 layer, GaP yielded slightly higher $P_{Tesc,in}$ as compared with the one without it, while the rest also yielded less $P_{Tesc,in}$ than without it. Between adding a 10-nm Al_2O_3 passivation layer and adding a 100-nm SiN_x ARC layer, the latter yielded a

more significant reduction. Therefore, sidewall deposition of the 100-nm ARC layer for MJSCs may help homogenize LC effect through photon escape reduction. However, it should be noted that the Al_2O_3 thickness may not yet be the optimum thickness; hence, it is still possible to reduce photon escape by adding this passivation layer at its optimum thickness. This is also considering that Al_2O_3 has a smaller refractive index (about 1.68 [259]) and is a wide bandgap material (6.4 eV, as reported in [260]).

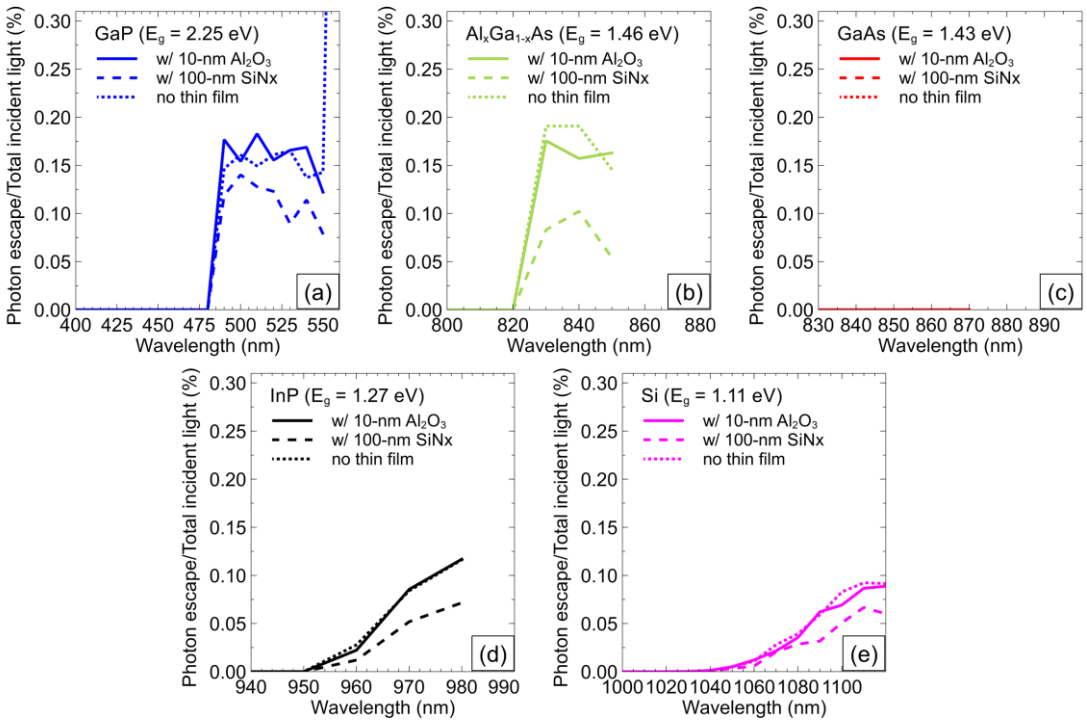

Fig. 8 Wavelength-resolved inbound photon escape probabilities of bare (dotted lines) and thin film-coated (Al_2O_3 - solid lines, SiN_x – dashed lines) (a) GaP, (b) $Al_xGa_{1-x}As$; x = 0.099, (c) GaAs, (d) InP, and (e) Si solar cell absorbers surrounded by air and having a cell width of 1 mm.

Table 4 Integrated inbound photon escape probabilities of various III-V, IV solar cell absorber materials with and without thin film coating. These structures are surrounded by air and have a width of 1 mm.

Semiconductor absorber material	Photon escape probability (%)		
	No thin film	10-nm Al_2O_3	100-nm SiN_x
Gallium Phosphide, GaP (E_g = 2.25 eV)	1.06	1.13	0.79
Aluminum Gallium Arsenide, $Al_xGa_{1-x}As$; x=0.099 (E_g = 1.46 eV)	0.53	0.50	0.24
Gallium Arsenide, GaAs (E_g = 1.43 eV)	0	0	0
Indium Phosphide, InP (E_g = 1.27 eV)	0.23	0.22	0.14
Silicon, Si (E_g = 1.11 eV)	0.41	0.38	0.31

The wavelength-resolved outbound photon escape probabilities for GaP, $Al_xGa_{1-x}As$ (x = 0.099), GaAs, InP, and Si are shown in Figs. 9(a) to (e), respectively. For all materials, it can be seen clearly that for photon emission originating within the solar cell absorber, photon escape is drastically higher for those with a 10-nm Al_2O_3 passivation layer as compared to those having no thin film layer or 100-nm SiN_x ARC layer. Meanwhile, 100-nm SiN_x ARC is noticeably higher for shorter wavelengths

(approximately between 300 nm to 400 nm), while no drastic reduction could be observed at emission wavelengths beyond 400 nm. Hence, 100-nm SiN_x ARC coating seems to be a better option, considering how adding this layer could reduce photon escape probability for incident inbound emission, as inferred from Fig. 8. To confirm these inferences in numbers, $P_{Tesc,out}$ was calculated using eq. (4) and are listed in Table 5. From these numbers, it can be seen that there are less than two times and more than ten times increase in $P_{Tesc,out}$ for SiN_x-coated and Al_2O_3-coated absorbers, respectively, than that of the bare, uncoated absorbers. This can be attributed to the refractive indices of the thin film layers being larger than that of air as a surrounding medium to the absorbers. In this sense then, adding thin film layers may even aggravate the inhomogeneity of the LC effect, having more photon escape towards the cell edges. Nevertheless, as discussed earlier, adding these layers may reduce photon escape in the case of external sunlight emission inward the absorbers.

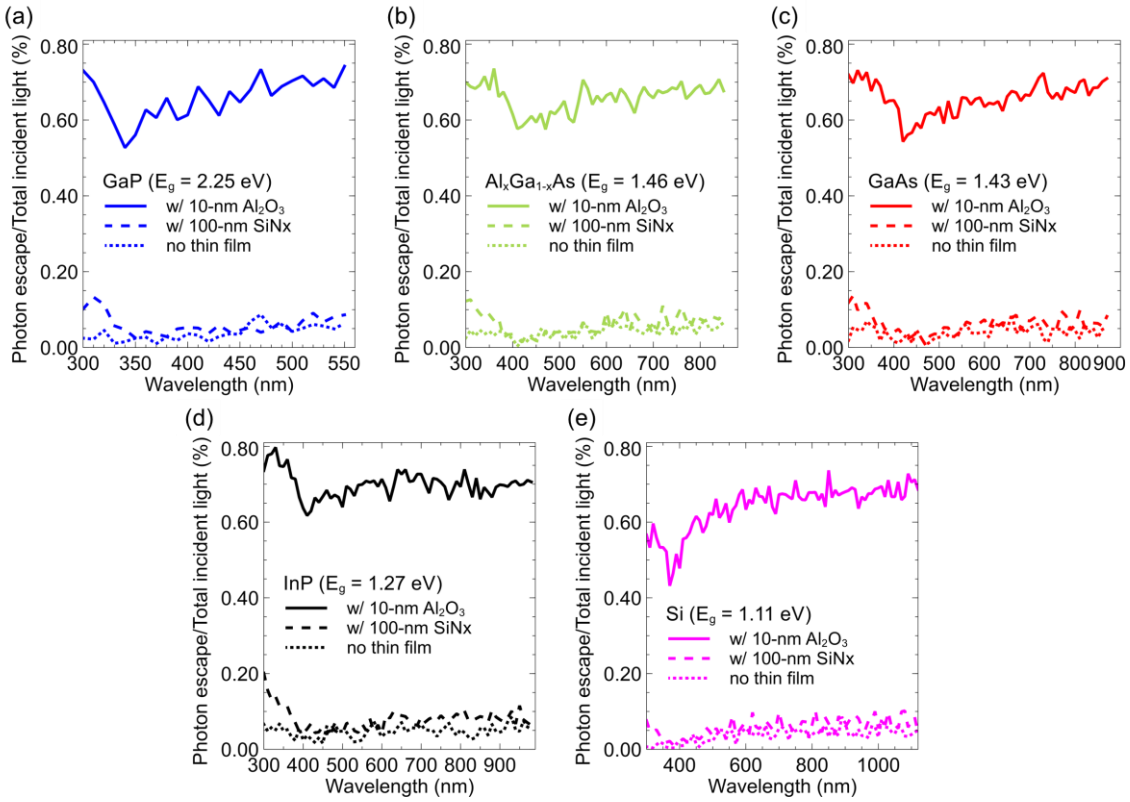

Fig. 9 Wavelength-resolved outbound photon escape probabilities of bare (dotted lines) and thin film-coated (Al_2O_3 - solid lines, SiN_x – dashed lines) (a) GaP, (b) $Al_xGa_{1-x}As$; x = 0.099, (c) GaAs, (d) InP, and (e) Si solar cell absorbers surrounded by air.

C.3.1.3. Case 3 – Photon escape in textured solar cell absorbers

It was also explored if photon escape will be alleviated by texturing the solar cell absorber surfaces, specifically the sidewalls. For a fixed cell width of 1 mm, the effect of different surface textures to photon escape was simulated using the 2D ray tracer. Figures 10 (a) to (e) show the wavelength-resolved inbound photon escape probabilities for GaP, $Al_xGa_{1-x}As$ (x = 0.099), GaAs, InP, and Si. Here, the different textures simulated were planar (solid line, same as those shown in Figs. 7 and 8), upright pyramid (dashed lines), inverted pyramid (dotted lines), and periodically or X-grooved (dashed-dot-dot lines)

textures. No photon escape calculated for GaAs regardless if its surface is textured or not, as shown in Fig. 10(c). For periodic texture (X-groove), photon escape probabilities increased by about twice as compared to having a planar texture. Hence, having a periodically-textured sidewall may worsen the LC effect nonuniformity in MJSCs. On the other hand, upright and inverted pyramid textures seem to benefit $Al_xGa_{1-x}As$, InP, and Si at shorter wavelengths – approximately between 820 and 845 nm, 950 and 965 nm, and 1045 and 1110 nm, respectively. Therefore, pyramid textures for sidewalls could help alleviate the nonuniformity of the LC effect in MJSCs. Meanwhile, no clear benefit could be observed for GaP having upright or inverted pyramid textures.

Table 5 Integrated outbound photon escape probabilities of various III-V, IV solar cell absorber materials with and without thin film coating. These structures are surrounded by air.

Semiconductor absorber material	Photon escape probability (%)		
	No thin film	10-nm Al_2O_3	100-nm SiN_x
Gallium Phosphide, GaP (E_g = 2.25 eV)	1.00	17.15	1.57
Aluminum Gallium Arsenide, $Al_xGa_{1-x}As$; x=0.099 (E_g = 1.46 eV)	2.39	36.82	3.45
Gallium Arsenide, GaAs (E_g = 1.43 eV)	2.35	38.13	3.61
Indium Phosphide, InP (E_g = 1.27 eV)	3.30	48.21	5.47
Silicon, Si (E_g = 1.11 eV)	3.14	53.18	4.81

To collectively quantify the benefit or the disadvantage of textured surfaces as compared with planar surfaces, the $P_{Tesc,in}$ for each absorber having different textures and at a fixed cell width of 1 mm was calculated using eq. (3). These calculations are summarized in Table 6. Except for GaAs, all absorbers with periodically-grooved texture yielded larger $P_{Tesc,in}$, by about 1.5 to 2 times larger, than with planar texture. As for pyramid-textured GaP surface, higher $P_{Tesc,in}$ was calculated as compared with the planar ones. Therefore, it is not desired to have a periodically-grooved surface for any of the materials simulated and pyramid texture for GaP. On the other hand, a slight reduction of $P_{Tesc,in}$ were calculated for $Al_xGa_{1-x}As$, InP, and Si. Hence, pyramid textures may slightly alleviate the inhomogeneity of the LC effect in these absorber materials.

Table 6 Integrated inbound photon escape probabilities of surface-textured III-V, IV solar cell absorber materials. These structures are surrounded by air and have a width of 1 mm.

Semiconductor absorber material	Photon escape probability (%)			
	Planar	Upright pyramid	Inverted pyramid	Periodically -grooved
Gallium Phosphide, GaP (E_g = 2.25 eV)	1.06	1.12	1.14	2.15
Aluminum Gallium Arsenide, $Al_xGa_{1-x}As$; x=0.099 (E_g = 1.46 eV)	0.53	0.50	0.50	0.93
Gallium Arsenide, GaAs (E_g = 1.43 eV)	0	0	0	0
Indium Phosphide, InP (E_g = 1.27 eV)	0.23	0.21	0.20	0.35
Silicon, Si (E_g = 1.11 eV)	0.41	0.32	0.27	0.49

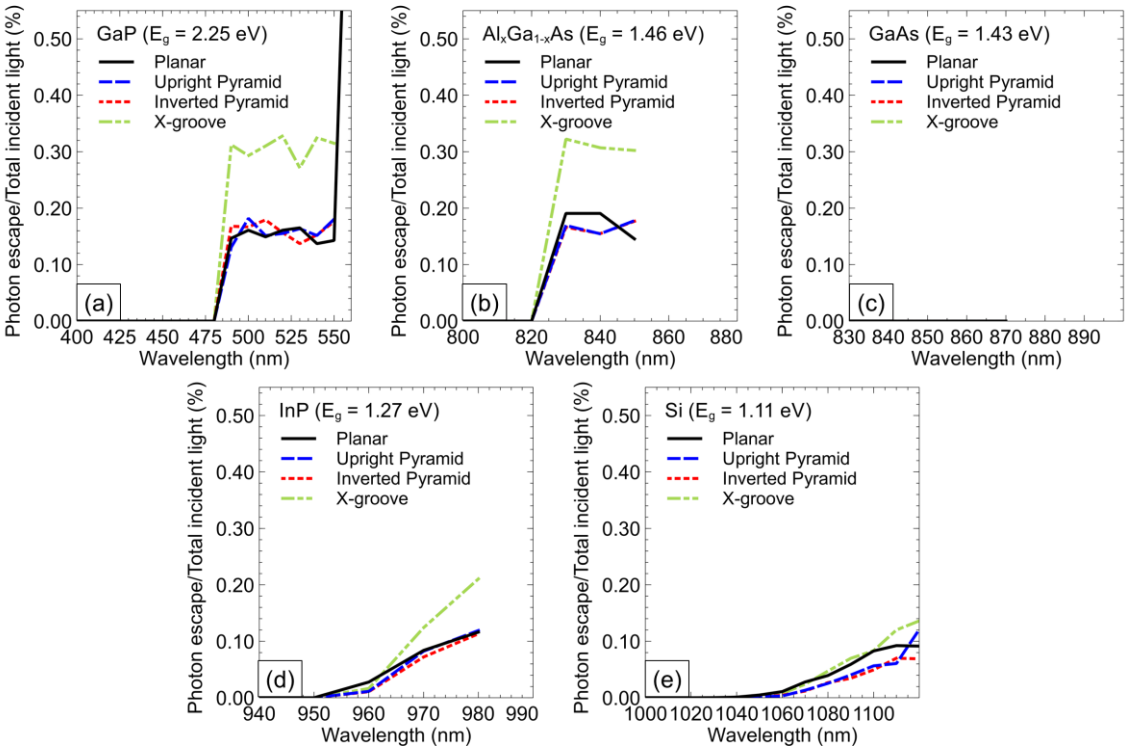

Fig. 10 Wavelength-resolved inbound photon escape probabilities of surface-textured (a) GaP, (b) $Al_xGa_{1-x}As$; x = 0.099, (c) GaAs, (d) InP, and (e) Si solar cell absorbers surrounded by air and having a cell width of 1 mm.

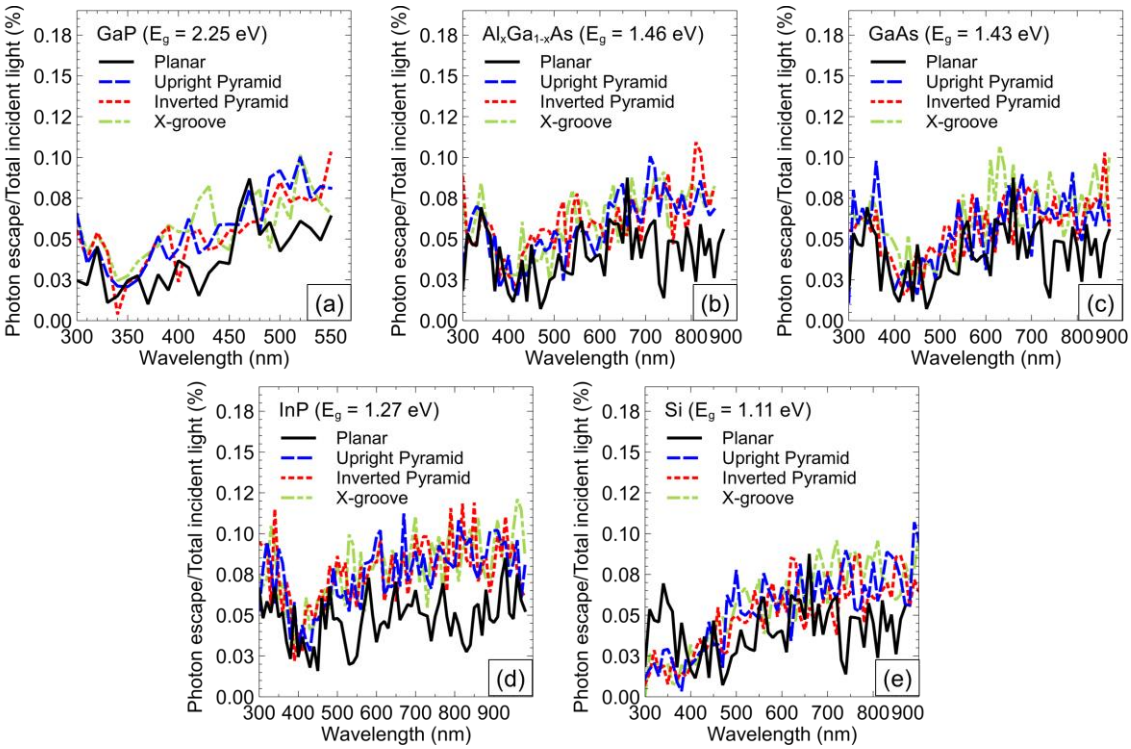

Fig. 11 Wavelength-resolved outbound photon escape probabilities of surface-textured (a) GaP, (b) $Al_xGa_{1-x}As$; x=0.099, (c) GaAs, (d) InP, and (e) Si solar cell absorbers surrounded by air and having a cell width of 1 mm.

Similarly, the outbound photon escape probability for GaP, $Al_xGa_{1-x}As$, GaAs, InP, and Si was determined across different emission wavelengths, as shown in Figs. 11(a) to (e), respectively. Here, it can be seen that per wavelength, textured surfaces for any absorber yielded higher photon escape probabilities than those with planar surfaces. Hence, the escape of light originating from the absorber is aggravated by having textured surfaces and may not be optically helpful in homogenizing the LC effect in MJSCs. These inferences are numerically supported by $P_{Tesc,out}$ values, which were calculated using eq. (4) and are listed in Table 7.

Table 7 Integrated outbound photon escape probabilities of surface-textured III-V, IV solar cell absorber materials. These structures are surrounded by air.

Semiconductor absorber material	Photon escape probability (%)			
	Planar	Upright pyramid	Inverted pyramid	Periodically-grooved
Gallium Phosphide, GaP (E_g = 2.25 eV)	1.00	1.47	1.40	1.52
Aluminum Gallium Arsenide, $Al_xGa_{1-x}As$; x=0.099 (E_g = 1.46 eV)	2.39	3.19	3.37	3.39
Gallium Arsenide, GaAs (E_g = 1.43 eV)	2.35	3.21	3.27	3.60
Indium Phosphide, InP (E_g = 1.27 eV)	3.30	5.16	5.29	5.39
Silicon, Si (E_g = 1.11 eV)	3.14	5.08	4.67	5.26

As no definite trend in photon escape probability of inbound and outbound emission were found, regardless if thin-film coatings or textured surfaces were implemented on the MJSC sidewalls, it can be concluded that photon escape could not be solved using direct approaches studied through 2D ray tracing. Nevertheless, this section only focused on photon escape, which is an optical aspect studied. Therefore, another angle that can be looked upon is the material properties using the SPICE electrical simulation model discussed in the next section. Here, being able to alleviate the nonuniform LC effect by electrical passivation or material quality improvement may be confirmed or disproved theoretically.

C.3.2. Electrical simulations using 3D distributed SPICE model

C.3.2.1. Middle cell current limiting case

Three-dimensional distributed SPICE simulation results considering the LC effect between the top cell as the HBG subcell and the middle cell as the LBG and current-limiting subcell are shown in Fig. 12. Here, it can be seen that the LC current is uniform regardless of the magnitude of the nonradiative recombination saturation current of the top cell and the shunt resistances of both top and middle cells. On the other hand, LC current distribution nonuniformity can be significant under the following conditions: (1) nonradiative recombination saturation current of the LBG middle cell is high [Fig. 12(b)], in the order of 10^{-1} mA/dA (dA is differential area) or higher, which may signify a larger number of recombination centers present in the middle cell and are most likely to be found in the perimeter region; and (2) R_{lat} [Fig. 12(c)] is sufficiently large, in the order of 1.0

Ω/*dA*, which represents the inhomogeneous lateral transport efficiency of carriers. Furthermore, this becomes more prominent when the operating voltage of the emitting subcell is close to V_{OC}, at high carrier injection voltage regime [154,186], having decreasing carrier transport efficiency towards the subcell perimeter. Between these two parameters, the effect of R_{lat} was found to be more significant over length. Here, the current variation at low R_{lat} is less drastic than that at high R_{lat}, suggesting a more uniform voltage distribution ascribed to a more uniform distribution of excess carriers at low R_{lat}.

Table 8 Summary of varied parameters in all regions of triple-junction solar cell modeled using 3D distributed SPICE electrical circuit for electrical investigation of nonuniform current production when the middle cell is made current-limiting. Here, *dA* is the differential cell area.

Varied Parameter		Low Value	High Value
Lumped lateral series resistance, R_{lat} (Ω/*dA*)		1.00×10^{-3} *	1.00
Nonradiative recombination diode coefficient, $J_{02,i}$ (mA/*dA*)			
	Top cell	1.00×10^{-15} *	1.00×10^{-3}
	Middle cell	1.00×10^{-9} *	1.00×10^{-1}
Shunt resistance, $R_{sh,i}$ (Ω/*dA*)			
	Top cell	1.00×10^{2}	1.00×10^{7} *
	Middle cell	1.00×10^{2}	1.00×10^{7} *

** Closer to ideal values.*

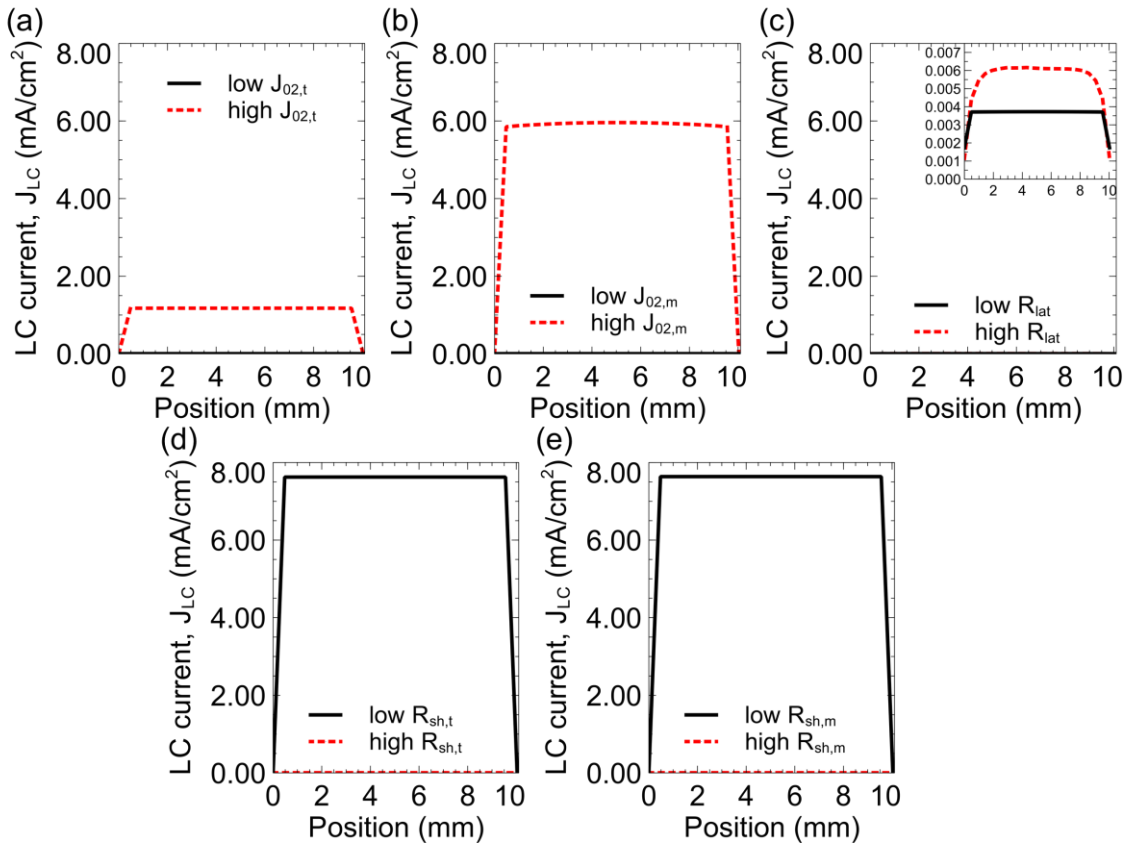

Fig. 12 3D distributed SPICE simulation results of limiting middle cell LC current having (a) top cell nonradiative recombination diode coefficient, $J_{02,t}$, varied from 1×10^{-15} (low) to 1×10^{-3} mA/*dA* (high), (b) middle cell nonradiative recombination diode coefficient, $J_{02,m}$, varied from 1×10^{-9} (low) to 1×10^{-1} mA/*dA*

(high), (c) lumped series lateral resistance, R_{lat}, varied from 1×10^{-3} (low) to 1.0 Ω/*dA* (high), (d) top cell shunt resistance, $R_{sh,t}$, varied from 1×10^{2} (low) to 1×10^{7} Ω/*dA* (high), and (e) middle cell shunt resistance, $R_{sh,m}$, varied from 1×10^{2} (low) to 1×10^{7} Ω/*dA* (high).

As for the higher middle cell current collection simulated with higher $J_{02,i}$ [Figs. 12(a) and (b)] and lower $R_{sh,i}$ [Figs. 12(d) and (e)] values for both the top cell and the current-limiting middle cell, this may be attributed to leakage current passing through the defects within the cell. The summary of low and high values simulated for varying $J_{02,t}$, $J_{02,m}$, R_{lat}, $R_{sh,t}$, and $R_{sh,m}$ shown in Figs. 12(a) to (e), respectively, are listed in Table 8.

From the presented electrical simulations of the middle cell current-limiting case, it may be inferred that sidewall or perimeter passivation of the solar cell absorbers may alleviate the nonuniform LC effect.

C.3.2.2. Bottom cell current limiting case

Three-dimensional distributed SPICE simulation results considering the LC effect between the middle cell as the HBG subcell and the bottom cell as the lower bandgap and current-limiting subcell are shown in Fig. 13. Simulation results revealed that in general, the LC current is uniform regardless of the magnitude of the nonradiative recombination saturation current of the middle cell and the shunt resistances of both middle and bottom cells. These results are consistent with those in the middle cell current-limiting case in the previous subsection. On the other hand, LC current distribution nonuniformity can be significant under the following conditions: (1) nonradiative recombination saturation current of the bottom cell is high [Fig. 13(b)], in the order of 10^{-1} mA/*dA* (*dA* is differential area) or higher, which may also signify a larger number of recombination centers present in the bottom cell and are most likely to be found in the perimeter region; and (2) R_{lat} [Fig. 13(c)] is sufficiently large, in the order of 1.0 Ω/*dA*, which represents the inhomogeneous lateral transport efficiency of carriers. Additionally, this becomes more prominent when the operating voltage of the emitting subcell is close to V_{OC}, at high carrier injection voltage regime [154,186], having decreasing carrier transport efficiency towards the subcell perimeter. Between these two parameters, the effect of R_{lat} was found to be more significant over length. Here, the current variation at low R_{lat} is less drastic than that at high R_{lat}, suggesting a more uniform voltage distribution ascribed to more uniform distribution of excess carriers at low R_{lat}. Meanwhile, the peak due to perimeter region current generation may be attributed to leakage current, which is usually observed in LBIC mapping of MJSCs near the busbar-active region or active region-perimeter boundaries as shown in the LBIC map results in Chapter 3. Another reason could be that the applied terminal voltage-dependent constant-current source may not be the most appropriate component to model the perimeter current in MJSCs. Last, it could be due to the drastic boundary condition imposed on the 3D distributed SPICE electrical model design itself.

In terms of current collection magnitude, simulation results for the bottom cell current-limiting case were inconsistent with those discussed for middle cell current-limiting case earlier. As for the higher bottom cell current collection simulated with higher $J_{02,m}$ [Fig. 13(a)] and lower $R_{sh,m}$ [Fig. 13(d)] values, this may be attributed to leakage current passing through the defects within the cell. Meanwhile, the larger bottom cell current collection at higher $R_{sh,b}$ [Fig. 13(e)] is more intuitive, since higher $R_{sh,b}$ indicates fewer shunt defects brought about during cell manufacturing. With this, the larger current collection may be attributed to the higher efficiency of the LC effect with the HBG middle

cell. The summary of low and high values simulated for varying $J_{02,t}$, $J_{02,m}$, R_{lat}, $R_{sh,t}$, and $R_{sh,m}$ shown in Figs. 13(a) to (e), respectively, are listed in Table 9.

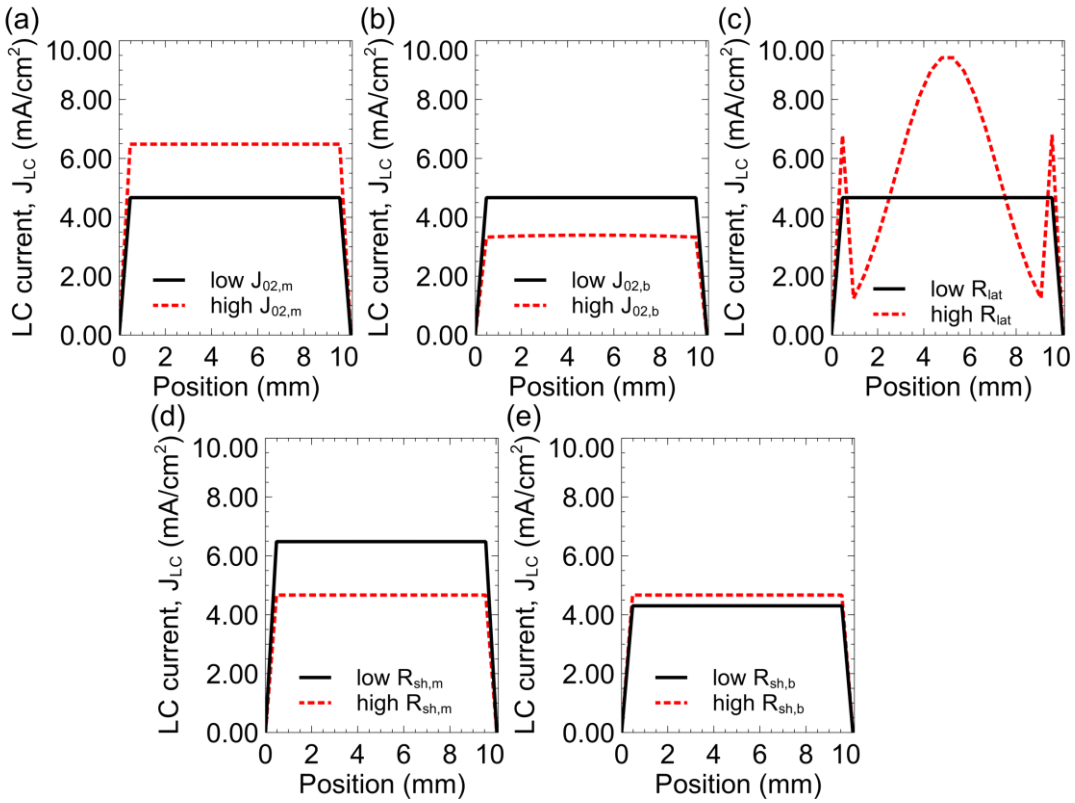

Fig. 13 3D distributed SPICE simulation results of limiting bottom cell LC current having (a) middle cell nonradiative recombination diode coefficient, $J_{02,m}$, varied from 1×10^{-9} (low) to 1×10^{-1} mA/dA (high), (b) bottom cell nonradiative recombination diode coefficient, $J_{02,b}$, varied from 1×10^{-4} (low) to 1×10^{-1} mA/dA (high), (c) lumped series lateral resistance, R_{lat}, varied from 1×10^{-3} (low) to 1.0 Ω/dA (high), (d) middle cell shunt resistance, $R_{sh,m}$, varied from 1×10^{3} (low) to 1×10^{7} Ω/dA (high), and (e) bottom cell shunt resistance, $R_{sh,b}$, varied from 1×10^{2} (low) to 1×10^{4} Ω/dA (high).

Table 9 Summary of varied parameters in all regions of triple-junction solar cell modeled using 3D distributed SPICE electrical circuit for electrical investigation of nonuniform current production when the bottom cell is made current-limiting. Here, dA is the differential cell area.

Varied Parameter		Low Value	High Value
Lumped lateral series resistance, R_{lat} (Ω/dA)		1.00×10^{-3} *	1.00
Nonradiative recombination diode coefficient, $J_{02,i}$ (mA/dA)			
	Middle cell	1.00×10^{-9} *	1.00×10^{-1}
	Bottom cell	1.00×10^{-4} *	1.00×10^{-1}
Shunt resistance, $R_{sh,i}$ (Ω/dA)			
	Middle cell	1.00×10^{3}	1.00×10^{7} *
	Bottom cell	1.00×10^{2}	1.00×10^{4} *

* *Closer to ideal values.*

In summary, the electrical circuit simulation results of the bottom cell current-limiting case presented suggest that sidewall or perimeter passivation of the solar cell absorbers may alleviate the nonuniform LC effect, which is consistent with the inferences made for middle cell current-limiting case in the previous subsection.

C.3.3. Empirical fitting of spatially-resolved LC current measurements into Q2DEP model

Simulated variation of the fraction of LC effect nonuniformity, β_{LC}, from 0% to 100% is shown in Fig. 14. Here, the LC factor, α_{LC}, was set to 0.69, which is the maximum α_{LC} fitted from the light *J-V* characteristics of the smaller sample discussed in Chapter 3, Sec. 3.3.3. As the β_{LC} is increased, the current distribution becomes less uniform.

In Chapter 3, the Q2DEP model was introduced as a tool for analyzing the LBIC measurements acquired by LC excitation. Figure 15(a) shows the measured and fitted LC current production in the Ge bottom cell of a 0.31-cm^2 InGaP/GaAs/Ge 3JSC at various 660-nm intensities upon GaAs middle cell, P_{660nm}, between 35.0 and 293.5 mW/cm^2, which in turn varies the LC strength towards the current-limiting Ge bottom cell. Using eq. (9), the goodness of fit, r^2, was calculated per LC current measurement, J_{gen}, fitted into the Q2DEP model. Most of the fitted J_{gen} yielded an $r^2 > 0.90$ for $P_{660nm} \geq 180.0$. However, for low P_{660nm} (35 mW/cm^2), low r^2 was obtained. This may be attributed to the larger amount of noise acquired during the low optical bias measurements. Nevertheless, r^2 values close to 1.0 suggest that the Q2DEP model is capable of theoretically predicting the inhomogeneous LC effect in MJSCs for varying LC strength.

Meanwhile, the measured and fitted LC current production in the Ge bottom cell of a 0.31-cm^2 InGaP/GaAs/Ge 3JSC at fixed P_{660nm} intensity of 293.5 mW/cm^2 upon the GaAs middle cell at various cell operating temperatures, T_c, between 18°C and 72°C is shown in Fig. 15(b). Same as for varying P_{660nm} intensities discussed earlier, r^2 values were calculated per J_{gen} at each T_c. All J_{gen} fitted yielded an $r^2 > 0.89$, indicating the goodness of model prediction for varying T_c.

Figure 16(a) shows the measured and fitted LC current production in the Si bottom cell of wafer-bonded InGaP/AlGaAs//Si 3JSC having different cell areas at fixed P_{660nm} of 9.17 suns equivalent upon AlGaAs middle cell. Using eq. (9), the goodness of fit, r^2, was calculated per LC current measurement, J_{gen}, fitted into the Q2DEP model. All fitted J_{gen} resulted in an r^2 of 0.89 and higher at various cell areas, suggesting that the Q2DEP model is capable of theoretically predicting the inhomogeneous LC effect in MJSCs for varying cell areas.

On the other hand, the measured and fitted LC current production in the Ge bottom cell of a 1.00-cm^2 wafer-bonded InGaP/AlGaAs//Si 3JSC at fixed P_{660nm} intensity of 9.17 suns equivalent upon the AlGaAs middle cell at various cell operating temperatures, T_c, between 15°C and 90°C is shown in Fig. 16(b). Same as for varying P_{660nm} intensities discussed earlier, r^2 values were calculated per J_{gen} at each T_c. All J_{gen} fitted yielded an $r^2 > 0.93$, indicating the goodness of Q2DEP model prediction for varying T_c. This agrees with the goodness of fit acquired for the InGaP/GaAs/Ge 3JSCs shown in Fig. 15(b) for varying T_c.

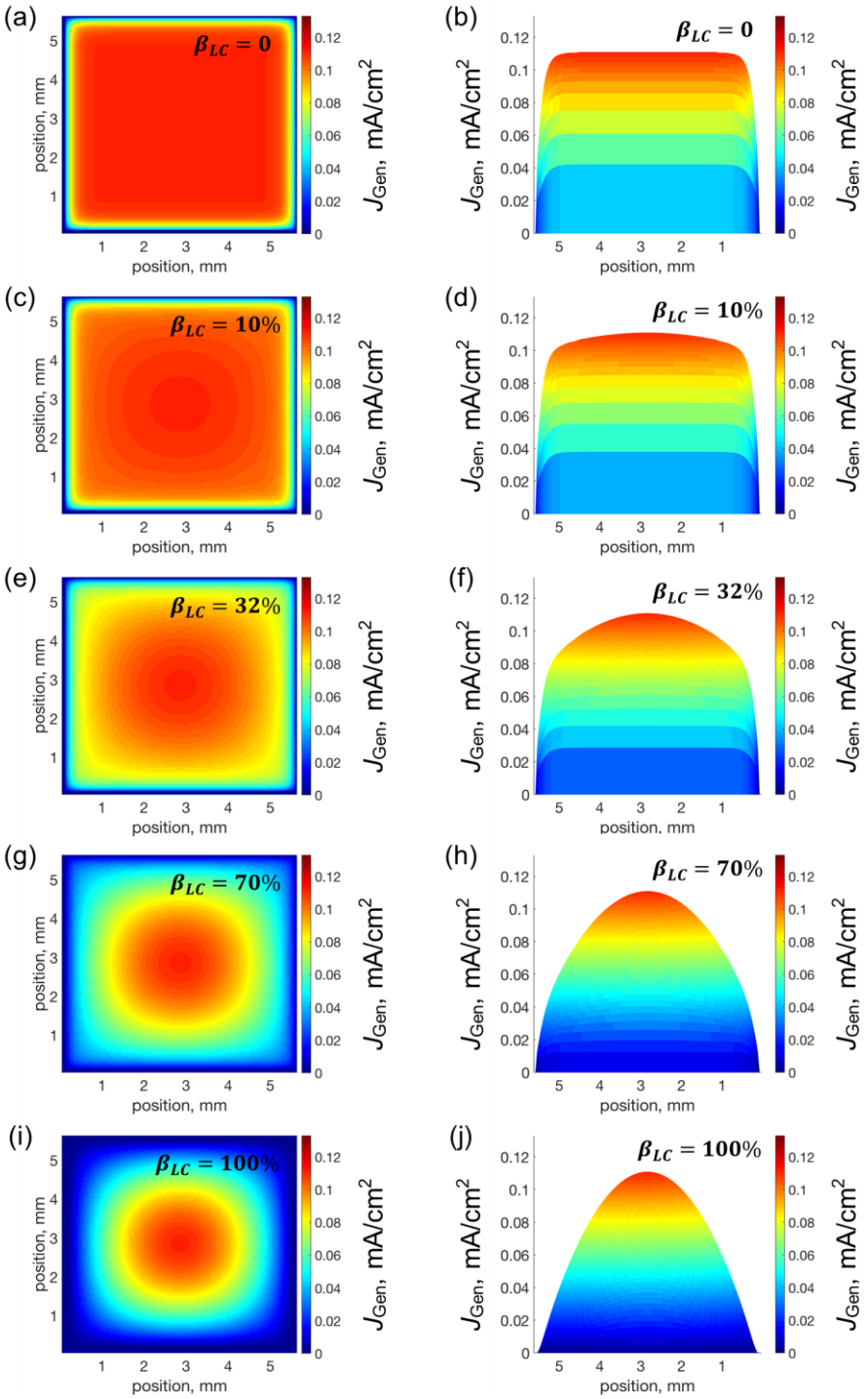

Fig. 14 Spatially-resolved color map representations and LC current, J_{Gen}, versus position plots whose fractions of nonuniformity, β_{LC}, are set to (a)-(b) 0%, (c)-(d) 10%, (e)-(f) 32% [185], (g)-(h) 70%, and (i)-(j) 100%, respectively. The α_{LC} for both LC current distributions is 0.69, which is the maximum acquired for 0.31 cm^2 sample discussed in Chapter 2, Sec. 2.3.3. The spatial resolution of the maps is 23.4 × 20.9 pixels/mm^2 and the applied InGaP/GaAs/Ge triple-junction solar cell terminal voltage is 1.5 V.

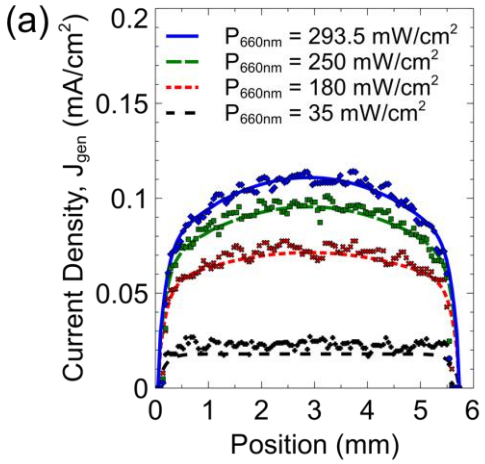

P_{660nm} (mW/cm^2)	r^2
35.0	0.7425
180.0	0.9060
250.0	0.9181
293.5	0.9205

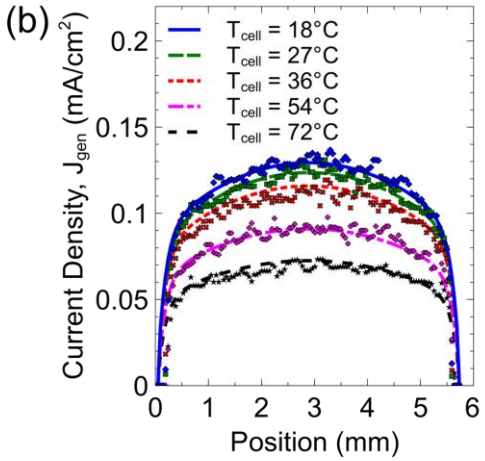

T_c (°C)	r^2
18	0.9283
27	0.9185
36	0.9228
54	0.9015
72	0.8923

Fig. 15 Measured and Q2DEP model fitted LC current collection in the Ge bottom cell of InGaP/AlGaAs//Si 3JSCs cross-section as a function of position (a) at various 660-nm LED intensities, P_{660nm} between 35.0 and 293.5 mW/cm^2 (b) at cell operating temperatures, T_c, of 18°C to 72°C. In both (a) and (b), r^2 is the coefficient of determination.

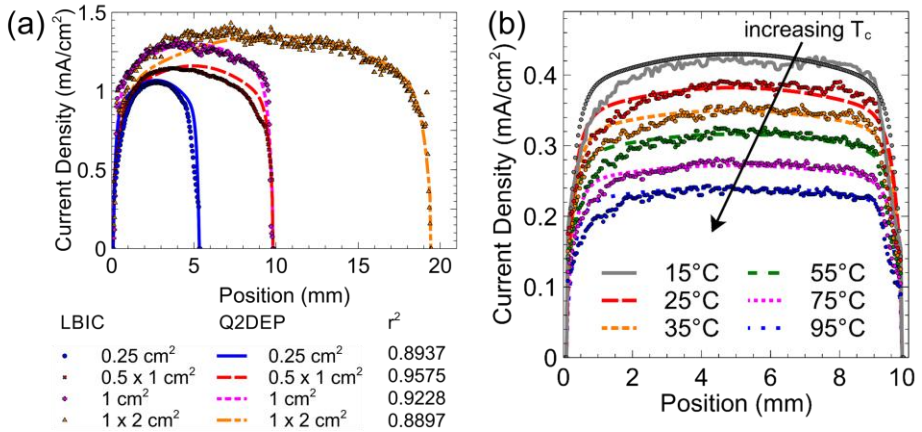

T_c (°C)	r^2
15	0.9455
25	0.9305
35	0.9369
55	0.9353
75	0.9379
95	0.9319

Fig. 16 Measured and Q2DEP model fitted LC current collection in the Si bottom cell of InGaP/AlGaAs//Si 3JSCs cross-section as a function of position (a) having different areas at 9.17 suns equivalent 660-nm LED intensity and (b) at cell operating temperatures, T_c, of 15°C to 95°C. In both (a) and (b), r^2 is the coefficient of determination.

C.4. Synthesis of Findings

The underlying carrier dynamics and light interactions possibly responsible for nonuniform LC current collection were theoretically investigated using various electrical and optical simulation models. The following were found to be the possible causes behind the nonuniform LC effect: (1) photon escape, (2) lateral series resistance leading to degraded carrier transport efficiency, and (3) high nonradiative recombination in the emitting HBG subcell. It was also found that depending on the solar cell absorber material, possible solutions to nonuniform LC could be the deposition of electrical passivation to the sidewalls of MJSCs or texturing the sidewalls with upright or inverted pyramid structures.

The aptness of the Q2DEP model for describing the LC effect having various uniformities was explored by fitting the measured LC current production into the said model. By varying the β_{LC}, one can fit and determine the degree of inhomogeneity of spatially-resolved LC current collection in an MJSC limiting subcell.

C.5. Supplementary Information

The succeeding images are the sample inputs and outputs to the free version of PV Lighthouse 2D Monto Carlo ray tracer for inbound and outbound light emissions with respect to the solar cell absorber material being simulated. Figures 17(a) and (b) correspond to the input of the inbound and outbound simulation of bare III-V and IV solar cell absorbers illustrated in Figs. 1(a) and (b), respectively. Figures 18(a) and (b) correspond to the output of the inbound and outbound simulation of bare III-V and IV solar cell absorbers illustrated in Figs. 1(a) and (b), respectively.

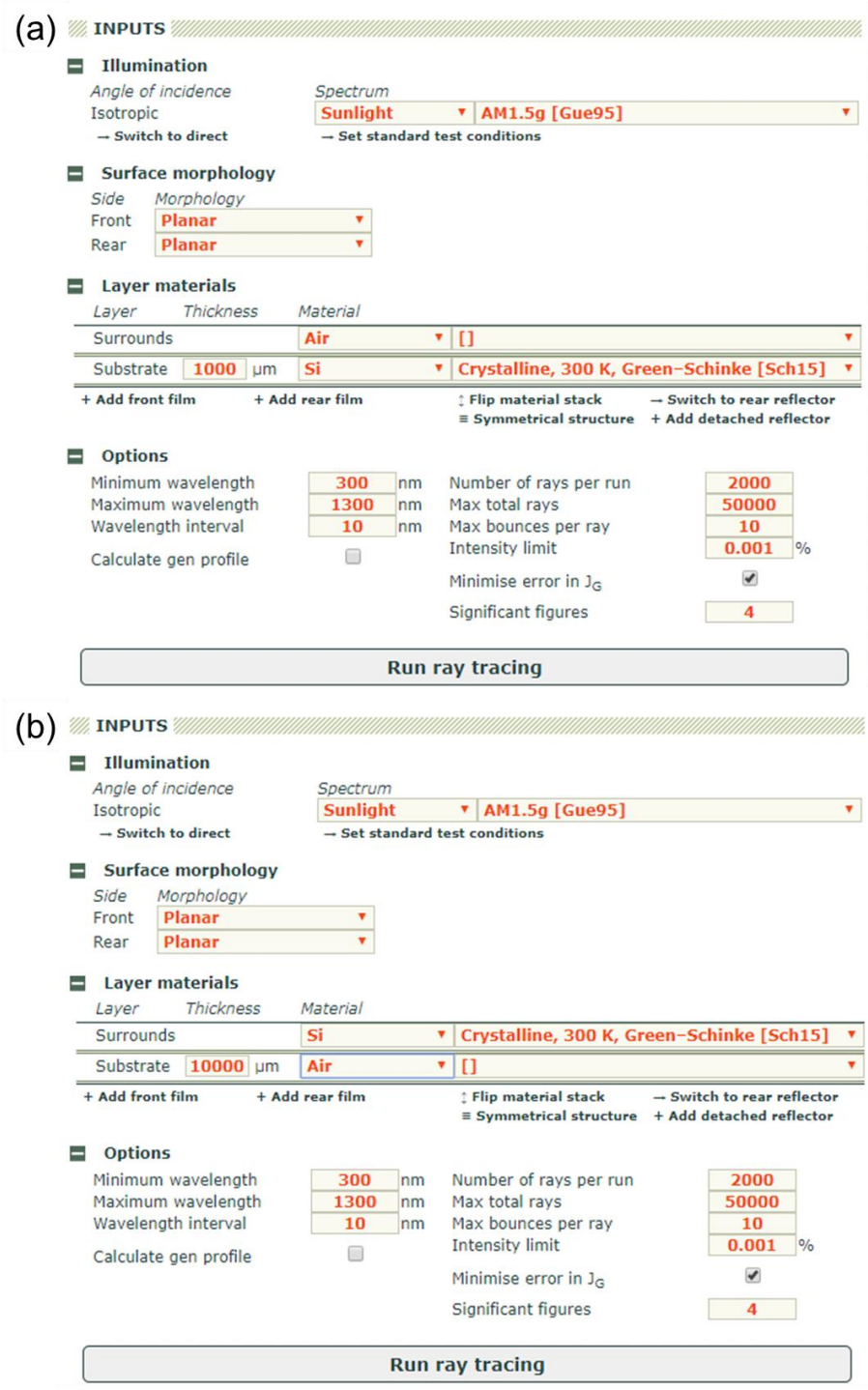

Fig. 17 Sample input sections for simulating (a) light emissions from the sun at AM 1.5G towards the bare, planar Si solar cell absorber, hence inbound, and (b) light emissions originating from the bare, planar Si solar cell absorber, thus outbound for photons escaping, as illustrated in Figs. 1(a) and (b), respectively.

(a)

OUTPUTS

Ray tracing complete.
Total rays traced: 50000.

Photon current densities

			Mean ± 95% CI (mA/cm^2)	Fraction of J_{inc} (%)
	Incident	J_{inc}	25.29 ± 0.1422	100.0
	Lost			
(1)	Reflected – external	$J_{R,ext}$	9.054 ± 0.1764	35.79
(2)	Reflected – escape	$J_{R,esc}$	0.5874 ± 0.04460	2.322
(3)	Transmitted	J_T	2.066± 0.04683	8.168
	Absorbed – front films	$J_{A,F}$	-± -	-
	Absorbed – rear films	$J_{A,R}$	-± -	-
	Absorbed – detached reflector	$J_{A,det\ refl}$	-± -	-
	Photogeneration (absorbed)	J_G	13.58± 0.1692	53.70
	Remainder		0.003822± 0.001005	0.01511

(b)

OUTPUTS

Ray tracing complete.
Total rays traced: 50000.

Photon current densities

			Mean ± 95% CI (mA/cm^2)	Fraction of J_{inc} (%)
	Incident	J_{inc}	25.38 ± 0.1757	100.0
	Lost			
(1)	Reflected – external	$J_{R,ext}$	24.25 ± 0.1812	95.53
(2)	Reflected – escape	$J_{R,esc}$	0.2824 ± 0.03900	1.113
(2)	Transmitted	J_T	0.8318± 0.06338	3.277
	Absorbed – front films	$J_{A,F}$	-± -	-
	Absorbed – rear films	$J_{A,R}$	-± -	-
	Absorbed – detached reflector	$J_{A,det\ refl}$	-± -	-
	Photogeneration (absorbed)	J_G	-± -	-
	Remainder		0.02009± 0.009224	0.07916

Fig. 18 Sample output sections for (a) inbound and (b) outbound simulation cases of bare III-V or IV solar cell absorber material surrounded by air, as illustrated in Figs. 1(a) and (b), respectively.

Figures 19(a) and (b) correspond to the input of the inbound and outbound simulation of thin film-coated III-V and IV solar cell absorbers illustrated in Figs. 2(a) and (b), respectively; Figures 20(a) and (b) correspond to the output of the inbound and outbound simulation of bare III-V and IV solar cell absorbers illustrated in Figs. 2(a) and (b), respectively.

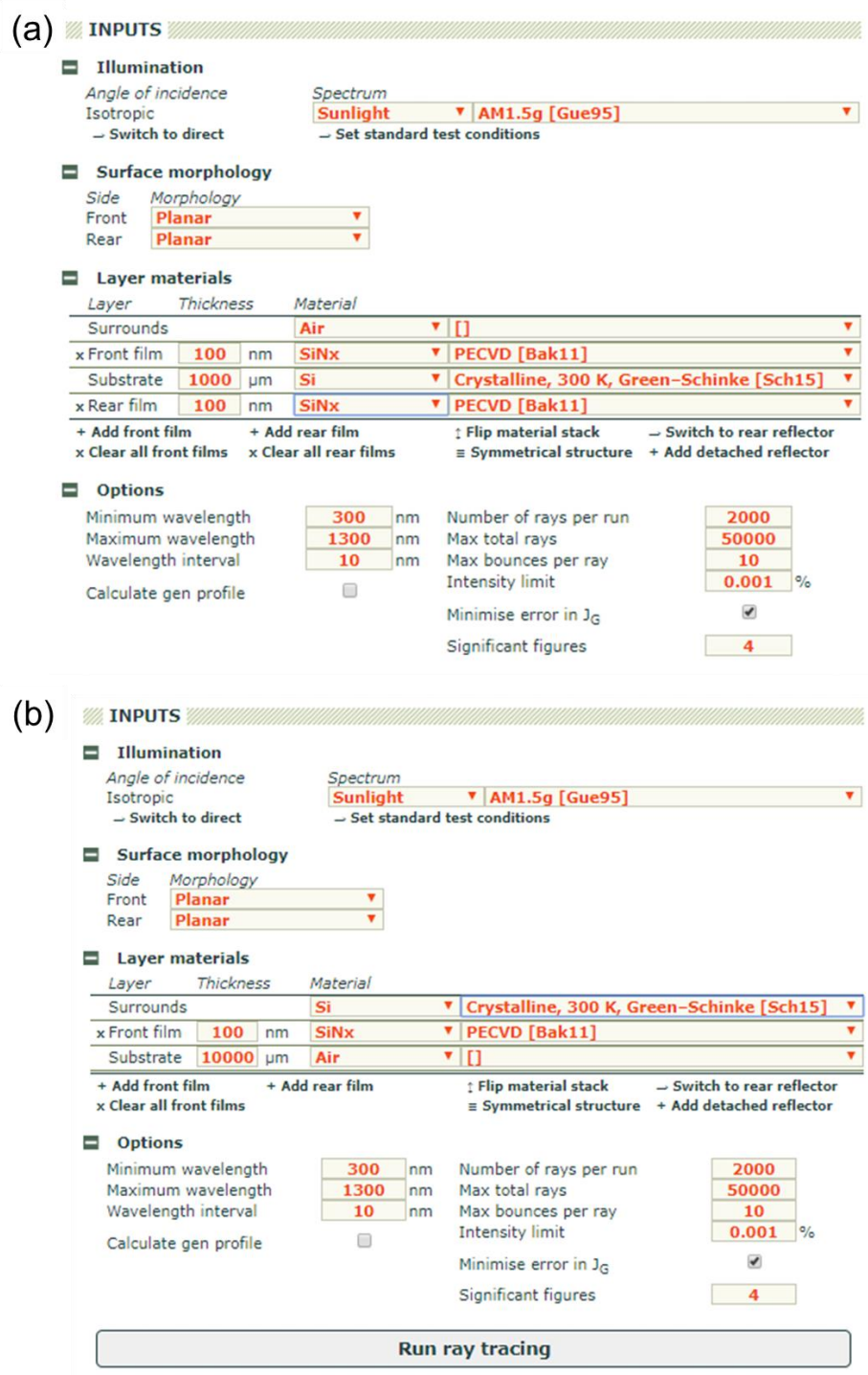

Fig. 19 Sample input sections for simulating (a) light emissions from the sun at AM 1.5G towards the SiN_x-coated Si solar cell absorber, hence inbound, and (b) light emissions originating from the SiN_x-coated Si solar cell absorber, thus outbound for photons escaping, as illustrated in Figs. 3(a) and (b), respectively.

(a)

OUTPUTS

Ray tracing complete.
Total rays traced: 50000.

Photon current densities

			Mean ± 95% CI (mA/cm^2)	Fraction of J_{inc} (%)
	Incident	J_{inc}	25.27 ± 0.1095	100.0
	Lost			
(1)	Reflected – external	$J_{R,ext}$	4.166 ± 0.07682	16.49
(2)	Reflected – escape	$J_{R,esc}$	0.4124 ± 0.02613	1.632
(3)	Transmitted	J_T	2.719± 0.04882	10.76
(4)	Absorbed – front films	$J_{A,F}$	0.2036± 0.001298	0.8056
(5)	Absorbed – rear films	$J_{A,R}$	0.03909± 0.0006551	0.1547
	Absorbed – detached reflector	$J_{A,det\ refl}$	–± –	–
	Photogeneration (absorbed)	J_G	17.73± 0.1266	70.15
	Remainder		0.002731± 0.0005603	0.01081

(b)

OUTPUTS

Ray tracing complete.
Total rays traced: 50000.

Photon current densities

			Mean ± 95% CI (mA/cm^2)	Fraction of J_{inc} (%)
	Incident	J_{inc}	25.30 ± 0.1709	100.0
	Lost			
(1)	Reflected – external	$J_{R,ext}$	23.69 ± 0.1559	93.64
(2)	Reflected – escape	$J_{R,esc}$	0.4809 ± 0.05189	1.901
(2)	Transmitted	J_T	0.9645± 0.06505	3.812
(3)	Absorbed – front films	$J_{A,F}$	0.1619± 0.001974	0.6398
	Absorbed – rear films	$J_{A,R}$	–± –	–
	Absorbed – detached reflector	$J_{A,det\ refl}$	–± –	–
	Photogeneration (absorbed)	J_G	–± –	–
	Remainder		0.0009518± 0.001813	0.003762

Fig. 20 Sample output sections for (a) inbound and (b) outbound simulation cases of a III-V or IV solar cell absorber material with thin film coating and then surrounded by air, as illustrated in Figs. 3(a) and (b), respectively.

Figures 21(a) and (b) correspond to the input of the inbound and outbound simulation of textured III-V and IV solar cell absorbers illustrated in Figs. 3(a) and (b), respectively; Figures 22(a) and (b) correspond to the output of the inbound and outbound simulation of bare III-V and IV solar cell absorbers illustrated in Figs. 3(a) and (b), respectively.

(a)

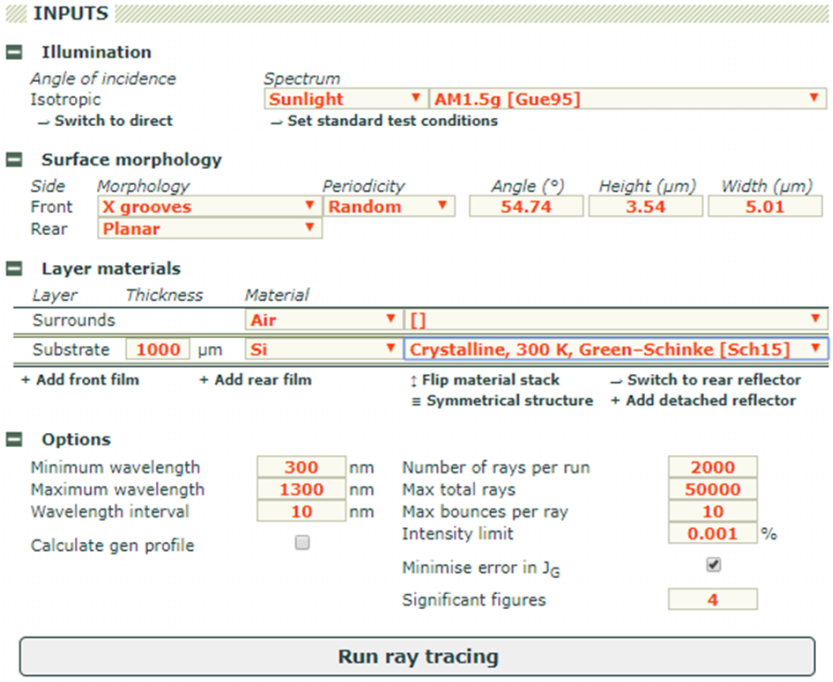

(b)

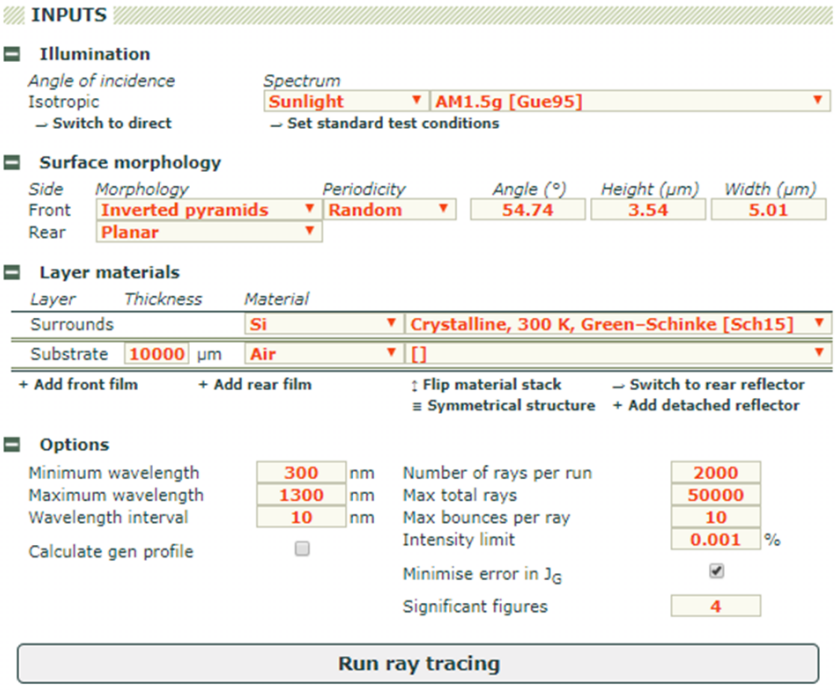

Fig. 21 Sample input sections for simulating (a) light emissions from the sun at AM 1.5G towards the surface-textured Si solar cell absorber surface, hence inbound, and (b) light emissions originating from the textured Si solar cell absorber surface, thus outbound for photons escaping, as illustrated in Figs. 5(a) and (b), respectively.

(a)

OUTPUTS

Ray tracing complete.
Total rays traced: 50000.

Photon current densities

			Mean ± 95% CI (mA/cm²)	Fraction of J_{inc} (%)
	Incident	J_{inc}	25.36 ± 0.1628	100.0
	Lost			
(1)	– Reflected – external	$J_{R,ext}$	5.059 ± 0.1169	19.95
(2)	– Reflected – escape	$J_{R,esc}$	1.069 ± 0.05039	4.214
(3)	– Transmitted	J_T	0.2784± 0.02760	1.098
	Absorbed – front films	$J_{A,F}$	–± –	–
	Absorbed – rear films	$J_{A,R}$	–± –	–
	Absorbed – detached reflector	$J_{A,det\ refl}$	–± –	–
	Photogeneration (absorbed)	J_G	17.44± 0.2008	68.77
	Remainder		1.514± 0.04730	5.969

(b)

OUTPUTS

Ray tracing complete.
Total rays traced: 50000.

Photon current densities

			Mean ± 95% CI (mA/cm²)	Fraction of J_{inc} (%)
	Incident	J_{inc}	25.35 ± 0.1475	100.0
	Lost			
(1)	– Reflected – external	$J_{R,ext}$	21.47 ± 0.1512	84.70
(2)	Reflected – escape	$J_{R,esc}$	0.7819 ± 0.03975	3.085
(2)	Transmitted	J_T	0.9421± 0.05178	3.717
	Absorbed – front films	$J_{A,F}$	–± –	–
	Absorbed – rear films	$J_{A,R}$	–± –	–
	Absorbed – detached reflector	$J_{A,det\ refl}$	–± –	–
	Photogeneration (absorbed)	J_G	–± –	–
	Remainder		2.155± 0.06075	8.502

Fig. 22 Sample output sections for (a) inbound and (b) outbound simulation cases of textured III-V or IV solar cell absorber material surrounded by air, as illustrated in Figs. 5(a) and (b), respectively.

Supplementary information

Appendix D

Appendix D – Tools and Specifications

D.1. MATLAB Codes

D.1.1. The goodness of prediction model fitting calculation

```
meanLBIC = mean(LBIC(:));
meanfit = mean(fit(:));
ssLBIC = sum((LBIC-meanLBIC).^2);
ssfit = sum((fit-meanfit).^2);

r=sum((LBIC-meanLBIC).*(fit-
meanfit)./sqrt(ssLBIC*ssfit));
rsquare = r*r;
```

D.1.2. General code for data point interpolation

```
x_low = -0.1;         % lower limit of x axis
x_high = 2.95;        % upper limit, x axis

x = transpose([
% paste your x data here...
]);

v = transpose([
% paste your y data here...
]);

% extrapolating x axis
xq = transpose([x_low:0.1:x_high]);
figure;
vq1 = interp1(x,v,xq);
plot(x,v,'o',xq,vq1,':.');
xlim([x_low x_high]);
```

D.1.3. Subcell current density calculation from external quantum efficiency measurements at various spectra

```
% -*- constants/presets -*- %
h = 6.62607015e-34;              % planck's constant, J s
c = 2.99792458e8;                % speed of light, m/s
q = 1.60217662e-19;              % electron charge, C

% -*- import spectra data (from NREL) -*- %
raw_lambda = csvread('current_density_calculator_files/ASTMG173.csv',
2, 0, [2, 0, 3343, 0]);              % unit: nm
```

```
raw_spectrum_AM0 =
csvread('current_density_calculator_files/ASTMG173.csv', 2, 1, [2, 1,
3343, 1]);         % unit: W/m^2?nm
raw_spectrum_AM1_5G =
csvread('current_density_calculator_files/ASTMG173.csv', 2, 2, [2, 2,
3343, 2]);       % unit: W/m^2?nm
raw_spectrum_AM1_5Direct =
csvread('current_density_calculator_files/ASTMG173.csv', 2, 3, [2, 3,
3343, 3]);  % unit: W/m^2?nm

% -*- toggle switches for AM spectrum selection -*- %
use_AM0 = 0;                      % calculate DBL for AM 0 (space)
use_AM1_5G = 1;                    % calculate DBL for AM 1.5 global
use_AM1_5Direct = 0;                % calculate DBL for AM 1.5 direct

integrated_top = 0;
integrated_mid = 0;
integrated_bot = 0;

% sample EQE measurement file import
lambda_meas =
transpose(csvread('current_density_calculator_files/190928 - SR2 PQD
3x 2nd run/Spectrum.csv', 20, 0, [20, 0, 177, 0]));      % unit: nm
EQE_meas_top =
transpose(csvread('current_density_calculator_files/190928 - SR2 PQD
3x 2nd run/Spectrum.csv', 20, 1, [20, 1, 177, 1])./100); % unit: nm
EQE_meas_mid =
transpose(csvread('current_density_calculator_files/190928 - SR2 PQD
3x 2nd run/Spectrum.csv', 20, 2, [20, 2, 177, 2])./100); % unit: nm
EQE_meas_bot =
transpose(csvread('current_density_calculator_files/190928 - SR2 PQD
3x 2nd run/Spectrum.csv', 20, 3, [20, 3, 177, 3])./100); % unit: nm

lambda_low = min(lambda_meas);
lambda_high = max(lambda_meas);

lambda_q = transpose([lambda_low:0.5:lambda_high]);
figure;
spectrum_AM1_5G_q1 =
round(interp1(raw_lambda,raw_spectrum_AM1_5G,lambda_q),1000);
EQE_top_q1 = round(interp1(lambda_meas,EQE_meas_top,lambda_q),1000);
EQE_mid_q1 = round(interp1(lambda_meas,EQE_meas_mid,lambda_q),1000);
EQE_bot_q1 = round(interp1(lambda_meas,EQE_meas_bot,lambda_q),1000);
plot(raw_lambda,raw_spectrum_AM1_5G,'o',lambda_q,spectrum_AM1_5G_q1,':
.');
figure;
plot(lambda_meas,EQE_meas_top,'o',lambda_q,EQE_top_q1,':.');
figure;
plot(lambda_meas,EQE_meas_mid,'o',lambda_q,EQE_mid_q1,':.');
figure;
plot(lambda_meas,EQE_meas_bot,'o',lambda_q,EQE_bot_q1,':.');

xlim([lambda_low lambda_high]);
upper_limit=size(lambda_q,1);

for count = 2:upper_limit-1
```

```
temp=lambda_q(count)*EQE_top_q1(count)*spectrum_AM1_5G_q1(count)*(lamb
da_q(count+1)-lambda_q(count-1))/2;
    integrated_top = integrated_top + temp;
end

integrated_J_AM1_5G_top = q/h/c*integrated_top*0.1/1e9;

for count = 2:upper_limit-1

temp=lambda_q(count)*EQE_mid_q1(count)*spectrum_AM1_5G_q1(count)*(lamb
da_q(count+1)-lambda_q(count-1))/2;
    integrated_mid = integrated_mid + temp;
end

integrated_J_AM1_5G_mid = q/h/c*integrated_mid*0.1/1e9;

for count = 2:upper_limit-1

temp=lambda_q(count)*EQE_bot_q1(count)*spectrum_AM1_5G_q1(count)*(lamb
da_q(count+1)-lambda_q(count-1))/2;
    integrated_bot = integrated_bot + temp;
end

integrated_J_AM1_5G_bot = q/h/c*integrated_bot*0.1/1e9;
```

D.1.4. SPICE netlist generator

```
% =*=*=*=*= % Measurement List Generator for LTSPICE Netlist %
=*=*=*=*= %

row = 100;                % number of rows in the active region
col = 100;                % number of columns in the active region
char = cell((row+2)*(col+2),1);     % cell array storage for the
netlist commands
counter=1;                % cell array counter

% *** perimeter region elements addressing *** %
% 10x1 edge module %
outer_element_counterL = 1;     % left
outer_element_counterR = 1;     % right
outer_element_counterB = 1;     % back
outer_element_counterF = 1;     % front
% 3JSC edge module %
inner_element_counterL = 1;     % left
inner_element_counterR = 1;     % right
inner_element_counterB = 1;     % back
inner_element_counterF = 1;     % front

% *** active region elements addressing *** %
outer_element_counterA = 1;     % 10x10 bulk module
inner_element_counterA = 1;     % 3JSC bulk module

% *** temporary storages for incrementing the element indeces *** %
temp_B=10;      % back perimeter
temp_F=10;      % front perimeter
```

```
temp_A=10;      % active region

module_column_A = 1;    % counter for 3JSC bulk module
last_element=1;         % counter for 10x10 bulk module

for i = 0:col+1
    for j = 0:row+1
        if i==0           % left perimeter commands
            if j==0           % back-left corner element
                char{counter}='.measure I_nodeR00C00 find Ix(XCBL:NODE)
when V1=Vout';
            elseif j==row+1     % front-left corner element
                char{counter}=['.measure I_nodeR', num2str(j), 'C00 find
Ix(XCFL:NODE) when V1=Vout'];
            else              % non-corner elements
                char{counter}=['.measure I_nodeR', num2str(j), 'C00 find
Ix(XL', num2str(outer_element_counterL), ':X',
num2str(inner_element_counterL) ':lat_top_edge) when V1=Vout'];
                if mod(inner_element_counterL,10)==0    % element counter
reset once index = 10
                    inner_element_counterL = 1;
                    outer_element_counterL = j/10+1;
                else                                    % while index /= 10 yet
                    inner_element_counterL = inner_element_counterL + 1;
                end
            end
        elseif i==col+1     % right side perimeter commands
            if j==0           % back-right corner element
                char{counter}=['.measure I_nodeR00C', num2str(i), ' find
Ix(XCBR:NODE) when V1=Vout'];
            elseif j==row+1     % front-right corner element
              char{counter}=['.measure I_nodeR', num2str(j),'C',
num2str(i),' find Ix(XCFR:NODE) when V1=Vout'];
            else              % non-corner elements
                char{counter}=['.measure InodeR', num2str(j), 'C',
num2str(i), ' find Ix(XR', num2str(outer_element_counterR), ':X',
num2str(inner_element_counterR) ':lat_top_edge) when V1=Vout'];
                if mod(inner_element_counterR,10)== 0   % element counter
reset once index = 10
                    inner_element_counterR = 1;
                    outer_element_counterR = j/10+1;
                else                                    % while index /= 10 yet
                    inner_element_counterR = inner_element_counterR + 1;
                end
            end
        elseif j==0         % back perimeter commands
            char{counter}=['.measure InodeR', num2str(j), 'C',
num2str(i), ' find Ix(XB', num2str(outer_element_counterB), ':X',
num2str(inner_element_counterB) ':lat_top_edge) when V1=Vout'];
            if mod(inner_element_counterB,10)== 0   % when index = 10
                temp_B = temp_B + 10;
                inner_element_counterB = 1;
                outer_element_counterB = temp_B/10;
            else                                  % while index /= 10 yet
                inner_element_counterB = inner_element_counterB + 1;
            end
        elseif j==row+1     % front perimeter commands
```

```
          char{counter}=['.measure InodeR', num2str(j), 'C',
num2str(i), ' find Ix(XF', num2str(outer_element_counterF), ':X',
num2str(inner_element_counterF) ':lat_top_edge) when V1=Vout'];
          if mod(inner_element_counterF,10)== 0   % when index = 10
              temp_F = temp_F + 10;
              inner_element_counterF = 1;
              outer_element_counterF = temp_F/10;
          else                                    % while index /= 10 yet
              inner_element_counterF = inner_element_counterF + 1;
          end
       else % active region
          char{counter}=['.measure InodeR', num2str(j), 'C',
num2str(i), ' find Ix(X', num2str(outer_element_counterA), ':X',
num2str(inner_element_counterA+300) ':NODE) when V1=Vout'];
          if mod(inner_element_counterA,10)== 0   % determine indeces
incrementing every inner index (3JSC module) = 10
              inner_element_counterA = 1+temp_A*last_element-10;
              if j==row
                  if module_column_A == row*10    % when last element of
a column is accessed
                      module_column_A = 0;          % reset to 0
                      last_element = last_element+1;  % increment to the
next column of 10x10 modules' indeces
                      outer_element_counterA = last_element;            %
assign new 10x10 module index
                      inner_element_counterA = 1+temp_A*last_element-
10;  % assign new 3JSC bulk module index
                  else
                      outer_element_counterA = last_element;  % still
within the same column of 10x10 modules
                  end
              else       % access the next 10x10 module in the same row
                  outer_element_counterA =
outer_element_counterA+temp_A;
              end
          else       % inner index /= 10 yet
              inner_element_counterA = inner_element_counterA + 1;
          end
          module_column_A = module_column_A + 1;  % increment 3JSC bulk
module counter
       end
       counter=counter+1;  % increment cell array element writing index
    end
end

% *** Write cell array contents to file *** %
fileID = fopen('netlist.txt','w');  % create file where to write
generated netlist commands
%[row,col] = size(char);
for i = 1:row
    temp_str = char{i,:};             % temporary storage for i'th
command
    fprintf(fileID ,'%s¥n', temp_str);  % write into the created file
end
fclose(fileID);                      % disconnect with the created file
```

D.1.5. Temperature dependent prediction models for semiconductor bandgap

D.1.5.1. Viña model

```
% *** % Vina model % *** %
% Purpose: AlGaAs top cell temperature dependence of Eg calculation
%          >>> https://doi.org/10.1117/1.JPE.9.015503, Fig. 5(b)
% Reference: https://doi.org/10.1103/PhysRevB.30.1979

% extrapolate thermal coefficient expansion, InGaP
x = transpose([0, 0.17, 0.3, 0.4]);
v1 = transpose([1576.6, 1802.4, 1975.7, 2081.2]);      % E_B published
v2 = transpose([59.7, 76.9, 85.9, 94.4]);      % electron-phonon
interaction strength
v3 = transpose([241, 275, 289, 317]);      % characteristic temperature
xq = transpose([0:0.005:1]);
vq1 = interp1(x,v1,xq, 'linear');
vq2 = interp1(x,v2,xq, 'linear');
vq3 = interp1(x,v3,xq, 'linear');
E_B = vq1(8);
alpha_B = vq1(8);
theta_B = vq1(8);

T = [15, 25, 35, 55, 75, 95];
T_K = 273.15 + T;

Eg_T = transpose((E_B-alpha_B*(1+2./exp(theta_B./T_K)-1))/1000);
h = 4.135667662e-15;    % Planck's constant, eV s
c = 299792458;         % speed of light, m/s

lambda_T = h*c./Eg_T*1e9;

Eg_Tadj = [1.4624 1.4600 1.4573 1.4510 1.4434 1.4345];
lambda_Tadj = h*c./Eg_Tadj*1e9;
```

D.1.5.2. Electron-phonon and volume interaction model

```
clc;
clear all;
close all;

% *** % Model considering electron-phonon coupling and volume thermal
expansion % *** %
% Purpose: InGaP top cell temperature dependence of Eg calculation
%          >>> https://doi.org/10.1117/1.JPE.9.015503, Fig. 5(b)
% Reference: Y. Ishitani, S. Minagawa, and T. Tanaka, "Temperature
% dependence of the bandgap energy of disordered GaInP," J. Appl.
Phys. 75, 5326-5331 (1994).

% extrapolate thermal coefficient expansion, InGaP
x = transpose([0, 0.236, 0.553, 0.783, 1]);
v = transpose([4.75e-6, 5.03e-6, 5.34e-6, 5.76e-6, 5.91e-6]);
xq = transpose([0:0.01:1]);
% figure;
vq1 = interp1(x,v,xq, 'linear');
% plot(x,v,'o',xq,vq1,':.');
```

```
alphaT = vq1(52);

% extrapolate thermal coefficient expansion, InGaP
y = transpose([0, 0.5, 0.7]);
w1 = transpose([7.25e11 8.04e11 8.36e11]);
w2 = transpose([11e-12 10.9e-12 10.8e-12]);
yq = transpose([0:0.01:1]);
wq1 = interp1(y,w1,yq, 'linear');
wq2 = interp1(y,w2,yq, 'linear');

volumeTexp = wq1(52)*wq2(52);

theta_1 = 515;                % K
theta_2 = 55;                 % K
E_0 = 2.0536;                 % eV
E_1 = 0.129;                  % eV
E_2 = 8.6/1000;               % eV

T = [15, 25, 35, 55, 75, 95];
T_K = 273.15 + T;

E_v = volumeTexp*alphaT*(T);

Eg_T = transpose(E_0-E_v-E_1*(1./(exp(theta_1./T_K)-1)+0.5)-
E_2*(1./(exp(theta_2./T_K)-1)+0.5));
h = 4.135667662e-15;    % Planck's constant, eV s
c = 299792458;          % speed of light, m/s

lambda_T = h*c./Eg_T*1e9;

Eg_Tadj = [1.9040 1.9000 1.8960 1.8879 1.8797 1.8714];
lambda_Tadj = h*c./Eg_Tadj*1e9;
```

D.1.6. Dipping cycle estimation from thin-film absorption

```
lambda = csvread('ch6_190927_glass_PPQD_abs.csv', 1, 0, [1, 0, 701,
0]);
absorb = csvread('ch6_190927_glass_PPQD_abs.csv', 1, 1, [1, 1, 701,
6]);

C_pqd = 5;          % PQD concentration, mg/mL
Avogadro = 6.022e23;
PQD_a = 0.587;      % CsPbX3 lattice constant

vol_fraction =  C_pqd*Avogadro*PQD_a*PQD_a*PQD_a/10e24;


% mu=0.0;
mu = zeros(6,1);
for count1=1:size(mu,1)
    for count2=2:size(lambda,1)-1
        temp=log(10)*absorb(count2,count1)*(lambda(count2+1)-
lambda(count2-1))/2/vol_fraction;
```

```
        mu(count1)=mu(count1)+temp;
    end
end

mu_ave = mean(mu(:));

Ireq = 1.35;

h_PPQD = 1/mu_ave*log(100/Ireq)*10000;
ndip = 1/0.3467*log(h_PPQD/0.336);
```

D.2. Voltage and current node extraction from 2D SPICE electrical model

From the 2D electrical circuit model built-in SPICE, it is possible to extract the current and the voltage maps. For the successful extraction of a log file containing the values of the node currents and voltages, two SPICE netlist commands need to be defined syntactically. First, in the outermost SPICE circuit, in which all of the circuit modules are joined together, the step parameter command must be defined as

$$.step\ param\ Vout\ list\ Vdummy\ Vrequired \qquad (a)$$

where Vout is the voltage across the InGaP/GaAs/Ge 3JSC terminals, V_{dummy} is any voltage value, usually 0 V for faster calculation, and $V_{required}$ is the applied voltage value at which the current or voltage map is desired to be extracted. Here, a dummy voltage value is initially required for the proper conversion of the log file in Fortran, which is discussed in subsection 4.4.2. Then, for each node, a measure command syntax for current must be defined as

$$.measure\ Isubcellx,y\ find\ I(x_1{:}\,x_2{:}\,\ldots{:}\,x_n)when\ Vsource = Vout \qquad (b)$$

and

$$.measure\ Vsubcellx,y\ find\ V(x_1{:}\,x_2{:}\,\ldots{:}\,x_n)when\ Vsource = Vout \qquad (c)$$

for voltage. Here *Vsource* is the name of the voltage source across the InGaP/GaAs/Ge 3JSC terminals, $I(x_1{:}x_2{:}\ldots{:}x_n)$ and $V(x_1{:}x_2{:}\ldots{:}x_n)$ are the measured current and voltages respectively, $x_1{:}x_2{:}\ldots{:}x_n$ is the address of the measured current or voltage node allocated by SPICE based on modular connections and $Isubcell_{x,y}$ and $Vsubcell_{x,y}$ are the user-defined current and voltage node names which must be unique to prevent extraction error.

D.3. Specification sheets

D.3.1. C3MJ Spectrolab sample specifications

SPECTROLAB

A **BOEING** COMPANY

CPV Point Focus Solar Cells

C3MJ Third Generation CPV Technology

Product Description

Typical Efficiency	38.5%
Recommended operating temperature	<110°C

Epitaxial Structure

Triple junction solar cell on Germanium substrate
GaInP (1.88 eV) / GaInAs (1.41 eV) / Ge (0.67 eV)

Metallization

Silver metallization on front busbar and grid fingers
Silver metallization with 500Å gold on back surface

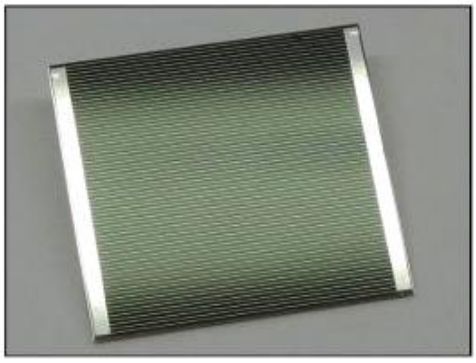

Qualification Tests Completed

Test	Test Conditions	Qty	Requirement
Performance Tests			
LIV	50 W/cm2 under ASTM 173G	100%	Avg η_{mp}>38.5%; Min η_{mp} > 36.2%
Temp Intensity	50, 75 & 100 W/cm^2, ASTM 173G at 10°C, 25°C, 65°C, and 110°C	20	Characterization
Weld Degradation	LIV test before and after weld	100% of scribed parts	NP_{mp} > 0.98
Spectral Response			Characterization
Angle of incidence	X25 or SR illumination source	10	Characterization
Solar Absorptance	Measure reflectance	10	Characterization
Accelerated Life Tests			
Damp Heat	85C, 85% RH for 2000 hours	30	NP_{mp} > 0.9
Thermal Cycle	IEEE 1513 (500 cycles –40°C to +110°C)	25	NP_{mp} > 0.9
High Temp Soak in Nitrogen	unbiased soak at 200°C and 250°C in Nitrogen	15 at each T	NP_{mp} > 0.95 after 25 yrs

* Full Qualification Report Is Available Upon Request

Mechanical Dimensions

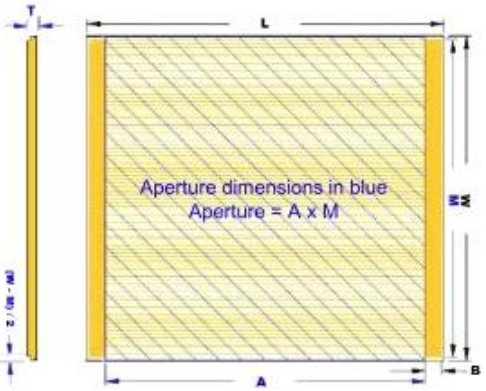

Product	Aperture Area	Aperture Dimensions (cm)			Mechanical Dimensions (cm)			Typical Efficiency
CPV Cell	(cm^2)	M	A	T	L	W	B	η
CDO-30 (045745)	0.308 cm^2	0.555	0.554	0.019	0.681	0.565	0.051	38.70 %
CDO-56 (045135)	0.564 cm^2	0.734	0.750	0.019	0.868	0.763	0.050	38.60 %
CDO-76 (045774)	0.763 cm^2	0.883	0.864	0.019	0.962	0.899	0.040	38.55 %
CDO-100 (045505)	0.969 cm^2	0.980	0.989	0.019	1.108	1.008	0.051	38.50 %
CDO-225 (045835)	2.226 cm^2	1.484	1.500	0.020	1.620	1.510	0.050	38.10 %

Specifications Subject to Change without Notice.

ISO9001:2000 REGISTERED

ENVIRONMENTAL MANAGEMENT SYSTEM CERTIFIED BY DNV ISO 14001

AS9100 REGISTERED

Spectrolab, Inc. 12500 Gladstone Avenue, Sylmar, California 91342 USA
● Phone 818.365.4611 ● FAX: 818.361.5102 ● Website : www.spectrolab.com

SPECTROLAB

A **BOEING** COMPANY

Typical Current-Voltage Characteristics

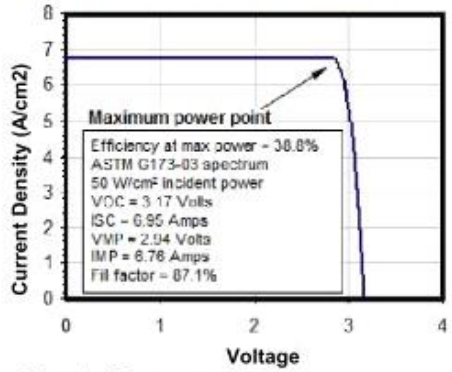

Typical Performance Over Temperature

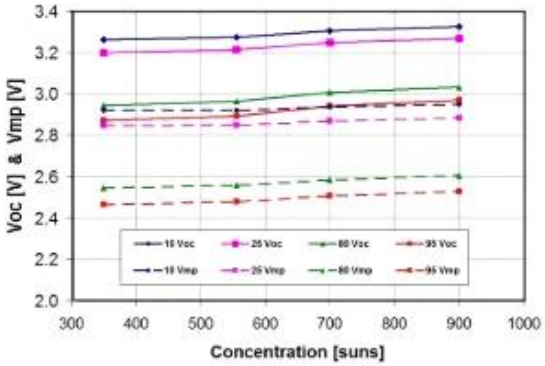

Spectral Response

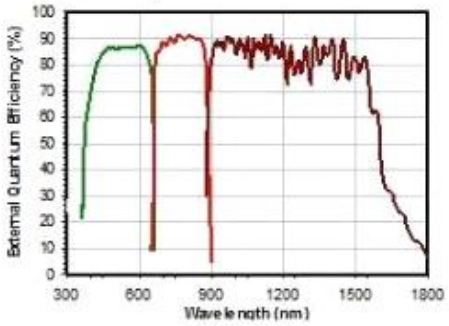

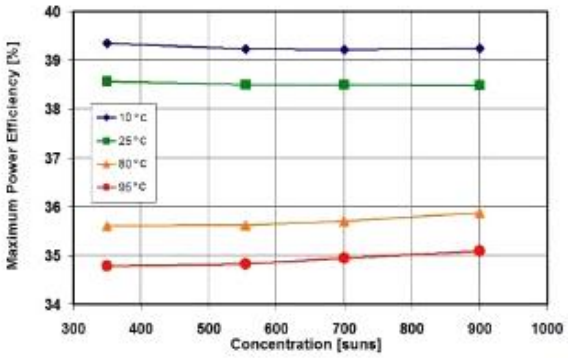

Response Versus Angle of Incidence

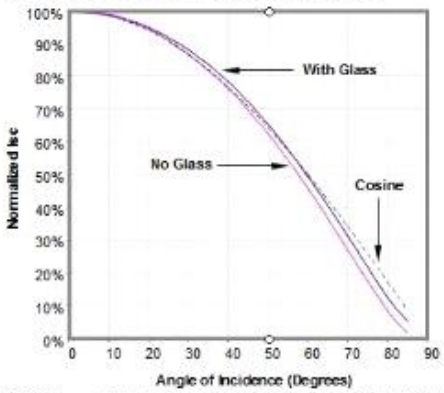

Typical Population Efficiency Distribution

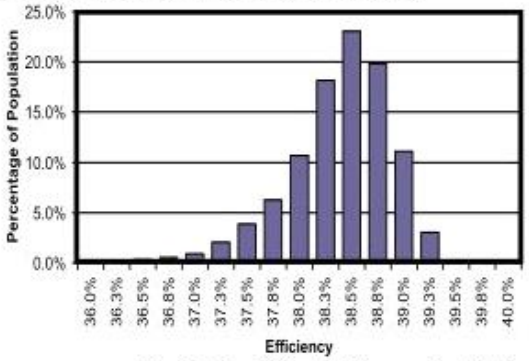

Specifications Subject to Change without Notice.

ISO9001:2000 REGISTERED

ENVIRONMENTAL MANAGEMENT SYSTEM CERTIFIED BY DNV ISO 14001

AS9100 REGISTERED

Spectrolab, Inc. 12500 Gladstone Avenue, Sylmar, California 91342 USA
● Phone 818.365.4611 ● FAX: 818.361.5102 ● Website : www.spectrolab.com

D.3.2. C3MJ+ Spectrolab sample specifications

SPECTROLAB A **BOEING** COMPANY

CPV Point Focus Solar Cells

C3MJ+ Improved Third Generation CPV Technology

✓*Enhanced efficiency of our C3MJ technology*
✓*Fully qualified and field-proven*

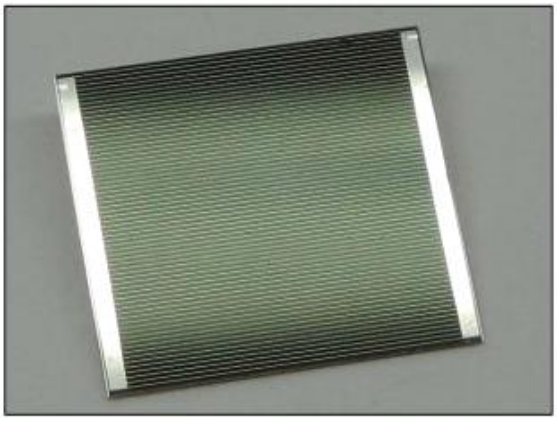

Product Description

Typical Efficiency	39.2%
Recommended operating temperature	<110°C

Epitaxial Structure
Triple junction solar cell on Germanium substrate
GaInP (1.88 eV) / GaInAs (1.41 eV) / Ge (0.67 eV)

Metallization
•Silver metallization on front busbar and grid fingers (optional gold flash finish)
•Silver metallization with 500Å gold on back surface

CPV Cell Ordering Guide

PP –MMMMMM– CCC

Mask Identifier

Packaging Format
11 – Processed Wafer
21 – Bare Cell in Waffle Tray

Configuration Options
311 – C3MJ+, Silver front contact finish, 100% Tested
321 – C3MJ+, Gold front contact finish, 100% Tested
310, 320 – Same as above, Untested

Example: 21 – 046191 – 321 Bare Cell in Waffle Tray – 9.99×9.95mm Aperture – C3MJ+ Gold Front Contact, 100% Tested

Mechanical Dimensions

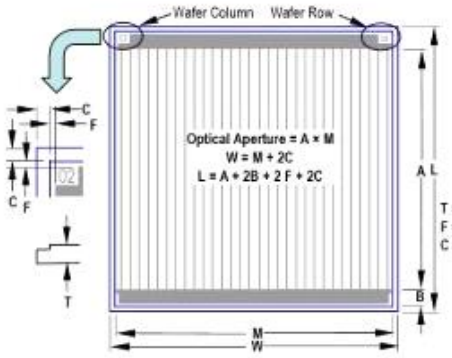

T = 19 µm in all cases
F = 25 µm in all cases
C = 38.2 µm in all cases

Product	Aperture Area	Aperture Dimensions (mm)		Busbar (µm)	Typical Efficiency
CPV Cell #	(mm ²)	M	A	B	η
PP- 046191 – CCC "CDO-100"	99.00	10.000	9.900	400 µm	39.20 %
PP- 046167 – CCC "CDO-086"	86.47	9.299	9.299	252 µm	39.22 %
PP- 046192 – CCC "CDO-076"	76.50	8.854	8.640	300 µm	39.25 %
PP- 046193 – CCC "CDO-020 "	30.74	5.547	5.542	300 µm	39.40 %

ISO9001:2000 REGISTERED
ENVIRONMENTAL MANAGEMENT SYSTEM CERTIFIED BY DNV ISO 14001
AS9100 REGISTERED

Spectrolab, Inc. 12500 Gladstone Avenue, Sylmar, California 91342 USA
● Phone 818.365.4611 ● FAX: 818.361.5102 ● Website : www.spectrolab.com

 Specifications Subject to Change without Notice.

SPECTROLAB

A **BOEING** COMPANY

Typical Current-Voltage Characteristics

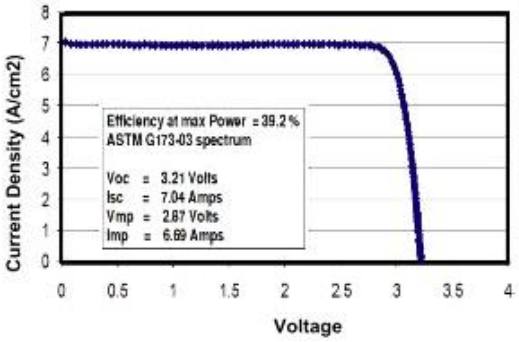

Spectral Response

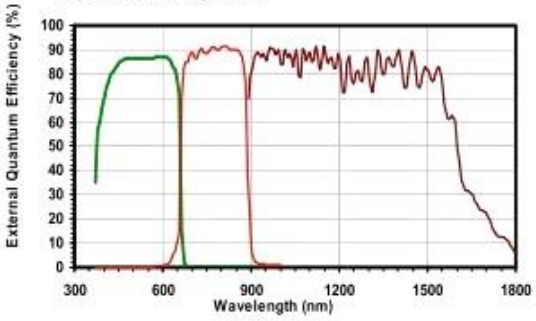

Qualification Tests Completed

Test	Test Conditions	Qty	Requirement
Performance Tests			
LIV	50 W/cm2 under ASTM 173G	100%	Avg η_{mp}>38.5%; Min η_{mp} > 36.2%
Temp Intensity	50, 75 & 100 W/cm^2, ASTM 173G at 10°C, 25°C, 65°C, and 110°C	20	Characterization
Weld Degradation	LIV test before and after weld	100% of scribed parts	NP_{mp} > 0.98
Spectral Response			Characterization
Angle of incidence	X25 or SR illumination source	10	Characterization
Solar Absorptance	Measure reflectance Refer to SR chart shown	10	Characterization
Accelerated Life Tests			
Damp Heat	85C, 85% RH for 2000 hours	30	NP_{mp} > 0.9
Thermal Cycle	IEEE 1513 (500 cycles –40°C to +110°C)	25	NP_{mp} > 0.9
High Temp Soak in Nitrogen	unbiased soak at 200°C and 250°C in Nitrogen	15 at each T	NP_{mp} > 0.95 after 25 yrs

* Full Qualification Report Is Available Upon Request

Typical Performance Over Temperature

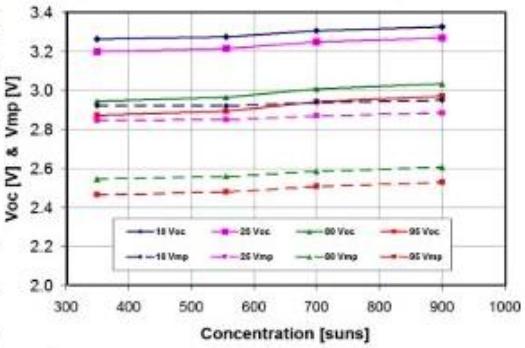

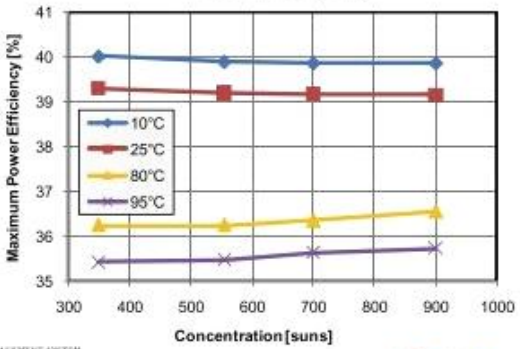

ISO9001:2000 REGISTERED

ENVIRONMENTAL MANAGEMENT SYSTEM CERTIFIED BY DNV ISO 14001

AS9100 REGISTERED

Spectrolab, Inc. 12500 Gladstone Avenue, Sylmar, California 91342 USA
● Phone 818.365.4611 ● FAX: 818.361.5102 ● Website : www.spectrolab.com

Specifications Subject to Change without Notice.

D.3.3. C4MJ Spectrolab sample specifications

SPECTROLAB A BOEING COMPANY

CPV Point Focus Solar Cells

C4MJ Metamorphic Fourth Generation CPV Technology

✓*First 40% production cell*
✓*First fully qualified metamorphic cell*

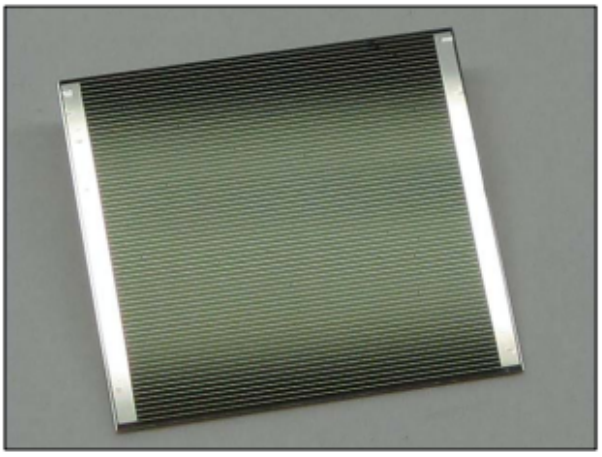

Product Description

Typical Efficiency	40%
Recommended operating temperature	<110°C

Epitaxial Structure

Triple junction solar cell on Germanium substrate
GaInP (1.82 eV) / GaInAs (1.33 eV) / Ge (0.66 eV)

Metallization

•Silver metallization on front busbar and grid fingers (optional gold flash finish)
•Silver metallization with 500Å gold on back surface

CPV Cell Ordering Guide

PP –MMMMMM– CCC
Mask Identifier

Packaging Format
11 – Processed Wafer
21 – Bare Cell in Waffle Tray

Configuration Options
401 – C4MJ, Silver front contact finish, 100% Tested
411 – C4MJ, Gold front contact finish, 100% Tested

Example: 21 – 046191 – 411 Bare Cell in Waffle Tray -- 9.99×9.95mm Aperture -- C4MJ Gold Front Contact, 100% Tested

Mechanical Dimensions

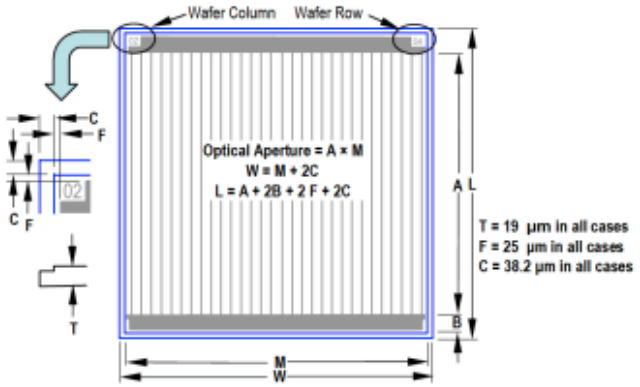

Product	Aperture Area	Aperture Dimensions (mm)		Busbar (µm)
CPV Cell #	(mm²)	M	A	B
PP- 046191 – CCC "CDO-100"	99.00	10.000	9.900	400 µm
PP- 046167 – CCC "CDO-086"	86.47	9.299	9.299	252 µm
PP- 046192 – CCC "CDO-076"	76.50	8.854	8.640	300 µm
PP- 046193 – CCC "CDO-030"	30.74	5.547	5.542	300 µm

ISO9001:2000 REGISTERED
ENVIRONMENTAL MANAGEMENT SYSTEM CERTIFIED BY DNV ISO 14001
AS9100 REGISTERED

Spectrolab, Inc. 12500 Gladstone Avenue, Sylmar, California 91342 USA
• Phone 818.365.4611 • FAX: 818.361.5102 • Website : www.spectrolab.com

Specifications Subject to Change without Notice. Rev. 7/12/11

SPECTROLAB A **BOEING** COMPANY

Spectral Response

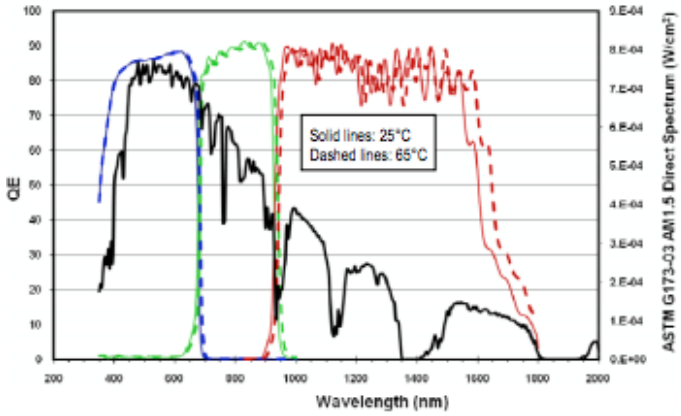

Typical Current-Voltage Characteristics

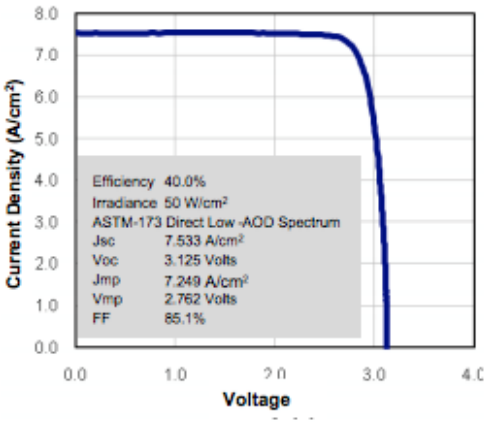

Typical Performance Over Temperature

Temperature coefficient of efficiency: < –0.06%/°C

Qualification Tests Completed

Full Qualification Report is available on request (May 2011)

Test	Conditions	Requirement	Results
Performance	50 W/cm^2	Effmp > 37.6% target avg = 40.0%	Avg = 39.8%
Thermal Cycle	1500 cycles, -40°C to +110°C with 10 m dwell	unprotected cell < 2% degradation	NEff = 1.0
Unprotected Cell Damp Heat	1000 hrs, 85°C/85% RH	characterization	NEff > 0.98
High Temperature Soak	Unbiased soak at 180° C, 200°C, 225°C and 250°C	< 0.5% degradation after 25 year lifetime	NEff = 1.0
Outdoor Field Trial	> 10 kW on sun for 6 months	characterization	> 10 kW total
High Temperature Reverse Bias	-0.8V and -1.6V @ 140° C until failure	characterization	Complete
HTOL	1 A & 4 A dark forward bias at 160°C	characterization	NEff > 0.99
ESD	HBM 4000 V, CDM 2000 V	characterization	NEff = 1.0

ISO9001:2000 REGISTERED

ENVIRONMENTAL MANAGEMENT SYSTEM CERTIFIED BY DNV ISO 14001

AS9100 REGISTERED

Spectrolab, Inc. 12500 Gladstone Avenue, Sylmar, California 91342 USA
• Phone 818.365.4611 • FAX: 818.361.5102 • Website : www.spectrolab.com

Specifications Subject to Change without Notice. Rev. 7/12/11

D.3.4. XTJ-Prime Spectrolab sample specifications

60th Anniversary!

SPECTROLAB

A BOEING COMPANY

XTJ PRIME

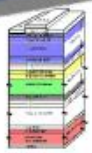

30.7% Triple Junction Space Grade Solar Cell

- Currently in full production
- Best In class - BOL & EOL
- AIAA-S111 & AIAA-S112 Qualified
- Heritage Upright Latice Matched XTJ Structure
- 26.7% EOL, 1E15 1MeV electron**
- Multiple sizes avilable (27cm² through 84 cm²)

Cell Thickness = 80 µm - 225 µm

Cell Mass = 50 – 84mg/cm²

XTJ Prime (US Standard- AIAA-S111-2005)

Parameters*	BOL	5E14	1E15	3E15	1E16
$Efficiency_{mp}$	30.7%	.88	.85	.76	.65
V_{OC} (V)	2.715	.89	.87	.83	.78
J_{sc} (mA/cm²)	18.1	.99	.98	.96	.93
V_{mp} (V)	2.390	.89	.87	.83	.76
J_{mp} (mA/cm²)	17.4	.99	.97	.92	.86

*Production Average; AM0 (135.3 mW/cm²) 28°C (Fluence 1MeV Electrons/cm²)

XTJ Prime (European Standard - ECSS)**

Parameters*	BOL	5E14	1E15	3E15	1E16
$Efficiency_{mp}$	30.7%	.90	.87	.80	.70
V_{OC} (V)	2.715	.90	.88	.85	.80
J_{sc} (mA/cm²)	18.1	.99	.99	.97	.94
V_{mp} (V)	2.390	.91	.89	.85	.80
J_{mp} (mA/cm²)	17.4	.99	.98	.94	.88

** Photon and temperature annealing according to ECSS-E-ST-20-08C

ENVIRONMENTAL MANAGEMENT SYSTEM CERTIFIED BY DNV ISO 14001

AS9100 REGISTERED

QS9001 2008

Spectrolab, Inc. 12500 Gladstone Avenue, Sylmar, California 91342 USA
• Phone: 818.365.4611 • FAX: 818.361.5102 • Website: www.spectrolab.com

60 th Anniversary!

XTJ PRIME

SPECTROLAB

A BOEING COMPANY

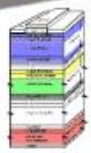

30.7% Triple Junction Space Grade Solar Cell

Temperature Coefficients (15°C - 75°C)

Parameters	5E14	1E15	3E15	1E16
$\Delta V_{oc}/\Delta T$ (mV/C°)	-6.2	-6.3	-6.5	-6.6
$\Delta J_{sc}/\Delta T$ (uA/cm²/C°)	10	11	11	12
$\Delta V_{mp}/\Delta T$ (mV/C°)	-6.5	-6.6	-6.7	-6.7
$\Delta J_{mp}/\Delta T$ (uA/cm²/C°)	8.9	10.3	12	12

Thermal Parameters	Value
Solar Absorptance	0.88
Emittance	0.85

Operates 2° C Cooler Than Other Space Grade Solar Cells

Standard Cell Sizes

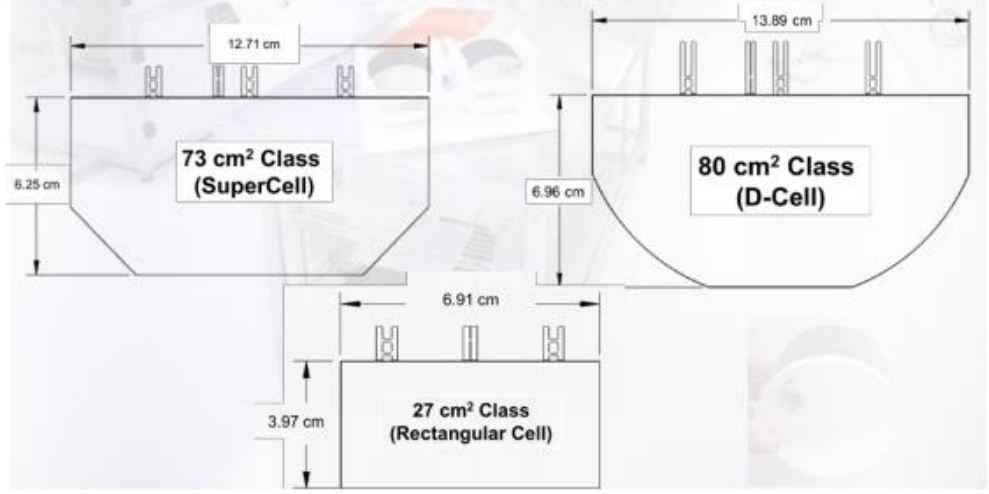

Spectrolab, Inc. 12500 Gladstone Avenue, Sylmar, California 91342 USA
• Phone: 818.365.4611 • FAX: 818.361.5102 • Website: www.spectrolab.com

D.3.5. 3C44 AzurSpace sample specifications

AZURSPACE
SOLAR POWER GMBH

Concentrator Triple Junction Solar Cell
Cell Type: 3C44 – 10 x 10mm²
Application: Concentrating Photovoltaic (CPV) Modules

Typical Average Electrical Data

Sun Concentration	I_{sc} [A]	V_{oc} [V]	I_{MPP} [A]	V_{MPP} [V]	P_{MPP} [W_{MPP}]	FF [%]	η [%]
Version MC/Air Grid optimized for medium concentration + Antireflective Coating adapted to air							
X 250	3,85	3,06	3,77	2,80	10,59	89,9%	42,1
X 500	7,66	3,11	7,54	2,81	21,20	88,9%	42,0
X 1000	15,35	3,15	15,07	2,69	40,56	83,8%	40,3
Version MC/Glass Grid optimized for medium concentration + Antireflective Coating adapted to glass							
X 250	3,82	3,07	3,76	2,80	10,55	89,9%	41,9
X 500	7,61	3,11	7,50	2,81	21,04	88,8%	41,8
X 1000	15,36	3,15	14,98	2,70	40,46	83,8%	40,2

Sun Concentration	I_{sc} [A]	V_{oc} [V]	I_{MPP} [A]	V_{MPP} [V]	P_{MPP} [W_{MPP}]	FF [%]	η [%]
Version HC/Air Grid optimized for high concentration + Antireflective Coating adapted to air							
X 250	3,76	3,06	3,68	2,83	10,44	90,7%	41,5
X 500	7,49	3,11	7,38	2,83	20,88	89,6%	41,4
X 1000	15,17	3,14	14,82	2,77	41,08	86,4%	40,8
Version HC/Glass Grid optimized for high concentration + Antireflective Coating adapted to glass							
X 250	3,75	3,06	3,68	2,82	10,39	90,5%	41,3
X 500	7,47	3,10	7,35	2,82	20,73	89,5%	41,2
X 1000	14,97	3,14	14,71	2,77	40,77	86,9%	40,5

Efficiency versus Sun Concentration

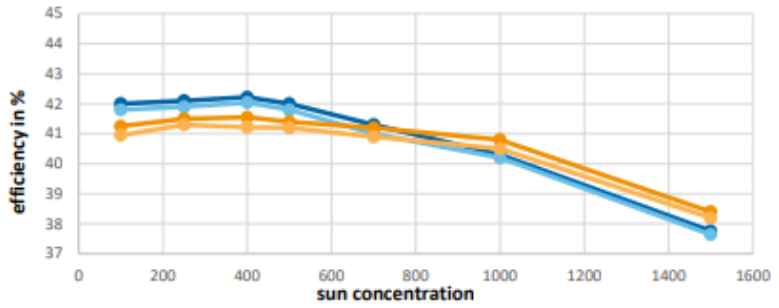

Measurement conditions: 1.5 AMd – 1000 W/m² (ASTM G 173-03), T = 25 °C, designated measurement area = 100,51 mm²

3C44

CPV

AZUR SPACE Solar Power GmbH
Theresienstr. 2
74072 Heilbronn
phone: +49 7131 67 2603
telefax: +49 7131 67 2727
e-mail: info@azurspace.com
website: www.azurspace.de

Certified Company
ISO 9001
ISO 14001
OHSAS 18001

DB 0004355-00-01
Issue: 2016-12-21
Page 1 of 4
AZUR DOCUMENT released for publication (Level 1 of 5)

Spectral Response

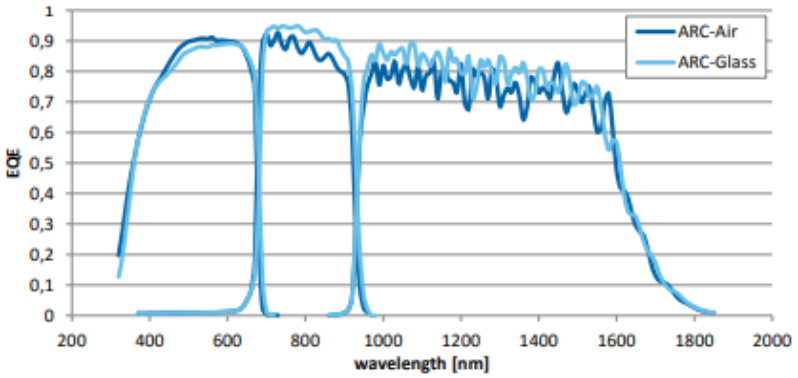

Typical Temperature Coefficients

Temperature range (25 – 80 °C)

Parameter	$(\Delta I_{sc} / I_{sc\,(25°C)}) / \Delta T$	$(\Delta V_{oc} / V_{oc\,(25°C)}) / \Delta T$	$(\Delta P_{mpp} / P_{mpp\,(25°C)}) / \Delta T$	$(\Delta \eta / \eta_{(25°C)}) / \Delta T$
Value	0,080%/K	-0,135%/K	-0,106%/K	$-0,106\%_{(rel)}$/K
Parameter	$\Delta I_{sc} / \Delta T$	$\Delta V_{oc} / \Delta T$	$\Delta P_{mpp} / \Delta T$	$\Delta \eta / \Delta T$
Value	6,1 mA/K	-4,2 mV/K	-22,5 mW/K	$-0,045\%_{(abs)}$/K

Exemplary values measured with version MC/Air, at 500 suns

Typical Performance over Temperature

Exemplary for version MC/Air

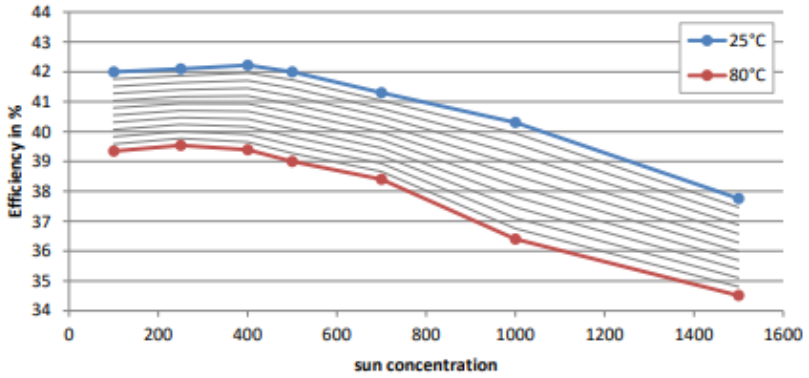

3C44

CPV

AZUR SPACE Solar Power GmbH
Theresienstr. 2
74072 Heilbronn
phone: +49 7131 67 2603
telefax: +49 7131 67 2727
e-mail: info@azurspace.com
website: www.azurspace.de

Certified Company
ISO 9001
ISO 14001
OHSAS 18001

Version Comparison

Opto Electrical Behaviour	
Antireflective Coating	Efficiency change on glass covered cells
Version Air	-3,2 %$_{(rel)}$
Version Glass	-0,4 %$_{(rel)}$

Efficiency comparison at 500 suns

Influence of Cell Dimension	
Active Area	Typical efficiency (Version MC/Air at 250 suns)
3 x 3 mm	44,0 %
5,5 x 5,5 mm	42,9 %
10 x 10 mm	42,1 %

Design and Mechanical Data

Base Material	GaInP/GaInAs/Ge on Ge substrate
AR coating	TiO_x/AlO_x
Chip size	10,1 mm x 10,5 mm = 106,05 mm²
Active Cell Area	10,0 mm x 10,0 mm = 100 mm²
Cell thickness	190 µm ± 20 µm
Polarity	N on P
Thickness of front contact	≥ 2,8 µm (finish is an Ag/Au alloy)
Thickness of back contact	≥ 2,6 µm (finish is an Ag/Au alloy)
Assembly methods	suitable for welding, soldering and bonding

Layout details

Drawing dimension are mm

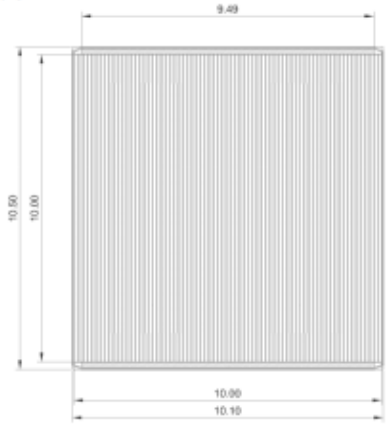

Sample drawing shows version with HC-grid design; More details in drawing HNR 0003782 and HNR 0003783, available on request.

3C44

CPV

AZUR SPACE Solar Power GmbH
Theresienstr. 2
74072 Heilbronn
phone: +49 7131 67 2603
telefax: +49 7131 67 2727
e-mail: info@azurspace.com
website: www.azurspace.de

Certified Company
ISO 9001
ISO 14001
OHSAS 18001

Storage and Operation Conditions Requirements

- Humidity protection is strongly recommended
- Storage in dry air or nitrogen atmosphere is requested
- As front side interconnector material we recommend gold or silver
- We recommend to use Sn96.5/Ag3.5-solder or another solder with saturated silver for rear side assembly
- A void free rear side assembly (heat sink) is requested to avoid hot spots
- The cell junction shall not exceed a maximum operation temperature of 110° C
- Secondary glass glue on the front side has to be flexible (prefer silicone glue or similar)

Additional Information

- Current values at specific operating voltage can be offered on customer request
- Explanation of ARC versions:
  - AIR:
    The antireflective coating on top of the solar cell is optimized for the interface to air. In this kind of application the light enters the solar cell directly from air. The indoor test measurement (flash test) will be done at air atmosphere.
  - GLASS:
    The antireflective coating on top of the solar cell is optimized for the interface to glass or similar (n≈1.43). At this kind of application the light enters the solar cell through a glass component or similar (e.g. secondary element, homogenizer element, cover glass). However, the indoor test measurement (flash test) will be done at air atmosphere without glass interface. Therefore the flash test results will underestimate the potential cell performance. The performance of a system with glass interfaces is expected to be higher using cells with ARC Glass than with ARC Air.
- Acceptance test rules for delivery lots:
  - Minimum average efficiency = typical average value minus 2% (rel.)
  - Minimum individual cell efficiency = typical average value minus 5% (rel.)

Order Information

Product Version	 wafer (not diced)	 diced wafer, mounted on a tape
MC/Air	81244	81245
MC/Glass	81246	81247
HC/Air	81248	81249
HC/Glass	81250	81251

3C44

AZUR SPACE Solar Power GmbH
Theresienstr. 2
74072 Heilbronn
phone: +49 7131 67 2603
telefax: +49 7131 67 2727
e-mail: info@azurspace.com
website: www.azurspace.de

Certified Company
ISO 9001
ISO 14001
OHSAS 18001

CPV

D.3.6. TOPAS® Cyclic Olefin Copolymer (COC) specifications

Cyclic Olefin Copolymer


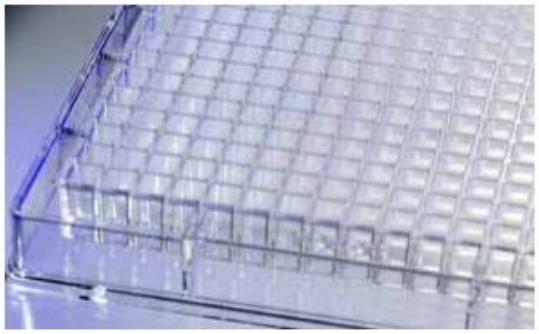
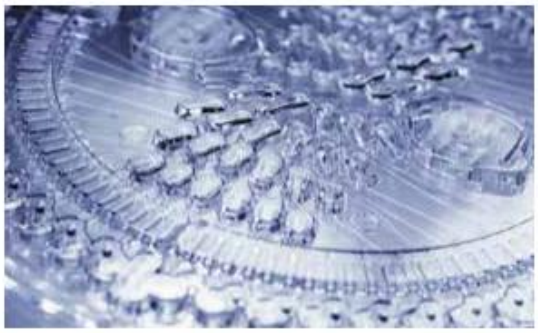


Important:

Properties of molded parts, sheets and films can be influenced by a wide variety of factors involving material selection, further additives, part design, processing conditions and environmental exposure. It is the obligation of the customer to determinewhether a particular material and part design is suit-able for a particular application. The customer is responsible for evaluating the performance of all parts containing plastics prior to their commercialization.Our products are not intended for use in medical ordental implants. – Unless provided otherwise, values shown merely serve as an orientation; such values alone do not represent a sufficient basis for any part design. – Our processing and other instructions must be followed. We do not hereby promise or guarantee specific properties of our products. Any existing industrial property rights must be observed.

Published in June 2019

Cyclic Olefin Copolymer

Effective January 1, 2006, the global COC business has been sold from Ticona/Celanese to the Japanese companies Daicel and Polyplastics and transfered into a new entity with the name Topas Advanced Polymers. The new company is located in Frankfurt/ Germany and Florence/USA and has about 100 people working in Research & Development, Marketing & Sales, Production and Administration.

The History of Topas® COC started in the early 90s at corporate research of Hoechst AG. In a new developed process first Norbornene will be synthesized from Dicyclopentadiene and Ethylene. In a second copolymerisation step with Etylene using Metallocene-Catalysts the final product Cyclic Olefin Copolymer is generated. The Topas® COC production plant in Oberhausen/ Germany went on stream in year 2000 with an annual capacity of 30,000 tons.

Topas Advanced Polymers is producing and marketing cyclic olefin copolymers under its trademarks Topas® COC and Crystal Dew® and a bi-cyclic olefin Norbornene.

1. Introduction

Topas® COC is the trade name for Topas Advanced Polymers' cyclic olefin copolymers (COC). The Topas® COC family, in contrast to the partially crystalline polyolefins PE and PP, consists of amorphous, transparent copolymers based on cyclic olefins and linear olefins.

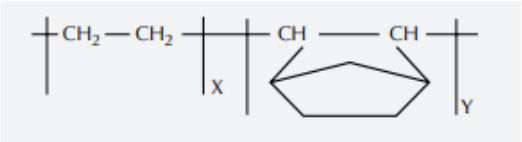

Cyclic olefin copolymers are a new class of polymeric materials with property profiles which can be varied over a wide range during polymerization.

These new materials exhibit a unique combination of properties of which can be customized by varying the chemical structure of the copolymer. Performance benefits include:

- **Low density**
- **High transparency**
- **Low birefringence**
- **Extremely low water absorption**
- **Excellent water vapour barrier properties**
- **Variable heat deflection temperature up to 170 °C**
- **High rigidity, strength and hardness**
- **Very good blood compatibility**
- **Excellent biocompatibility**
- **Very good resistance to acids and alkalis**
- **Very good electrical insulating properties**
- **Very good melt processability/flowability**

Topas® COC resins are suitable for the production of transparent moldings for use in optical data storage, optics, e.g. lenses, sensors, and industrial products e. g. in the construction and lighting sectors.

These materials are also of particular interest for primary packaging of pharmaceuticals, medical devices and diagnostic disposables.

(Co)-extruded films made from Topas® COC offer opportunities in blister packaging, shrink sleeves, shrink films and stand-up pouches.

New applications have been developed for blends of Topas® COC, with a variety of polyolefins.

2. Grades, supply form, colors

Topas® COC resin is currently supplied as an unreinforced water-clear transparent material. Glass-filled, tinted and pigmented formulations are also under development.

Currently available basic grades differ primarily in their heat deflection temperature HDT/B. The heat deflection temperature is determined by the ratio of the comonomers. Topas® COC grades with higher cyclo-olefin content have higher heat resistance. Flow characteristics may be adjusted independently of heat resistance.

The product nomenclature contains a 4 digit number. The first two digits indicate the viscosity number, the last two digits describe the heat deflection temperature HDT/B. The flowability decreases with increasing viscosity number.

The table on the right lists the Topas® COC basic grades. Of these grades, specific sub-grades are avail-able on request, which are particularly well suited for optical, medical and diagnostic applications, for extrusion and injection blow molded applications.

Grade	Description
8007	Clear grade with a heat deflection temperature HDT/B of 75 °C. It is especially suited for packaging of moisture-sensitive products because of its low water absorption and very good barrier properties. Grade 8007 has a lo-wer elastic modulus and higher elongation than other Topas® COC grades.
5013	Clear grade with a heat deflection temper-ature HDT/B of 130 °C. This grade is char-acterized by high flowa-bility and excellent optical properties. Recommended for applications such as optical parts, e. g. lenses, and optical storage media, where low birefringence and high molding accuracy (pit replication) are essential, as well as for medical and diagnostic applications.
6013	Clear grade with a heat deflection temperature HDT/B of 130 °C, a value which cannot be attained by many amor-phous polymers. Its combination of high purity, chemi-cal resistance, high transparency and high HDT/B makes this material useful for prod-ucts such as labware. Parts made from 6013 can be gamma- and steam-sterilized.
6015	Clear grade similar to 6013, with a heat deflection tem-perature HDT/B of 150 °C, a value which cannot be at-tained by many amorphous polymers.
6017	Clear grade with a heat deflection temper-ature HDT/B of 170 °C. For parts requiring resistance to short-term, high-temperature exposure.

3. Physical properties

The physical property values of Topas® COC are given in Table 1 below. Most of the properties were determined by standard test methods, as indicated in the table.

Although the typical values shown in Table 1, determined on development specimens by various standard test methods, are guide values and can be used as a basis for comparing different materials, in-service testing, using finished molded parts, is recommended. Also, mold shrinkage should be evaluated in proto-type parts.

3.1 Mechanical properties

Topas® COC resin is a clear thermoplastic resin with high strength, rigidity and, depending on the grade, heat deflection temperature. Because of its amorphous character, these properties are retained over a wide temperature range, from -50 °C to near the glass transition temperature. Fig. 1 shows shear modulus curves, which are particularly useful in characterizing the temperature-dependent behaviour of a plastic.

3.1.1 Behaviour under short-term stress

The behaviour of materials under short-term stress can be evaluated by the tensile test according to ISO 527. This test enables yield stress, tensile strength and elongation at break to be determined. Fig. 2 shows the stress-strain curves for Topas® COC grades. Note that grades 5013, 6013, 6015 and 6017 display similar behaviour.

Fig. 1: Shear modulus curves determined by DIN 53445 for various Topas® COC grades as a function of temperature

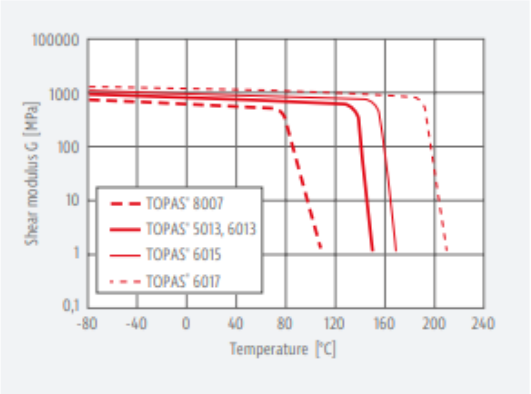

Fig. 2: Stress-strain curves according to ISO 527 for Topas® COC resins

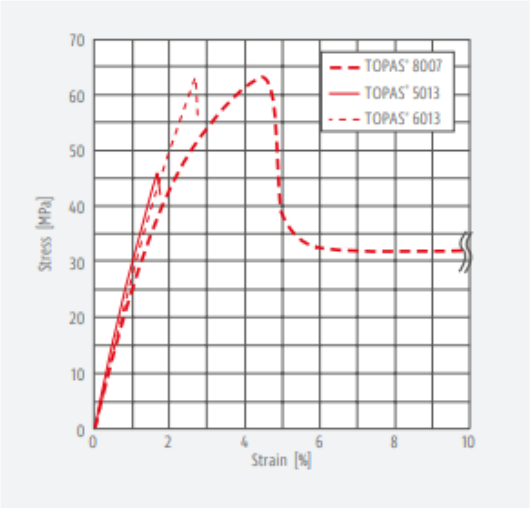

Table 1: Physical properties of Topas® COC

Property	Unit	Test method	8007	6013	6015	5013	6017
Volume flow index MVR at 260 °C, 2.16 kg	ml/10 min	ISO 1133	32	14	4	48	1.5
Volume flow index MVR at HDT +115 °C, 2.16 kg	ml/10 min	ISO 1133	2	6	5	24	5
Density	g/cm³	ISO 1183	1.02	1.02	1.02	1.02	1.02
Water absorption (24 h immersion in water at 23 °C)	%	ISO 62	< 0.01	< 0.01	< 0.01	< 0.01	< 0.01
Water vapour permeability (at 23 °C and 85% relative humidity)	g · mm/ m² · d	DIN 53 122	0.023	0.035	0.035	0.030	0.045
Mold shrinkage (ϑ_W = 60 °C, 2 mm wall thickness)	%	–	0.1 - 0.5	0.4 - 0.7	0.4 - 0.7	0.4 - 0.7	0.4 - 0.7
Mechanical properties, measured under standard conditions, ISO 291 – 23/50							
Tensile strength [5 mm/min]	MPa	ISO 527 parts 1 and 2	63	63	60	46	58
Elongation at break [5 mm/min]	%	ISO 527, parts 1 and 2	10*)	2.7	2.5	1.7	2.4
Tensile modulus [1 mm/min]	MPa	ISO 527, parts 1 and 2	2600	2900	3000	3200	3000
Impact strength (Charpy)	kJ/m²	ISO 179/1eU	20	15	15	13	15
Notched impact strength (Charpy)	kJ/m²	ISO 179/1eA	2.6	1.8	1.6	1.6	1.6
Ball indentation hardness, 30-sec value	N/mm²	ISO 2039 part 1, applied load 961N	130	184	184	184	191
Thermal properties							
Heat deflection temperature HDT/B (0.45 MPa)	°C	ISO 75 parts 1 and 2	75	130	150	130	170
Coefficient of linear thermal expansion	K^{-1}	ISO 11 359 parts 1 and 2	$0.7 \cdot 10^{-4}$	$0.6 \cdot 10^{-4}$	$0.6 \cdot 10^{-4}$	$0.6 \cdot 10^{-4}$	$0.6 \cdot 10^{-4}$
Electrical properties							
Relative permittivity ε_r at 1-10 kHz	–	IEC 60250	2.35	2.35	2.35	2.35	2.35
Comparative tracking index CTI	–	IEC 60112	> 600	> 600	> 600	> 600	> 600
Volume resistivity	Ω · m	IEC 60093	$> 10^{14}$	$> 10^{14}$	$> 10^{14}$	$> 10^{14}$	$> 10^{14}$
Flammability							
UL Flammability Rating	Class	UL 94	HB (1.6mm)	HB (1.6mm)	HB (1.6mm)	HB (1.6mm)	HB (1.6mm)
Optical properties							
Light transmission (2 mm wall thickness)	%	ISO 13468-2	91	91	91	91	91
Refractive index	–	–	–	–	–	1.53	–
Abbe number	–	–		–	–	56	–

*) Yield strain: 4.5%

Fig. 3 and 4: Effect of temperature on the elastic modulus and tensile strength of Topas® COC resin compared with other transparent amorphous thermoplastics. This is valid with good approximation for grades 5013, 6013, 6015 and 6017

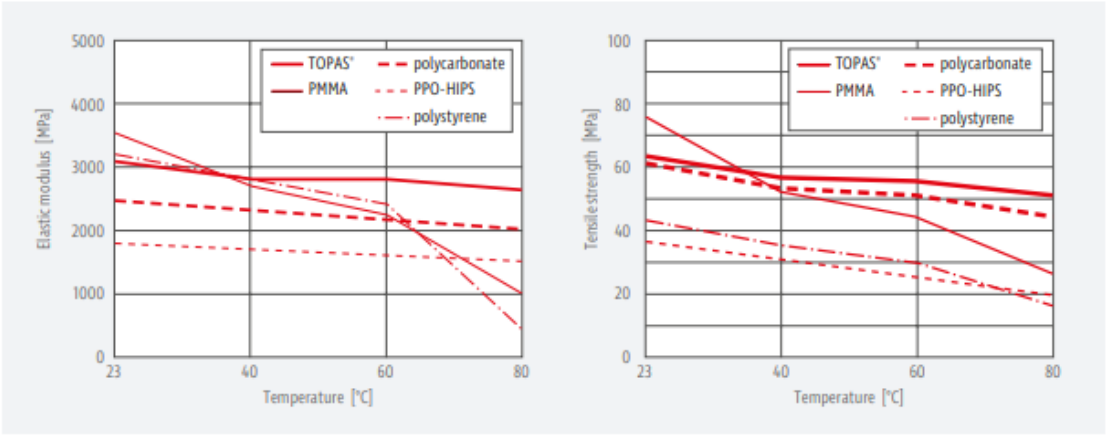

Figures 3 and 4 show the effect of temperature on the elastic modulus and tensile strength of Topas® COC resins compared with other transparent amorphous thermoplastics.

3.1.2 Behaviour under long-term stress

The results of long-term tests carried out under various conditions provide the design engineer with a basis for calculation when designing components subjected to prolonged stress. The behaviour of plastics under long-term tensile stress is tested by two basis methods:

- **Creep rupture test according to DIN 53 444**
- **Stress relaxation test according to DIN 53 441 (stress decay in specimen held under constant strain).**

The results are plotted as creep curves, creep modulus curves, time-stress curves and isochronous stress-strain curves. The graphs show initial results offering a preliminary guide to behaviour.

Fig. 5 shows the flexural creep modulus of Topas® COC grades (valid with good approximation for grades 5013, 6013, 6015 and 6017) compared with selected other transparent resins. Note the modulus level and low creep tendency of Topas® COC polymers in comparison with the other polymers shown.

Fig. 5: Flexural creep modulus over time for Topas® COC polymer grades and other polymers as a function of time

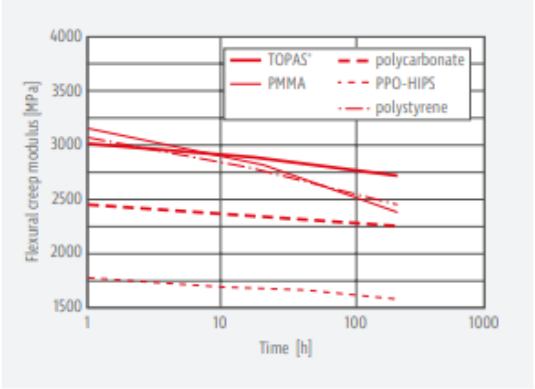

3.2 Thermal properties

The outstanding feature of this new class of polymer materials is the ability to vary its glass transition temperature. The Topas® COC development product line covers a wide range of glass transition temperatures from about 80 °C to 180 °C or, expressed in terms of the more meaningful heat deflection temperature under load, a HDT/B range of 75 °C to about 170 °C. The permissible service temperature for short-term heat stress comes close to the glass transition temperature.

The high transparency of the material remains unaffected by temperature. However, the maximum permissible service temperature should be assessed for the specific grade and stress conditions that the molded part will encounter in actual service. Values determined by standard test methods are designed to serve only as a general guide.

Thermal conductivity

The thermal conductivity of the Topas® COC grades at 20 °C varies between 0.12 to 0.15 W/m · K (dependent on grade). The thermal conductivity value is temperature dependent.

Coefficien fo linear thermal expansion

The coefficient of linear thermal expansion is about
$a = 0.6 \cdot 10^{-4}/°C$.

Fig. 6: Heat deflection temperature HDT/B of Topas® COC and other amorphous polymers

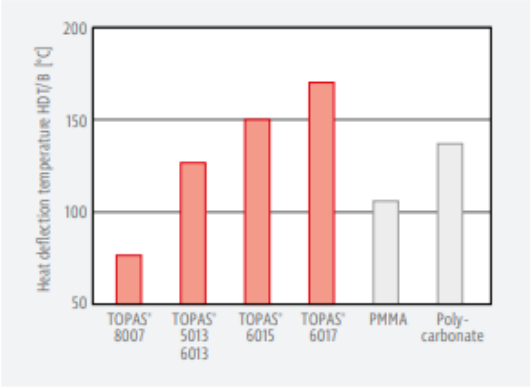

3.3. Electrical properties

Topas® COC has very good electrical insulating properties and a low dissipation factor. It is therefore suit-able for use as an insulating material, particularly at higher end of its temperature capabilities. The dielectric constant of Topas® COC is around 2.35, which is typical of the values obtained with olefinic materials (Fig. 7). It stays constant in the high frequency area up to 20 GHz. The very low temperature dependence of the dielectric constant and dissipation factor is shown by measurements on biaxially oriented film (Fig. 8). At 10 kHz and 100 °C, a value of 0.2 · 10—4 was determined.

Volume resistivity

The volume resistivity of all Topas® COC grades at
23 °C $r_D > 10^{16}$ V · m.

Surface resistivity

Surface resistivity gives an indication of the insulation resistance across the surface of a material. The dependence of this value on humidity and surface contamination must be taken into account. The surface resistivity of all grades Topas® COC is $> 10^{14}$ V.

CTI value

The comparative tracking index for Topas® COC polymer is
CTI > 600 V.

Fig. 7: Effect of temperature on the dielectric constant of various polymers

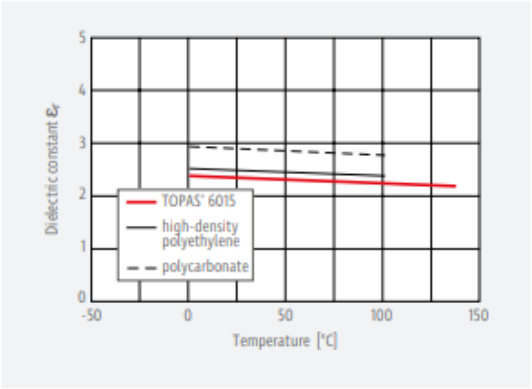

Fig. 8: Effect of temperature on the dissipation factor tand of various polymers

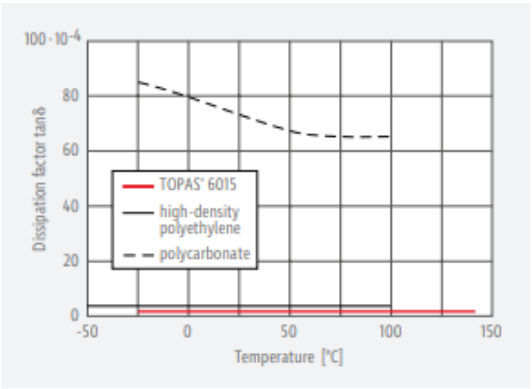

3.4. Optical properties

Transmission and refractive index

Light transmission in the visible region is an important optical property for optical applications such as lenses, prisms or optical storage media but is not the only important optical property. The high transparency of Topas® COC in the visible and near ultraviolet regions coupled with a refractive index of 1.53 (Topas® 5013) makes the polymer attractive for optical components. The chromatic aberration of Topas® COC, evidenced by a high Abbe number of 56 for Topas® 5013, is very low. Topas® COC is, therefore, suitable for the production of high-quality optical components for cameras and office machines.

Stress-optical constant and birefringence

Optical birefringence is a critical factor which must be controlled in a range of applications; from optical storage media and lenses to films.

Because of its aliphatic structure and the low optical anisotropy associated with this type of structure, Topas® COC has inherently low birefringence. This material property is accompanied by a low stress-optical constant. Fig. 10 shows the effect of applied tensile strength on the birefringence of various plastics. The following table shows that the stress-optical constant of Topas® COC is in the same range as that for PMMA but only around one tenth of the value for PC.

The advantageous optical properties of Topas® COC resin, combined with its very low moisture absorption, high elastic modulus and the possibility of tailoring flow make it especially suitable even for very thin optical parts. Very good molding accuracy (replication) is attained.

Fig. 9: Light transmission of Topas® 6015 as a function of wavelength

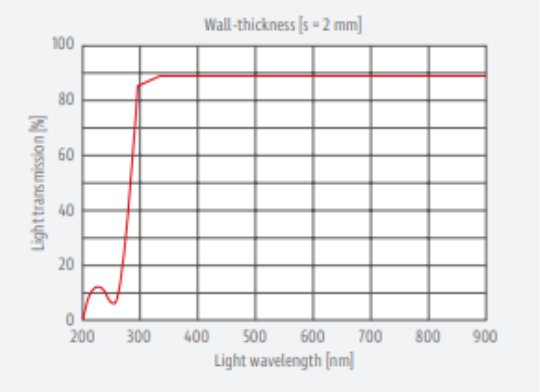

Fig. 10: Stress birefringence of various plastics (birefringence as a function of tensile stress)

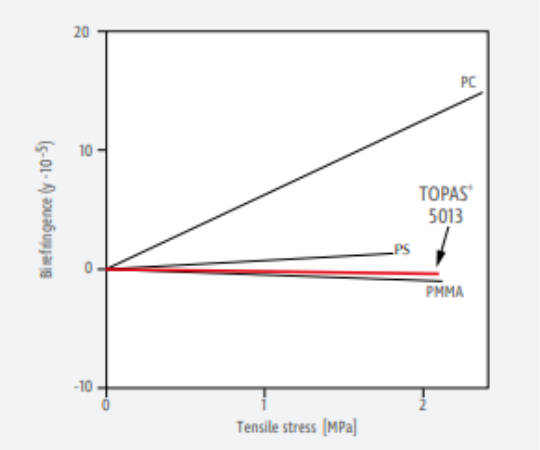

Stress-optical constant C

MATERIAL	C [10^{-6} mm²/N]
TOPAS® COC	-2 to -7
PMMA[1])	-4.5 to -4.8
PS[1])	4 to 7
PC[2])	66 to 70

1) Kunststoff Handbuch vol. 1, published by B. Carlowitz, Hanser Verlag München 1990, page 779.

2) M.-J. Brekner, "Polymers in Information Storage Technology" pub-lished by K. L. Mittal, Plenum Press, New York 1989, page 199.

4. Effect of service environment on properties of Topas® COC

This section describes the effects on the properties of Topas® COC by:

- Air at elevated temperature
- Water
- Motor fuels
- Chemicals
- Weathering
- High-energy radiation
- Flammability

4.1 Behaviour in air and water at elevated temperatures

Air

Most grades are stabilized against thermooxidative degradation to ensure that both the melt, during processing, and finished parts, in service, can withstand heat stresses. Progressive deterioration in properties through heat ageing is influenced in various ways by many service condition factors. Terms such as "heat resistance" and "continuous service temperature" do not, therefore, describe material constants but should be regarded only in the context of particular application requirements.

However, molded parts made from Topas® COC remain dimensionally stable almost to the glass transition temperature of the particular grade on short-term exposure to high-temperature stresses.

Water

Topas® COC is water-repellent (hydrophobic) and therefore exhibits only negligible swelling when immersed in water. Changes in the relative humidity of the environment have virtually no effect on material properties. The very slight water uptake that can be measured when there is a change of temperature in a warm, humid atmosphere mainly results from traces of moisture on the surface. If this situation is encountered the pellets need to be dried before molding.

Water absorption after immersion for 24 h/23 °C is 0.01 %; after immersion in demineralized water for 28 days/80 °C, it is 0.11 %. The water absorption of PC is about four times greater and that of PMMA about 10 times greater under identical conditions.

Topas® COC has excellent water vapour barrier properties (fig. 11).

Fig. 11: Water vapour permeability of various polymers (measured at 40 °C/90 % RH)

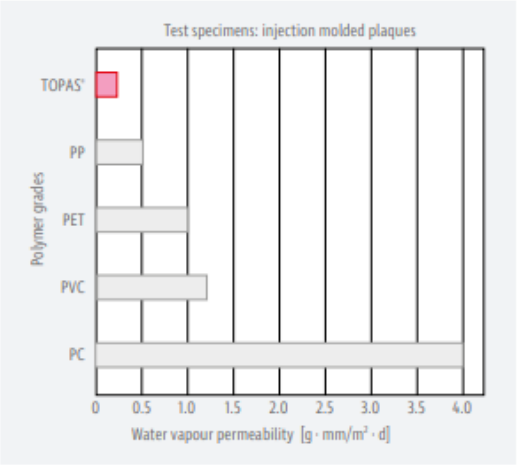

4.2 Chemical resistance

Because of their olefinic character, all Topas® COC grades are resistant to hydrolysis, acids and alkalis, as well as to polar solvents such as methanol. However, Topas® COC is attacked by non-polar organic solvents such as toluene and naphtha. Decisions to use COC resins in the presence of certain chemicals should always be made with knowledge of the requirement profile, and in cases where suitability is in doubt, resistance should always be confirmed by end-use testing.

The resistance of Topas® COC to selected chemicals tested at room temperatures is shown in Table 2.

Cyclic Olefin Copolymer

Table 2: Chemical resistance of Topas® COC

Medium	
Soap solution	⊕
Hydrochloric acid 36%	⊕
Sulphuric acid 40%	⊕
Acetic acid > 99%	⊕
Nitric acid 65%	⊕
Caustic soda solution 50%	⊕
Ammonia solution 33%	⊕
Methanol	⊕
Ethanol	⊕
Isopropanol	⊕
Acetone	⊕
Butanone	⊕
Benzaldehyde	⊙
Methylene chloride	⊖
n-Pentane	⊖
Heptane	⊖
Toluene	⊖
Hexane	⊖
Naphtha	⊖
Oleic acid	⊖

Assessment is based on the following criteria:

⊕ resistant	⊙ limited resistance	⊖ not resistant
weight increase < 3 % or weight loss < 0.5 %	weight increase 3 to 8 % or weight loss 0.5 to 5 %	weight increase > 8 % or weight loss > 5 %
elongation at break not substantially altered	elongation at break reduced by < 50 %	elongation at break reduced by > 50 %

4.3 Stress cracking resistance

The combined action of certain media with internal molded-in stresses and, in some cases, with imposed mechanical stresses, can result in chemically induced stress cracking in moldings made from Topas® COC resins. Temperature, duration of exposure to the medium and the level of internal and external stresses in the molded part all have an influence on stress crack initiation. Vegetable and animal fats and continuous contact with hot water, for example, can initiate stress cracking. It is therefore essential to carry out end-use tests to assess the suitability of a molded part for the specific service conditions.

Experience with injection molded parts has shown that resistance to stress cracking may be improved by the following measures:

- Processing with the highest possible melt temperature
- Filling the mold cavity rapidly
- Correct adjustment of in-mold residence time and pressure
- Carefully designed mold cooling system.

Parts can be designed to minimize stress cracking by:

- Avoiding large wall thickness variations
- Radiusing corners and edges
- Avoiding stress concentration peaks (notches).

4.4 Light and weathering resistance

Like most plastics, Topas® COC resin undergoes little or no change when exposed to radiation in the visible light region. However, prolonged exposure to direct sunlight can have an adverse effect on the properties of Topas® COC due to ultraviolet rays. For parts likely to be exposed to outdoor weathering, UV-stabilized grades are under development.

Table 3

TOPAS® COC	Hot steam			ETO	High-energy radiation	
	121 °C	134 °C	143 °C		gamma	electron
8007	–	–	–	+	+	+
5013	+	–	–	+	+	+
6013	+	–	–	+	+	+
6015	+	+	+	+	+	+

The data presented herein show the typical effects of sterilization procedures on the nominal physical properties, using standardized test specimens. The actual sterility of the parts have not been evaluated for either single or multiple use applications. It is the responsibility of the medical device manufacturer to determine the necessary steps to ensure the safe and efficacious use of their products and to obtain the necessary regulatory approvals for the intended applications.

5. Food packaging, medical and diagnostic

Topas® COC exhibits a unique combination of properties – glass-clear transparency, superior water vapour barrier, low water absorption and good chemical resistance to aqueous media, acids and alkalis and to polar organics. Thus, together with their excellent biocompatibility, these materials are of particular interest for primary packaging of pharmaceuticals, medical devices and diagnostic disposables.

5.1 Sterilizability

The use of plastics in the pharma and diagnostics sector in many cases requires sterilizability of the plastic material.

The effect of various sterilization methods, using high energy radiation (gamma and electron beam), ETO, hot air and hot steam, has been investigated for Topas® COC . Standard test specimens were subjected to conditions simulating one time exposure. Table 3 summarizes the results of these testings. Topas® COC should not be used in applications requiring more than one or two sterilization cycles.

Topas® COC test specimens maintain mechanical properties after exposure to gamma radiation doses of 50 kGy. Like many other plastics, Topas® COC shows a dose-dependent discoloration after exposure to gamma radiation. Grades with improved color stability in gamma irradiation can be requested.

5.2 Biocompatibility

Criteria for the use of plastics in the pharma and diagnostics sector are specified in the national pharmacopoeias (US, EU and JP), and by the appropriate regulatory agencies. Material test program guidelines are given by the FDA, and the International Organization for Standardization (ISO 10993). The test program depends on the particular application and the duration of contact with the human body.

Topas® COC material biocompatibility testing was carried out according to guidelines given in the FDA Blue Book Memorandum, and by the International Organization for Standardization (ISO 10993). A range of Topas® COC grades were subjected to this material biocompatibility test program. The protocol included the following: Acute Systemic and Intra-cutaneous Toxicity, Muscle Implantation, Physico-Chemical tests, Blood Compatibility (Hemolysis), and Cytotoxicity. These grades meet the specification of US Pharmacopoeia XXIII – Class VI. Corresponding certificates for specific grades are available.

Chemical characterization and extraction tests have been carried out successfully according to the protocols described in the US, EU and Japanese Pharmacopoeia.

These tests are intended as a general screening of the materials. The information discussed here should only be used as a starting point for the package/device manufacturer's consideration of the protocol to be used for testing specifically to the particular application. The presentation of these results is thus not intended to replace the testing required of the manufacturer of the package or device. Nor should it be considered a recommendation of the material for any particular application. It is the package/device manufacturer's responsibility to ensure that the materials used for a particular application are suitable for the intended use.

Topas® COC products are not be used in any kind of implants in the human body.

5.3 Regulatory

Approval for use in food contacting applications has been obtained. The monomers used for manu-facturing the material are listed in the EU directives 90/128/EEC, 92/39/EEC, 93/9/EEC, 95/3/EEC, 96/11/EEC, 99/91/EEC and 2002/72/EC.

Effective May 20, 2004 the FDA is amending the food additive regulations to allow for the safe use of norbornene-ethylene copolymers for dry food applications. The FDA regulation number is 21 CFR 177.1520.

In the USA, a Drug Master File (number 12132) and a Device Master File (number 1043) have been established for Topas® COC.

6. Processing

Topas® COC can be processed by all commonly used methods for thermoplastics such as injection molding, extrusion (film, sheet and profile), blow molding and injection blow molding.

6.1 Safety and health information

Before starting the injection molding process, obtain and read the appropriate Material Safety Data Sheet (MSDS) for detailed safety and health information.

Use process controls, work practices, and protective measures described in the MSDS sheets to control workplace exposure to dust, volatiles, etc..

6.2 Injection molding

6.2.1 Machine requirements

Topas® COC can be processed on conventional injection molding machines. The plasticizing cylinders can be fitted with standard screws. Three – section screws with a compression ratio 1:2.3 should be preferred.

Drying

Special pretreatment (drying prior to molding) generally is not necessary. Topas® COC that has become moist as a result of unsuitable storage conditions must be dried in a dehumidifying oven at 80 °C to remove surface moisture. For special applications imposing high surface quality requirements, Topas® COC should be predried in a dehumidifying oven at temperatures of > 100 °C for a period of 4 - 6 hours. Grade 8007 should be dried at lower temperatures (max. 60 °C) because of its lower glass transition temperature.

6.2.2 Flow behaviour

The melt index is commonly employed to characterize the flow behaviour of Topas® COC grades under processing conditions. However, a more practical method of determining flow behaviour is the non-standardized spiral flow test. The spiral length measured in this test provides a meaningful guide to flowability. Figure 12 shows the spiral length of the Topas® COC grades for a wall thickness of s = 2 mm under different processing conditions.

However it is important to note that the rheological properties of any thermoplastic material are strongly influenced by processing parameters such as injection pressure, injection speed, melt and mold temperature and on mold design (and machine operating data).

Fig. 12: Spiral flow length of Topas® COC grades with different glass transition temperatures as a function of pressure (2 mm-thick test spiral). The processing parameters (q_M5 melt temperature, q_W5 mold wall temperature) were matched to the glass transition temperature of the Topas® COC grades

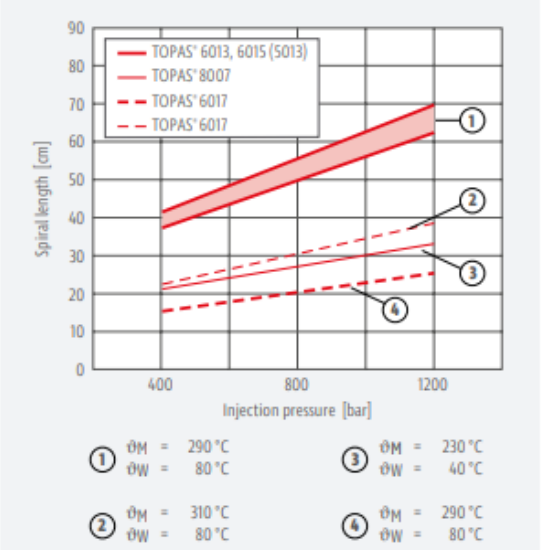

6.2.3 Gate and mold design

The suitability of a plastic molding for a particular application is basically determined by the following factors:

- Properties of the molding material
- Processing of the molding material
- Design of the molded part and mold.

Only optimization of all three factors will ensure a high-quality molded part. This requires close cooperation between the material manufacturer, designer and end user.

The type of gate and its location are determined by various factors such as:

- Wall thickness
- Flow path
- Flow direction
- Weld lines
- Sink marks, etc.

The size of the gate depends on the wall thickness of the molded part. If the gate is too large, cooling time and hence cycle time may be unacceptably long.An undersized gate may cause premature freeze-off or may cause excessive shear heating of the melt.

With submarine and pinpoint gates, no finishing is required. Submarine gates must be matched as closely as possible to the deformation behaviour of the Topas® COC resin, which is a hard, rigid material. They are in effect like undercuts and can obstruct part removal from the mold.

6.2.4 Range of processing conditions

The melt temperature range varies for the different Topas® COC grades according to the glass transition temper-ature and flowability (viscosity). Melt temperature can be adjusted over a wide range. The following table gives a guide:

TOPAS® 8007	190 °C	<	melt temperatur	<	250 °C
TOPAS® 5013	240 °C	<	melt temperatur	<	300 °C
TOPAS® 6013	240 °C	<	melt temperatur	<	300 °C
TOPAS® 6015	260 °C	<	melt temperatur	<	310 °C
TOPAS® 6017	270 °C	<	melt temperatur	<	320 °C

Excessive mold residence times or melt temperatures may cause yellowing of the melt. When the cycle is only briefly interrupted, barrel temperatures should be reduced to 170 °C.

Mold wall temperatures have to be adjusted to each Topas® COC grade respectively. Improved surfaces can be realised with wall temperatures 10 °C below the transition temperature and high injection speed

Typical injection molding conditions for the standard grade 6015 are shown in Fig. 13.

Fig. 13: Processing conditions for Topas® 6015

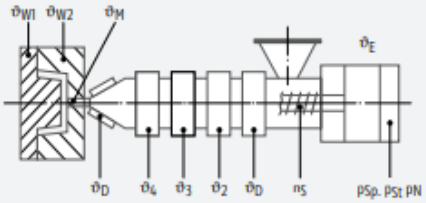

ϑ_E = 110 °C
ϑ_1 = 240-270 °C
ϑ_2 = 250-290 °C
ϑ_3 = 260-310 °C
ϑ_4 = 260-310 °C
ϑ_D = 250-310 °C
ϑ_M = 260-310 °C
Maximum residence time: < 15 min.
Short interruption pressure to cycle: reduce ϑ_X to 170 °C!
p_{Sp} = Injection pressure 500-1000 bar (specif.)
p_N = Hold-on pressure 300-600 bar (specif.)
p_{St} = Back pressure < 150 bar (specif.)
n_S = Screw speed 50-200 1/min
Injection speed: moderate to fast (50 mm/s-150 mm/s)
ϑ_{W1}, ϑ_{W2}: 110-145 °C
Nozzle type: free-flow
Note: typical shrinkage value 0.4-0.7 %

To obtain low-stress moldings, phased injection speeds, relatively low pressure and relatively high mold temperatures are recommended. Injection hold time should be set just long enough to avoid sink marks. Since stress cracking resistance depends to a large extent on the stress condition of the molded part, it is important to try and avoid internal stresses and to verify the results by tests under end-use conditions.

6.2.5 Shrinkage

Shrinkage of Topas® COC resin depends on the volume contraction of the melt due to cooling. The additional contraction as a result of crystallization which typifies partially crystalline molding materials does not occur. Mold shrinkage of unreinforced Topas® COC grades is grade dependent and typical of amorphous resins. Typical values are 0.1-0.7.

6.2.6 Demolding

Undercuts in the part or runner system should be kept to a minimum. A sufficient number of large-area ejectors or stripper devices should be provided.

The greatest possible draft angle should be employed, such as is used for polystyrene.

6.2.7 Compatibility with thermoplastics

Contamination or mixture with other, even transparent, thermoplastics causes severe turbidity. When changing material, special cleaning is not normally necessary. The material is simply purged. Polypropylene has been found to be a good purge material.

6.3 Extrusion/injection blow molding/extrusion blowing

Topas® COC resin can be processed by injection molding and is also suitable for extrusion and injection blow molding.

6.3.1 Film extrusion

Extrusion conditions/temperatures for Topas® COC are determined primarily by softening point and molecular weight, as well as by specific machine requirements. Flowability data for the individual Topas® COC grades are given in table 4 (measured volume flow indices). For specific recommendations for individual Topas® COC grades please refer to the corresponding processing data sheet.

Topas® COC grades can be processed by extrusion into flat films or blown films. Their properties can be considerably improved by stretching at temperatures of 20-30 °C above the glass transition temperature (see table 5).

Table 4: Volume flow indices for Topas® COC

TOPAS® grade	Volume flow indices (ml/10min)/2.16 kg			Extrusion temperatures [°C]
	190 °C	230 °C	260 °C	
8007	2	10	30	220 - 250
6013	–	3	13	240 - 260
6015	–	< 1	4	260 - 280

Table 5: Mechanical properties of extruded flat films and biaxially oriented films

Property	Unoriented flat film	Biaxially oriented Film
Tensile modulus (GPa)	1.5 - 2.2	3.0 - 4.0
Tensile strength (MPa)	60 - 70	100 - 150
Elongation at break (%)	2 - 5	50 - 90

Topas® COC provides high shrink and high stiffness for shrinkable round-about labels (sleeves). In addition PET bottles and Topas® COC based sleeves can easily be separated and recycled by flotation due to their density difference.

In addition Topas® COC is used in special packaging films where high twist retention is required.

(Co)-extruded films, COC-Blends, respectively Topas® COC as an additive in polyolefins offer new opportunities, by adding additional film stiffness, seal- and hot tack strength, while keeping high clarity.

6.3.2 Injection blow molding/extrusion blowing

Injection blow molding technology can be used to produce bottles and vials from Topas® COC. These bottles open the medical market by offering high water vapour barrier, high transparency and chemical resistance. They are a shatter-resistant alternative to pharmaceutical glass. Unlike glass, they contain no traces of metals or free alkali-oxides and do not chip or craze in production. In particular 8007 and 6013 grades are well suited for injection blow molding.

6.4 Secondary operations

6.4.1 Welding

Various welding methods, except for high-frequency welding, can be used to join molded parts made from Topas® COC resin. The most suitable welding method will depend primarily on the specific part.

6.4.2 Adhesive bonding

Topas® COC shows in principle the same behavior in respect to adhesive bonding as other polyolefins like polyethylene or polypropylene. Due to the low surface energy pretreatment such as plasma or flame treatment is typically required.

6.4.3 Metallization

Topas® COC shows good adhesion to metals. Reflective metal surfaces can be achieved by common vacuum metallizing methods. In many cases metallization can be done without pretreatment. Aluminium layers produced by vacuum deposition provide high glass surfaces.

7. Typical applications

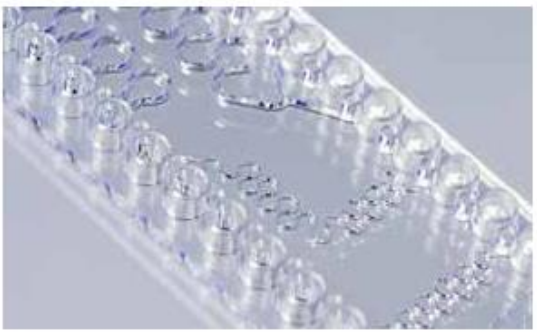

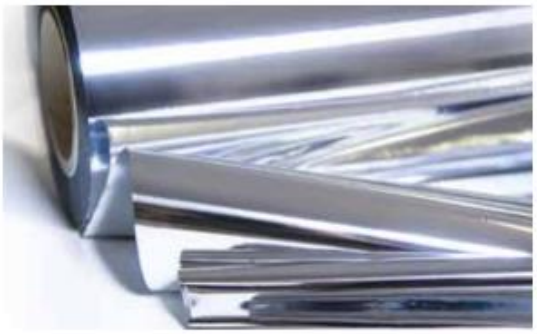

7. Typical applications